

# The Landscape of Stellar Mergers with Time-domain Surveys

Thesis by  
Viraj Karambelkar

In Partial Fulfillment of the Requirements for the  
Degree of  
Doctor of Philosophy

The Caltech logo, consisting of the word "Caltech" in a bold, orange, sans-serif font.

CALIFORNIA INSTITUTE OF TECHNOLOGY  
Pasadena, California

2025  
Defended April 22, 2025

© 2025

Viraj Karambelkar  
ORCID: 0000-0003-2758-159X

All rights reserved

## ACKNOWLEDGEMENTS

The journey of this thesis has been a rollercoaster, with its fair share of ups and downs, but undoubtedly, the most rewarding part of this experience has been the interactions with incredible individuals who have kept me motivated and inspired along the way.

First and foremost, I would like to express my heartfelt gratitude to my advisor, Mansi Kasliwal, who has been an incredibly thoughtful and supportive mentor ever since I first met her seven years ago. Mansi — your endless enthusiasm for science, fearless leadership, and pragmatic approach to astronomy have always inspired me and guided me from an eager undergraduate to the scientist that I am today. It has been a great privilege to explore the dynamic universe under your guidance and I will forever cherish (most of) this experience!

I am indebted to several individuals who provided scientific and career guidance throughout my PhD — Patrick Tisserand, my first scientific collaborator, for being incredibly patient with me, teaching me everything I know about RCB stars, and a wonderful two-hour lunch in Paris; Geoff Clayton, for the insightful discussions and help with papers on RCB stars; Rob Simcoe for the invaluable guidance on all WINTER-related issues and a great MIT campus tour; and Shrinivas Kulkarni, for advice on scientific and life matters, and for organizing the OVRO workshop that sparked ideas for my future projects. I would also like to thank Kishalay De for teaching me observing, answering my endless questions during the early years of graduate school, and offering guidance as I navigated my next steps in the final year.

I am grateful to members of my thesis committee, Shrinivas Kulkarni, Jim Fuller, Gregg Hallinan, and Andrew Howard for their guidance throughout my PhD, and to Lynne Hillenbrand for her support as option representative during graduate school, and for insightful discussions about infrared variable stars.

I would like to thank the wonderful WINTER team for all their work on the challenging task of building this new telescope. I am grateful to Robert Stein for sharing the experience of coding the WINTER pipeline, teaching me Github, and being an amazing colleague and friend over the last three years. I am also grateful to the members of the WINTER crew at MIT — Danielle, Nate, Rob, Geoffrey, Jill, Erik, Drew, Gabor - for answering my hardware-related questions and all their help with the WINTER pipeline. I will always remember the two weeks we all spent at

Palomar for WINTER commissioning.

I am grateful to several collaborators without whom this thesis would not have been possible — Nadejda Blagorodnova for introducing me to the world of stellar mergers; Ryan Lau and Jacob Jencson for all the help with JWST proposals and data analysis; Hugo Tranin and Max Wavaseur for their help with LRN-science and excellent restaurant recommendations in Barcelona; Lars Bildsten and the ZTF Theory Network group for useful discussions on stellar mergers and RCB stars; Courtney Crawford and Sunny Wong for explaining the theory of RCB stars; the core multimessenger crew at Caltech — Tomas Ahumada, Shreya Anand, Robert Stein, and Theophile du Laz, for partaking in the wild experience of planning and executing gravitational wave followup; Michael Coughlin for the assistance with Kowalski and Skyportal; and members of the GROWTH collaboration for all the help with gravitational wave followup. I would like to thank Igor Andreoni for teaching me the ropes of the GW followup game and for being an amazing colleague and mentor.

This thesis uses data from almost all telescopes at Palomar Observatory. I am incredibly grateful to the amazing Observatory staff, including Carolyn, Isaac, Kathleen, Diana, Paul, and Joel, for keeping the telescopes running even during the pandemic, and providing support on my observing runs. I would like to thank Brian and Alex for the fantastic meals at the monastery. Palomar Observatory is truly magical and will always have a special place in my heart.

I am grateful to the PGIR and ZTF teams for building these amazing survey telescopes that have enabled a large portion of this thesis. I would also like to thank members of the larger TDA group at Caltech — Christoffer Fremling, Lin Yan, Yujing Qin, and Ashish Mahabal — who provided guidance on various ZTF and WINTER-related topics. I've also been fortunate to share this journey with a wonderful group of current and former student members of the TDA group — Yuhan Yao, Shreya Anand, Kaustav Das, Sam Rose, Nicholas Earley, Yashvi Sharma, William Meynardie, and Andy Tzanidakis — whose camaraderie and support have made this experience more enjoyable. I would like to thank Judy McClain for prompt assistance with all administrative matters.

I am incredibly grateful for the amazing community of astronomy graduate students at Caltech that greatly enriched my time here. I am thankful to my seniors Kishalay De, Jacob Jencson, Chris Bochenek, Kaew Tinyanont, and Yuguang Chen for guidance at several junctures during my PhD. I would like to thank friends from my

cohort Sam, Evan, Max, Zhuyun, Yashvi, and Sarah for help with homework, fun times in the first year office, and their support throughout grad school. I am indebted to Dillon Dong for teaching me driving and Dee Dunne for teaching me skiing.

I am grateful to have had the opportunity to work with some extremely talented undergraduate students Kayton Truong, Sulekha Kishore, Aswin Suresh, and Advait Mehla, whose curiosity, enthusiasm and insightful questions increased my understanding of astronomy.

I would like to thank Adam Lustick, Brian Brophy, and the improv crew at Caltech for introducing me to the fascinating world of improv theatre; Ashish and Anu Mahabal for inviting me to the LAMAL writing club and taking me along to see Marathi plays; and Robert Stein for joining in a reading of a three-hour long play in the Cahill observing room on a weathered out observing night. I am also grateful to Forte Shinko and other members of the Caltech Badminton Club for fun badminton outings and boardgame nights during the pandemic.

I am grateful to Pranav Kulkarni, for being a great friend throughout grad school. It has been a lot of fun figuring out the American life with you.

I am deeply grateful to Yashvi Sharma for her unwavering support and encouragement throughout grad school, for being a sweet cheese, and for patiently putting up with all my nonsense for the last five years. You have been the best companion I could have asked for on this wild journey. I would like to thank Merry and Pippin for being delightful little distractions along the way.

I would like to thank my mentors from my pre-grad school days — Varun Bhalerao for kickstarting my astronomy journey, and Subha Majumdar, Scott Adams, and Vikram Rentala for setting me on the path that made this thesis possible. I would also like to thank my friends from college and high school — Ashay, Arnesh, Hari, Nitin, Murali, Archit, Gurbir, Anish, Smit, Pushan, Shubhang, and others whose support was key to get through the pandemic and persevere through tough times.

Finally, I would like to thank my parents for always supporting and fueling my curiosity for physics. Without your support and countless sacrifices, none of this would have been possible.

## ABSTRACT

Stellar mergers result in a wide range of outcomes, from luminous cosmic transients to peculiar variable stars. Mergers provide valuable insights into a broad range of astrophysical phenomena, from stellar evolution to gravitational waves to the origins of the universe’s heaviest elements. In this thesis, I systematically explore the outcomes of merging white dwarfs, merging neutron stars, and merging massive stars, using robotic survey telescopes to fill gaps in our understanding of the diverse merger landscape.

In Part I of this thesis, I present the first infrared census of dusty variable stars formed from low-mass white dwarf mergers. This population offers new insights into the binary white dwarfs that will be detected by the upcoming Laser Interferometer Space Antenna (LISA). I also present the least luminous thermonuclear supernova discovered to date, which possibly originated in the merger of two massive white dwarfs.

In Part II of this thesis, I present the data processing pipeline of the novel Wide-field Infrared Transient Explorer (WINTER) surveyor at Palomar Observatory, designed for infrared followup of gravitational wave events from neutron star mergers. I present results from WINTER’s first search for an infrared counterpart to a neutron star merger recently detected by the International Gravitational Wave Network.

In Part III of this thesis, I present the first systematic study of extragalactic transient eruptions from massive stellar mergers and estimate their volumetric rate and luminosity function. I also present the first infrared observations of such mergers with the *James Webb Space Telescope*, which suggest that stellar mergers could be significant contributors to the cosmic dust budget. Additionally, I present a slow-evolving infrared transient identified by WINTER that originated in a merger involving a giant star primary, revealing a new class of events that have been overlooked by previous optical surveys.

Together, these studies set the stage for more comprehensive explorations of the merger landscape in the future, with i) the Vera Rubin Observatory to study large populations of low luminosity transients from massive stellar mergers and white-dwarf mergers, and ii) the upcoming suite of ground and space-based infrared surveys to discover the dustiest stellar mergers and quantify their contributions to the cosmic dust budget.

## PUBLISHED CONTENT AND CONTRIBUTIONS

Frostig, D., Karambelkar, V. & Stein, R. et al. (Apr. 2025). “WINTER on S250206dm: A near-infrared search for an electromagnetic counterpart”. In: *PASP [Submitted]*, arXiv:2504.12384.

VK coordinated the follow-up observations, wrote the pipeline that processed the data, participated in candidate vetting, and wrote the manuscript with DF and RS. VK, DF, and RS are joint first-authors on this paper, which is under review in *PASP*.

Karambelkar, V. R. et al. (Apr. 2025). “The slow brightening of WNTR23bzdiq / WTP19aalzlk : Possible onset of common-envelope evolution in an asymptotic giant branch star?” In: *ApJ [Submitted]*.

VK wrote the pipeline that led to the identification of this source, contributed to data acquisition, reduction, and analysis, and wrote the manuscript. This paper is under review in *ApJ*.

Karambelkar, V. R. et al. (Aug. 2024). “An Infrared Census of R Coronae Borealis Stars II—Spectroscopic Classifications and Implications for the Rate of Low-mass White Dwarf Mergers”. In: *PASP* 136.8, 084201, p. 084201. doi: 10.1088/1538-3873/ad6210.

VK contributed to the conception of the project, data acquisition, reduction, and analysis, and wrote the manuscript.

Karambelkar, V. R. et al. (May 2023). “Volumetric Rates of Luminous Red Novae and Intermediate-luminosity Red Transients with the Zwicky Transient Facility”. In: *ApJ* 948.2, 137, p. 137. doi: 10.3847/1538-4357/acc2b9.

VK contributed to the program that led to the identification of the sources, contributed to data acquisition, reduction, and analysis, and wrote the manuscript.

Karambelkar, V. et al. (Nov. 2022). “R Coronae Borealis and dustless hydrogen-deficient carbon stars likely have different oxygen isotope ratios”. In: *A&A* 667, A84, A84. doi: 10.1051/0004-6361/202142918.

VK contributed to the conception of the project, data acquisition, reduction, and analysis, and wrote the manuscript.

Karambelkar, V. R. et al. (Apr. 2021a). “Census of R Coronae Borealis Stars. I. Infrared Light Curves from Palomar Gattini IR”. In: *ApJ* 910.2, 132, p. 132. doi: 10.3847/1538-4357/abe5aa.

VK defined the selection criteria for this project, contributed to data acquisition, reduction, and analysis, and wrote the manuscript.

Karambelkar, V. R. et al. (Nov. 2021b). “Faintest of Them All: ZTF 21aaoryiz/SN 2021fcg-Discovery of an Extremely Low Luminosity Type Iax Supernova”. In: *ApJ* 921.1, L6, p. L6. doi: 10.3847/2041-8213/ac2e90.

VK contributed to the program that led to the identification of this source, contributed to data acquisition, reduction, and analysis, and wrote the manuscript.

## TABLE OF CONTENTS

Acknowledgements . . . . .	iii
Abstract . . . . .	vi
Published Content and Contributions . . . . .	vii
Table of Contents . . . . .	viii
List of Illustrations . . . . .	xi
List of Tables . . . . .	xv
Chapter I: Introduction . . . . .	1
1.1 White dwarf mergers . . . . .	2
1.2 Neutron star mergers . . . . .	6
1.3 Massive star mergers . . . . .	9
1.4 Discovery engines for studying the merger landscape . . . . .	13
1.5 Thesis outline . . . . .	14
Chapter II: Census of R Coronae Borealis stars I: Infrared light curves from Palomar Gattini IR . . . . .	17
2.1 Introduction . . . . .	18
2.2 IR lightcurve-based prioritization . . . . .	21
2.3 IR color-based prioritization . . . . .	23
2.4 Pilot NIR spectroscopic follow-up . . . . .	28
2.5 Preliminary implications for progenitors . . . . .	35
2.6 Summary and way forward . . . . .	45
2.7 Acknowledgements . . . . .	47
Chapter III: An infrared census of R Coronae Borealis Stars II – Spectroscopic classifications and implications for the rate of low-mass white dwarf mergers . . . . .	48
3.1 Introduction . . . . .	50
3.2 Candidate selection . . . . .	52
3.3 NIR Spectroscopic observations . . . . .	55
3.4 NIR spectroscopic classifications . . . . .	55
3.5 Discussion . . . . .	67
3.6 Summary and way forward . . . . .	78
3.7 Acknowledgements . . . . .	79
3.8 Data Availability . . . . .	80
3.9 Appendix: Candidate RCB and DY Per type stars . . . . .	80
3.10 Appendix: Source classifications . . . . .	80
Chapter IV: R Coronae Borealis and dustless hydrogen-deficient carbon stars have different oxygen isotope ratios . . . . .	84
4.1 Introduction . . . . .	85
4.2 Data . . . . .	87
4.3 NIR spectra of dLHdC stars . . . . .	88
4.4 $^{16}\text{O}/^{18}\text{O}$ : Analysis and results . . . . .	91

4.5 Discussion . . . . .	97
4.6 Summary and way forward . . . . .	105
4.7 Acknowledgements . . . . .	107
Chapter V: Faintest of Them All: Discovery of an Extremely Low Luminosity	
Type Iax Supernova . . . . .	108
5.1 Introduction . . . . .	109
5.2 Discovery and follow-up observations . . . . .	110
5.3 Light-curve analysis . . . . .	112
5.4 Spectroscopic evolution . . . . .	116
5.5 Discussion . . . . .	117
5.6 Conclusions . . . . .	121
5.7 Acknowledgements . . . . .	121
Chapter VI: A data reduction pipeline for the WINTER surveyor . . . . .	
6.1 Introduction . . . . .	125
6.2 WINTER observatory infrastructure . . . . .	127
6.3 Data Reduction Framework - <code>mirar</code> . . . . .	130
6.4 The WINTER Pipeline ( <code>winterdrp</code> ) . . . . .	136
6.5 WINTER Pipeline performance . . . . .	147
6.6 Planned upgrades for performance improvements . . . . .	151
6.7 Early Science with WINTER . . . . .	153
6.8 Summary and way forward . . . . .	157
6.9 Acknowledgements . . . . .	158
Chapter VII: WINTER on S250206dm: A near-infrared search for an elec-	
tromagnetic counterpart . . . . .	159
7.1 Introduction . . . . .	160
7.2 WINTER follow-up campaign . . . . .	162
7.3 Comparison with kilonova models . . . . .	168
7.4 Summary and way forward . . . . .	170
7.5 Acknowledgments . . . . .	171
Chapter VIII: Volumetric Rates of Luminous Red Novae and Intermediate-	
luminosity Red Transients with the Zwicky Transient Facility . . . . .	173
8.1 Introduction . . . . .	175
8.2 Sample Selection . . . . .	177
8.3 Volumetric rate . . . . .	202
8.4 Discussion . . . . .	209
8.5 Summary and the future . . . . .	216
8.6 Acknowledgements . . . . .	218
8.7 Data availability . . . . .	219
8.8 Appendix: Properties of Sources Classified as Possible LBV Outbursts	219
Chapter IX: Hot springs and dust reservoirs: <i>JWST</i> reveals the dusty, molec-	
ular aftermath of extragalactic massive star mergers . . . . .	222
9.1 Introduction . . . . .	223
9.2 The Luminous Red Novae . . . . .	225
9.3 Observations and data reduction . . . . .	226
9.4 Analysis . . . . .	230

9.5 Discussion . . . . .	237
9.6 Summary and way forward . . . . .	245
9.7 Appendix: Modeling the dust and molecular emission . . . . .	246
Chapter X: The slow brightening of WNTR23bzdiq / WTP19aalzlk : Possible onset of common-envelope evolution in an asymptotic giant branch star? .	253
10.1 Introduction . . . . .	254
10.2 Observations . . . . .	256
10.3 Analysis . . . . .	261
10.4 Discussion . . . . .	267
10.5 Summary and way forward . . . . .	274
10.6 Acknowledgements . . . . .	276
Chapter XI: Summary and path forward . . . . .	277
11.1 Uncovering the demographics of He-CO WD mergers . . . . .	278
11.2 Populating the landscape of low-luminosity SNe Iax . . . . .	280
11.3 The infrared quest for the next kilonova . . . . .	280
11.4 The (IR) bright future of common-envelope transients . . . . .	281
Bibliography . . . . .	286

## LIST OF ILLUSTRATIONS

<i>Number</i>	<i>Page</i>
1.1 The formation and brightness variations of R Coronae Borealis-type stars. . . . .	4
1.2 Infrared emission from kilonovae. . . . .	8
1.3 Common-envelope evolution in massive stellar binaries. . . . .	11
2.1 Examples of PGIR J-band lightcurves for candidates in each of the lc-based priority groups described in Section 2.2. . . . .	24
2.2 The WISE W1–W2 vs W3–W4 and 2MASS $K$ vs $J - K$ color-color diagrams for all candidates in the Tisserand et al. (2020) catalog. . . . .	25
2.3 Schematic of light curve-based priorities and IR color based priorities for RCB candidates. . . . .	26
2.4 PGIR $J$ Band light curves for 8 known RCB stars. . . . .	30
2.5 NIR spectra of 8 known RCB stars . . . . .	31
2.6 PGIR $J$ band light curves of new RCB stars identified in this paper. . . . .	32
2.7 NIR spectra of new RCB stars identified in this paper. . . . .	33
2.8 Maximum light spectral energy distributions (SEDs) for six RCB stars from our sample. . . . .	37
2.9 Best-fits to the $K$ band spectra of RCB stars. . . . .	39
2.10 Distribution of $^{16}\text{O}/^{18}\text{O}$ ratios of RCB and HdC stars. . . . .	40
2.11 Pulsation periods against effective temperatures for RCB stars. . . . .	42
2.12 He I $\lambda 10830$ line profiles of RCB stars analysed in this paper. . . . .	44
2.13 Distribution of the radial velocities of RCB stars. . . . .	45
2.14 A schematic of our strategy for an NIR survey of Galactic RCB stars. . . . .	47
3.1 Lightcurve and color-based priorities for RCB candidates. . . . .	54
3.2 PGIR $J$ -band lightcurves of new RCB stars. . . . .	59
3.3 PGIR $J$ -band lightcurves of new RCB stars (continued from Figure 3.2). . . . .	60
3.4 NIR spectra of new RCB stars. . . . .	61
3.5 NIR spectra of new RCB stars (continued from Fig. 3.4). . . . .	62
3.6 Lightcurves and spectra of new DYPer type stars. . . . .	63
3.7 Distributions of RCB and DYPer-type stars. . . . .	66
3.8 Detection thresholds of PGIR for Galactic RCB stars. . . . .	70

3.9	Periodograms of RCB and dLHdC stars using PGIR lightcurves . . . . .	72
3.10	TESS lightcurves of RCB and dLHdC stars. . . . .	74
3.11	NIR spectra of the 8 candidate RCB stars. . . . .	81
3.12	PGIR J-band lightcurves of candidate DY Per type stars. . . . .	82
4.1	Near-infrared spectra of the newly discovered dLHdC stars. . . . .	90
4.2	Zoom-in of the spectral region around the He I(10833 Å) triplet. . . . .	92
4.3	Zoom-in of the $^{12}\text{C}^{16}\text{O}$ and $^{12}\text{C}^{18}\text{O}$ absorption bands of all seven dLHdC stars (left) and six representative RCB stars (right) from our sample. . . . .	97
4.4	Model fits to the CO absorption bandheads of the dLHdC star A166 and RCB stars ASAS-RCB-17, WXCrA and ASAS-RCB-7. . . . .	98
4.5	Zoom-in of the spectra of the RCB star WXCrA . . . . .	99
4.6	Zoom-in of the spectra of the RCB star ASAS-RCB-7 . . . . .	100
4.7	Cumulative distribution plot showing the fraction of dLHdC and RCB stars that have $^{16}\text{O}/^{18}\text{O}$ below a given value. . . . .	101
5.1	ZTF <i>r</i> -band science, reference and difference discovery images of SN 2021fcg. . . . .	111
5.2	Lightcurve of SN 2021fcg compared to other low luminosity SNe Iax. . . . .	114
5.3	Bolometric luminosity evolution (derived from blackbody fitting) of SN 2021fcg compared with the blackbody luminosities of SNe 2008ha, 2010ae and 2019gsc. . . . .	115
5.4	Spectroscopic observations of SN 2021fcg. . . . .	118
5.5	SN 2021fcg in the context of thermonuclear supernovae. . . . .	120
6.1	The WINTER telescope at Palomar Observatory. . . . .	128
6.2	Illustration of the data structure usage in <i>mirar</i> . . . . .	132
6.3	An illustration of a typical <i>Processor</i> sequence. . . . .	133
6.4	An example of a raw WINTER image as it is processed through different stages of the pipeline. . . . .	136
6.5	Variation of median dark counts for the Port C sensor taken in a continuous eighteen hour timespan from noon to sunrise the next day, plotted as a function of sun altitude. . . . .	139
6.6	A mosaic with a stack of five WINTER sensors, where the images were calibrated using a master flat made by stacking all sky frames from the night. . . . .	141

6.7	An example page from the WINTER Grafana dashboard that interacts with the WINTER database and allows for realtime monitoring of pipeline and survey performance. . . . .	144
6.8	WINTER alerts on Skyportal. . . . .	145
6.9	Distribution of astrometric residuals . . . . .	148
6.10	Distribution of the limiting magnitudes for each of the six WINTER sensors . . . . .	149
6.11	Limiting magnitudes as a function of exposure time for all WINTER data taken during 2024. . . . .	150
6.12	Distribution of residuals computed by measuring the standard deviation of the difference between instrumental magnitude and reference magnitude in photometrically calibrated WINTER stacks . . . . .	151
6.13	Improvements in performance after applying the current version of non-linearity corrections (NLC). . . . .	152
6.14	Examples of two extragalactic transients detected by WINTER. . . .	154
6.15	Galactic transients detected by WINTER. . . . .	154
6.16	Multi-band lightcurve of the flaring blazar PKS 0446+11 that is located within the localization region of the high-energy neutrino alert IC 240105A. . . . .	156
7.1	WINTER <i>J</i> -band coverage of S250206dm. . . . .	163
7.2	WINTER observations compared to kilonova models . . . . .	169
8.1	Forced-photometry light curves of the 11 LRNe in our sample. . . .	184
8.2	Optical spectra of LRNe presented in this paper. . . . .	185
8.3	NIR spectra of LRNe presented in this paper. . . . .	186
8.4	Pre-explosion <i>g</i> , <i>r</i> , and <i>i</i> detections for ZTF19adakuot. . . . .	189
8.5	Evolution of Ca III line profiles of ZTF21aaekeqd. . . . .	196
8.6	Forced-photometry light curves of the 10 ILRTs in our sample. . . .	202
8.7	Optical spectra of ILRTs presented in this paper. . . . .	203
8.8	NIR spectra of ILRTs presented in this paper. . . . .	204
8.9	Distribution of the peak absolute magnitudes of LRNe ( <i>left</i> ) and ILRTs ( <i>right</i> ) in our sample. . . . .	205
8.10	The volumetric rates of LRNe and ILRTs. . . . .	208
8.11	The rate of LRNe brighter than a given absolute magnitude . . . .	210
8.12	Host galaxies of the ILRTs in our sample. . . . .	215
8.13	Host galaxies of the LRNe in our sample. . . . .	217
8.14	Light curves of transients that are possible LBV outbursts. . . . .	220

8.15	Optical spectra of transients that are possible LBV outbursts. . . . .	220
9.1	The infrared spectral energy distributions of the four LRNe. . . . .	229
9.2	Comparison of the spectral energy distributions of the four LRNe to Galactic stellar mergers. . . . .	232
9.3	Range of best-fit models from MCMC fits to the SEDs. . . . .	234
9.4	Dust masses inferred for the four LRNe in this paper compared with CCSNe and Galactic LRNe. . . . .	238
9.5	Late-time evolution of LRN properties. . . . .	243
9.6	A breakdown of the different model components for AT 2021blu . .	248
9.7	Posterior probability distributions of parameters for AT 2021blu. . .	249
9.8	Posterior probability distributions of parameters for AT 2021biy. . .	250
9.9	Posterior probability distributions of parameters for AT 2018bwo. .	251
9.10	Posterior probability distributions of parameters for M31-LRN-2015. .	252
10.1	The location of WNTR23bzdiq. . . . .	256
10.2	Multiband lightcurve of WNTR23bzdiq. . . . .	258
10.3	Optical-NIR spectra of WNTR23bzdiq . . . . .	260
10.4	Modeling the progenitor of WNTR23bzdiq. . . . .	261
10.5	The <i>r</i> -band lightcurve of WNTR23bzdiq showing an indication of periodicity at the end of the first eruption in 2023, with two successive bumps of $\approx 0.2$ mag amplitude. . . . .	264
10.6	Comparison of properties of WNTR23bzdiq to the giant star merger OGLE-BLG and classical LRNe V838 Mon, V1309 Sco, and M31- LRN-2015. . . . .	270
10.7	HR-diagram with the progenitors of classical LRNe, OGLE-BLG, and WNTR23bzdiq with MIST stellar evolutionary tracks. . . . .	273
11.1	A schematic of the landscape of merging stars, merging white dwarfs, and merging neutron stars explored in this thesis. . . . .	279
11.2	The landscape of LRNe in the Rubin era. . . . .	282
11.3	The landscape of stellar merger discovery for Rubin and upcoming infrared surveys. . . . .	283
11.4	Searching for missing mergers in the Milky Way with NEOWISE and SPHEREx. . . . .	284

## LIST OF TABLES

<i>Number</i>	<i>Page</i>
2.1 Light curve (LC) based priorities, sub-classifications and IR color based priorities for spectroscopic followup of candidates in Tisserand et al. (2020) catalog. We assign color-based priorities to all 2194 candidates in the catalog, and lightcurve-based priorities to 1209 candidates that have PGIR coverage. . . . .	23
2.2 Properties of newly identified RCB stars . . . . .	31
2.3 Properties derived from the spectra of RCB stars. The three stars V391 Sct, WISE-ToI-6 and WISE-ToI-1309 do not show strong CO absorption features. . . . .	43
3.1 Updated priorities of WISE-selected candidates based on PGIR lightcurves (full table available online, see Sec. 3.8) . . . . .	55
3.2 Spectroscopic classifications of candidates selected for followup (full table available online, see Sec. 3.8) . . . . .	55
3.3 RCB and DY Per stars identified/confirmed from our NIR census (continued in Table 3.4) . . . . .	64
3.4 RCB and DY Per stars identified/confirmed from our NIR census (continued from Table 3.3) . . . . .	65
3.5 Total number of RCB stars identified in the T20 catalog for different color and lightcurve priorities. * marks categories which were not covered in our spectroscopic followup. The numbers in these categories were determined as described in Sec. 3.5 . . . . .	68
3.6 Pulsation periods using PGIR lightcurves . . . . .	73
3.7 Radial velocities derived from C absorption lines in the NIR spectra. Sources marked with * denote revised values from the ones reported previously in Karambelkar et al. (2021) . . . . .	76
3.8 Strong RCB and DY Per candidates identified from our NIR census. .	80
4.1 Log of spectroscopic observations . . . . .	88
4.2 Range of model parameters that best fit the observed spectra . . . . .	95
5.1 Photometric measurements of SN 2021fcg ( $> 3\sigma$ detections and $5\sigma$ limits, data behind Figure 5.2) . . . . .	113
7.1 Summary of WINTER images which overlap transients reported to TNS. The image-wide limiting magnitude is also reported, though all transients had underlying hosts which complicate recovery. . . . .	166

7.2	Statistics for source cuts using the three independent candidate search methods. Given that sources can be selected by multiple searches, we also give the combined total in the right-most column. . . . .	167
8.1	Properties of the 34 ZTF transients of interest . . . . .	178
8.2	Observation log of spectra presented in this paper . . . . .	182
8.3	Photometric properties of LRN and ILRTs <sup>a</sup> . . . . .	197
8.4	Spectroscopic properties of LRN and ILRTs . . . . .	200
9.1	Infrared fluxes of the four LRNe . . . . .	228
9.2	Inferred dust and molecular parameters for the four LRNe . . . . .	235

## Chapter 1

### INTRODUCTION

In the textbook picture of stellar evolution, a star’s fate is primarily determined by its mass and composition at the onset of core hydrogen burning (Hansen et al. 2004). These properties set the luminosities and temperatures of stars — placing them along the stellar main sequence — and govern their evolutionary pathways and final outcomes. Low-mass stars ( $\leq 8 M_{\odot}$ ) ultimately shed their outer layers, leaving behind compact, degenerate cores known as white dwarfs (WDs), while more massive stars ( $\geq 10 M_{\odot}$ ) end their lives forming neutron stars (NSs) and black holes (BHs)<sup>1</sup>, that can be accompanied by spectacular supernova explosions (SNe, Heger et al. 2003).

This simple but effective framework can be substantially altered by stellar multiplicity. A large fraction of stars in our universe harbor gravitationally bound companions, with the multiplicity fraction rising from  $\sim 50\%$  for solar-mass stars (Raghavan et al. 2010) to nearly  $100\%$  for stars above  $10 M_{\odot}$  (Sana et al. 2012). Stellar companions can significantly influence the evolution of stars and compact objects through a remarkable interplay of interaction processes such as mass transfer, tidal forces, magnetic effects, and gravitational wave radiation (Paczynski 1976; Soberman et al. 1997; Lidov 1962; Misner et al. 1973; Postnov et al. 2014).

These interactions can drive stars and compact objects in binary systems to merge, giving rise to some of the most magnificent phenomena observed in our universe. Mergers of NS and BH binaries radiate gravitational waves that are now being routinely detected on Earth (Abbott et al. 2016; Abbott et al. 2017c), offering an exciting new messenger for studying the expansion of the universe (Abbott et al. 2017a), testing the foundations of general relativity, and tracing the cosmic origins of the heaviest elements (Kasliwal et al. 2017a). Massive WD mergers can produce some of the most luminous explosions in the universe (Webbink 1984), influencing the chemical enrichment of galaxies and serving as standard candles for cosmology (Riess et al. 1998; Perlmutter et al. 1999). Lower-mass WD binaries merge by radiating gravitational waves that will soon be detected by space-based detectors (Amaro-Seoane et al. 2017) and can give rise to exotic variable stars with

---

<sup>1</sup>Some massive stars can explode leaving behind no remnant (Woosley et al. 2002).

unusual chemical compositions (Clayton 1996). Stellar mergers mark transformative episodes in the lives of stars, capable of rejuvenating them (Schneider et al. 2016), altering their evolutionary pathways and final fates (Vigna-Gómez et al. 2019; Schneider et al. 2024), and enriching their host galaxies with dust (Lü et al. 2013).

Despite the astrophysical significance of stellar and compact-object mergers, there remain several gaps in our understanding of how these mergers unfold and what they leave behind. This thesis aims to address some of these gaps by conducting systematic searches for explosive and variable outcomes of merging white dwarfs, merging neutron stars, and merging massive stars. These searches leverage the armada of optical and infrared robotic survey telescopes at Palomar Observatory in Southern California and offer insights into processes ranging from mass transfer in binary stars to the formation of gravitational wave sources and the origins of the heaviest elements in the periodic table. I begin by reviewing the current observational and theoretical landscape of stellar and compact-object mergers and outlining key open questions that this thesis seeks to address.

### 1.1 White dwarf mergers

Double white dwarf (DWD) systems form through interactions in stellar binaries with low- to intermediate-mass stars, typically involving one or more phases of unstable mass transfer between the stars (Webbink 1979; Webbink 1984; Iben et al. 1984; Lipunov et al. 1988; Tutukov et al. 1994; Yungelson et al. 1994; Han et al. 1995; Iben et al. 1997; Han 1998a; Sun et al. 2018; Li et al. 2019; Scherbak et al. 2023). The final outcomes depend on the progenitor masses: He-He DWDs form from low-mass stars ( $\leq 2 M_{\odot}$ ), CO-He systems arise from primaries in the  $\sim 2$ – $4 M_{\odot}$  range, and more massive stars can produce CO-CO or ONe-bearing DWDs (Webbink 1984). Gravitational wave (GW) radiation can cause the closest of these DWD systems to shrink further and initiate mass transfer within the Hubble time (Misner et al. 1973). Whether the mass transfer is stable or not depends on the mass ratio, mode of accretion (disk versus direct impact), and the timescale at which the angular momentum is transferred back to the orbit (Marsh et al. 2004; Dan et al. 2011; Dan et al. 2014). In a large fraction of systems, the mass transfer is unstable, causing the WDs to merge with each other<sup>2</sup>. These WD mergers produce a broad range of outcomes – from Type Ia supernovae (SNe Ia) in high-mass CO-CO WD mergers (Webbink 1984; Fryer et al. 2008; Toonen et al. 2012; Fink et al. 2007; Sim

---

<sup>2</sup>Shen (2015) suggest that even for stable mass transfer, DWDs can merge due to nova-like outbursts on the accretor.

et al. 2010; Shen et al. 2018) and exotic thermonuclear explosions in more massive mergers (e.g., SNe Ia (Shen et al. 2010), SNe Iax (Foley et al. 2013; Kashyap et al. 2018), runaway electron-captures via accretion induced collapse (Fryer et al. 1999)), to hot He-rich subdwarfs in the lowest mass He-He WD mergers (Webbink 1984; Saio et al. 2000; Han et al. 2002; Han et al. 2003; Zhang et al. 2012), and helium and carbon-rich supergiant stars for intermediate mass He-CO WD mergers (Webbink 1984; Clayton 1996). This thesis focuses on the outcomes of intermediate-mass He-CO and the most massive ONe-CO WD mergers.

### Remnants of He-CO WD mergers: R Coronae Borealis stars

When He-CO WD binaries merge, their remnants are expected to go through a supergiant-sized phase lasting  $10^4 - 10^5$  years powered by shell helium burning around the C/O core (see Figure 1.1) (Webbink 1984; Jeffery et al. 2011; Schwab 2019). The Galactic population of these supergiant-sized merger remnants can provide valuable insights about the underlying population of He-CO DWD systems in the Milky Way. This is particularly relevant for GW observations in the next decade, as close He-CO WD binaries are predicted to be the dominant population of GW sources that will be detected by the Laser Interferometric Space Antenna (LISA Amaro-Seoane et al. 2017; Lamberts et al. 2019; Burdge et al. 2020).

R Coronae Borealis (RCB) stars are an enigmatic class of supergiant-sized stars believed to originate in He-CO WD mergers (Clayton 1996; Webbink 1984). They are characterized by a peculiar chemical composition – an acute deficiency of hydrogen and an overabundance of carbon and helium (Clayton 1996; Clayton 2012; Asplund et al. 2000). Additionally, RCB stars show large photometric variations (up to 8 mag in V band, Figure 1.1) caused by erratic mass loss and dust formation episodes (Clayton 2012; Feast et al. 1997). Historically, two possible formation scenarios were developed to explain the chemical compositions of HdC stars — 1) the merger of a He-core and a CO-core WD (Webbink 1984; Clayton 2012), and 2) a final helium flash (FF) in a post-AGB star (Iben et al. 1996). However, theoretical modeling and observations in the last decade, specifically the discovery of unusually large  $^{18}\text{O}$  abundances in RCB stars ( $\sim 100$  times larger than normal stars) have favored the WD merger model (Clayton et al. 2005; García-Hernández et al. 2009; García-Hernández et al. 2010).  $^{18}\text{O}$  can naturally be explained as a product of partial He burning during a WD merger (Crawford et al. 2020; Jeffery et al. 2011; Clayton et al. 2007) but is expected to be destroyed at the temperatures reached in a FF event.

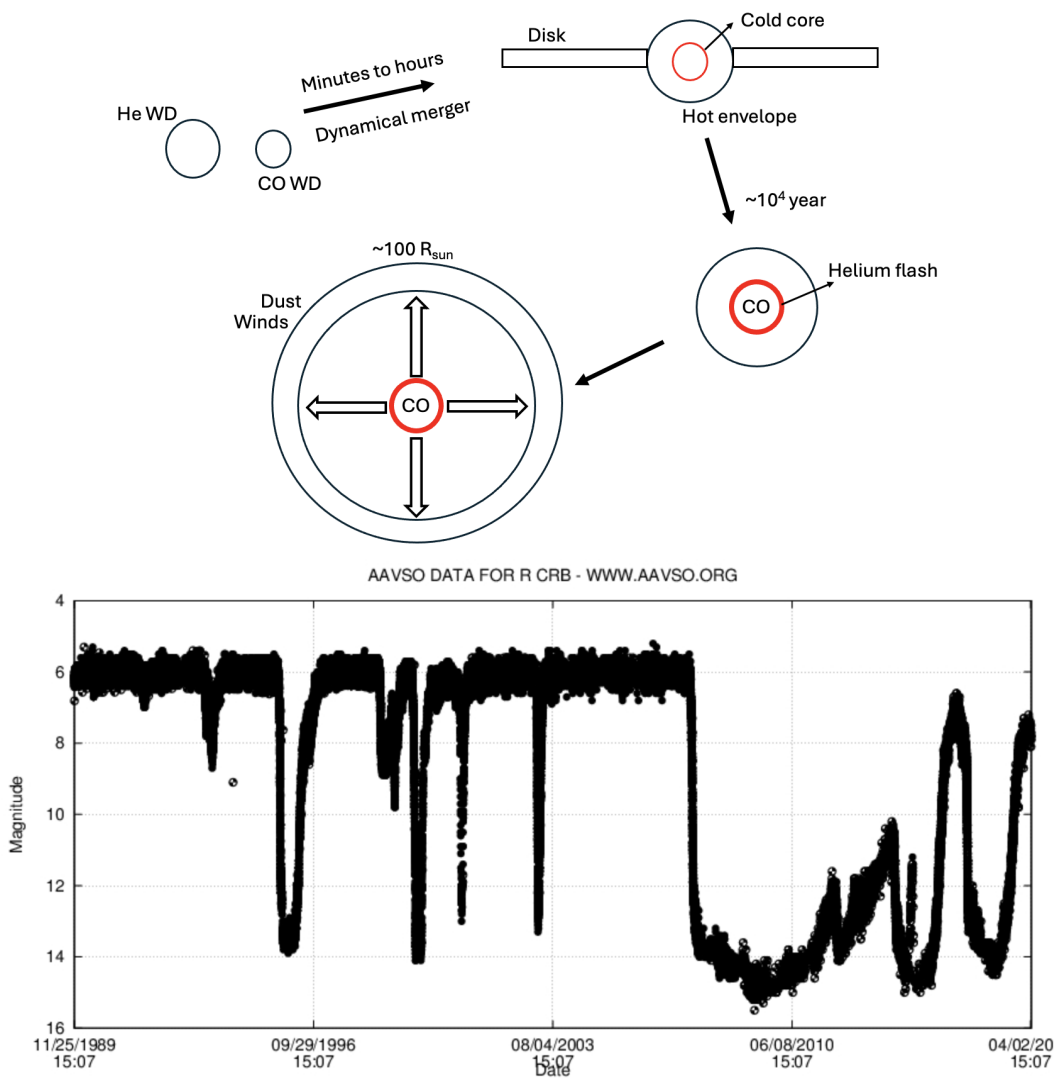


**Figure 1.1: The formation and brightness variations of R Coronae Borealis-type stars.** *Top:* A schematic showing the formation of RCB-type stars from He-CO WD mergers (figure adapted from Zhang et al. 2014). *Bottom:* The thirty-year visible lightcurve of R Coronae Borealis showing erratic large amplitude variations due to dust-formation. Lightcurve plot reproduced from the AAVSO archive.

Despite the identification of their formation channel, many mysteries surrounding RCB stars remain unresolved. Most fundamentally, their total number in the Milky Way was unknown. Prior to 2019, about a hundred Galactic RCB stars were known (Tisserand et al. 2020), while the estimated number of such stars in the Milky Way ranged from 300–5400 (Han 1998b; Clayton 2012; Tisserand et al. 2020), suggesting a large fraction of RCB stars could have been missed by previous searches. These searches primarily relied on optical surveys (Alcock et al. 2001; Zaniewski et al. 2005; Tisserand et al. 2004; Tisserand et al. 2008; Tisserand et al. 2009; Lee 2015; Tisserand et al. 2013; Shields et al. 2019; Otero et al. 2014; Lee et al. 2020), which are inherently disadvantaged in the search for dusty RCB stars located in dusty regions of the Milky Way. Instead, infrared (IR) searches are better suited to identify these dusty variable stars and provide an unbiased view of their populations. In Chapters 2 and 3 of this thesis, I present results from the first systematic infrared (IR) search for Galactic RCB stars to estimate their total number in the Milky Way, and use this to measure the He-CO WD merger rate, and validate predictions for the DWD sources that will be detected by LISA.

A second puzzle relates to dust formation around RCB stars. A small number of stars have been discovered with chemical compositions similar to RCB stars, but without any dust signatures (Warner 1967; Feast et al. 1997). These stars are termed dustless Hydrogen-deficient Carbon (dLHdC) stars<sup>3</sup>. It is still a mystery as to why both these classes have identical chemical compositions, suggesting the same formation channels, but RCB stars form dust while dLHdC stars do not (Clayton 2012). The chemical differences that might trigger dust formation in RCB stars as opposed to dLHdC stars are not known. Studies have suggested dLHdC stars could have a lower  $^{16}\text{O}/^{18}\text{O}$  ratios than RCB stars (García-Hernández et al. 2010), however, they have been limited by the small sample of four dLHdC stars known at the time. The number of dLHdC stars has now grown to 27 (Tisserand et al. 2021), and it is only now becoming possible to conduct statistical studies to identify differences between these two classes. In Chapter 4 of this thesis, I present a comparison of the oxygen isotope ratios for the largest sample of RCB and dLHdC stars.

---

<sup>3</sup>Together, dLHdC and RCB-type stars constitute the class of Hydrogen-deficient Carbon (HdC) stars (Tisserand et al. 2022).

## Possible outcomes of CO-ONe WD mergers: low-luminosity type Iax supernovae

In the last decade, time domain surveys have uncovered a diverse array of thermonuclear explosions, including both standard Type Ia supernovae (SNe Ia) and several related, but distinct, classes of explosions (Kasliwal 2011; Taubenberger 2017). These classes share several observational features with standard SNe Ia but differ significantly in properties such as peak luminosities and expansion velocities. Type Iax supernovae (SNe Iax) form the most common subclass of such ‘peculiar’ thermonuclear SNe and are thought to be explosions in which the white dwarf survives the explosion (Foley et al. 2013; Foley et al. 2014; Stritzinger et al. 2015). SNe Iax are less energetic compared to normal SNe Ia, with slower expansion speeds and a broad luminosity distribution ranging from  $M_{r,peak} \approx -19$  to  $-14$  mag (Jha 2017). The progenitors of SNe Iax are still unknown. Two main models to explain SNe Iax are 1) a failed detonation (or “deflagration”) of an accreting white dwarf with mass close to the Chandrasekhar limit (Jordan et al. 2012; Kromer et al. 2013; Fink et al. 2014; Kromer et al. 2015); or 2) a failed detonation during the merger of a CO and ONe white dwarf. While deflagration models can explain the more luminous SNe Iax, they struggle to account for the least luminous members of this class ( $M_{peak} \approx -14$  mag), as they cannot eject sufficiently low masses of radioactive nickel (Kromer et al. 2013; Kromer et al. 2015). In contrast, in the CO-ONe WD merger model, the inert core of the ONe primary suppresses the ignition flame in the carbon-rich material from the CO WD<sup>4</sup>, resulting in a failed detonation that ejects very low amounts of nickel and produces subluminous explosions with  $M_{peak}$  as low as  $-11$  mag (Kashyap et al. 2018). Prior to 2020, only three SNe were known at this extremely low luminosity end — SN 2008ha (Foley et al. 2009), SN 2010ae (Stritzinger et al. 2014) and SN 2019gsc (Srivastav et al. 2020). In Chapter 5 of this thesis, I present the discovery of the least luminous SN Iax observed to date, which challenges existing WD deflagration models and instead hints at a WD merger origin.

### 1.2 Neutron star mergers

Binary neutron stars (BNS) and neutron star-black hole (NSBH) systems merge by emitting GWs (Misner et al. 1973), which are now being routinely detected by the International Gravitational-Wave Observatory Network (Abbott et al. 2023; Abbott

---

<sup>4</sup>This behavior has also motivated deflagration models with hybrid CONe WDs, though the existence of such objects in nature remains uncertain (Kromer et al. 2015).

et al. 2021a). These mergers can also be accompanied by electromagnetic (EM) signatures, such as short-duration gamma-ray bursts (GRBs) powered by relativistic jets (Narayan et al. 1992), multiwavelength afterglows powered by interactions of the jets with the interstellar medium (ISM, Fong et al. 2015), and optical-NIR transients called kilonovae powered by radioactive decay of heavy elements in the neutron-rich ejecta (Kasen et al. 2013; Metzger et al. 2010; Barnes et al. 2013; Kulkarni 2005; Li et al. 1998). The high density of free neutrons in the merger ejecta enables rapid capture of neutrons on seed nuclei, facilitating the *r*-process (Johnson et al. 2020): a nuclear reaction sequence responsible for synthesizing the heaviest elements in the periodic table (atomic mass number  $A \geq 80$ ). Thus, BNS and NSBH mergers can potentially explain the origins of the heaviest elements in the universe. Furthermore, joint GW and EM detections of these “multi-messenger” sources can probe the neutron star equation of state (Margalit et al. 2017; Coughlin et al. 2019b; Coughlin et al. 2018), test predictions of general relativity, and provide a new class of standard sirens for measuring the Hubble constant (Abbott et al. 2017a; Coughlin et al. 2020b; Dietrich et al. 2020).

Despite these rich scientific yields, only one confirmed multi-messenger source has been found to date. GW 170817, discovered on August 17, 2017 by the LIGO and Virgo detectors (Abbott et al. 2017c), was a BNS merger that was accompanied by a short-GRB (Abbott et al. 2017b), a multiwavelength afterglow (Haggard et al. 2017; Hallinan et al. 2017; Margutti et al. 2017; Mooley et al. 2018; Pozanenko et al. 2018; Troja et al. 2017), and a fast-fading kilonova AT 2017gfo at a distance of  $\approx 40$  Mpc (Coulter et al. 2017). The optical and infrared observations of this source revealed signatures of radioactive decay from heavy elements (Kasliwal et al. 2017a; Kasen et al. 2017), unambiguously establishing BNS mergers as sites of *r*-process nucleosynthesis (Hotokezaka et al. 2018) and constrained the Hubble constant to  $\approx 20\%$  precision (Abbott et al. 2017a). These results sparked an excitement for discovering more multi-messenger events to study heavy element production across a broad range of BNS and NSBH mergers and increase the precision on  $H_0$ .

During LIGO-Virgo-Kagra (LVK) Collaboration’s subsequent O3 observing run, high-significance GWs were detected from one BNS and four NSBH mergers (Abbott et al. 2023). However, no kilonovae were discovered for these events despite several searches (e.g., Kasliwal et al. 2020; Goldstein et al. 2019; Levan et al. 2020; Gompertz et al. 2020; Antier et al. 2020; Dobie et al. 2019). These observations revised the BNS merger rate down to  $50 - 440 \text{ Gpc}^{-3} \text{ yr}^{-1}$  (Abbott et al. 2023) and

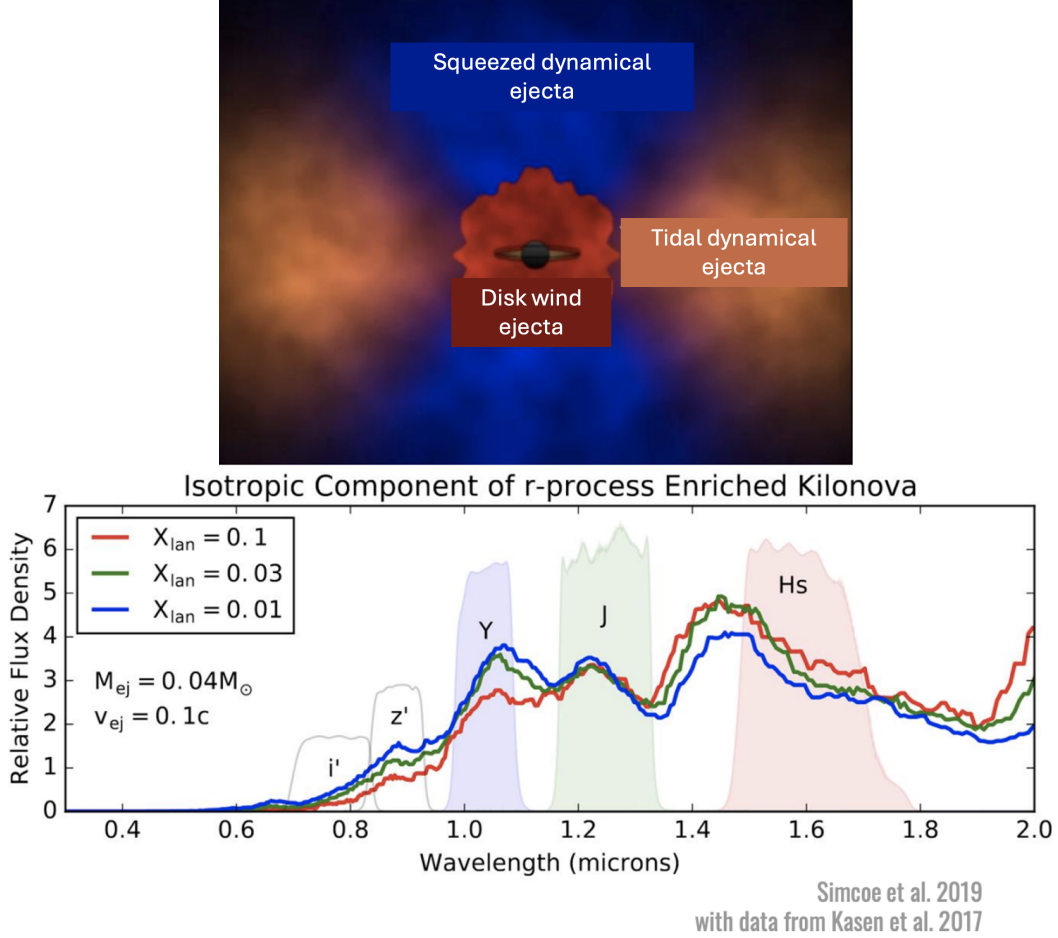


Figure 1.2: **Infrared emission from kilonovae.** *Top:* A schematic showing the distribution of ejecta from a BNS merger. The optical blue emission primarily comes from ejecta along polar directions, while the infrared emission comes from tidally stripped ejecta that is more isotropically distributed. Figure adapted from Kasen et al. (2017). *Bottom:* GW170817-like kilonova models at 2 days post-merger, showing that kilonovae are significantly brighter in the near-infrared bands than optical. Figure reproduced with permission from Simcoe et al. (2019a).

showed that GW 170817 was an unusual kilonova, with the fraction of GW 170817-like kilonovae constrained to less than 25%. (Kasliwal et al. 2020).

A possible factor limiting kilonova detection is that previous electromagnetic follow-up searches have predominantly been conducted at optical wavelengths. The optical emission from a kilonova comes primarily from ejecta with low opacities and light *r*-process elements that are distributed along polar directions. The optical emission is thus expected to be angle-dependent, fade rapidly (<1 week), and may not be present in all BNS and NSBH mergers (Metzger 2020; Kasen et al. 2013; Kasen

et al. 2017; Barnes et al. 2016; Kasliwal et al. 2020). In contrast, infrared emission originates in more isotropically distributed tidally stripped ejecta, rich in heavy *r*-process elements with high opacities and long diffusion timescales. IR emission is thus expected to be isotropic, long-lived ( $>1$  week), and ubiquitous in models regardless of mass ratio, viewing angle, or remnant lifetime (Kasen et al. 2017). The detection rates of kilonovae in the near-infrared could be up to  $\sim$ 8–10 times higher than in optical wavebands (Zhu et al. 2021a). However, the high cost of infrared detectors has hindered wide-field infrared cameras that can effectively tile the large sky-localization regions of GW events to search for the associated kilonovae.

As part of this thesis, I will present the Wide-field Infrared Transient Explorer (WINTER) — a new near-infrared surveyor at Palomar Observatory that had first light on June 10, 2023, and is designed for EMGW follow-up at NIR wavelengths during IGWN’s fourth observing run (O4; from 2023–2025). WINTER achieves a wide field-of-view (FOV) using novel, cheaper alternatives to traditional IR sensors. In Chapter 6 of this thesis, I describe the development of the automated data processing pipeline for WINTER. In Chapter 7 of this thesis, I describe a near-IR follow-up campaign of the gravitational wave alert S250206dm conducted with WINTER.

### 1.3 Massive star mergers

The high binary fraction in stars ( $>70\%$  for  $>10 M_{\odot}$  stars, Moe et al. 2017; Sana et al. 2012) suggests that a substantial fraction  $\approx 30\%$  of them interact with each other and can merge (de Mink et al. 2014; Schneider et al. 2015). Stellar mergers can explain a wide variety of unusual stars such as blue and red stragglers (McCrea 1964; Hills et al. 1976; Schneider et al. 2015) rapidly rotating spotted FKCom stars (Bopp et al. 1981), magnetic stars (Ferrario et al. 2009; Schneider et al. 2019), blue supergiant progenitors of 1987A-like SNe (Morris et al. 2007), and luminous blue variables (LBV) such as  $\eta$ -Car (Smith et al. 2018).

Stellar mergers are initiated when the primary star overfills its Roche Lobe and undergoes unstable mass transfer onto its companion. This can cause the primary star to engulf the secondary, initiating a phase called common-envelope evolution (CEE; Paczynski 1976; Webbink 1975; van den Heuvel 1976; Podsiadlowski et al. 2003; Justham et al. 2006; Ivanova et al. 2013a), where the two stars orbit inside a shared common envelope. Dynamical friction between the cores and envelope triggers a rapid dynamical inspiral of the binary system. This can eventually lead to the merger of the binary or ejection of the common envelope and the formation

of a much smaller stable binary. Thus, CEE can bring about the rapid orbital shrinkage required to explain the formation of double compact-object systems that are compact enough to radiate GWs and merge within the Hubble time (Ivanova et al. 2013a). However, when does CEE lead to a merger and when does it lead to envelope ejection is still not understood. In the standard picture of CEE (termed the energy formalism; van den Heuvel 1976; Webbink 1984; Livio et al. 1988; Iben et al. 1993), the outcome of CEE depends on the efficiency  $\alpha_{CE}$  with which the orbital energy is transferred to the common envelope. If the transferred energy exceeds the envelope binding energy, the envelope is ejected, otherwise, the stars merge. However, the exact values of  $\alpha_{CE}$  across a wide range of stellar binaries, the contributions of energy sources other than orbital energy, and the overall validity of this formalism<sup>5</sup> remain uncertain (Ivanova et al. 2013a). The uncertainty is largely due to a lack of direct observations of the short-lived CE phase that is expected to last for  $\sim$ 100–1000 years. Thus, despite its crucial role in the formation of GW sources (see, e.g., Broekgaarden et al. 2021), CEE remains one of the most poorly understood phases of binary star evolution.

### Luminous Red Novae as probes of CEE

The final step of CEE, merger or envelope ejection, is accompanied by energetic mass ejections that can power electromagnetic transient eruptions. The class of transients termed Luminous Red Novae (LRNe; Kulkarni et al. 2007; Kasliwal et al. 2011; Tylenda et al. 2011a; Pastorello et al. 2019a) have been associated with CEE (Ivanova et al. 2013b). These transients are characterized by low peak luminosities (between novae and supernovae, earning them the name ‘gap transients’; Kasliwal 2011), long durations ( $\sim$ hundred days), and a rapid transition to red color due to dust formation in the ejecta (Kamiński et al. 2011; Kamiński et al. 2015; Loebman et al. 2015). The prototypical member of this class instrumental in establishing the link to CEE was V 1309 Sco (Mason et al. 2010), an eclipsing binary in the Milky Way, whose period decreased exponentially over several years prior to its eruption (Tylenda et al. 2011a). LRNe thus present a valuable observational window into the otherwise elusive phase of CEE (Ivanova et al. 2013b).

Over the last thirty years, about two dozen extragalactic (Rich et al. 1989; Mould et al. 1990; Kulkarni et al. 2007; Smith et al. 2016; Mauerhan et al. 2018; Blagorodnova et al. 2017; Pastorello et al. 2019a; Blagorodnova et al. 2021; Pastorello et al. 2021a; Pastorello et al. 2021b; Pastorello et al. 2022) and four Galactic LRNe (Martini

---

<sup>5</sup>See, e.g., Hirai et al. (2022) for an alternate formalism of CEE.

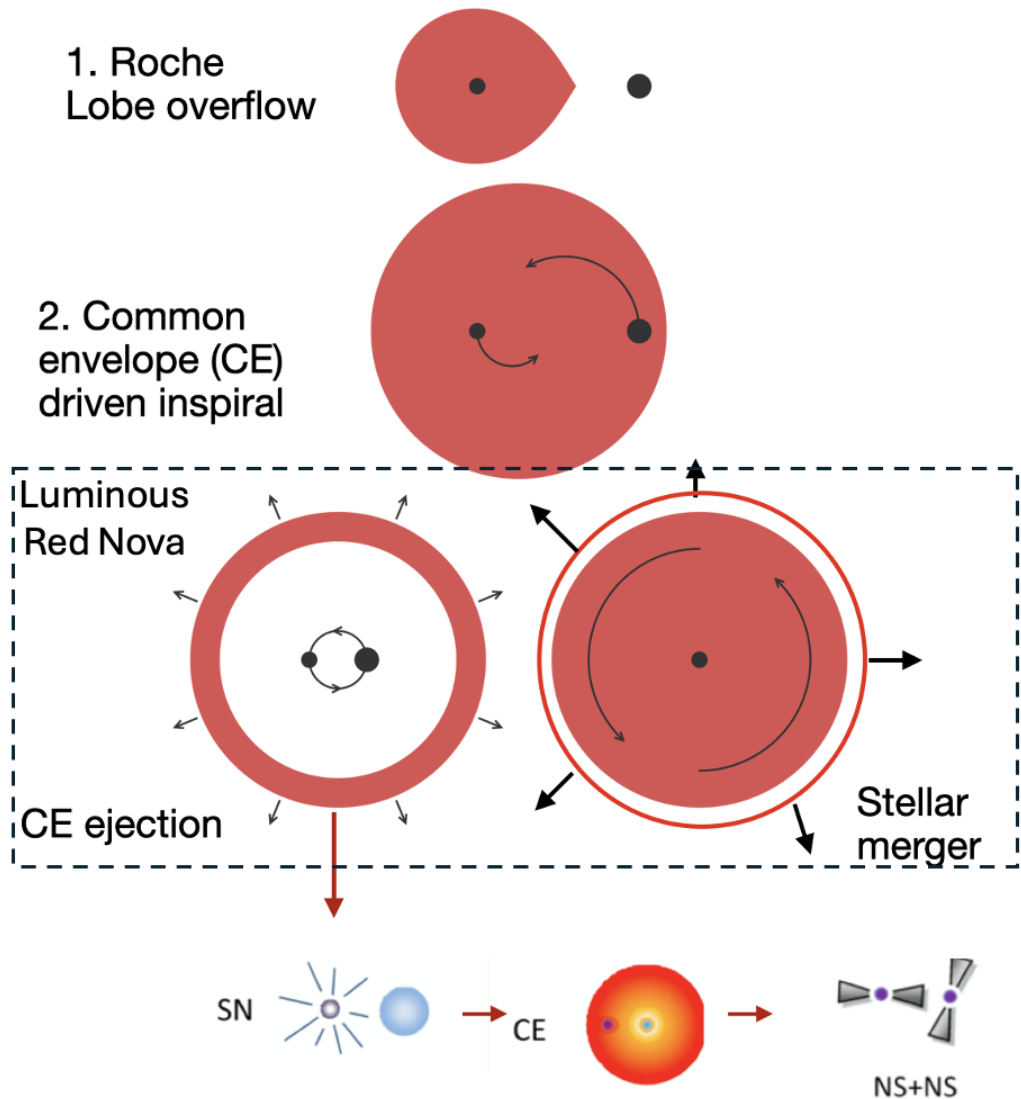


**Figure 1.3: Common-envelope evolution in massive stellar binaries.** A schematic of a massive binary system undergoing common-envelope evolution, that can result in a stellar merger, or envelope ejection which eventually leads to the formation of compact object binaries that radiate gravitational waves and merge within the Hubble time. The final stages of CEE, merger or envelope ejection, are accompanied by electromagnetic transient eruptions called Luminous Red Novae (LRNe).

et al. 1999; Munari et al. 2002; Mason et al. 2010; Tylenda et al. 2013) have been discovered, that have enabled detailed studies of these transients<sup>6</sup>. Archival pre-eruption data has revealed that progenitors of most of the Galactic LRNe have hot, low-mass, main-sequence primaries, while extragalactic LRNe have massive ( $>10 M_{\odot}$ ) yellow-giant primaries crossing the Hertzsprung Gap (Pastorello et al. 2019a; Blagorodnova et al. 2021). Pre-eruption brightenings are detected wherever data is available (Blagorodnova et al. 2020; Pastorello et al. 2021b), pointing to dynamical mass loss, possibly from the L<sub>2</sub> Lagrangian point of the binary (MacLeod et al. 2017; Pejcha 2014). The main eruption is believed to be powered by hydrogen recombination in the ejected material (Ivanova et al. 2013b; Matsumoto et al. 2022) or shocks between the ejecta and pre-eruption mass loss during the CE phase (MacLeod et al. 2017; Pejcha 2014; Metzger et al. 2017). Despite these, there are three major open questions about LRNe and their connection to CEE :

First, the volumetric rates of LRNe are poorly constrained due to a lack of systematic searches. The best available estimate is based on three Galactic events discovered in the last 30 years (Kochanek et al. 2014), which suggests that the Galactic rate of low luminosity LRNe ( $M_{V,\text{peak}} = -3$  mag) is fairly high ( $\sim 0.5 \text{ yr}^{-1}$ ), but the rate drops steeply for higher luminosities. The rate of the massive, extragalactic LRNe has not been measured, and extrapolations based on the Galactic rate disagree by several orders of magnitude with the expectations from population synthesis (Howitt et al. 2020). The observed rate of LRNe can constrain several CEE parameters used in binary population synthesis models (Howitt et al. 2020), and a lack of systematic searches for extragalactic LRNe have precluded their use in probing CEE parameters in massive binary systems. In Chapter 8 of this thesis, I present the first systematic search for LRNe to measure their volumetric rate and luminosity function.

Second, late time observations of LRNe are severely limited by the lack of sensitive IR telescopes. At late times, dust formation in the ejecta suppresses the optical emission, and the remnants of LRNe manifest as dusty, long-lived IR sources. Late-time observations can be used to estimate the dust masses of LRNe, which give an independent measurement of their ejected masses (Blagorodnova et al. 2020). Comparing these masses to the envelope masses of the progenitor stars can shed light on the outcome of CEE (merger versus envelope ejection). However, only the Galactic LRNe have been studied extensively at late times, and the dust content of extragalactic massive LRNe remains unexplored. In Chapter 9 of this thesis, I

---

<sup>6</sup>The historical eruptions of CK Vul and  $\eta$ Car have also been suggested to be members of this class (Tylenda et al. 2013; Smith et al. 2018)

present the first late-time observations of LRNe conducted with the *James Webb Space Telescope* to measure their dust masses.

Third, it is surprising that all extragalactic LRNe have progenitors involving moderately evolved main-sequence or subgiant primaries (MacLeod et al. 2022; Blagorodnova et al. 2021). Such stars have radiative envelopes with high binding energies that cause the engulfed companion to spiral in and merge (Dominik et al. 2012), while successful envelope ejections require giant primaries with convective envelopes and low binding energies (Klencki et al. 2021). All known LRNe progenitors are subgiants (Blagorodnova et al. 2021), suggesting that optical surveys miss giant stars capable of ejecting their envelopes and eventually forming compact-object binaries. Simulations show that for giant primaries, companions spiral slowly through the extended envelope, gradually stripping material (Lau et al. 2022) that forms dust and obscures the binary in the optical (MacLeod et al. 2022). The resulting giant envelope ejections or mergers manifest as slow infrared transients (Tylenda et al. 2013; MacLeod et al. 2022) but remain unexplored due to the lack of infrared surveys. In Chapter 10 of this thesis, I present one such slow IR transient in M31 identified by WINTER that possibly originated in the onset of CEE in an AGB star.

#### 1.4 Discovery engines for studying the merger landscape

Having outlined the scientific questions addressed in this thesis, I now briefly describe the observational resources that form its backbone. This thesis leverages the following three robotic surveyors at Palomar Observatory to conduct systematic searches for white dwarf mergers, neutron star mergers, and massive star mergers :

- Palomar Gattini IR (PGIR, Moore et al. 2016; De et al. 2020a) is a *J*-band camera with a 25 sq. deg. field-of-view (FOV) mounted on a 30-cm robotic telescope. PGIR has been surveying the entire northern sky to a depth of  $J = 15.7$  mag (AB) at a cadence of  $\approx 3$  days since 2018, and has compiled *J*-band lightcurves for over 60 million stars in the Milky Way. This makes PGIR an ideal instrument to conduct systematic searches for dusty variable R Coronae Borealis stars in the Milky Way (see Chapters 2 and 3).
- The Zwicky Transient Facility (ZTF, Bellm et al. 2018; Graham et al. 2019) comprises a 47 sq. deg. camera mounted on the 48-inch Samuel Oschin Schmidt Telescope at Palomar Observatory. ZTF has been systematically surveying the entire northern sky in the optical *g*, *r*, and *i* bands at a cadence

of 2–3 days since 2018 to a depth of  $\approx$ 20.5 mag. This thesis focuses on the Census of the Local Universe experiment conducted at Caltech (De et al. 2020c; Das et al. 2023), which aimed to spectroscopically classify all ZTF transients within 150 Mpc. This systematic experiment is well-suited to build samples of transients such as LRNe to study their demographics (see Chapter 8).

- The Wide-field Infrared Transient Explorer (WINTER, (Lourie et al. 2020a; Frostig et al. 2024a)) is a new near-infrared (NIR) surveyor installed on a dedicated at Palomar Observatory in June 2023. WINTER uses novel InGaAs sensors for the first time in astronomy to demonstrate the use of a potentially cheaper alternative to traditional HgCdTe IR sensors. WINTER has a field-of-view of 1.2 sq. deg. and operates in the NIR Y, J, and shortened-H (Hs) filters (1–1.7  $\mu$ m), and is well-suited to search for IR transients such as dust-enshrouded stellar mergers and followup of GW alerts (see Chapters 6 and 7).

In addition to these surveys, the spectra presented in this thesis come from the suite of optical and infrared spectrographs on the 200-inch Hale Telescope at Palomar Observatory, and the 10-m Keck telescopes and the NASA Infrared Telescope Facility at the Mauna Kea Observatory in Hawaii. Finally, this thesis also makes use of mid-infrared observations from the *James Webb Space Telescope (JWST)*.

## 1.5 Thesis outline

This thesis is organized as follows:

Part I focuses on white-dwarf mergers. In Chapters 2 and 3, I describe the candidate selection and spectroscopic follow-up of a systematic IR campaign to search for Galactic RCB stars using PGIR. In Chapter 4, I present a comparison of oxygen isotope ratios for the largest sample of RCB and dIhdC stars to date. In Chapter 5, I present a low-luminosity thermonuclear supernova that possibly originated in a massive white-dwarf merger.

Part II focuses on neutron star mergers. In Chapter 6, I present the data-reduction pipeline for the WINTER surveyor and describe its on-sky performance and early science results. In Chapter 7, I describe results from an infrared follow-up campaign conducted with WINTER to search for a kilonova associated with the recent GW alert S250206dm.

Part III focuses on massive stellar mergers. Chapter 8 focuses on a systematic search for LRNe using ZTF and presents the volumetric rate and luminosity function of these mergers. In Chapter 9, I present infrared observations of four LRNe from the *JWST* to study their dust masses and contributions to the cosmic dust budget. In Chapter 10, I present an IR transient identified by WINTER that possibly originated in a giant star merger.

I conclude with a summary and a discussion of the path forward in Chapter 11.

## Part I : White dwarf mergers

## Chapte r 2

# CENSUS OF R CORONAE BOREALIS STARS I: INFRARED LIGHT CURVES FROM PALOMAR GATTINI IR

Karambelkar, V. R. et al. (Apr. 2021). “Census of R Coronae Borealis Stars. I. Infrared Light Curves from Palomar Gattini IR”. In: *ApJ* 910.2, 132, p. 132. doi: 10.3847/1538-4357/abe5aa.

Viraj R. Karambelkar<sup>1</sup>, Mansi M. Kasliwal<sup>1</sup>, Patrick Tisserand<sup>2</sup>, Kishalay De<sup>1</sup>, Shreya Anand<sup>1</sup>, Michael C. B. Ashley<sup>3</sup>, Alex Delacroix<sup>1</sup>, Matthew Hankins<sup>4</sup>, Jacob E. Jencson<sup>5</sup>, Ryan M. Lau<sup>6</sup>, Dan McKenna<sup>1</sup>, Anna Moore<sup>7</sup>, Eran O. Ofek<sup>8</sup>, Roger M. Smith<sup>1</sup>, Roberto Soria<sup>9,10</sup>, Jamie Soon<sup>7</sup>, Samaporn Tinyanont<sup>11</sup>, Tony Travouillon<sup>7</sup>, Yuhan Yao<sup>1</sup>

<sup>1</sup>Cahill Center for Astrophysics, California Institute of Technology, Pasadena, CA 91125, USA

<sup>2</sup>Sorbonne Universites, UPMC Univ. Paris 6 et CNRS, UMR 7095, Institut d’Astrophysique de Paris, IAP, 75014 Paris, France

<sup>3</sup>School of Physics, University of New South Wales, Sydney, NSW 2052, Australia

<sup>4</sup>Arkansas Tech University, 203 W O St, Russellville, AR 72801, USA

<sup>5</sup>University of Arizona, Steward Observatory, 933 N. Cherry Avenue, Tucson, AZ 85721, USA

<sup>6</sup>Institute of Space and Astronautical Science, Japan Aerospace Exploration Agency, 3-1-1 Yoshinodai, Chuo-ku, Sagamihara, Kanagawa 252-5210, Japan

<sup>7</sup>Research School of Astronomy and Astrophysics, Australian National University, Canberra, ACT 2611, Australia

<sup>8</sup>Department of Particle Physics and Astrophysics, Weizmann Institute of Science, Rehovot 76100, Israel

<sup>9</sup>College of Astronomy and Space Sciences, University of the Chinese Academy of Sciences, Beijing 100049, China

<sup>10</sup>Sydney Institute for Astronomy, School of Physics A28, The University of Sydney, Sydney, NSW 2006, Australia

<sup>11</sup>University of California Santa Cruz, 1156 High St, Santa Cruz, CA 95064

## Abstract

We are undertaking the first systematic infrared (IR) census of R Coronae Borealis (RCB) stars in the Milky Way, beginning with IR light curves from the Palomar Gattini IR (PGIR) survey. PGIR is a 30-cm *J*-band telescope with a  $25 \text{ deg}^2$  camera that is surveying  $18000 \text{ deg}^2$  of the northern sky ( $\delta > -28^\circ$ ) at a cadence of 2 days. We present PGIR light curves for 922 RCB candidates selected from a mid-IR color-based catalog (Tisserand et al. 2020). Of these 922, 149 are promising RCB candidates as they show pulsations or declines similar to RCB stars. Majority of the candidates that are not RCB stars are either long period variables (LPVs) or RV Tauri stars. We identify IR color-based criteria to better distinguish between RCB stars and LPVs. As part of a pilot spectroscopic run, we obtained NIR spectra for 26 out of the 149 promising candidates and spectroscopically confirm 11 new RCB stars. We detect strong He I  $\lambda 10830$  features in spectra of all RCB stars, likely originating within high velocity ( $200\text{--}400 \text{ km s}^{-1}$ ) winds in their atmospheres. Nine of these RCB stars show  $^{12}\text{C}^{16}\text{O}$  and  $^{12}\text{C}^{18}\text{O}$  molecular absorption features, suggesting that they are formed through a white dwarf merger. We detect quasi-periodic pulsations in the light curves of 5 RCB stars. The periods range between 30–125 days and likely originate from the strange-mode instability in these stars. Our pilot run results motivate a dedicated IR spectroscopic campaign to classify all RCB candidates.

## 2.1 Introduction

R Coronae Borealis (RCB) stars form a distinct class of variable stars (Clayton 2012). These stars are notable for their extreme photometric variations and characteristic chemical compositions. They are characterised by deep, rapid declines in their brightness ( $\approx 9$  mag in *V* band, Clayton 1996), that can last for hundreds of days before they emerge from the low state back to the initial brightness. RCB stars also belong to the class of hydrogen-deficient stars, with helium being the most abundant element in their atmospheres, followed by carbon, nitrogen and oxygen (Asplund et al. 2000). Most RCB stars are thought to be remnants of white dwarf (WD) mergers (Webbink 1984; Clayton 2012), however, some could originate from a final helium shell flash in an evolved low mass star (Iben et al. 1996). RCB stars are thus potential low mass counterparts of type Ia supernovae in the double-degenerate (DD) scenario (Fryer et al. 2008).

Photometric and spectroscopic properties of RCB stars have been studied extensively. While at maximum light, they are known to pulsate with periods between 40–100 days and amplitudes of a few tenths of a magnitude (Lawson et al. 1996). The stars can then undergo mass loss episodes that eject “puffs” of dust around them

(Feast et al. 1997). If the dust is ejected along the line of sight to a star, its brightness decreases rapidly. The dust is eventually blown away by radiation pressure and the star rises back to its initial brightness Clayton et al. 1992. Spectra of RCB stars taken at maximum light suggest that most of them are F-G type supergiants (Iben et al. 1996) (although a few “hot” RCB stars with  $T > 10000$  K exist De Marco et al. 2002; Tisserand et al. 2020). RCB stars with effective temperatures  $T_{\text{eff}} < 6800$  K show spectra with absorption features of molecules such as CO, CN and C<sub>2</sub> (Morgan et al. 2003; Tisserand et al. 2020). Most RCB stars do not show any Hydrogen features in their spectra. However, a few exceptions exist. The stars V854Cen, VCrA, U Aqr and DY Cen are relatively more hydrogen-rich and their spectra show H-Balmer lines (Kilkenny et al. 1989; Lawson et al. 1989). During a photometric decline, the dust enshrouded RCB star shows a mostly featureless spectrum with a few emission lines.

There are two contending theories to explain the formation of RCB stars — double degenerate (DD) and the final flash (FF). In the DD scenario, RCB stars are proposed to be remnants of the merger of a He-core WD and a CO-core WD. In the FF scenario, they are proposed to be the product of a final helium flash in the central star of a planetary nebula. The DD scenario is supported by the discovery of large abundances of <sup>18</sup>O in atmospheres of some RCB stars (Clayton et al. 2007; García-Hernández et al. 2009). Using the CO bandhead in the near-infrared (NIR) spectra, these studies measured an <sup>16</sup>O/<sup>18</sup>O ratio of order unity in several RCB stars. For comparison, this ratio is  $\approx 500$  in the solar system (Geiss et al. 2002). Such high quantities of <sup>18</sup>O can be produced during a white dwarf merger (Clayton et al. 2007; Jeffery et al. 2011). In contrast, there is no such model in the FF scenario that can explain the <sup>18</sup>O overabundance (García-Hernández et al. 2009). However, the FF scenario is supported by the detection of Li and <sup>13</sup>C in few RCB stars (Asplund et al. 2000; Rao et al. 2008). Thus, the DD scenario could account for most of the RCB stars while a small fraction, those without an <sup>18</sup>O overabundance, may be formed through the FF channel.

There is a big discrepancy between the number of known and predicted Galactic RCB stars. 117 Galactic RCB stars are currently known (Tisserand et al. 2020), while the total number is expected to be much larger. Assuming a DD origin with a WD merger rate of  $\approx 10^{-2}$  yr<sup>-1</sup> from Han 1998b, Clayton 2012 estimate that there are  $\approx 5400$  RCB stars in the Milky Way. This number is consistent with that extrapolated from the RCB population of the Large Magellanic Cloud (Alcock et

al. 2001). From a campaign to identify Galactic RCB stars using mid-IR colors, Tisserand et al. (2020) estimate the total number to be  $\approx 380$ – $550$ . This suggests a lower WD merger rate of  $\sim 10^{-3}$  yr $^{-1}$ , which is consistent with theoretical estimates made from population synthesis via the DD channel (Ruiter et al. 2009; Karakas et al. 2015). An accurate estimate of the number of RCB stars is important to shed further light on their progenitors. In the DD scenario, this number will provide an independent probe of the rate of mergers of white dwarf binaries. This will be particularly useful as close white-dwarf binaries will be important gravitational wave sources for LISA (Amaro-Seoane et al. 2017; Burdge et al. 2020).

Modern time domain surveys provide an attractive avenue for resolving this discrepancy. The high cadence, long baseline photometric observations are ideal to flag RCB stars (from their declines). These can be further followed up spectroscopically to study their chemical compositions. Such studies have been carried out in the past with data from optical surveys such as the Massive Compact Halo Object project (MACHO, Alcock et al. 2001; Zaniewski et al. 2005), EROS-2 (Tisserand et al. 2004; Tisserand et al. 2008; Tisserand et al. 2009), the Catalina Survey (Lee 2015), All Sky Automated Survey for Supernovae (ASASSN, Tisserand et al. 2013; Shields et al. 2019; Otero et al. 2014) and the Zwicky Transient Facility (ZTF, Lee et al. 2020). In this paper, we use data from Palomar Gattini IR (PGIR), an infrared time domain facility to conduct the first near-infrared (NIR) search for RCB stars.

Palomar Gattini IR (PGIR, De et al. 2020a; Moore et al. 2019) is a 25 sq. degree J-band camera on a 30 cm telescope located atop Mt. Palomar. PGIR was commissioned in September 2018 and commenced survey operations in July 2019. PGIR surveys the entire northern sky (18000 sq. degrees,  $\delta > -28^\circ$ ) to a depth of  $J \approx 16$  mag (AB) and a cadence of  $\approx 2$  days. In the Galactic Plane, the limiting magnitude drops to  $J \approx 14$  mag (AB) due to confusion noise. RCB stars are inherently brighter in the J band compared to the optical. 95% of all known Galactic RCB stars have 2MASS J band magnitudes brighter than 14 mag. Even during a photometric decline, the J band brightness decreases by  $\approx 3$  mag (Feast et al. 1997) as opposed to 9 mag in the optical. Of the known Galactic RCB stars, 66% are brighter than 11 mag in the J band. This puts a majority of the Galactic RCB stars above the sensitivity of PGIR. Additionally, a large number of RCB stars are expected to be located towards the Galactic Center, in regions of high dust-extinction (Tisserand et al. 2020). The extinction due to dust is significantly lower in the IR compared to optical wavelengths. This makes PGIR an ideal instrument to conduct a systematic

search for Galactic RCB stars. In the first part of this search, we focus on PGIR  $J$ –band light curves for objects in a pre-existing catalog of candidate Galactic RCB stars (Tisserand et al. 2020).

The remainder of this paper is structured as follows— in Section 2.2, we describe our source catalog and present PGIR  $J$ –band light curves of 922 objects from this catalog. We use the light curves to identify promising RCB candidates from contaminants such as long period variables (LPVs) and RV Tauri stars. In Section 2.3, we use our lightcurve-based classifications to identify IR color-criteria to distinguish between RCB stars and LPVs to subsequently prioritise our spectroscopic followup. In Section 2.4 we present results from a pilot NIR spectroscopic campaign to identify new RCB stars from our list. In Section 2.5 we analyse the NIR spectra and light curves of several RCB stars to derive their radial velocities, photospheric temperatures,  $^{16}\text{O}/^{18}\text{O}$  ratios, pulsation periods and discuss the implications of these quantities on their formation channels. We conclude with a summary of our results and future prospects in Section 2.6.

## 2.2 IR lightcurve-based prioritization

Our source catalog comes from the Tisserand et al. (2020) list of 2194 Galactic RCB candidates selected based on their WISE colors. We performed forced aperture photometry using a 3 pixel ( $\approx 13''$ ) aperture on all J-band PGIR images since November 2018 at the locations of these candidates to generate light curves for each of them. The average cadence between observations is  $\approx 2$  days. The baseline of observations is  $\approx 500$  days, which corresponds to two observing seasons of the Galactic plane. Further details of the imaging and photometric pipeline can be found in De et al. (2020a). We note that the photometry for sources brighter than  $J \approx 8.5$  mag may not be accurate due to non-linearity effects in the detector.

Of the 2194 targets of interest, 1209 sources lie in the on-sky area covered by PGIR ( $\delta \gtrapprox -28^\circ$ ). Of these, 287 are fainter than the detection limit of PGIR. The remaining 922 sources have J-band light curves. In addition to RCB stars, this list also contains several contaminants. These mainly include Miras, dust enshrouded RV Tauri stars and T Tauri stars (cf. Section 2.4 in Tisserand et al. 2020). Miras are long-period variables (LPVs) with periods longer than 150 days. RV Tauri and T Tauri stars show pulsations on timescales of a few weeks (Grankin et al. 2007). In this aspect, their light curves are similar to RCB stars at maximum light. However, unlike RCB stars, some RV Tauri stars show subsequent deep and shallow minima. Some also

exhibit a long term periodic trend in addition to the shorter periodic variations<sup>1</sup>. To weed out these periodic impostors, we fit sinusoids to the J band light curves of all candidates using the GATSPY (VanderPlas et al. 2015) implementation of the Lomb Scargle method (Lomb 1976; Scargle 1982). We visually examine the fits to determine the reliability of the derived period.

With this information in hand, we find that the 1209 candidates can be divided into the following priority groups based on their PGIR light curves –

- **Priority A** : The lightcurve shows sharp, deep declines or rises, or pulsations at timescales of few weeks, and resembles that of an RCB star. We identify 149 candidates in this category. We further divide this category into 3 sub-categories based on the trends shown by their light curves as of July 2020 — 48 candidates that are *declining*, 53 candidates that are *rising* and 48 candidates that are *pulsating* (with periods  $\leq 100$  days).
- **Priority B** : The lightcurve is ambiguous, not sufficient for any firm classification. There are 279 candidates in this category. Of these 279, 58 candidates show an overall rise in their brightness and 44 show an overall decline. 29 candidates have too large photometric errors to identify any trend. 148 sources show erratic photometric variations.
- **Priority C** : The lightcurve shows no significant photometric evolution ( $<\approx 0.1$  mag) for the last 500 days. There are 199 candidates in this category.
- **Priority D** : There are no detections in PGIR data. 287 candidates belong to this category.
- **Priority E** : The lightcurve is consistent with that of an RV Tauri or a T Tauri star. 23 candidates belong to this category.
- **Priority F** : The lightcurve is consistent with an LPV. There are 272 candidates in this category.

The groups are listed in order of priority for spectroscopic followup. Figure 2.1 shows examples of lightcurves in each priority group. The Priority A group is expected to be rich in RCB stars. Some objects in this group could be LPVs that show non-sinusoidal variations. Priority B, C and D groups are also expected to

---

<sup>1</sup>[http://ogle.astrow.edu.pl/atlas/RV\\_Tau.html](http://ogle.astrow.edu.pl/atlas/RV_Tau.html)

Table 2.1: Light curve (LC) based priorities, sub-classifications and IR color based priorities for spectroscopic followup of candidates in Tisserand et al. (2020) catalog. We assign color-based priorities to all 2194 candidates in the catalog, and lightcurve-based priorities to 1209 candidates that have PGIR coverage.

WISE ToI	R.A (deg)	Dec (deg)	LC-based Priority	LC-based sub-class	IR-color based priority
1	2.1755	63.0093	A	pulsating	1-b
2	4.7942	52.0343	F		1-a
3	7.3382	64.8141	C		1-a
4	9.7554	59.4681	B	erratic	1-a
5	11.6178	58.9057	C		1-a
6	12.0930	74.2992	A	declining	1-b
...					

This table is published online in its entirety in the machine-readable format.

contain RCB stars. Additional PGIR observations will help identify candidates with RCB-like declines or pulsations in these groups. Table 2.1 lists the lightcurve based priorities and sub-priorities for each of the 1209 candidates. All 1209 lightcurves are publicly available online<sup>2</sup>

### 2.3 IR color-based prioritization

In Section 2.2, we prioritized 1209 of the 2194 candidates from Tisserand et al. (2020)’s catalog based on their PGIR light curves. Importantly, we identified 272 LPVs and 23 RV Tauri stars from their light curves. Here, we explore the positions of these contaminants in the WISE and 2MASS color diagrams. We use this to identify color criteria that distinguish between RCB stars, LPVs and RV Tauri stars. We then assign a color-based priority to each of the 2194 candidates to optimise further NIR spectroscopic follow-up. This priority will be particularly useful for the 985 candidates that do not have PGIR coverage.

The WISE and 2MASS color-color diagrams were used previously by Tisserand et al. (2020) to divide their catalog into different groups (their Figure 4). Group 1 occupies the bottom-right region in the WISE [3.4]–[4.6] vs [12]–[22] diagram. This group is expected to contain the maximum number of RCB stars. Group 2

<sup>2</sup><https://doi.org/10.5281/zenodo.4480376>

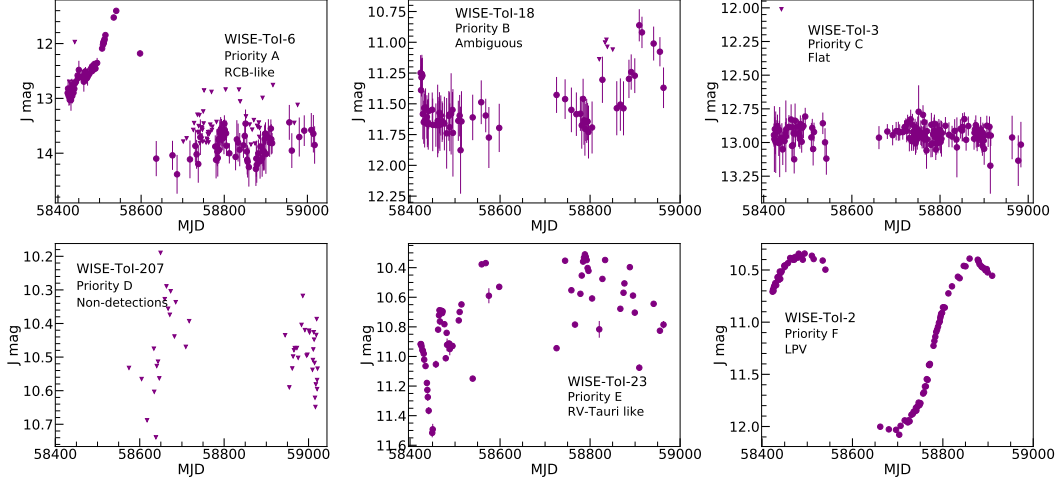


**Figure 2.1: Examples of PGIR J-band lightcurves for candidates in each of the lc-based priority groups described in Section 2.2.** The solid dots represent detections and triangles represent  $5\sigma$  upper limits. Of the 1209 candidates from Tisserand et al. (2020) catalog that have PGIR coverage, we assign 149 candidates Priority A (RCB-like), 279 candidates Priority B (ambiguous light curves), 199 candidates Priority C (flat light curves), 287 candidates Priority D (no detections), 23 candidates Priority E (RV Tauri-like) and 272 candidates Priority F (LPV-like). The Priority A group is expected to be rich in RCB stars, but the groups B, C and D could also contain RCB stars.

occupies the top-left region in the diagram and is expected to contain rare RCB stars that are surrounded by thin or cold dust shells ( $T < 500$  K). Finally, Group 3 comprises objects that are reported with upper limits in at least one WISE band and objects that have prior classifications. We analyse the candidates in each of these groups separately<sup>3</sup>.

Figure 2.2 shows the WISE [3.4]–[4.6] vs [12]–[22] and 2MASS  $K$  vs  $J - K$  color-color diagrams for all 2194 candidates in the source catalog. We plot these diagrams separately for Groups 1, 2 and 3. All candidates in a group are plotted as gray background points. On each plot we highlight the candidates with lightcurve-based priority A (RCB-like, blue dots), priority E (RV Tauri, red dots) and priority F (LPVs, orange dots). We also indicate the position of known RCB stars in these diagrams (black crosses). In the [3.4]–[4.6] vs [12]–[22] diagram, we also mark the “disk-box” region, which is expected to contain RV Tauri stars with dust disks around them (Gezer et al. 2015). We note that our lightcurve-Priority E (RV Tauri) candidates lie in this region.

<sup>3</sup>Tisserand et al. (2020) further divide Group 1 and 3 into two subgroups each

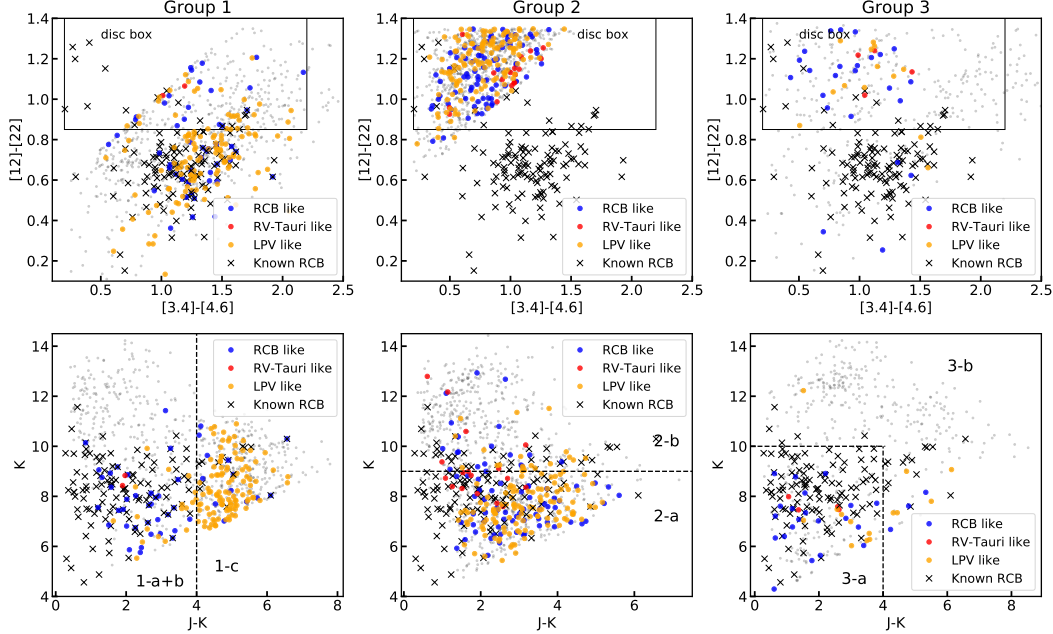


**Figure 2.2: The WISE  $[3.4]-[4.6]$  vs  $[12]-[22]$  and 2MASS  $K$  vs  $J - K$  color-color diagrams for all candidates in the Tisserand et al. (2020) catalog.** The left column shows the plots for candidates in Group 1, middle column shows candidates in Group 2 and the right column shows candidates in Groups 3. All candidates in each group are plotted as gray background points. On each color-color diagram, we highlight candidates that have light curves similar to RCB stars (Priority A, blue circles), RV Tauri stars (Priority E, red circles) and LPVs (Priority F, orange circles) present in the respective group. In addition, we also plot all known RCB stars as black crosses. We assign a new color based priority to each candidate based on its position in the  $K$  vs  $J - K$  diagram, as indicated. In the WISE color-color plots, we also indicate the “disc-box” where RV Tauri stars surrounded by dust discs are expected to lie (Gezer et al. 2015). In Group 1,  $J - K = 4$  line separates LPVs from the known RCB stars and lc-Priority A candidates. We assign all candidates in Group 1 that have  $J - K < 4$  mag and lie outside the RV Tauri disc box to “Group-1-a” and those inside the disc box to “Group-1-b”. For Groups 2 and 3, we cannot identify a similar distinction between LPVs and RCB candidates. Instead, we use the positions of known RCB stars and our light curve based priority A candidates to prioritise these groups for spectroscopic followup (see text). We prioritise candidates in Group-1-a, Group-2-a and Group-3-a for spectroscopic followup.

Light curve based priorities for 1209 candidates							
	Priority A RCB-like 149	Priority B ambiguous 279	Priority C flat 199	Priority D no detect. 287	Priority E RV-Tauri 23	Priority F LPV 272	
IR color based priorities for 2194 candidates	1-a 252	21	38	37	34	0	11
	1-b 111	14	18	10	11	2	7
	1-c 422	13	33	22	87	0	106
	2-a 548	58	72	1	13	11	114
	2-b 439	19	55	91	48	6	20
	3-a 101	21	39	5	2	4	8
	3-b 321	3	24	33	92	0	6

**Figure 2.3: Schematic of light curve-based priorities and IR color based priorities for RCB candidates.** We assign light curve based priorities (A–F) to 1209 of the 2194 candidates in Tisserand et al. (2020) catalog. We also divide the full catalog into 7 groups based on the IR colors of the candidates. In this figure, we indicate the overlap between each lightcurve based and IR color based group. For our campaign, we aim to observe all 149 candidates with lightcurve-priority A. We will also observe 241 additional candidates that have lc-Priorities B, C, D and belong to IR-color Groups 1-a, 2-a and 3-a. We highlight these 390 candidates in green.

Based on these diagrams, we assign a color-based classification to each of the 2194 candidates as follows:

- **Group 1** : This group has 785 candidates, and are expected to contain the maximum number of RCB stars. The left column in Fig. 2.2 shows the color-color diagrams for candidates in this group. These candidates lie in the bottom-right part of the [3.4]–[4.6] vs [12]–[22] diagram. We first note that the  $K$  vs  $J - K$  diagram can be used to separate most LPVs from RCB stars in this group. If we apply a cut of  $J - K < 4$  mag, we eliminate 90% LPVs, while retaining 90% of known RCB stars and 73% of priority A candidates. We assign all 422 candidates with  $J - K > 4$  mag the priority “Group-1-c”. For the few RCB stars lying within this group, the 2MASS observations were likely obtained while they were in a deep decline phase, being, consequently, highly reddened. Of the remaining 363 candidates, 111 candidates lie in the RV Tauri disk box. We assign a priority “Group-1-b” to these stars. We give the highest priority for spectroscopic follow-up to the

remaining 252 candidates : “Group-1-a”.

- **Group 2** : This group alone has 987 candidates, and is expected to have the highest contamination. The middle column in Fig. 2.2 shows the color-color diagrams for candidates in Group 2. These candidates lie in the top left part of the  $[3.4] - [4.6]$  vs  $[12] - [22]$  diagram. Although this group contains the largest number of candidates, very few known RCB stars (7 out of 117) lie in this region of the diagram. The disk box is not a particularly useful metric for prioritization as almost all of these candidates lie in the disk box. Unlike Group 1, no clear distinction can be made between the LPVs, known RCB stars and photometric RCB candidates in the  $K$  vs  $J - K$  diagram. If we apply a cut of  $K < 9$  mag, we retain 70% of known RCB stars and 75% of lc-priority A candidates. In absence of any other criteria, we prioritise the sources with  $K < 9$  mag over the remaining candidates. We assign 548 candidates with  $K < 9$  mag to the higher priority “Group-2-a” and the remaining 439 candidates to the lower priority “Group-2-b”.
- **Group 3** : This group has 422 candidates. The last column in Fig. 2.2 shows the color-color diagrams for candidates in Groups 3. Based on the  $K$  vs  $J - K$  diagram, we prioritise sources that lie inside the box defined by  $4 < K < 10$  and  $J - K < 4$  mag. This box contains 85% of known RCB stars, 88% of priority A candidates and only 50% of LPVs. We assign 150 candidates that lie in this box priority “Group-3-a” and the remaining 272 candidates “Group-3-b”.

We list these candidates with their color-based priorities in Table 2.1. For spectroscopic followup, we prioritise candidates in Group-1-a, Group-2-a and Group-3-a in decreasing order. Group-1-b is also expected to contain RCB stars but is likely contaminated by RV Tauri stars. The IR colors thus provide an additional metric to prioritise the candidates for spectroscopic followup.

Our spectroscopic campaign focuses on candidates in the northern hemisphere that lie in the area covered by PGIR. First, we aim to spectroscopically follow-up all 149 candidates that have light curve-based Priority A. From the 765 candidates that have light curve-Priority B, C or D, we will follow-up only 241 candidates that belong to our top three IR-color based groups (Groups-1-a, 2-a and 3-a). This leaves us with a sample of 390 candidates for spectroscopic followup. The distribution of the candidates among the different priority groups is illustrated in Figure 2.3.

## 2.4 Pilot NIR spectroscopic follow-up

In Sections 2.2 and 2.3, we reprioritised candidates in the Tisserand et al. (2020) catalog based on their IR light curves and colors. We aim to spectroscopically followup the candidates in the top priorities to confirm their true nature. Traditionally, large-scale spectroscopic campaigns for identifying RCB stars have made use of optical spectra. As noted in Section 2.1, RCB stars are significantly brighter in the NIR compared to the optical. Thus, NIR wavebands are better suited to efficiently observe a large number of candidate RCB stars. In addition, NIR spectral features such as the  $^{12}\text{C}^{16}\text{O}$  and  $^{12}\text{C}^{18}\text{O}$  bandheads can provide useful diagnostics about the progenitors of these stars. Thus, a NIR spectroscopic campaign promises to be highly productive in identifying and characterising RCB stars. No such campaign has been conducted in the past. As a pilot for such a campaign, we obtained NIR spectra for eight known RCB stars and 31 of our top lightcurve-based priority candidates. Of the 31 candidates, 26 have lightcurve-priority A and five have lightcurve-priority B. Here, we present results from this pilot run.

We used Triplespec (Herter et al. 2008), a medium resolution ( $R \approx 2700$ ) *JHK* band spectrograph on the 200-inch Hale telescope at Mt. Palomar. We observed eight known RCB stars and 21 candidates on 2019 October 23, and three additional candidates on 2020 February 3. We further observed seven more candidates on 2020 June 28 with the Spex spectrograph ( $R \approx 1500$ ) on the NASA Infrared Telescope Facility (IRTF; Rayner et al. 2003) at Mauna Kea. The IRTF observations were acquired as part of program 2020A111 (PI: K. De). All spectra were extracted using the IDL package `spextool` (Cushing et al. 2004). The extracted spectra were flux calibrated and corrected for telluric absorption with standard star observations using `xtellcor` (Vacca et al. 2003).

### NIR spectral features of known RCB stars

We obtained NIR spectra of eight known RCB stars (as listed on SIMBAD<sup>4</sup>) – A0 Her, V391 Sct, NSV 11154, WISE J184158.40-054819.2 (WISE J18+), WISE J175749.76-075314.9 (WISE J17+), ASAS-RCB-21, WISE J194218.38-203247.5 (WISE J19+) and ASAS-RCB-20.

Figure 2.4 shows the *J* band light curves of these stars. Seven of the known RCB stars have been reported as cold ( $T_{\text{eff}} < 6800\text{K}$ ) – AO Her (Tisserand P., private communication), NSV11154 (Kijbunchoo et al. 2011), ASAS-RCB-20, ASAS-RCB-21

---

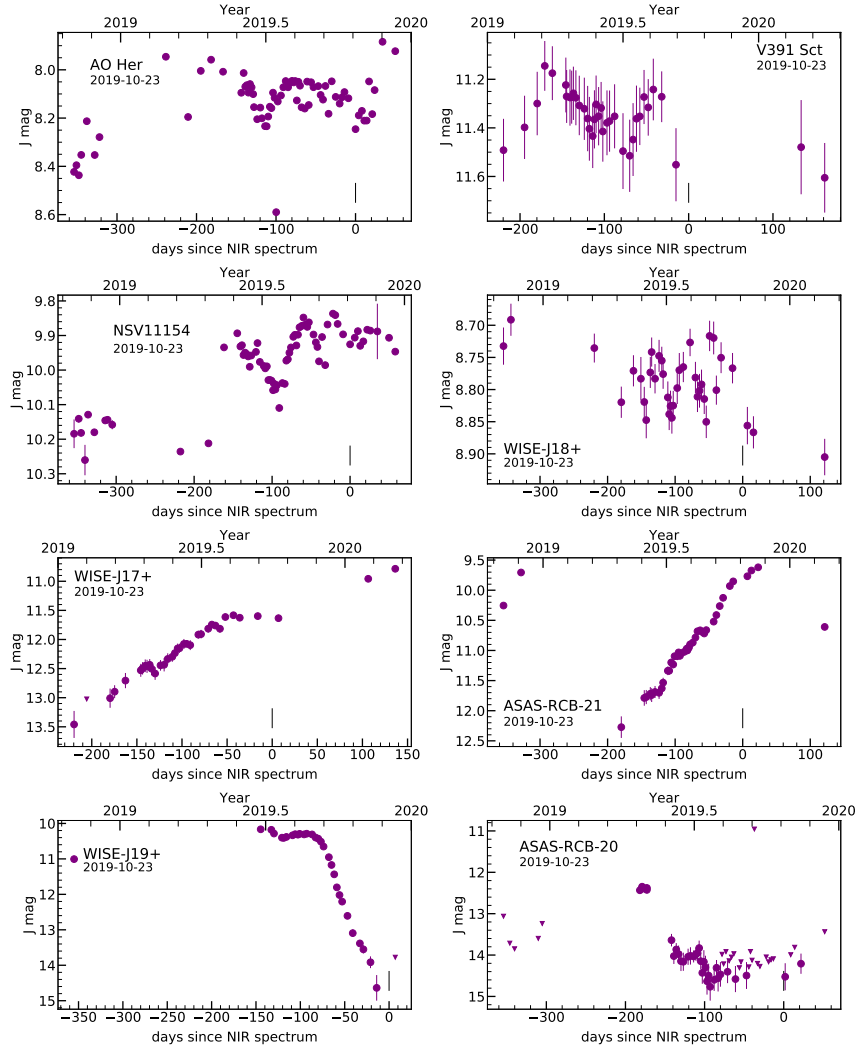
<sup>4</sup><https://simbad.u-strasbg.fr>

(Tisserand et al. 2013), WISE-J17+, WISE-J18+ and WISE-J19+ (Tisserand et al. 2020). The star V391 Sct has been reported as a warm RCB by Tisserand et al. (2013). Four out of the eight RCB stars – V391Sct, NSV11154, AOHer and WISE-J18+ were at the maximum light phase when the spectra were obtained. All four stars exhibit quasi-periodic pulsations with periods between 40–140 days. The RCB stars WISE-J19+ and ASAS-RCB-20 were in the photometric minimum phase. WISE-J17+ and ASAS-RCB-21 were rising out of a photometric minimum towards maximum light. Figure 2.5 shows the NIR spectra of these stars, grouped by their photometric phase. We note the following characteristic features in these spectra –

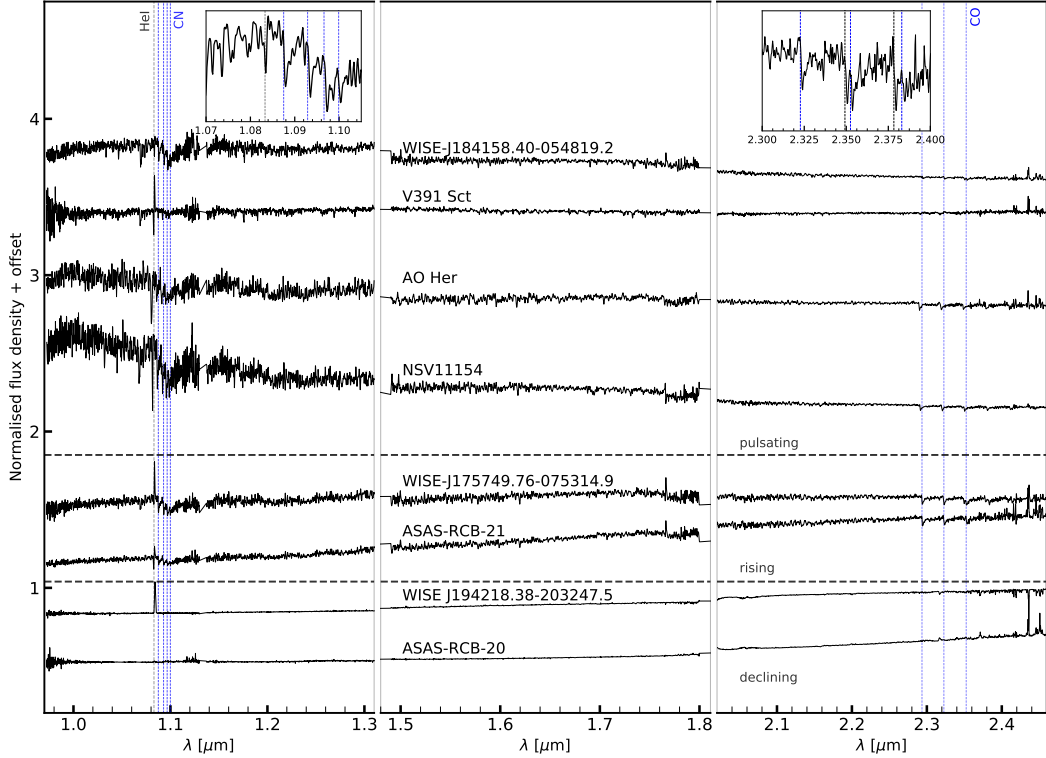
- All RCB stars show He I ( $\lambda 10830$ ) emission or absorption features. The two stars inside a photometric minimum show helium emission. The emission is strong for WISE-J19+ (just entering the minimum) and very weak for ASAS-RCB-20 (deep inside the minimum, featureless spectrum). The pulsating and rising stars show either a fully developed P Cygni profile or strong blueshifted absorption. We discuss the He I line profiles in more detail in Section 2.5.
- The RCB stars inside a minimum show a mostly featureless reddened spectrum with He I emission. If the star has entered the minimum recently, other emission lines such as Si I and C<sub>2</sub> are detected. These features are absent if the star is deep inside the minimum.
- The rising and pulsating RCB stars show a variety of atomic absorption lines. These include C I (most prominently at 1.0686 and 1.0688  $\mu\text{m}$ ) along with Fe I, Si I and K I.
- Of the rising and pulsating RCB stars, all but V391 Sct show the CN (1.0875, 1.0929, 1.0966 and 1.0999  $\mu\text{m}$ ) and <sup>12</sup>C<sup>16</sup>O (2.2935, 2.3227, 2.3525, 2.3829, 2.4141  $\mu\text{m}$ ) absorption bandheads. The presence of these molecular bandheads suggests that these stars have cold photospheres ( $T_{\text{eff}} < 6800$  K). Importantly, we also detect <sup>12</sup>C<sup>18</sup>O absorption features in the K band of all these stars. We discuss the CO bandhead in more detail in Section 2.5.
- None of the 8 RCB stars show any Hydrogen features in their NIR spectra.

### New RCB stars

We obtained NIR spectra for 31 RCB candidates – 26 with lightcurve-priority A and five with lightcurve-priority B. None of the five priority B candidates show



**Figure 2.4: PGIR J Band light curves for 8 known RCB stars.** The black vertical lines at 0 days mark the epoch at which the NIR spectra were acquired (indicated in each plot). We note that photometry brighter than 8.5 mag may not be reliable due to non-linearity effects in the detector. The J-band magnitudes are in Vega system.



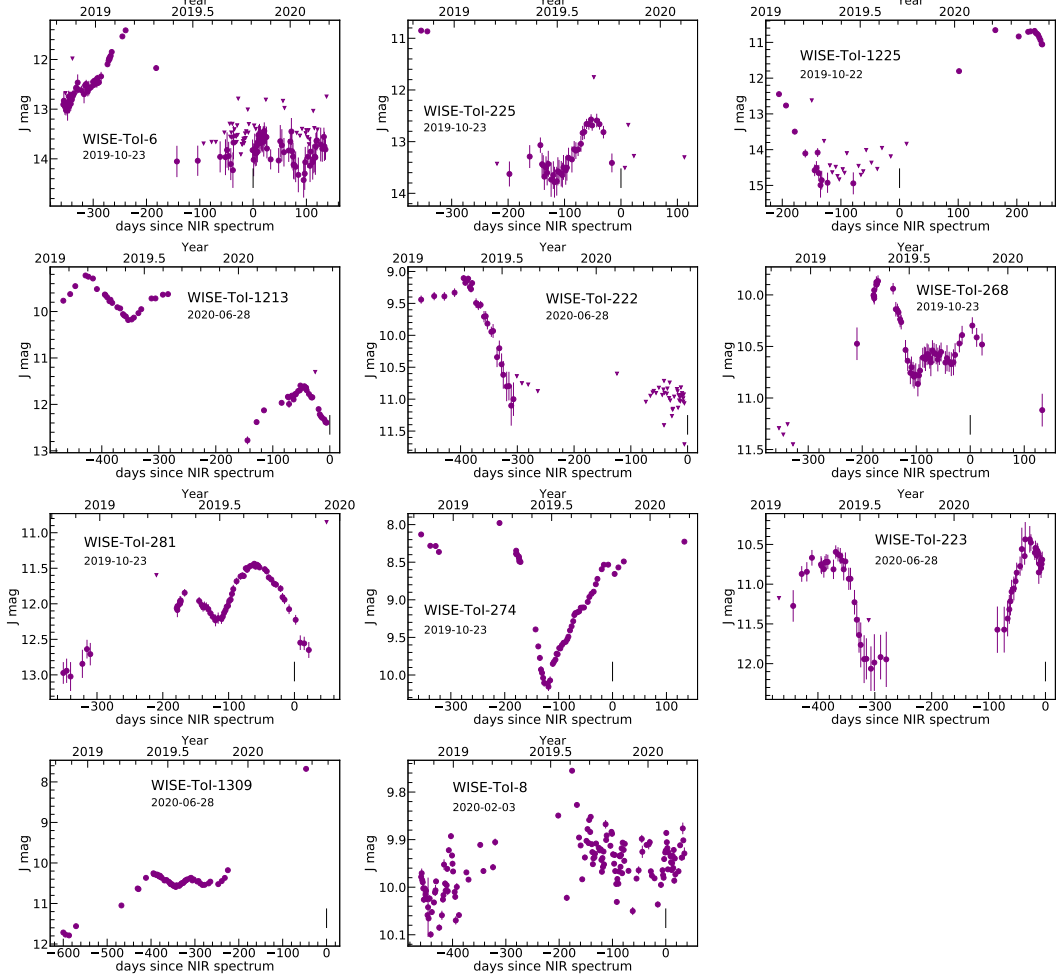
**Figure 2.5: NIR spectra of 8 known RCB stars on 2019 November 23.** The stars are grouped by their photometric phase - 4 pulsating, 2 rising and 2 fading. We also show a zoom in of the J-band and K-band spectra of the RCB star WISE-J18+. In the J-band inset plot, we mark the positions of the CN absorption bandhead in blue and He I absorption in gray. In the K-band inset, we mark the position of  $^{12}\text{C}^{16}\text{O}$  and  $^{12}\text{C}^{18}\text{O}$  absorption bandheads in blue and black respectively.

Table 2.2: Properties of newly identified RCB stars

WISE Name	WISE ToI	RA (deg)	Dec (deg)	Light-curve Phase <sup>a</sup>	Temperature	$A_V^b$ mag	Comments
J004822.34+741757.4	6	12.0931	74.2993	Declining	cold	4.3	
J005128.08+645651.7	8	12.8670	64.9477	Pulsating	hot	1.2	pulsating with period $\approx 30$ days
J181836.38-181732.8	222	274.6516	-18.2925	Declining		8.7	
J182010.96-193453.4	223	275.0457	-19.5815	Rising	cold	4.9	
J182235.25-033213.2	225	275.6469	-3.5370	Declining		6.5	
J190813.12+042154.1	268	287.0547	4.3650	Declining	cold	6.8	
J191243.06+055313.1	274	288.1795	5.8870	Rising	cold	7.7	sharp rise out of a decline
J192348.98+161433.7	281	290.9541	16.2427	Declining	cold	22	
J170552.81-163416.5	1213	256.4701	-16.5713	Declining		1.3	
J173737.07-072828.1	1225	264.4045	-7.4745	Declining		2.8	
J185726.40+134909.4	1309	284.3600	13.8193	Rising	cold	2.4	rising from 600 day long minimum

a : The photometric phase when the spectrum was obtained.

b : Line of sight extinction, values taken from Schlafly et al. (2011)



**Figure 2.6: PGIR J band light curves of new RCB stars identified in this paper.** The black vertical lines at 0 days mark the epochs at which the NIR spectra were acquired. For each RCB star, we also indicate the date when the spectrum was obtained. We note that photometry brighter than 8.5 mag may not be reliable due to non-linearity effects in the detector. All J-band magnitudes are in Vega system.

spectra resembling RCB stars. Of the 26 priority A candidates, we identify 11 new RCB stars using the spectral features described in Section 2.4. These stars are – WISE-Tol-6, 8, 222, 223, 225, 268, 274, 281, 1213, 1225 and 1309. Table 2.2 summarises the properties of these stars. Figure 2.6 shows the light curves of these stars and Figure 2.7 shows their spectra. Here, we discuss the properties of these newly identified RCB stars. We group the stars by their photometric phase at the time the spectra were obtained.

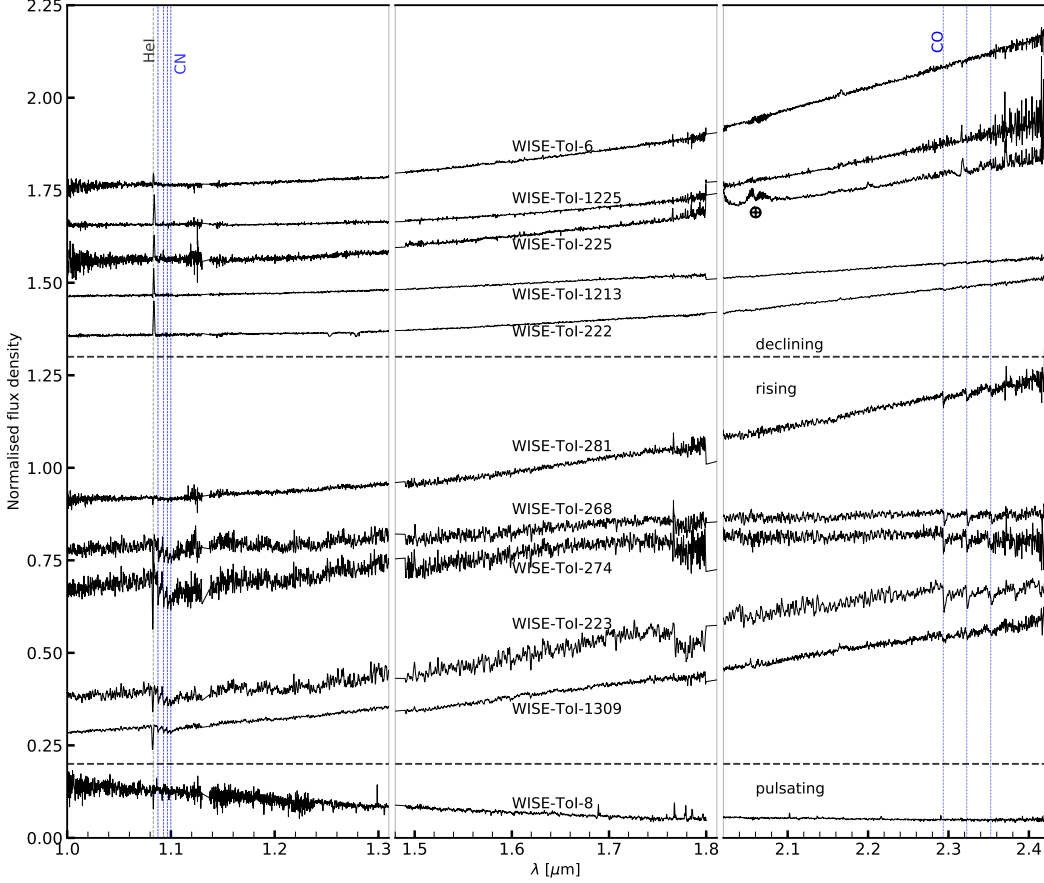


**Figure 2.7: NIR spectra of new RCB stars identified in this paper.** All RCB stars show He I  $\lambda 10830$  features. 5 RCB stars that were in a deep decline show strong emission, while others show either fully developed P Cygni profiles or strong blueshifted absorption. 4 RCB stars show the CO absorption bandhead, suggesting that they are cold.

### Declining

Seven of the 11 new RCB stars – WISE-Tol-6, 222, 225, 268, 281, 1213 and 1225 were in a photometric minimum or were undergoing a photometric decline when the spectra were obtained. The light curves of WISE-Tol-6, 222, 225 and 1225 indicate that these stars were in a photometric minimum for more than a hundred days before the spectra were taken. These stars showed photometric declines of  $\approx 3$  mag in the J band and present featureless spectra with strong He I emission. WISE-Tol-268 and 281 show shallower declines ( $\approx 1.5$  mag) and also show brief recoveries from the declines. Their spectra show strong blueshifted He I absorption and  $^{12}\text{C}^{16}\text{O}$  and  $^{12}\text{C}^{18}\text{O}$  absorption bands, suggesting that they are cold RCB stars. The lightcurve of WISE-Tol-1213 shows a complex photometric evolution where the star underwent

shallow declines and recoveries of 1 mag *and* a deep decline of  $> 3$  mag. The spectrum obtained during this decline shows He I with a P Cygni profile. We also detect the  $^{12}\text{C}^{16}\text{O}$  absorption bandhead with traces of  $^{12}\text{C}^{18}\text{O}$ , suggesting that this is an RCB star.

We note that WISE-ToI-225, 222 and 281 lie in highly extinguished regions of the Galaxy. The integrated line of sight extinction in their direction ( $A_V$ ) is 6.5, 8.7 and 22 mag respectively (Schlafly et al. 2011). Their 2MASS  $J$  band magnitudes are 10.8, 9.0, 10.9 mag and PanSTARRS  $g$  band magnitudes are 19.9, 20.2 and 22.4 mag respectively. These stars thus have  $J - g \gtrsim 10$  mag and illustrate the advantage that NIR searches offer over even very deep optical searches for RCB stars.

### Rising

Three stars WISE-ToI-223, 274 and 1309 were rising out of a photometric decline when the spectra were obtained. ToI 223 was at constant minimum brightness for 200 days before it rose out of the minimum, brightening by 2.5 mag in  $J$  band. ToI 274 previously underwent a decline of 2 mag but recovered sharply without flattening at the minimum brightness. This variation is similar to the one observed with DYPer type stars (Tisserand et al. 2009). The  $J$  band lightcurve of ToI 1309 suggests that this star was in a minimum for at least 600 days before our spectrum was obtained. The spectra of these stars show strong blueshifted He I absorption, CN,  $^{12}\text{C}^{16}\text{O}$  and  $^{12}\text{C}^{18}\text{O}$  absorption features. ToI 274 also shows a small redshifted He I emission component.

ToI 223 and 274 have been listed as strong RCB candidates by Tisserand et al. (2020). They note that these stars are the fifth and sixth brightest RCB stars in the  $12\text{ }\mu\text{m}$  band. They have WISE [12] = 1.0 and 1.2 mag respectively, indicative of a very bright circumstellar dust shell. The integrated Galactic extinction in their direction ( $A_V$ ) is 4.9 and 7.7 mag respectively, suggesting that they lie in regions of high dust extinction.

### Pulsating

The lightcurve of WISE-ToI-8 was showing quasi-periodic variations when the spectrum was obtained. We identify a tentative period of  $\approx 30\text{ d}$  for this star. This star was photometrically identified as an RCB candidate on AAVSO and by the ASAS-SN survey (Jayasinghe et al. 2018), as it underwent photometric declines in 1999 and 2012. This star has not shown any obvious photometric declines at least

for the last 500 days. The spectrum shows blueshifted helium absorption and no Hydrogen absorption lines. No CO or CN features are present in our spectrum taken at maximum-light, suggesting that this is not a cold RCB star. The spectrum shows several emission lines, resembling spectra of hot ( $T_{\text{eff}} > 10000$  K) RCB stars. We identify CI emission at  $1.68 \mu\text{m}$ , CII emission at  $1.784 \mu\text{m}$ , FeII emission at  $1.766$  and  $1.778 \mu\text{m}$  and possibly Ne I emission at  $1.7961 \mu\text{m}$ . Similar to other hot RCB stars, the emission lines are double-peaked, which could indicate the presence of an equatorial outflow around the star (De Marco et al. 2002).

Our pilot campaign has demonstrated the utility of NIR spectra in searches for RCB stars. We will continue this spectroscopic followup campaign in the future, aiming for completeness in the top priority classes. The NIR spectra of all RCB stars from our pilot campaign are publicly available online<sup>5</sup>.

## 2.5 Preliminary implications for progenitors

In this paper, we have presented NIR spectra for 19 RCB stars (eight previously known, 11 newly identified). We have also presented long baseline ( $\approx 500$  days) high cadence ( $\approx 2$  day) light curves for these stars. In this section, we analyse the NIR spectra to derive diagnostic quantities about the nature of RCB stars. In particular, we focus on photospheric temperatures, oxygen isotope ratios and helium line profiles. We also derive maximum-light pulsation periods for 5 RCB stars. We discuss the implications of these quantities on the progenitors and nature of RCB stars. Although our sample size is not sufficient for any quantitative insights, the results are indicative of the potential of the NIR campaign. Future observations will increase our sample size and shed more light on the open questions about RCB stars.

### Photospheric Temperatures and Isotope ratios

#### SED modeling

We searched archival data from optical, NIR and mid-IR surveys for maximum-light photometric measurements of RCB stars analysed in this paper. For optical wavebands we used data from AAVSO, ZTF and ASAS-SN sky surveys. For NIR wavebands, we compare the 2MASS J-band magnitudes to PGIR lightcurves to identify RCB stars for which the 2MASS measurements correspond to maximum light. For mid-IR wavebands, we use the WISE magnitudes directly as the mid-IR fluxes of RCB stars do not vary significantly (Feast et al. 1997). We corrected

---

<sup>5</sup><https://doi.org/10.5281/zenodo.4480376>

the WISE 4.6  $\mu\text{m}$  magnitudes for saturation effects based on the prescription in Tisserand (2012). As the distances to these stars are not known accurately ( $\approx 30\%$  uncertainty from GAIA-DR2, Bailer-Jones et al. 2018), we cannot estimate the line-of-sight extinction in their direction. We restrict our analysis to only those stars that have integrated  $E_{B-V}$  values smaller than 1.5 mag. We assume 10% uncertainties on the photometric measurements to account for variations in the light curve and uncertainties in extinction. We construct maximum light spectral energy distributions (SEDs) for six RCB stars analysed in this paper. This includes five previously known RCB stars – AOHer, NSV11154, ASAS-RCB-21, WISE-J17+, WISE-J19+ and one new RCB WISE-ToI-1213.

We model the SEDs with the radiative transfer code DUSTY (Ivezic et al. 1997; Ivezic et al. 1999; Elitzur et al. 2001). In our models, DUSTY is embedded in a Markov Chain Monte Carlo (MCMC) wrapper using the python package emcee (Foreman-Mackey et al. 2013a). We modeled the star as a blackbody corrected for molecular absorption. We used synthetic spectra of RCB stars (see Sec. 2.5) to calculate the molecular absorption fractions. The dust is treated as a shell with density profile  $\rho \propto r^{-2}$ . We fix the outer radius of the shell to be ten times the inner radius (Clayton et al. 2011). We examine optical depth values in the visual band within the range  $0 < \tau_V < 10$  and dust temperatures in the range  $300 \text{ K} < T_{\text{dust}} < 1200 \text{ K}$ . We assume amorphous carbonaceous dust with a standard MRN size distribution (Mathis et al. 1977). One limitation of this analysis is the assumption of spherical symmetry. Therefore, the estimated dust optical depth could be an over or underestimation depending on the viewing angle.

The SEDs and best fit models from the dust analysis are shown in Figure 2.8. The model parameters and their  $1-\sigma$  uncertainties are listed in Table 2.3. The stars are consistent with temperatures between 4500 and 6000 K, surrounded by dust shells of temperatures between 700 – 900 K. With improved distance estimates from the next GAIA data release and additional monitoring from optical and NIR surveys, we will be able to estimate the temperatures for several more RCB stars. Accurate distance measurements will also enable us to derive luminosities of these stars and place them on the Hertzsprung-Russell (HR) diagram.

## NIR spectral modeling

The NIR spectra of cold RCB stars provide a host of information about their compositions. Here, we model the CO bandhead in the K band to constrain the temperatures

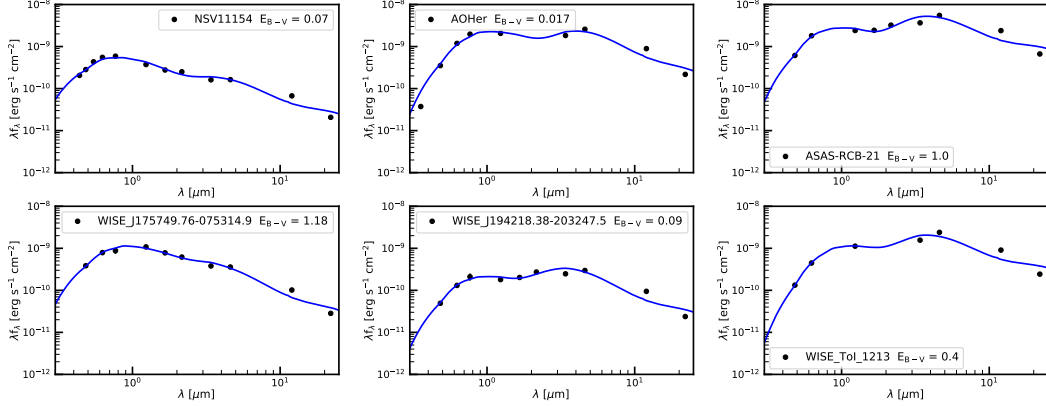


**Figure 2.8: Maximum light spectral energy distributions (SEDs) for six RCB stars from our sample.** We plot the best-fit DUSTY models in blue. For each star, we also indicate the assumed values of  $E_{B-V}$ . The derived model parameters are listed in Table 2.3

and oxygen isotope ratios of these stars. However, the circumstellar dust shells of RCB stars can contribute significantly to the observed K-band fluxes (up to 80% of the total flux, Tisserand 2012). The observed absorption depth of the CO bands depends largely on the assumed dust contribution. We defer a detailed characterisation of dust shells around these stars to a future paper. Instead, we leave the dust contribution as a free parameter in our model, and report a range of effective temperatures and oxygen isotope ratios for these stars. Secondly, given the medium resolution of our spectra, it is possible that  $^{12}\text{C}^{16}\text{O}$  bandheads of some RCB stars are saturated (García-Hernández et al. 2009). It is thus possible that the values of the oxygen isotope ratios are lower limits for some stars.

We use a grid of Hydrogen deficient spherically symmetric MARCS (Model Atmospheres in Radiative and Convective Scheme) atmospheric models with input compositions characteristic of RCB stars ( $\log \epsilon(\text{H}) = 7.5$ , C/He ratio of 1%; Gustafsson et al. 1975; Gustafsson et al. 2008; Bell et al. 1976; Plez 2008). We generated the synthetic spectra using the package TURBOSPECTRUM (Alvarez et al. 1998). We set  $\log g = 1.0$  and varied the effective temperatures from 4000 to 7500 K in intervals of 250 K. We chose values of 0.5, 1, 2, 5, 10, 20, 50, 500 and infinity for the  $^{16}\text{O}/^{18}\text{O}$  ratio. We also introduce an additional parameter  $f_{\text{dust}} = \frac{F_{\text{shell,K}}}{F_{\text{total,K}}}$  to quantify the dust shell contribution to the K-band flux, and vary it between 0 to 0.8 in steps of 0.1.

We fit the synthetic spectra to the continuum normalised NIR spectra in the region 2.26-2.4  $\mu\text{m}$ . For each star, we visually selected the spectra that best fit the data for

each value of  $f_{\text{dust}}$ . We used these fits to derive upper limits on the photospheric temperature and a range of  $O^{16}/O^{18}$  ratios, irrespective of the dust contribution of the star. Figure 2.9 shows the best-fit synthetic spectra together with the continuum normalised NIR spectra. The five RCB stars WISE-J17+, WISE-J18+, WISE-ToI-223, ASAS-RCB-21 and WISE-ToI-268 show the strongest  $^{12}\text{C}^{18}\text{O}$  absorption features. The first three are consistent with having  $^{16}\text{O}/^{18}\text{O}$  in the range 0.5 – 10 while ASAS-RCB-21 and WISE-ToI-268 are consistent with  $^{16}\text{O}/^{18}\text{O}$  in 2 – 50 and 5 – 50 respectively (higher value for higher assumed dust contribution). Using the temperature range for NSV11154 derived in Sec. 2.5, we constrain the  $^{16}\text{O}/^{18}\text{O}$  ratio in the range 10-50. For the remaining stars, the  $^{12}\text{C}^{18}\text{O}$  absorption is weaker. Given the uncertainty in the dust contribution, we cannot put similar constraints on  $^{16}\text{O}/^{18}\text{O}$  of these stars using our medium resolution spectra. For these stars, we only indicate a lower limit on the oxygen isotope ratios from our fits. Table 2.3 lists the derived effective temperature constraints and oxygen isotope ratio ranges. In Section 2.5, we modeled the SEDs of four of the nine stars analysed here (AOHer, NSV11154, WISE-J17+ and ASAS-RCB-21). We note that the temperatures derived from SED modeling are consistent with constraints derived from NIR spectra.

The high  $^{18}\text{O}$  abundances in RCB stars could be key to identifying their formation mechanism. The reaction  $^{14}\text{N}(\alpha, \gamma) \text{F}^{18}(\beta^+ \nu)^{18}\text{O}$  is an important channel for synthesizing  $^{18}\text{O}$ . The cores of intermediate mass stars just before He burning commences can reach the temperatures required for this reaction (Warner 1967; Crawford et al. 2020). However, if a star undergoes a final helium flash, the temperature becomes high enough for all  $^{18}\text{O}$  to be destroyed. The FF scenario is thus unlikely to explain the high  $^{18}\text{O}$  abundances (García-Hernández et al. 2009). On the other hand, dynamically accreting material in mergers of CO-core and He-core white dwarfs can be sites for synthesis of  $^{18}\text{O}$  (Clayton et al. 2007). Jeffery et al. (2011) suggest that even a cold white dwarf merger (i.e., without any nucleosynthesis) could explain large quantities of  $^{18}\text{O}$  in the remnant. These merger models successfully predict the high  $^{12}\text{C}/^{13}\text{C}$  ratio observed for most RCB stars (Asplund et al. 2000). Most RCB stars are thus thought to be formed from the DD channel. García-Hernández et al. (2010) suggest that the DD scenario could link RCB stars with Hydrogen-deficient carbon (HdC) stars. This is supported by the high  $^{18}\text{O}$  abundances measured in HdC stars (Clayton et al. 2005).

There are a few challenges to the DD picture. Lithium has been detected in the spectra of one HdC (Rao et al. 1996) and four RCB stars (Asplund et al. 2000).

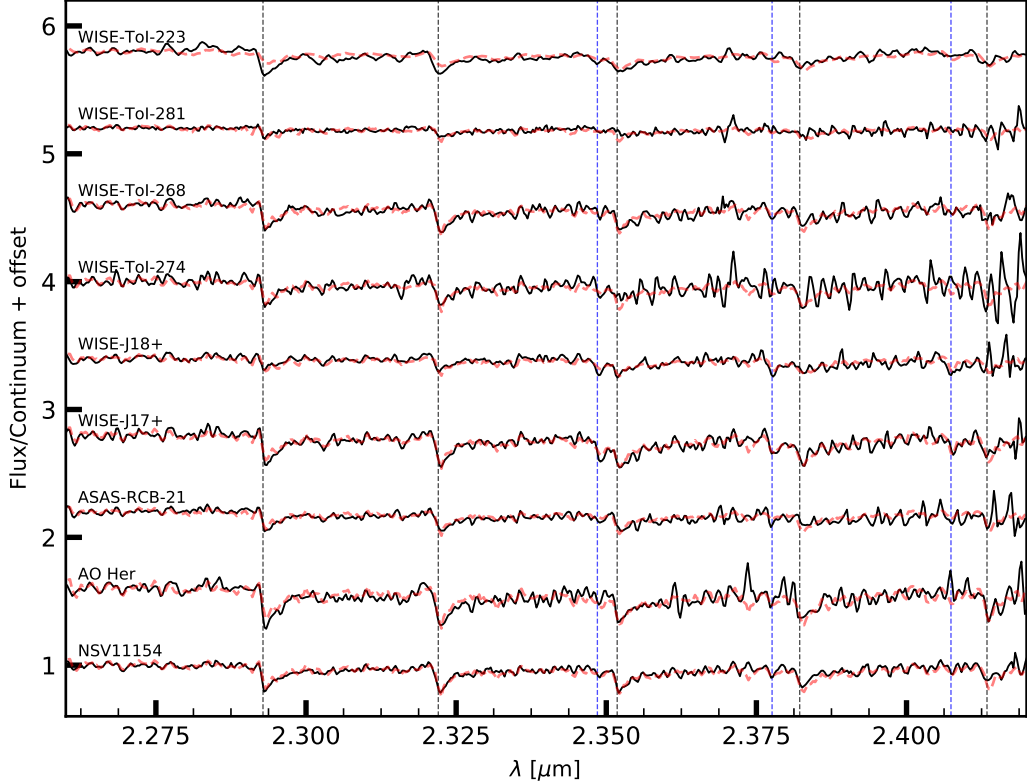


**Figure 2.9: Best-fits to the K band spectra of RCB stars.** The continuum normalised spectra are plotted as black solid lines and the best-fit synthetic spectra are plotted as red dashed lines. We mark the positions of  $^{12}\text{C}^{16}\text{O}$  (black lines) and  $^{12}\text{C}^{18}\text{O}$  (blue lines) absorption bandheads. The derived ranges of best-fit temperatures and oxygen isotope ratios are listed in Table 2.3.

The RCB stars VCrA, V854 Cen, VZ Sgr and UX Ant have a high  $^{13}\text{C}$  abundance (Rao et al. 2008; Hema et al. 2017). The presence of Li and  $^{13}\text{C}$  in these stars was considered to be inconsistent with DD models, and instead favourable for the FF scenario (Asplund et al. 2000; Clayton 2012). However, recently Crawford et al. (2020) showed that it is possible to produce the required Li abundances in WD merger models for specific ranges of Helium burning temperatures. None of these anomalous RCB stars show the CO bandheads, as most of them are warm.

Oxygen isotope ratios have been previously measured for six known Galactic RCB stars and three HdC stars (Clayton et al. 2007; García-Hernández et al. 2009; García-Hernández et al. 2010; Bhowmick et al. 2018). We have reported constraints on the ratios of six more RCB stars and provided lower limits for three RCB stars. Figure 2.10 shows a histogram of  $^{16}\text{O}/^{18}\text{O}$  ratios for all of these RCB stars. We also indicate

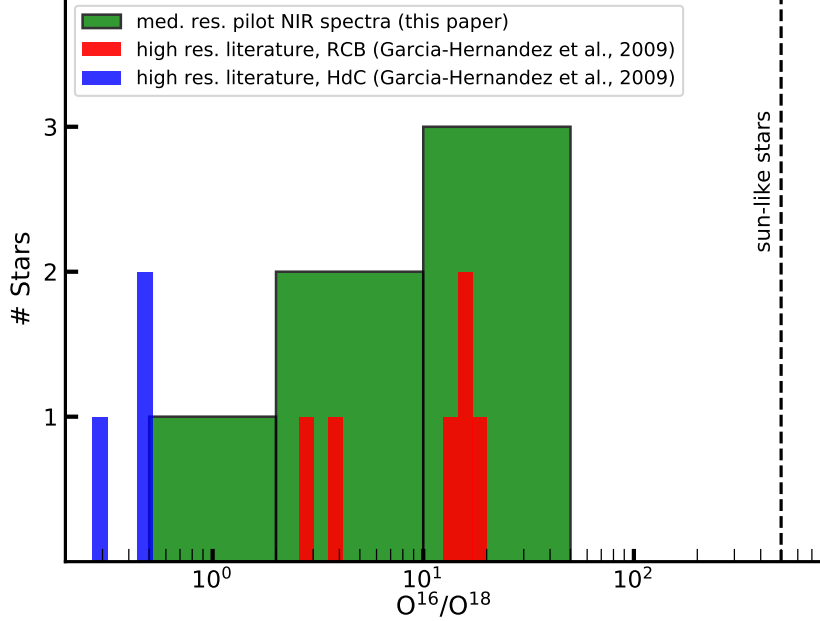


Figure 2.10: **Distribution of  $^{16}\text{O}/^{18}\text{O}$  ratios of RCB and HdC stars.** In red, we plot all 6 previously available measurements of the isotope ratios in RCB stars derived from high resolution spectra García-Hernández et al. (2009). In this paper, we report preliminary constraints on  $^{16}\text{O}/^{18}\text{O}$  for 4 new RCB stars. We indicate these new measurements in green. We note that 5 additional RCB stars reported in this paper show weak  $^{12}\text{C}^{18}\text{O}$  absorption features, and are consistent with  $^{16}\text{O}/^{18}\text{O} > 10$ . In blue, we plot the isotope ratios measured for HdC stars, taken from García-Hernández et al. (2009). The high  $^{18}\text{O}$  content of RCB stars compared to sun-like stars favours a white dwarf merger origin for them. Further NIR spectroscopic observations that populate this diagram will provide additional clues about the formation channels of RCB stars.

ratios for the two HdC stars, and mark the solar  $^{16}\text{O}/^{18}\text{O}$  value. The oxygen isotope ratios in the six RCB stars are at least an order of magnitude lower than the solar value. These stars also do not show any  $^{13}\text{C}^{16}\text{O}$  features, further indicating that they originate in a WD merger. Additional NIR spectroscopic observations that populate this diagram will provide clues the evolutionary channels of RCB stars.

In particular, measuring the isotope ratios for anomalous cold RCB stars will help illuminate the multiple possible channels for RCB-formation.

### Pulsation Periods and effective temperatures

At maximum light, some RCB stars are known to pulsate with periods between 40-100 days and amplitudes of a few magnitudes (Lawson et al. 1997). These pulsations

can be fairly irregular – the star can exhibit multiple pulsation modes or undergo changes in the dominant period. R CrB has shown pulsations with periods of 33, 44, 52 and 60 days (Lawson et al. 1996). Saio (2008) suggest that these semi-regular or irregular pulsations can be explained by the onset of the strange instability in the remnant of a WD merger. They also find that longer period ( $P > 100$  days) non-radial modes could be excited in these stars. Using WD merger models, they find that pulsation periods together with effective temperatures of RCB stars can be indicative of their mass. These values have been measured previously for only three RCB stars – R CrB, RY SGr and UW Cen.

The high cadence PGIR light curves are ideal for identifying maximum-light pulsations in RCB stars. Of the 19 RCB stars analysed in this paper, we can measure pulsations for five – AO Her, NSV11154, V391 Sct, WISE-J18+ and WISE-ToI-8. Four of these are previously known RCB stars but their pulsation periods and temperatures have not been reported. WISE-J18+ has the most well-defined period of 41 days with a Lomb-Scargle (LS) score of 0.4. AO Her shows a period of 56 days (LS score = 0.2), but with significant scatter that could be attributed partly to non-linearity effects in the PGIR detector. For NSV11154, we detect two distinct pulsation modes. The lightcurve shows one full cycle with a period of 96 days (LS score 0.5) followed by another cycle with a period of 48 days (LS score 0.5) and slightly smaller amplitude. It is possible that the first period is an overtone of the second. V391 Sct shows a full cycle with a period of 124 days (LS score = 0.4). WISE-ToI-8 shows a period of 30 days at low significance (LS score = 0.13).

Using our NIR spectra, we have put constraints on effective temperatures of 3 of these stars – AO Her, NSV11154 and WISE-J18+ (Table 2.3). WISE-ToI-8 shows several strong emission lines, suggesting that it has  $T_{\text{eff}} > 10000$ K. Tisserand et al. (2013) suggest that V391 Sct has  $T_{\text{eff}} > 7500$  K based on the presence of metal absorption lines in its spectrum. In Figure 2.11, we plot the periods of these stars against their effective temperatures. This figure is similar to Fig. 32 of Lawson et al. 1990 and Fig. 15 of Rao et al. 2015.

### Dust driven winds in RCB stars

Clayton et al. (2003) showed that most (if not all) RCB stars have winds. These winds are thought to be driven by the dust surrounding the star. RCB stars undergo frequent dust formation episodes (a photometric decline results if dust condenses along the line of sight to the star). Radiation pressure from the star can accelerate

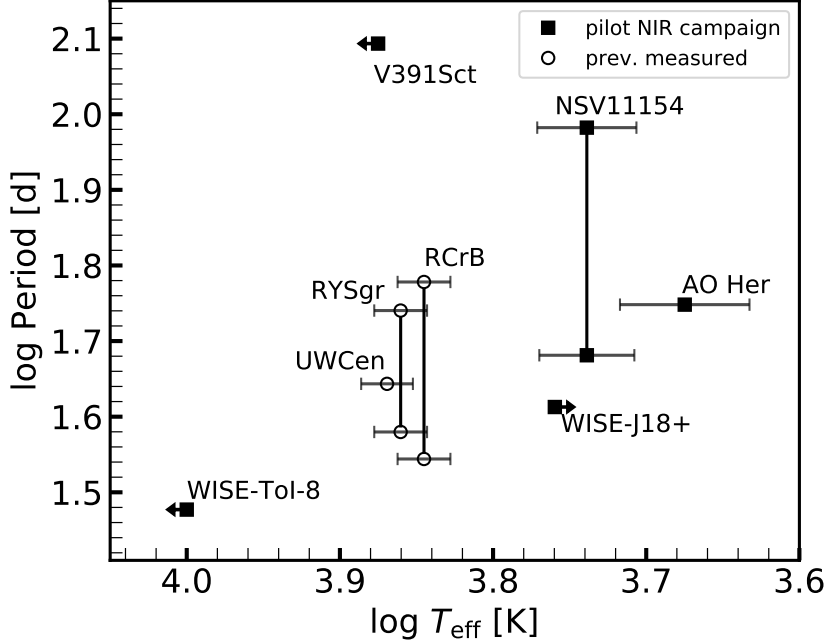


**Figure 2.11: Pulsation periods against effective temperatures for RCB stars.** The hollow circles indicate the 3 previously known positions of RCB stars (R CrB, RY Sgr, UW Cen) in this diagram. The solid circles indicate RCB stars analysed in this paper. The positions of RCB stars in this diagram can be compared to white dwarf merger models to infer the masses of the remnants (cf. Saio 2008).

these dust particles to supersonic velocities. The dust particles drag the gas along with them, giving rise to a wind. Consequently, HdC stars – close relatives of RCB stars that do not undergo major dust formation episodes are not expected to show such winds.

The helium  $\lambda 10830$  line is an important tracer of winds in RCB stars for the following reasons – 1) helium is the most abundant elements in RCB stars, 2) The upper level for this line is 20eV above the ground state, and is thus unlikely to be populated by photospheric radiation of F-G type RCB stars. However, this level can be populated by collisional excitation in high velocity winds around these stars. Clayton et al. (2003) first observed this line and noted its ubiquitous presence in RCB stars in their sample. While some stars show a clear P Cygni profile, most show only a strong blueshifted absorption component, as the emission component is affected by other photospheric absorption. They model these profiles to find wind velocities of 200–350 km·s<sup>-1</sup>, with column densities of 10<sup>12</sup>cm<sup>-2</sup>. Clayton et al. (2013) observed a larger sample and noted that winds are usually strongest when the RCB is undergoing a decline.

Table 2.3: Properties derived from the spectra of RCB stars. The three stars V391 Sct, WISE-ToI-6 and WISE-ToI-1309 do not show strong CO absorption features.

RCB Name	RV <sup>a</sup> km-s <sup>-1</sup>	$T_{\text{eff}}^b$ K	$T_{\text{dust}}^b$ K	$\tau_V^b$	$T_{\text{eff}}^c$ K	$\text{O}^{16}/\text{O}^{18}$ <sup>c</sup>
AO Her	$430 \pm 20$	$4730^{+240}_{-200}$	$830^{+35}_{-45}$	$1.25^{+0.14}_{-0.15}$	< 5750	>10
NSV11154	$260 \pm 20$	$5480^{+140}_{-170}$	$770^{+33}_{-35}$	$0.38^{+0.05}_{-0.04}$	4750–5750	10–50
WISE J17+	$-70 \pm 20$	$4850^{+160}_{-130}$	$830^{+45}_{-60}$	$0.36^{+0.08}_{-0.05}$	< 5750	1–5
ASAS-RCB-21	$-100 \pm 20$	$5790^{+300}_{-390}$	$800^{+25}_{-35}$	$2.10^{+0.16}_{-0.22}$	< 6250	2–50
WISE J19+	$-50 \pm 50$	$5440^{+350}_{-350}$	$920^{+30}_{-50}$	$1.67^{+0.16}_{-0.21}$		
WISE-ToI-1213	$-50 \pm 50$	$4980^{+360}_{-400}$	$790^{+40}_{-60}$	$2.21^{+0.25}_{-0.46}$		
WISE J18+	$-170 \pm 30$				< 6250	0.5–2
WISE-ToI-223	$-100 \pm 50$				4750–5750	2–10
WISE-ToI-268	$-170 \pm 30$				< 6000	5–50
WISE-ToI-274	$-30 \pm 20$				< 6000	>10
WISE-ToI-281	$0 \pm 50$				< 6250	>5
WISE-ToI-1309	$-30 \pm 50$	..	..			
WISE-ToI-6	$0 \pm 50$	..	..			
V391 Sct	$-20 \pm 40$	..	..			

*a* : Radial velocity of the RCB star, rounded to nearest 50 km-s<sup>-1</sup>.

*b* : Quantities derived from modeling of maximum-light SEDs (Sec. 2.5).

*c* : Quantities derived from NIR spectral modeling (Sec. 2.5).

Our NIR spectroscopic campaign is ideal to monitor the HeI  $\lambda 10833$  line in a number of RCB stars in various evolutionary phases. Similar to Clayton et al. (2003) and Clayton et al. (2013), we detect strong HeI features in spectra of all RCB stars analysed in this paper. Of the 19 total RCB stars analysed, 7 are in a deep decline and show the helium line only in emission. As these stars do not have any other spectral features, we cannot measure their radial velocities. We are thus unable to measure wind velocities for these 7 stars. Figure 2.12 shows the line profiles for the remaining 12 RCB stars. We note that some stars show terminal velocities as high as 400–500 km s<sup>-1</sup>. Such high He I velocities were reported previously by Clayton et al. 2013 for some RCB stars in their sample. We will present a detailed analysis of the He I profiles in a future paper.

### Radial Velocities of RCB stars

The distribution of RCB stars and their velocities will shed further light on their formation channels. Of the 19 RCB stars (11 new + 8 previously known) analysed in this paper, we measure radial velocities for eight by cross-correlating the barycentric-

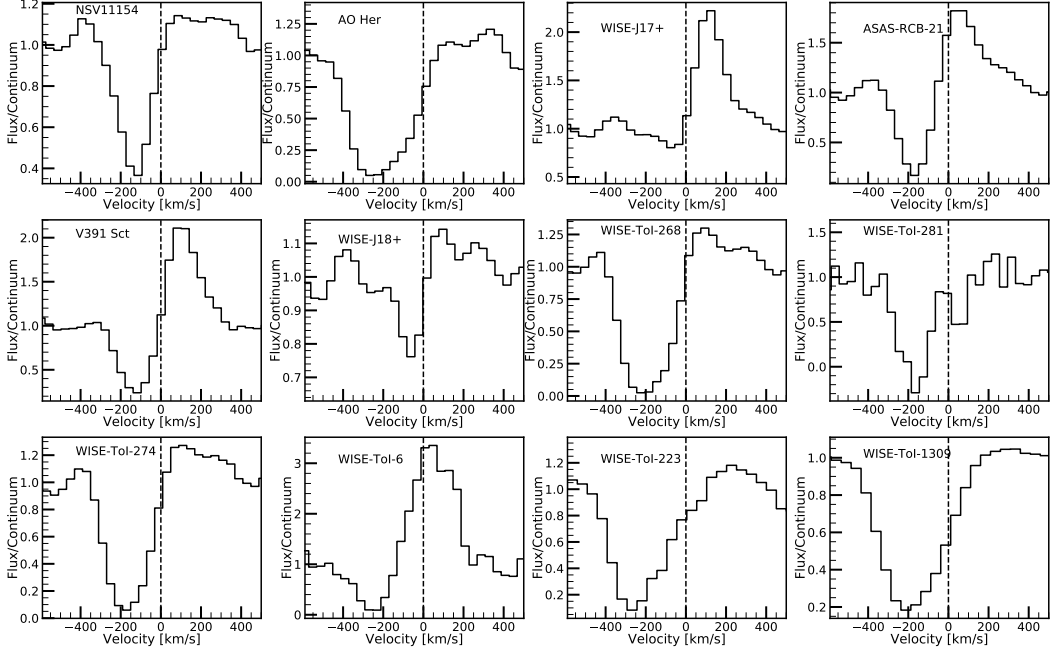


**Figure 2.12:  $\text{He I } \lambda 10830$  line profiles of RCB stars analysed in this paper.** The helium line is an almost ubiquitous feature of RCB stars. This line originates in high velocity winds in the atmospheres of these stars. Some RCB stars show a fully developed P Cygni profile, while some stars show only the blueshifted component. In the latter case, other photospheric absorption reduces the emission component. Here, we have excluded the 7 RCB stars that are in a dust enshrouded dip, as we cannot derive radial velocities for them. These stars show the helium line in emission. The absorption component is absent as almost all the continuum is extinguished due to dust.

velocity corrected J and K band spectral orders separately with synthetic spectra (see Sec. 2.5). Three additional RCB stars were in the decline phase, but show weak C I absorption lines in the J band. We use these lines to measure the radial velocities for these stars. The measured radial velocities are listed in Table 2.3.) Figure 2.13 shows a histogram of the measured velocities. In this figure, we also indicate velocity measurements of other known RCB stars from GAIA DR2. We note that the stars AO Her and NSV11154 have particularly high radial velocities ( $\gtrsim 300 \text{ km s}^{-1}$ ). Such high velocities could be indicative that these stars could be part of a halo population. Additional measurements that probe the velocity distribution of RCB stars will provide better insights about their formation mechanisms.

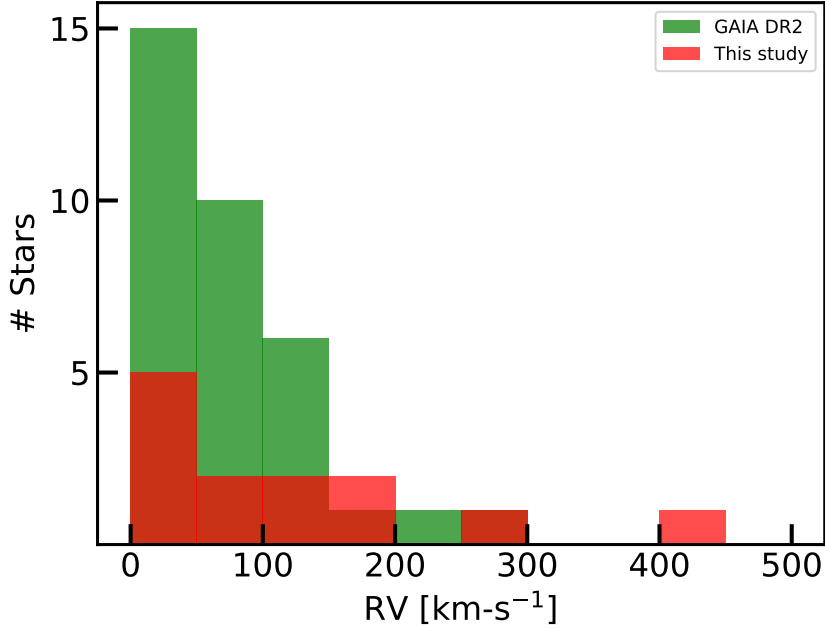


Figure 2.13: **Distribution of the radial velocities of RCB stars.** Previously known velocity measurements from GAIA DR2 are plotted in green and measurements from this study are plotted in red. We note that two RCB stars have very high radial velocities ( $\gtrsim 300$  km/s), which could be indicative of a halo population for these objects.

## 2.6 Summary and way forward

The population of RCB stars in the Milky Way is largely unexplored – only about a third of Galactic RCB stars are currently known. A systematic census of RCB stars is necessary to shed light on the nature of these mysterious objects. Major advances in this direction were made by Tisserand et al. (2020) with a catalog of 2194 WISE sources expected to contain  $\approx 85\%$  of the RCB stars in the Milky Way. In this paper, we used data from Palomar Gattini IR, a J band time domain survey, to prioritise this catalog for spectroscopic followup. 1209 candidates have PGIR coverage, of which 922 are above the sensitivity of PGIR. Based on their light curves, we assigned a “lightcurve-based priority” to each of the 922 candidates. The top priority comprises 149 candidates that show light curves similar to RCB stars. The lowest priority consists of 272 candidates that we classified as long period variables and 23 as RV Tauri stars. Using our lightcurve-based classification, we identified IR color-based criteria that help separate the RCB stars from the LPVs. We then assigned a second “color-based priority” to each of the 2194 candidates in the catalog. These priorities will aid the process of spectroscopic followup and

maximise the yield of RCB stars.

We then obtained NIR spectra for eight known RCB stars and 26 of our top lightcurve-based priority RCB candidates. This was a pilot run for the first NIR spectroscopic campaign to identify RCB stars. We spectroscopically confirmed 11 new RCB stars and analyzed NIR spectral features of these stars. In particular, we report constraints on the effective temperatures and oxygen isotope ratios for these stars. These quantities serve as useful diagnostics about the compositions and formation mechanisms of RCB stars. We derive maximum-light pulsation periods for 5 RCB stars, and plot them in the period-effective temperature space. The position of an RCB star in this phase space can be used to derive the mass of the RCB star. Although the sample analysed in this pilot run is small, it is indicative of the potential of a full NIR spectroscopic campaign for classifying RCB stars.

It is evident that NIR searches promise to be productive in identifying and characterising RCB stars. NIR time domain surveys are particularly well suited to discover highly dust enshrouded RCB stars and those lying in highly extinguished regions of the Galactic Bulge and plane. The lightcurve and color-based priorities identified in this paper will help identify the remaining RCB stars in the Tisserand et al. 2020 catalog. We aim to complete the spectroscopic followup of top candidates in these priority classes. Further observations from PGIR will help improve the lightcurve-based classifications for the (922) bright candidates visible in the northern hemisphere. The successor to PGIR in the northern hemisphere is Wide-field Infrared Transient Explorer (WINTER; Simcoe et al. 2019a), a more sensitive J-band time domain survey (lim.  $J \approx 20$  mag). WINTER will start operating at Mt. Palomar by December 2021, and will help characterise the (287) fainter candidates in the northern hemisphere. The Dynamic Red All-sky Monitoring Survey (DREAMS) survey will be an analog of WINTER in the southern hemisphere at the Siding Springs Observatory. DREAMS will help characterise the 985 candidates that are accessible only from the south. Figure 2.14 shows a schematic of this strategy for our NIR census of RCB stars.

Moreover, systematic blind searches using data from these telescopes will help discover RCB stars outside this catalog. This includes the more exquisite RCB stars with double dust shells around them (Montiel et al. 2018) and DY Per stars – the colder cousins of RCB stars (Bhowmick et al. 2018). The NIR census thus promises to uncover the Galactic RCB population.

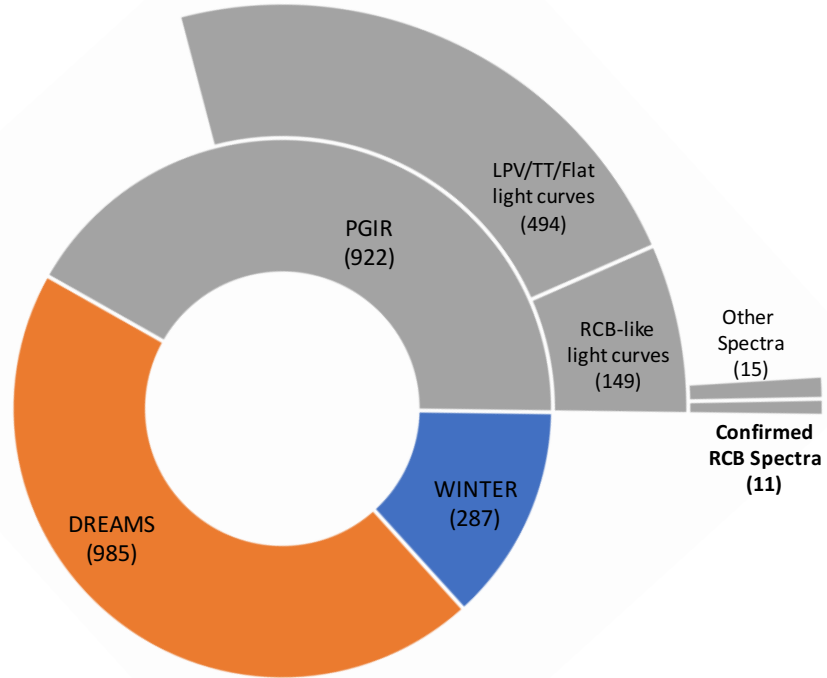


**Figure 2.14: A schematic of our strategy for an NIR survey of Galactic RCB stars** focusing on the Tisserand et al. (2020) catalog. 1209 candidates from this catalog are accessible from the northern hemisphere. Of these, 922 candidates are bright enough to be characterised by PGIR. The remaining 287 fainter candidates will be characterised by WINTER – a deeper ( $J \approx 20$ ) NIR time domain survey starting December 2021. The candidates in the southern hemisphere will be characterised by DREAMS, an analog of WINTER in Australia.

## 2.7 Acknowledgements

We thank our referee, Geoff Clayton, for valuable feedback that improved the manuscript. Palomar Gattini-IR (PGIR) is generously funded by Caltech, Australian National University, the Mt Cuba Foundation, the Heising Simons Foundation, the Bi-national Science Foundation. PGIR is a collaborative project among Caltech, Australian National University, University of New South Wales, Columbia University and the Weizmann Institute of Science. MMK acknowledges generous support from the David and Lucille Packard Foundation. J. Soon acknowledges the support of an Australian Government Research Training Program (RTP) scholarship. Some of the data presented here were obtained with Visiting Astronomer facility at the Infrared Telescope Facility, which is operated by the University of Hawaii under contract 80HQTR19D0030 with the National Aeronautics and Space Administration.

## Chapte r 3

AN INFRARED CENSUS OF R CORONAE BOREALIS STARS II  
 – SPECTROSCOPIC CLASSIFICATIONS AND IMPLICATIONS  
 FOR THE RATE OF LOW-MASS WHITE DWARF MERGERS

Karambelkar, V. R. et al. (Aug. 2024). “An Infrared Census of R Coronae Borealis Stars II—Spectroscopic Classifications and Implications for the Rate of Low-mass White Dwarf Mergers”. In: *PASP* 136.8, 084201, p. 084201. doi: 10.1088/1538-3873/ad6210.

Viraj R. Karambelkar<sup>1</sup>, Mansi M. Kasliwal<sup>1</sup>, Patrick Tisserand<sup>2</sup>, Shreya Anand<sup>1</sup>, Michael C. B. Ashley<sup>3</sup>, Lars Bildsten<sup>4,5</sup>, Geoffrey C. Clayton<sup>6,7</sup>, Courtney C. Crawford<sup>8</sup>, Kishalay De<sup>9</sup>, Nicholas Earley<sup>1</sup>, Matthew J. Hankins<sup>10</sup>, Xander Hall<sup>1</sup>, Astrid Lamberts<sup>11,12</sup>, Ryan M. Lau<sup>13</sup>, Dan McKenna<sup>1</sup>, Anna Moore<sup>14</sup>, Eran O. Ofek<sup>15</sup>, Roger M. Smith<sup>1</sup>, Roberto Soria<sup>16,17,18</sup>, Jamie Soon<sup>14</sup>, Tony Travouillon<sup>14</sup>

<sup>1</sup>Cahill Center for Astrophysics, California Institute of Technology, Pasadena, CA 91125,  
 USA

<sup>2</sup>Sorbonne Université, CNRS, UMR 7095, Institut d’Astrophysique de Paris, 98 bis bd  
 Arago, 75014 Paris, France

<sup>3</sup>School of Physics, University of New South Wales, Sydney, NSW 2052, Australia

<sup>4</sup>Department of Physics, University of California, Santa Barbara, CA 93106, USA

<sup>5</sup>Kavli Institute for Theoretical Physics, University of California, Santa Barbara, CA  
 93106, USA

<sup>6</sup>Department of Physics & Astronomy, Louisiana State University, Baton Rouge, LA  
 70803, USA

<sup>7</sup>Space Science Institute, 4765 Walnut St, Suite B, Boulder, CO 80301, USA

<sup>8</sup>Sydney Institute for Astronomy (SIfA), School of Physics, University of Sydney, Sydney,  
 NSW 2006, Australia

<sup>9</sup>MIT-Kavli Institute for Astrophysics and Space Research, 77 Massachusetts Ave.,  
 Cambridge, MA 02139, USA (NASA Einstein Fellow)

<sup>10</sup>Arkansas Tech University, Russellville, AR 72801, USA

<sup>11</sup>Laboratoire Lagrange, Université Côte d’Azur, Observatoire de la Côte d’Azur, CNRS,  
 Bd de l’Observatoire, 06300 Nice, France

<sup>12</sup>Laboratoire Artemis, Université Côte d’Azur, Observatoire de la Côte d’Azur, CNRS, Bd  
 de l’Observatoire, 06300 Nice, France

<sup>13</sup>NSF's National Optical-Infrared Astronomy Research Laboratory, 950 N. Cherry Ave., Tucson, AZ 85719, USA

<sup>14</sup>Research School of Astronomy and Astrophysics, Australian National University, Canberra, ACT 2611, Australia

<sup>15</sup>Department of Particle Physics and Astrophysics, Weizmann Institute of Science, Rehovot 76100, Israel

<sup>16</sup>College of Astronomy and Space Sciences, University of the Chinese Academy of Sciences, Beijing 100049, China

<sup>17</sup>INAF-Osservatorio Astrofisico di Torino, Strada Osservatorio 20, I-10025 Pino Torinese, Italy

<sup>18</sup>Sydney Institute for Astronomy, School of Physics A28, The University of Sydney, Sydney, NSW 2006, Australia

## Abstract

We present results from a systematic infrared (IR) census of R Coronae Borealis (RCB) stars in the Milky Way, using data from the Palomar Gattini IR (PGIR) survey. R Coronae Borealis stars are dusty, erratic variable stars presumably formed from the merger of a He-core and a CO-core white dwarf (WD). PGIR is a 30 cm *J*-band telescope with a  $25 \text{ deg}^2$  camera that surveys  $18000 \text{ deg}^2$  of the northern sky ( $\delta > -28^\circ$ ) at a cadence of 2 days. Using PGIR *J*-band lightcurves for  $\sim 60$  million stars together with mid-IR colors from WISE, we selected a sample of 530 candidate RCB stars. We obtained near-IR spectra for these candidates and identified 53 RCB stars in our sample. Accounting for our selection criteria, we find that there are a total of  $\approx 350^{+150}_{-100}$  RCB stars in the Milky Way. Assuming typical RCB lifetimes, this corresponds to an RCB formation rate of  $0.8\text{--}5 \times 10^{-3} \text{ yr}^{-1}$ , consistent with observational and theoretical estimates of the He-CO WD merger rate. We searched for quasi-periodic pulsations in the PGIR lightcurves of RCB stars and present pulsation periods for 16 RCB stars. We also examined high-cadenced *TESS* lightcurves for RCB and the chemically similar, but dustless hydrogen-deficient carbon (dLHdC) stars. We find that dLHdC stars show variations on timescales shorter than RCB stars, suggesting that they may have lower masses than RCB stars. Finally, we identified 3 new spectroscopically confirmed and 12 candidate Galactic DY Per type stars — believed to be colder cousins of RCB star — doubling the sample of Galactic DY Per type stars.

### 3.1 Introduction

R Coronae Borealis (RCB) stars are an enigmatic class of stellar variables, notable for extreme brightness variations and peculiar chemical compositions (Clayton 2012). They show deep, rapid declines in their optical brightness ( $\lesssim 9$  mag in  $V$  band), which can last hundreds of days before rising back to their initial state (Clayton 1996). In addition, they have helium-rich atmospheres with an acute deficiency of hydrogen and an overabundance of carbon (Asplund et al. 2000). The chemical compositions of RCB stars point to them being remnants of white dwarf (WD) mergers between a He-WD and a CO-WD (Webbink 1984; Clayton et al. 2005; Clayton et al. 2007), possibly making them low-mass analogs of type Ia supernova progenitors (Fryer et al. 2008). Furthermore, close He-CO WD binaries are expected to be the dominant population of gravitational wave sources detected by LISA (Lamberts et al. 2019). RCB stars represent the fate of this population and can potentially be used to infer the merger rates of these.

RCB stars have several intriguing properties that present challenges to models of stellar evolution. Their photometric declines are the result of mass-loss episodes that produce dust and obscure the star (Clayton et al. 1992). The origin of these mass-loss episodes is still not known. While at maximum light, some RCB stars pulsate with periods between 40–100 days (Lawson et al. 1997), with the pulsation periods likely depending on their effective temperatures ( $T_{\text{eff}}$ ) which range from 4000 – 8000 K (Tisserand et al. 2024b; Crawford et al. 2023). The origin of these pulsations is still not known — they have been attributed either to the strange-mode instability (Saio 2008; Gautschy 2023), or thought to be solar-like oscillations in helium-rich envelopes (Wong et al. 2024).

RCB stars are closely related to the class of dustless Hydrogen-deficient Carbon stars (dLHdC stars, Warner 1967; Tisserand et al. 2022). dLHdC stars have similar chemical compositions to RCB stars, but show no signs of dust-formation. Together, RCB and dLHdC stars constitute the class of Hydrogen-deficient Carbon (HdC) stars. The differences between RCB stars and dLHdC stars have been explored only recently, based on their positions in the HR diagram (Tisserand et al. 2022), their oxygen isotope ratios (Karambelkar et al. 2022), their strontium-abundances (Crawford et al. 2022) and their H and Li content (Crawford et al. 2023). These initial results suggest that RCB stars may be more massive than dLHdC stars. These results are based on small samples of these stars, and it still remains a mystery as to why RCB stars form dust, while dLHdC stars do not.

A third class of stars called DY Per type stars is thought to be a colder sub-class of RCB stars (with  $T_{\text{eff}} \approx 3500$  K), marked by shallower and more symmetric declines in their lightcurves (Alcock et al. 2001). Only 3 DY Per type stars have been confirmed in the Milky Way (Tisserand et al. 2008; Tisserand et al. 2013), while about a dozen have been confirmed in the Magellanic Clouds (Alcock et al. 2001; Tisserand et al. 2004; Tisserand et al. 2009). These stars have a hydrogen-deficiency, a high carbon-abundance (Začs et al. 2007) and have been recently found to have a high  $^{18}\text{O}$  abundance (Bhowmick et al. 2018; García-Hernández et al. 2023) — resembling RCB stars. On the other hand, their luminosities and infrared colors are very similar to cool N-type carbon stars and differ significantly from RCB stars (Alcock et al. 2001; Soszyński et al. 2009; Tisserand et al. 2009). It is debated whether DY Per type stars are colder RCB stars originating in WD mergers, or classical carbon stars undergoing strong dust-formation.

When RCB stars are enshrouded by dust, they appear brighter at infrared wavelengths than the optical (Feast 1997). The photometric declines are also shallower in the infrared ( $\lesssim 3$  mag in  $J$ -band) than in the optical (Karambelkar et al. 2021). Despite this, most previous searches for RCB stars have focused on optical surveys such as MACHO (Alcock et al. 2001; Zaniewski et al. 2005), OGLE (Tisserand et al. 2011), EROS-2 (Tisserand et al. 2004; Tisserand et al. 2008; Tisserand et al. 2009), the Catalina Survey (Lee 2015), All Sky Automated Survey for Supernovae (ASASSN, Tisserand et al. 2013; Shields et al. 2019; Otero et al. 2014), the Palomar Transient Facility (Tang et al. 2013) and the Zwicky Transient Facility (Lee et al. 2020).

The first IR-search for RCB stars was carried out by Tisserand (2012), who used WISE and 2MASS colors to publish a list of RCB candidates. Tisserand et al. (2020) subsequently refined the selection criteria and published a catalog of 2356 RCB candidates and 40 new RCB stars confirmed via optical spectroscopy, suggesting that there are 300 – 500 RCB stars in the Milky Way. In our previous paper (Karambelkar et al. 2021), near-IR (NIR)  $J$ -band lightcurves from Palomar Gattini IR (De et al. 2020a) together with WISE colors yielded 394 promising candidates for spectroscopic follow-up. Using NIR spectra for a 26 of these, 11 new RCB stars were presented.

In this paper, we complete the NIR census of RCB stars and present NIR spectra (1– $2.4\ \mu\text{m}$ ) of the full sample of RCB candidates listed in Karambelkar et al. (2021). Additionally, we conduct a WISE-color independent search for RCB stars using PGIR lightcurves to find RCB stars missed by the color-selection criteria. We also

use the PGIR lightcurves to search for new DY Per type stars in the Milky Way. We describe our candidate selection criteria in Section 3.2, the NIR spectroscopic observations in Section 3.3 and the classifications in Section 3.4. We use this complete census of RCB stars to derive the total number of RCB stars expected in the Milky Way and infer the rate of He and CO white dwarf mergers in Section 3.5. We use the NIR spectra and lightcurves to measure their radial velocities, their positions in the color-magnitude diagram and pulsation periods. We also examine high cadenced *TESS* lightcurves of a sample of RCB and dLHdC stars. We conclude with a summary of our results in Section 3.6

### 3.2 Candidate selection

#### IR color + PGIR lightcurve-based selection

Our candidate selection is described in detail in Karambelkar et al. (2021). Briefly, we re-prioritize the WISE color-selected catalog of 2194 RCB candidates from Tisserand et al. (2020) (T20 catalog hereafter) using PGIR light-curves. First, we exclude 304 candidates that show large-amplitude periodic variations resembling AGB stars and 23 candidates whose lightcurves resemble those of RV-Tauri stars. Of the remaining candidates, we identify 177 candidates that show significant, non-periodic variations in their lightcurves, 230 candidates that show no significant variations and 253 candidates where the lightcurve is ambiguous (i.e. shows some variations that are not obviously periodic or large-amplitude). Using the location of known RCBs and LPVs in the WISE and 2MASS color diagrams, we further subdivide Priorities A, B, C and D into seven color-based sub-categories. We prioritize categories A, 1-a, 2-a and 3-a comprising 383 candidates in total for spectroscopic follow-up.

The top panel of Fig. 3.1 shows a table with the distribution of candidates in these categories. This table differs slightly from the one presented in Karambelkar et al. (2021), as we updated the lightcurve-based priorities based on more recent PGIR *J*-band lightcurves with additional  $\approx 1.5$  years of data. The categories prioritized for NIR spectroscopic followup are marked in green. We also indicate the number of candidates for which we obtained NIR spectra in each category, and the number of RCB stars spectroscopically confirmed within each category (by red numbers). The bottom panel of Fig. 3.1 shows a pie-chart with the spectroscopic classifications of all sources we observed (discussed in Sec. 3.4.)

As the color-criteria were chosen to search for RCB stars, we do not expect to find

any DY Per type stars in this category.

### Color independent PGIR lightcurve-based selection

To search for possible RCB stars missed by the T20 color-selected catalog, we searched for RCB stars in the PGIR lightcurve database, independent of any color-criteria. The PGIR lightcurve database contains aperture-photometry lightcurves spanning June 2018 to July 2021 for  $\sim$ 70 million stars that were detected in the PGIR reference images. We search for stars that show RCB-like large-amplitude, erratic variations in their PGIR lightcurves. Unfortunately, the completeness of the lightcurve database is not well-quantified, especially in dense Galactic fields that are limited by confusion noise. Therefore, we cannot use this lightcurve-selection alone for a systematic RCB search. Instead, we use this to search for possible populations of RCB stars missing from the T20 catalog.

For each lightcurve in the PGIR database, we calculate the von-neumann ratio ( $\eta$ , Neumann 1941) and peak-to-peak amplitude (ptp).  $\eta$  measures the degree of correlation between successive data-points in the lightcurve, and is well-suited to identify stars showing large-amplitude variations. Non-variable stars are expected to have  $\eta$  close to 2, while smaller  $\eta$  values suggest significant correlations in successive variations. We select 1200 stars with  $\eta < 0.5$  and  $\text{ptp} > 2.5$  mag (informed by known RCB stars). We then inspect their lightcurves to reject periodic variability and select 75 stars that show large-amplitude variations and are not present in the color-selected T20 catalog for further spectroscopic follow-up. As no color-information was used in the selection, we expect to find both RCB and DY Per type stars in this category. The spectroscopic classifications of all 75 variables will be presented in a forthcoming paper (Earley et al., in prep). Here, we focus on RCB and DY Per type stars found within these sources.

### PGIR lightcurves of known carbon-stars

As RCB stars have spectral features resembling carbon stars, we examined PGIR-J band lightcurves for 9975 stars classified as “carbon-star” or “candidate carbon stars” on Simbad, to search for RCB-like variations in them. We were not able to obtain NIR spectra for interesting stars identified in this category. For this reason, we report them as candidate RCB and DY Per type stars in Section 3.4, pending spectroscopic confirmation.

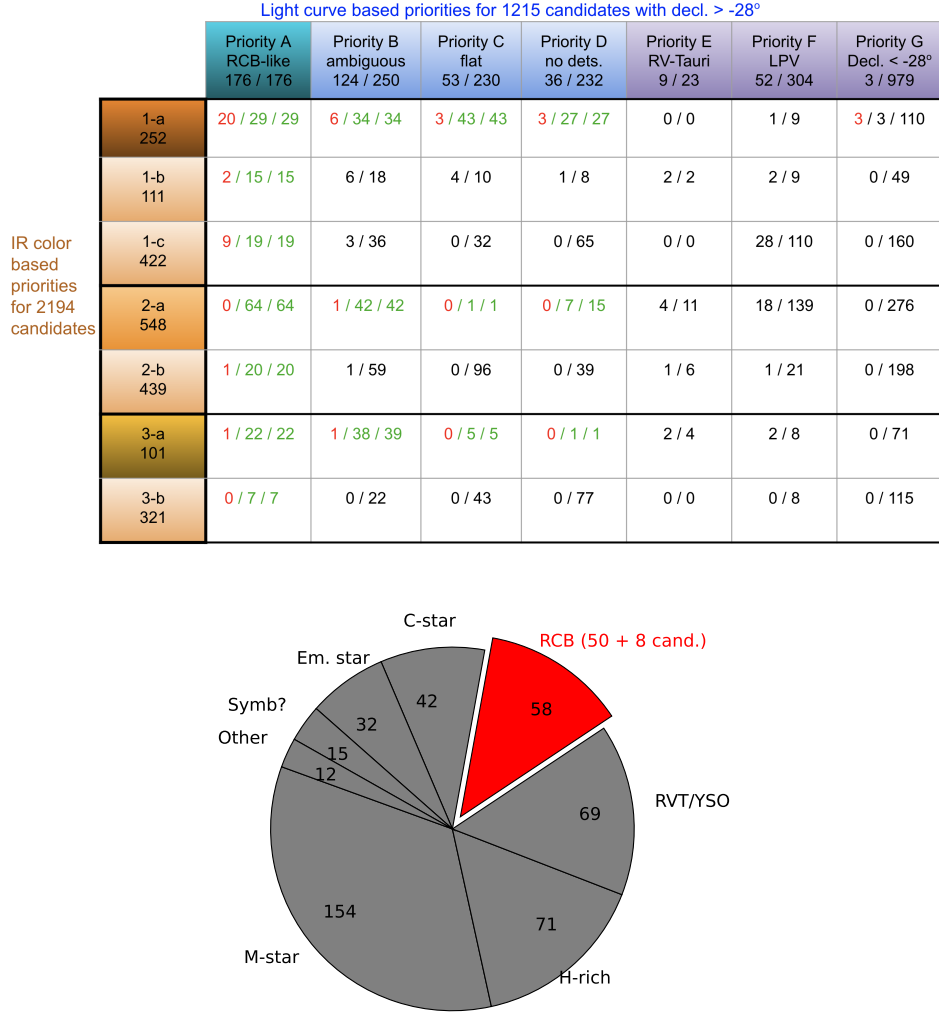


Figure 3.1: (Top:) **Lightcurve and color-based priorities for RCB candidates** (updated from Karambelkar et al. (2021) using more recent PGIR lightcurves). The categories prioritized for spectroscopic follow-up are numbered in green. In each category, we indicate the total number of candidates and the number of candidates for which we obtained NIR spectra. We also indicate the number of RCB stars identified in each category in red. We obtained NIR spectra for a total of 453 candidates. 375 of the 383 prioritized candidates have NIR spectra, corresponding to an overall completeness of  $\approx 98\%$ . 3 candidates from Priority G (decl.  $< -28^\circ$ ) were observed spectroscopically because they were listed as strong RCB candidates in T20. (Bottom:) Pie-chart showing our NIR spectroscopic classifications of all 453 stars.

Table 3.1: Updated priorities of WISE-selected candidates based on PGIR lightcurves (full table available online, see Sec. 3.8)

ToI-ID	RA	Dec	Priority
	deg	deg	
23	37.5679	12.28989	A
..			

Table 3.2: Spectroscopic classifications of candidates selected for followup (full table available online, see Sec. 3.8)

ToI-ID	RA	Dec	Class.	Date	Inst.
	deg	deg			
23	37.5679	12.28989	RV-Tauri		
..					

### 3.3 NIR Spectroscopic observations

We obtained medium resolution NIR spectra for a total of 453 of our color-selected candidates from the T20 catalog. This includes 375 of the 383 prioritized candidates described in Section 2.1, and 81 stars from the other priorities. All but 3 observed candidates have declination  $> -28^\circ$ . These 3 candidates belong to Priority G and were observed because they were listed as strong RCB candidates in T20. Fig. 3.1 shows the priority-wise distribution of stars for which we obtained NIR spectra.

The NIR spectra were obtained on several nights from October 2019 to December 2021 with the Triplespec spectrograph ( $R \approx 2700$ , Herter et al. 2008) on the 200-inch Hale telescope at Palomar Observatory and the SpeX spectrograph ( $R \approx 1500$ ) on the NASA Infrared Telescope Facility (IRTF, Rayner et al. 2003). The IRTF spectra were observed as part of programs 2020A111 and 2021B074. We obtained a total of 389 spectra with P200/Triplespec and 69 spectra with IRTF/SPeX. All spectra were extracted using the IDL package `spextool` (Cushing et al. 2004). The extracted spectra were flux calibrated and corrected for telluric absorption with standard star observations using `xtellcor` (Vacca et al. 2003).

### 3.4 NIR spectroscopic classifications

We classify the 453 sources using their spectra and lightcurves. We find that these sources include a mix of RCB stars, Mira variables, carbon-rich (C-rich) AGB stars, RV Tauri stars, possible giant stars in symbiotic binaries, possible young

stellar objects (YSOs) and Wolf-Rayet (WR) stars. The bottom panel of Fig. 3.1 shows the distribution of the source classifications. We discuss the classifications and properties of these sources in Appendix 3.10. Here, we focus on the sources classified as RCB stars.

As discussed in Karambelkar et al. (2021), RCB stars are characterised by the following NIR spectral features :

- RCB stars show He I ( $\lambda 10830$ ) emission or absorption. The RCB stars undergoing a photometric minimum usually show He I emission, however this can be suppressed by the circumstellar dust. The stars at or rising to maximum light show either a P-cygni profile or strong blueshifted absorption.
- RCB stars in a minimum exhibit a mostly featureless, reddened spectrum with emission lines of He I, and sometimes Si I and C<sub>2</sub>.
- At maximum light, the spectra of RCB stars resemble F-G type supergiants, with the absence or significantly weak hydrogen lines. Prominent features include absorption lines of C I (most prominently at 1.0686 and 1.0688 $\mu\text{m}$ ), Fe I, Si I and K I. Stars with cold effective ( $T_{\text{eff}} \leq 6800$  K) temperatures show molecular absorption features due to CN (1.0875, 1.0929, 1.0966 and 1.0999 $\mu\text{m}$ ), <sup>12</sup>C<sup>16</sup>O (2.2935, 2.3227, 2.3525, 2.3829, 2.4141 $\mu\text{m}$ ) and <sup>12</sup>C<sup>18</sup>O.

### IR color + PGIR lightcurve - based selection

We examine our spectra and identify 74 stars that show some or all of the spectroscopic features described above. In cases where the spectra are not sufficient to determine a robust classification, we examine the lightcurves. We mainly use the PGIR *J*-band light-curves, and also examine publicly available optical light-curves from the Zwicky Transient Facility (ZTF, Bellm et al. 2019a) and ATLAS (Tonry et al. 2018; Smith et al. 2020a) surveys to search for large amplitude variations. RCB stars can also show large amplitude variations at mid-IR wavelengths due to dust formation episodes. To search for these, we use publicly available 3.6 and 4.5  $\mu\text{m}$  data from the NEOWISE survey.

First, we classified 11 of these stars as RCBs in Karambelkar et al. (2021). Of the remaining stars, 27 show RCB-like variations in the PGIR *J*-band data. We classify 26 of these as RCB stars, as the NIR spectral features are consistent with the photometric phases as suggested by the light curve. The last one — WISE-ToI-1007 shows large amplitude RCB-like variations, but does not show He I in its spectrum.

As the spectrum otherwise resembles that of a carbon-star, and we suggest that this is a dust-forming carbon star and not an RCB.

26 stars do not show any large amplitude variations in PGIR data, but have spectra with features seen in those of RCB stars. Of these, we classify 8 stars as RCB stars because their spectra very closely resemble RCB stars that haven't undergone photometric declines in a long time, or the ZTF, ATLAS or NEOWISE lightcurves show clear evidence of declines or variability in the past. Of the remaining 18 sources, the spectra of 8 show strong He emission — unlike RCB stars that haven't undergone a large-amplitude photometric decline in a long time. The ZTF and ATLAS light-curves of these 8 stars show pulsations on timescales of  $\sim$ 10–100 days superposed on smooth longer-timescale variations, similar to those seen in RV-Tauri stars<sup>1</sup>. These 8 stars are most likely RV-Tauri stars. Of these, we highlight the source WISE-ToI-3012, as it shows a slow rise in the optical and NIR wavelengths for the last 2000 days, and shows a large amplitude dip in the NEOWISE data. The 10 remaining stars have spectra with low S/N and no conclusive features in their lightcurves to enable a confident classification. 5 of these stars show strong He emission and some strong narrow H emission lines in their spectra, suggesting that they are likely RV-Tauri stars. We list the remaining 5 — WISE-ToI-28, 41, 228, 293 and 1257 as candidate RCB stars. WISE-ToI-28 shows uncharacteristically large helium emission, but also shows periodic 1 mag variations in NEOWISE. WISE-ToI-293 shows a short timescale decline in ZTF data. WISE-ToI-41 shows weak He emission and erratic NEOWISE variations. WISE-ToI-1257 shows a steep rising red continuum with small variations in the *J*-band.

7 stars have no detections in the PGIR data: WISE-ToI-195, 270, 245, 288, 317, 321 and 323. Their spectra show the helium emission line. No strong hydrogen features are evident, but we cannot rule out their presence as the spectra have low S/N. Of the seven, WISE-ToI-195 and WISE-ToI-270 show RCB-like declines in their ZTF lightcurves. We classify these two as RCB stars. WISE-ToI-317 and 321 do not show any significant declines in their ZTF and ATLAS lightcurves. These two stars have distance estimates from *Gaia* (Bailer-Jones et al. 2018) which suggest that their absolute magnitudes are  $M_r \approx 4.1$  and 1.8 mag, respectively — inconsistent with them being RCB stars. For this reason, we exclude them as RCB stars<sup>2</sup>. The

---

<sup>1</sup>[https://ogle.astrouw.edu.pl/atlas/RV\\_Tau.html](https://ogle.astrouw.edu.pl/atlas/RV_Tau.html)

<sup>2</sup>We note that the significance of the *Gaia* parallax measurement for WISE-ToI-317 is low ( $\text{Plx}/e_{\text{Plx}} = 2.9$ ). Nevertheless, there is no compelling evidence, so we do not classify this as an RCB star.

remaining three — WISE-ToI-245, 288 and 323 do not show any declines in their ZTF and ATLAS lightcurves, and do not have any additional information from Gaia. We list these three as strong RCB candidates.

Finally, we observed 3 stars — WISE-ToI-164, 181 and 264 — that lie outside the area covered by PGIR (i.e. have  $\delta < -28^\circ$  and belong to Priority G), but are listed as strong RCB candidates in Tisserand et al. (2020). Our NIR spectra confirm that they are RCB stars.

To summarize, we identify a total of 50 RCB stars and 8 strong RCB candidates using the PGIR-lightcurve-based prioritization of the T20 catalog. We note that of the 50 RCB stars, 19 were identified previously as RCB stars from their optical spectra by Tisserand et al. (2020). Our NIR spectra independently confirm their nature as RCBs. 6 additional RCB stars were listed as strong candidates by Tisserand et al. (2020), which we unambiguously classify as RCB stars based on their NIR spectra. Two stars WISE-ToI-185 and WISE-ToI-226 were listed as a potential RCBs based on their optical lightcurves by Eyer et al. (2023) and Maíz Apellániz et al. (2023), respectively, and are now spectroscopically classified as RCBs based on our NIR spectra. All 50 RCB stars identified or confirmed by our NIR spectra are listed in Table 3.3 and 3.4. The PGIR lightcurves of the 45 RCB stars that have PGIR detections are plotted in Figures 3.2, 3.3. The NIR spectra of all 50 RCB stars are plotted in Figures 3.4 and 3.5. The 8 strong RCB candidates are listed in Table 3.8, and their lightcurves and spectra are shown in Fig. 3.11.

### Color-independent, PGIR lightcurve-only selection

#### New RCB stars

Of the 75 lightcurve-selected candidates, we identify 2 new RCB stars PGIRV663-2-3-2970 (PGIRV663 hereafter) and PGIRV526-1-0-2033 (PGIRV526 hereafter). Their lightcurves and spectra are included in Fig. 3.3 and 3.5, respectively. The *J*-band lightcurves of both these stars shows a slow rise of  $\approx 3$  mag over 1500 days. The ZTF lightcurve of PGIRV663 shows a 2 mag. decline, 1700 days prior to the epoch of our NIR spectrum. Based on the ZTF lightcurve, this candidate was flagged as a possible RCB star on AAVSO by G. Murakawski. The NIR spectra of both stars are similar to RCB stars that are recovering from a photometric decline, consistent with their lightcurves. Both stars have WISE and 2MASS detections, but were missed by the color-selection criteria of Tisserand et al. (2020). PGIRV526 has  $W2 - W3 = 0.85$  — failing the criterion  $W2 - W3 > 1.1$  mag, suggesting that it

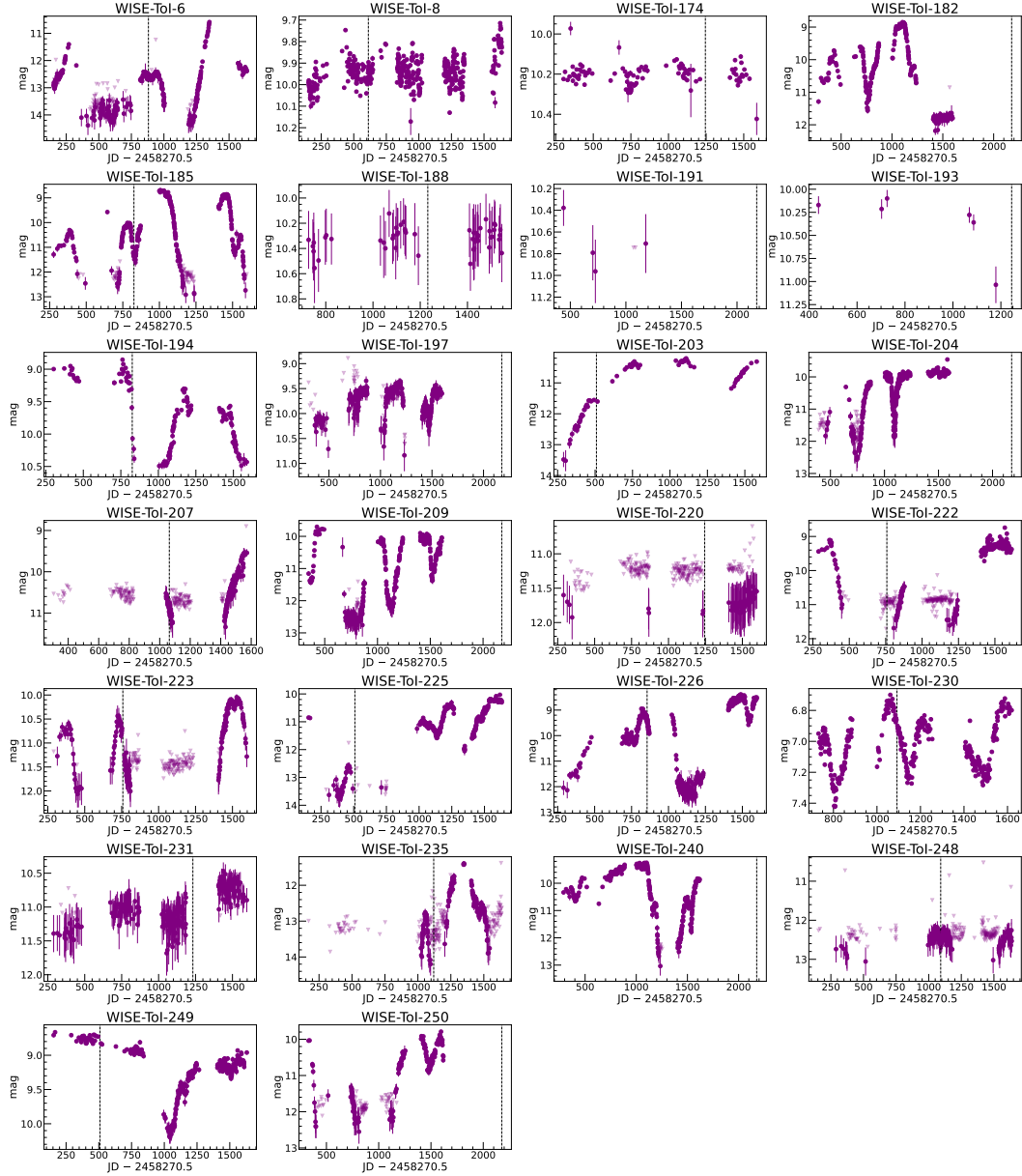


**Figure 3.2: PGIR *J*-band lightcurves of new RCB stars.** Circles denote detections, while triangles denote upper limits (continued in Fig. 3.3). The dotted black vertical line marks the epoch when the NIR spectrum was obtained.

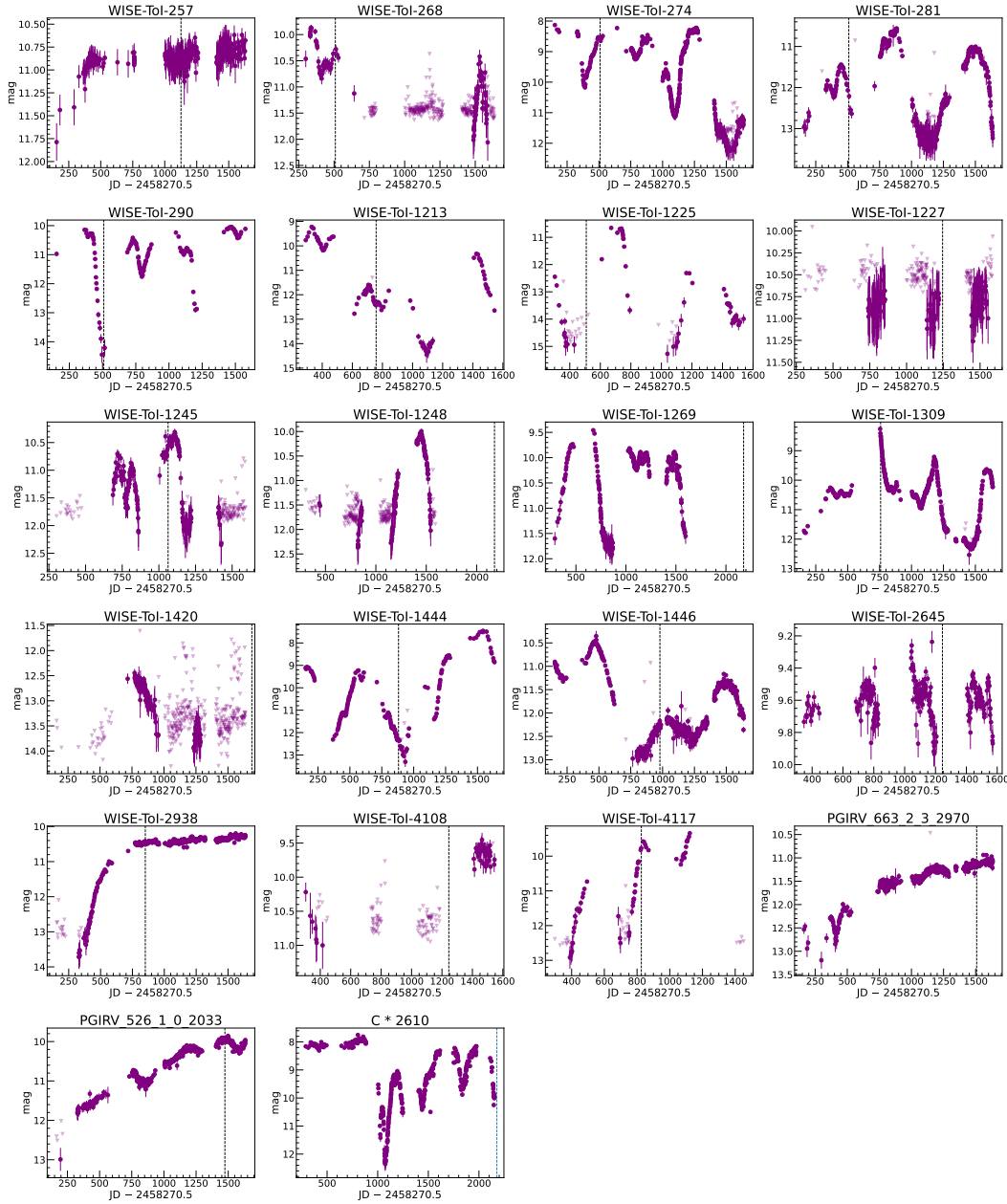


**Figure 3.3: PGIR *J*-band lightcurves of new RCB stars (continued from Figure 3.2).**

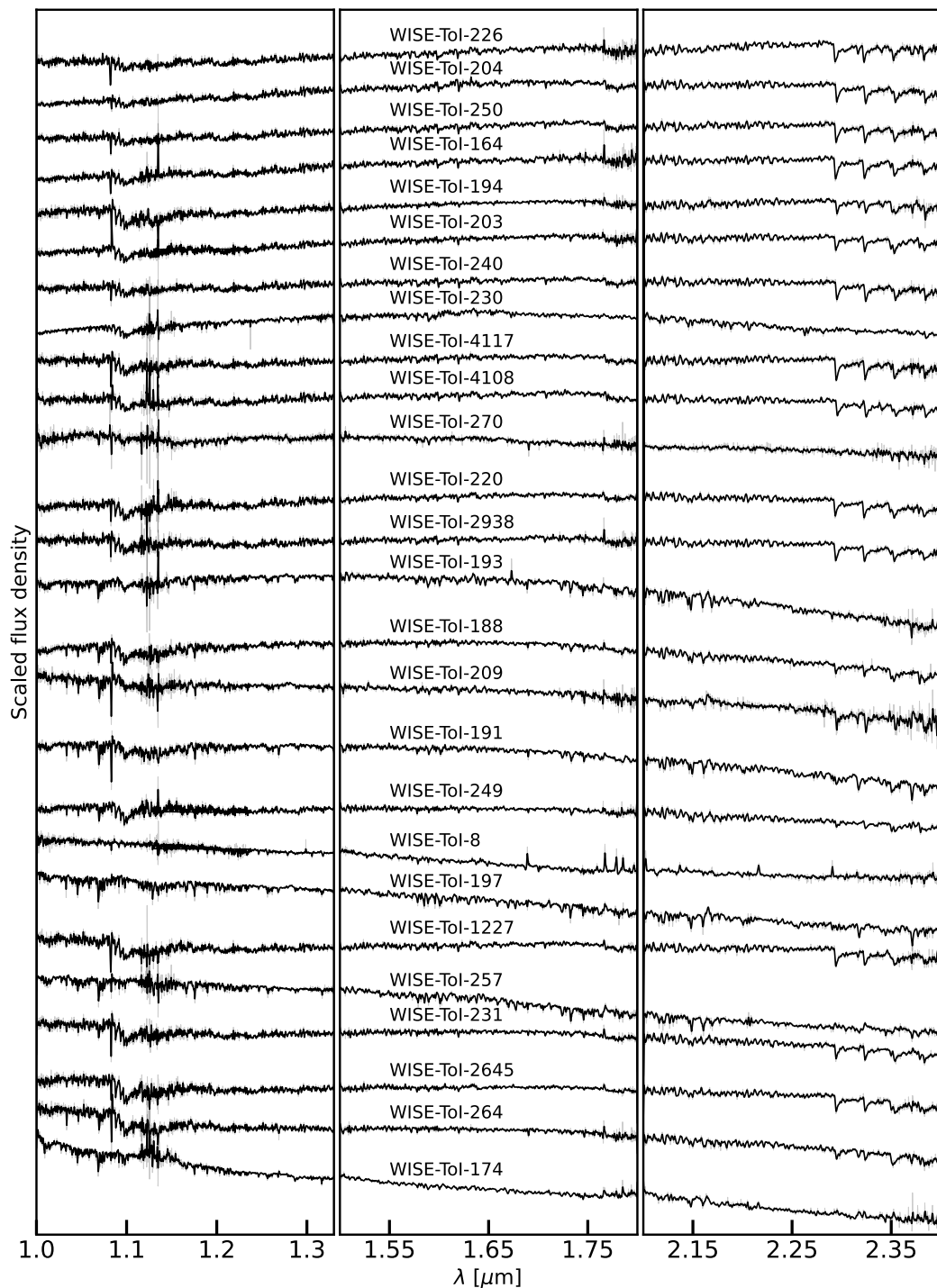


Figure 3.4: **NIR spectra of new RCB stars.**

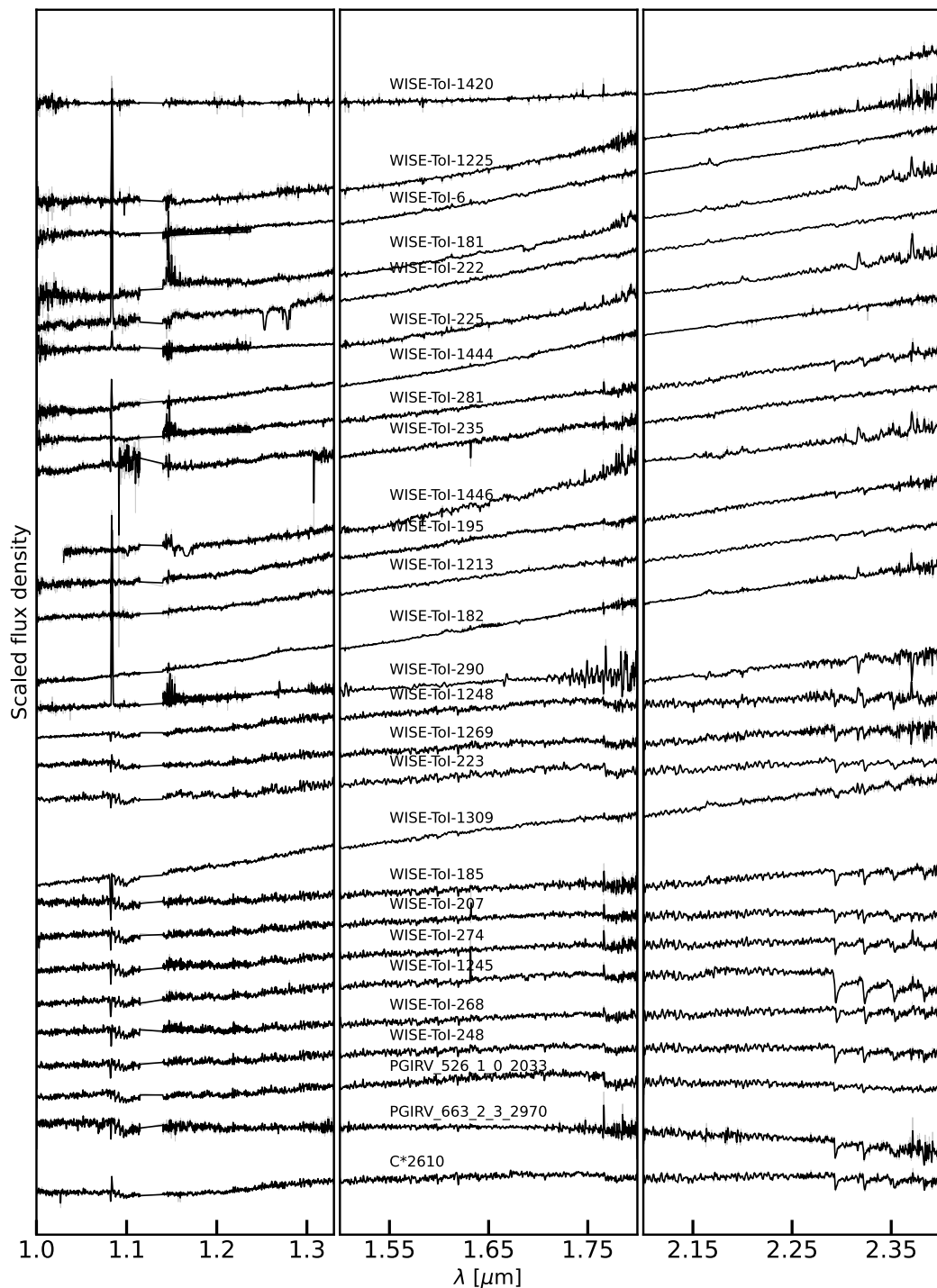
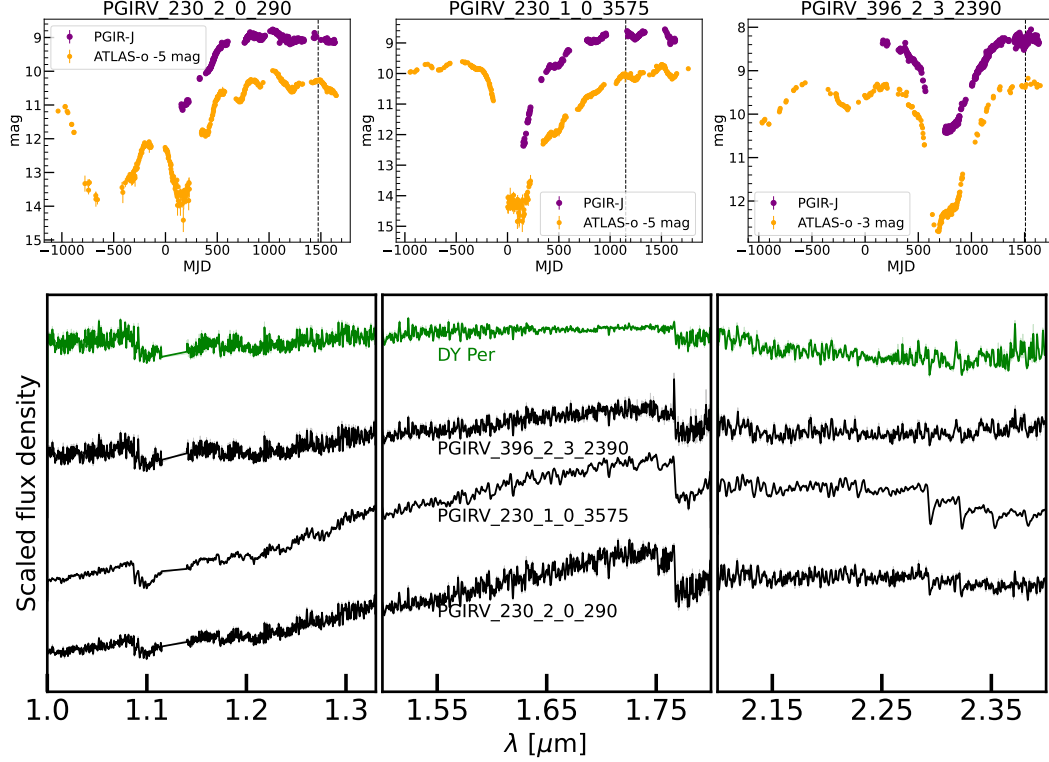


Figure 3.5: NIR spectra of new RCB stars (continued from Fig. 3.4).



**Figure 3.6: Lightcurves and spectra of new DYPer type stars.** *Top:* Lightcurves of new DYPer type stars. Purple dots show the PGIR data and orange dots show the shifted ATLAS-o band data. *Bottom:* NIR spectra of the new DYPer type stars (black) and DY Per itself (green). The spectra of the new stars closely resemble that of DY Per and N-type carbon stars.

has hot dust ( $T > 1000$  K) around it. PGIRV663 has  $J - H = 0.70$  and  $H - K = 0.43$  mag, failing the criterion  $J - H < (H - K) + 0.2$  — suggesting that it is a warm RCB star with a thin dust shell.

### New DY Per type stars

DY Per type stars are thought to be a colder sub-class of RCB stars (with  $T_{\text{eff}} \approx 3500$  K), marked by shallower and more symmetric declines in their lightcurves than RCB stars (Alcock et al. 2001). From our PGIR lightcurve-selected candidates, we identified three stars that show lightcurves and spectra resembling DY Per type stars. Fig. 3.6 show the PGIR-J band and ATLAS-o band lightcurves of these stars. For two of them, the PGIR lightcurves sample only the rise out of the decline, but the longer baseline ATLAS lightcurves show DY Per-like variations. The NIR spectra of these stars very closely resemble N-type carbon star templates from the IRTF

Table 3.3: RCB and DY Per stars identified/confirmed from our NIR census (continued in Table 3.4)

Name	ToI-ID/ PGIR Name	RA deg	Dec deg	NIR spec. class	Comments
WISE J174317.52-182402.4	185	265.82303	-18.40068	RCB	a
WISE J175317.73-194632.5	195	268.32389	-19.77572	RCB	
WISE J182501.85-230803.9	226	276.25772	-23.13444	RCB	b
WISE J182801.05-100916.7	230	277.00438	-10.15464	RCB	
WISE J183213.53+050454.5	235	278.05638	5.08181	RCB	
WISE J184102.48-004136.3	248	280.26034	-0.69344	RCB	
WISE J190918.81+030531.2	270	287.32838	3.09201	RCB	
WISE J175725.03-230426.4	1245	269.35429	-23.07402	RCB	
WISE J180021.11-232202.9	1248	270.08797	-23.36749	RCB	
WISE J203825.90+514140.7	1420	309.60795	51.69464	RCB	
WISE J221558.89+422246.2	1444	333.99538	42.37950	RCB	
WISE J223517.61+593812.7	1446	338.82341	59.63688	RCB	
WISE J202514.28+472731.5	2938	306.30950	47.45877	RCB	
WISE J181706.84-235751.3	4108	274.27851	-23.96426	RCB	h
WISE J175136.80-220630.6	194	267.90335	-22.10852	RCB	c
WISE J180313.12-251330.1	207	270.80467	-25.22505	RCB	c
WISE J183631.25-205915.1	4117	279.13024	-20.98755	RCB	c
WISE J172044.89-315031.7	164	260.18707	-31.84215	RCB	c, g
WISE J173837.00-281734.5	181	264.65417	-28.29292	RCB	c, g
WISE J190309.89-302037.1	264	285.79123	-30.34365	RCB	c, g
WISE J004822.34+741757.4	6	12.09309	74.29928	RCB	e
WISE J005128.08+645651.7	8	12.86702	64.94770	RCB	e
WISE J175749.76-075314.9	203	269.45737	-7.88750	RCB	d, e
WISE J181836.38-181732.8	222	274.65160	-18.29247	RCB	e
WISE J182010.96-193453.4	223	275.04570	-19.58150	RCB	e
WISE J182235.25-033213.2	225	275.64690	-3.53701	RCB	e
WISE J184158.40-054819.2	249	280.49336	-5.80535	RCB	d, e
WISE J190813.12+042154.1	268	287.05469	4.36503	RCB	e
WISE J191243.06+055313.1	274	288.17945	5.88698	RCB	e
WISE J192348.98+161433.7	281	290.95410	16.24270	RCB	e
WISE J194218.38-203247.5	290	295.57660	-20.54654	RCB	d, e
WISE J170552.81-163416.5	1213	256.47005	-16.57125	RCB	e
WISE J173737.07-072828.1	1225	264.40446	-7.47449	RCB	e
WISE J185726.40+134909.4	1309	284.36004	13.81930	RCB	e
WISE J172951.80-101715.9	174	262.46586	-10.28778	RCB	d
WISE J174645.90-250314.1	188	266.69128	-25.05392	RCB	d
WISE J175107.12-242357.3	193	267.77967	-24.39927	RCB	d
WISE J181538.25-203845.7	220	273.90938	-20.64604	RCB	d
WISE J182943.83-190246.2	231	277.43263	-19.04617	RCB	d
WISE J185525.52-025145.7	257	283.85636	-2.86271	RCB	d
WISE J173819.81-203632.1	1227	264.58255	-20.60893	RCB	d
WISE J181252.50-233304.4	2645	273.21875	-23.55124	RCB	d
WISE J182723.38-200830.1	1269	276.84744	-20.14172	RCB	d
WISE J180550.49-151301.7	209	271.46038	-15.21714	RCB	d
WISE J175558.51-164744.3	197	268.99382	-16.79565	RCB	d
WISE J175749.98-182522.8	204	269.45827	-18.42300	RCB	d
WISE J175031.70-233945.7	191	267.63210	-23.66270	RCB	d

a : Listed as a RCB candidate based on the *Gaia* lightcurve by Eyer et al. (2023). b : Listed as a RCB candidate based on its lightcurve by Maíz Apellániz et al. (2023). c : Listed as strong RCB candidates by Tisserand et al. (2020), d: Classified as RCB stars from optical spectra by Tisserand et al. (2020), e: Also presented in our previous pilot NIR spectroscopic paper Karambelkar et al. (2021), f: Flagged as a possible RCB star on AAVSO by Gabriel Murakowski. g: Targets with declination  $< -28^\circ$  that were observed as they were listed as strong RCB candidates, h: Listed as RCB star V2331 Sgr in Crawford et al. (2023).

Table 3.4: RCB and DY Per stars identified/confirmed from our NIR census (continued from Table 3.3)

Name	ToI-ID/ PGIR Name	RA deg	Dec deg	NIR spec. class	Comments
WISE J184246.26-125414.7	250	280.69277	-12.90409	RCB	d
WISE J174138.87-161546.4	182	265.41199	-16.26291	RCB	d
WISE J183649.54-113420.7	240	279.20645	-11.57244	RCB	d
IRAS 19437+2812	PGIRV_526_1_0_2033	296.4334005	28.33476509	RCB	
MGAB-V209	PGIRV_663_2_3_2970	288.3546954	17.61718824	RCB	f
C*2610		278.80827	-15.60382	RCB	a
IRAS 21210+4922	PGIRV_230_2_0_290	320.699761	49.58775202	DY Per	
BC 279	PGIRV_230_1_0_3575	316.0404598	51.96017409	DY Per	
NC50_6	PGIRV_396_2_3_2390	300.5364042	36.46534761	DY Per	

*a* : Listed as a RCB candidate based on the *Gaia* lightcurve by Eyer et al. (2023). *b* : Listed as a RCB candidate based on its lightcurve by Maíz Apellániz et al. (2023). *c* : Listed as strong RCB candidates by Tisserand et al. (2020), *d*: Classified as RCB stars from optical spectra by Tisserand et al. (2020), *e*: Also presented in our previous pilot NIR spectroscopic paper Karambelkar et al. (2021), *f*: Flagged as a possible RCB star on AAVSO by Gabriel Murakawski.

spectral library (Rayner et al. 2003). All three stars have NIR colors similar to known DY Per type stars (Tisserand et al. 2013). We classify these three as new Galactic DY Per type stars.

## PGIR lightcurves of known carbon-stars

### New RCB star

Using the PGIR lightcurves of stars classified as “carbon-stars” on Simbad, we identified one previously unknown RCB candidate — C\*2610 — that shows large-amplitude RCB-like declines in its lightcurve. We classify it as an RCB star based on its NIR spectrum which resembles RCB stars undergoing declines. This source was also listed as a possible RCB star based on its *Gaia* lightcurve by Eyer et al. (2023), and appears in the carbon-star catalogs of Stephenson (1973) and Alksnis et al. (2001). This star is listed in Table 3.3 and its PGIR lightcurve and NIR spectra are included in Fig. 3.3 and 3.5, respectively.

### New DY Per candidates

From the Simbad “carbon-star” lightcurves, we identify 15 stars that show variations resembling DY Per. We list these stars as candidate DY Per type stars in Table 3.8, as we do not have spectroscopic observations for them. These PGIR lightcurves of these stars are shown in Fig. 3.12.

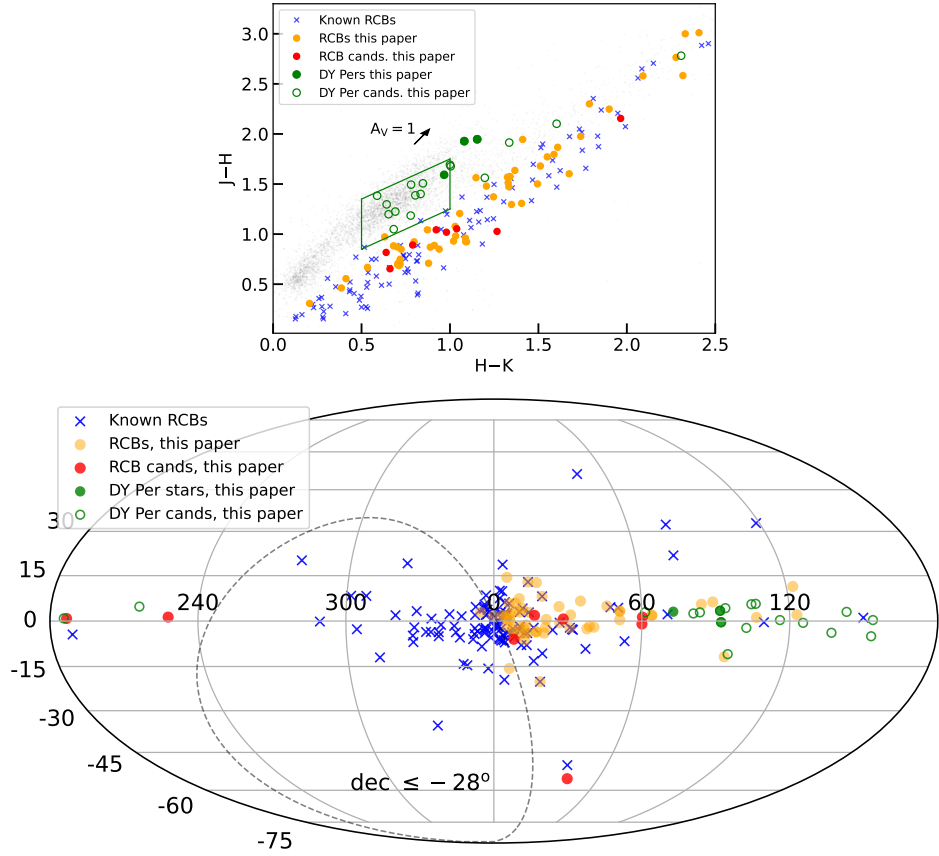


**Figure 3.7: Distributions of RCB and DYPer-type stars.** *Top:* 2MASS color-color diagram for known RCB stars (blue crosses), new RCB stars (orange dots), new RCB candidates (red dots), new DY Per type stars (green solid dots) and new DY Per candidates (hollow green circles). The green box marks the DY Per-selection region from Tisserand et al. (2013), and the black arrow indicates the direction of interstellar extinction of  $A_V = 1$  mag. The DY Per type stars follow a distinct trend than the RCB stars. *Bottom :* Galactic distribution of RCB and DY Per type stars. Most RCB stars are located towards the center of the Milky Way, consistent with a bulge population, while most DY Per type stars are located at high Galactic longitudes, indicative of a disk population.

### 3.5 Discussion

#### Total number of Galactic RCB stars

#### Total RCB stars in the T20 catalog

First, we determine the total number of RCB stars in the T20 catalog. We identified a total of 50 RCB stars (see Sec. 3.4 and Fig. 3.1). As noted earlier, 3 of these belong to Priority G ( $\text{decl.} < -28^\circ$ ) which is not amongst our prioritized categories, so we do not use these to determine the total number. The remaining 47 RCB stars come from our systematic followup of prioritized categories highlighted in Fig. 3.1.

For lightcurve Priority A (see Fig. 3.1), we observed all 176 candidates and identified 33 RCB stars. For lightcurve priorities (lc-pri) B, C and D, we only observed the color-priorities (col-pri) 1-a, 2-a and 3-a. We use these observations to estimate the numbers in col-pri 1-b, 2-b and 3-b.

First, in col-pri 1-a and lc-pri B+C+D, we observed all 104 candidates and identified 12 RCB stars. For col-pri 1-b and lc-pri B+C+D, we observed 11 out of 36 candidates and identified no RCB stars, but 1 strong RCB candidate. Scaling to the total number of candidates in this category, we expect no more than  $\approx 3$  RCB stars in 1-b. The efficiency is expected to be lower in 1-b than 1-a as 1-b is more contaminated by RV-Tauri stars. For col-pri 1-c and lc-pri B+C+D, we expect the contamination of LPVs to be much higher than 1-a+1-b. Based on the estimate in Karambelkar et al. (2021), we expect 1-c to have 5 times more LPVs and 10 times fewer RCBs than 1-a and 1-b combined. Therefore, for the ambiguous and non-detection lightcurves (lc-pri B and D) in 1-c, we estimate the RCB-occurrence rate to be 50 times lower than 1-a and 1-b. For flat lightcurves (lc-pri C), we assume the same RCB-occurrence rate in 1-c as in 1-a + 1-b. This gives a total expected number of 3 RCB stars in 1-c.

Second, in col-pri 2-a and lc-pri B+C+D, we observed 50 candidates and identified 1 RCB star. Assuming this RCB-occurrence rate, we expect 1 RCB star in col-pri 2-a and 4 RCB stars in col-pri 2-b.

Finally, for col-pri 3-a and lc-pri B+C+D, we observed 44 out of 45 candidates and identified 1 RCB star. The low efficiency is expected, as these are the brightest targets in group 3, which coincide with stars with a classification listed on Simbad. Category 3-b groups the candidates with at least one upper limit in the 4 WISE bands. Optimistically, we choose an RCB efficiency of  $\approx 20\%$  for this category (following Tisserand et al. 2020), we estimate another 29 RCB stars from colpri 3-b and lc-pri B+C+D to account for a population of highly dust enshrouded RCB

Table 3.5: Total number of RCB stars identified in the T20 catalog for different color and lightcurve priorities. \* marks categories which were not covered in our spectroscopic followup. The numbers in these categories were determined as described in Sec. 3.5

col-pri	lc-pri	lc-pri
	A	B+C+D
1-a	20	12
1-b	2	3*
1-c	9	3*
2-a	0	1
2-b	1	4*
3-a	1	1
3-b	0	29*

stars. Table 3.5 shows a summary of number of RCB stars in each of the categories discussed above.

In total, we estimate there are  $\approx 86$  RCB stars (95% confidence interval  $60 - 150$ ) out of the 1215 candidates from the T20 catalog with northern declinations ( $\delta > -28^\circ$ ). Accounting for southern candidates, 85% completeness and adding the 77 known RCB stars gives a total of  $86 \times (100/85) \times (2194/1215) + 77 = 260$  (95 % confidence interval  $200 - 390$ ). Including the 8 strong RCB candidates gives a total of 280 (95% CI 210 – 400) RCB stars in the full T20 catalog.

### Total Galactic RCB stars

We now discuss possible biases associated with our search, and correct for them to determine the total number of Galactic RCB stars. First, as noted in Tisserand et al. (2020), the detection efficiency of the catalog drops within a few degrees of the Galactic center and along the Galactic plane at low Galactic latitude due to high interstellar extinction. We used the white-dwarf binary population synthesis model from Lamberts et al. (2019) to estimate the number of RCB stars within this region. From the simulated white-dwarf binaries, we calculate the number of He-CO WD binaries that are within 2 degrees of the Galactic center, or within  $1^\circ$  of the Galactic plane. We find that  $\approx 20\%$  of all He-CO WD binaries lie within this region. Assuming that RCB stars follow a similar distribution, we estimate that

there are  $\approx$ 70 RCB stars within this region that are missed by our search. We derive a similar number using star counts generated from the Besancon model of the Milky Way (Czekaj et al. 2014). Future high-spatial resolution observations (e.g., with the *Roman* space telescope) can accurately measure the number of RCB stars in this highly crowded region. Our rough estimate suggests a total of  $\approx$ 350 (C.I. 250 – 500) RCB stars in the Milky Way. This estimate agrees well with the estimate of 300–500 from Tisserand et al. (2020).

Second, the T20 catalog is expected to contain 85% of RCB stars based on previously known RCB stars, that come from a non-homogenous sample. We use our color-independent PGIR lightcurve-based search to test this 85% completeness estimate. After applying our lightcurve selection criteria ( $\eta < 0.5$  and  $\text{ptp} > 2$ ) on lightcurves in the PGIR database, we recover a total of 24 RCB stars. 22 of them are either previously known RCB stars or present in the T20 catalog. Only 2 RCBs are previously unknown and are not present in the catalog. Other than these 2, we do not find any RCBs in the lightcurve selected candidates. This suggests that the 85% completeness estimate of the T20 catalog is reasonable. We note that the completeness of the PGIR lightcurve database is not well quantified, but it is unlikely that we are missing a substantial population of RCB stars.

Finally, we quantify the efficiency of PGIR in detecting RCB stars. We created a simulated distribution of 10000 RCB stars in the Milky Way assuming that the distribution traces the Galactic stellar mass. We use the SED of the prototype star R CrB together with interstellar extinction values from Green et al. (2019) to predict the expected distribution of the brightness of RCB stars visible from the northern hemisphere ( $\delta > -28^\circ$ ). Fig. 3.8 shows the distribution of apparent magnitudes of the simulated RCB stars in the *J* and optical *g* and *r* bands. We find that PGIR with a limiting magnitude  $m_{\text{lim}} \approx 13 - 15$  mag is sensitive enough to detect  $> 90\%$  of RCB stars at maximum light. PGIR will thus detect almost all RCB stars in the northern hemisphere that brightened to maximum light over its five year baseline. Declines longer than 5 years are seen in known RCB stars, such as the historic 10-year dimming of R CrB itself in 2007. Examining declines in all known RCB stars using long-baseline AAVSO lightcurves, Crawford et al. (2024, in prep.) finds that 30 out of 1039 ( 3%) declines are longer than 5 years, and additionally that the coldest RCB stars are prone to both more frequent declines and spending more than 80% of observed time in decline phase. These cool stars occasionally not show any brightness variations and would thus not be identified as large amplitude

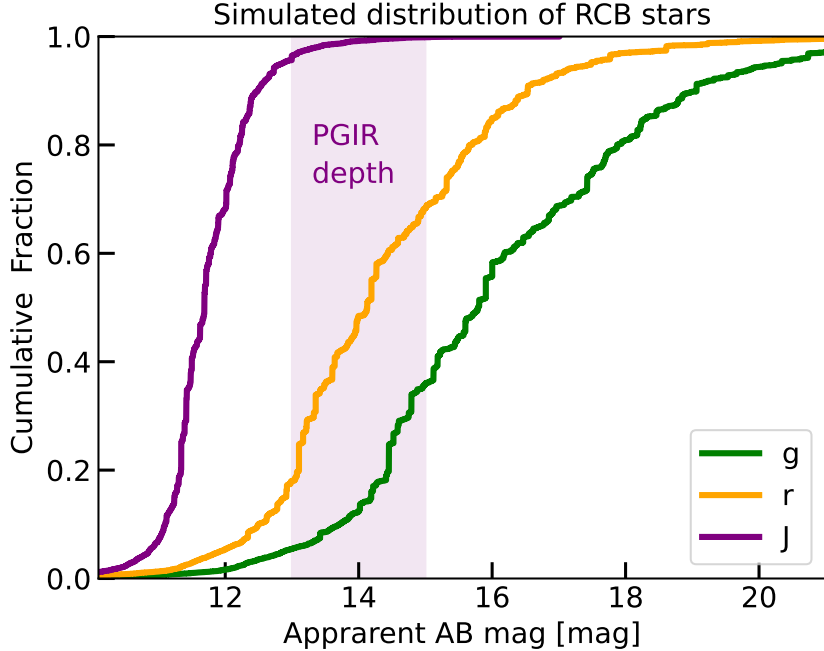


**Figure 3.8: Detection thresholds of PGIR for Galactic RCB stars.** Distribution of the apparent magnitudes of simulated Galactic RCB stars at maximum light, that are visible from the northern hemisphere. The shaded purple region shows the typical range of PGIR limiting magnitudes (which varies depending on the extent of confusion). PGIR is sensitive enough to detect  $> 90\%$  of RCB stars at maximum light. PGIR can detect almost all RCB stars that brightened to maximum light in the last five years. PGIR has the same RCB-detection efficiency as an optical survey with a much deeper limiting magnitude ( $\approx 20$  mag) — illustrating the advantages of a NIR search for dusty RCB stars.

variables. However, they would still pass the lightcurve-independent color-selection criteria. Specifically, as mentioned in Sec. 5.1.1, col-pri 3-b accounts for highly dust-enshrouded cold RCB stars that spend most of their time in a dust-enshrouded phase and do not rise to maximum light. Interestingly, Fig. 3.8 shows that PGIR has the same RCB-detection efficiency as an optical survey with a much deeper limiting magnitude ( $m_{\text{lim}} \approx 20$  mag, e.g., ZTF) — illustrating the advantages of a NIR search at finding dusty RCB stars in dusty regions of the Milky Way.

To summarize, we determine that there are a total of 350 RCB stars in the Milky Way (C.I. 250–500). Despite the biases associated with our search listed here, the total number of Galactic RCB stars is unlikely to be substantially larger than this estimate.

### Comparisons with the rate of He-CO WD mergers

Using our derived number of 350 (C.I. 250–500) Galactic RCB stars and assuming typical RCB lifetimes of  $1 - 3 \times 10^5$  yr (Schwab 2019; Crawford et al. 2020; Wong et al. 2024), the formation rate of RCB stars, in the Milky Way is between  $0.8 - 5 \times 10^{-3}$  yr $^{-1}$ . This is consistent with observational and theoretical estimates of the He-CO WD merger rate. Using observations of low-mass WD binaries in the Milky Way disk from the ELM survey, Brown et al. (2020) estimate a lower limit of  $2 \times 10^{-3}$  yr $^{-1}$  on the rate of He-CO WD mergers. Using binary population synthesis models, Karakas et al. (2015) estimate a He-CO WD merger rate of  $\sim 1.8 \times 10^{-3}$  yr $^{-1}$ .

The population of RCB stars can provide useful information for future gravitational wave missions like LISA. Recently, Lamberts et al. (2019) found that close He-CO double white dwarfs (DWDs) will constitute the majority of sources detectable with LISA, and predicted over 5000 He-CO DWD resolvable over a 4 year baseline. As RCB stars are remnants of He-CO WD mergers, they serve as an independent probe of these predictions. We start with the simulated short-period (lower than few hours) He-CO WD binaries from Lamberts et al. (2019) and evolve them assuming gravitational wave radiation dominates the binary evolution, and find a He-CO WD merger rate of  $\approx 1 \times 10^{-3}$  yr $^{-1}$ . Assuming RCB-lifetimes as above, this corresponds to an expected number of 100–300 RCB stars in the Milky Way. It is encouraging that this estimate is broadly consistent with the observed number of RCB stars despite simplified assumptions about WD binary evolution. More detailed simulations that account for different RCB-lifetimes, RCB progenitor-mass ranges and WD-merger physics such as mass transfer can provide observationally-grounded predictions for the dominant population of DWDs that should be detectable with LISA.

Missing from this picture are dLHdC stars. As noted in Tisserand et al. (2022), there could be as many, if not more, dLHdC stars in the Milky Way as RCB stars. There are several indications that the population of WDs that merge to form RCB stars have distinct properties from those that form dLHdC stars (Karambelkar et al. 2022; Tisserand et al. 2022; Crawford et al. 2022). The lower luminosities and oxygen isotope ratios suggest that dLHdC stars could come from lower mass mergers than RCB stars. From BPS simulations, Tisserand et al. (2022) find that the distribution of total masses of WD merger remnants is bimodal, with the higher end ( $\approx 0.9 M_\odot$ ) coming from hybrid-CO + CO WD mergers. If RCB stars form preferentially from these higher mass mergers, the RCB formation rate derived here

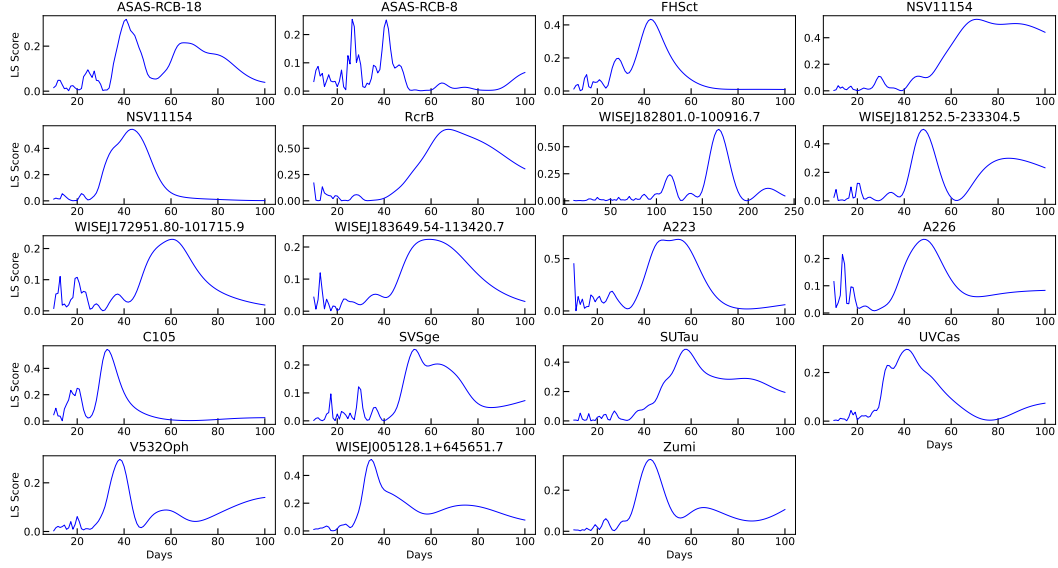


Figure 3.9: **Periodograms of RCB and dLHdC stars** using PGIR lightcurves reported in Table 3.6

corresponds to the rate of hybrid-CO + CO WD mergers rather than the full rate of He-CO WD mergers. Accurate mass measurements of RCB and dLHdC stars will help understand the implications of the RCB formation rate on the rate of WD mergers.

### Pulsation periods

At maximum light, some RCB stars are known to pulsate with periods between 40-100 days and amplitudes of a few tenths of a magnitude (Lawson et al. 1997; Alcock et al. 2001; Percy 2023). These pulsations can be fairly irregular – the star can exhibit multiple pulsation modes or undergo changes in the dominant period (e.g., R CrB has shown pulsations with periods of 33, 44, 52 and 60 days (Lawson et al. 1996)). Initially, these semi-regular or irregular pulsations were suggested to originate from the strange-mode instability in non-adiabatic and radiation-pressure dominated envelopes (Saio 2008; Gautschy 2023). Recently, Wong et al. (2024) modeled the RCB-dLHdC pulsations as solar-like oscillations excited by convection in a helium-rich envelope. They find that the frequencies with maximum power ( $\nu_{\max}$ ) for such oscillations matches the observed range of periods in RCBs and dLHdCs. These models show that the pulsation periods can be used as diagnostics of the mass of the stars, with lower periods generally indicative of lower masses.

We examined the *J*-band PGIR light curves of the RCB stars presented in this paper,

Table 3.6: Pulsation periods using PGIR lightcurves

Name	PGIR Period days
ASAS-RCB-8	$27 \pm 6$
ASAS-RCB-18	$41 \pm 8$
FH Sct	$44 \pm 11$
NSV 11154	$70 \pm 20, 45 \pm 5$
R CrB	$67 \pm 10$
SU Tau	$58 \pm 10$
SV Sge	$53 \pm 10$
UV Cas	$41 \pm 10$
V532 Oph	$38 \pm 10$
WISE J005128.09+645651.73	$34 \pm 6$
WISE J182801.05-100916.71	$170 \pm 10$
WISE J181252.50-233304.47	$48 \pm 15$
WISE J172951.80-101715.9	$60 \pm 19$
WISE J183649.54-113420.7	$59 \pm 9$
Z Umi	$42 \pm 10$
C105	$33 \pm 10$

70 previously known RCB stars to search for maximum-light periodic variations. We identified windows in the light curves that show periodic variations, and derived the periods using the Lomb-Scargle implementation in the python package `gatspy`. We derive pulsation periods for 16 RCB. To derive errorbars on the periods, for each star, we used the measured brightness and uncertainties to generate 100 simulations of the lightcurve assuming a normal distribution and measured the periods for each lightcurve. The median periods and standard deviations are listed in Table 3.6. The periods typically lie between 30–100 days. Periods of some of these stars have been previously reported based on optical photometry — SU Tau ( $\sim 40$  d, Lawson et al. 1990), FH Sct ( $\sim 47$  d, Percy 2023), R CrB (multiple periods ranging from  $\sim 35$ –60 d Lawson et al. 1996), C105 ( $\sim 40$  d, Tisserand et al. 2022). The PGIR periods of these stars are consistent with those reported previously.

In addition to the PGIR lightcurves, we also examined lightcurves of RCB and dLHdC stars from the Transiting Exoplanet Satellite Survey (*TESS*, Ricker et al. 2015) to search for short-timescale variability from them. We downloaded calibrated, short-cadence *TESS* lightcurves from the Quicklook Pipeline (QLP) for

known RCB and dLHdC stars from the Mikulski Archive for Space Telescopes<sup>3</sup> using astroquery. We examined simple aperture photometry (SAP) lightcurves for each star and removed lightcurves which have bad photometric flags, large photometric scatter and rapid increases or decreases of flux that are likely not astrophysical. Additionally, we also use the python package `lightkurve` to download the *TESS* target pixel files and extract aperture photometry at the locations of known RCB and dLHdC stars. We find that the QLP lightcurves agree well with those extracted using `lightkurve`, where available. We use the DREAMS-RCB monitoring website to determine the photometric phase of the RCB stars at the time of *TESS* observations and use only those lightcurves that were observed at maximum light. We are then left with 6 RCB stars and 6 dLHdC stars. The *TESS* lightcurves have cadences of 10 and 30 minutes, and a baseline of  $\approx 22$ –27 days per sector. Some stars were observed in multiple sectors. As it is challenging to stitch data from different sectors together if they are not observed continuously, we analyze the different sectors individually.

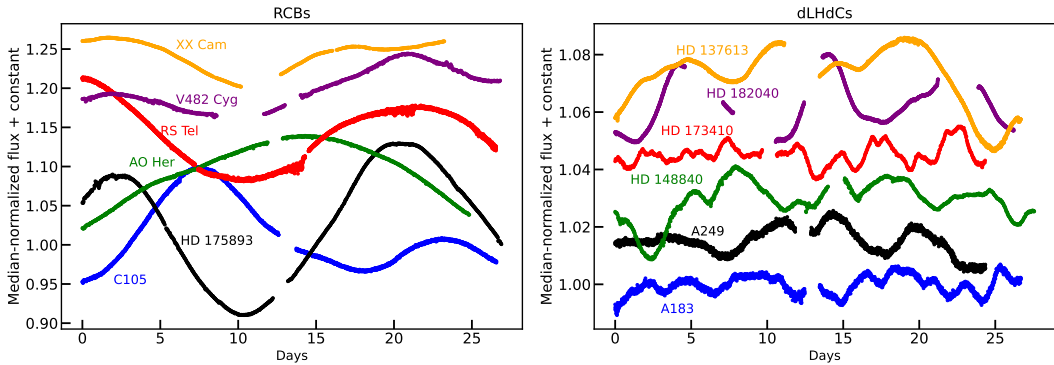


Figure 3.10: **TESS lightcurves of RCB and dLHdC stars.** *Top* : Examples of *TESS* lightcurves of RCB stars (*left*) and dLHdC stars (*right*). *Bottom* : Lomb-Scargle periodograms of RCB stars (*left*) and dLHdC stars (*right*). dLHdC stars in general show variability on timescales shorter than RCB stars. A possible explanation is that dLHdC stars have lower mass than RCB stars.

Figure 3.10 shows the median-normalized *TESS* lightcurves of six RCB and six dLHdC stars. The *TESS* lightcurves show that both RCB and dLHdC stars do not show variability at very short ( $< 1$  day) timescales. Interestingly, these high-cadence lightcurves show that dLHdC stars generally exhibit variability on timescales shorter than RCB stars. In the picture that dLHdC stars have lower masses than RCB stars, they are expected to have smaller pulsation periods than RCB stars (Wong et al. 2024). The differences seen in the *TESS* lightcurves of RCBs and dLHdCs may

<sup>3</sup><https://mast.stsci.edu>

therefore point towards the different masses of this class of objects, as suggested in Tisserand et al. (2022) and Karambelkar et al. (2022). Studying the variations of a larger sample of dLHdC and RCB stars will provide an important clue towards identifying their masses and possible differences.

### Radial velocities

We use our NIR spectra to derive the radial velocities (RVs) of the newly identified RCB stars. We correct the spectra for barycentric motion, examine them to identify strong carbon absorption lines, and fit a Gaussian profile to derive the line centers. We then compare the line-centers to rest-wavelengths (taken from NIST) to measure the RVs. For each spectrum, we determined the statistical uncertainty on the RV using by calculating the standard deviation of the velocities measured from each carbon line examined. These uncertainties are small (typically  $< 5 \text{ km s}^{-1}$ ). To determine the systematic uncertainty on how precisely line centroids can be measured due to instrumental resolution, we use the sky-emission lines in our spectra. The dispersion on the sky line centroids is  $20 \text{ km s}^{-1}$  (approx. a third of a pixel). We add the statistical and systematic uncertainties in quadrature and report those as uncertainties on the RVs in Table 3.7.

We also note an error in the RVs reported in our previous paper (Karambelkar et al. 2021) — the signs of the values in Table 3 there should be flipped. Additionally, we note that the previous values were measured by cross-correlating the entire spectrum with synthetic RCB spectra, while here, we measure the values using only strong carbon absorption lines. We find that the RVs measured using carbon lines are more reliable, as the spectral features in the synthetic models are highly dependent on the assumed elemental abundances of the RCB star. Indeed, we find that the RVs reported here agree better with those reported by other sources wherever available (e.g., *Gaia*, see Tisserand et al. 2024a). Table 3.7 also lists the revised RVs for these stars. Most RCB stars in Table 3.7 have low RVs ( $\leq 50 \text{ km s}^{-1}$ ), consistent with other RCB stars with RV measurements (Tisserand et al. 2024a). AO Her and NSV 11154 have very high RVs, and are located towards the Galactic halo. The RVs reported here will be useful in constructing the 3D-distribution of Galactic RCB stars (similar to Tisserand et al. 2024a).

### Are RCB and DY Per type stars related?

First, we note that neither DY Per, nor the three spectroscopically confirmed DY Per type stars show the He I ( $\lambda 10830$ ) line that is ubiquitous in RCB stars. In RCB stars,

Table 3.7: Radial velocities derived from C absorption lines in the NIR spectra. Sources marked with \* denote revised values from the ones reported previously in Karambelkar et al. (2021)

Name	Radial velocity km/s
WISE-ToI-164	$-27 \pm 20$
WISE-ToI-174	$-96 \pm 25$
WISE-ToI-185	$-68 \pm 20$
WISE-ToI-188	$-9 \pm 20$
WISE-ToI-193	$-122 \pm 20$
WISE-ToI-194	$120 \pm 20$
WISE-ToI-207	$-40 \pm 20$
WISE-ToI-220	$-101 \pm 20$
WISE-ToI-226	$-146 \pm 20$
WISE-ToI-231	$7 \pm 25$
WISE-ToI-248	$-44 \pm 25$
WISE-ToI-257	$27 \pm 20$
WISE-ToI-264	$120 \pm 20$
WISE-ToI-270	$69 \pm 22$
WISE-ToI-323	$-119 \pm 20$
WISE-ToI-1227	$-43 \pm 20$
WISE-ToI-1241	$-74 \pm 20$
WISE-ToI-1245	$3 \pm 20$
WISE-ToI-2645	$40 \pm 20$
WISE-ToI-2938	$-39 \pm 20$
WISE-ToI-4108	$173 \pm 20$
WISE-ToI-4117	$18 \pm 20$
*AO Her	$-524 \pm 20$
*ASAS-RCB-21	$20 \pm 20$
*NSV 11154	$-326 \pm 22$
*V391 Sct	$-36 \pm 25$
*WISE-ToI-249 <sup>a</sup>	$81 \pm 20$
*WISE-ToI-203 <sup>a</sup>	$-18 \pm 20$
*WISE-ToI-290 <sup>a</sup>	no C lines
*WISE-ToI-6	$-101 \pm 20$
*WISE-ToI-223	$37 \pm 20$
*WISE-ToI-268	$95 \pm 20$
*WISE-ToI-274	$-36 \pm 20$
*WISE-ToI-1309	$-13 \pm 20$
*WISE-ToI-281	no C lines
*WISE-ToI-1213	no C lines

<sup>a</sup> : The stars WISE-ToI-203, 249 and 290 are listed as WISE-J17+, WISE-J18+ and WISE-J19+ in Karambelkar et al. (2021).

this line is collisionally excited in high velocity ( $\approx 400 \text{ km s}^{-1}$ ) He-rich dust-driven winds (Clayton et al. 2013; Karambelkar et al. 2021). DY Per type stars resemble classical carbon-stars in this aspect. However, even in the cold-RCB picture, the absence of this line can possibly be explained by the low-luminosity of DY Per type stars compared to RCB stars. As DY Per type stars are  $\approx 10$  times dimmer than RCBs, the radiation pressure can accelerate only low velocity winds ( $\approx 40 \text{ km s}^{-1}$ ), which is not sufficient to excite the helium atoms to the lower energy level of the He I transition.

Second, Fig. 3.7 (bottom panel) shows the Galactic distribution of the RCB and DY Per type stars identified in this paper together with known RCB and DY Per type stars. Most RCB stars lie towards the Galactic center, with a small number at higher Galactic latitudes suggestive of a small halo population. In contrast, the DY Per type stars and candidates lie at high Galactic longitudes, suggesting that they are part of a disk population. This is consistent with the findings of Tisserand et al. (2024a) who studied the distribution of RCB and DY Per type stars using *Gaia* DR3. The top panel of Fig. 3.12 shows the NIR color-color diagram for RCB and DY Per type stars. We find that the new DY Per type stars and DY Per candidates occupy a distinct region in this diagram from RCB stars and have colors similar to classical carbon stars, consistent with Tisserand et al. (2013).

We also note that the new DY Per type stars and candidates show some diversity in their lightcurves. We plot longer baseline ATLAS-o band lightcurves of the DY Per type stars and candidates in Fig. 3.6 and Fig. 3.12. Some stars (e.g., PGIRV\_396, PGIRV\_230\_1\_0\_3575, NIKC 2-77, V\*FL Per, Fuen C 157) show well-defined brightness-declines that are clearly distinguishable from other small-amplitude variations, while some stars (e.g., IRAS 04193+, IRAS 07113+, C\*2905, Fig. 3.12) generally show large-amplitude erratic variations without well-defined declines. The lightcurves of some stars such as PGIRV\_230\_2\_0\_290 (Fig. 3.6), C2905 and ATO J308.8118 (Fig. 3.12) show large-amplitude pulsations that are seen in carbon stars. The stars V2060 Cyg, KISO C1-139, IRAS22137+ (Fig. 3.12) show declines at periodic intervals. Based on the lightcurves of classical carbon stars in the LMC, (Soszyński et al. 2009) suggest that DY Per variability is part of the continuum of carbon-star variability. Spectroscopic observations of the different classes of DY Per candidates will help understand which, if any, of these stars show RCB-like elemental abundances (esp.  $^{18}\text{O}$ ).

### 3.6 Summary and way forward

In this paper, we presented results from a systematic infrared census for RCB stars in the Milky Way. We selected RCB candidates using NIR  $J$ -band lightcurves from PGIR, mid-IR colors from WISE and obtained medium resolution NIR spectra for them. We identified 53 RCB stars from our candidates. We use this number to estimate the total number of RCB stars in the Milky Way. This has been a longstanding open question - with estimates ranging from a few thousand (Clayton 2012; Han 1998b; Alcock et al. 2001) to a few hundred (Tisserand et al. 2020). Our systematic infrared census provides an excellent way to address this question. Using our selection criteria, we estimate that there are a total of  $\approx 350$  RCB stars with a 95% confidence interval of 250 – 500 in the Milky Way. This corresponds to a formation rate of  $0.8 - 5 \times 10^{-3} \text{ yr}^{-1}$ . This is consistent with observational and theoretical estimates of the rate of He-CO WD mergers in the Milky Way. Using binary population synthesis models, the measured RCB-formation rate can be used to draw insights about the population of He-CO WD binaries detectable with future gravitational-wave experiments such as *LISA*. However, in addition to RCB stars, it is important to understand the contribution of the dustless dLhdC stars and colder DY Per type stars to the population of He-CO WD merger remnants.

It is still not clear whether DY Per type stars are colder RCB stars or classical carbon stars. Only 3 Galactic DY Per type stars were known in the Milky Way. In this paper, we identified 3 spectroscopically confirmed and 15 candidate DY Per type stars. The new DY Per type stars and candidates have distinct NIR colors and appear to have a different Galactic distribution than RCB stars. Future analysis of the spectra and long-term photometric variations of these stars will be useful to understand their relation to RCB stars. dLhdC stars have been conclusively associated with He-CO WD merger remnants, but their number is uncertain. As noted in (Tisserand et al. 2022), there could potentially be as many dLhdC stars as RCB stars in the Milky Way. A systematic search for dLhdC stars is required to interpret the number of RCB-dLhdC stars in the context of the He-CO WD merger rate.

The differences between dLhdC and RCB stars have only recently started to be explored. The differences in their luminosities and chemical compositions suggest that dLhdC stars could be less massive than RCB stars (Tisserand et al. 2022; Karambelkar et al. 2022; Crawford et al. 2022). In this picture, we would expect the maximum-light pulsation periods of these stars to differ. The *TESS* lightcurves for six dLhdC and six RCB stars show that dLhdC stars show variations on timescales

shorter than RCB stars, consistent with the picture that they have lower masses. Comparing these pulsation data to theoretical models (e.g., Wong et al. 2024; Saio 2008) to estimate their masses will provide useful information towards understanding why dLHdCs form dust and RCBs do not.

Finally, we have presented NIR spectra for 44 RCB stars, which can be useful for measuring their elemental abundances. In addition to oxygen isotope ratios (e.g., Karambelkar et al. 2021; Karambelkar et al. 2022), it would be interesting to see if the NIR spectra can be used to solve the long-standing carbon problem in RCBs (Asplund et al. 2000). NIR spectra also probe the helium line, which can be used to study mass-loss in RCB stars (Clayton et al. 2011).

NIR observations are an efficient way to identify and characterize RCB stars. Ongoing and upcoming NIR surveys such as the Wide-field Infrared Transient Explorer (WINTER, Lourie et al. 2020a), the Dynamic Red All-sky Monitoring Survey (DREAMS), Cryoscope in Antarctica will help uncover the population of RCB stars in the Milky Way. Future missions such as the *Nancy Grace Roman Space Telescope* will help study the RCB stars in the most crowded central region of the Milky Way. In the optical, the Vera Rubin Observatory has the sensitivity to discover all Galactic RCB stars in the southern hemisphere, as well as RCB stars in other galaxies out to  $\approx 5$  Mpc, shedding light on the DWD populations of these galaxies.

### 3.7 Acknowledgements

We thank the anonymous referee for useful suggestions that improved this paper. VK thanks Sunny Wong and Yashvi Sharma for useful discussions. Palomar Gattini-IR (PGIR) is generously funded by Caltech, Australian National University, the Mt Cuba Foundation, the Heising Simons Foundation, the Bi-national Science Foundation. PGIR is a collaborative project among Caltech, Australian National University, University of New South Wales, Columbia University and the Weizmann Institute of Science. MMK acknowledges generous support from the David and Lucille Packard Foundation. J. Soon acknowledges the support of an Australian Government Research Training Program (RTP) scholarship. Some of the data presented here were obtained with Visiting Astronomer facility at the Infrared Telescope Facility, which is operated by the University of Hawaii under contract 80HQTR19D0030 with the National Aeronautics and Space Administration. This work was supported, in part, by the National Science Foundation through grant PHY-2309135 to the Kavli Institute for Theoretical Physics, and by the Gordon and

Table 3.8: Strong RCB and DY Per candidates identified from our NIR census.

Name	ToI-ID/ PGIR Name	RA deg	Dec deg	NIR spec. class	Comments
WISE J060405.01+233304.7	28	91.02088	23.55132	RCB-cand	
WISE J072356.66-124014.0	41	110.98611	-12.67058	RCB-cand	
WISE J182649.64-244532.8	228	276.70684	-24.75912	RCB-cand	
WISE J184016.09-035608.9	245	280.06707	-3.93583	RCB-cand	
WISE J193929.35+244504.0	288	294.87231	24.75113	RCB-cand	
WISE J194739.93+232638.7	293	296.91639	23.44410	RCB-cand	
WISE J222704.54-165948.4	323	336.76892	-16.99678	RCB-cand	
WISE J181400.05-134254.4	1257	273.50025	-13.71511	RCB-cand	
Kiso C1-139		18.13093	62.18622	DY Per-cand	Maehara et al. (1987)
NIKC 2-77		55.08234	59.09781	DY Per-cand	Soyano et al. (1991)
Fuen C 157		90.42725	24.56634	DY Per-cand	Fuenmayor (1981)
V* FL Per		59.90524	46.46239	DY Per-cand	Lee et al. (1947)
Case 492		330.83864	62.30802	DY Per-cand	Nassau et al. (1957)
IRAS 22137+6311		333.83008	63.44256	DY Per-cand	Alksnis et al. (2001)
IRAS 07113-0025		108.47103	-0.51654	DY Per-cand	Alksnis et al. (2001)
V* AR Vul		293.93229	26.55986	DY Per-cand	Nassau et al. (1957)
IRAS 04193+4959		65.78151	50.10781	DY Per-cand	Putney (1997)
V* V2060 Cyg		317.43137	54.17533	DY Per-cand	Alksnis et al. (2001)
Kiso C1-24		357.80148	62.38434	DY Per-cand	Maehara et al. (1987)
ABC90 cep 7		335.68037	54.59463	DY Per-cand	Alksnis et al. (2001)
Case 749		334.65993	43.77903	DY Per-cand	Blanco (1958)
C* 2905		307.02683	42.91874	DY Per-cand	Stephenson (1973)
ATO J308.8118+45.2629		308.81182	45.26292	DY Per-cand	Alksnis et al. (2001)

All strong RCB candidates are sources from the WISE color-selected catalog of Tisserand et al. (2020). For the DY Per-type candidates, we list the papers that first classified them as carbon stars.

Betty Moore Foundation through grant GBMF5076.

### 3.8 Data Availability

The PGIR *J*-band lightcurves of all 1215 candidates, lightcurves of new RCB stars, NIR spectra of all 453 sources, spectroscopic classifications of all 453 sources (Table 3.2) and updated priorities of the T20 candidates (Table 3.1) are publicly available at Zenodo at 10.5281/zenodo.12683154.

### 3.9 Appendix: Candidate RCB and DY Per type stars

Table 3.8 lists the candidate RCB and DY Per type stars identified in our paper. Fig. 3.11 shows the lightcurves and spectra of the stars listed as strong RCB candidates. Fig. 3.12 shows the lightcurves of stars listed as candidate DY Per type stars.

### 3.10 Appendix: Source classifications

We now discuss classifications of the 453 spectra presented in this paper.

*M stars* — A total of 154 stars have M-type spectra (with broad TiO, VO features)

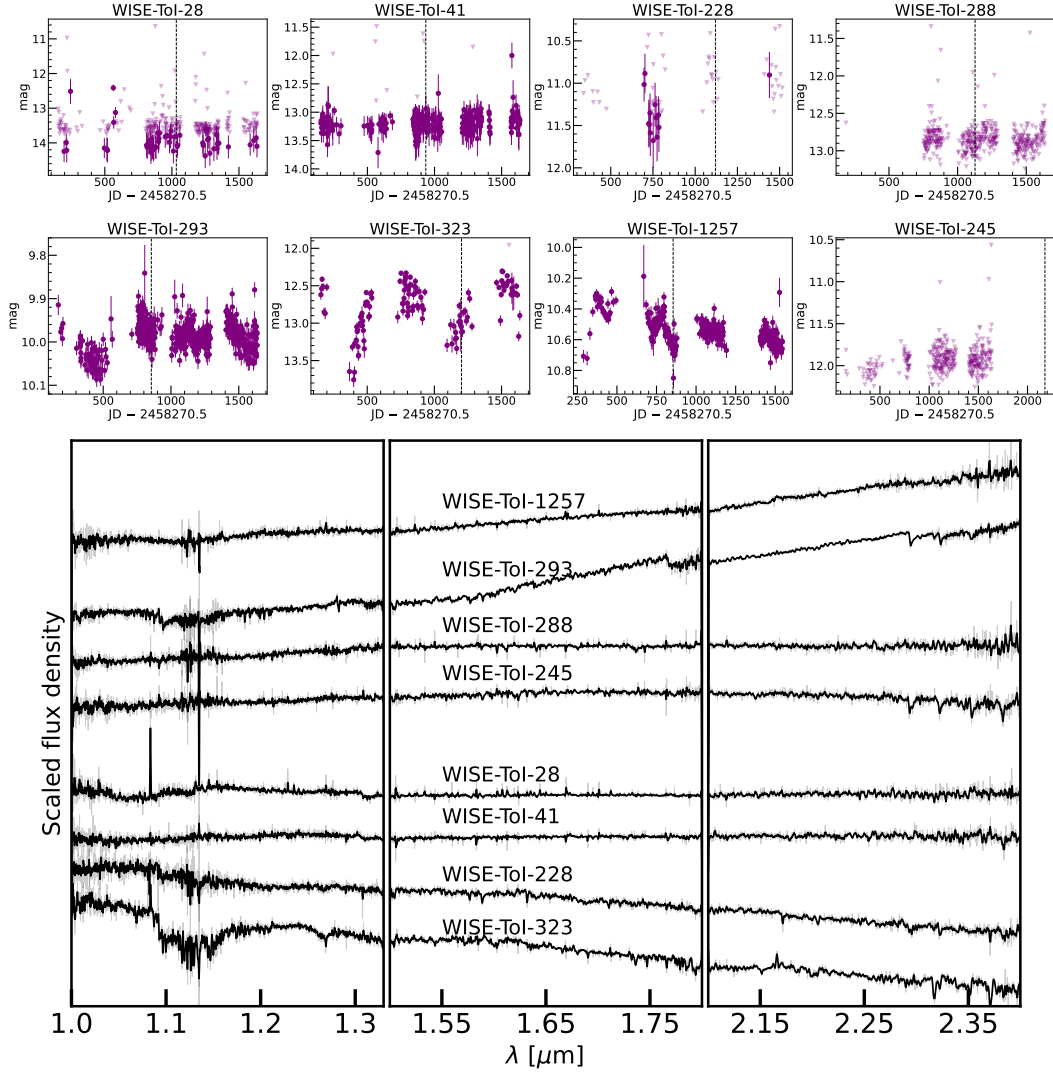


Figure 3.11: **NIR spectra of the 8 candidate RCB stars listed in Table 3.3.** The broad absorption feature seen in the spectrum of WISE-Tol-323 from  $1.1 - 1.2\mu\text{m}$  is likely due to imperfect telluric correction.

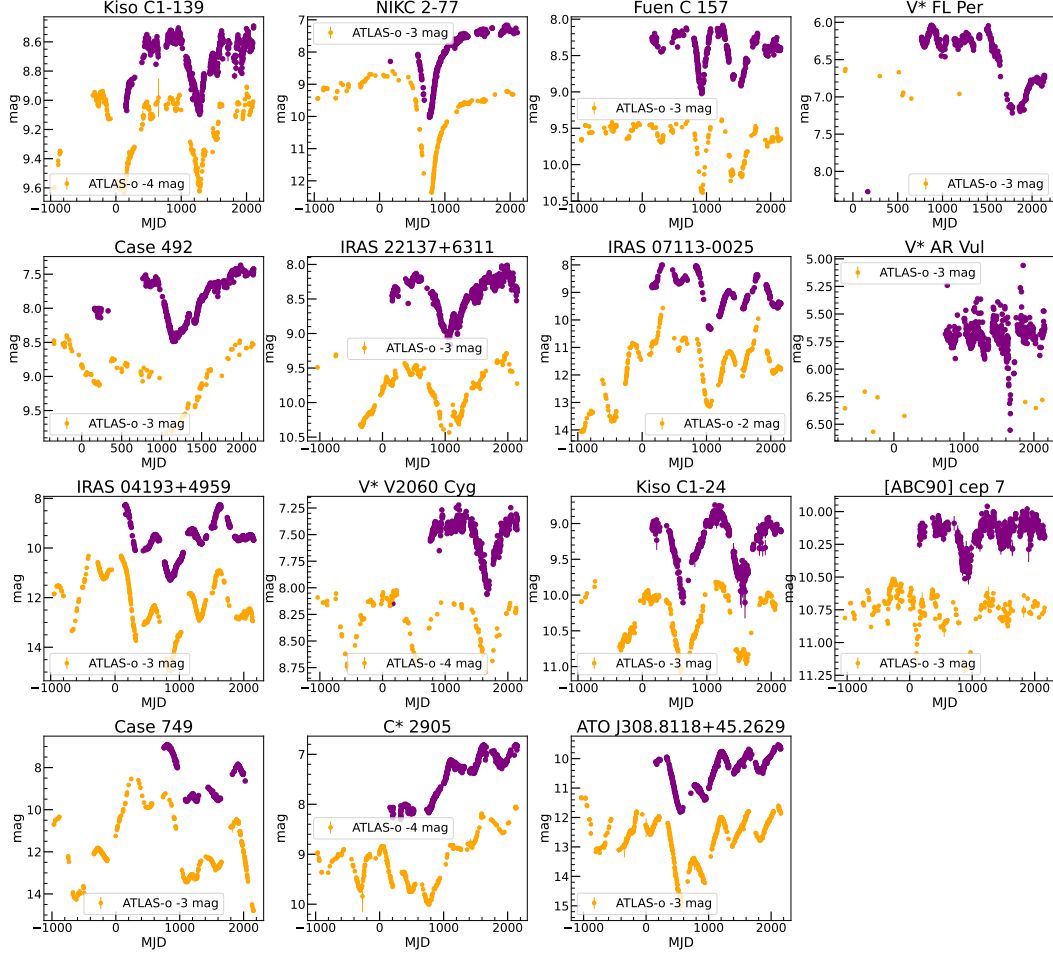


Figure 3.12: PGIR J-band lightcurves of candidate DY Per type stars.

and are thus O-rich AGB stars. We compare the spectra to the IRTF spectral library (Rayner et al. 2009), and determine the best-fit match by performing a least-squares fit. The spectral types of these stars range between M5–M9. Several of these stars show H emission lines — commonly seen in Miras. The strength of these emission lines are known to vary with pulsation phase, and likely originate in pulsation-driven shock heating of the atmospheres (Gray et al. 2009).

*Possible symbiotic binaries* — 15 stars show AGB-star-like spectra together with strong emission lines, particularly the He I  $\lambda 10830$  emission line. These stars are possibly symbiotic stars, where the helium line collisionally excited in high velocity winds around the star. 8 stars have spectra similar to M-type stars, while 7 stars have spectra resembling C stars.

*Emission stars* — 32 stars show spectra dominated by emission lines, we classify

them as emission stars.

*Dust forming carbon stars* — 42 stars show spectra resembling carbon-stars. 39 of these show a broad absorption feature at  $1.5\mu\text{m}$ . This feature is likely due to HCN + C<sub>2</sub>H<sub>2</sub> and has been previously noted in several carbon stars Gonneau et al. (2016) and Gautschy-Loidl et al. (2004).

*CO emitters : Possible RV-Tauri or young-stellar objects (YSOs)* — 69 stars show CO emission bands in their spectra. Some of these stars show short-period variations on top of a long-period, large amplitude variation, characteristic of RV-Tauri stars. The remaining stars are likely a combination of RV-Tauri stars and young stellar objects (YSOs) that are known to exhibit CO emission in their spectra.

*H-rich* — 71 stars have spectra with strong absorption lines of hydrogen. These stars are most likely RV-Tauri stars.

*Other* — We identify 2 Wolf-Rayet and 1 post-AGB star. 9 additional stars do not show any obvious strong features in their spectra except some hydrogen lines and no brightness variations, suggesting that they are not RCB stars.

## Chapter 4

**R CORONAE BOREALIS AND DUSTLESS  
HYDROGEN-DEFICIENT CARBON STARS HAVE DIFFERENT  
OXYGEN ISOTOPE RATIOS**

Karambelkar, V. et al. (Nov. 2022). “R Coronae Borealis and dustless hydrogen-deficient carbon stars likely have different oxygen isotope ratios”. In: *A&A* 667, A84, A84. doi: 10.1051/0004-6361/202142918.

V. Karambelkar<sup>1</sup>, M. M. Kasliwal<sup>1</sup>, P. Tisserand<sup>2</sup>, G. C. Clayton<sup>3</sup>, C. L. Crawford<sup>3</sup>, S. G. Anand<sup>1</sup>, T. R. Geballe<sup>4</sup>, E. Montiel<sup>5</sup>

<sup>1</sup>Cahill Center for Astrophysics, California Institute of Technology, Pasadena, CA 91125,  
USA

<sup>2</sup>Sorbonne Universités, UPMC Univ Paris 6 et CNRS, UMR 7095, Institut d’Astrophysique  
de Paris, IAP, F-75014 Paris, France

<sup>3</sup>Department of Physics & Astronomy, Louisiana State University, Baton Rouge, LA  
70803, USA

<sup>4</sup>Gemini Observatory/NSF’s NOIRLab, 670 N A’ohoku Pl, Hilo HI 96720, USA

<sup>5</sup>SOFIA-USRA, NASA Ames Research Center, MS 232-12, Moffett Field, CA 94035, USA

**Abstract**

R Coronae Borealis (RCB) and dustless Hydrogen-deficient Carbon (dLHdC) stars are believed to be remnants of low mass white dwarf mergers. These supergiant stars have peculiar hydrogen-deficient carbon-rich chemistries and stark overabundances of  $^{18}\text{O}$ . RCB stars undergo dust formation episodes resulting in large-amplitude photometric variations that are not seen in dLHdC stars. Recently, the sample of known dLHdC stars in the Milky Way has more than quintupled with the discovery of 27 new dLHdC stars. It has been suggested that dLHdC stars have lower  $^{16}\text{O}/^{18}\text{O}$  than RCB stars. We aim to compare the  $^{16}\text{O}/^{18}\text{O}$  ratios for a large sample of dLHdC and RCB stars to examine this claim. We present medium resolution ( $R \approx 3000$ ) near-infrared spectra of 20 newly discovered dLHdC stars. We also present medium resolution ( $R \approx 3000\text{--}8000$ ) *K*-band spectra for 49 RCB stars. Due to the several free

parameters and assumptions in our fitting strategy, we provide wide range estimates on the  $^{16}\text{O}/^{18}\text{O}$  ratios of seven dLHdC and 33 RCB stars that show  $^{12}\text{C}^{16}\text{O}$  and  $^{12}\text{C}^{18}\text{O}$  absorption bands, and present the largest sample of such  $^{16}\text{O}/^{18}\text{O}$  wide-range values for dLHdC and RCB stars to date. We find that six of the seven dLHdC stars have  $^{16}\text{O}/^{18}\text{O} < 0.5$ , while 28 of the 33 RCB stars have  $^{16}\text{O}/^{18}\text{O} > 1$ . We also confirm that unlike RCB stars, dLHdC stars do not show strong blueshifted ( $> 200 \text{ km s}^{-1}$ ) He I 10833 Å absorption, suggesting the absence of strong, dust-driven winds around them. Although we only can place wide range estimates on the  $^{16}\text{O}/^{18}\text{O}$  and these are more uncertain in cool RCBs, our medium resolution spectra suggest that most dLHdC stars have lower  $^{16}\text{O}/^{18}\text{O}$  than most RCB stars. This confirms one of the first, long-suspected spectroscopic differences between RCB and dLHdC stars. The different oxygen isotope ratios rule out the existing picture that RCB stars represent an evolved stage of dLHdC stars. Instead, we suggest that whether the white dwarf merger remnant is a dLHdC or RCB star depends on the mass ratios, masses and compositions of the merging white dwarfs. Future high resolution spectroscopic observations will help confirm and more precisely quantify the difference between the oxygen isotope ratios of the two classes.

#### 4.1 Introduction

R Coronae Borealis (RCB) and dustless Hydrogen-deficient Carbon (dLHdC)<sup>1</sup> stars are supergiants characterized by a peculiar chemical composition — an acute deficiency of hydrogen and an overabundance of carbon (Clayton 1996; Feast 1996; Lambert et al. 1994). Together, they form the class of Hydrogen-deficient Carbon (HdC) stars. Their chemical compositions suggest that they are remnants of He-core and CO-core white dwarf (WD) mergers (Webbink 1984; Iben et al. 1984; Saio et al. 2002), making them low mass counterparts of type Ia supernovae in the double-degenerate (DD) scenario (Fryer et al. 2008). In addition to peculiar chemical compositions, RCB stars experience rapid photometric declines (up to 8 mag in V band) that are attributed to dust formation episodes (Clayton 2012). dLHdC stars do not show any such declines or any significant infrared (IR) excess, suggesting that they do not undergo any dust formation (Warner 1967; Goswami et al. 2010; Tisserand 2012). Why RCB stars produce dust while dLHdC stars do not, despite having no other known chemical differences is still a mystery.

It has been relatively easier to identify RCB stars than dLHdC stars owing to their

---

<sup>1</sup>Historically, dLHdC stars were referred to as HdC stars. Here, we follow the updated nomenclature of Tisserand et al. 2021.

spectacular photometric variations. There are 128 RCB stars known in the Milky Way, while only five Galactic dLHdC stars had been known for the last four decades (Clayton 2012; Tisserand et al. 2020; Karambelkar et al. 2021). However, the sample of Galactic dLHdC stars has more than quintupled in the last year with the discovery of 27 new dLHdC stars (Tisserand et al. 2021). Additionally, several new RCB stars have been discovered and observed spectroscopically at near-infrared (NIR) wavelengths (Karambelkar et al. 2021).

NIR spectroscopic observations were key to identifying He-core and CO-core WD mergers as the progenitors of dLHdC and RCB stars. The K-band spectra of these stars show anomalously strong  $^{12}\text{C}^{18}\text{O}$  first overtone bands in addition to the  $^{12}\text{C}^{16}\text{O}$  first overtone bands (Clayton et al. 2005). The values of  $^{16}\text{O}/^{18}\text{O}$  in dLHdC and RCB stars cover a remarkably wide range (from 0.3 to 50), thus in all cases 1–3 orders of magnitude smaller than the solar value ( $\sim 500$ ). The large amount of  $^{18}\text{O}$  is thought to be produced by partial helium burning in a thin shell around the core of the WD merger remnant, which is convectively dredged up to the surface (Clayton et al. 2007; Crawford et al. 2020).

It has been suggested that in addition to dust production,  $^{16}\text{O}/^{18}\text{O}$  ratios could be a second difference between RCB and dLHdC stars. Clayton et al. 2007 and García-Hernández et al. (2009) noted that dLHdC stars have  $^{16}\text{O}/^{18}\text{O} < 1$  and most RCB stars have  $^{16}\text{O}/^{18}\text{O} > 1$ . However, this analysis is based on a small sample of only two dLHdC and five RCB stars<sup>2</sup>. Both dLHdC stars in the sample have  $^{16}\text{O}/^{18}\text{O} < 1$ , while three of the five RCB stars have  $^{16}\text{O}/^{18}\text{O} > 1$ . Karambelkar et al. (2021) measured the ratios for six additional RCB stars using medium resolution spectra and found that they had  $^{16}\text{O}/^{18}\text{O} > 1$ . However, additional measurements of these ratios for dLHdC stars were not possible in the past because of the five dLHdC stars known at the time, only three had temperatures cold enough to show the CO bands (Clayton et al. 2007; García-Hernández et al. 2009; García-Hernández et al. 2010).

In this paper, we present the largest sample of  $^{16}\text{O}/^{18}\text{O}$  values in dLHdC and RCB stars measured to date. We use medium resolution NIR spectra to measure  $^{16}\text{O}/^{18}\text{O}$  for seven dLHdC and 33 RCB stars. We also present *JHK*-band spectra of 21 (20 new, one previously known) dLHdC stars for the first time. Our results conclusively show that most dLHdC stars have lower  $^{16}\text{O}/^{18}\text{O}$  than most RCB stars. In Section 4.2, we describe our spectroscopic observations, which include data collected over

---

<sup>2</sup>Note that the star HD 175893 was originally classified as a dLHdC star but is now known to be an RCB star based on an IR excess found by Tisserand (2012)

the last 15 years. In Section 4.3, we describe the NIR spectral features of dLHdC stars. We outline our methods for measuring  $^{16}\text{O}/^{18}\text{O}$  in Section 4.4. We discuss the implications of the different oxygen isotope ratios for formation scenarios of RCB and dLHdC stars in Section 4.5, and conclude with a summary of our results in Section 4.6.

## 4.2 Data

Our data comprise medium resolution NIR spectra of 24 dLHdC stars and 49 RCB stars. All but two of the stars are resident in the Milky Way; the others are in the Magellanic Clouds. The complete log of spectroscopic observations together with the S/N for each spectrum is presented in Table 4.1.

The spectra of 18 of the 20 newly discovered dLHdC stars were taken with the Triple-spec spectrograph (Herter et al. 2008,  $R \approx 3000$ ) on the 200-inch Hale telescope at Palomar observatory on several nights between June and October 2021. Two newly discovered dLHdC star (A166 and A183) were observed with the SpeX spectrograph ( $R \approx 2500$ ) on the 3-m NASA Infrared Telescope Facility (IRTF, Rayner et al. 2003) on UT 20210623. We include a previously unpublished spectrum of the previously known dLHdC star HD 137613 taken with the UKIRT Imager Spectrometer (UIST, Ramsay Howat et al. 2004,  $R \approx 3100$ ) on the 3.8-m United Kingdom Infrared Telescope (UKIRT) on UT 20050309. We also include spectra of three other previously known dLHdC stars obtained with the Gemini Near-infrared Spectrograph (GNIRS, Elias et al. 2006) on the 8.1-m Gemini-South telescope in the long-slit mode with  $R \approx 5900$  in 2005, reported by Clayton et al. (2007).

The spectra of the RCB stars were collected over the last 15 years at three telescopes with four different instruments. We include spectra of six RCB stars obtained with Gemini South/GNIRS in September 2005 (Clayton et al. 2007) and 4 more RCB stars observed with the Flamingos 2 spectrograph (Eikenberry et al. 2004) on the Gemini-South telescope in 2015 and 2016. We observed the RCB star Z Umi with GNIRS on the Gemini-North telescope in 2011. In 2013, we observed nine RCB stars with IRTF/SpeX at  $R \approx 2500$ . We observed 12 more RCB stars in 2014 and 26 RCB stars in 2015 with IRTF/Spex at  $R \approx 5000$ .

The Triplespec and IRTF spectra were reduced using the IDL package `spextool` (Cushing et al. 2004), and were flux calibrated and corrected for telluric absorption with standard star observations using `xtellcor` (Vacca et al. 2003). The UKIRT spectrum of HD 137613 was reduced in a standard manner using the Figaro software

Table 4.1: Log of spectroscopic observations

Name	Class	Date	S/N	Tel./Inst.	Name	Class	Date	S/N	Tel./Inst.
HD 137613	dLHdC	09/03/2005	>100	UKIRT/UIST	ASAS-RCB-17	RCB	08/2013,06/2015	27	IRTF/Spex
HD 182040	dLHdC	09/2005	>100	GS/GNIRS	ASAS-RCB-4	RCB	08/2013,06/2015	25	IRTF/Spex
HD 148839	dLHdC	09/2005	>100	GS/GNIRS	MACHO-401.48170.2237	RCB	08/2013,06/2015	36	IRTF/Spex
HD 173409	dLHdC	09/2005	>100	GS/GNIRS	ASAS-RCB-14	RCB	08/2013,08/2014	51	IRTF/Spex
A183	dLHdC	23/06/2021	92	IRTF/Spex	ASAS-RCB-18	RCB	08/2014	42	IRTF/Spex
A166	dLHdC	23/06/2021	48	IRTF/Spex	IRAS18135.5-2419	RCB	08/2014	39	IRTF/Spex
C17	dLHdC	25/06/2021	44	P200/TSpec	EROS2-CG-RCB-4	RCB	08/2014	48	IRTF/Spex
A223	dLHdC	25/06/2021	116	P200/TSpec	MACHO-308.38099.66	RCB	08/2014,06/2015	22	IRTF/Spex
B42	dLHdC	25/06/2021	109	P200/TSpec	WISE_J194218.38-203247.5	RCB	08/2014	68	IRTF/Spex
A226	dLHdC	25/06/2021	50	P200/TSpec	OGLE-GC-RCB-1	RCB	08/2014,06/2015	62	IRTF/Spex
C38	dLHdC	29/06/2021	64	P200/TSpec	EROS2-CG-RCB-9	RCB	08/2014	40	IRTF/Spex
C20	dLHdC	29/06/2021	39	P200/TSpec	EROS2-CG-RCB-11	RCB	08/2014	41	IRTF/Spex
C105	dLHdC	02/07/2021	140	P200/TSpec	WISE_J183649.54-113420.7	RCB	08/2014	31	IRTF/Spex
F75	dLHdC	02/07/2021	49	P200/TSpec	V739 Sgr	RCB	08/2014,06/2015	52	IRTF/Spex
B565	dLHdC	15/09/2021	70	P200/TSpec	V3795 Sgr	RCB	08/2014	67	IRTF/Spex
B566	dLHdC	15/09/2021	90	P200/TSpec	ASAS-RCB-5	RCB	06/2015	58	IRTF/Spex
C528	dLHdC	15/09/2021	20	P200/TSpec	ASAS-RCB-7	RCB	06/2015	62	IRTF/Spex
C539	dLHdC	15/09/2021	46	P200/TSpec	ASAS-RCB-16	RCB	06/2015	59	IRTF/Spex
A811	dLHdC	15/09/2021	65	P200/TSpec	ASAS-RCB-19	RCB	06/2015	42	IRTF/Spex
B567	dLHdC	15/09/2021	74	P200/TSpec	ASAS-RCB-20	RCB	06/2015	42	IRTF/Spex
A798	dLHdC	15/10/2021	47	P200/TSpec	EROS2-CG-RCB-3	RCB	06/2015	73	IRTF/Spex
C542	dLHdC	15/10/2021	89	P200/TSpec	EROS2-CG-RCB-10	RCB	06/2015	24	IRTF/Spex
B563	dLHdC	15/10/2021	60	P200/TSpec	EROS2-CG-RCB-13	RCB	06/2015	41	IRTF/Spex
A814	dLHdC	15/10/2021	50	P200/TSpec	FH Sct	RCB	06/2015	62	IRTF/Spex
HD 175893	RCB	09/2005	>100	GS/GNIRS	GU Sgr	RCB	06/2015	45	IRTF/Spex
S Aps	RCB	09/2005	>100	GS/GNIRS	RS Tel	RCB	06/2015	32	IRTF/Spex
SV Sge	RCB	09/2005	>100	GS/GNIRS	V482 Cyg	RCB	06/2015	25	IRTF/Spex
ES Aql	RCB	09/2005	>100	GS/GNIRS	V854 Cen	RCB	06/2015	39	IRTF/Spex
WX CrA	RCB	09/2005	>100	GS/GNIRS	V1783 Sgr	RCB	06/2015	40	IRTF/Spex
U Aqr	RCB	09/2005	>100	GS/GNIRS	V2552 Sgr	RCB	06/2015	40	IRTF/Spex
Z Umi	RCB	03/2011	>100	GN/NIRI	VZ Sgr	RCB	06/2015	40	IRTF/Spex
ASAS-RCB-11	RCB	08/2013	34	IRTF/Spex	WISE_J174328.50-375029.0	RCB	06/2015	42	IRTF/Spex
EROS2-CG-RCB-6	RCB	08/2013	26	IRTF/Spex	V532 Oph	RCB	06/2015	57	IRTF/Spex
V517 Oph	RCB	08/2013	32	IRTF/Spex	HV 5637	RCB	11/2015	>50	GS/F-2
V1157 Sgr	RCB	08/2013	39	IRTF/Spex	EROS2-SMC-RCB-1	RCB	12/2015	>100	GS/F-2
NSV 11154	RCB	08/2013	22	IRTF/Spex	EROS2-SMC-RCB-2	RCB	10/03/2016	> 50	GS/F-2
					EROS2-SMC-RCB-3	RCB	10/09/2016.	> 50	GS/F-2

package for flatfielding, removal of the effects of cosmic ray hits, spectral and spatial rectification of the spectral images, wavelength calibration using an argon lamp, and ratioing by the spectrum of a standard star. The Gemini spectra were reduced similarly, but used a combination of IRAF and Figaro as described in Clayton et al. (2007).

### 4.3 NIR spectra of dLHdC stars

We present *JHK*-band NIR spectra of the 20 new dLHdC stars in Figure 4.1. We also include in the figure spectra of the previously known dLHdC star HD 137613 (green) and the RCB star NSV11154 (red, taken from Karambelkar et al. 2021).

The spectra of the dLHdC stars closely resemble NIR spectra of RCB stars taken at maximum light. The continuum shapes resemble those of F-G type stars. Numerous absorption lines are present. We identify strong absorption features attributed to C I

(most prominently at 1.06883, 1.0686, 1.0688 and 1.06942  $\mu\text{m}$  in the J-band and 1.73433, 1.74533 and 1.75104  $\mu\text{m}$  in the H-band) and a blend of numerous Fe I, K I and Si I lines (see Rayner et al. (2003) for the wavelengths). H lines are absent in the NIR spectra of the dLHdC stars<sup>3</sup>. Only five of the twenty new dLHdC stars show  $^{12}\text{C}^{16}\text{O}$  and  $^{12}\text{C}^{18}\text{O}$  molecular features (presumably because the others are too hot for CO to exist in detectable amounts). Of the five, all but A166 also show the  $^{12}\text{C}^{14}\text{N}$  bands at 1.0875, 1.0929, 1.0966, 1.0999  $\mu\text{m}$ . Two additional stars B565 and A811 show CN but no CO bands.

### Helium 1.0833 $\mu\text{m}$ triplet

Our NIR spectra cover the He I 1.0833  $\mu\text{m}$  triplet. This feature can serve as a tracer of high velocity winds around RCB and dLHdC stars. The levels of this transition are 20 eV above the ground state, and cannot be populated by photospheric radiation of dLHdC and RCB stars. Instead, they can be collisionally excited in high velocity winds around these stars. The He I feature has been observed in several RCB stars either as blueshifted absorption or as a P-Cygni profile with velocities as high as 500  $\text{km s}^{-1}$  (Clayton et al. 2003; Clayton et al. 2011; Karambelkar et al. 2021). The strength and velocity of the winds around RCB stars are greatest when the stars have just emerged from dust enshrouded minima, and decrease with time thereafter. This suggests that the winds around RCB stars are dust-driven; that is, the gas is dragged to high velocities by dust grains that are accelerated by radiation pressure. As dLHdC stars do not show dust excesses in their spectral energy distributions, we do not expect to see dust-driven winds around them. Geballe et al. (2009) observed the four previously known dLHdC stars and found no evidence for strong RCB-like He I absorption lines in their spectra.

Figure 4.2 shows a zoom-in of the NIR spectra of the new dLHdC stars around the He I 1.0833  $\mu\text{m}$  triplet. We do not detect RCB-like (width  $> 200 \text{ km s}^{-1}$ ) helium absorption in the NIR spectra for any of the newly discovered dLHdC stars, except possibly A166. We cannot determine whether a lower velocity He I component is present in this star from our medium resolution spectra, as we cannot resolve possible contribution of He I to the Si I (1.0831  $\mu\text{m}$ ) line. A166 is the only dLHdC star that shows signs of an extended absorption component in addition to Si I absorption. If this is indeed the He I line, it would imply a wind velocity of  $\approx 400 \text{ km s}^{-1}$ . Higher resolution observations are necessary to identify the sources of this absorption.

---

<sup>3</sup>See <https://www.gemini.edu/observing/resources/near-ir-resources/spectroscopy/hydrogen-recombination-lines> for a list of NIR H lines.

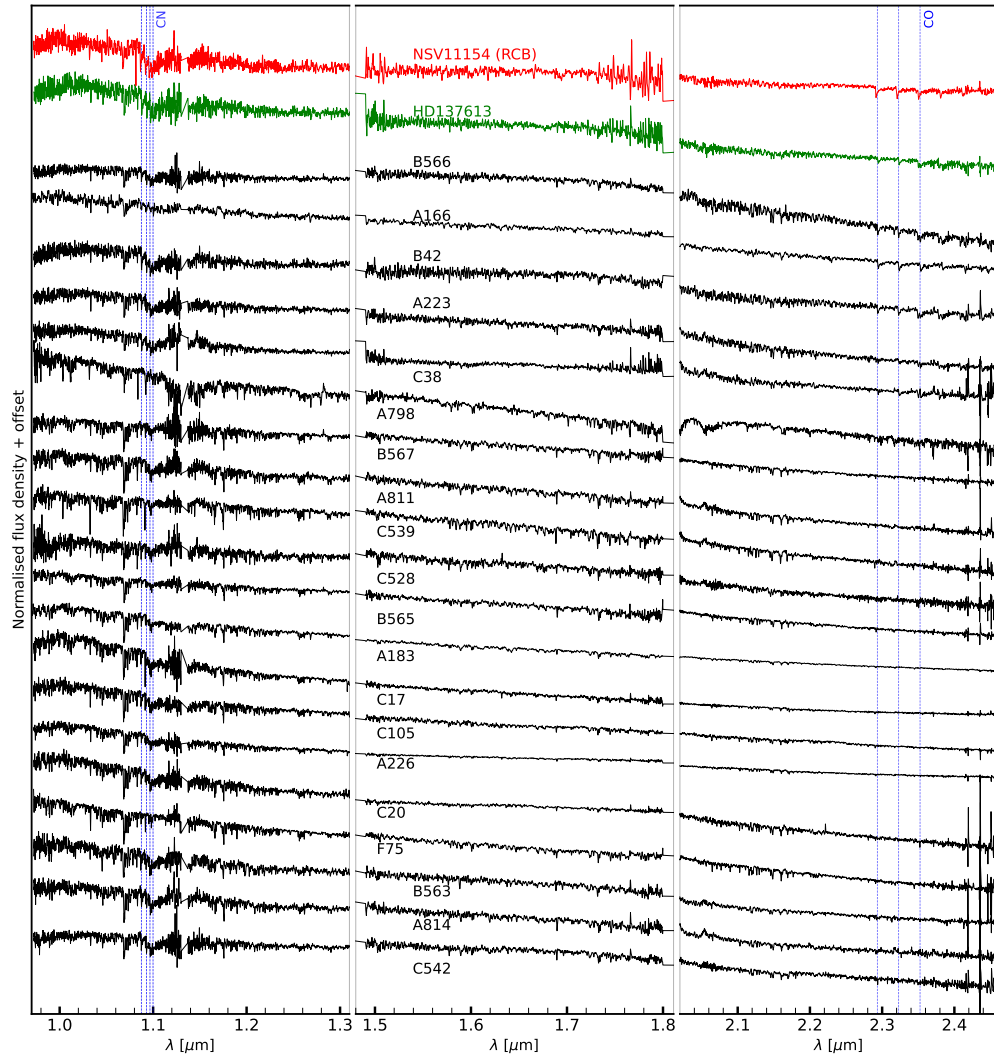


**Figure 4.1: Near-infrared spectra of the newly discovered dLHdC stars.** Near-infrared spectra of the RCB star NSV11154 and the previously known dLHdC star HD137613 are also shown for comparison. The rest-frame positions of the CN and  $^{12}\text{C}^{16}\text{O}$  absorption bands are indicated by dashed vertical lines.

Although we cannot completely resolve any possible low velocity He I component, our observations rule out the presence of strong, RCB-like dust-driven mass loss in dLHdC stars. This is expected, as none of these stars (except A166) shows a significant IR excess (Tisserand et al. 2021). We note, however, that this does not rule out the possibility that dLHdC stars were forming dust at some point in their history ( $\gtrsim 10$  years ago). Observations of XX Cam — an RCB star that has not entered a dust-enshrouded decline for the last six decades — do not show any significant He I features, similar to dLHdC stars (Geballe et al. 2009). The dust-driven He I wind is thus only a tracer of recent (few years to decades) dust-formation.

#### 4.4 $^{16}\text{O}/^{18}\text{O}$ : Analysis and results

##### Analysis

In this section we constrain the  $^{16}\text{O}/^{18}\text{O}$  ratios of the five newly discovered dLHdC stars that show  $^{12}\text{C}^{16}\text{O}$  and  $^{12}\text{C}^{18}\text{O}$  bands, the previously known dLHdC stars HD 137613 and HD 182040 and 33 RCB stars that show the CO bands. Figure 4.3 shows the first four overtone CO bandheads of the seven dLHdC stars and six representative RCB stars. Even from visual inspection of the spectra, it is evident that in general the  $^{12}\text{C}^{18}\text{O}$  absorptions are stronger in dLHdC stars than RCB stars. Here, we describe our procedure to derive constraints on the  $^{16}\text{O}/^{18}\text{O}$  ratios from these and other spectra.

We follow the procedure described in Karambelkar et al. (2021). We first generated synthetic spectra using a grid of hydrogen-deficient spherically symmetric MARCS (Model Atmospheres in Radiative and Convective Scheme) atmospheric models with input compositions characteristic of RCB and dLHdC stars ( $\log \epsilon(\text{H}) = 7.5$ ,  $\log \epsilon(\text{He}) = 11.5$ ,  $\log \text{C/He} = 0.01$ , Gustafsson et al. 1975; Gustafsson et al. 2008; Bell et al. 1976; Plez 2008). The models assumed a solar metallicity to derive compositions of other elements, a total mass of  $1 \text{ M}_\odot$ ,  $\xi = 5 \text{ km s}^{-1}$  and surface gravity  $\log g = 1.0$ . We generated synthetic spectra using the package TURBOSPECTRUM (Alvarez et al. 1998) and line lists from Goorvitch (1994), B. Plez 2010 (private communication and described in Hedrosa et al. 2013) and Yurchenko et al. (2018) for CO, CN and C<sub>2</sub> molecules, respectively. We varied the effective temperatures from 4000 to 7500 K in intervals of 250 K. The C, N and O abundances are relevant to measure the oxygen isotope ratios. However, we cannot measure these abundances from our low to medium resolution spectra directly. We assumed a C/He ratio of 0.01 (Asplund et al. 2000), corresponding to  $\log \epsilon(\text{C}) = 9.5$ . We also fixed the total oxygen abundance to  $\log \epsilon(\text{O}) = 8.8$  (consistent with the range of observed

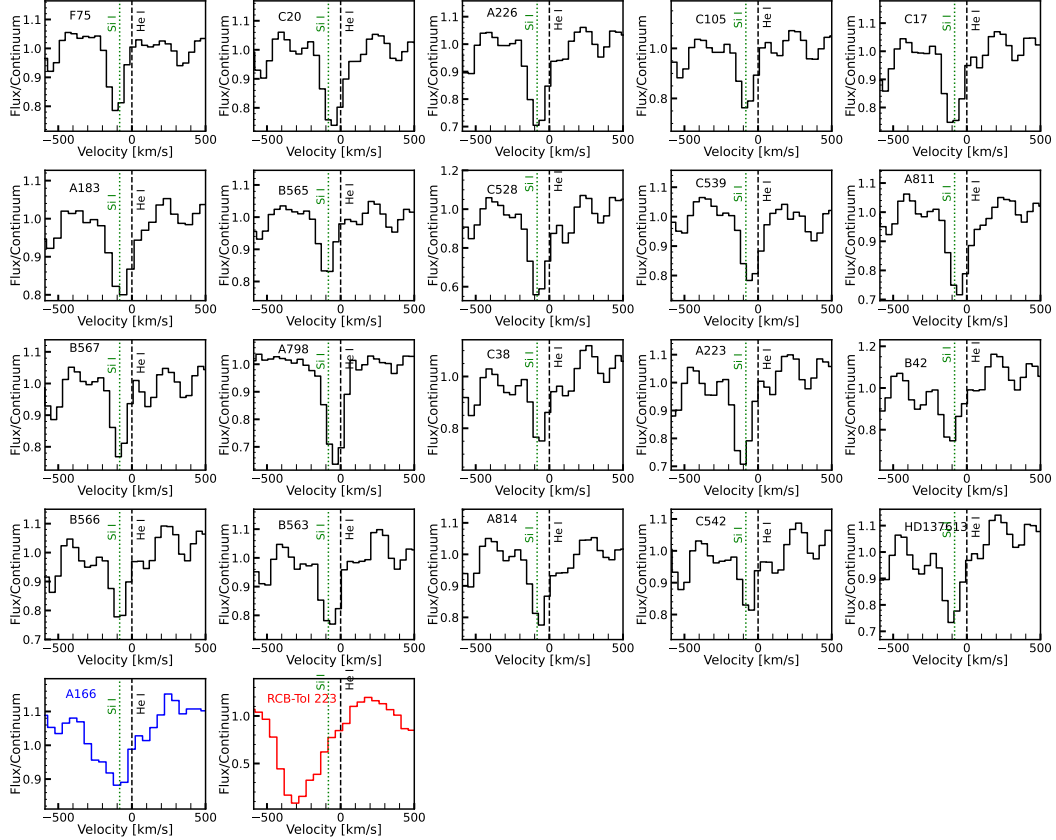


**Figure 4.2: Zoom-in of the spectral region around the He I (10833 Å) triplet.** The velocity is measured with respect to 1.0833  $\mu\text{m}$ . The same spectral region of He I profile of an RCB star is shown in red — RCB-ToI-223 (a.k.a. WISE J182010.96-193453.4), at a phase when it has just emerged from a dust decline. We cannot resolve the contribution from the Si I line to any He I features from our low resolution spectra. However, it is evident that we do not detect any strong ( $> 200 \text{ km s}^{-1}$ ), RCB-like winds in any dLHdC star, suggesting that there are no dust-driven winds around them. This is consistent with no hot dust excesses seen in the SEDs of any of these stars. A166 is the only dLHdC star that shows a possible high velocity He I absorption profile (plotted in blue).

O abundances for RCB stars Asplund et al. 2000), and only varied the oxygen isotope ratios to vary the relative contribution of  $^{16}\text{O}$  and  $^{18}\text{O}$ . We chose  $^{16}\text{O}/^{18}\text{O}$  values of 0.01, 0.05, 0.1, 0.2, 0.5, 1, 2, 5, 10, 20, 50, 500 and infinity (no  $^{18}\text{O}$ ). Finally, to partially mitigate the effects of fixing the abundances, we varied the nitrogen abundances, choosing values of  $\log \epsilon(\text{N}) = 7.0, 7.5, 8.0, 8.5$  and  $9.4$  (Asplund et al. 2000) Additionally, for RCB stars, the warm dust shell can contribute significantly to the K-band flux (up to 80%, Tisserand et al. 2013), veiling the absorption bands. To account for this, we introduced an additional parameter  $f_{\text{dust}} = \frac{F_{\text{shell,K}}}{F_{\text{total,K}}}$ , and varied it between 0 to 0.8 in steps of 0.1 for RCB stars. We do not expect this to be a significant effect for dLHdC stars as they do not have infrared dust excesses. We fit the synthetic spectra to continuum-normalised NIR spectra and visually examine each of the fits to determine the range of isotope ratios that is consistent with the observed spectra. We are only able to place wide range estimates on the oxygen isotope ratios owing to the several free parameters and assumptions in our fitting. Future higher resolution spectra will determine the CNO abundances precisely and provide precise oxygen isotope ratios for the stars presented here. The derived values of  $^{16}\text{O}/^{18}\text{O}$  are listed in Table 4.2, and Fig. 4.4, Fig. 4.5 and Fig. 4.6 show some examples of the model fits.

As noted in García-Hernández et al. (2009), it is challenging to measure the  $^{16}\text{O}/^{18}\text{O}$  ratios accurately from medium resolution spectra. The  $^{12}\text{C}^{16}\text{O}$  and  $^{12}\text{C}^{18}\text{O}$  absorption bands can be contaminated by absorption from other molecules such as  $^{12}\text{C}^{14}\text{N}$  and  $\text{C}_2$ . The absorption lines of CN and  $\text{C}_2$  are densely packed in the K band. It is also possible that the  $^{12}\text{C}^{16}\text{O}$  absorption bands are saturated, resulting in a smaller measured  $^{16}\text{O}/^{18}\text{O}$  ratios than the true value. There is also a degeneracy between the effects of the effective temperatures and nitrogen abundances on the depths of the CO absorption bands. For these reasons, we are not able to tightly constrain  $^{16}\text{O}/^{18}\text{O}$ , but instead provide a range of values combining the effects of the temperatures, nitrogen abundances and  $f_{\text{dust}}$ . Wherever possible, we use estimates of temperature ranges from the literature to tighten the constraints. Despite the wide range of ratios for each star, our measurements strongly suggest that most dLHdC stars have significantly lower  $^{16}\text{O}/^{18}\text{O}$  than RCB stars.

## Results

### dLHdC stars

With the exception of A166, the depths of the  $^{12}\text{C}^{18}\text{O}$  absorption bands in the dLHdC stars are comparable to those of the  $^{12}\text{C}^{16}\text{O}$  bands (see Figure 4.3). We use temperature estimates from the  $V - I$  color calibration of the HdC spectral classification system found in Crawford et al. (in prep). From comparisons to synthetic spectra we derive  $^{16}\text{O}/^{18}\text{O}$  ratios in the ranges 0.05–0.2 for B42, C38 and B566, 0.1–0.5 for A223, HD 182040 and HD 137613. Our derived values for HD 137613 and HD 182040 are consistent with those reported by Clayton et al. (2007) from medium resolution and García-Hernández et al. (2009) from high resolution spectra.

For B42, none of the spectral models fit the CO features at 2.349  $\mu\text{m}$  and 2.352  $\mu\text{m}$ . This could be because the 2.352  $\mu\text{m}$   $^{12}\text{C}^{16}\text{O}$  band is saturated. Fits to the 2.378 and 2.383  $\mu\text{m}$  bands suggest  $^{16}\text{O}/^{18}\text{O} = 0.05\text{--}0.2$ , but the only models that fit these bands have a low nitrogen abundance of  $\log \epsilon(\text{N}) = 7.0$ . The optical spectrum of B42 shows strong CN bands (see Tisserand et al. 2021), suggesting that the nitrogen abundance may not be so low. It is possible that the 2.383  $\mu\text{m}$   $^{12}\text{C}^{16}\text{O}$  band in B42 is also saturated, and the value we report is lower than the true  $^{16}\text{O}/^{18}\text{O}$ . If this is the case, our reported uncertainty on the  $^{16}\text{O}/^{18}\text{O}$  of B42 is also likely underestimated, as it does not include the systematic uncertainty associated with the saturated bands and the nitrogen abundances. Higher resolution observations are necessary to measure the true nitrogen abundance and the true  $^{16}\text{O}/^{18}\text{O}$  value of B42.

Unlike the other dLHdC stars, A166 shows significantly weaker  $^{12}\text{C}^{18}\text{O}$  absorptions than the  $^{12}\text{C}^{16}\text{O}$  absorption; we constrain  $^{16}\text{O}/^{18}\text{O} > 20$  for this star. Tisserand et al. 2021 note that A166 is an outlier among the newly discovered dLHdC stars. In the HR diagram, it is located near two cool RCB stars and is distant from most dLHdC stars. It also has IR excesses in the WISE W3 and W4 bands. This, together with its high, RCB-like value of  $^{16}\text{O}/^{18}\text{O}$  and possible broad He I absorption suggests that it is an RCB star. However, the lack of IR excesses in the NIR and WISE W1 and W2 bands indicates that it is in a phase of low dust production, similar to XX Cam (see Section 4.6 of Tisserand et al. 2021).

### RCB stars

Of the 33 RCB stars that show the CO overtone absorption bands, estimates of effective temperatures are available for 19 (Crawford et al., in prep). We are able to

Table 4.2: Range of model parameters that best fit the observed spectra

Name	Class	Temperature	$\log(\epsilon(N))$	$f_{\text{dust}}$	$^{16}\text{O}/^{18}\text{O}$
B42 <sup>a</sup>	dLHdC	4500-5000 <sup>c</sup>	7.0-7.5	0	0.01-0.1
C38	dLHdC	5000-5800 <sup>c</sup>	9.4	0	0.05-0.2
B566	dLHdC	5000-5800 <sup>c</sup>	9.4	0	0.05-0.5
HD 137613	dLHdC	4500-5000 <sup>c</sup>	7.5-9.4	0	0.05-0.5
A223	dLHdC	5000-5800 <sup>c</sup>	9.4	0	0.2-1
HD 182040	dLHdC	5000-5800 <sup>c</sup>	8.5-9.4	0	0.1-0.5
A166	dLHdC	4000-6000 <sup>d</sup>	7.0-9.4	0	> 20
HD 175893	RCB	4500-5000 <sup>c</sup>	7.0-9.4	0-0.5	0.01 - 0.2
ASAS-RCB-11	RCB	4500-5000 <sup>c</sup>	7.0-9.4	0-0.3	0.01 - 0.2
WX Cra	RCB	4100-4500 <sup>c</sup>	7.0-9.4	0-0.2	0.05 - 1
EROS2-CG-RCB-6	RCB	4500-5750 <sup>d</sup>	7.0-9.4	0-0.8	0.2 - 5
IRAS 1813.5-2419	RCB	3900-4100 <sup>c</sup>	7.0-9.4	0-0.5	0.2 - 20
S Aps <sup>a</sup>	RCB	4100-4500 <sup>c</sup>	7.0	0-0.8	1 - 5
SV Sge <sup>a</sup>	RCB	3900-4100 <sup>c</sup>	7.0-9.4	0	1 - 5
HV 5637	RCB	4500-5750 <sup>d</sup>	7.0-9.4	0-0.8	1 - 50
ES Aql <sup>a</sup>	RCB	4500-6000 <sup>d</sup>	7.0-9.4	0-0.3	2 - 20
Z Umi	RCB	4750-5500 <sup>d</sup>	9.4	0.5-0.8	1 - 20
EROS2-SMC-RCB-2	RCB	4500-6000 <sup>d</sup>	7.0-9.4	0-0.8	2 - 50
EROS2-SMC-RCB-3	RCB	5250-6000 <sup>d</sup>	9.4	0.5-0.8	5 - 50
V1783 Sgr	RCB	4100-4500 <sup>c</sup>	9.4	0.7-0.8	5 - 50
U Aqr	RCB	4100-4500 <sup>c</sup>	9.4	0.4-0.8	5 - 50
EROS2-CG-RCB-10	RCB	4500-5750 <sup>d</sup>	7.0-9.4	0-0.8	5 - 50
ASAS-RCB-17	RCB	4100-4500 <sup>c</sup>	7.0-9.4	0-0.1	5 - 50
NSV 11154	RCB	5250-5500 <sup>c</sup>	7.0-9.4	0-0.2	10 - 50
V1157 Sgr	RCB	3900-4100 <sup>c</sup>	7.0-9.4	0-0.8	> 10
ASAS-RCB-16	RCB	4100-4500 <sup>c</sup>	7.0	0	> 20
MACHO-401.48170.2237	RCB	4500-6000 <sup>d</sup>	7.0-9.4	0-0.8	> 20
ASAS-RCB-18	RCB	3750-3900 <sup>c</sup>	7.0-9.4	0-0.8	> 20
WISE_J174328.50-375029.0	RCB	3900-4100 <sup>c</sup>	7.0-9.4	0-0.6	> 50
ASAS-RCB-19	RCB	3750-3900 <sup>c</sup>	7.0-9.4	0.5-0.6	> 50
MACHO-308.38099.66	RCB	4000-5500 <sup>d</sup>	7.0-9.4	0-0.8	> 50
ASAS-RCB-4	RCB	3750-3900 <sup>c</sup>	7.0-9.4	0-0.2	> 50
EROS2-CG-RCB-13 <sup>f</sup>	RCB	4500-5500 <sup>d</sup>	7.0-9.4	0-0.8	> 500
EROS2-CG-RCB-3 <sup>f</sup>	RCB	6000-6500 <sup>d</sup>	9.4	0-0.3	> 500
EROS2-CG-RCB-4 <sup>b,f</sup>	RCB	4500-5500 <sup>d</sup>	7.0-9.4	0-0.8	> 500
V517 Oph <sup>f</sup>	RCB	4500-5500 <sup>d</sup>	7.0-9.4	0-0.8	> 500
ASAS-RCB-7 <sup>f</sup>	RCB	3750-3900 <sup>c</sup>	7.0-9.4	0-0.8	> 500
OGLE-GC-RCB-1 <sup>f</sup>	RCB	4100-4500 <sup>c</sup>	7.0-9.4	0-0.4	> 500
ASAS-RCB-5 <sup>f</sup>	RCB	3900-4100 <sup>c</sup>	7.0-9.4	0-0.6	> 500
WISE_J194218.38-203247.5 <sup>f</sup>	RCB	3900-4100 <sup>c</sup>	7.0-9.4	0-0.8	> 500

*a* : The  $^{12}\text{C}^{16}\text{O}$  absorption bands are possibly saturated, and the  $^{16}\text{O}/^{18}\text{O}$  is likely underestimated.

*b* : EROS2-CG-RCB-4 shows  $^{13}\text{C}^{16}\text{O}$  absorption bands.

*c* : Photometry based temperature range estimates from Crawford et al. 2022 (in prep).

*d* : Temperature ranges based on the models that are good fits to the NIR spectra.

*e* : Temperature range from SED fit in (Karambelkar et al. 2021).

*f* : The medium resolution spectra do not show any strong  $^{12}\text{C}^{18}\text{O}$  bandheads, but it is possible that these bands are not detected due to a combination of low resolution, low S/N, saturation and dust-dilution of CO bandheads (see Sec. 4.4).

derive the tightest constraints on  $^{16}\text{O}/^{18}\text{O}$  for them. For most of the remaining 12, we can only derive lower limits on  $^{16}\text{O}/^{18}\text{O}$ .

Most of the RCB stars in our sample have much weaker  $^{12}\text{C}^{18}\text{O}$  absorption bands relative to  $^{12}\text{C}^{16}\text{O}$ , than dLHdC stars. A total of 28 of the 33 RCB stars have  $^{16}\text{O}/^{18}\text{O} > 1$ . Eight of them do not show any  $^{12}\text{C}^{18}\text{O}$  bandheads in our medium resolution spectra, and are consistent with the  $^{16}\text{O}/^{18}\text{O} \gtrsim 500$  models. Fig. 4.6 shows a zoom-in of the spectrum of one such star. However, it is possible that these measurements are not accurate for the following reasons. First, it is possible that the resolution and S/N of these spectra is not sufficient to resolve a weak  $^{12}\text{C}^{18}\text{O}$  bandhead from the  $^{12}\text{C}^{14}\text{N}$  bands (that are possibly enhanced by the low effective temperatures) in this region of these cold stars. Second, it is possible that the strong CO bandheads in the spectra of these cold RCB stars are saturated. As our medium resolution spectra cannot resolve the weaker, unsaturated CO lines, we cannot accurately measure their oxygen isotope ratios. Third, it is also possible that the spectra of these cold stars suffer strong dust dilution, making it difficult to detect the diluted  $^{12}\text{C}^{18}\text{O}$  bandheads at medium resolution. We caution that a combination of these resolution, saturation and dilution effects could be preventing the detection of  $^{12}\text{C}^{18}\text{O}$  bands in our spectra of these cold stars. Higher resolution spectra are required to obtain reliable measurements of oxygen isotope ratios in these stars, which we highlight in Table 4.2. However, it is unlikely that they have very strong dLHdC-like  $^{12}\text{C}^{18}\text{O}$  bands. Thus, the medium resolution spectra suggest that a large majority of RCB stars have higher  $^{16}\text{O}/^{18}\text{O}$  than dLHdC stars.

Five RCB stars — HD 175893, ASAS-RCB-11, IRAS 18135.5-2419, WX CrA and EROS2-CG-RCB-6 — have prominent  $^{12}\text{C}^{18}\text{O}$  absorption features and are consistent with  $^{16}\text{O}/^{18}\text{O} < 1$ . We derive  $^{16}\text{O}/^{18}\text{O}$  values of 0.01–0.2, 0.01–0.2, 0.5–5, 0.05–1 and 0.2–5 for these stars, respectively. These values are similar to those of dLHdC stars. We note that our derived  $^{16}\text{O}/^{18}\text{O}$  values for HD 175893, S Aps, SV Sge, ES Aql, U Aqr, Z Umi and WX Cra agree with previous medium resolution measurements from Clayton et al. (2007). Our derived values also agree with high resolution measurements for all of these except S Aps, SV Sge and ES Aql, as the  $^{12}\text{C}^{16}\text{O}$  bandheads are saturated in these three (García-Hernández et al. 2010). Finally, the RCB star EROS2-CG-RCB-4 shows the  $^{13}\text{C}^{16}\text{O}$  absorption bandhead at 2.345, 2.374, 2.404 and 2.434  $\mu\text{m}$  (see Figure 4.3).

To summarize, we find that most dLHdC stars have  $^{16}\text{O}/^{18}\text{O} < 1$ , lower than most RCB stars. However, there is an overlap — a small fraction of dLHdC stars have

$^{16}\text{O}/^{18}\text{O} > 1$  while a small fraction of RCB stars have  $^{16}\text{O}/^{18}\text{O} < 1$ . We illustrate this in Figure 4.7. Finally, we emphasize that high resolution spectra are required to confirm the oxygen isotope ratio measurements, especially in the case of stars that have low effective temperatures. High-resolution spectra will help identify the stars for which the bandheads are saturated, and also provide accurate O and N abundance measurements which are crucial for precise  $^{16}\text{O}/^{18}\text{O}$  measurements. These observations should help confirm our conclusion that most dLHdC stars have smaller  $^{16}\text{O}/^{18}\text{O}$  than most RCB stars.

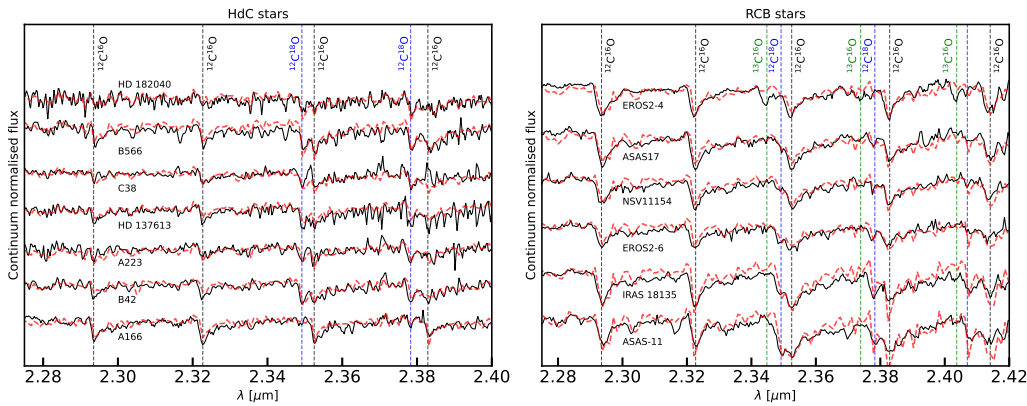


**Figure 4.3: Zoom-in of the  $^{12}\text{C}^{16}\text{O}$  and  $^{12}\text{C}^{18}\text{O}$  absorption bands of all seven dL-HdC stars (left) and six representative RCB stars (right) from our sample.** All dLHdC stars except A166 show strong  $^{12}\text{C}^{18}\text{O}$  absorption, comparable in strength to the  $^{12}\text{C}^{16}\text{O}$  absorption. The RCB stars show a range of  $^{12}\text{C}^{18}\text{O}$  absorption strengths. Shown are two RCB stars where the  $^{12}\text{C}^{18}\text{O}$  absorption is strongest, two where it is of intermediate strength and two where the absorption is weak. Of the 33 RCB stars analyzed here, only five have strong dLHdC-like  $^{12}\text{C}^{18}\text{O}$  absorption, while the remaining majority has intermediate or weak  $^{12}\text{C}^{18}\text{O}$  absorption. We also plot examples of synthetic spectra that fit the observed spectra as red dashed lines. Note that the RCB star EROS2-CG-RCB4 shows  $^{13}\text{C}^{16}\text{O}$  absorption bands (right panel).

## 4.5 Discussion

Our NIR spectroscopic observations have revealed that in addition to dust-formation, dLHdC and RCB stars can in most cases be distinguished based on their values of  $^{16}\text{O}/^{18}\text{O}$ . dLHdC stars in general have a lower  $^{16}\text{O}/^{18}\text{O}$  than RCB stars. It is not surprising that the oxygen isotope ratios are an important factor in the study of dLHdC and RCB stars. Anomalously low  $^{16}\text{O}/^{18}\text{O}$  in dLHdC and RCB stars was key to identifying the merger of a He-core and a CO-core white dwarf as their formation channel.

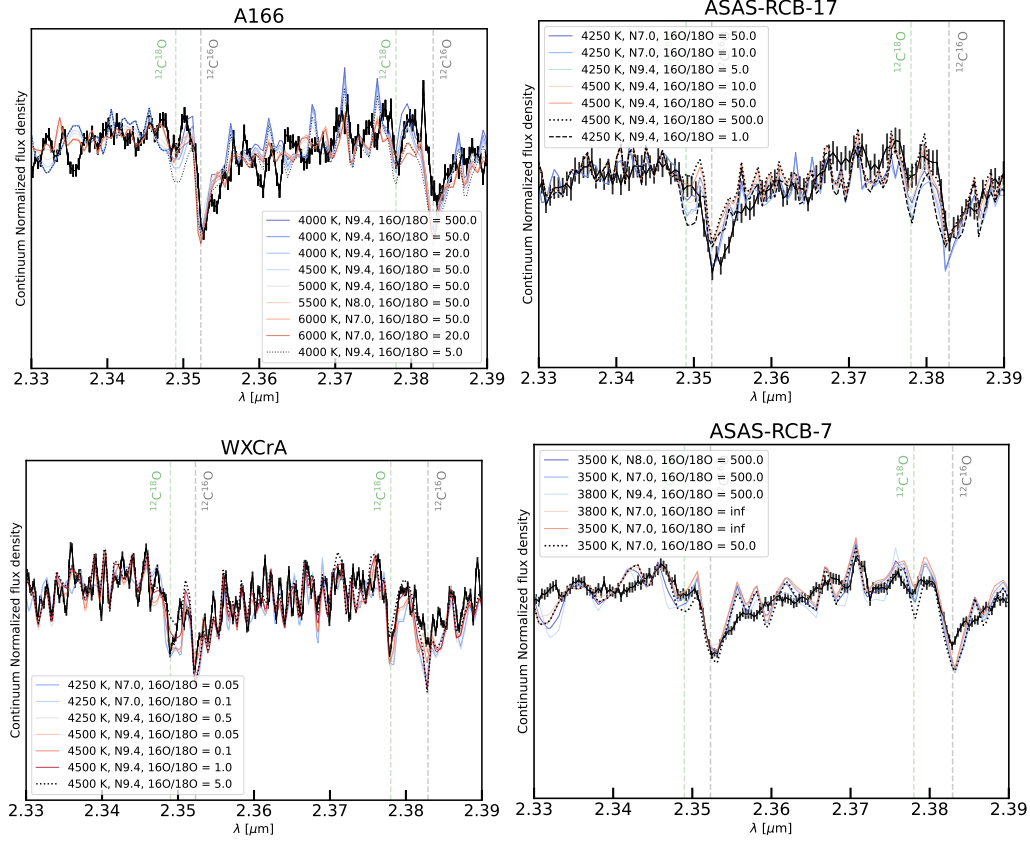


**Figure 4.4: Model fits to the CO absorption bandheads of the dLHdC star A166 and RCB stars ASAS-RCB-17, WXCrA and ASAS-RCB-7.** The spectra (with errorbars) are plotted in black, and the best-fit models for a wide allowed range of model parameters (Table 4.2) are plotted as solid colored lines. The measured  $^{16}\text{O}/^{18}\text{O}$  for these stars are  $> 20$ ,  $5 - 50$ ,  $0.05 - 1$  and  $> 500$ , respectively. The dotted and dashed lines show models with oxygen isotope ratios outside these derived ranges ( $^{16}\text{O}/^{18}\text{O} = 10$  for A166, 1 and 500 for ASAS-RCB-17, and 5 for WXCrA). It is challenging to distinguish between models with different N abundances given the medium resolution and S/N of the spectra. We focus on the regions around the  $^{12}\text{C}^{18}\text{O}$  and  $^{12}\text{C}^{16}\text{O}$  bandheads (dashed green and gray lines) and report the range of values consistent with the observed spectra.

$^{18}\text{O}$  is synthesized by the partial helium burning reaction  $^{14}\text{N}(\alpha, \gamma) \text{F}^{18}(\beta^+ \nu)^{18}\text{O}$ . This reaction is efficient at temperatures of  $\approx 10^8$  K (Clayton et al. 2007; Jeffery et al. 2011). At higher temperatures,  $^{18}\text{O}$  is burnt to  $^{22}\text{Ne}$ . These conditions can be achieved in a thin helium burning shell around the merger remnant of a He-core and a CO-core white dwarf (Clayton et al. 2007). The  $^{18}\text{O}$  is convectively dredged up to the surface of the star within the first few hundred years after the white dwarf merger (Crawford et al. 2020; Munson et al. 2021; Lauer et al. 2019). The photospheric

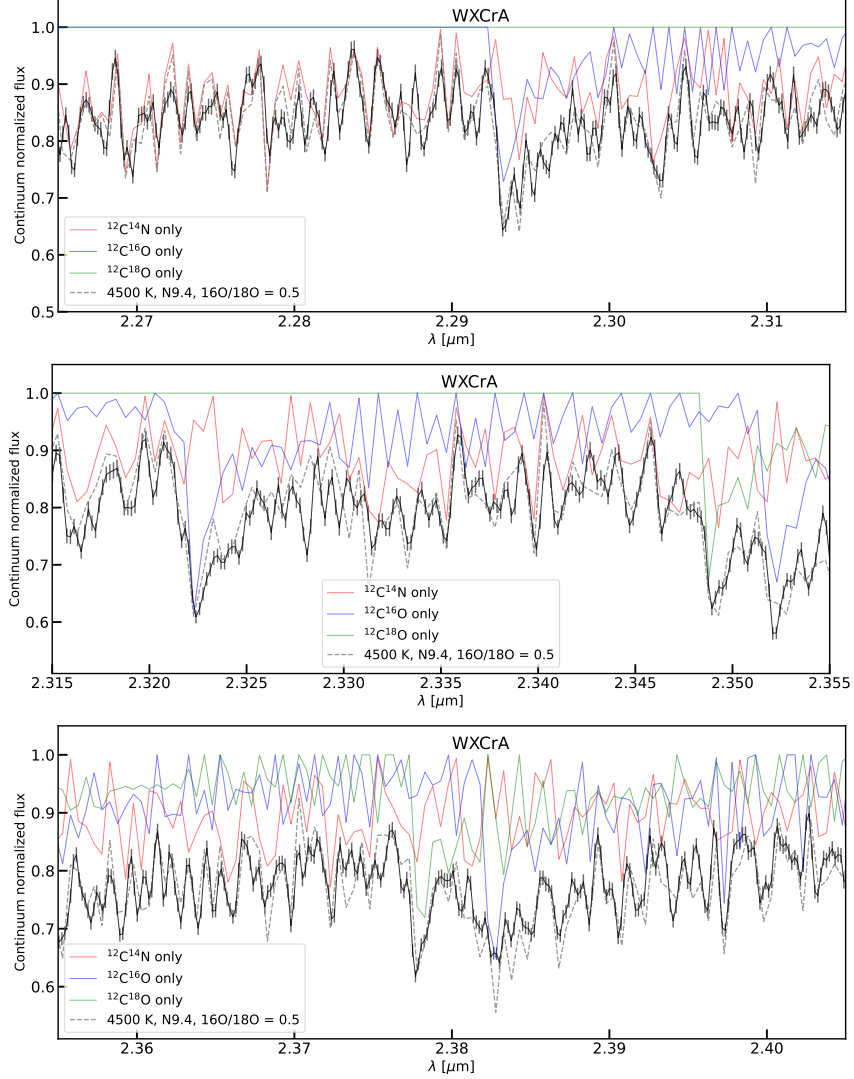


**Figure 4.5: Zoom-in of the spectra of the RCB star WXCrA (solid black line).** We plot the best fit-model synthetic spectrum to this star (gray, dashed line), and show the contribution of  $^{12}\text{C}^{14}\text{N}$  (solid red),  $^{12}\text{C}^{16}\text{O}$  blue and  $^{12}\text{C}^{18}\text{O}$  green. The top, middle and bottom panels show different spectral regions.

value of  $^{16}\text{O}/^{18}\text{O}$  in dLHdC and RCB stars is thus set within the first hundred years and remains constant for the rest of their lifetimes ( $\approx 10^{4-5}$  years). Here, we explore the properties of the merging white dwarfs that set the values of  $^{16}\text{O}/^{18}\text{O}$  in the remnant supergiants. We also discuss the implications of our observations on the dLHdC-RCB connection.

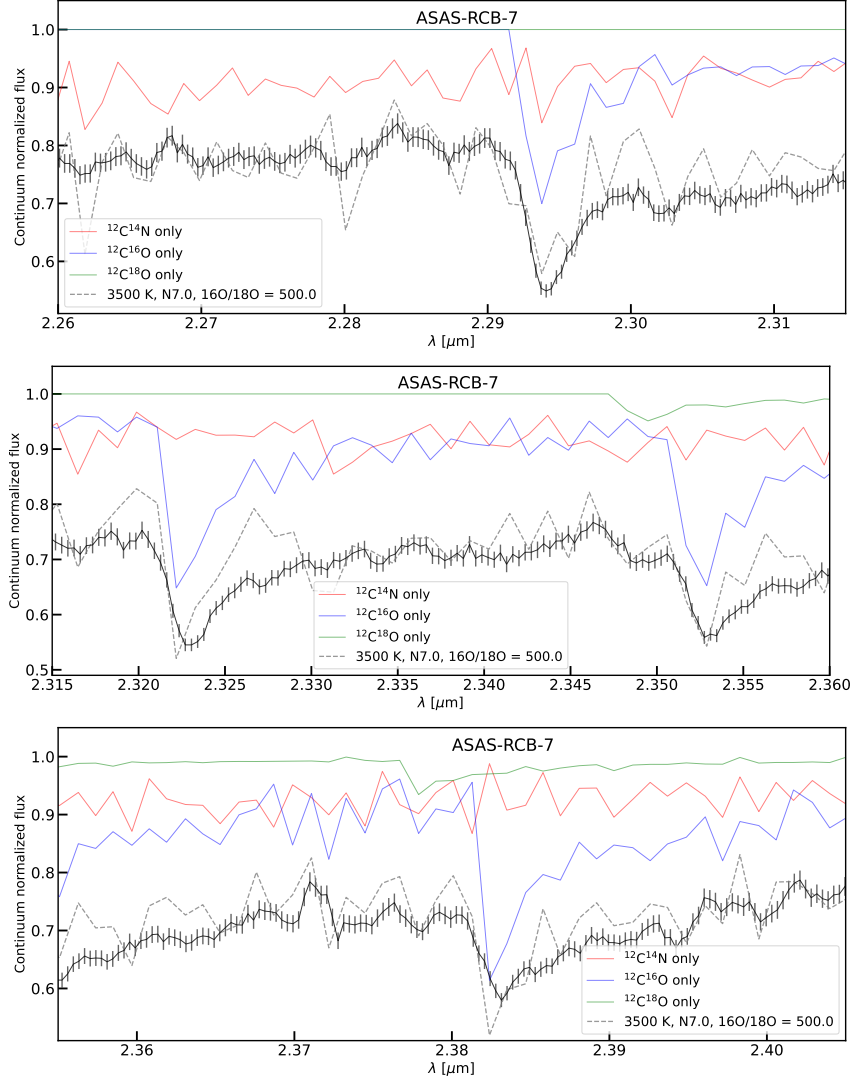


**Figure 4.6: Zoom-in of the spectra of the RCB star ASAS-RCB-7 (solid black line).** We plot the best fit-model synthetic spectrum to this star (gray, dashed line), and show the contribution of  $^{12}\text{C}^{14}\text{N}$  (solid red),  $^{12}\text{C}^{16}\text{O}$  blue and  $^{12}\text{C}^{18}\text{O}$  green. Unlike WXCrA (Fig. 4.5), this spectrum does not show very strong  $^{12}\text{C}^{18}\text{O}$  bandheads. As our oxygen ratio measurements are based on these bandheads, we estimate  $^{16}\text{O}/^{18}\text{O} \geq 500$  for this source. It is possible that the low spectroscopic resolution and S/N of this spectrum cannot resolve the blended weak bandhead. Higher resolution spectra are required to measure the ratio accurately. The other targets with  $^{16}\text{O}/^{18}\text{O} \geq 500$  could also be affected by a similar issue.

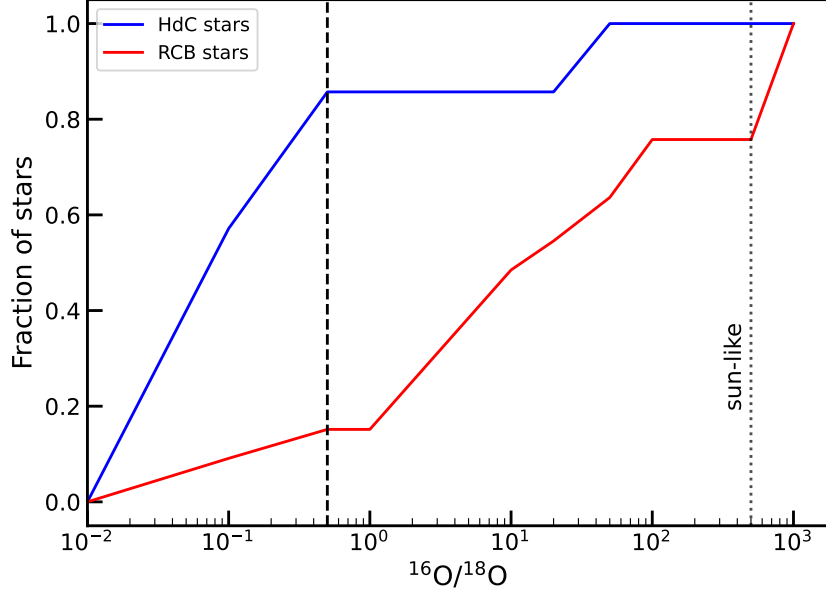


Figure 4.7: **Cumulative distribution plot showing the fraction of dLHdC and RCB stars that have  $^{16}\text{O}/^{18}\text{O}$  below a given value.** Of the dLHdC stars, 85% (6 out of 7) have  $^{16}\text{O}/^{18}\text{O} < 0.5$  (black dashed line) while only  $\approx 15\%$  of RCB stars (5 out of 33) are consistent with such low  $^{16}\text{O}/^{18}\text{O}$  values. Most dLHdC stars have a lower  $^{16}\text{O}/^{18}\text{O}$  than most RCB stars. A166 is the only dLHdC star that has  $^{16}\text{O}/^{18}\text{O} > 1$ . This star is an outlier amongst the newly discovered dLHdC stars, and is likely an RCB star in a low phase of dust production (see Sec. 4.1).

### The origin of different $^{16}\text{O}/^{18}\text{O}$ for dLHdC and RCB stars

Studies have just begun to examine the quantities that affect  $^{16}\text{O}/^{18}\text{O}$  in white dwarf merger remnants. The effects on  $^{16}\text{O}/^{18}\text{O}$  of the helium burning shell temperature, convective extent of the supergiant envelope and the amount of hydrogen in the shell have been explored (Crawford et al. 2020; Munson et al. 2021). Their values in turn depend on the properties of the merging He-core and CO-core white dwarfs, such as their masses, mass ratios and compositions. The different values of  $^{16}\text{O}/^{18}\text{O}$  in dLHdC and RCB stars thus suggest a correlation between the progenitor white dwarfs' properties and dLHdC/RCB formation, which we discuss here. Note however that there are several additional factors that could contribute to the oxygen isotope ratios and remain to be modeled. A large unmodeled source of uncertainty is the effect of the initial composition of the progenitor white dwarfs and post-merger remnant on  $^{16}\text{O}/^{18}\text{O}$ . The correlations that we discuss below are based on current understanding and are hence preliminary. Nevertheless, they demonstrate that different properties of merging white dwarfs can result in different values of  $^{16}\text{O}/^{18}\text{O}$ , possibly providing

a natural explanation for dLHdC versus RCB formation. Additional modeling will help establish robust relations between progenitor properties and dLHdC-RCB stars.

Crawford et al. (2020) explored the effect of the temperature of the helium burning shell ( $T_{\text{He}}$ ) on  $^{16}\text{O}/^{18}\text{O}$ . In particular,  $^{16}\text{O}/^{18}\text{O}$  drops below unity for shell temperatures in the range  $T_{\text{He}} \approx 2.5\text{--}3.5 \times 10^8 \text{ K}$ . Thus, dLHdC stars could be associated with WD merger remnants that have  $T_{\text{He}}$  in this range. For shell temperatures outside this range,  $^{16}\text{O}/^{18}\text{O}$  increases to RCB-like values, suggesting that RCB stars either have  $T_{\text{He}} < 2.5 \times 10^8 \text{ K}$  or  $T_{\text{He}} > 3.5 \times 10^8 \text{ K}$ .

From simulations of white dwarf mergers, Staff et al. (2012) found that  $T_{\text{He}}$  is inversely correlated with the mass ratio ( $q = M_{\text{He}}/M_{\text{CO}}$ , where  $M_{\text{He}}$  and  $M_{\text{CO}}$  are the masses of the He white dwarf and CO white dwarf, respectively). They derive values of  $T_{\text{He}} = 3, 2.5$  and  $1.5 \times 10^8 \text{ K}$  for  $q = 0.5, 0.6$  and  $0.7$ , respectively. The helium shell temperatures of dLHdC stars are consistent with mass ratios  $0.5 < q < 0.6$ . RCB stars are consistent either with  $q > 0.6$  or  $q < 0.5$  depending on whether they have  $T_{\text{He}} < 2.5 \times 10^8 \text{ K}$  or  $T_{\text{He}} > 3.5 \times 10^8 \text{ K}$ , respectively. However the Staff et al. (2012) analysis does not include an important factor — additional energy contributions from nucleosynthesis in the shell. This additional energy will increase the shell temperature, and thus the above estimates of  $T_{\text{He}}$  are likely lower limits, and the  $q$  ranges are unrealistic. No studies of temperature increase due to nucleosynthesis exist in literature.

To first order, we can estimate the temperature increase timescale assuming triple- $\alpha$  burning is the dominant nucleosynthetic energy source (Hansen et al. 2004). Assuming the shell parameters from Staff et al. (2012) and a 100% energy to temperature conversion, we find that the temperature of a  $q = 0.7$  merger with initial  $T_{\text{He,init}} = 1.5 \times 10^8 \text{ K}$  doubles within the first few years after merger. This time reduces to a few days for  $q = 0.6$  ( $T_{\text{He,init}} = 2 \times 10^8 \text{ K}$ ) and a few minutes for  $q = 0.5$  ( $T_{\text{He,init}} = 3 \times 10^8 \text{ K}$ ). The shell-burning temperatures for  $q < 0.6$  mergers can thus exceed  $4 \times 10^8 \text{ K}$ . RCB stars would then be consistent with low mass-ratio ( $q < 0.6$ ) mergers and dLHdC stars would be consistent with higher mass-ratio mergers ( $q > 0.7$ )<sup>4</sup>. More detailed studies of nucleosynthetic energy production are required to determine the exact ranges of  $q$  that might form RCB and dLHdC stars.

$T_{\text{He}}$  also depends on the total mass of the white dwarf merger (Staff et al. 2018);

---

<sup>4</sup>Note that for mergers where  $T_{\text{He}} > 4.5 \times 10^8 \text{ K}$ , other elemental abundances predicted by models do not agree with the observed RCB abundances (Crawford et al. 2020). This suggests that there is a lower limit on the mass-ratios of white dwarf binaries that can produce RCB/dLHdC stars.

however, the exact dependence has not been studied extensively. The Staff et al. (2012) estimates mentioned above assumed  $M_{\text{tot}} \approx 0.9 M_{\odot}$ . Without including nucleosynthetic energy, Staff et al. (2018) found that a  $M_{\text{tot}} = 0.7 M_{\odot}$ ,  $q = 0.5$  merger has  $T_{\text{He}} < 2 \times 10^8$  K — lower than the estimate of  $3 \times 10^8$  K for the  $0.9 M_{\odot}$ ,  $q = 0.5$  merger. This suggests that lower mass mergers have lower  $T_{\text{He}}$  than higher mass mergers. Adding nucleosynthetic energy can increase  $T_{\text{He}}$  for the  $0.7 M_{\odot}$  merger to the dLHdC range ( $2.5 - 3.5 \times 10^8$  K) and the  $0.9 M_{\odot}$  merger outside this range. dLHdC stars would then be consistent with arising from lower mass mergers than RCB stars. This would be consistent with the observation in Tisserand et al. (2021) that the population of dLHdC stars has lower luminosities than RCB stars, which they interpret as a consequence of dLHdC stars originating from lower mass mergers than RCB stars.

In addition to  $T_{\text{He}}$ ,  $^{16}\text{O}/^{18}\text{O}$  can also depend on the extent of the convective envelope and the mass of hydrogen in the helium burning shell (Zhang et al. 2014; Munson et al. 2021). Munson et al. explored the effect of convective overshoot factor ( $f$ ) on  $^{16}\text{O}/^{18}\text{O}$ . They found that for  $f < 0.07$ ,  $^{16}\text{O}/^{18}\text{O} \approx 1$ , but increases rapidly for  $f > 0.07$ . Large values of  $f$  correspond to cases where the convective envelope extends all the way to the CO core and dredges up additional  $^{16}\text{O}$  from the core into the envelope. The high values of  $^{16}\text{O}/^{18}\text{O}$  in RCB stars could be partly explained due to such a deep convective dredge up. That will also reduce C/O in RCB stars compared to dLHdC stars. The initial conditions of a merging system that would give rise to a deep convective zone remain to be explored. Munson et al. (2021) also showed that  $^{16}\text{O}/^{18}\text{O}$  increases with increasing mass of hydrogen in the helium-burning shell. The presence of hydrogen leads to a decrease of  $^{18}\text{O}$  and increase in  $^{16}\text{O}$  due to proton capture reactions. The source of this hydrogen is a thin hydrogen envelope around the progenitor He white dwarf (Zhang et al. 2014). The mass of the hydrogen envelope is inversely correlated with the mass of the He white dwarf (Staff et al. 2012; Driebe et al. 1998). However, a significant fraction of this hydrogen is expected to be burned during the merger. How much of the envelope hydrogen actually reaches the helium shell is not known.

In conclusion, the  $^{16}\text{O}/^{18}\text{O}$  values in white dwarf merger remnants are affected by the properties of the merging white dwarfs such as their total mass, mass ratios and individual compositions. In this context, the different values of  $^{16}\text{O}/^{18}\text{O}$  in dLHdC and RCB stars indicate that they are formed from distinct populations of progenitor white dwarf binary mergers.

### The evolutionary link between dLHdC and RCB stars

García-Hernández et al. (2010) speculated the possibility of an evolutionary link between dLHdC and RCB stars. This was based on their surface abundances, together with the assumptions that dLHdC→RCB (→ Extreme Helium Stars) is the common sequence and that their surface abundances change with evolution. They note that depending on the masses and compositions of the merging white dwarfs, the merger remnant will have different initial temperatures on the supergiant track. They associate dLHdC stars with the cooler parts of the supergiant track and RCB stars with hotter temperatures. In their model, depending on merger conditions the merger may first form a cold dLHdC star and eventually evolve to an RCB star, or directly form an RCB star.

The new observations, if corroborated by high-resolution spectroscopy, would show that the picture of a dLHdC-RCB evolutionary link could be incorrect. First, several newly discovered dLHdC stars have higher photospheric temperatures than many RCB stars (Tisserand et al. 2021). Second, the spectra presented and analyzed here demonstrate that dLHdC stars in general may have different values of  $^{16}\text{O}/^{18}\text{O}$  than RCB stars (Section 4.4). In addition, recent theoretical modeling by Crawford et al. (2020) suggest that the surface abundances of dLHdC and RCB stars remain constant throughout their lifetimes; that is, it would not be possible for one class to evolve into another.

Instead, we propose that whether a white dwarf merger forms a dLHdC or an RCB depends solely on the properties of the merging white dwarfs. The merger forms a dLHdC star (no significant dust formation, low  $^{16}\text{O}/^{18}\text{O}$ ) or an RCB star (dust formation, high  $^{16}\text{O}/^{18}\text{O}$ ) based on the mass ratios, masses and compositions of the white dwarfs. In this picture, it is still a mystery why RCB stars form large amounts of dust while dLHdC stars do not. It seems reasonable to expect that only those white dwarf mergers that are more massive than a certain threshold or have particular ranges of chemical compositions form remnants that can undergo dust formation. Future theoretical models and studies that more precisely identify the differences between dLHdC and RCB star progenitors could provide an answer to this question.

### The overlap between dLHdC and RCB stars

An intriguing observation is the five RCB stars (classified based on their observed IR excesses and brightness declines) that show low, dLHdC-like  $^{16}\text{O}/^{18}\text{O}$ . These

“overlap” stars may be a consequence of there being several different factors that contribute to  $^{16}\text{O}/^{18}\text{O}$ . For example, they could arise from typical RCB-like mass-ratio mergers but with a smaller total mass, smaller convective envelope or a smaller hydrogen content than typical. Another interesting possibility is that some dLHdC stars undergo a short-lived, dust forming phase. During this phase, these stars would be observed as dust-forming RCB-like stars with low  $^{16}\text{O}/^{18}\text{O}$  - similar to the five RCB stars mentioned above. This scenario does not contradict the observation that dLHdC stars do not show significant excesses in the mid-IR WISE bands. Tisserand et al. 2021 show that the emission from a circumstellar dust shell ejected from the surface of a star shifts from the mid-IR to longer wavelengths within a few decades. Thus, even if some dLHdC stars experienced dust formation  $\sim$ 10 years before their WISE observations, they would not show any excesses in the WISE bands. The dust around them would have cooled to  $< 50$  K (see Montiel et al. 2018) and would be observable only at very long wavelengths. Only one dLHdC star has been observed at far-infrared (FIR) wavelengths to date — HD 173409 which did not show any FIR excess (Montiel et al. 2018). Far-infrared and sub-mm observations of the newly identified dLHdC stars will help confirm or rule out the presence of a cold dust shell around them.

Finally, we note that four newly discovered dLHdC stars (A166, C526, F75 and F152) show definite signs of dust formation from their mid-IR colors and light curves (see Sec. 4.5 of Tisserand et al. 2021). Of these, A166 is an outlier within the dLHdC population (see Sec. 4.4), has RCB-like  $^{16}\text{O}/^{18}\text{O}$  and is likely an RCB star in a low dust-production phase. The three other stars are not outliers, but are too hot to sustain  $^{12}\text{C}^{16}\text{O}$  and  $^{12}\text{C}^{18}\text{O}$  in their photospheres so their  $^{16}\text{O}/^{18}\text{O}$  cannot be constrained. Sub-mm searches for the colder circumstellar medium of these stars can determine whether they have dLHdC-like or RCB-like  $^{16}\text{O}/^{18}\text{O}$  values. Additional studies of such “overlap” stars are necessary to understand the dust-formation connection between dLHdC and RCB stars.

#### 4.6 Summary and way forward

$^{18}\text{O}$  has been key to understanding the origins of the enigmatic dLHdC and RCB stars. The anomalously large  $^{18}\text{O}$  abundance in them can be explained by invoking a He-core and a CO-core white dwarf merger model for their formation. Although there were indications that RCB and dLHdC stars have different values of  $^{16}\text{O}/^{18}\text{O}$ , the limited sample of dLHdC stars prevented a quantitative comparison. In this paper, we have utilized the revolutionary discovery of 27 new Galactic dLHdC stars

to revisit this question.

We analyzed NIR spectra of 24 dLHdC stars together with unpublished spectra of 49 RCB stars. Owing to the several free parameters and assumptions in our fitting methodology, we obtained wide range estimates of the  $^{16}\text{O}/^{18}\text{O}$  ratios for 7 dLHdC and 33 RCB stars whose spectra contain the  $^{12}\text{C}^{16}\text{O}$  and/or  $^{12}\text{C}^{18}\text{O}$  bands. We find that six of the seven dLHdC stars have  $^{16}\text{O}/^{18}\text{O} < 0.5$ , while 28 of the 33 RCB stars have  $^{16}\text{O}/^{18}\text{O} > 1$ . Thus, the wide range estimates on the  $^{16}\text{O}/^{18}\text{O}$  ratios (although more uncertain in the coolest RCBs) obtained from the medium resolution spectra analyzed here suggest that most dLHdC stars have lower  $^{16}\text{O}/^{18}\text{O}$  than most RCB stars. If corroborated by future high resolution spectroscopic observations, this will be the first established chemical difference between the two classes of HdC stars. It remains to be seen if and how the lower  $^{16}\text{O}/^{18}\text{O}$  can be related to the lack of dust formation in dLHdC stars.

The different oxygen isotope ratios suggest that there is no evolutionary link between the class of dLHdC and RCB stars. Instead, this observation is consistent with the picture that dLHdC and RCB stars are formed from merging white dwarfs with distinct masses, mass ratios and compositions. Further theoretical studies are required to accurately determine the properties of white dwarfs that merge to form dLHdC versus RCB stars. A small number of RCB stars have uncharacteristically low, dLHdC-like  $^{16}\text{O}/^{18}\text{O}$  values. This could be a consequence of multiple white dwarf properties that can affect the value of  $^{16}\text{O}/^{18}\text{O}$  in the merger product, or can be explained by a short-lived dust formation phase in dLHdC stars. Theoretical models will test the former scenario, while FIR and sub-mm observations will confirm or rule out the latter. Further investigations of these “overlap” stars will shed light on the dLHdC-RCB dust formation mystery.

Future higher resolution NIR spectroscopy of the newly discovered dLHdC stars with CO bands will allow accurate determinations of their  $^{16}\text{O}/^{18}\text{O}$  ratios and will help validate the results presented here. High resolution optical spectroscopy should allow the determination of accurate fluorine abundances in them. As fluorine is also a signature of a white dwarf merger (Pandey et al. 2007), these observations will help determine the properties of progenitors of the hot dLHdC stars that do not show CO overtone bands. High resolution spectroscopy also will potentially identify additional chemical differences between dLHdC and RCB stars (e.g., between their H and N abundances as indicated in Tisserand et al. (2021).) and shed further light on their progenitor white dwarf populations.

#### 4.7 Acknowledgements

We thank the anonymous referee for helpful comments that improved the quality of this paper. We thank Bradley Munson for useful comments and discussions. PT acknowledges financial support from “Programme National de Physique Stellaire” (PNPS) of CNRS/INSU, France. MMK acknowledges the Heising-Simons foundation for support via a Scialog fellowship of the Research Corporation. MMK acknowledges generous support from the David and Lucille Packard Foundation. SA acknowledges support from the GROWTH PIRE grant 1545949. GC and CC are grateful for support from National Science Foundation Award 1814967. This research is based in part on observations for programs GS-2005B-Q-20, GN-2011A-Q-112, GS-2015B-FT-1 and GS-2016B-FT-6 obtained at the international Gemini Observatory, a program of NSF’s NOIRLab, which is managed by the Association of Universities for Research in Astronomy (AURA) under a cooperative agreement with the National Science Foundation, on behalf of the Gemini Observatory partnership: the National Science Foundation (United States), National Research Council (Canada), Agencia Nacional de Investigación y Desarrollo (Chile), Ministerio de Ciencia, Tecnología e Innovación (Argentina), Ministério da Ciência, Tecnologia, Inovações e Comunicações (Brazil), and Korea Astronomy and Space Science Institute (Republic of Korea).

## FAINTEST OF THEM ALL: DISCOVERY OF AN EXTREMELY LOW LUMINOSITY TYPE IAX SUPERNOVA

Karambelkar, V. R. et al. (Nov. 2021). “Faintest of Them All: ZTF 21aaoryiz/SN 2021fcg-Discovery of an Extremely Low Luminosity Type Iax Supernova”. In: *ApJ* 921.1, L6, p. L6. doi: 10.3847/2041-8213/ac2e90.

V. R. Karambelkar<sup>1</sup>, M. M. Kasliwal<sup>1</sup>, K. Maguire<sup>2</sup>, S. G. Anand<sup>1</sup>, I. Andreoni<sup>1</sup>, K. De<sup>1</sup>, A. Drake<sup>1</sup>, D. A. Duev<sup>3</sup>, M. J. Graham<sup>1</sup>, E. C. Kool<sup>4</sup>, R. R. Laher<sup>5</sup>, M. R. Magee<sup>2</sup>, A. A. Mahabal<sup>3,6</sup>, M. S. Medford<sup>7,8</sup>, D. Perley<sup>9</sup>, M. Rigault<sup>10</sup>, B. Rusholme<sup>5</sup>, S. Schulze<sup>11</sup>, Y. Sharma<sup>1</sup>, J. Sollerman<sup>12</sup>, A. Tzanidakis<sup>1</sup>, R. Walters<sup>13</sup>, Y. Yao<sup>1</sup>

<sup>1</sup>Cahill Center for Astrophysics, California Institute of Technology, Pasadena, CA 91125, USA

<sup>2</sup>School of Physics, Trinity College Dublin, the University of Dublin, College Green, Dublin, Ireland

<sup>3</sup>Division of Physics, Mathematics, and Astronomy, California Institute of Technology, Pasadena, CA 91125, USA

<sup>4</sup>The Oskar Klein Centre, Department of Astronomy, Stockholm University, AlbaNova, SE-10691 Stockholm, Sweden

<sup>5</sup>IPAC, California Institute of Technology, 1200 E. California Blvd, Pasadena, CA 91125, USA

<sup>6</sup>Center for Data Driven Discovery, California Institute of Technology, Pasadena, CA 91125, USA

<sup>7</sup>Department of Astronomy, University of California, Berkeley, Berkeley, CA 94720, USA

<sup>8</sup>Lawrence Berkeley National Laboratory, 1 Cyclotron Rd., Berkeley, CA 94720, USA

<sup>9</sup>Astrophysics Research Institute, Liverpool John Moores University, 146 Brownlow Hill, Liverpool, L3 5RF, UK

<sup>10</sup>Univ Lyon, Univ Claude Bernard Lyon 1, CNRS, IP2I Lyon / IN2P3, UMR 5822, F-69622, Villeurbanne, France

<sup>11</sup>The Oskar Klein Centre, Department of Physics, Stockholm University, AlbaNova, SE-10691 Stockholm, Sweden

<sup>12</sup>The Oskar Klein Centre, Department of Astronomy, Stockholm University, AlbaNova, SE-10691 Stockholm, Sweden

<sup>13</sup>Caltech Optical Observatories, Pasadena, CA 91125, USA

## Abstract

We present the discovery of ZTF21aaoryiz/SN 2021fcg — an extremely low-luminosity Type Iax supernova. SN 2021fcg was discovered by the Zwicky Transient Facility in the star-forming galaxy IC0512 at a distance of  $\approx 27$  Mpc. It reached a peak absolute magnitude of  $M_r = -12.66 \pm 0.20$  mag, making it the least luminous thermonuclear supernova discovered to date. The E(B–V) contribution from the underlying host galaxy is unconstrained. However, even if it were as large as 0.5 mag, the peak absolute magnitude would be  $M_r = -13.78 \pm 0.20$  mag — still consistent with being the lowest luminosity SN. Optical spectra of SN 2021fcg taken at 37 and 65 days post maximum show strong [Ca II], Ca II and Na I D emission and several weak [Fe II] emission lines. The [Ca II] emission in the two spectra has extremely low velocities of  $\approx 1300$  and  $1000 \text{ km s}^{-1}$ , respectively. The spectra closely resemble those of the very low luminosity Type Iax supernovae SN 2008ha, SN 2010ae and SN 2019gsc taken at similar phases. The peak bolometric luminosity of SN 2021fcg is  $\approx 2.5_{-0.3}^{+1.5} \times 10^{40} \text{ erg s}^{-1}$  which is a factor of three lower than that for SN 2008ha. The bolometric lightcurve of SN 2021fcg is consistent with a very low ejected nickel mass ( $M_{\text{Ni}} \approx 0.8_{-0.5}^{+0.4} \times 10^{-3} M_{\odot}$ ). The low luminosity and nickel mass of SN 2021fcg pose a challenge to the picture that low luminosity SNe Iax originate from deflagrations of near  $M_{\text{ch}}$  hybrid carbon-oxygen-neon white dwarfs. Instead, the merger of a carbon-oxygen and oxygen-neon white dwarf is a promising model to explain SN 2021fcg.

### 5.1 Introduction

Type Iax supernovae (SNe) are a peculiar subclass of Type Ia SNe (Foley et al. 2013). These events are named after the prototypical SN 2002cx (Li et al. 2003) and are characterised by slower expansion speeds ( $2000\text{--}8000 \text{ km s}^{-1}$ ) and a diverse range of luminosities compared to normal SNe Ia (Jha 2017). The luminosities of SNe Iax vary from  $M_r \approx -19$  at the bright end (SN 2008A, McCully et al. 2014) to  $M_r \approx -14$  at the faint end (SN 2008ha, Valenti et al. 2009; Foley et al. 2009). SNe Iax account for  $\sim 31\%$  of the total SN Ia rate (Foley et al. 2013) and are believed to be associated with thermonuclear explosions of white dwarfs (Jha 2017). However, their exact progenitors and explosion mechanisms still remain unknown.

Four SNe Iax have been discovered with very low luminosities ( $M_V \approx -14$ ) and explosion energies — SN 2008ha ( $M_V = -14.2$ , Valenti et al. 2009; Foley et al. 2009), SN 2010ae ( $-13.8 > M_V > -15.3$ ; Stritzinger et al. 2014), SN 2019gsc ( $M_r = -13.9$ ; Srivastav et al. 2020; Tomasella et al. 2020) and SN 2019ttf ( $M_r \approx -14$ ; De et al. 2020c), although only the first three have been studied extensively. These SNe have low ejected nickel masses ( $\sim 10^{-3} M_\odot$ ) and a faster evolution than their brighter counterparts. Several explosion mechanisms have been proposed to account for the low luminosities and nickel masses of faint SNe Iax — partial deflagration of a hybrid CONe white dwarf (Kromer et al. 2015), merger of a CO and ONe white dwarf (Kashyap et al. 2018), a helium-nova (McCully et al. 2014), an ultra-stripped electron-capture SN (Pumo et al. 2009), a “fallback” massive star SN (Moriya et al. 2010). However, the small sample of these events makes it difficult to distinguish between these models.

In this Letter, we present the discovery of ZTF21aaoryiz or SN 2021fcg — the least luminous member of the SN Iax class. SN 2021fcg has peak  $M_r = -12.66 \pm 0.20$  and is the lowest luminosity thermonuclear SN discovered to date. Here, we present optical photometric and spectroscopic follow-up of this transient. In Section 5.2, we describe the discovery and details of our follow-up observations. In Section 5.3 we analyse the light curve to derive ejecta masses. In Section 5.4, we present the spectroscopic evolution of this SN. In Section 5.5, we discuss this SN in the context of different formation scenarios. We conclude with a summary of our results in Section 5.6.

## 5.2 Discovery and follow-up observations

### Discovery

SN 2021fcg was discovered by the Zwicky Transient Facility (ZTF, Bellm et al. 2019a; Graham et al. 2019; Dekany et al. 2020), which runs on the Palomar 48-inch (P48) Oschin Schmidt telescope. The first real-time alert (Patterson et al. 2019) was generated on 20210308.22 UT (MJD 59281.22) at J2000 coordinates of  $\alpha = 09^{\text{h}}04^{\text{m}}32.37^{\text{s}}$ ,  $\delta = +85^{\text{d}}29^{\text{m}}48.44^{\text{s}}$ . The transient was automatically tagged as a supernova candidate by a machine-learning-based Alert-Classifying Artificial Intelligence program (ACAI; Duev et al. in prep). It was later flagged by the Census of Local Universe program (CLU, see De et al. 2020c for details) that identifies transients associated with nearby ( $< 200$  Mpc) galaxies on the Fritz portal (Walt et al. 2019a; Duev et al. 2019a; Kasliwal et al. 2019a). Figure 5.1 shows the ZTF discovery image of this transient.

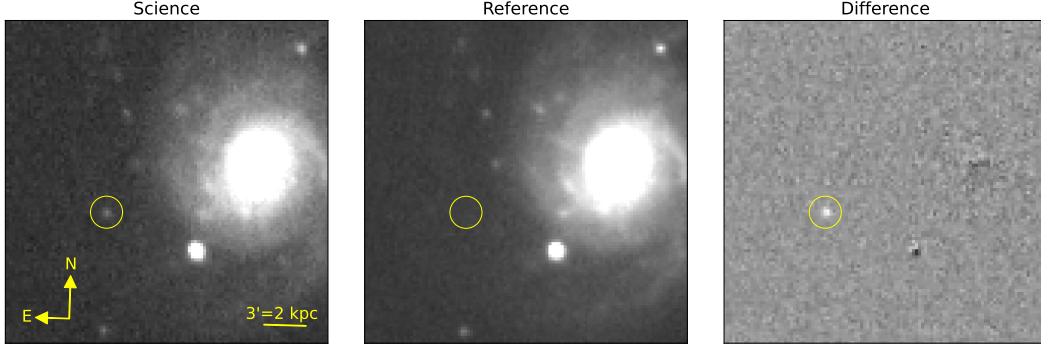


Figure 5.1: **ZTF  $r$ -band science, reference and difference discovery images of SN 2021fcg.** The position of the supernova is marked with a yellow circle. The science image was taken on MJD 59281.22.

### Host Galaxy and Extinction

SN 2021fcg is located on the outskirts of the star forming spiral galaxy IC0512 at a physical separation of  $\approx 7.5$  kpc (angular separation  $\approx 53''$ ) from the nucleus (Figure 5.1). The host galaxy has a redshift of  $z = 0.005384$  and a heliocentric velocity of  $1614 \pm 10 \text{ km s}^{-1}$  (Kourkchi et al. 2017). Correcting for the Virgo Infall, Shapley cluster and Great Attractor (Mould et al. 2000) gives a distance modulus  $\mu = 32.14 \pm 0.15$  mag (we use  $H_0 = 73 \text{ km s}^{-1} \text{ Mpc}^{-1}$  in this paper)<sup>1</sup>.

The Galactic extinction along the line of sight to this galaxy is  $A_V = 0.208$  mag (Schlafly et al. 2011), for a standard reddening law with  $R_V = 3.1$ . We cannot estimate extinction due to the host galaxy accurately as our spectra do not show any absorption lines from the host. However, the supernova is located in the outskirts of the host galaxy where the host extinction is likely low (Figure 5.1). We thus adopt  $E(B-V)_{\text{tot}} = E(B-V)_{\text{MW}} = 0.068$  mag. We discuss the implications of host extinction on our absolute magnitude estimates in Section 5.3.

### Follow-up observations

The field containing SN 2021fcg was observed on several epochs by the ZTF camera on P48 in the  $g$ ,  $r$  and  $i$  bands. The images were processed by the ZTF Data System Pipelines (Masci et al. 2019) which perform image subtraction based on the ZOGY algorithm (Zackay et al. 2016a). We performed forced point spread function photometry at the location of the transient in all subtracted ZTF images.

<sup>1</sup>Theureau et al. (2007) report a Tully-Fisher distance modulus of  $31.82 \pm 0.41$  mag using  $H_0 = 57 \text{ km s}^{-1} \text{ Mpc}^{-1}$ . Adopting  $H_0 = 73 \text{ km s}^{-1} \text{ Mpc}^{-1}$  will reduce this distance modulus, making SN 2021fcg even lower luminosity than reported here

We obtained additional  $g$ ,  $r$ ,  $i$  bands photometric observations with the Spectral Energy Distribution Machine (SEDM, Blagorodnova et al. 2018; Rigault et al. 2019) mounted on the 60-inch telescope at Palomar (P60) on MJD 59306 and 59318. We also observed the field in  $r$ -band with the Alhambra Faint Object Spectrograph and Camera (ALFOSC) at the 2.56-m Nordic Optical Telescope (Spain) on MJD 59367. We reduced the data with the PyNOT<sup>2</sup> pipeline. Finally, the field was also observed by the ATLAS survey (Tonry et al. 2018; Smith et al. 2020b). We used the ATLAS forced photometry service<sup>3</sup> to query all photometric measurements at the location of SN 2021fcg. We combined measurements from same-day observations by taking a weighted mean of the flux using the inverse of the square of the flux uncertainties as weights. All photometric measurements ( $3\sigma$  detections and  $5\sigma$  upper limits) are listed in Table 5.1.

Our spectroscopic followup comprises of two optical spectra obtained with the Low Resolution Imaging Spectrograph (LRIS, Oke et al. 1995) on the Keck I 10-m telescope. The spectra were obtained on MJD 59318 and 59344 corresponding to +37 day and +63 day after the  $r$ -band maximum of SN 2021fcg. The spectra were reduced using the IDL-based tool 1pipe (Perley 2019).

### 5.3 Light-curve analysis

Figure 5.2 shows the light-curve of SN 2021fcg.

We constrain the explosion time between  $MJD 59265.28 < t_{\text{exp}} < 59275.16$  (based on the latest, deepest non-detection and the first detection). The  $g$ -band light curve of SN 2021fcg has only three points that do not show significant evolution and hence samples the supernova around the peak. We report the mean of the three detections as the peak  $g$ -band magnitude. We also report the mean of the first two  $o$ -band detections as the peak  $o$  magnitude, however this is poorly constrained as the latest  $o$  upper limit prior to first detection is shallower than the first detection. We cannot constrain the  $c$ -band peak from our two detections. To determine the peak brightness in the  $r$ -band, we use the light curve of SN 2019gsc as a template and fit the stretched-scaled template to the observed light curve of SN 2021fcg.

The extinction corrected peak apparent magnitudes of SN 2021fcg are  $m_o^{\text{peak}} = 19.54 \pm 0.28$ ,  $m_g^{\text{peak}} = 20.16 \pm 0.24$  and  $m_r^{\text{peak}} = 19.48 \pm 0.14$  on  $MJD 59284.0 \pm 1.5$  days. This corresponds to  $M_o^{\text{peak}} = -12.60 \pm 0.32$ ,  $M_g^{\text{peak}} = -11.66 \pm 0.42$  and

---

<sup>2</sup> <https://github.com/jkrogager/PyNOT>

<sup>3</sup><https://fallingstar.com>

Table 5.1: Photometric measurements of SN 2021fcg ( $> 3\sigma$  detections and  $5\sigma$  limits, data behind Figure 5.2)

MJD	Phase <sup>a</sup>	<i>g</i>	<i>r</i>	<i>i</i>	<i>c</i>	<i>o</i>	Instrument
59256.25	-27.7	> 20.77	> 20.90	-	-	-	ZTF
59265.28	-18.7	> 20.59	> 20.62	-	-	-	ZTF
59270.45	-13.5	-	-	-	-	> 19.27	ATLAS
59275.16	-08.8	$20.58 \pm 0.23$	> 19.96	-	-	-	ZTF
59276.61	-07.4	-	-	-	-	$19.63 \pm 0.24$	ATLAS
59278.25	-05.7	$20.25 \pm 0.22$	-	-	-	-	ZTF
59278.49	-05.5	-	-	-	-	$19.79 \pm 0.31$	ATLAS
59281.22	-02.8	$20.39 \pm 0.28$	$19.72 \pm 0.08$	-	-	-	ZTF
59284.36	+00.4	-	-	-	$20.30 \pm 0.22$	-	ATLAS
59288.35	+04.3	-	-	-	$20.75 \pm 0.23$	-	ATLAS
59291.34	+07.3	-	$20.10 \pm 0.12$	-	-	-	ZTF
59293.23	+09.2	> 20.64	$20.35 \pm 0.22$	-	-	-	ZTF
59296.26	+12.3	-	-	$20.01 \pm 0.30$	-	-	ZTF
59302.31	+18.3	-	-	$19.87 \pm 0.22$	-	-	ZTF
59304.32	+20.3					$20.47 \pm 0.31$	ATLAS
59306.14	+22.1	-	$20.59 \pm 0.11$	-	-	-	SEDM
59307.16	+23.2	> 20.83	-	-	-	-	ZTF
59308.32	+24.3	-	-	$20.39 \pm 0.24$	-	-	ZTF
59309.24	+25.2	-	$20.79 \pm 0.30$	-	-	-	ZTF
59311.26	+27.3	-	-	$20.57 \pm 0.27$	-	-	ZTF
59315.18	+31.2	-	-	$20.81 \pm 0.30$	-	-	ZTF
59317.65	+33.7	-	$21.27 \pm 0.21$	$20.63 \pm 0.21$	-	-	SEDM
59366.88	+82.9	-	$22.84 \pm 0.12$	-	-	-	NOT

*a* : Phase is given in days since *r*-band peak.

$$M_r^{\text{peak}} = -12.66 \pm 0.20 \text{ mag.}$$

This makes SN 2021fcg the lowest luminosity SN discovered to date. The faintest previously known SN-Iax are SN 2019gsc ( $M_g^{\text{peak}} = -13.58 \pm 0.15$ ,  $M_r^{\text{peak}} = -14.28 \pm 0.15$ , Tomasella et al. 2020; Srivastav et al. 2020), SN 2010ae ( $M_g^{\text{peak}} = -14.2 \pm 0.5$ ,  $M_r^{\text{peak}} = -14.6 \pm 0.5$ , Stritzinger et al. 2014) and SN 2008ha ( $M_g^{\text{peak}} = -13.89 \pm 0.14$ ,  $M_r^{\text{peak}} = -14.25 \pm 0.14$ , Valenti et al. 2009). SN 2021fcg is more than a magnitude fainter than these SNe (see Figure 5.5).

We note that extinction from the host galaxy can increase our estimate of the peak brightness. In the absence of any host extinction indicators (Sec. 2.2), we use the  $(g - r)$  color of SN 2021fcg to examine the effect of host extinction on our measurements. The  $(g - r)$  color of SN 2021fcg at the *r*-band peak corrected for Galactic extinction is  $0.60 \pm 0.29$  mag. The corresponding value for SN 2008ha is  $0.57 \pm 0.03$  mag, SN 2019gsc is  $0.42 \pm 0.12$  mag and SN 2010ae is  $0.42 \pm 0.04$  mag (Srivastav et al. 2020; Foley et al. 2009; Stritzinger et al. 2014). SN 2008ha

and SN 2019gsc had no significant host extinction, while  $E(B - V)_{\text{host}} = 0.3$  is the most appropriate value for SN 2010ae (Srivastav et al. 2020; Stritzinger et al. 2014). If SN 2021fcg has similar peak colors as the other low luminosity SNe, the host extinction is  $E(B - V)_{\text{host}} \approx 0.2^{+0.3}_{-0.2}$ . Using  $E(B - V)_{\text{host}} = 0.2$  gives  $M_{r,\text{peak}} = -13.16 \pm 0.20$ . Even with the  $E(B - V) = 0.5$ , SN 2021fcg has  $M_{r,\text{peak}} = -13.78 \pm 0.20$  and is still among the lowest luminosity thermonuclear supernova discovered to date. However, no relation between SN Iax peak colors has been established, so these extinction estimates are representative at best.

The right panel of Figure 5.2 shows the  $r$ -band photometric evolution of SN 2021fcg compared to other low luminosity SN Iax. The overall evolution of SN 2021fcg is broadly consistent, albeit slightly slower than the other three SNe. However, the slow apparent evolution might be an effect of the epoch of peak brightness not being constrained accurately. We note that the  $r$  and  $i$ -band light curve flattened between  $+9$  d and  $+22$  d, a behaviour that is not seen for the other three SNe (Figure 5.2). From  $+25$  d to  $+80$  d, the  $r$ -band light curve declined at a rate of  $\approx 0.04 \text{ mag d}^{-1}$ .

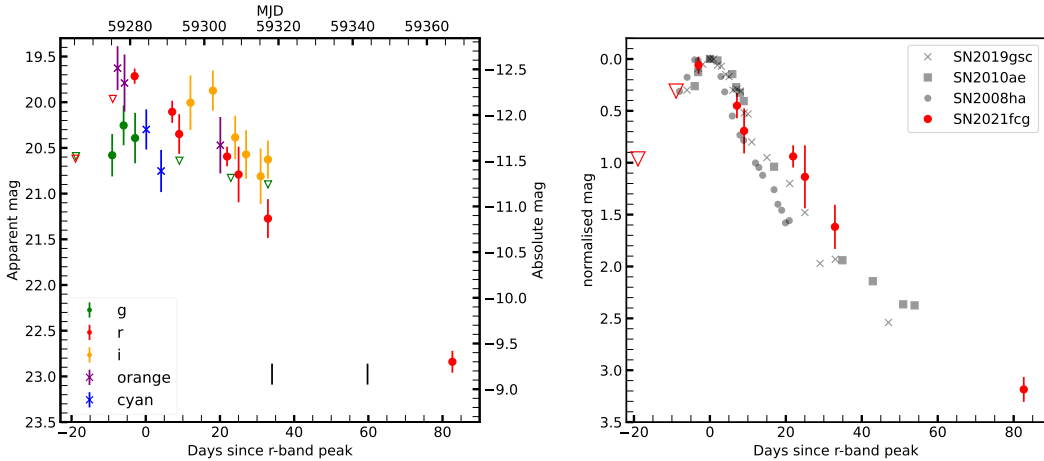


**Figure 5.2: Lightcurve of SN 2021fcg compared to other low luminosity SNe Iax.** *Left* :  $g$ ,  $r$ ,  $i$ ,  $o$  and  $c$  band light curve of SN 2021fcg. The epochs of our spectroscopic observations are marked with a black vertical line. *Right* : Comparison of the  $r$ -band photometric evolution to other low luminosity SN Iax (SNe 2008ha, 2019gsc and 2010ae). In the first 12 days post maximum, the evolution of SN 2021fcg is similar to SNe 2010ae and 2019gsc, but slower than SN 2008ha. After 12 days, the evolution of SN 2021fcg slows down, with a possible plateau between 12 and 22 days. This plateau is also seen in the  $i$ -band measurements (left panel). Data for the comparison objects is taken from Valenti et al. (2009), Stritzinger et al. (2015) and Srivastav et al. (2020), respectively.

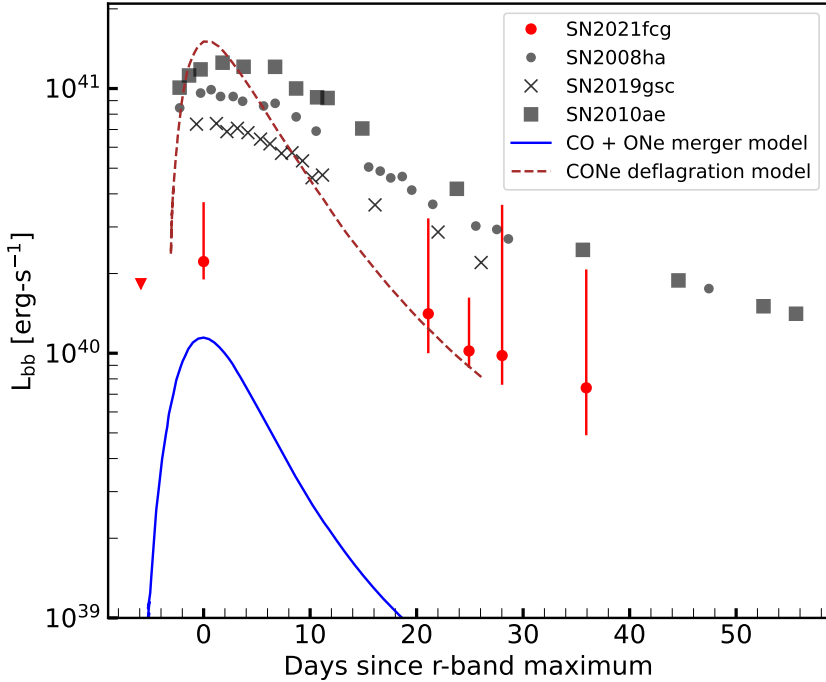


**Figure 5.3: Bolometric luminosity evolution (derived from blackbody fitting) of SN 2021fcg compared with the blackbody luminosities of SNe 2008ha, 2010ae and 2019gsc (Srivastav et al. 2020). The peak luminosity of SN 2021fcg is smaller than the other low-luminosity SN Iax by a factor of  $\sim 3$ . Also plotted are the theoretical bolometric luminosities of explosions from deflagration of a near- $M_{\text{ch}}$  white dwarf (dashed-brown line, Kromer et al. 2015) and the merger of a  $1.1 M_{\odot}$  CO and a  $1.2 M_{\odot}$  ONe white dwarf (solid blue line, Kashyap et al. 2018).**

### Bolometric luminosity

We fit the photometric measurements with a blackbody function to derive the bolometric luminosity of the supernova. As our lightcurve sampling is sparse, we do not have contemporaneous multiband observations. We interpolate between the *r* and *i*-band detections using a gaussian process with a radial basis function (RBF) kernel to generate synthetic measurements wherever necessary. The Gaussian process model was implemented using `scikit-learn`<sup>4</sup> We then fit a blackbody function to these measurements with a Markov Chain Monte Carlo (MCMC) analysis using the python package `emcee` (Foreman-Mackey et al. 2013b) to derive the effective temperatures, photospheric radii and bolometric luminosities. We note that the systematic uncertainties on our estimates are large as they are derived using data for only two filters. Additionally, we do not have any ultraviolet (UV) or near-infrared

<sup>4</sup>[https://scikit-learn.org/stable/modules/gaussian\\_process.html](https://scikit-learn.org/stable/modules/gaussian_process.html)

(NIR) photometric coverage. For SN2019gsc, Srivastav et al. (2020) estimated that the UV and NIR contribution increases the optical blackbody luminosity by a factor of  $\approx 1.5$ . Assuming a similar contribution for SN 2021fcg, we add a 50% systematic uncertainty to our luminosity estimates. We note that the late time spectra do not resemble a blackbody. However, we use simple blackbody estimates as the data available is limited.

Figure 5.3 shows the evolution of the bolometric luminosity of SN 2021fcg compared to SN 2008ha, SN 2010ae and SN 2019gsc (taken from Srivastav et al. 2020). The peak bolometric luminosity is  $2.5_{-0.3}^{+1.5} \times 10^{40}$  erg s $^{-1}$  which is  $\sim 3$  times lower than SN 2019gsc. We model the bolometric luminosity evolution using the relations from Arnett (1982) reformulated as in Valenti et al. (2008). This model assumes that the light curve is powered by radioactive decay of  $^{56}\text{Ni}$  and  $^{56}\text{Co}$  in the ejecta. The ejecta are assumed to be spherically symmetric, homologously expanding and have constant opacity (see Valenti et al. 2008 for additional details). Under these assumptions, the evolution of the bolometric luminosity can be described using three parameters — the total nickel mass  $M_{\text{Ni}}$ , the lightcurve timescale ( $\tau_M$ ) and the explosion time ( $\tau_{\text{exp}}$ ). We use emcee to estimate the best-fit parameters for SN 2021fcg. We derive a nickel mass of  $M_{\text{Ni}} = 0.8_{-0.5}^{+0.4} \times 10^{-3} M_{\odot}$ . This is lower than the nickel mass in SN 2019gsc ( $1.4 - 2.4 \times 10^{-3} M_{\odot}$ ), SN 2008ha ( $3 \times 10^{-3} M_{\odot}$ ) and SN 2010ae ( $3 - 4 \times 10^{-3} M_{\odot}$ , derived in Srivastav et al. 2020).

The total ejecta mass ( $M_{\text{ej}}$ ) can be derived using the relation  $M_{\text{ej}} = \frac{1}{2} \tau_M^2 \frac{\beta c v_{\text{peak}}}{k_{\text{opt}}}$  (Valenti et al. 2008), where  $\beta = 13.8$ ,  $c$  is the speed of light,  $v_{\text{peak}}$  is the peak photospheric velocity and  $k_{\text{opt}}$  is the net opacity. We cannot estimate  $v_{\text{peak}}$  for SN 2021fcg as we do not have spectroscopic coverage near maximum light. We assume  $v_{\text{peak}} = 3500 \text{ km s}^{-1}$  and  $k_{\text{opt}} = 0.1 \text{ cm}^2 \text{ g}^{-1}$  similar to SN 2019gsc (Srivastav et al. 2020), we derive  $M_{\text{ej}} = 0.05 - 0.4 M_{\odot}$ .

Finally, we note that for  $E(B-V) = 0.2$  and  $0.5$ , respectively, the peak luminosity of SN 2021fcg is  $4.3_{-0.6}^{+2.0} \times 10^{40}$  erg s $^{-1}$  and  $1.1_{-0.3}^{+3.0} \times 10^{41}$  erg s $^{-1}$ , respectively.

#### 5.4 Spectroscopic evolution

Figure 5.4 shows the +37 d and +63 d (rest frame phase from peak) optical spectra of SN 2021fcg. Both spectra show characteristics of late-time SN Iax spectra and closely resemble similar phase spectra of SN 2008ha and SN 2019gsc (Valenti et al. 2009; Tomasella et al. 2020). We do not detect any hydrogen, helium or oxygen lines in our spectra that could be indicative of a nova. In the nebular phases, the calcium

lines in SN 2021fcg have velocities of  $\approx 1500 \text{ km s}^{-1}$  — much smaller than those measured for Ca-rich SNe ( $\approx 5000 \text{ km s}^{-1}$ ; De et al. 2020c). Overall, our spectra strongly indicate that SN 2021fcg is a low luminosity SN Iax.

The +37d spectrum shows a slightly reddened continuum with several emission lines. The strongest emission features are the [Ca II] doublet and Ca II NIR triplet. Both of the [Ca II] doublet lines have a FWHM of  $\approx 1300 \text{ km s}^{-1}$  (measured using Gaussian fits). We also detect a possible absorption feature for these lines at a velocity of  $-3500 \text{ km s}^{-1}$  (see Figure 5.4). For the Ca II NIR triplet, the 8498 and 8548 Å lines are blended together, with a FWHM of  $1330 \text{ km s}^{-1}$ . These lines also show a P-cygni profile with the emission maximum at  $\sim 1500 \text{ km s}^{-1}$  and the absorption minimum at  $-2500 \text{ km s}^{-1}$ . However, the absorption is likely affected by blending from other absorption lines. For the 8662 Å line, only an emission component is detected with a FWHM of  $2620 \text{ km s}^{-1}$ . Similar features are also seen in the spectra of SN 2019gsc and SN 2008ha. The spectrum also shows strong Na I D emission with a P-cygni profile, although this absorption is also affected by blending. In addition, we detect several [Fe II] emission lines. We note that the O I emission is weak and no Ni or He features are detected.

The +63d spectrum is similar, with a very weak continuum. The [Ca II] doublet is the strongest emission feature with a FWHM of  $\approx 1000 \text{ km s}^{-1}$ . The Ca II NIR triplet is also detected in emission, with a FWHM of  $\approx 1050 \text{ km s}^{-1}$  (8498 and 8548 Å) and  $1850 \text{ km s}^{-1}$  (8662 Å). Compared to the +37 d spectrum, the Na I emission is very weak.

These spectral features and FWHM velocities are similar to those seen in other low-luminosity SN Iax. We also note that in both spectra, the peak wavelengths of the [Ca II] emission lines are blueshifted by  $\approx 100 \text{ km s}^{-1}$  with respect to the rest wavelength.

## 5.5 Discussion

The extremely low luminosity of SN 2021fcg makes it a remarkable member of the class of thermonuclear supernovae. In Figure 5.5 (left panel), we compare the peak absolute magnitude and decline rate of SN 2021fcg to other thermonuclear supernovae. While the peak absolute magnitude of SN 2021fcg is  $\approx 1.5$  mag fainter than all other supernovae, its decline rate is not extreme ( $\Delta m_{15,r} = 0.7 \pm 0.3$  mag), and is similar to the other three low luminosity SN Iax.

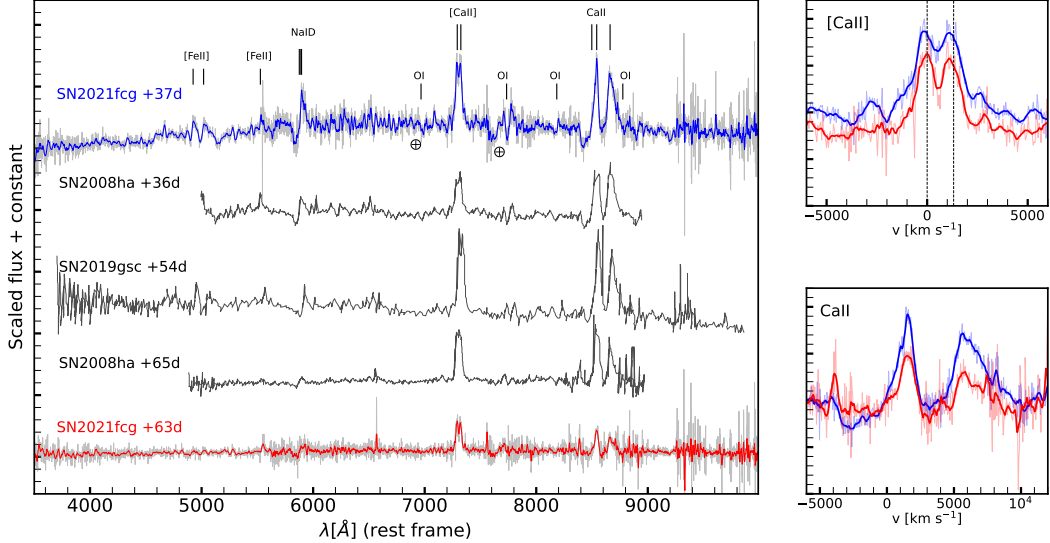


**Figure 5.4: Spectroscopic observations of SN 2021fcg.** *Left* : Late-time optical spectra of SN 2021fcg at +37 d (blue) and +63 d (red). Also plotted are similar phase spectra of SN 2008ha and SN 2019gsc (gray, taken from Valenti et al. 2009; Tomasella et al. 2020). The spectra of SN 2021fcg closely resemble the spectra of the other low-luminosity SN Iax. *Right*: Zoom-in of the [CaII] (*top*) and CaII (*bottom*) emission lines. These are the strongest features in the spectra (37 d : blue, 63 d : red). In both spectra, the peak wavelengths of [CaII] emission are blueshifted from the rest wavelengths (black dashed lines in top panel) by  $\approx 100 \text{ km s}^{-1}$ .

### What is the progenitor of SN 2021fcg?

The exact origin of SN Iax is debated, however it is generally accepted that they are associated with thermonuclear explosions of white dwarfs (Jha 2017). In particular, models involving the deflagration of a near Chandrasekhar ( $M_{\text{ch}}$ ) accreting white dwarf that leaves behind a bound remnant have been able to reproduce some observed properties of SN Iax. Failed deflagrations of a near  $M_{\text{ch}}$  CO white dwarf successfully explain several features of the luminous SN Iax (Jordan et al. 2012; Kromer et al. 2013; Fink et al. 2014). However, this model cannot explain the lower luminosity 08ha-like explosions – the faintest supernova from the CO deflagration model has  $M_V = -16.8$  mag (Fink et al. 2014).

Kromer et al. (2015) proposed that the low luminosity SN Iax could be deflagrations of hybrid COnE white dwarfs (Chen et al. 2014; Denissenkov et al. 2015). The presence of the ONe layer can quench the burning to suppress the amount of nickel produced. They simulated the deflagration of a  $1.4 M_{\odot}$  COnE white dwarf with five ignition cores and found that this results in a low luminosity ( $M_V \approx -14.2$ )

transient roughly consistent with SN 08ha, 10ae and 19gsc. However, they derive a total ejecta mass of  $0.014 M_{\odot}$  — an order of magnitude smaller than SN 08ha, 10ae and 19gsc. Consequently, the transient in their simulations evolves faster than these three SN (see Figure 5.3).

SN 2021fcg is fainter than the CONe deflagration model by  $\approx 1.5$  mag. In order to explain the luminosity and timescale of SN 2021fcg as the outcome of a white dwarf deflagration, the nickel ejecta mass has to be lower by a factor of  $\sim 3$  and the total ejecta mass has to be at least 10 times larger than the value obtained by Kromer et al. (2015). It remains to be seen if lower number of ignition cores or a larger ONE mass than the one used by Kromer et al. (2015) can reduce the nickel yield enough to explain the low luminosity of SN 2021fcg. However, a lower total ejecta mass will make the transient even faster evolving and inconsistent with the slow decline rate of SN 2021fcg. SN 2021fcg is thus a challenge to the existing picture of hybrid white dwarf deflagration and warrants further investigation of this channel.

An alternative picture for formation of low luminosity SNe Iax is the double-degenerate scenario. Kashyap et al. (2018) showed that the merger of a CO and ONE white dwarf yields a failed detonation of the ONE core producing small amounts of ejecta. This gives rise to a very faint, rapidly evolving transient. They modeled the merger of a  $1.1 M_{\odot}$  CO and a  $1.2 M_{\odot}$  ONE white dwarf and derive a very low nickel yield ( $5.7 \times 10^{-4} M_{\odot}$ ). The resulting transient has peak  $M_V = -11.3$ , an ejecta velocity of  $\sim 4000 \text{ km s}^{-1}$  and a total ejecta mass of  $\sim 0.08 M_{\odot}$ .

The observed luminosity of SN 2021fcg is  $\sim 3$  times brighter than that predicted by Kashyap et al. (2018) (see Figure 5.3), while the nickel and total ejecta masses are roughly consistent with their estimates. The double-degenerate channel is thus a promising model to explain SN 2021fcg, as a merger involving a more massive ONE white dwarf could give a brighter and longer lived transient than the one modelled in Kashyap et al. (2018). However, the requirement of a more massive ONE white dwarf may decrease the expected rate of such explosions. Additional studies of this model are necessary to test its viability as the progenitor of SN 2021fcg. In this channel, the remnant is a high velocity super-Chandrasekhar star with an ONE core embedded in the nebulosity of the SN ejecta. Recently, Oskinova et al. (2020) identified a candidate super- $M_{\text{ch}}$  remnant at the center of the nebula IRAS00500+6713. They posit that this source is the remnant of a SN Iax resulting from an ONE and CO white dwarf merger. If SN 2021fcg is the result of a white dwarf merger, the remnant would be a similar super- $M_{\text{ch}}$  star that will eventually end its life as an electron-capture SN.

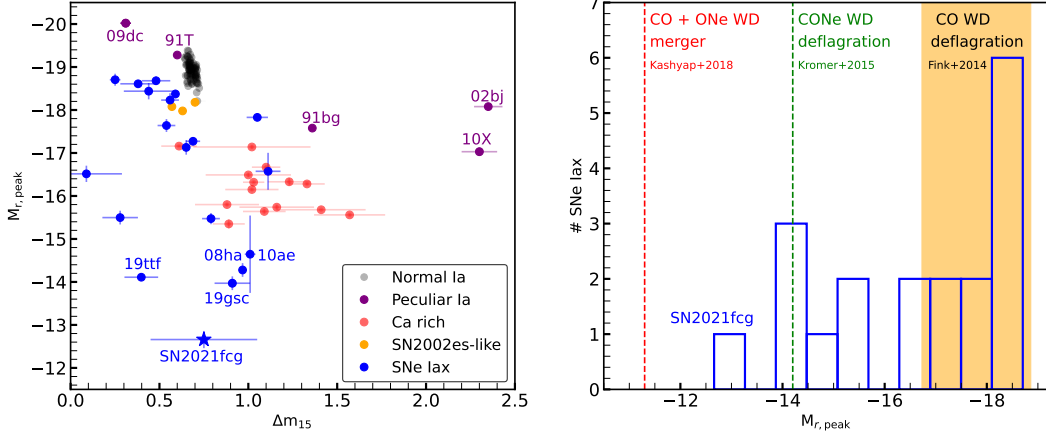


**Figure 5.5: SN 2021fcg in the context of thermonuclear supernovae.** *Left:* Peak  $r$ -band absolute magnitudes against  $r$ -band decline rates ( $\Delta m_{15}$ ) of thermonuclear supernovae. SN 2021fcg (blue star) is the least luminous thermonuclear SN discovered to date. We also plot the values for normal SNe Ia (black circles, Yao et al. 2019), the peculiar SNe Ia 1991bg (Filippenko et al. 1992), 1991T (Lira et al. 1998), 2009dc (Taubenberger et al. 2011), 2010x (Kasliwal et al. 2010) and 2002bj (Poznanski et al. 2010) (purple circles), calcium-rich gap transients (red circles, De et al. 2020c), 02es-like transients (orange circles, White et al. 2015), SNe Iax (blue circles, Magee et al. 2016; Foley et al. 2013; Srivastav et al. 2020). We use the Tully Fisher distance modulus for SN 2021fcg, while we use  $H_0 = 73 \text{ km s}^{-1} \text{ Mpc}^{-1}$  for all other SNe.

*Right:* A histogram of peak SN Iax absolute magnitudes together with the predictions of existing progenitor models. The bright ( $M_r < -16.8$  mag) SN Iax are consistent with simulations of deflagrations of near  $M_{\text{ch}}$  CO white dwarfs (orange region, Fink et al. 2014). The lower luminosity 08ha-like SNe are consistent with the simulation of a deflagration of hybrid CONe white dwarf (green line, Kromer et al. 2015). SN 2021fcg is even fainter, and it is unclear if it could be explained by different initial conditions of the CONe WD deflagration. A promising alternative is the double degenerate model involving the merger of a  $1.1 M_{\odot}$  CO and  $1.2 M_{\odot}$  ONe white dwarf. A more massive ONe white dwarf could give rise to more luminous transients such as SN 2021fcg.

In any of these scenarios, the surviving bound remnant can drive winds from its surface through delayed radioactive decay (Shen et al. 2017). These winds can be the dominant source of luminosity at late times ( $\approx 1$  year post explosion) lasting for at least a decade. Recent *Hubble Space Telescope* (HST) observations of SN 2012Z revealed an excess in its late-time luminosity that could be a result of remnant-driven winds (McCully et al. 2021). Late time HST observations of SN 2021fcg will be valuable in probing the nature of its bound remnant.

We summarize these possible formation scenarios in the right panel of Figure 5.5. Additional scenarios that do not invoke a white dwarf have also been proposed to explain other low luminosity SNe Iax. For example, Valenti et al. 2009 note that SN 2008ha has similarities with models of low luminosity core-collapse SN such as a fallback massive star SN (Moriya et al. 2010) or an ultra-stripped electron-capture SN (Pumo et al. 2009). NIR spectra can help distinguish between a thermonuclear and core-collapse origin for these supernovae (Stritzinger et al. 2015).

## 5.6 Conclusions

We have presented optical photometry and late-time optical spectroscopy for SN 2021fcg — the lowest luminosity SN-like transient discovered to date. The photometric and spectroscopic evolution of SN 2021fcg closely resembles low luminosity SN Iax such as SN 2008ha, SN 2010ae and SN 2019gsc. SN 2021fcg has  $M_r = -12.66 \pm 0.20$  mag and is the faintest of the faint SN Iax, fainter than the other members by more than a magnitude. The lower luminosity, lower nickel ejecta mass and slightly slower photometric evolution of SN 2021fcg represent a challenge to theoretical models of low luminosity SN Iax. Existing hybrid CONe white dwarfs deflagration models are overluminous by a factor of  $\sim 3$ . A double degenerate scenario in which the SN is an outcome of a CO and ONe white dwarf merger is a promising model. Formation channels that involve a core-collapse origin are also plausible, but unlikely.

Additional observations of SNe Iax with extremely low luminosities ( $M \approx -12.5$  mag) are required to identify the explosion mechanisms of these mysterious transients. ZTF can detect these SNe to a distance of  $\approx 40$  Mpc. The Vera Rubin Observatory (VRO, Ivezić et al. 2019a) will significantly increase the discovery distance to  $\approx 275$  Mpc. However, given the fast evolution of these transients, rapid followup observations will be required to derive useful insights about them. An experiment similar to the Census of the Local Universe (De et al. 2020c) that keeps track of VRO transients in catalogued galaxies will be instrumental in discovering such low luminosity SNe.

## 5.7 Acknowledgements

We thank the anonymous reviewer for comments that helped improve the paper. We thank Harsh Kumar, Varun Bhalerao and G.C. Anupama for photometric observations with the GROWTH-India telescope<sup>5</sup>. This paper is based on observations

---

<sup>5</sup><https://sites.google.com/view/growthindia/>

obtained with the Samuel Oschin Telescope 48-inch and the 60-inch Telescope at the Palomar Observatory as part of the Zwicky Transient Facility project. ZTF is supported by the National Science Foundation under Grant No. AST-2034437 and a collaboration including Caltech, IPAC, the Weizmann Institute for Science, the Oskar Klein Center at Stockholm University, the University of Maryland, Deutsches Elektronen-Synchrotron and Humboldt University, the TANGO Consortium of Taiwan, the University of Wisconsin at Milwaukee, Trinity College Dublin, Lawrence Livermore National Laboratories, and IN2P3, France. Operations are conducted by COO, IPAC, and UW. SED Machine is based upon work supported by the National Science Foundation under Grant No. 1106171. This work is also based on observations made with the Nordic Optical Telescope, owned in collaboration by the University of Turku and Aarhus University, and operated jointly by Aarhus University, the University of Turku and the University of Oslo, representing Denmark, Finland and Norway, the University of Iceland and Stockholm University at the Observatorio del Roque de los Muchachos, La Palma, Spain, of the Instituto de Astrofisica de Canarias. SED Machine is based upon work supported by the National Science Foundation under Grant No. 1106171. The ZTF forced photometry service was funded under the Heising-Simons Foundation grant 12540303 (PI: Graham). KM is funded by the EU H2020 ERC grant no. 758638. SS and ECK acknowledge support from the G.R.E.A.T research environment, funded by *Vetenskapsrådet*, the Swedish Research Council, project number 2016-06012. ECK acknowledges support from The Wenner-Gren Foundations. MR has received funding from the European Research Council (ERC) under the European Union’s Horizon 2020 research and innovation programme (grant agreement 759194 - USNAC).

## Part II : Neutron star mergers

## Chapte r 6

# A DATA REDUCTION PIPELINE FOR THE WINTER SURVEYOR

To be submitted to PASP.

V. Karambelkar<sup>a,1</sup>, R. Stein<sup>a,2,3,4</sup>, M. M. Kasliwal<sup>1</sup>, R. A. Simcoe<sup>7</sup>, D. Frostig<sup>6</sup>, N. Lourie<sup>7</sup>, S. Rose<sup>1</sup>, T. Ahumada<sup>1</sup>, M. Sheshadri<sup>1</sup>, J. Purdum<sup>1</sup>, S. Kishore<sup>1</sup>, A. Suresh<sup>5</sup>, G. Mo<sup>7,8</sup>, S. Hall<sup>5</sup>, J. Soon<sup>9</sup>

*a* : These authors contributed equally.

<sup>1</sup>Cahill Center for Astrophysics, California Institute of Technology, Pasadena, CA 91125,  
USA

<sup>2</sup>Department of Astronomy, University of Maryland, College Park, MD 20742, USA

<sup>3</sup>Joint Space-Science Institute, University of Maryland, College Park, MD 20742, USA

<sup>4</sup>Astrophysics Science Division, NASA Goddard Space Flight Center, Mail Code 661,  
Greenbelt, MD 20771, USA

<sup>5</sup>CIERA, Northwestern University, 1800 Sherman Ave 8th Floor, Evanston, IL 60201, USA

<sup>6</sup>Center for Astrophysics | Harvard & Smithsonian, 60 Garden Street, Cambridge, MA  
02138, USA

<sup>7</sup>Department of Physics and Kavli Institute for Astrophysics and Space Research,  
Massachusetts Institute of Technology, 77 Massachusetts Ave, Cambridge, MA 02139,  
USA

<sup>8</sup>MIT LIGO Laboratory, Massachusetts Institute of Technology, Cambridge, MA 02139,  
USA

<sup>9</sup>Research School of Astronomy and Astrophysics, Australian National University,  
Canberra, ACT 2611, Australia

## Abstract

We present the data reduction and transient detection pipeline for the Wide-field Infrared Transient Explorer (WINTER) surveyor and report its on-sky performance. WINTER is a 1-m robotic telescope at Palomar Observatory equipped with a six-detector, 1.2 sq. deg. field-of-view near-infrared camera operating in the Y, J, and

shortened-H bands, using cost-effective InGaAs sensors as alternatives to traditional IR sensors. WINTER had first light in June 2023 and has been operating robotically since. The WINTER data processing pipeline (`winterdrp`) has been implemented within a broader framework `mirar`: a modular, open-source python package developed for realtime processing of images from time-domain surveys. `winterdrp` performs dark and flat calibration, astrometric calibration using `Astrometry.net` and `Scamp`, photometric calibration relative to 2MASS, and image subtraction using the ZOGY algorithm relative to archival images from public UKIRT surveys. Transient alerts in Avro format are broadcast to `Skyportal` for scanning and follow-up. During a year of observations in 2024, WINTER achieved *J*-band median depths ranging from 18.0–18.6 mag (AB) on its six detectors in 960 seconds integrations,  $\approx$ 2 mag shallower than expected due to a ten times lower quantum efficiency than design specifications. We achieve astrometric residuals of  $\approx$ 0.2 arcsec (a fifth of a pixel) and photometric residuals of  $\approx$ 0.2 mag. The large photometric residuals are primarily due to non-linearity effects and dark current variations in the detectors. We outline ongoing efforts to correct for these effects and improve performance. We present early science results from WINTER, which include the identification of a possible stellar merger in M 31, dust-enshrouded outbursting young stellar objects and classical novae in the Galactic plane, NIR followup of known transients, and multi-messenger followup of gravitational wave alerts, gamma-ray bursts, and X-ray transients.

## 6.1 Introduction

Time-domain astronomy is undergoing an epochal transition to an era of ‘big data’. The last decade has seen the advent of several automated wide-field optical surveys such as the Zwicky Transient Facility (ZTF; Bellm et al. 2019b), the Asteroid Terrestrial-impact Last Alert System (ATLAS; Tonry et al. 2018), the All-Sky Automated Survey for Supernovae (ASAS-SN, Shappee et al. 2014), PanSTARRS (Chambers et al. 2016a), BlackGem (Groot et al. 2024), The Gravitational-wave Optical Transient Observer (GOTO, Steeghs et al. 2022), and the Large Area Survey Telescope (LAST, Ofek et al. 2023), that survey large areas of the sky every night to search for transient cosmic explosions. The large data volume generated by these surveys has necessitated the development an infrastructure ecosystem to support real-time processing of astronomical images, image subtraction relative to reference templates to identify candidate transient alerts (Zackay et al. 2016b; Hu et al. 2022; Becker 2015), and rapid disbursements of these alerts to the wider astronomy

community for follow-up studies (e.g., Coughlin et al. 2023a; Nordin et al. 2019. The upcoming Legacy Survey of Space and Time (LSST) with the Vera C. Rubin Observatory will represent another leap forward (Ivezić et al. 2019b), providing deep optical survey data that is over an order of magnitude larger than existing surveys.

Unlike rapid advancements in optical time-domain surveys, the dynamic infrared (IR) sky has remained largely unexplored with far fewer IR time-domain surveys. This is primarily because of the substantially larger cost of IR cameras compared to optical CCDs. Most existing IR surveys have targeted small areas of the sky. The Spitzer Infrared Intensive Transients Survey (SPIRITS, Kasliwal et al. 2017b) surveyed  $\sim$ 100 nearby galaxies at 3.6 and 4.5  $\mu$ m and uncovered a plethora of dusty IR transients that did not have any optical counterparts (Jencson et al. 2019b). The VISTA Variables in Via Lactae (VVV, Minniti et al. 2010) and VVV extended (VVVX, Saito et al. 2024) surveys targeted regions towards the Galactic bulge and mid-plane from 2009 to 2023 at near-IR (NIR) wavebands to characterize transients and variable stars in the dustiest regions of the Milky Way. The Supernova Unmasked by IR Detections (SUNBIRD, Kool et al. 2018) survey used adaptive optics on the Gemini South telescope to identify supernovae (SNe) in the dense, dusty nuclei of ultra-luminous infrared galaxies.

The first all-sky, high-cadence exploration of the dynamic IR sky was provided by the Palomar Gattini-IR (PGIR, De et al. 2020a) surveyor, that has been surveying the entire northern sky at a cadence of  $\approx$ 2–3 days with its 25 sq. deg *J*-band camera mounted on a 30 cm telescope since 2018. PGIR reached a median depth of  $m_J = 15.7$  mag (AB), and has been instrumental in uncovering hidden populations of dusty Galactic novae and variable stars. In addition to PGIR, a recent pipeline to identify mid-IR transients in the decade-long observations from the NEOWISE reactivation of the WISE satellite surveyor (Mainzer et al. 2014a) has discovered a large number of mid-IR transients over the entire sky (De et al. 2023). These studies have demonstrated the immense potential of IR surveys in identifying large population of dusty cosmic explosions that are missed by optical surveys, and highlighted the need for further systematic IR time-domain exploration.

In addition to dusty transients, IR surveys can be particularly effective for electromagnetic followup of gravitational waves (EMGW). The kilonovae associated with binary neutron star and neutron star black hole mergers are expected to exhibit viewing-angle-dependent blue emission that fades rapidly (<1 week), while the

NIR emission is predicted to be more isotropic and longer-lived (Kasen et al. 2013; Kasen et al. 2017; Metzger 2020). This was confirmed for GW 170817, that had significantly longer-lived IR emission compared to the optical (Tanvir et al. 2017). Thus kilonovae are more detectable in the near-infrared than the optical (Zhu et al. 2021a; Frostig et al. 2022a), yet EMGW followup has primarily focused on optical wavelengths. The benefits of IR surveys have fueled efforts to build ground-based wide-field IR surveyors in the last few years, such as the PRime Focus Infrared Microlensing Experiment (PRIME, Kondo et al. 2023), and Wide-field Infrared Transient Explorer (WINTER, Lourie et al. 2020a; Frostig et al. 2024a).

WINTER is a new NIR camera installed on a dedicated 1 m robotic telescope at Palomar Observatory in Southern California. The WINTER camera has a field of view of 1.2 sq deg, and employs novel Indium-Gallidium-Arsenide (InGaAs) sensors as a cheaper alternative to traditional IR detectors for the first time in astronomy. WINTER is equipped with the Y, J, and shortened-H (H<sub>s</sub>) filters, covering the 1–1.7  $\mu$ m wavelength range. WINTER was designed for EMGW followup during the International Gravitational Wave Network’s O4 observing run. Additionally, WINTER’s wide FOV and NIR sensitivity enables it to conduct systematic searches for dusty NIR transients. WINTER had first light in June 2023 and has been operating robotically since.

Here, we describe the data reduction and transient detection pipeline for WINTER and report the system performance during the commissioning period of the camera. This pipeline is implemented in an open-source modular python framework (`mirar`) that has been developed for real time processing of images from time-domain surveys. The paper is organized as follows: Section 6.2 describes the WINTER observatory and a dedicated API for interacting with the observatory. 6.3 introduces the `mirar` data reduction framework, and Section 6.4 outlines the exact pipeline used to process WINTER images. Section 6.5 outlines WINTER’s on-sky performance, Section 6.6 describes ongoing upgrades to improve performance, and Section 6.7 presents early science results from WINTER. We conclude with a summary of the lessons learnt from WINTER in Section 6.8.

## 6.2 WINTER observatory infrastructure

### The WINTER observatory

The WINTER camera is mounted on a dedicated 1 m telescope at Palomar Observatory, and consists of six InGaAs detectors that produce a field-of-view of 1.2 deg.

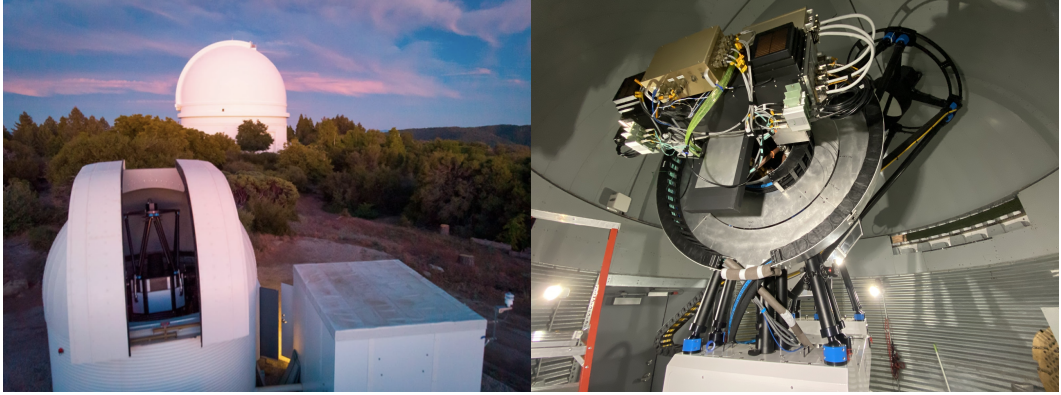


**Figure 6.1: The WINTER telescope at Palomar Observatory.** *Left:* A picture of the WINTER dome and 1 m. telescope, with the 200-inch Hale telescope in the background. *Right:* The WINTER camera mounted on the 1 m. telescope.

$\times 1$  deg. The pixel scale of the camera is 1.13" per pixel. The WINTER telescope has been running robotically on sky since June 2023 (Frostig et al. 2024a), featuring new InGaAs sensor technology and a custom read out (Frostig et al. 2022b; Malonis et al. 2020), a novel fly's-eye optical design (Lourie et al. 2020a), and custom opto-mechanics (Hinrichsen et al. 2020). More details about the WINTER camera and the InGaAs detectors can be found in Frostig et al. (2024a). Figure 6.1 shows the WINTER dome, telescope, and camera at Palomar Observatory.

## WINTER API

WINTER observation requests and data access are handled by a dedicated API server, hosted on a dedicated winter server at Caltech. The API is built using the `fastapi` python framework (Ramírez 2024), and includes automated generation of OpenAPI-compliant metadata. These metadata are used to create an interactive documentation of the API using the Swagger UI<sup>1</sup>. The documentation is hosted on a web page for WINTER users. The API ensures that minimal human intervention is required to support user interaction, and enables Target-of-Opportunity (ToO) and other user-generated scheduling requests to be handled with very low latency. All requests for observations with WINTER require a validity window and priority, and are passed on with this information as ‘ToO requests’ to the WINTER scheduler.

A dedicated python package, `wintertoo`<sup>2</sup>, provides a single shared framework for these ToO requests. `wintertoo` is used by the WINTER API server, as well as the

<sup>1</sup><https://swagger.io/tools/swagger-ui/>

<sup>2</sup><https://github.com/winter-telescope/wintertoo>

WINTER camera software and `mirar`. `wintertoo` contains a standardized format for ToO requests as well as a set of functions to ensure that the ToO requests are valid. These include checking that the target is observable within the requested window above the requested airmass limit, that the program has sufficient unexpired time, as well as more low-level checks such as requiring the requested filters to actually be one of those mounted on the camera. Once validated by the WINTER API server, ToO requests are copied to the WINTER computer at Palomar, where they are then read by the WINTER scheduler. Additional validation checks are repeated at this stage, and valid requests are added to the queue. The API server monitors the status of these requests, which can be either ‘QUEUED’ or ‘ATTEMPTED’. To prevent repeats of failed observations, each individual ToO observation is only attempted once. Unsuccessful ToO requests, for example due to hardware failures that prevent data acquisition, are not charged to respective programs. A WINTER log provides a complete list of all data that was successfully taken and these observations are charged to the respective programs.

Once the data has been processed and updated in the `winterdrp` database, it becomes available for users to access. This process is also handled by the `winter` API server. Users can query the API to find available images for a given program at the five stages of data processing described in Section 6.4. Users can also query for the complete set of Avro alerts generated for a given WINTER difference image. These queries can either provide all images associated to a program, or users can select subsets based on target name and/or observation date. Users can then perform a separate API request to download a list of these images as a ZIP file. For security, each user requires unique user credentials to interact with the API, and each WINTER program has an associated set of unique program credentials. Both sets of credentials are required to request observations for a program or access data from a program.

Users primarily interact with the WINTER API server through a separate python package, `winterapi`<sup>3</sup>. This package has simple wrapper functions for interacting with the WINTER API server, as well as example Jupyter notebooks illustrating the various features. Beyond allowing using to manually interact with the API server in a simple way, `winterapi` is designed to be easily imported as a dependency into user-built python scripts, simplifying automated interactions with the API. `winterapi` is an essential component of the software infrastructure supporting automated GRB follow-up with WINTER, as well as MMA follow-up of gravitational wave and

---

<sup>3</sup><https://github.com/winter-telescope/winterapi>

neutrino events. Alternative API access is available through `skyportal` (Walt et al. 2019b; Coughlin et al. 2023b), the Swagger UI documentation page or directly via the server.

### 6.3 Data Reduction Framework - `mirar`

A data reduction framework has been developed that was explicitly designed to be modular, flexible and telescope-agnostic. The Modular Image Reduction and Analysis Resource (`mirar`) is an open-source code built using python 3.12, and is available on Github<sup>4</sup> and PyPi. It has extensive unit tests to ensure reproducibility, and relies on systematic type hinting to reduce end-user errors. `mirar` is built around a series of discrete configurable operational units known as *Processors*, which act in sequence on data.

#### `mirar` Data Structure

`mirar` depends on handling data with a uniform format. Each *Processor* receives groups of standardised data known as a *DataBlocks*, performs a specific operation on that data, and then returns a *DataBlock*. Several key fields are required by `mirar` to be in every *DataBlock*, and these are added as raw images as read in. These include a full processing history, which is continuously updated as data passes through processors, and other vital metadata such as raw image path and time of exposure. There are two basic types of *DataBlock*:

1. *Image*: An *Image* object contains image data in a numpy array (Harris et al. 2020), as well as an astropy ‘header’ (Astropy Collaboration et al. 2013; Astropy Collaboration et al. 2018; Astropy Collaboration et al. 2022). There is a only one header and one 2D array per *Image*, so multi-extension fits files are converted to multiple individual *Image* objects when read in by `mirar`.
2. *SourceTable*: A *SourceTable* object contains a table of sources in a pandas DataFrame format (Pandas Development Team 2024), as well as a ‘metadata’ dictionary that is analogous to the *Image* header. The metadata in a *SourceTable* typically contains information which is common to all sources in the *SourceTable*.

At the highest level, all data forms part of a single *DataSet*. Each *Processor* receives a *DataSet* as input, and returns a *DataSet* as output. Within a *DataSet*, the individual

---

<sup>4</sup><http://www.github.com/winter-telescope/mirar>

*DataBlocks* are grouped into *DataBatches*, each containing at least one *DataBlock*. After receiving a *DataSet*, *Processors* will typically act on each *DataBatch* in turn. For example, a processor to stack images may receive a *DataBatch* containing eight *Images* corresponding to eight dithers, and then generate a *DataBatch* containing one *Image* which is the combined stack of those dithers. *Processors* will typically treat each *DataBatch* within the *DataSet* independently, and can act on different *DataBatches* simultaneously thorough multi-processing. However, some *Processors* act instead on the entire *DataSet* at once, such as the *Processors* used to reorganize *DataBatches*.

When errors are encountered, `mirar` will drop the entire *DataBatch* from further processing, so the *Image* are often repeatedly reordered into different *DataBatch* groups during the processing sequence. For example, each *Image* from a dither set may each be in an individual *DataBatch* for astrometric and photometric calibration, then reordered into a single combined *DataBatch* before being passed to a stacking *Processor*. Then, even if one dither *Image* produces an error, the remaining *Images* will still be used to generate a stacked *Image*. An example of the data structure is illustrated in Figure 6.2.

### `mirar` *Processors*

From the two core *DataBlock* types (*Images* and *SourceTables*), there are three basic types of *Processor*:

1. *Image Processors* receive *Images* as an input, and produce *Images* as an output.
2. *Source Generators* receive *Images* as an input, and produce *SourceTables* as an output.
3. *Source Processors* receive *SourceTables* as an input, and produce *SourceTables* as an output.

Because the data format is consistent across processors, they can be performed sequentially and in arbitrary orders. This provides substantial flexibility to recycle processors across different instruments and tasks. A typical workflow within `mirar` might consist of a series of image processors to detrend images, perform astrometric and photometric calibration, perform image subtraction against reference images from another survey, followed by a source detector to extract transients in the image, and finally a series of candidate processors to filter those detected sources

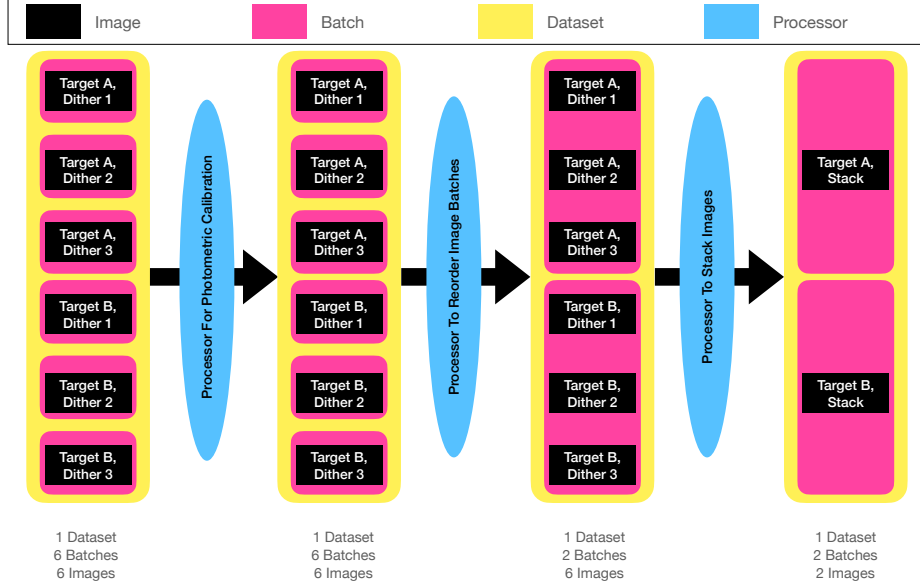


Figure 6.2: **Illustration of the data structure usage in `mirar`.** In the above example, a dataset initially consists of six images. These correspond to three images of Target A, and another three images of Target B. The images begin grouped into six separate batches, and undergo photometric calibration. The images are then reorganised into two batches (one batch per target). Finally, each batch is stacked together, yielding one stacked image per batch.

and exported them to external services such as a database and an alert broker. An example *Processor* sequence is shown in Figure 6.3, combining all three *Processor* classes.

By virtue of the modular structure in `mirar`, many individual *Processors* exist which are simply wrappers of software packages which are widely used in astronomy or industry. However, because of the uniform data standards and consistent *Processor* structure, it is simple to combine these different components with minimal complexity. It is similarly straightforward to add a new *Processor* which applies a new software package. Some prominent *Processors* based on external libraries include:

- SExtractor for the extraction of sources in images (Bertin et al. 1996).
- Scamp for providing astrometric solutions to images (Bertin 2006).
- Astrometry.net for providing astrometric solutions (Lang et al. 2010).
- Swarp for image interpolation and stacking (Bertin et al. 2002).
- PSFEx for measuring PSFs (Bertin 2011).

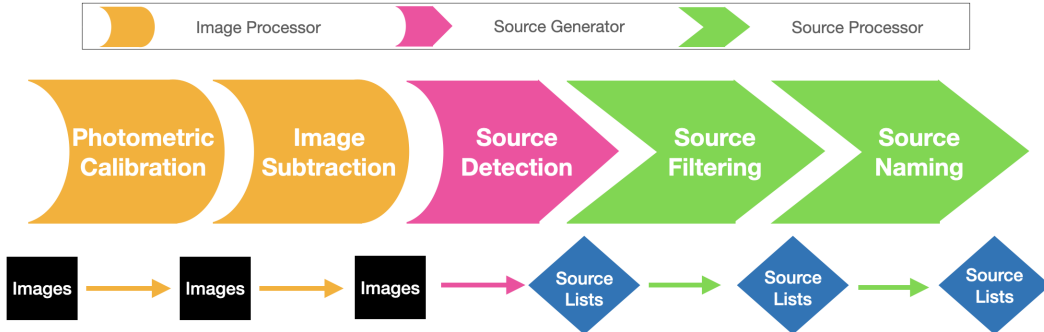


Figure 6.3: **An illustration of a typical *Processor* sequence.** A series of *Image-Processors* are applied to *Images*, resulting in a set of final *Images* (these could be calibrated science images or subtraction images depending on the use case). A *SourceGenerator* is then applied to each of these final *Images*, resulting in one *SourceTable* for each parent *Image*. Finally, a series of additional *SourceProcessors* are applied to the *SourceTables*.

- ZOGY for image subtraction against reference images (Zackay et al. 2016b).
- pytorch for machine-learning classification (Ansel et al. 2024).
- *Apache Avro* for generating a serialised ‘alert stream’ of detections.
- Skyportal for interacting with external ‘marshal’ instances (Walt et al. 2019b; Coughlin et al. 2023b).
- PostgreSQL for interacting with postgres databases.
- Autoastrometry

Key native `mirar` *Processors* include:

- *RawImageLoader* and *MEFloader* for loading raw fits files and converting them to *Images*.
- *CalHunter* for finding and loading missing calibration images.
- *ImageSaver* for writing an *Image* to a fits file.
- *ImageBatcher*, *ImageDebatcher* and *ImageRebatcher* for reorganising *Images* into different *DataBatches*.

- *ImageSelector* and *ImageRejector* for removing *Images* that match user-specified criteria.
- *CSVLog* for generating a csv log of *Images* in a *DataSet*, with user-selected columns.
- *AperturePhotometry* and *PSFPhotometry* to perform aperture/PSF photometry at the position of sources in a *SourceTable*.
- *PhotometricCalibrator* for performing photometric calibration against a user-selected reference catalogue.
- *DarkCalibrator*, *BiasCalibrator* and *FlatCalibrator* for performing dark-subtraction, bias-subtraction and flat correction, respectively.
- *CustomImageBatchModifier* as a catch-all for applying any user-provided python function to *DataBatches*.
- *SourceExporter*, *JsonExporter*, *CSVExporter* and *ParquetExporter* for exporting *SourceTables* to pickle, JSON, CSV or Parquet files, respectively.
- *SourceLoader*, *JsonLoader*, *CSVLoader* and *ParquetLoader* for loading *SourceTables* from pickle, JSON, CSV or Parquet files, respectively.

### **mirar pipelines and configurations**

While users can analyses data with any arbitrary series of processors, `mirar` contains a series of tailored sequences for selected instruments. A *Pipeline* class is created for each new instrument, containing all of the telescope-specific information that is needed for data processing. Most importantly, each *Pipeline* has a function to read in raw data from the corresponding telescope, and ensure that the image and header are formatted correctly for the *ImageProcessors*. In this way, multiple different telescopes can use the same sequence of processors to reduce images.

A single chain of *Processors* is known as a ‘configuration,’ and a given *Pipeline* may have several pre-built configurations to choose from. For example, one configuration might simply generates a CSV log for a particular night of data, while another configuration completely reduces this raw data to produce difference images, and a third might reduce the data without subtraction and produce lists of detected sources. Each configuration must have a name, and can be selected based on the

unique combination of instrument and configuration. In addition to the aforementioned pipelines for WINTER and SUMMER, `mirar` also has already-implemented pipelines for the following instruments:

- Spectral Energy Distribution Machine V2 (SEDMV2) optical camera on the 2.1m Kitt Peak telescope.
- Wide Field Infrared Camera (WIRC) on the Palomar 200-inch telescope (Wilson et al. 2003a).
- Wafer-Scale Imager for Prime (WaSP) on the Palomar 200-inch telescope.
- Gemini Multi-Object Spectrographs (GMOS) on the Gemini-North telescope (Hook et al. 2004).

### **mirar execution and monitor**

Pipelines can be run via the command line on a particular night of data, in which case that night’s data will be processed sequentially. Calibration image requirements can be specified in advance, and if any of these are missing within a night’s data, the *CalHunter* processor can be used to search for suitable calibration images in previous nights. `mirar` uses python’s inbuilt `logger` class throughout, so that output at a chosen verbosity can be printed to the terminal or saved to a file. In addition, `mirar` has systematic error catching, handling and aggregation, so any errors raised during processing will be tracked. After processing has been completed, a dedicated error log can be produced which groups errors raised by type, and aggregates the list of images for which that error was raised. This feature is useful for gathering statistics to understand where processing might be failing.

In addition to the ‘offline’ mode, `mirar` has a *Monitor* class for real-time processing. This mode can also be called from the command line, and uses the python `watchdog` module to watch a specified directory for new images. After checking to ensure the images are complete (i.e they are not partially transferred), the monitor will then run the image through a specified real-time pipeline. After a chosen number of hours, a post-processing step can be run to provide an email summary of the processing. Typically, a new monitor instance would be created each afternoon to process the upcoming night of observation data, with the post-processing summary step then run the next morning when no new images are expected. The monitor class can persist for a user-selected duration, which could be several days, to ensure that even if data is delayed it can still ultimately be processed.

## Documentation

`mirar` is documented through in-code comments and docstrings, which are rendered by ReadTheDocs<sup>5</sup>. These are augmented by dedicated doc pages describing high-level information and installation instructions. Pipeline configurations are automatically rendered as a flowchart for visualization, and each flowchart is included in automatically-generated documentation pages for that instrument. Users can browse available instruments<sup>6</sup>, and all available configurations for these instruments.

## 6.4 The WINTER Pipeline (`winterdrp`)

In this section, we describe the `winterdrp` flow of data processing for WINTER, from raw photoelectrons to uploaded transient candidates in Skyportal.

### Raw WINTER data

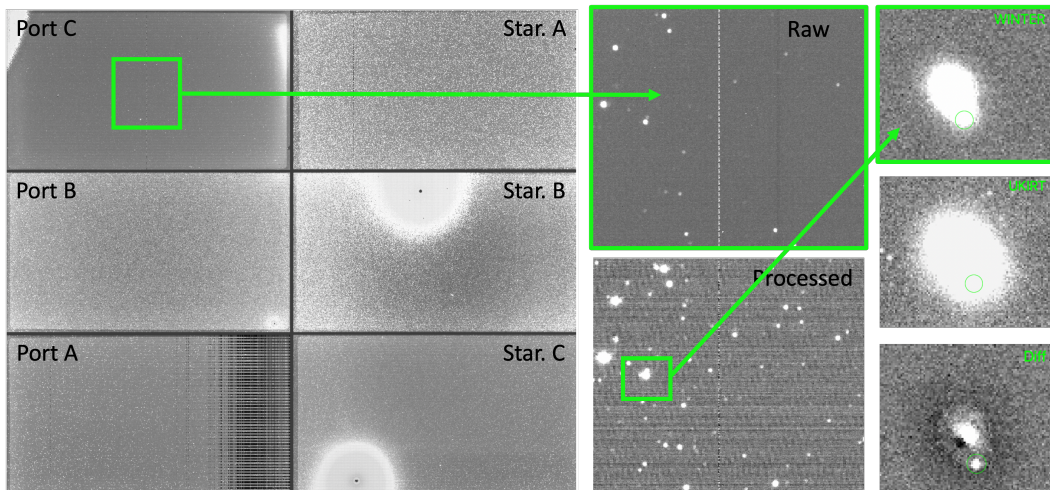


Figure 6.4: **An example of a raw WINTER image as it is processed through different stages of the pipeline.** The MEF file with all six labelled sensors is shown in the *left* panel, and the smaller images show zoom-ins of the raw, processed, reference, and difference images around a transient. The big white spots on the Star B and Star C sensors mark glow spots. The Star B sensor was replaced in April 2024 with a new sensor that does not have the glow spot, but has one nonfunctional output of its eight readout channels.

Observations are coordinated by the WINTER scheduler (Lourie et al. 2020a), with user discretion in terms of exposure time and dither sequencing. However, for both routine survey observations and ToO observations conducted by the WINTER, observations are conducted with exposure times of 120s. Our standard sequence

<sup>5</sup><https://mirar.readthedocs.io/en/latest/>

<sup>6</sup><https://mirar.readthedocs.io/en/latest/autogen/pipelines.html>

uses 8 dithers (16 minutes), used uniformly for all surveys, while our follow-up observations occasionally use 30 dithers (60 minutes) for deep imaging. The single dither exposure time was chosen to keep the counts in each exposure close to the well center ( $\approx 20000$  counts). The number of dithers is chosen based on the total integration time required to achieve the required depth. The dither distance is also user configurable, but based on the physical scale of detector imperfections almost all observations are conducted with our recommended 90'' dither step.

Images are acquired using proprietary sensor software on the ITAR-controlled *Freya* computer, physically located in the WINTER control room at Palomar Observatory. The resultant exposures are sent to the neighboring non-ITAR *Odin* machine, which is more widely accessible. Raw WINTER exposures are initially saved as six-frame multi-extension fits files (one frame per WINTER sensor). These images are then transferred from *Odin* to Caltech using the High Performance Wireless Research and Education Network (HPWREN) via an `rsync` command that runs every minute. The images are copied to the dedicated *WINTER* server at Caltech, with raw data organized into a separate directory for each night.

After raw images arrive, all subsequent processing of data is done with the realtime WINTER pipeline (`winterdrp`), built using the `mirar` framework. A `winterdrp monitor` is started each day at 1AM PDT, and is assigned to watch the directory for that night's data. As images appear on the dedicated WINTER machine at Caltech, they are assigned to one of 40 available multi-processing threads. The images are grouped by dither set, and then processed as a single *DataBatch*.

Every raw image is a multi-extension fits file with each extension corresponding to one of the six detectors, identified as Port A/B/C or Star A/B/C (see Figure 6.4). The Star C and Star B detectors have unusable areas due to glow spots. The Star B detector was replaced in April 2024 with a new engineering grade sensor that does not have glow spots, but one of its eight readout channels is nonfunctional. Glow spots are also visible on Port C, but they are limited to the detector edges, while Port A has a large number of dead pixels towards its right edge. Additionally, a large number of hot pixels are visible in several detectors. We attempt to mitigate the effect of these detector outages using aggressive masking (see Sec. 6.4) and dithering. Given the different outage patterns, sensitivities, and dark current levels of each detector, the `winterdrp` pipeline processes each detector independently. Figure 6.4 shows a zoom-in of the raw image as it goes through the pipeline to identify a transient in the image. The next subsections describe specifics of the steps

involved.

### Dark subtraction

The first step in the calibration routine is dark subtraction. This seemingly straightforward step has proven to be challenging for WINTER. The operating temperatures of the on-sky WINTER detectors range from  $-30^{\circ}$  C to  $-15^{\circ}$  C, substantially warmer than the design requirement of  $-50^{\circ}$  C (see Frostig et al. 2024a for possible causes). As a result, the dark current of WINTER is comparable to the sky background counts and is thus an important source of noise. Furthermore, the dark counts are unstable and correlate with several environmental parameters. Figure 6.5 shows the variation of counts in 120 sec dark exposures taken over a 18 hour period starting from noon local time to sunrise of next day. Dark images taken during the day have substantially larger counts (often exceeding the dark+sky counts of images taken during the night) pointing to a light leak in the optical system. To mitigate the effect of the light leak, darks are taken at midnight. The dark counts also correlate strongly with the ambient temperature (distinct from the detector temperature), suggesting that the detectors are sensitive to thermal emission from components in the optical system. To mitigate night-to-night temperature variations, dark images are acquired on a nightly basis. This strategy does not correct for temperature variations within a night that are substantial from sunset to midnight, but relatively stable from midnight to sunrise. Such thermal IR pickup has also been observed by SPIRIT InGaAs camera at the SPECULOOS Southern Observatory (Pedersen et al. 2024). Additionally, we observe a third effect, where even at constant temperature the dark current seemingly fluctuates between two possible states. This effect is currently undiagnosed and we do not have a way of correcting for it. Together, these variations in the dark current of  $\approx 5\text{--}10\%$  currently set the uncertainty floor for any WINTER measurements.

In summary, dark frames are taken every night at midnight local time. Five sets of dark exposures for all integration times of science exposures for the night (typically 120 sec. for *J*-band observations) are acquired and median stacked to generate a master dark that is subtracted from the raw exposures. On a clear night, between 2500–3000 sky counts are detected in the dark subtracted images. Dark subtracted images with counts lower than 500 are marked as bad and are dropped from the pipeline.

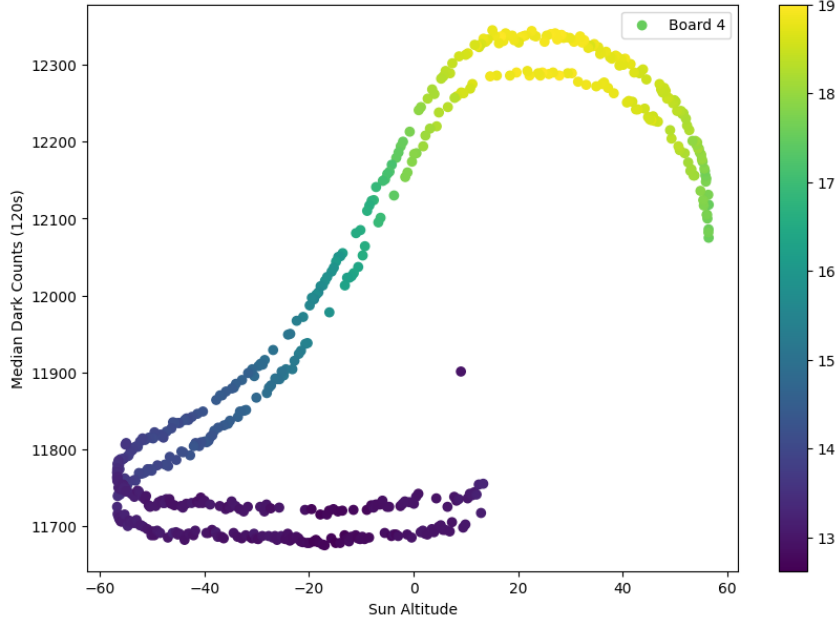


**Figure 6.5: Variation of median dark counts for the Port C sensor taken in a continuous eighteen hour timespan from noon to sunrise the next day, plotted as a function of sun altitude.** The points are color-coded by the ambient temperature. It is evident that the dark counts vary significantly with sun altitude and ambient temperature. WINTER uses dark frames taken at midnight every day to reduce the effect of this. Additionally, the dark counts randomly jump between two distinct curves. This variation remains undiagnosed, and sets a noise floor for the WINTER images.

### Masking

We aggressively mask areas around glow spots on all detectors. Additionally, we construct a bad pixel mask using dithered frames for each exposure by identifying pixels that are  $3\sigma$  outliers in every dithered exposure from that observation. We find that this strategy identifies majority of the hot and dead pixels in the image. These bad pixels constitute  $\approx 10\%$  of the entire detector. In addition to these, we also find a small number of transient bad pixels that are present in some but not all images. These are possibly correlated with the undiagnosed fluctuations in the dark current. These pixels seem to appear randomly in some dithers, and comprise  $\sim 1\%$  of the entire detector.

### Flat Calibration and sky subtraction

The WINTER detectors have a pattern of eight interweaved readout channels, each with different (unquantified) gain values, together with non-negligible pixel-to-pixel

gain variations. There is also a strong vignetting pattern across the focal plane. We attempt to calibrate for these effects through flat-fielding. We experimented with three strategies for constructing a flat field — 1) Dome flats taken using a lamp installed in the WINTER dome, 2) Twilight flats taken during twilight, 3) Nightly flats using science exposures from the night. The dome flats were not used as the WINTER dome lamp did not provide uniform illumination. The twilight flats had substantially larger sky counts than the majority of the science images taken later in the night. Non-linearity effects in the WINTER detectors (see Sec. 6.6) precluded the use of twilight flats, as large residuals were visible in the science images that were flat calibrated using them, leaving nightly flats as the only viable option. We first constructed master flats by stacking all science images taken during a night and used them to calibrate the science images. However, we find a residual circular pattern across the focal plane in all calibrated images (Figure 6.6). The morphology of this pattern changes with telescope pointing and is likely due to position-dependent scattered light from the telescope. To mitigate this, instead of stacking all nightly science images, we constructed flat frames for each dither-set by stacking all dithered exposures in that observation set. This successfully removes the circular arcs and other trends from the images. However, we observe dark residual wings around bright stars and galaxies in the flat-calibrated images. To correct for this, we perform astrometry and stack these flat-calibrated images (see Sec. 6.4 and 6.4) and perform image segmentation on the stacked image using SExtractor to generate source masks covering the brightest sources in the image. We then go back and apply the source masks to the to dark-calibrated images and stack them to regenerate sky flats, this time with bright sources masked. This strategy reduces the dark residuals around bright sources.

Finally, a 2D background is estimated and subtracted from each flat-calibrated image using SExtractor. At this stage, the images are fully detrended.

### Astrometric Calibration

Astrometric calibration is performed in multiple phases within `winterdrp` to ensure an accurate solution is found. An initial solution is obtained through use of `astrometry.net` (Lang et al. 2010), using the standard Tycho 2/Gaia DR2 (Høg et al. 2000; Marrese et al. 2019) reference index catalogue stored locally on the Caltech winter machine. For this, `astrometry.net` is configured to use SExtractor to identify sources, and not measure distortion corrections. As a second step, SExtractor is run on the image again, and full astrometric solutions including distortion coeffi-

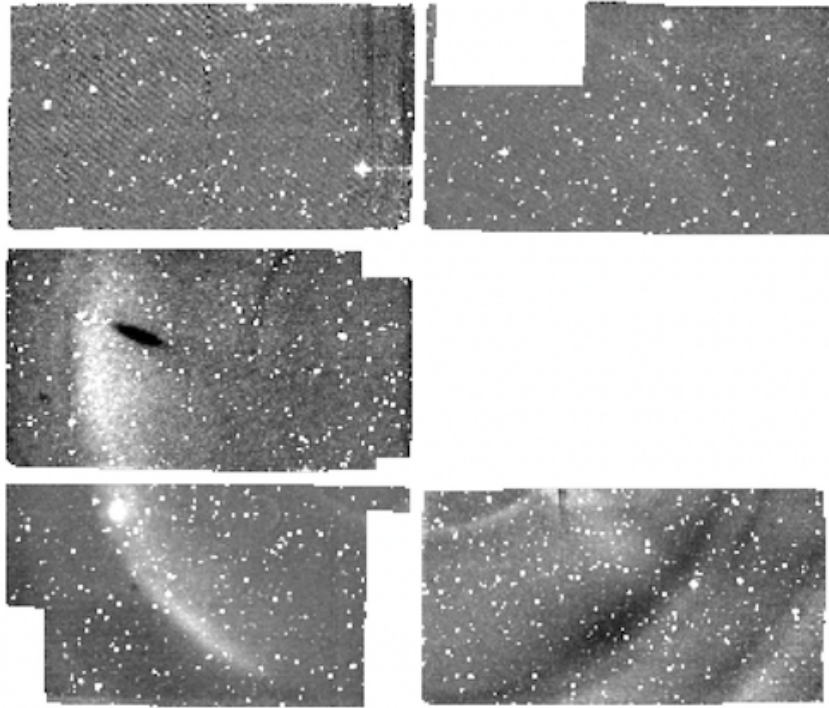


**Figure 6.6: A mosaic with a stack of five WINTER sensors, where the images were calibrated using a master flat made by stacking all sky frames from the night.** We find circular patterns across the focal plane, likely originating in scattered light. We find that the morphology of this pattern changes with telescope pointing. This precludes the use of the all-night-sky-frames strategy for flat-fielding. Instead, we create flats by stacking dithered observations for each pointing.

ients are calculated using `Scamp` (Bertin 2006). The joint Gaia/2MASS catalog (Skrutskie et al. 2006; Marrese et al. 2019) is used as the reference catalog for `Scamp`. At this stage, a significant fraction of the images still had poor astrometric solutions. We found that running a second iteration of `Scamp` on these images solved this issue. In summary, our astrometric calibration consists of three steps — `astrometry.net` followed by two iterations of `Scamp`. The astrometric accuracy is computed for each image by calculating the median offset between the image coordinates and the reference coordinates, and images with poor astrometric solutions at this stage are dropped from further processing.

### Image Stacking and Photometric Calibration

Images are grouped by dither set, and stacked using `SWarp` (Bertin et al. 2002). Header information is propagated from the component images. Photometric calibration is then performed against reference stars from Gaia/2MASS (Marrese et al.

2019; Skrutskie et al. 2006) for J-band and Hs-band) or PS1 (Chambers et al. 2016a) for y-band. In all cases, a colour correction of the following form is applied:

$$M_{\text{ref}} - M_{\text{img}} = \text{ZP} + C \times (\text{colour}_{\text{ref}}) \quad (6.1)$$

where J-band uses reference J–H colour, Hs band uses reference H–K colour, and y-band uses y–z colour. The gradient value of C is newly fit for each image using the available stars with the `optimize` package of `scipy` (Virtanen et al. 2020).

### Image Subtraction and Transient Detection

Image subtraction on the J and Hs-band is performed relative to publicly available images from the United Kingdom Infrared Telescope (UKIRT Murdin 2000). Most J-band reference images are from the UKIRT Hemisphere Survey (UHS, Dye et al. 2018), while a small number of reference images are from the UKIRT Infrared Deep Sky Survey (UKIDSS) Data Release 11. The UHS images are stored locally on the WINTER server at Caltech, while the UKIDSS images are downloaded in realtime from the WFCAM Science Archive<sup>7</sup>. For y-band, we use reference images from PANSTARRs-1 (Chambers et al. 2016a). The reference images are resampled and scaled to match the pixel scales and sensitivities of the science image using SWarp (Bertin et al. 2002). After matching the two images, image subtraction is performed using a python implementation of ZOGY (Zackay et al. 2016b), which yields a final ‘difference image’ and a significance ‘SCorr’ image.

Source detection is not performed directly on the difference, but rather on the corresponding SCorr image (Zackay et al. 2016b). We run SExtractor on the Scorr image to identify sources, with a peak scorr value greater than 5. Aperture and PSF photometry is then performed at these positions in the difference image and all sources with these values are compiled in a *SourceTable*. Each row of the *SourceTable* also includes three ‘cutout images’, which are 64x64 pixel arrays centered on the source with image data from the parent science, reference and difference image. Metadata regarding the the detection itself, for example the FWHM and the number of bad pixels in the difference cutout, are also included in the *SourceTable*. Finally, the sources are filtered to remove bad detections.

---

<sup>7</sup><http://wsa.roe.ac.uk/>

### Crossmatching and WINTER AVRO alerts

Detected sources are cross-matched to a variety of external catalogues to provide contextual information, in particular through queries to the kowalski database at Caltech (Duev et al. 2019b). These include crossmatches to the 2MASS point source catalogue (Skrutskie et al. 2006), PS1 point source catalogue (Chambers et al. 2016a), the PS1-based star/galaxy classification catalogue (Tachibana et al. 2018a), the Gaia EDR3 source catalogue (Gaia Collaboration et al. 2021) and a database of ZTF-detected sources (Bellm et al. 2019b). Sources are also cross-matched to previous WINTER detections, providing a complete detection history of each source. At this stage, if sources have no previous detection, they are assigned a unique sequential name of the form *WNTR25abcde*. Sources that do have previous detections will instead inherit their previous name.

Each detection is then converted to an *Apache Avro* alert, adopting the same data format used by ZTF (Bellm et al. 2019b), Gattini (De et al. 2020b) and the upcoming Rubin observatory (Ivezić et al. 2019b). The WINTER alerts contain information about both the latest detection and historical detections, as well as the contextual data, the source name, and the latest cutout images. All Avro alerts are contain a full schema detailing the data products, and the WINTER alerts contain additional information about schema version. These Avro alerts are written to disk.

### Filters, Streaming and Skyportal Integration

Due to the large number of raw WINTER detections (a typical night might produce 20000 detections), substantial additional filtering is required to useful scientific results. Cuts are applied based on the source metadata, including parameters such as the FWHM and bad pixel count, which serve as a proxy for bad detections. Moreover, as the differencing infrastructure is designed to identify transients, additional cuts are applied based on the crossmatching results to remove known stars. Ultimately, approximately 150 alerts survive these cuts and are deemed potentially interesting.

After applying the cuts, the Avro alerts for the remaining sources are sent to IPAC, which serves as a broker that distributes these detections more widely as a Kafka ‘alert stream’. The instance of Skyportal (Walt et al. 2019b; Coughlin et al. 2023b) used by the ZTF and WINTER collaborations receives these alerts, and applies a series of filters to identify possible transients within the alerts. These filters can overlap, but each is focused on particular science cases such as ‘transients in nearby galaxies’, ‘transients with a ZTF crossmatch’, or ‘extragalactic transients’. Human

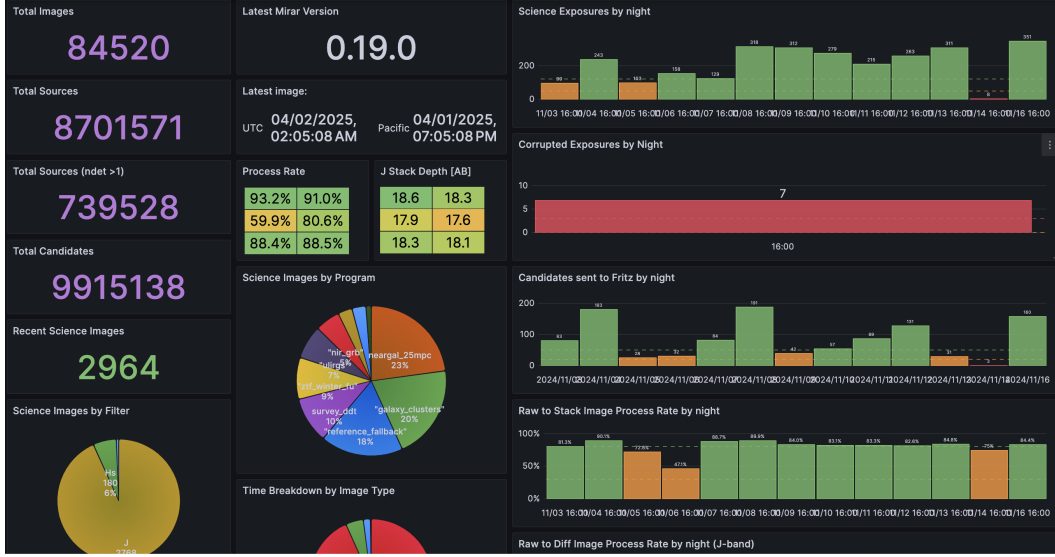


Figure 6.7: An example page from the WINTER Grafana dashboard that interacts with the WINTER database and allows for realtime monitoring of pipeline and survey performance. The dashboard has panels showing performance metrics such as processing success rates for stacks and difference images, limiting magnitudes, and number of candidates broadcast to Skyportal; accounting metrics like total number of images processed, number of candidates generated, program-wise distribution of observations; and low-level debugging metrics like the number of science exposures, and number of corrupted images.

scanners vet detections which pass these filters, of which there are typically 120 per night, and bona fide sources are saved for further followup. An example source page of a WINTER transient is shown in Figure 6.7.

## WINTER Database

A single PostgreSQL database is used to store metadata about WINTER data, with a table and field structure that is automatically generated by `mirar` through the SQLAlchemy python package (Bayer 2012). The database tables are indexed by spatial position using Q3C (Koposov et al. 2006), increasing the speed of spatial queries and crossmatching. The database includes separate tables corresponding to images at five stages of processing:

- **Exposure** — The original WINTER camera images, with 6 multi-extension fits frames corresponding to the six individual camera sensors.
- **Raw** — The individual WINTER camera images, after the multi-extension file has been split into six separate images and pixel masking has been applied.

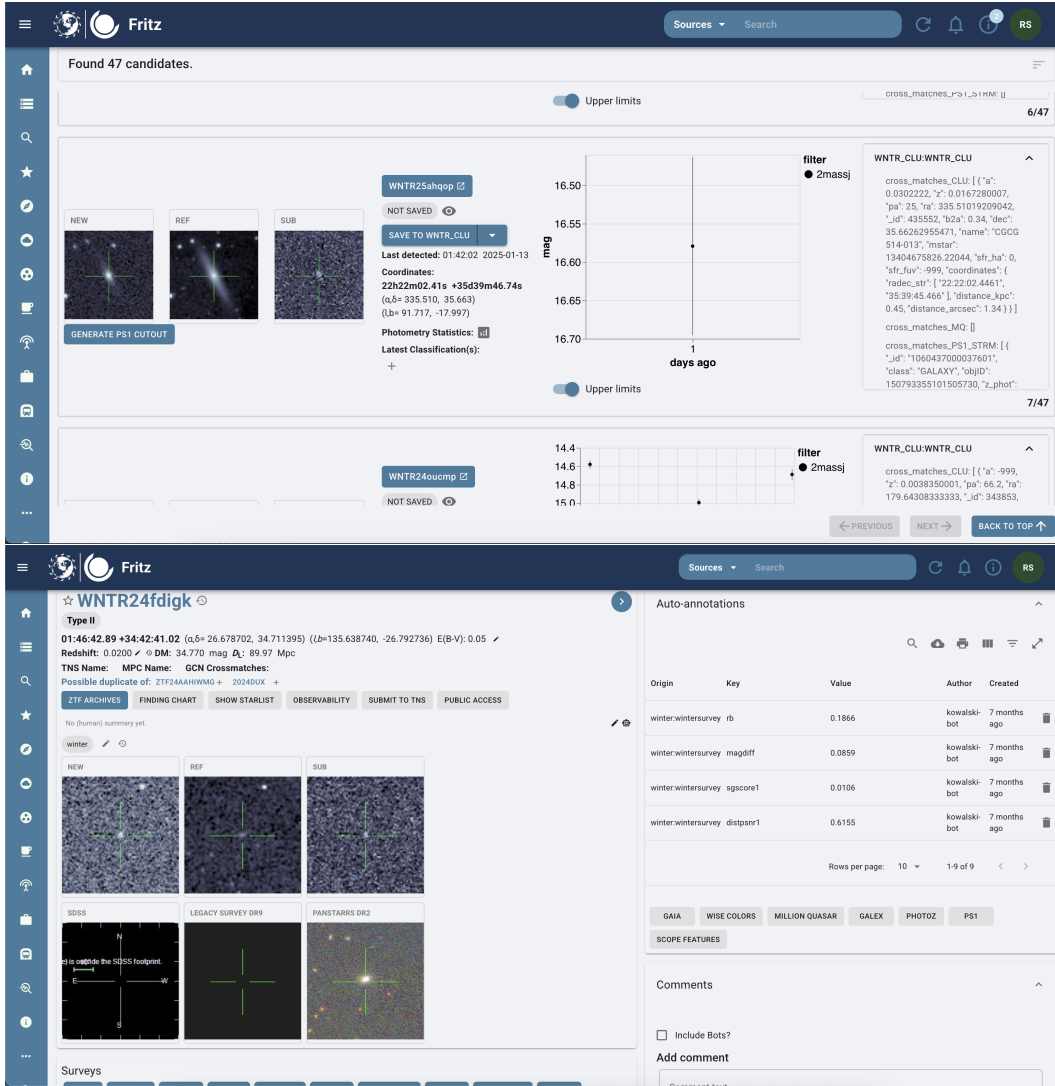


**Figure 6.8: WINTER alerts on Skyportal.** *Top:* An example scanning page on Skyportal showing the new, reference, and difference cutouts of candidate WINTER transients, their photometry, and ancillary information such as cross-matches to external catalogs and subtraction quality metrics. *Bottom:* Skyportal source page for WNTR24fdigk/AT2024dux, a Type II supernova that was detected by both WINTER and ZTF and flagged for further followup.

- **Science** — Science-ready WINTER camera images, after detrending and astrometric/photometric calibration has been applied.
- **Stack** — The stacks of all individual WINTER science images for a given detector, including each image in the dither set.
- **Diff** — The difference images generated for WINTER stack images, after image subtraction against a reference image.

Further tables include ones for filters, fields and active survey programs. There are two additional tables relating to transients:

- **Sources** — All objects detected at least once by WINTER, including a unique name for each.
- **Candidates** — Every individual detection by WINTER. A single source must have one or more detections associated with it.

These database tables are used by both the Grafana dashboard (Section 6.4) and the API (Section 6.2). Most `mirar` interactions with the database come via unidirectional *Processors* which simply copy metadata to an individual database table. However, `mirar` also queries the source table to determine whether a named object already exists at the position of each detected transient, and the candidate table to retrieve the complete detection history of sources which have been detected before.

### Grafana Dashboard and Alerts

`winterdrp` performance is monitored through a dedicated *Grafana*<sup>8</sup> dashboard, which provides live visualisation of the database. An example of a dashboard pages is shown in Figure 6.7. The dashboard provides processing efficiency, an aggregate log of all recent ToO requests, as well as photometric/astrometric performance, and overall statistics about the time usage of each survey program. The Grafana dashboard has been configured to provide automated email alerts for a variety of data problems including a lack of new images for a given night, an abnormally low processing rate, or images arriving with corrupted or missing header information. These notifications help to promptly identify data-taking issues that may arise, so they can be resolved promptly.

---

<sup>8</sup><https://grafana.com>

## 6.5 WINTER Pipeline performance

### Processing Rates and Latency

The average successful processing rate from raws to stacks is  $\approx 85\%$  across all detectors during periods when no detectors are affected by undiagnosed technical issues. Processing failures primarily occur in images affected by clouds or bad weather, or images taken during twilight with high background counts. The average stack-to-difference image rate from routine operations is  $\approx 70\%$ . Failures include fields that were not covered by the UKIRT surveys (usually  $\delta \geq 60$  deg, but also some southern fields with  $\delta < -25$  deg), and stacked images affected by weather with shallow depths that cannot be matched to the deeper UKIRT reference images. We note that during periods of good weather with observations limited to regions with reference coverage (e.g., GW followup of S250206dm, see Sec. 6.7) stacks-to-difference rates are much higher ( $\geq 90\%$ ).

As WINTER requires dark images to be taken at midnight, the processing of the data begins at 1 am Pacific time every night, and the full night's data processing typically finishes before 8 am Pacific. A daily email notifies the WINTER users of the completion of the pipeline.

### Astrometric accuracy

We achieve a median astrometric precision of  $\approx 0.2''$ , corresponding to a fifth of one WINTER pixel. Fig. 6.9 shows the distribution of median astrometric residuals calculated by comparing the image coordinates to reference coordinates for 16300 representative images taken between 2025-02-15 to 2025-02-25.

### Limiting magnitudes and photometric accuracy

Figure 6.10 shows the distribution of  $5\sigma$   $J$ -band limiting magnitudes for 960 second exposures (8 dithers, 120 seconds each) of the routine WINTER survey taken during a one year span in 2024. The median limiting magnitudes range from 18.6 mag (AB) on the most sensitive detector Port C to  $\sim 18.0$  mag (AB) on the least sensitive Star B detector. Figure 6.11 shows the dependence of limiting magnitude with total integration times for  $Y$ ,  $J$ , and  $Hs$  bands measured using data taken in 2024 (colored lines). First principles calculations of the limiting magnitudes for all three filters are shown as the solid black line. The observed depth is shallower than these calculations by  $\approx 2.5$  mag. We note that this calculation incorporates all known differences between design and observed WINTER parameters such as mirror reflectivity, detector gain, and FWHM (see Frostig et al. 2024a for more

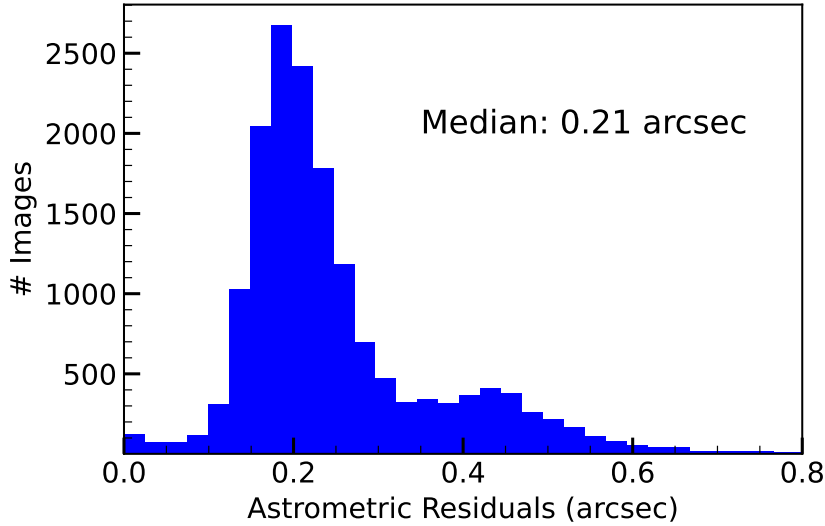


Figure 6.9: **Distribution of astrometric residuals** from  $\sim 16000$  images taken in February 2025. The median astrometric residual is  $0.21''$ , corresponding to a fifth of one WINTER pixel.

details). The observed depths are consistent with a first-principles calculation if we artificially lower the system throughput by a factor of ten, shown by the dashed line in Figure 6.11. Thus, WINTER’s on-sky throughput is mysteriously lower than expected by a factor of ten. Frostig et al. (2024a) suggest that this reduced efficiency could be attributed to lower performance in one or more of the following factors: detector conversion gain, quantum efficiency, or throughput of the telescope and instrument optics. Further testing has revealed a reduced QE of  $\sim 10\%$ , compared to the 80% design requirement as a possible culprit (Frostig et al. 2025, in prep.).

Figure 6.12 shows the distribution of photometric residuals measured by calculating the standard deviation of the differences between the instrumental and reference 2MASS magnitudes after photometric calibration of stacked  $J$ -band images taken during 2025-02-15 to 2025-02-25. The median photometric residuals range from 0.1 mag on Star A to  $\sim 0.2$  mag on the other detectors. These large residuals even for bright 2MASS sources (12–16 mag (AB)) are caused due to a combination of non-linearity effects in the detector (Section 6.6), dark current variations (Section 6.4), imperfect gain corrections due to sub-optimal flat-fielding strategies, and the undiagnosed pick-up noise from electronic components. These residuals set an uncertainty floor of  $\approx 0.2$  mag on any photometry measured using the WINTER camera currently. We are in the process of testing several strategies to improve this, described in the Section 6.6.

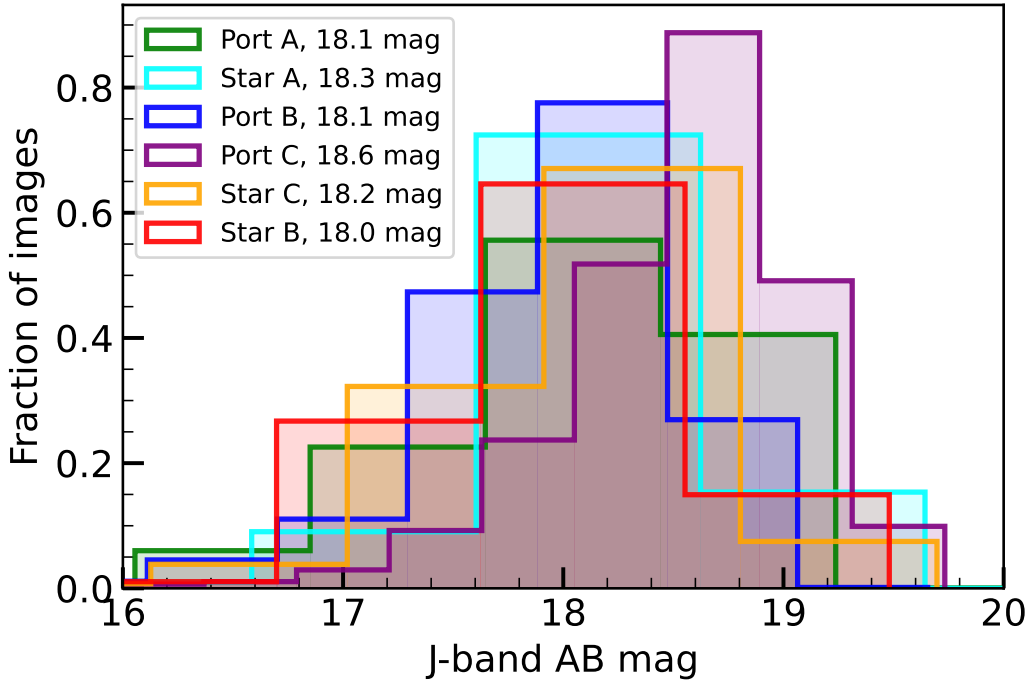
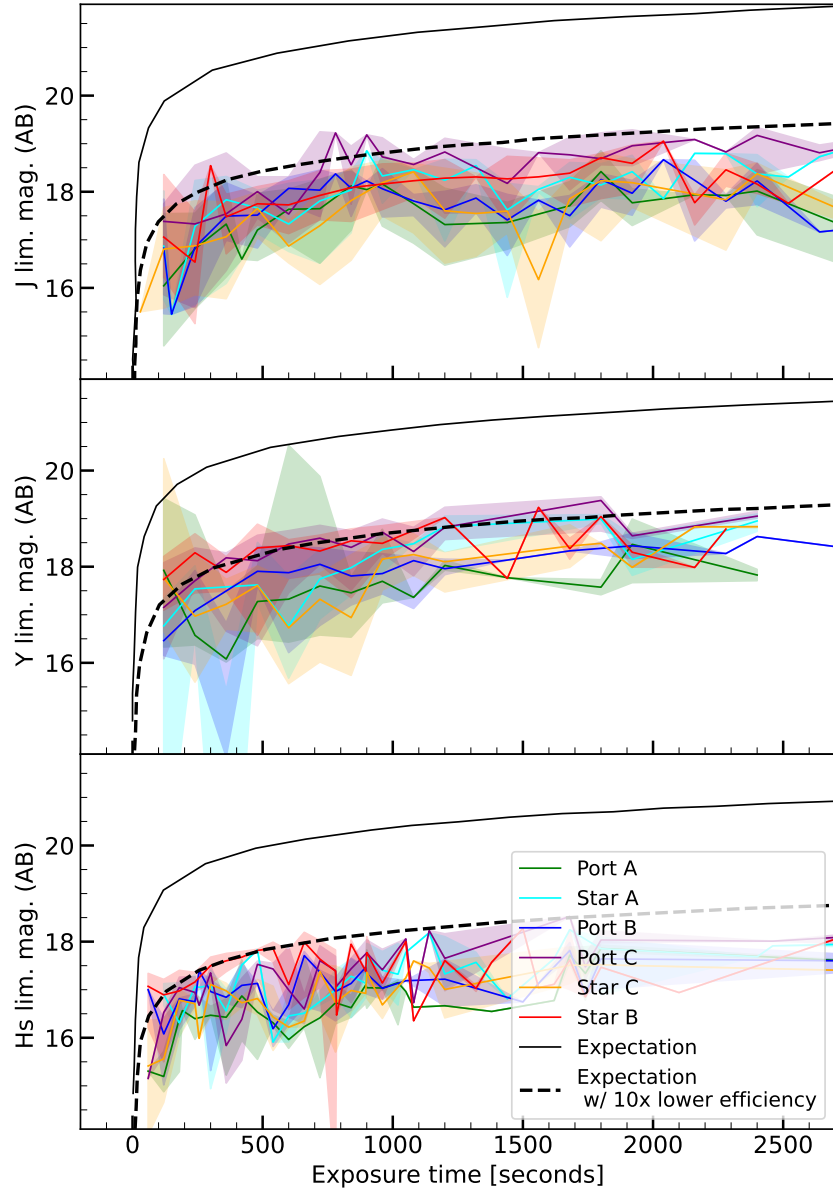


Figure 6.10: **Distribution of the limiting magnitudes for each of the six WINTER sensors**, for data taken during 2024. The median values of the limited magnitudes range from 18.0 to 18.6 mag (AB), and are listed in the legend.

### Image subtraction and candidate detection

We find that image subtraction relative to UKIRT reference images can detect isolated transients, transients offset from bright host galaxies, and faint stars that have brightened since the UKIRT epochs. However, the difference images have large residuals at the locations of bright stars and nuclei of bright galaxies. While some residuals are expected for such sources, they are exacerbated by the non-linearity of WINTER detectors. For a given science image, the reference image scaling factor depends on the brightness of stars, and different scaling factors are required to cleanly subtract faint and bright stars, respectively. This effect limits our ability to detect nuclear transients and bright variable stars. In addition to these nuclear and bright star artifacts, we also find several artifacts due to noisy pixels, especially around detector outages, and a small number of spurious detections due to dark spots in the UKIRT images. Examples of real transients identified by the pipeline are shown in Figure 6.7.



**Figure 6.11: Limiting magnitudes as a function of exposure time for all WINTER data taken during 2024 in the  $J$ -band (top),  $Y$ -band (middle), and the  $H_s$ -bands (bottom). Solid lines mark the median limiting magnitudes and shaded regions show the 16<sup>th</sup> and 84<sup>th</sup> percentiles. Different colors indicate the six different sensors. WINTER’s sensitivity is substantially lower than expected (solid black line). Instead, the depths match the expectation depth if the WINTER throughput is lower than the design specifications by a factor of ten (dashed black line). This is consistent with lab-testing which shows that the QE of the sensors is ten times lower than the design specs.**

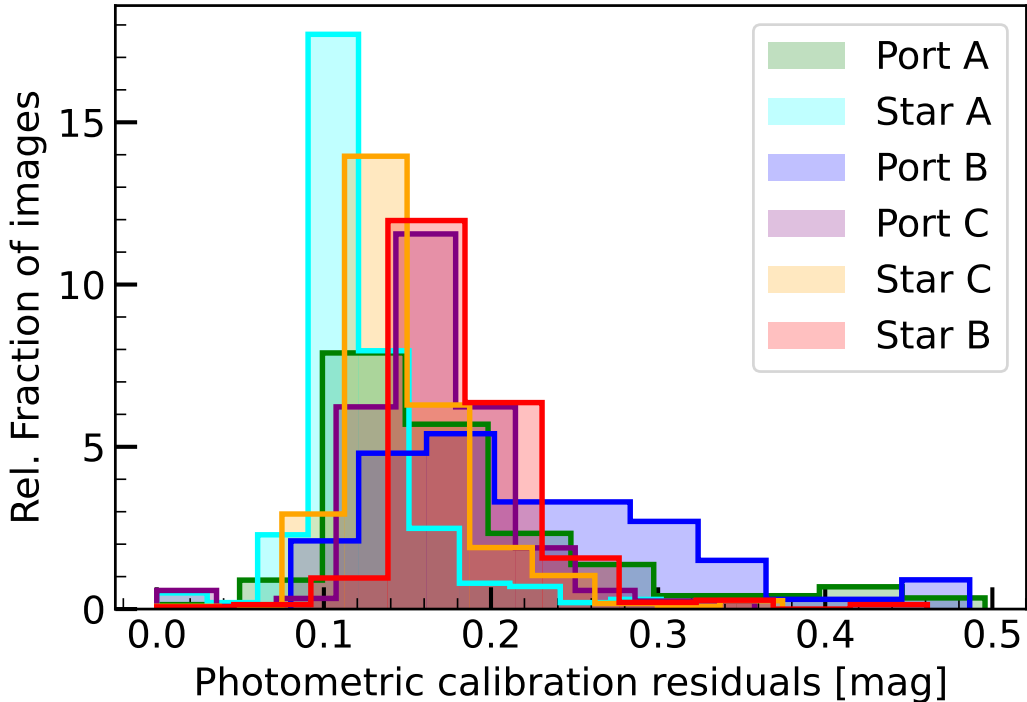
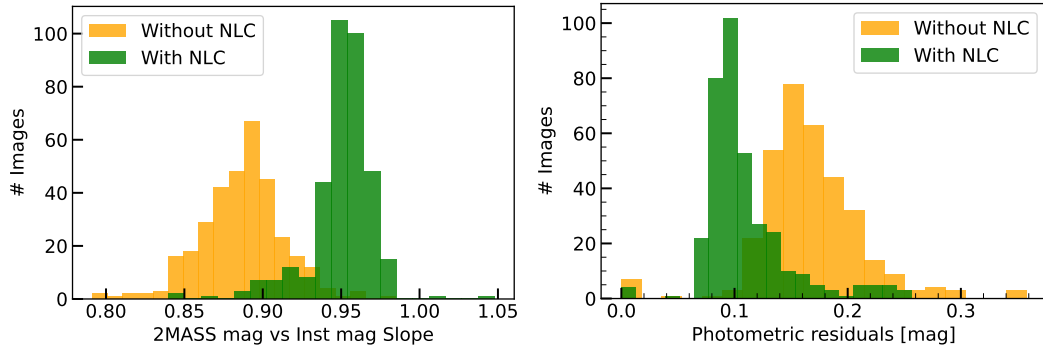


Figure 6.12: **Distribution of residuals computed by measuring the standard deviation of the difference between instrumental magnitude and reference magnitude in photometrically calibrated WINTER stacks** from February 15 to 25, 2025. Different colors show different boards. The median of the residuals range from 0.1–0.2 mag. These residuals are due to a combination of the non-linear response of the detectors, variation in dark counts, and other noise sources, and set a systematic uncertainty for any photometry measured using the WINTER stacks.

## 6.6 Planned upgrades for performance improvements

### Non-linearity corrections

WINTER’s detectors exhibit more nonlinearity than expected. The strongest deviations appear at lower signal levels (9000 – 14000 counts), but significant deviations persist in the most linear region (28000 to 44000 counts), well before the expected high-end nonlinearity near saturation. To correct for these effects, a six parameter rational calibration function is applied to each pixel, approximating a linear response. More details about WINTER non-linearity and derivation of the rational coefficients are described in a dedicated instrument paper (Frostig et al. 2025, in prep). Briefly, for a particular hardware configuration, a series of increasingly bright flats are taken to measure the pixel response, and these data are used to fit the underlying curve parameters. Having measured these parameters, any raw count value can then be converted back to a ‘linearised’ count value. Here, we describe



**Figure 6.13: Improvements in performance after applying the current version of non-linearity corrections (NLC).** *Left:* Distribution of slopes obtained by fitting a linear function to the instrumental magnitudes as a function of reference magnitudes. It is clear that the slopes after applying the corrections are closer to perfect linearity (1) than the slopes without NLC. *Right:* Photometric residuals after NLC are lower than those without NLC. Efforts are underway to further characterize the NLC of the WINTER sensors.

the pipeline implementation and early results from these non-linearity corrections.

A dedicated Python package, `winternlc`<sup>9</sup>, was created to implement these non-linearity corrections. The parameter maps are stored as six-frame fits files, and these are downloaded locally when the package is run. Crucially, the parameters themselves depend on the exact settings of the hardware and firmware, meaning that they change over time as settings are adjusted. The package therefore has strict versioning and includes multiple versions of the correction maps corresponding to different hardware states. The non-linearity correction is applied in `mirar` to every individual WINTER image, including both calibration and science images.

We reprocessed data taken in a ten-day window during 2025 February 15 to February 25 using these non-linearity corrections. The non-linearity is quantified by measuring the slope between measured instrumental magnitudes and 2MASS reference magnitudes in the stacked images. Figure 6.13 shows a comparison of the slopes before and after non-linearity corrections for detector Port C. We find that using non-linearity corrections shifts the slopes closer to one than before (median value 0.96 vs 0.88), suggesting a more linear response. We also find lower photometric residuals (Figure 6.13) of  $\approx 0.1$  mag compared to 0.16 mag without non-linearity corrections. We also find substantially fewer bad pixels in the dark-calibrated images than before. These results demonstrate the efficacy of our non-linearity correction strategy

<sup>9</sup><https://github.com/winter-telescope/winternlc>

in improving the detector response. Efforts to improve the non-linear correction coefficients and extend them to other detectors are underway.

### Other upgrades

In addition to the non-linearity corrections, efforts are ongoing to model the thermal dependence of dark current, and also to identify the source of mysterious seemingly random variations in the dark counts. There are also efforts to improve the flat-fielding strategy by measuring gain variations across pixels using higher S/N flats taken in the lab. On the image subtraction side, we are working on building a better real-bogus classifier to reduce the scanning load and more efficiently identify real transient and variable sources in the data.

## 6.7 Early Science with WINTER

Since first light in June 2023, WINTER has been operating robotically to observe a mix of long-term surveys and target-of-opportunity (ToO) sources. Long-term surveys include the WINTER survey of Nearby Galaxies, the WINTER Galactic plane survey, and the WINTER reference building survey. ToO observations include a dedicated program for electromagnetic followup of gravitational waves (EMGW), followup of gamma-ray bursts and X-ray transients detected by the Einstein Probe mission, followup of high-energy neutrino candidates from the Icecube Neutrino Experiment, and followup of the reddest ZTF transients. We list examples and lessons learnt from these observing programs.

### ToO science

#### Observations of known transients

There is a program to systematically follow-up the reddest extragalactic transients identified by ZTF with WINTER, to identify signs of dust formation in them. Figure 6.14 shows examples of two such transients. So far, we have obtained *J*-band observations for 80 ZTF transients with WINTER and continue to compile this systematic sample. WINTER also observes Galactic transients identified by different surveys such as ZTF, Gaia, and NEOWISE (Mainzer et al. 2014a; De et al. 2023). Figure 6.15 shows two examples of Galactic transients identified by WINTER. Follow-up NIR spectroscopic observations show that one of them is an outbursting young stellar object, while the other is a classical nova.

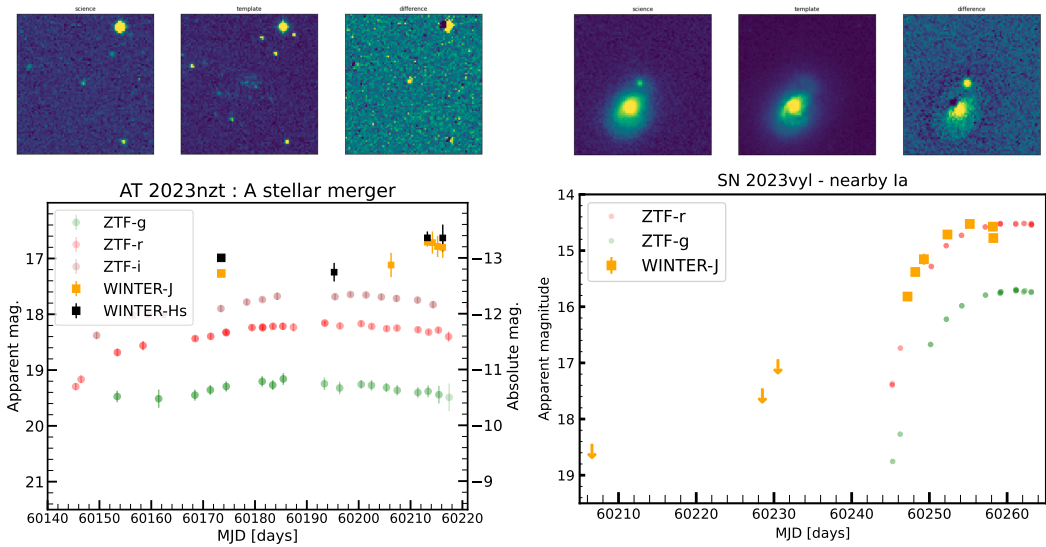


**Figure 6.14: Examples of two extragalactic transients detected by WINTER.** The top panels show cutouts of WINTER science, reference, and difference images for the two transients, and the bottom panels show the multiband lightcurves including WINTER *J* and *Hs* band data.

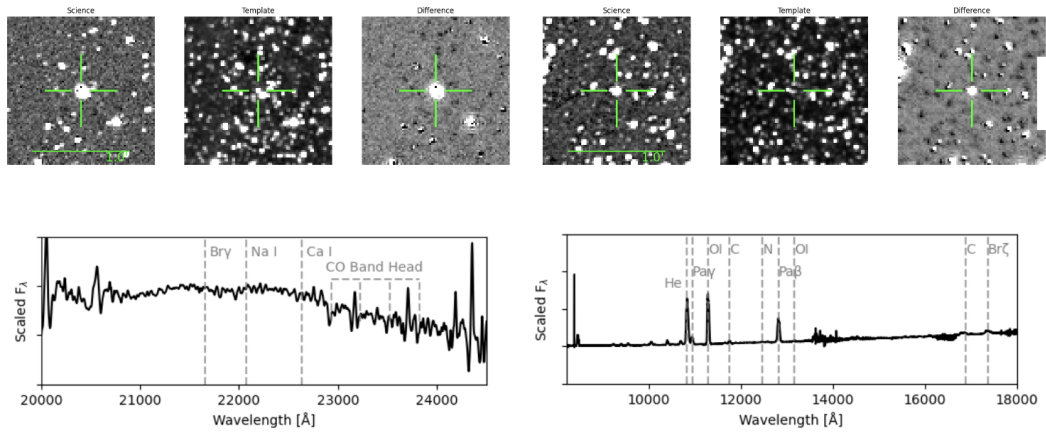


**Figure 6.15: Galactic transients detected by WINTER.** *Left:* WNTR24jheuy (Gaia18dvy/WTP17aadrne), a young stellar object outbursting with follow-up MMIRs spectrum. *Right:* WNTR24fzjjq (ZTF24aaomlx), a galactic classical nova with a WINTER detection and FIRE spectrum. Image credit: Danielle Frostig.

### Multi-messenger followup

WINTER was designed for EMGW followup of GW alerts out to a distance of 200 Mpc and localized to better than 300 sq. deg (Frostig et al. 2022b). With its reduced on-sky sensitivity, WINTER can detect kilonovae only to a distance of  $\approx$ 100 Mpc. There has not been a GW alert matching these criteria in LVK’s ongoing O4 observing run. The recent BNS/NSBH GW alert S250206dm at a distance of  $\approx$ 373 Mpc and a 50% sky-localization area of 38 sq. deg. is one of nearest and best localized GW triggers identified so far. We used WINTER to follow-up this trigger, covering a total of  $\approx$ 43% of the integrated probability of the sky localization and did not find any compelling counterpart candidate (Frostig et al. 2025 in prep). While our upper limits are not deep enough to constrain kilonova models at the distance of this event, our search demonstrates WINTER’s capabilities to tile GW localizations, and highlights the promise of NIR EMGW followup.

In addition to EMGW followup, we have programs for automated triggering of WINTER for Swift GRBs and EP X-ray transients. The localization regions (typically 1–3 arcmin) of these sources are small enough to be covered by the most sensitive WINTER detector (Port C). So far, we have reported *J*-band observations for 22 GRBs and EP sources (e.g., Mo et al. 2024; Ahumada et al. 2024; Karambelkar et al. 2024). The automated triggering ensures we can begin observations within a few minutes of the event being observable from Palomar. We continue to automatically trigger these alerts.

We also have a program for automated triggering of high-energy neutrino alerts from Icecube. Figure 6.16 shows an example from the follow-up campaign of the neutrino alert IC 240105A. The blazar PKS 0446+11 lies within the localization region and was reported to undergo a flare possibly coincident with the neutrino alert. We detect the flaring of this blazar in our WINTER observations, with the *J*-band magnitude being 2 mag brighter than the optical *r*-band (Stein et al. 2024).

Automated realtime triggering of NIR observations is one of WINTER’s unique capabilities. We are now routinely triggering WINTER on such alerts and look forward to start detecting GRB afterglows and infrared counterparts to EP X-ray transients on a regular basis.

### Survey science

The design plan for WINTER survey science was to conduct an all-sky survey to  $J = 21$  mag (AB) for serendipitous NIR discovery of type Ia SNe, tidal disruption

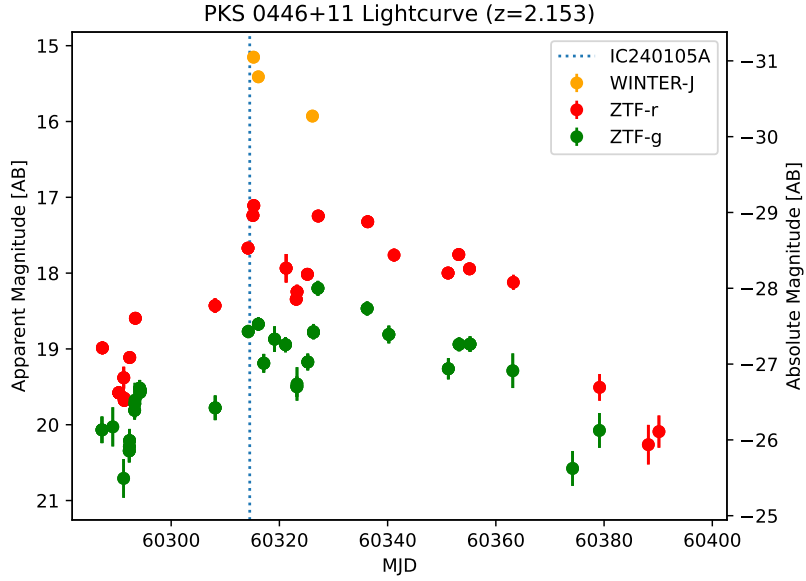


**Figure 6.16: Multi-band lightcurve of the flaring blazar PKS 0446+11 that is located within the localization region of the high-energy neutrino alert IC 240105A.** The dotted line marks the epoch of the neutrino detection, and WINTER detections of the flare are shown in orange.

events, and core-collapse SNe that could be missed by optical surveys. However, the lower on-sky depth of WINTER reduces the volumetric survey speed and discovery rate for an all-sky survey extremely<sup>10</sup>. Therefore, we opted to conduct a targeted survey of nearby galaxies to search for dusty transients. The galaxies were selected using a two-tiered strategy, with the first tier comprising five pointings covering the M31 group observed at daily cadence, and the second tier comprising 90 pointings covering galaxies out to 25 Mpc, 30 pointings of ultra-luminous infrared galaxies (ULIRGS) and 90 pointings of galaxy clusters out to 100 Mpc observed with a two week cadence. The survey ran from late-2023 to late-2024, with a break from May to July 2024 when we switched to Galactic plane observations. This survey yielded WNTR 23bzdiq: a slow varying star in M 31 that resembles a stellar merger involving an AGB star primary (Karambelkar et al. 2025 in prep). Several other slowly varying stars in M 31 that had brightened since their decade-old UKIRT epochs were also flagged. No other transients were identified in other galaxies, likely due to a combination of shallow depth, poor subtractions on bright galaxy backgrounds due to non-linearity effects, and commissioning breaks. Novae in M 31

<sup>10</sup>The most efficient strategy for an all sky survey was 225 sec. exposures reaching 17.5 mag (AB), which give an expected rate of 7 SNe Ia and 1 TDE per year.

were missed as they typically remained above WINTER’s detection limit only briefly before fading, making them vulnerable to weather and other commissioning-related downtimes.

## 6.8 Summary and way forward

In this paper, we presented the data reduction and transient detection pipeline for the WINTER near-infrared time-domain surveyor. The `winterdrp` pipeline was implemented using `mirar`: a modular, open-source python-based framework designed to process images from any telescope and find transients in them. `mirar`’s modular approach to the task enables users to plug in any telescope and go from raw frames to Avro alerts, by reusing *Processors* for performing tasks such as calibrations, resampling, stacking, image subtraction, and source detection. `mirar` has built-in *Processors* for widely-used astronomy software such as `astrometry.net`, `SExtractor`, `Scamp`, `Swarp`, and also supports interactions with the data visualization interface `Skyportal`. `mirar` is open-source and heavily tested, and additional capabilities can be easily added as needed.

The `winterdrp` implemented in `mirar` processes images from the WINTER surveyor at Palomar Observatory to identify transients in them by using template images from the UKIRT public surveys. WINTER’s InGaAs sensors present several calibration challenges, and we describe strategies used to mitigate some of these effects. We quantify the performance of the InGaAs sensors using year-long observations from 2024, and find  $5\sigma$  limiting magnitudes ranging from  $\approx 18$ – $18.6$  mag (AB) for the six detectors for a total integration time of 960 seconds. The limiting magnitudes range from  $\approx 17.5$ – $18.5$  mag (AB) in the Y-band, and  $16.5$ – $17.5$  mag (AB) in the Hs-band. This sensitivity is lower than expected by a factor of ten, likely due to ten times lower QE of the InGaAs sensors than the design requirements. We also find a systematic uncertainty of 0.2 mag on *J*-band photometry due to non-linearity effects in the detector and transient variations in dark frames. Initial tests using non-linearity corrections demonstrate significant improvements in linearity and reduced photometric residuals, and efforts are underway to better characterize the non-linearity response of the detectors.

We present initial science results from WINTER operations. These include the identification of a possible giant star merger in M31, dust-enshrouded YSO outbursts and a classical nova in the Milky Way, NIR followup of a possible NSBH gravitational wave trigger, automated followup of several GRBs, X-ray transients, and

high-energy neutrino alerts, and NIR followup of several ZTF supernovae. WINTER continues to survey nearby galaxies and galaxy clusters to search for dusty transients, and conduct automated ToO followup of a wide variety of transients and multi-messenger alerts.

Looking ahead, WINTER is part of the emerging landscape of new and upcoming ground-based NIR time-domain surveys such as PRIME (Kondo et al. 2023), DREAMS (Soon et al. 2022; Travouillon et al. 2020), and Cryoscope (Kasliwal et al. 2025a). Together, these surveys will systematically explore the dynamic infrared sky and set the stage for more sensitive searches with the *Nancy Grace Roman Space Telescope*.

## 6.9 Acknowledgements

WINTER’s construction is made possible by the National Science Foundation under MRI grant number AST-1828470 with early operations supported by AST-1828470. Significant support for WINTER also comes from the California Institute of Technology, the Caltech Optical Observatories, the Bruno Rossi Fund of the MIT Kavli Institute for Astrophysics and Space Research, the David and Lucille Packard Foundation, and the MIT Department of Physics and School of Science.

# WINTER ON S250206DM: A NEAR-INFRARED SEARCH FOR AN ELECTROMAGNETIC COUNTERPART

under review in PASP.

D. Frostig<sup>a,1</sup>, V. Karambelkar<sup>a,2</sup>, R. Stein<sup>a,3,4,5</sup>, N. Lourie<sup>6</sup>, M. M. Kasliwal<sup>2</sup>, R. A. Simcoe<sup>6</sup>, M. Bulla<sup>7,8,9</sup>, T. Ahumada<sup>2</sup>, G. Mo<sup>6,10</sup>, J. Purdum<sup>2</sup>

*a* : These authors contributed equally.

<sup>1</sup>Center for Astrophysics | Harvard & Smithsonian, 60 Garden Street, Cambridge, MA 02138, USA

<sup>2</sup>Cahill Center for Astrophysics, California Institute of Technology, Pasadena, CA 91125, USA

<sup>3</sup>Department of Astronomy, University of Maryland, College Park, MD 20742, USA

<sup>4</sup>Joint Space-Science Institute, University of Maryland, College Park, MD 20742, USA

<sup>5</sup>Astrophysics Science Division, NASA Goddard Space Flight Center, Mail Code 661, Greenbelt, MD 20771, USA

<sup>6</sup>Department of Physics and Kavli Institute for Astrophysics and Space Research, Massachusetts Institute of Technology, 77 Massachusetts Ave, Cambridge, MA 02139, USA

<sup>7</sup>Department of Physics and Earth Science, University of Ferrara, via Saragat 1, I-44122 Ferrara, Italy

<sup>8</sup>INFN, Sezione di Ferrara, via Saragat 1, I-44122 Ferrara, Italy

<sup>9</sup>INAF, Osservatorio Astronomico d'Abruzzo, via Mentore Maggini snc, 64100 Teramo, Italy

<sup>10</sup>MIT LIGO Laboratory, Massachusetts Institute of Technology, Cambridge, MA 02139, USA

## Abstract

The Wide-Field Infrared Transient Explorer (WINTER) is a near-infrared time-domain survey designed for electromagnetic follow-up of gravitational-wave sources localized to  $\leq 300 \text{ deg}^2$ . The instrument's wide field of view (1.2  $\text{deg}^2$ ), dedicated

1-m robotic telescope, and near-infrared coverage (0.9-1.7 microns) are optimized for searching for kilonovae, which are expected to exhibit a relatively long-lived near-infrared component. We present WINTER follow-up observations of the International Gravitational Wave Network (IGWN) event S250206dm—the only neutron star merger in the fourth observing run (to date) that is localized to  $\leq 300 \text{ deg}^2$  and has a False Alarm Rate lower than one per year. This event is predicted to have a 55% probability of being a neutron star black hole merger (NSBH) and a 37% probability of being a binary neutron star (BNS) merger with a 50% sky-localization area of 38  $\text{deg}^2$  and estimated distance of 373 Mpc with a false alarm rate of about 1 in 25 years. WINTER covered 43% of the probability area at least once and 35% at least three times. Through automated and human candidate vetting, all transient candidates found in WINTER coverage were rejected as kilonova candidates. Unsurprisingly, given the large estimated distance of 373 Mpc, the WINTER upper limits do not constrain kilonova models. This study highlights the promise of systematic infrared searches and the need for future wider and deeper infrared surveys.

## 7.1 Introduction

The discovery of GW170817 during the second Advanced LIGO-Virgo observing run (O2) marked a breakthrough in multi-messenger astronomy, providing the first confirmed detection of a kilonova powered by r-process nucleosynthesis in the neutron-rich ejecta of a binary neutron star (BNS) merger (Abbott et al. 2017d; Abbott et al. 2017f; Abbott et al. 2017e). This event established the importance of joint observations of gravitational wave (GW) alerts and identifying electromagnetic (EM) counterparts and investigating the physics of compact object mergers, the neutron star equation of state, and heavy-element production (e.g., Abbott et al. 2017e; Barnes et al. 2016; Coulter et al. 2017; Barnes et al. 2013; Evans et al. 2017; Goldstein et al. 2017; Grossman et al. 2014; Haggard et al. 2017; Hallinan et al. 2017; Kasen et al. 2017; Kasen et al. 2013; Kasliwal et al. 2019b; Li et al. 1998; Margutti et al. 2017; Metzger et al. 2010; Metzger 2020; Roberts et al. 2011; Rosswog 2005; Tanaka et al. 2013; Tanvir et al. 2017; Troja et al. 2017).

Despite extensive optical and infrared follow-up campaigns, subsequent LIGO-Virgo observing runs (e.g., the third observing run, O3) yielded no confirmed EM counterparts to BNS or neutron star-black hole (NSBH) mergers (e.g., Coughlin et al. 2020a; Kasliwal et al. 2020; Abbott et al. 2021a; Abbott et al. 2021b; Collaboration et al. 2021; Zhu et al. 2021b). Many of these events were predicted to be too faint for detection by optical telescopes, as kilonovae exhibit viewing-angle-dependent

blue emission that fades rapidly (<1 week), while a longer-lived near-infrared (NIR) signal is predicted to be more isotropic (Kasen et al. 2013; Kasen et al. 2017; Metzger 2020). Indeed, GW170817 had significantly longer-lived infrared emission compared to optical emission (Tanvir et al. 2017). Zhu et al. 2021a predicts kilonovae may be up to  $\sim$ 8–10 times more detectable in the near-infrared compared to optical wavelengths. However, systematic sensitive wide-field infrared searches have been limited by high detector costs and high sky backgrounds. Some shallow searches were performed by the Palomar Gattini-IR survey (Moore et al. 2016; De et al. 2020a) (Coughlin et al. 2019a). Two new wide-field IR surveyors have come online in the fourth observing run, including the Wide-field Infrared Transient Explorer (WINTER), discussed in this study, and PRIME a new NIR survey on a 1.8-meter telescope with four large-format HgCdTe sensors covering a  $1.56 \text{ deg}^2$  field of view (Durbak et al. 2024; Kutyrev et al. 2023; Yama et al. 2023).

WINTER is a 1-meter telescope and camera at Palomar Observatory designed for rapid-response NIR transient discovery, with a wide field of view ( $1.2 \text{ deg}^2$ ) and infrared sensitivity ( $J_{AB} \sim 18.5$  mag) (Lourie et al. 2020b). WINTER’s InGaAs-based detectors provide an efficient, cost-effective alternative to traditional HgCdTe NIR sensors, enabling systematic follow-up of GW events in Y, J, and shortened-H bands (0.9–1.7 microns) (Simcoe et al. 2019b).

WINTER is designed around the discovery of EM counterparts to GW events, with a wide field of view, infrared sensitivity, and rapid robotic follow-up to enable efficient tiling of GW localization regions (Frostig et al. 2020). Frostig et al. 2022a presents a comprehensive simulation of WINTER’s capability to follow up BNS mergers during the fourth International Gravitational Wave Network (IGWN) observing run (O4). The analysis predicts that near-infrared kilonovae will persist longer than their optical counterparts, with red kilonovae detectable at distances approximately 1.5 times greater in the NIR. This study offers detailed projections of WINTER’s effectiveness in identifying new kilonovae. However, issues manufacturing the new-to-astronomy InGaAs detectors resulted in a decreased final sensitivity ( $J_{AB} \sim 18.5$  instead of  $J_{AB} \sim 21.0$  magnitudes), impacting WINTER’s effectiveness following up kilonovae (Frostig et al. 2024b).

In this paper, we present results from WINTER follow-up of the LIGO-Virgo-KAGRA (LVK; Aasi et al. 2015; Acernese et al. 2014; Somiya 2012; Aso et al. 2013; Akutsu et al. 2020) gravitational wave trigger S250206dm (LIGO–Virgo–KAGRA Collaboration 2025a). S250206dm was first detected by the LVK at 2025–

02-06T21:25:30.439 UT, as part of the ongoing O4 run. The event was recovered by the GW search pipelines GstLAL (Messick et al. 2017; Sachdev et al. 2019; Hanna et al. 2020; Cannon et al. 2021; Ewing et al. 2024; Tsukada et al. 2023), MBTA (Adams et al. 2016b; Aubin et al. 2021) and PyCBC Live (Allen et al. 2012; Allen 2005; Dal Canton et al. 2020; Usman et al. 2016; Nitz et al. 2017; Davies et al. 2020), with an estimated distance of 373 Mpc and a false alarm rate of about 1 in 25 years. The event, as reported by the LVK, has a 55% probability of being a NSBH merger, with a 37% probability of being a BNS merger (LIGO–Virgo–KAGRA Collaboration 2025a); in addition, the probability that the lighter compact object is a neutron star is  $> 99\%$  (LIGO–Virgo–KAGRA Collaboration 2025b). S250206dm’s localization underwent several revisions, with the latest (released 36 hours after merger) having a 50% localization area of  $38 \text{ deg}^2$ , and a 90% area of  $547 \text{ deg}^2$ . With its relatively precise localization and confident detection, S250206dm is one of the most promising merger candidates in O4 with a high probability of containing a neutron star.

In addition to the gravitational wave properties of S250206dm which suggested a possible electromagnetic counterpart, the IceCube Neutrino Observatory (Aartsen et al. 2017) promptly reported the detection of two neutrinos in spatial and temporal coincidence with the event (IceCube Collaboration 2025), as part of its realtime search for neutrino-gravitational wave coincident detections (see, e.g., Abbasi et al. 2023). Neutrino 1 was detected 109s before merger, while neutrino B was detected 289s after merger<sup>1</sup>. We performed additional ToO observations of neutrino fields, similar to other teams (Becerra et al. 2025; Masi 2025).

In this paper, we report on the nondetection of an EM counterpart to S250206dm, observed with WINTER during O4. We describe our observational strategy, data processing, and implications for future NIR follow-up of GW events.

## 7.2 WINTER follow-up campaign

### WINTER observatory

The WINTER camera is mounted on a dedicated 1 m telescope at Palomar Observatory, and comprises six InGaAs detectors that together produce a field-of-view of 1.2 deg.  $\times$  1 deg with a pixel scale of 1.13" per pixel. The WINTER telescope has been running robotically on sky since June 2023 (Frostig et al. 2024b), featuring new InGaAs sensor technology and a custom read out (Frostig et al. 2022b; Malo-

---

<sup>1</sup>[https://roc.icecube.wisc.edu/public/LvkNuTrackSearch/output/2025\\_02\\_06\\_S250206dm-7-Update.html](https://roc.icecube.wisc.edu/public/LvkNuTrackSearch/output/2025_02_06_S250206dm-7-Update.html)

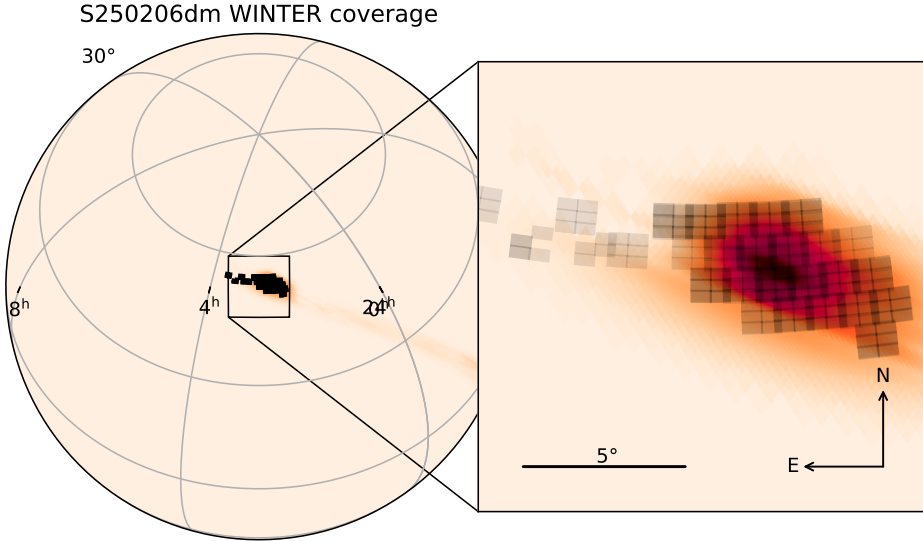


Figure 7.1: **WINTER J-band coverage of S250206dm.** The probability skymap is plotted in red overlaid with WINTER pointings shown as black rectangles. Each rectangle corresponds to a single WINTER detector and six detectors combine to produce a 1 deg.  $\times$  1.2 deg. FOV in a single WINTER pointing. Our observations covered a total of 43% of the skymap probability for this gravitational wave event, of which 40% was observed at least twice.

nis et al. 2020), a novel fly’s-eye optical design (Lourie et al. 2020b), and custom opto-mechanics (Hinrichsen et al. 2020).

The WINTER telescope is operated by the WINTER Supervisory Program (WSP), a multithreaded Python-based control system that manages scheduling and observations using PyQt5 for interfacing with the Qt framework. Cron jobs on the observatory’s control PC initiate WSP, which automates key observatory functions, including nightly scheduling, target-of-opportunity (ToO) handling, and priority-based command execution, while allowing manual overrides when necessary. Drawing on methodologies from MINERVA (Swift et al. 2015), Robo-AO (Riddle et al. 2012), and GOTO (Dyer et al. 2018), WSP facilitates automated decision-making for telescope operations, including dome control and observation execution. Target of opportunity (ToO) observations are submitted automatically through a dedicated API service.

### S250206dm observations

WINTER observations of the GW localization region commenced on UT 2025-02-08T04:05:52,  $\approx$ 30.5 hours after the merger. No observations were possible on

the first night after the merger due to poor weather at Palomar Observatory, which continued to limit observations throughout the follow-up campaign. WINTER observations are conducted on a predefined field grid. An optimal schedule to tile the GW skymap using WINTER fields was computed using `gwemopt` (Coughlin et al. 2018; Coughlin et al. 2019b; Dietrich et al. 2020). Each WINTER field was observed in the *J*-band with a set of eight two-minute long dithered exposures, corresponding to a combined integration time of sixteen minutes per field. These fields were subsequently reobserved on the nights of UT 2025 Feb 9, 10, 11, 16, and 17. All WINTER pointings overlaid on the GW-skymap are shown in Figure 7.1. The full details of the pointings are available on TreasureMap Wyatt et al. 2020. Within ten days of merger, a total of 43% of the probability enclosed within the latest available GW skymap at the time of writing<sup>2</sup> was observed with WINTER at least once, 40% of the total probability was observed at least twice, and 35% was observed at least three times.

### Data processing and transient detection

The WINTER images were processed by the WINTER data reduction pipeline implemented in `mirar`<sup>3</sup> (Karambelkar & Stein et al., in prep) — a modular, python-based framework designed for real-time, end-to-end processing of astronomical images to search for transients. A detailed description of the processing steps will be provided in a forthcoming publication. Briefly, the pipeline begins by performing dark subtraction, flat calibration and sky-subtraction on the raw WINTER images. Astrometric solutions are then computed using the packages `Astrometry.net` (Lang et al. 2010) and `Scamp` (Bertin 2006). Eight astrometry-calibrated dithers are then stacked using the software `Swarp` (Bertin et al. 2002), and the stacked images are photometrically calibrated relative to the Two Micron All-Sky Survey (2MASS; Skrutskie et al. 2006) point source catalog (Cutri et al. 2003). Images from each of WINTER’s six detectors are reduced separately, so each sixteen-minute observation of a field produces six stacked images each with dimensions 0.6 deg x 0.3 deg. The median depths achieved during our observations of S250602dm for the six detectors were 17.6, 17.6, 17.4, 18.0, 17.5, and 17.4 mag (AB), respectively. Of the total GW skymap probability, 41% was observed to a depth of 17 mag or deeper, 38% was observed to a depth of 17.5 mag or deeper, 31% was observed to a depth of 18 mag or deeper, and 11% was observed to a depth of 18.5 mag or deeper.

---

<sup>2</sup><https://gracedb.ligo.org/api/superevents/S250206dm/files/Bilby.offline1.multiorder.fits>

<sup>3</sup><https://github.com/winter-telescope/mirar>

Image subtraction is then performed on these stacked images relative to archival *J*-band reference images from the United Kingdom InfraRed Telescope (UKIRT) Hemisphere Survey (UHS; Dye et al. 2018) using the optimal image-subtraction algorithm ZOGY (Zackay et al. 2016b). Sources identified in the difference image are cataloged in a SQL database, cross-matched to external point-source catalogs such as 2MASS, Pan-STARRS (PS1; Chambers et al. 2016b), as well as to transient alerts from ZTF and the Transient Name Server, packaged as alerts in the `avro` format, and broadcast to the Fritz.science instance of Skyportal for scanning and visual vetting (Coughlin et al. 2023c).

During the ten day observational campaign, the WINTER images were processed every night in real-time and the alerts were examined to identify interesting transients. Separately, at the end of the campaign, we reprocessed the WINTER images by stacking repeat observations of the same field from multiple nights to increase the depth of our search. The median depths for these “super-stacks” was 17.8, 17.7, 17.7, 18.0, 17.8, and 17.5 mag for the six detectors, respectively.

### **Candidate Searches**

A total of 62991 individual alerts were generated by our standard observations, of which 62675 lay within the 95% contour reported by LVK. We perform three complementary searches for possible transients in our data.

### **Candidates With Multiple WINTER detections**

Our data reduction pipeline cross-matches each new detection to a dynamically-updated table of WINTER ‘sources,’ with each source having an assigned name. The new detections are then crossmatched to all previous detections of the same source, with each `avro` alert including a complete history of detections in our data. The 62675 alerts were grouped into 57670 unique sources. We select those sources with multiple detections, in order to reject moving objects and reduce the number of bogus sources. Of 57670 sources, we select the 4141 sources with at least 2 detections.

### **Candidates with a ZTF crossmatch**

Every WINTER detection is crossmatched to all archival ZTF alerts (Bellm et al. 2018), providing a ZTF source name if available. 9608 of the WINTER sources have a pre-assigned ZTF name. For this event, we perform an additional crossmatch on

Name	RA	Dec	Date	Limiting Magnitude [AB]
AT2025bmq	38.518	54.572	2025-02-08T06:44:50.635	18.3
			2025-02-10T05:15:34.858	17.7
AT2025bbp	153.782	-22.882	2025-02-08T11:04:14.707	17.3
			2025-02-11T09:29:20.609	17.0
AT2025ban	152.918	-18.952	2025-02-09T08:58:45.274	14.4
AT2025baj	156.517	-28.346	2025-02-08T11:21:47.004	14.6
			2025-02-11T10:39:07.412	17.3

Table 7.1: Summary of WINTER images which overlap transients reported to TNS. The image-wide limiting magnitude is also reported, though all transients had underlying hosts which complicate recovery.

all ZTF alerts detected in the same 2 week period post-merger, providing additional matches in cases where the WINTER detection precede ZTF detections. A total of 116161 ZTF alerts were detected within 14 days of merger in the 95% contour, for which no additional cuts were applied. These including both ToO and serendiptious detections of the ZTF public survey. The additional crossmatch yields 1275 matches, of which 65 are new. In total, 9673/57670 WINTER sources have a ZTF crossmatch.

### Candidates with a TNS cross-match

We select all candidates included on the TNS event page for S250206dm, which was 116 at the time of writing<sup>4</sup>. Of these, 95 lie within the 95% contour, though just four TNS transients fell within fields observed by WINTER. We crossmatch all WINTER candidates to the TNS transients with a radius of 3", but find no coincident detections.

In Table 7.1 we list each WINTER image which overlapped with a TNS transient. Only one of the 4 transients fell in a region with both WINTER coverage and reference image coverage (AT2025bmq), and this is the only transient that could potentially have produced an alert. However, as described above, none was found. Looking directly at the science images, the apparent transient is a nuclear with an IR-bright host, and we clearly recover this host in science images at  $mj \sim 14.5$  mag AB in both images. This is consistent with the archival magnitude of this source, so we cannot resolve whether there is any excess flux from a nuclear transient.

<sup>4</sup>[https://www.wis-tns.org/system/files/ligo/o4/S250206dm\\_20250206\\_212530/S250206dm\\_20250206\\_212530\\_AFTER.json](https://www.wis-tns.org/system/files/ligo/o4/S250206dm_20250206_212530/S250206dm_20250206_212530_AFTER.json)

	WINTER + WINTER	WINTER + ZTF	WINTER + TNS	Combined Total
Initial Sources	4141	9673	0	11802
After Stellar Cuts	140	140	0	274
After WINTER predection cuts	140	140	0	274
After ZTF predection cuts	135	4	0	139
After human vetting	0	0	0	0

Table 7.2: Statistics for source cuts using the three independent candidate search methods. Given that sources can be selected by multiple searches, we also give the combined total in the right-most column.

For the other three sources (AT2025bbp, AT2025ban and AT2025baj), no reference images were available, so no image subtraction was performed. All three have apparent underlying hosts, but given the depths of our images, neither the host nor transient were recovered in our science images. Only one of these three transients (AT2025baj) has a host bright enough to be detected in 2MASS. However, at  $m_J=17.4$  AB, this host is fainter than the limiting magnitudes of our science images.

### Candidate Vetting

Though many sources remain at this stage, the vast majority will be stellar. For all 11802 candidates selected by our three independent methods, we perform a series of algorithmic cuts:

- We crossmatch all sources to PS1 to a star/galaxy morphology classifier trained using PS1 data (Tachibana et al. 2018b). We reject WINTER sources within 7" of bright ( $m_r < 15$ ) stars, and those within 3" of fainter stars.
- We reject sources within 3" of sources detected in Gaia-DR3 (Gaia Collaboration et al. 2023) with  $> 3\sigma$  parallax.
- We finally remove sources within 20" of very bright Gaia-DR3 stars, defined as  $M_G < 14$ .
- We reject sources which are ‘old’, defined as having either a WINTER or ZTF detection prior to merger.

For sources passing these cuts, we perform visual inspection. We were aided by crossmatches to Gaia-DR3 (Gaia Collaboration et al. 2023), SDSS (York et al. 2000) and WISE (Wright et al. 2010) for identifying known variable sources. We reject candidates based on the following criteria:

- Candidates which are nuclear are classified as probable AGN if the host galaxy is either a spectroscopic AGN in SDSS (York et al. 2000), is listed as a quasar in Milliquas (Flesch 2023) or has AGN-like WISE colours of  $W1-W2>0.7$  (Stern et al. 2012).
- Bogus sources with poor subtraction residuals, especially those detections close to poorly-subtracted reference image sources. We require candidates to have at least two detections which pass visual inspection and appear to be plausibly real.

On this basis, every WINTER candidate is rejected as a possible transient. A full summary of cut statistics is given in Table 7.2.

### 7.3 Comparison with kilonova models

We generate model light curves for kilonovae using NSBH and BNS models presented in Ahumada et al., in prep. These models are simulated with the latest version (Bulla 2023) of the 3D Monte Carlo radiative transfer code `POSSIS` (Bulla 2019) assuming a two-component (dynamical+wind) ejecta configuration and using state-of-the-art heating rates (Rosswog et al. 2024) and opacities (Tanaka et al. 2020). The kilonova grids span the expected parameter space, with the NSBH grid varying the average velocity of the dynamical ejecta and the masses of the dynamical and wind ejecta (for a total of 108 models) and the BNS grid the mass, average velocity and average electron fraction for both components (for a total of 3072 models). To account for distance uncertainties, we sample 100 distances from the probability distribution function for S250206dm, as provided by the multi-order `Bilby` skymap (LIGO–Virgo–KAGRA Collaboration 2025b). For each sampled distance, we compute a full model grid of calculated ejecta properties to explore the range of possible emission scenarios.

Figure 7.2 presents the resulting marginalized model prediction, obtained by interpolating all light curves onto a common time grid and computing summary statistics at each epoch. We present the J-band median light curve and confidence intervals and compare to the r-band median light curve to demonstrate the relatively bright and persistent NIR plateau. Additionally, we overlay the limiting magnitudes of all WINTER follow-up observations (as described in Section 7.2) to assess whether the models are observationally constrained.

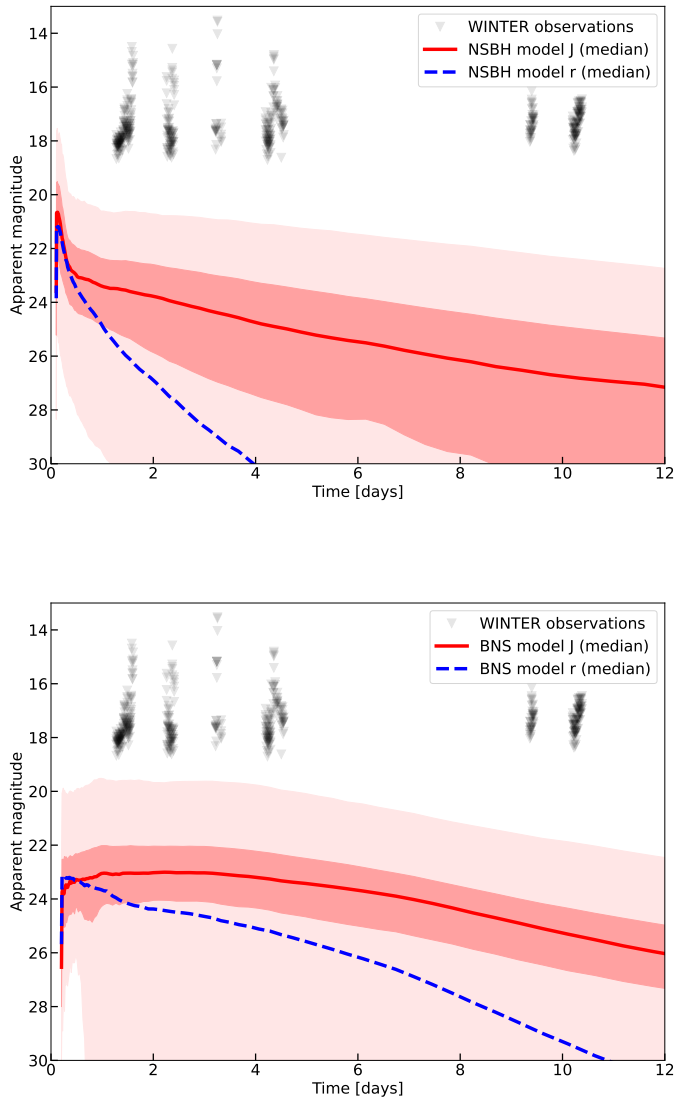


Figure 7.2: **WINTER observations compared to kilonova models** for NSBH (top) and BNS (bottom) mergers from Ahumada et al., in prep, computed using the radiative transfer code POSSIS (Bulla 2023). The kilonova light curve models are marginalized over the full parameter grid and 100 distances sampled from the event probability distribution function for the estimated distance. The median J-band light curve across all distance realizations and the full model grid is shown as a red line, while the shaded regions represent the  $1\sigma$  (68%) and  $3\sigma$  (99.7%) credible intervals. For comparison, the r-band light curve is shown from the same exercise to demonstrate the extended NIR plateau in kilonova models. The limiting magnitudes of WINTER observations are shown for comparison and do not constrain any of the presented models.

The absence of a detected kilonova in WINTER observations is consistent with the predicted NSBH and BNS model grids. At the estimated distance of S250206dm, the WINTER observations are not sufficiently deep to place meaningful constraints on any of the kilonova models explored in this study.

#### 7.4 Summary and way forward

In this study, we present results from the WINTER’s NIR follow-up observations of the gravitational wave event S250206dm, a candidate NSBH or BNS merger detected during the fourth LIGO-Virgo-KAGRA GW observing run. We conducted a targeted follow-up campaign to search for a potential EM counterpart. With systematic coverage of 43% of the probability region within ten days post-merger, we recover no EM counterpart.

The nondetection is consistent with the modeled light curves of kilonovae and our observational depths (median  $J_{AB} \sim 17.4$ –18.0 mag by WINTER sensor), which were insufficient to place strong constraints on kilonova models at these distances. With more typical weather conditions and reduced latency—particularly if follow-up had occurred within 1–2 hours post-merger—WINTER could have been sensitive to the brighter end of predicted models, potentially placing meaningful constraints. Furthermore, no confirmed counterpart was reported by other optical or infrared facilities, highlighting the challenges of detecting EM counterparts to distant compact object mergers with current facilities.

This study underscores the need for deeper infrared follow-up capabilities to improve kilonova detection prospects. WINTER, as a dedicated NIR transient survey, provides an important step toward systematic NIR follow-up of gravitational wave events. However, the development of future instruments with greater sensitivity, wider fields of view, and improved sky coverage will be critical for detecting and characterizing kilonovae from NSBH and BNS mergers. The upcoming Cryoscope surveyor in Antarctica will cover a  $50 \text{ deg}^2$  field of view in the K-dark to a depth of 24.1 mag AB in one hour (Kasliwal et al. 2025b) and the Nancy Grace Roman Space Telescope will provide a depth of 27.60 mag in an hour in the F129 filter over a field of  $0.281 \text{ deg}^2$ <sup>5</sup>. Furthermore, more precise and rapid gravitational wave sky localizations from future observing runs will improve targeting strategies for electromagnetic counterpart searches. Finally, next-generation ground-based observatories, such as the Vera C. Rubin Observatory (Ivezic et al. 2019b), will offer

---

<sup>5</sup>[https://roman.gsfc.nasa.gov/science/WFI\\_technical.html](https://roman.gsfc.nasa.gov/science/WFI_technical.html)

complementary optical coverage, further expanding the capability to identify and study transient astrophysical phenomena.

Although WINTER did not detect a counterpart S250206dm, this follow-up campaign demonstrates a systematic NIR multi-messenger approach. Future attempts, coupled with advancing technology, will further improve our odds of identifying and characterizing the electromagnetic signatures of compact object mergers, deepening our understanding of neutron star physics, nucleosynthesis, and the transient universe.

## 7.5 Acknowledgments

WINTER’s construction is made possible by the National Science Foundation under MRI grant number AST-1828470 with early operations supported by AST-1828470. Significant support for WINTER also comes from the California Institute of Technology, the Caltech Optical Observatories, the Bruno Rossi Fund of the MIT Kavli Institute for Astrophysics and Space Research, the David and Lucille Packard Foundation, and the MIT Department of Physics and School of Science. D.F.’s contribution to this material is based upon work supported by the National Science Foundation under Award No. AST-2401779. This research award is partially funded by a generous gift of Charles Simonyi to the NSF Division of Astronomical Sciences. The award is made in recognition of significant contributions to Rubin Observatory’s Legacy Survey of Space and Time. M.B. acknowledges the Department of Physics and Earth Science of the University of Ferrara for the financial support through the FIRD 2024 grant.

## Part III : Stellar mergers

## VOLUMETRIC RATES OF LUMINOUS RED NOVAE AND INTERMEDIATE-LUMINOSITY RED TRANSIENTS WITH THE ZWICKY TRANSIENT FACILITY

Karambelkar, V. R. et al. (May 2023). “Volumetric Rates of Luminous Red Novae and Intermediate-luminosity Red Transients with the Zwicky Transient Facility”. In: *ApJ* 948.2, 137, p. 137. doi: 10.3847/1538-4357/acc2b9.

V. R. Karambelkar<sup>1</sup>, M. M. Kasliwal<sup>1</sup>, N. Blagorodnova<sup>2</sup>, J. Sollerman<sup>3</sup>, R. Aloisi<sup>4</sup>, S. G. Anand<sup>1</sup>, I. Andreoni<sup>5,6,7</sup>, T. G. Brink<sup>8</sup>, R. Bruch<sup>9</sup>, D. Cook<sup>10</sup>, K. K. Das<sup>1</sup>, K. De<sup>11</sup>, A. Drake<sup>1</sup>, A. V. Filippenko<sup>8</sup>, C. Fremling<sup>1,12</sup>, G. Helou<sup>10</sup>, A. Ho<sup>13</sup>, J. Jencson<sup>14</sup>, D. Jones<sup>15,16,17</sup>, R. R. Laher<sup>10</sup>, F. J. Masci<sup>10</sup>, K. C. Patra<sup>8</sup>, J. Purdum<sup>12</sup>, A. Reedy<sup>1</sup>, T. Sit<sup>18</sup>, Y. Sharma<sup>1</sup>, A. Tzanidakis<sup>19</sup>, S. J. van der Walt<sup>20</sup>, Y. Yao<sup>1</sup>, C. Zhang<sup>21</sup>

<sup>1</sup>Cahill Center for Astrophysics, California Institute of Technology, Pasadena, CA 91125,  
USA

<sup>2</sup>Department of Astrophysics/IMAPP, Radboud University, Nijmegen, The Netherlands

<sup>3</sup>The Oskar Klein Centre, Department of Astronomy, Stockholm University, AlbaNova,  
SE-10691 Stockholm, Sweden

<sup>4</sup>Department of Astronomy, University of Wisconsin-Madison, 475 North Charter Street,  
Madison, WI 53706, USA

<sup>5</sup>Joint Space-Science Institute, University of Maryland, College Park, MD 20742, USA

<sup>6</sup>Department of Astronomy, University of Maryland, College Park, MD 20742, USA

<sup>7</sup>Astrophysics Science Division, NASA Goddard Space Flight Center, Mail Code 661,  
Greenbelt, MD 20771, USA

<sup>8</sup>Department of Astronomy, University of California, Berkeley, CA 94720-3411, USA

<sup>9</sup>Department of Particle Physics and Astrophysics, Weizmann Institute of Science, 234  
Herzl St, 76100 Rehovot, Israel

<sup>10</sup>IPAC, California Institute of Technology, 1200 E. California Blvd, Pasadena, CA 91125,  
USA

<sup>11</sup>MIT-Kavli Institute for Astrophysics and Space Research, 77 Massachusetts Ave.,  
Cambridge, MA 02139, USA

<sup>12</sup>Caltech Optical Observatories, California Institute of Technology, Pasadena, CA 91125,  
USA

<sup>13</sup>Department of Astronomy, Cornell University, Ithaca, NY 14853, USA

<sup>14</sup>Department of Physics and Astronomy, Johns Hopkins University, 3400 North Charles Street, Baltimore, MD 21218, USA

<sup>15</sup>Instituto de Astrofísica de Canarias, E-38205 La Laguna, Tenerife, Spain

<sup>16</sup>Departamento de Astrofísica, Universidad de La Laguna, E-38206 La Laguna, Tenerife, Spain

<sup>17</sup>Nordic Optical Telescope, Rambla José Ana Fernández Pérez 7, 38711, Breña Baja, Spain

<sup>18</sup>Department of Astronomy, The Ohio State University, 140 West 18th Avenue, Columbus, OH 43210, USA

<sup>19</sup>Department of Astronomy, University of Washington, Seattle, WA 98195, USA

<sup>20</sup>Berkeley Institute for Data Science, University of California, Berkeley

<sup>21</sup>Center for Gravitation, Cosmology, and Astrophysics, Department of Physics, University of Wisconsin, Milwaukee, WI 53201, USA

## Abstract

Luminous red novae (LRNe) are transients characterized by low luminosities and expansion velocities, and are associated with mergers or common-envelope ejections in stellar binaries. Intermediate-luminosity red transients (ILRTs) are an observationally similar class with unknown origins, but generally believed to either be electron-capture supernovae (ECSNe) in super-asymptotic giant branch (AGB) stars, or outbursts in dusty luminous blue variables (LBVs). In this paper, we present a systematic sample of 8 LRNe and 8 ILRTs detected as part of the Census of the Local Universe (CLU) experiment on the Zwicky Transient Facility (ZTF). The CLU experiment spectroscopically classifies ZTF transients associated with nearby ( $< 150$  Mpc) galaxies, achieving 80% completeness for  $m_r < 20$  mag. Using the ZTF-CLU sample, we derive the first systematic LRNe volumetric rate of  $7.8_{-3.7}^{+6.5} \times 10^{-5} \text{ Mpc}^{-3} \text{ yr}^{-1}$  in the luminosity range  $-16 \leq M_r \leq -11$  mag. We find that in this luminosity range, the LRN rate scales as  $dN/dL \propto L^{-2.5 \pm 0.3}$  — significantly steeper than the previously derived scaling of  $L^{-1.4 \pm 0.3}$  for lower-luminosity LRNe ( $M_V \geq -10$  mag). The steeper power law for LRNe at high luminosities is consistent with the massive merger rates predicted by binary population synthesis models. We find that the rates of the brightest LRNe ( $M_r \leq -13$  mag) are consistent with a significant fraction of them being progenitors of double compact objects (DCOs) that merge within a Hubble time. For ILRTs, we derive a volumetric rate of  $2.6_{-1.4}^{+1.8} \times 10^{-6} \text{ Mpc}^{-3} \text{ yr}^{-1}$  for  $M_r \leq -13.5$  mag, that scales as  $dN/dL \propto L^{-2.5 \pm 0.5}$ .

This rate is  $\sim$ 1–5% of the local core-collapse supernova rate, and is consistent with theoretical ECSN rate estimates.

## 8.1 Introduction

The advent of time-domain surveys in the last few decades has led to the discovery of “gap transients” — a new class of explosions that have  $-16 \leq M_V \leq -10$  mag and occupy the luminosity gap between novae and supernovae (SNe) (Kasliwal et al. 2011; Pastorello et al. 2019c). This class includes a diverse variety of transients such as faint core-collapse SNe (Yang et al. 2021), Ia-like SNe (Bildsten et al. 2007), low-luminosity Iax SNe (Karambelkar et al. 2021), luminous red novae (LRNe; Kulkarni et al. 2007), intermediate-luminosity red transients (ILRTs, Thompson et al. 2009), and outbursts in luminous blue variable (LBV) stars (Smith et al. 2011). Among gap transients, there is a subclass of hydrogen-rich explosions characterized by low expansion velocities and interaction with surrounding circumstellar material (CSM). This subclass comprises LRNe, ILRTs, and LBV outbursts.

LRNe are transients associated with the final stages of common-envelope evolution (CEE) in a stellar binary system (Ivanova et al. 2013b; Tylenda 2005; Pastorello et al. 2019a). The loss of angular momentum in a binary can initiate CEE that terminates with the inspiral of the binary on dynamical timescales. This can either lead to the merger of the two stars or the ejection of the CE and formation of a stable binary in a tighter orbit. Both cases are accompanied by energetic outbursts that are powered primarily by shocks or recombination in the ejected material (Ivanova et al. 2013b; MacLeod et al. 2017; Pejcha et al. 2017; Soker 2020; Soker et al. 2021; Matsumoto et al. 2022). The association of LRNe with CE-related outbursts was supported by the discovery of V 1309Sco, a Galactic LRN with archival photometric data showing a binary with a rapidly decaying orbital period in the years leading to the transient (Tylenda et al. 2011a). LRNe thus present an opportunity to probe the poorly understood physics of CEE; see Ivanova et al. (2013a). This is of particular importance because CEE is a crucial phase in the formation of double compact objects (DCOs; Vigna-Gómez et al. 2020) that merge to radiate gravitational waves, which are being detected regularly by LIGO (The LIGO Scientific Collaboration et al. 2021a).

LRNe generally have low expansion velocities ( $< 1000 \text{ km s}^{-1}$ ), a wide range of luminosities ( $-3 < M_V < -16$  mag), and long-lasting ( $\sim 100$  days) multipeaked light curves that redden rapidly due to dust formation (Kamiński et al. 2011; Kamiński

et al. 2015). Prior to 2021, only 4 Galactic and 11 extragalactic LRNe were known (Kochanek et al. 2014; Blagorodnova et al. 2021, and references therein). The extragalactic LRNe have  $-9 \leq M_{\text{peak}} \leq -15$  mag, while the Galactic LRNe in general have much lower luminosities. Progenitor primary stars have been identified for 7 LRNe so far and have revealed interesting correlations between the masses and peak luminosities (Blagorodnova et al. 2021; Pastorello et al. 2019a). Despite these advances, the volumetric rates of LRNe are largely unconstrained. The best estimate of the rate comes from Kochanek et al. (2014), who used 3 Galactic LRNe that had  $-4 < M_V < -10$  mag discovered over the last 30 yr to determine their rate in the Milky Way. They find that very low-luminosity events ( $M_{r/V,\text{peak}} \approx -3$  mag) are fairly common ( $\sim 0.5 \text{ yr}^{-1}$ ), but the rate drops  $\propto L^{-1.4}$  with increasing luminosity. The rate of the more-luminous, extragalactic LRNe has not been measured yet, and extrapolations based on the Galactic rate disagree by orders of magnitude with the expectations from population synthesis (Howitt et al. 2020). An accurate measurement of the rate and luminosity function of LRNe is needed to probe several CEE parameters (see Howitt et al. 2020 for examples).

ILRTs are an observationally related class of transients that are also characterized by low expansion velocities and reddening photometric evolution, but have single-peaked light curves and a narrower luminosity range ( $-11 < M_V < -15$  mag) compared to LRNe (Cai et al. 2021). The origin of ILRTs still remains a mystery. They have been proposed to be electron-capture SNe (ECSNe) in super-asymptotic giant branch (AGB) stars (Botticella et al. 2009; Cai et al. 2021) or eruptions of massive luminous blue variable (LBV) stars<sup>1</sup>. Both explanations are supported by the peculiar progenitors of ILRTs. The ILRTs SN 2008S, NGC 300 OT, and AT 2019abn have been associated with extremely dusty, infrared (IR)-bright progenitors (Botticella et al. 2009; Prieto et al. 2008; Jencson et al. 2019a) consistent with super-AGB stars, while the proposed ILRT AT 2019krl was associated with a blue supergiant or LBV progenitor (Andrews et al. 2021). About a dozen ILRTs have been studied extensively in the last decade (see Cai et al. 2021 and references therein). Similar to LRNe, the volumetric rate has not been reliably measured. Based on two ILRTs (SN 2008S and NGC 300 OT), Thompson et al. (2009) estimate the ILRT rate to be  $\sim 20\%$  of the core-collapse SN (CCSN) rate. Cai et al. (2021) use a sample of 5 ILRTs reported by different surveys over the last decade and estimate a lower limit of  $\sim 8\%$  of the CCSN rate.

---

<sup>1</sup>ILRTs are also proposed to be failed supernovae in massive stars (Tsuna et al. 2020), but this model does not have strong evidence supporting it yet.

Reliable LRN and ILRT rate measurements have been hindered by their heterogeneous sample. The existing rate estimates have used transients reported by different surveys, and have not accounted for effects of survey completeness or selection biases (Kochanek et al. 2014; Cai et al. 2021). A systematic sample of LRNe and ILRTs, preferably from a single survey, is required to accurately constrain their rate. Such studies are now possible with experiments like the Census of the Local Universe (CLU; De et al. 2020c) on the Zwicky Transient Facility (ZTF; Bellm et al. 2019a; Graham et al. 2019; Dekany et al. 2020). ZTF is an optical time-domain survey with a 47 sq. deg field of view that surveys the entire accessible northern sky at a cadence of  $\sim$ 2–3 days in the  $g$  and  $r$  bands down to a depth of 20.5 mag. The CLU experiment aims to build a spectroscopically complete sample of transients detected by ZTF that are associated with galaxies in the CLU galaxy catalog (Cook et al. 2019) to a depth of  $m_r \approx 20$  mag. The CLU experiment is ideal for detecting low-luminosity ( $M_r \leq -16$  mag) transients like LRNe and ILRTs out to large distances ( $\sim$ 100 Mpc), consequently building a large sample of such rare transients.

In this paper, we present a systematic sample of LRNe and ILRTs detected by the ZTF CLU experiment from 2018 June 1 to 2022 February 20<sup>2</sup>. We utilize this sample and the actual observation history of ZTF to derive the rates of LRNe and ILRTs. In Sec. 8.2, we describe the selection criteria used to construct our LRN and ILRT samples. Sec. 8.2 also discusses the photometric and spectroscopic properties of LRNe and ILRTs identified in the CLU experiment. Our methods for deriving the luminosity function and volumetric rates of LRNe and ILRTs are described in Sec. 8.3. Sec. 8.4 compares our results to previous measurements and theoretical predictions, and discusses the implications for progenitors of LRNe and ILRTs. We conclude with a summary of our results in Sec. 8.5.

## 8.2 Sample Selection

### Candidate Filtering

We focus our search on transients discovered as part of the ZTF CLU experiment (De et al. 2020c). Briefly, CLU aims to build a spectroscopically complete sample of transients associated with galaxies in the local universe ( $< 200$  Mpc). The CLU experiment uses alerts generated from all three (public, collaboration, and Caltech) components of the ZTF survey (see De et al. 2020c for details). CLU uses the platform `skyportal` to save and coordinate follow-up observations of sources (Walt et al. 2019a). During ZTF Phase I (2018 June 01 – 2020 October 30), the experiment

---

<sup>2</sup>UTC dates are used throughout this paper.

Table 8.1: Properties of the 34 ZTF transients of interest

ZTF Name	AT Name	$M_{\text{abs}}$ at peak	multippeak/ plateau	Archival (PTF/ATLAS)	Gal type <sup>a</sup>	$\text{H}\alpha$ -FWHM <sup>b</sup> [km s <sup>-1</sup> ]	[Ca II]	Mol. feats.	Classification
ZTF18acbwfza*	18hs0	$-13.82 \pm 0.15$	mp	–/no	SB(r)a pec	500	em?	yes <sup>c</sup>	LRN-gold
ZTF19adakuot	19zhd	$-9.60 \pm 0.15$	pl	no/yes	SA(s)b			yes <sup>c</sup>	LRN-gold
ZTF20aawdwch*	20hat	$-11.43 \pm 0.15$	pl	no/no	SAB(rs)cd	130	no	yes	LRN-gold
ZTF21aancgbm*	21biy	$-13.86 \pm 0.15$	mp	yes/no	SB(s)d.	500	em?	yes	LRN-gold
ZTF21aagppze*	21blu	$-13.50 \pm 0.15$	mp	no/no	starforming	500	no	yes	LRN-gold
ZTF21acpkzcc*	21aess	$-15.12 \pm 0.15$	mp	–/no	SB(s)m?	500	no	–	LRN-gold
ZTF18abwxrhi*	18gzz	$-14.50 \pm 0.16$	mp	no/no	(R')SB(rs)ab	300	no	no	LRN-silver
ZTF21aaekeqd*	21afy	$-13.95 \pm 0.16$	pl	–/no	starforming	700	no	no	LRN-silver
ZTF18aaajgqmr	20ifb	$-15.36 \pm 0.17$	mp	–/no	starforming				LRN-bronze
ZTF20abjgdec	20afdb	$-14.37 \pm 0.16$	mp	–/no	starforming				LRN-bronze
ZTF21aabfwwl	21iy	$-15.72 \pm 0.16$	mp	–/no	starforming				LRN-bronze
ZTF18acdyopn	18hcj	$-14.33 \pm 0.19$	no	–/no	SAdm.	300	em	no	ILRT-gold
ZTF19aadyppr*	19abn	$-14.73 \pm 0.15$	no	yes/no.	Sa	700	em	no	ILRT-gold
ZTF19acoaiub*	19udc	$-14.62 \pm 0.15$	no	–/no	SAB(s)a	1250	em	no	ILRT-gold
ZTF19acdrkbh	19sfo	$-14.62 \pm 0.20$	–	–/no	starforming	600	em	no	ILRT-gold
ZTF19aagqkrq*	19ahd	$-13.72 \pm 0.15$	no	–/no.	SA(s)cd	700	em	no	ILRT-gold
ZTF21aclzzex*	21adlx	$-15.68 \pm 0.16$	no	yes/no	Sb	700	em	no	<b>ILRT-gold</b>
ZTF21abtduh*	21vdr	$< -14.96$	–	no/no	SB(s)d:	1300	no	no	ILRT-silver
ZTF21abfxjld	21prj	$< -14.21$	–	no/no.	starforming	< 300	no	no	ILRT-silver
ZTF18acrygkg	18lqq	$< -14.14$	no	–/no	SA(s)bc				ILRT-bronze
ZTF19aavwbxs	19fxy	$-14.44 \pm 0.17$	no	–/no	starforming				ILRT-bronze
ZTF19acpmvbd	19wbg	$-14.66 \pm 0.15$	mp	yes/yes	SAB(r)a	1700			LBV?
ZTF20abwilhb	20swt	$-13.87 \pm 0.16$	no.	no/no	Scd	3300	no	no	LBV/Type II?
ZTF21aagydmn	21bug	$-14.36 \pm 0.15$	no	yes/no	SAd	2600	no	no	LBV?
ZTF21aantupk	21efb	$-14.71 \pm 0.15$	no	–/yes	–				LBV/AGN?
ZTF21aclyyfm	21adlw	$-16.03 \pm 0.15$	no	–/yes	SA(rs)b		no	no	LBV?
ZTF21aaitlhy	21afm	$-15.44 \pm 0.15$	mp	yes/yes	SBb				LBV?
ZTF18aawoeho	21ahuh	$-15.51 \pm 0.15$	no	no/no	starburst				?
ZTF20ablmyzj	20afdc	$-15.95 \pm 0.30$	no	–/no	S				?
ZTF20acfxfnmv	20afdd	$-14.67 \pm 0.15$	–	–/no	SB(s)cd				?
ZTF20acivtfy	20afde	$-13.72 \pm 0.16$	–	–/no	starforming				?
ZTF21aapngrj	21gcg	$-12.75 \pm 0.15$	no	–/no					?
ZTF21aakbdzz	21czz	$-14.83 \pm 0.10$	no	–/no	S				?
ZTF21aamwyxf	21dtz	$-15.98 \pm 0.15$	no	no/no	E				?

– or unfilled entries indicate instances for which data are not available.

\*: Events used for rate calculation, in Sec. 8.3; *a*: Galaxy morphologies are taken from NED. *b*: Where multiple spectra are available, the maximum FWHM is reported. *c*: The molecular features are visible in spectra from the literature (see Sec. 8.2).

was limited to all transients that (1) were within  $100''$  of known galaxies in the CLU galaxy catalog (Cook et al. 2019), (2) had more than two detections in ZTF- $g$  or  $r$  filters, and (3) were brighter than  $m_r = 20$  mag. Starting 2020 October 30 (ZTF Phase II), the filtering criteria were updated to select transients that were (1) within 30 kpc of CLU galaxies closer than 140 Mpc, (2) brighter than  $m_r = 20.5$  mag, and (3) less luminous than  $M_r = -17$  mag. A total of 3442 transients were saved by the CLU experiment since the start of the ZTF survey. The experiment achieved a spectroscopic completeness of 88.5% in ZTF Phase I and 79% in ZTF Phase II for sources brighter than 20 mag.

Candidate LRNe and ILRTs were selected from their real-time ZTF alert photometry using the following selection criteria:

- the transient must pass the CLU selection criteria,
- the transient must be less luminous than  $M_r = -16$  mag, and
- the transient must have two ZTF alerts (i.e., two  $> 5\sigma$  detections) brighter than 20 mag in either  $g$  or  $r$ .

The sample presented in this paper is restricted to events saved before 2022 February 20.

523 transients satisfied the selection criteria listed above. 109 of these were found to lie on top of faint underlying galaxies that are not present in the CLU catalog. These transients were excluded as they are likely SNe in distant host galaxies. 55 additional candidates were excluded because they were flagged as image-processing artifacts on visual inspection of the difference images. 73 candidates were eliminated because they showed small, long-term ( $> 1$  yr) variations in brightness without significant color changes, and were coincident with stars in the Milky Way or nearby galaxies (M31 or M33).

To further filter our candidates, we used follow-up spectroscopic observations (either from our own follow-up campaigns or on TNS). In addition to the CLU experiment, some of our spectra were collected as part of the ZTF Bright Transient Survey (BTS; Fremling et al. 2020; Perley et al. 2020). The BTS classifications are already public, while all CLU classifications will be presented in separate papers focusing on different subsamples (e.g., De et al. 2020c; Tzanidakis et al., in prep.; Sit et al., submitted). Of the CLU transients that pass our criteria, seven sources

were spectroscopically classified [based on the presence or absence of broad ( $v \geq 5000 \text{ km s}^{-1}$ ) H emission lines, and other characteristics] as active galactic nuclei (AGNs), 65 as hydrogen-poor SNe (Ia, Iax, Ca-rich, Ib, and Ic SNe), 11 as classical novae, 128 as Type II SNe. Two additional candidates were studied in detail (Reguitti et al. 2021; Yang et al. 2021) as low-luminosity Type II SNe showing low-velocity H lines. We were now left with 73 sources that did not match any of the above categories.

We ran forced point-spread-function (PSF) photometry at the location of these 73 sources on all ZTF difference images (Masci et al. 2019). This provides more-accurate photometry than the real-time ZTF alerts, and also enables the recovery of subthreshold ( $> 3\sigma$ ) detections. From this set, 14 candidates were ruled out as their forced photometry revealed them to have absolute magnitudes brighter than  $-16$ . 18 additional sources were eliminated because their forced-photometry light curves revealed slow, small-amplitude, long-term ( $> 500$  days) variations. These slowly varying sources are likely foreground variable stars, but some could also be long duration giant outbursts in LBV stars such as  $\eta$  Car or UGC 2773-OT (Humphreys et al. 1999; Smith et al. 2016). One additional source at redshift  $z = 0.002$  showed fast, erratic variations in ZTF data. Finally, five sources had  $M_r \geq -10$  mag and rapidly fading light curves ( $< 10$  d), suggesting that they are classical novae. Of the remaining sources, one showed a declining light curve with  $g - r < 0$  mag, similar to late-time SN light curves but unlike LRNe or ILRTs. The remaining 34 sources are promising LRN and ILRT candidates, and are listed in Table 8.1.

## Classification

The list of 34 transients in Table 8.1 consists of LRNe, ILRTs, LBV outbursts, and possibly some SNe observed at late phases. Here, we discuss the classifications of these transients using their ZTF light curves, spectroscopic data, and archival photometry.

LRNe typically exhibit multipeaked light curves (Pejcha et al. 2017; Matsumoto et al. 2022) which allow them to be photometrically differentiated from ILRTs (Cai et al. 2021). Table 8.1 indicates the transients that show multiple peaks in their ZTF light curves.

Searching for previous outbursts in archival data can help distinguish LBV eruptions from LRNe/ILRTs, as LBV outbursts can be recurring. While LRNe are also known to show precursor emission in the years leading up to the merger, the precursors

usually have much lower luminosities than the actual merger. The detection of historic outbursts comparable in brightness to the latest outburst is thus suggestive of an LBV eruption. We checked for historical activity at the locations of these sources using data from the ATLAS (Tonry et al. 2018; Smith et al. 2020a, depth  $\sim 19.5$  mag, dating back to  $\sim 2014$ ) and PTF (Law et al. 2009; Rau et al. 2009, depth  $\sim 21.5$  mag, dating back to  $\sim 2009$ ) surveys. All 34 sources have ATLAS data while 15 have PTF data. Table 8.1 indicates which transients were detected in the archival ATLAS or PTF data. The full forced-photometry light curves will be available online (see Sec. 8.7).

Spectroscopic data is available for 19 of the 34 transients. The low spectroscopic completeness of this sample compared to the full CLU experiment is discussed in Sec. 8.3. 11 of these sources only have medium-resolution optical spectra, while the remaining 8 also have medium-resolution near-infrared (NIR) spectra. The optical spectra were taken with the Low-Resolution Imaging Spectrograph (LRIS; Oke et al. 1995, resolution  $R \approx 750$ ) on the Keck I 10 m telescope, the Double Beam Spectrograph (DBSP; Oke et al. 1982,  $R \approx 1000$ ) on the 200-inch Hale telescope (P200) on Mount Palomar, the Alhambra Faint Object Spectrograph and Camera (ALFOSC;  $R \approx 360$ ) on the 2.56 m Nordic Optical Telescope (NOT), the Kast Double Spectrograph on the Shane 3 m telescope at Lick Observatory ( $R \approx 1000$ ), and the Spectrograph for Rapid Acquisition of Transients (SPRAT;  $R \approx 350$ ) on the Liverpool Telescope. For ZTF 21acpkzcc, we obtained a high-resolution ( $R \approx 15,000$ ) spectrum with the South African Large Telescope High Resolution Spectrograph (HRS; Bramall et al. 2010). The NIR spectra were taken with the Near-Infrared Echelle Spectrograph (NIRES; Wilson et al. 2004;  $R \approx 2700$ ) on the Keck II 10 m telescope and the Triplespec spectrograph (Herter et al. 2008;  $R \approx 2500$ ) on P200. The log of the spectroscopic observations is listed in Table 8.2. In addition to these, we obtained several low-resolution ( $R \approx 100$ ) spectra with the Spectral Energy Distribution Machine (SEDM; Blagorodnova et al. 2018; Rigault et al. 2019; Kim et al. 2022) on the 60-inch telescope at Palomar Observatory. These spectra are not discussed here as their resolution is too low for a useful analysis. All of our spectra (including those having low resolution) will be made available online (Sec. 8.7).

LRNe, ILRTs, and LBV outbursts can have similar spectroscopic properties, especially at early times. However, some LBV eruptions have expansion velocities exceeding  $\sim 2000 \text{ km s}^{-1}$ , while LRNe and ILRTs have lower expansion velocities

Table 8.2: Observation log of spectra presented in this paper

Name	Tel./ Inst.	Date	Resolution	Name	Tel./ Inst.	Date	Resolution
ZTF18abwxrhi	P200/DBSP	2018-09-18	1500	ZTF21aancgbm	Keck/NIRES	2021-04-18	1000
ZTF18abwxrhi	P200/DBSP	2018-10-10	1000	ZTF21aagppzg	Keck/NIRES	2021-04-18	1000
ZTF18acbwfza	Gemini/GMOS	2018-11-02	2000	ZTF21aaekeqd	Keck/LRIS	2021-05-09	750
ZTF18acbwfza	P200/DBSP	2018-11-02	1000	ZTF21abfxjld	Keck/LRIS	2021-07-06	750
ZTF18acbwfza	Keck/LRIS	2018-11-10	750	ZTF21abfxjld	Keck/LRIS	2021-08-14	750
ZTF18acdyopn	Keck/LRIS	2018-11-10	750	ZTF21abfxjld	Keck/NIRES	2021-09-25	1000
ZTF19aadypypr	P200/DBSP	2019-01-26	1000	ZTF21abtduah	P200/DBSP	2021-11-06	1000
ZTF19aagqkrq	NOT/ALFOSC	2019-02-11	350	ZTF21aclyyfm	P200/DBSP	2021-11-06	1000
ZTF19aagqkrq	P200/DBSP	2019-02-12	1000	ZTF21aclzzex	Shane/KAST	2021-11-12	1000
ZTF19aadypypr	NOT/ALFOSC	2019-02-23	350	ZTF21acpkzcc	Keck/NIRES	2021-11-17	1000
ZTF19aadypypr	Keck/LRIS	2019-03-07	750	ZTF21acpkzcc	SALT/HRS	2021-11-29	15000
ZTF19aadypypr	P200/DBSP	2019-03-16	1000	ZTF21acpkzcc	P200/DBSP	2021-12-01	1000
ZTF19aadypypr	P200/DBSP	2019-04-13	1000	ZTF21abtduah	P200/DBSP	2021-12-01	1000
ZTF19aadypypr	P200/DBSP	2019-05-13	1000	ZTF21aclzzex	P200/DBSP	2021-12-01	1000
ZTF19acdrkbh	Keck/LRIS	2019-10-27	750	ZTF21aagppzg	P200/TSpec	2021-12-12	1000
ZTF19acoaiub	P200/DBSP	2019-11-05	1000	ZTF21acpkzcc	P200/DBSP	2022-01-12	1000
ZTF19acoaiub	Keck/NIRES	2019-12-04	1000	ZTF21acpkzcc	P200/TSpec	2022-01-20	1000
ZTF19acpmbvd	LT/SPRAT	2019-12-23	350	ZTF21aclzzex	Keck/LRIS	2022-01-26	750
ZTF20aawdwch	NOT/ALFOSC	2020-05-15	300	ZTF21aclyyfm	P200/DBSP	2022-02-02	1000
ZTF20abwilhb	Keck/LRIS	2020-10-20	750	ZTF21aancgbm	Keck/LRIS	2022-02-03	750
ZTF21aagppzg	P200/DBSP	2021-02-08	1000	ZTF21acpkzcc	Keck/LRIS	2022-02-03	750
ZTF21aaekeqd	Keck/LRIS	2021-02-17	750	ZTF21abtduah	Keck/LRIS	2022-02-03	750
ZTF21aagppzg	P200/DBSP	2021-02-20	1000	ZTF21aclzzex	Keck/LRIS	2022-03-01	750
ZTF21aagydmn	P200/DBSP	2021-02-20	1000	ZTF21abtduah	Keck/LRIS	2022-03-03	750
ZTF21aagppzg	LT/SPRAT	2021-03-19	350	ZTF21aclzzex	Keck/LRIS	2022-03-03	750
ZTF21aancgbm	P200/DBSP	2021-04-09	1000	ZTF21aagppzg	Keck/NIRES	2022-03-16	1000
ZTF21aagppzg	P200/DBSP	2021-04-09	1000	ZTF21aancgbm	Keck/NIRES	2022-03-17	1000
ZTF21aaekeqd	Keck/LRIS	2021-04-14	750	ZTF21aclzzex	Keck/NIRES	2022-03-17	1000
ZTF21aaekeqd	Keck/NIRES	2021-04-18	1000	ZTF21aclzzex	Keck/NIRES	2022-04-15	1000

(typically  $\sim 1000 \text{ km s}^{-1}$ ). The full width at half-maximum intensity (FWHM) velocities of the H $\alpha$  emission line in the transients with spectroscopic coverage are listed in Table 8.1. For transients with multiple spectra, the maximum velocity is listed. Early-time spectra of both LRNe and ILRTs are characterized by narrow H $\alpha$  ( $v_{\text{FWHM}} \leq 1000 \text{ km s}^{-1}$ ) emission. [Ca II] emission was thought to be a defining feature of ILRTs; however, it was recently discovered that some LRNe can show [Ca II] emission (Cai et al. 2019), while some ILRTs do not exhibit [Ca II] at certain phases (Andrews et al. 2021). Late-time spectroscopic observations can help confidently distinguish between LRNe and ILRTs. In LRNe, H $\alpha$  emission grows narrower and weaker with time since peak brightness, disappears, and eventually reemerges (Blagorodnova et al. 2020). Late-time spectra of LRNe also exhibit molecular absorption features. On the contrary, ILRTs have persistent narrow H emission throughout their evolution. Their late-time spectra do not show molecular features, but have strong H $\alpha$  and Ca II emission lines.

Provided that not all of our sources have late-time spectroscopic coverage, we use

the available spectra (from the literature wherever necessary) together with the light curves to create a classification scheme for these transients. We classify the 34 transients into eight categories: Possible LBV outbursts, LRN-gold, LRN-silver, LRN-bronze, ILRT-gold, ILRT-silver, ILRT-bronze, and Ambiguous. We describe these categories in detail below. Briefly, for LRNe and ILRTs, the gold sample comprises transients that we can confidently classify in either category, the silver sample comprises transients that have photometry and spectra indicative of their class but lack smoking-gun signatures associated with the class, and the bronze category comprises transients that have photometric evolution similar to their class but do not have any spectroscopic data. The “Ambiguous” category consists of 7 sources that have poor-quality data (no spectra *and* low-quality sparse photometric coverage owing to bad weather or solar conjunction of the transient), rendering us unable to place them in any of the other categories. Table 8.1 lists the classification of these sources based on this scheme. We describe the sources in each category below.

### Possible LBV Eruptions

This category includes sources that show broad ( $v_{\text{FWHM}} \geq 2000 \text{ km s}^{-1}$ ) H $\alpha$  emission in their spectra, *or* have historic outbursts in archival data. A total of 6 transients in our short list satisfy these criteria. Two of these (ZTF 21aagydmn and ZTF 20abwilhb) show broad H $\alpha$  emission with FWHM velocities of 2600 and 3300 km s $^{-1}$  and are likely LBV outbursts. The ATLAS and PTF data classify four additional sources as potential LBVs (ZTF 19acpmbvd, ZTF 21aantupk, ZTF 21aclyyfm, and ZTF 21aaithy). We describe these sources in the Appendix 8.8.

### LRN-gold

This category includes six spectroscopically confirmed LRNe detected in ZTF data in the last three years. Three of these have been studied in detail previously — ZTF 18acbwfza (AT 2018hso; Cai et al. 2019), ZTF 19adakuot (AT 2019zhd; Pastorello et al. 2021a), and ZTF 20aawdwch (AT 2020hat; Pastorello et al. 2021b). Three other transients — ZTF 21aancgbm (AT 2021biy; Cai et al. 2022), ZTF 21aagppzg (AT 2021blu; Pastorello et al. 2022), and ZTF 21acpkzcc (AT 2021aess; Davis et al. 2021) were identified as possible LRNe in 2021. We initiated optical and NIR photometric and spectroscopic follow-up campaign for these objects, which confirmed

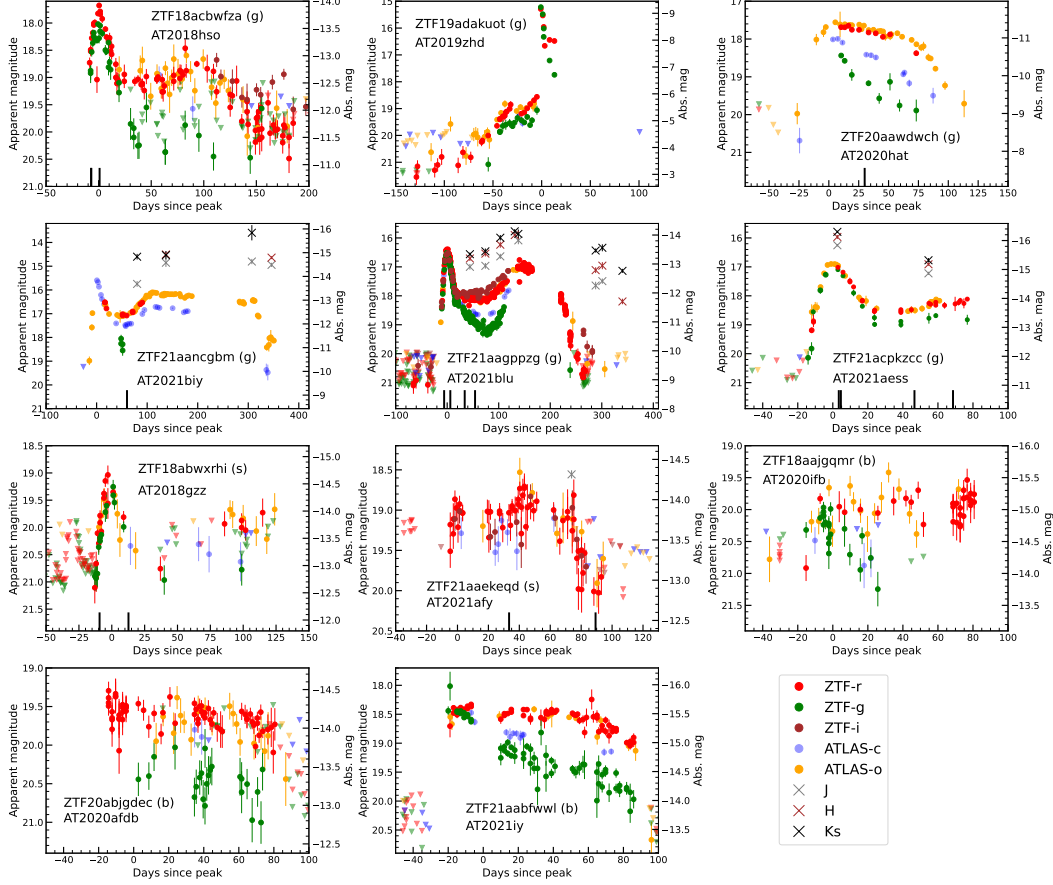


**Figure 8.1: Forced-photometry light curves of the 11 LRNe in our sample.** The transients in the gold, silver, and bronze samples are marked in parentheses with “g,” “s,” and “b”, respectively. The ZTF-*g*, ZTF-*r*, ZTF-*i*, ATLAS-*c*, and ATLAS-*o* data are plotted as green, red, brown, blue, and orange points, respectively. The *J*, *H*, and *K<sub>s</sub>* magnitudes are plotted as gray, brown, and black crosses, respectively. Downward-pointing triangles indicate  $5\sigma$  upper limits. Days are in the observer frame. The light curves have been corrected for extinction using the values listed in Table 8.3. Solid black vertical lines indicate epochs at which spectra were obtained.

their nature as LRNe.

Our light curves of these transients are shown in Fig. 8.1. For all our calculations, we use host-galaxy redshifts corrected for local velocity flows from the NASA Extragalactic Database (NED), and assume  $H_0 = 73 \text{ km s}^{-1} \text{ Mpc}^{-1}$ . We use Milky Way line-of-sight extinction values from Schlafly et al. (2012). Host-galaxy extinctions for LRNe are calculated using Na I D equivalent widths in their early-time spectra (see discussion of individual objects below). We calculate the peak magnitudes and epoch of maximum brightness by fitting polynomials to the near-peak light curve.

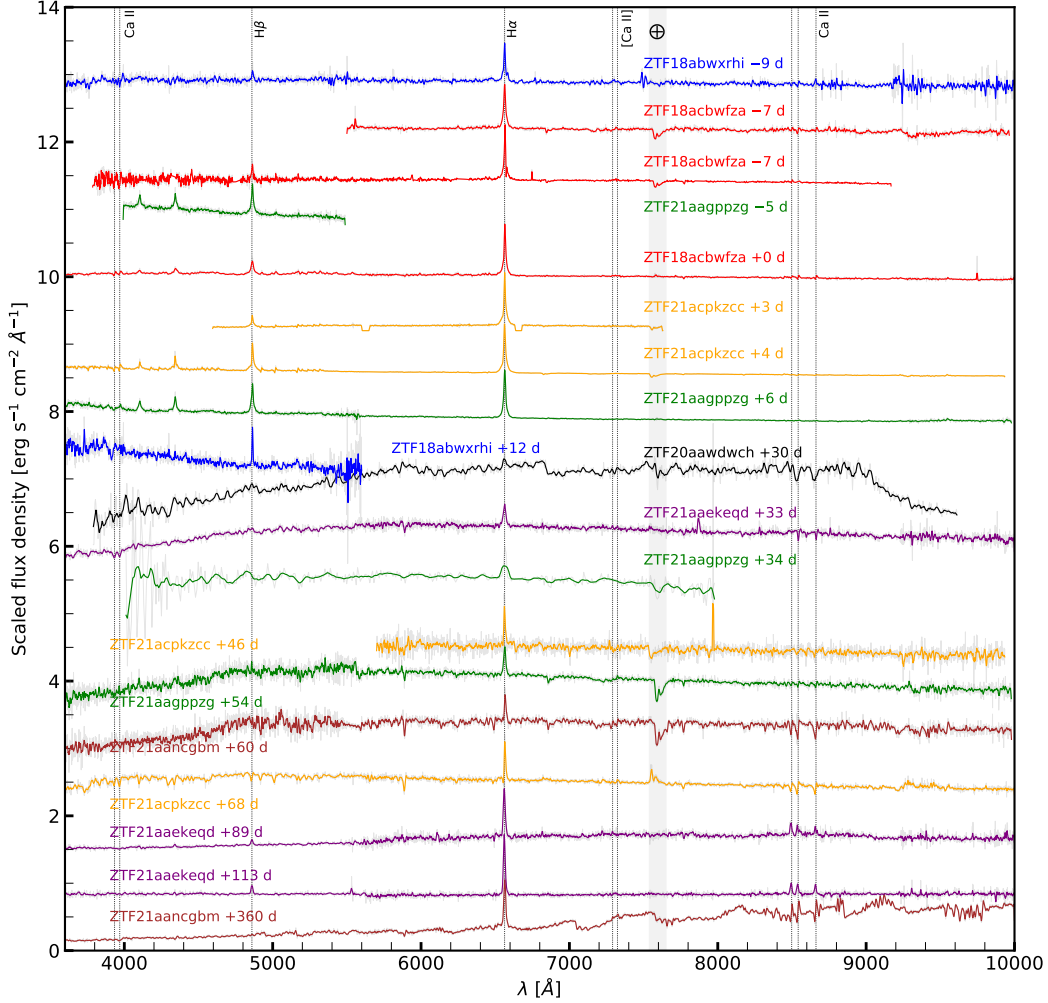


**Figure 8.2: Optical spectra of LRNe presented in this paper.** In plots of spectra throughout, we indicate the locations of telluric features with an “Earth” symbol.

We calculate the pseudobolometric light curves by fitting blackbodies to the available optical data. The derived photometric properties and the adopted distances and extinctions for the LRNe in our sample are listed in Table 8.3.

Our spectra of these transients are shown in Fig. 8.2 and 8.3. We analyze the optical spectra and derive the hydrogen Balmer line velocities by fitting Lorentzian profiles (which are better fits than Gaussian profiles) and corrected the velocities for instrumental broadening. We also measure the Balmer decrement ( $\beta$ ) as the ratio of H $\alpha$  to H $\beta$  line fluxes in the spectra where both lines are detected. The spectroscopic properties are listed in Table 8.4. We now briefly describe individual members of our sample.

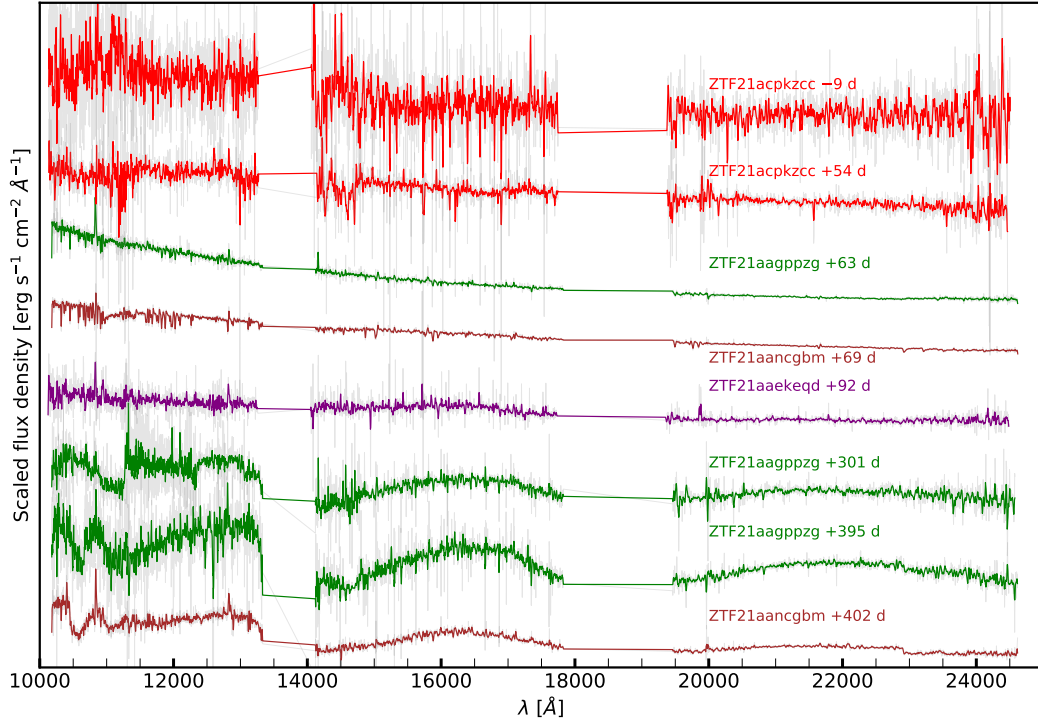


Figure 8.3: NIR spectra of LRNe presented in this paper.

**1. ZTF 18acbwfza (AT 2018hs0)** is located in the star-forming galaxy NGC 3729. Our earliest spectrum (7 days before peak brightness) shows Na I D absorption with an equivalent width of  $1.5 \pm 0.4 \text{ \AA}$ . Assuming this gas is associated with dust in the interstellar medium and using the correlation from Turatto et al. (2003), we derive  $E(B - V)_{\text{host}} = 0.23 \pm 0.06 \text{ mag}$ . This is consistent with the value used by Cai et al. (2019). The light curve is characteristic of LRNe, with an early blue peak lasting for  $\sim 20$  days, followed by a prolonged plateau where the transient evolves rapidly to redder colors. We note that the transient shows signs of evolving back to bluer colors at late times, when the  $r$ -band light curve is declining but the  $g$ -band light curve has plateaued. However, we caution that the  $g$ -band detections at this phase from ZTF have low significance ( $3\sigma$ ). Our spectra sample only the first blue peak, and show strong Balmer emission lines with  $v_{\text{FWHM}} \approx 500 \text{ km s}^{-1}$ . These spectra also exhibit narrow Ca II NIR triplet lines with a P Cygni profile. The absorption of the P Cygni profile extends to a maximum velocity  $v_{\text{max}} \approx 400\text{--}500 \text{ km s}^{-1}$ . Cai et al. (2019) report weak [Ca II] in this transient. We find marginal evidence for [Ca II] emission in only one of our spectra, taken 1 day post peak. Late-time spectra from Cai et al. (2019) show strong molecular absorption features.

**2. ZTF 19adakuot (AT 2019zhd)** is located in M31. Following Pastorello et al. (2021a), we assume that the total extinction is dominated by the Milky Way. The transient has the lowest luminosity in our sample (peaking at  $M_r \approx -9.5$  mag). We do not have any spectroscopic data for this transient, but late-time spectra presented by Pastorello et al. (2021a) show molecular absorption features.

As noted by Pastorello et al. (2021a), this transient shows precursor activity for a few months leading up to the explosion. In these months, the field of ZTF 19adakuot was imaged with the ZTF camera several times per night. We stack the ZTF forced photometry from images taken on the same night, and recover several additional detections than the ones reported by Pastorello et al. (2021a), which are plotted in Fig. 8.4. We further bin the photometry in bins of ten days to increase the significance of the detections. The ZTF detections date back to 160 days before the  $r$ -band peak, when the transient was first detected at  $m_r \approx 22.7 \pm 0.3$  mag. The binned ZTF light curve shows that the transient went through a gradual, bumpy brightening phase for  $\sim 160$  days before the main explosion. Three bumps can be identified in the  $r$ -band light curve, each with a duration of  $\sim 50$  days. During each of these bumps, the transient brightens by an increasing amount ( $\sim 0.5$ , 1, and 2.5 mag, respectively) before plateauing or declining by a modest amount ( $\sim 0.5$  mag) at the end of each bump. After the third bump, the transient brightens gradually by  $\sim 1$  mag for 25 days before brightening rapidly by 4 mag as it transitions into the main explosion. This bumpy rise is reminiscent of the pre-outburst evolution of M31-LRN-2015 (Blagorodnova et al. 2020), V838 Mon (Munari et al. 2002; Tylenda 2005), and AT 2020hat (Pastorello et al. 2019b).

At the end of the first bump (MJD 58759), fitting a single blackbody to the  $g$  and  $r$  detections suggests a source with  $T_{\text{eff}} = 6600^{+2400}_{-1600}$  K, a radius  $R = 17^{+14}_{-7}$   $R_{\odot}$ , and a luminosity of  $5.5^{+1.3}_{-0.7} \times 10^2 L_{\odot}$ . This photosphere is most likely formed by mass outflowing from the outer Lagrangian (L2) point (for example, Pejcha et al. 2017 or MacLeod et al. 2022). On the second bump, the transient is only detected in  $r$ , with the most constraining  $g$ -band upper limit giving  $g - r > 0.8$  mag, suggesting that the optically thick photosphere has cooled. This likely continues up to the beginning of the third bump on MJD 58837, where the temperature has cooled down to  $T = 3900^{+700}_{-700}$  K, the photosphere has expanded to  $R = 170^{+140}_{-70}$   $R_{\odot}$ , and  $L = 6.1^{+3.9}_{-1.7} \times 10^3 L_{\odot}$ . This would imply a photospheric expansion speed of  $\sim 10$ –30  $\text{km s}^{-1}$ . After this, the temperature increases quickly in the next 12 days on the third bump to  $5700^{+300}_{-300}$  K with  $L = 7.5^{+0.3}_{-0.3} \times 10^3 L_{\odot}$ , and reduced  $R = 90^{+12}_{-12}$   $R_{\odot}$ .

on MJD 58849, suggesting the temperature increase was accompanied by a drop in opacity. This is followed by a surprisingly sharp decline in the redder ( $r$ ,  $o$ ) bands but a slow brightening in  $g$ . During this decline, the temperature increases to  $6900^{+1100}_{-1000}$  K but the radius drops to  $69^{+27}_{-16}$   $R_{\odot}$  with an increased luminosity of  $9.5^{+0.8}_{-0.6} \times 10^3$   $L_{\odot}$  on MJD 58871. This is followed by an increase in luminosity and photospheric radius accompanied by a slight decrease in temperature, to  $L = 1.7^{+0.2}_{-0.1} \times 10^4$   $L_{\odot}$  on MJD 58887. In the next five days, the transient brightens rapidly to its peak luminosity of  $\sim 5.2 \times 10^5$   $L_{\odot}$ .

A full analysis of this complex precursor photometric evolution is outside the scope of this paper. A possible explanation for the abrupt temperature increases in this final phase is shocks owing to collisions within the L2 stream, as suggested by Pejcha et al. (2017). The total energy radiated during this  $\sim 40$  day duration is  $\sim 10^{44}$  erg. Assuming an L2 velocity of  $30 \text{ km s}^{-1}$ , the mass required in the L2 stream is  $\geq 10^{-2} M_{\odot}$ .

**3. ZTF20aawdwch (AT 2020hat)** is located in NGC 5068. We follow Pastorello et al. (2021b) and assume that the extinction is dominated by the Milky Way. The ZTF light curve samples the post-peak decline, starting at  $m_r = 17.90 \pm 0.06$  mag. Our sole spectrum was taken at a phase of 30 days since peak, which shows a reddened continuum, extremely weak H $\alpha$  emission, some broad but weak molecular absorption features, and Ca II NIR triplet absorption lines — characteristic of LRNe on the red plateau phase. Molecular absorption features are clearly detected in late-time spectra presented by Pastorello et al. (2021b).

**4. ZTF 21aancgbm (AT 2021biy, Smith et al. 2021a; Cai et al. 2022)** is located in the galaxy NGC 4631. We do not have spectra at early phases, so we adopt the host extinction derived by Cai et al. (2022) using Na I D absorption. The light curve is characteristic of LRNe, with an initial blue peak lasting for  $\sim 50$  days, followed by a rebrightening and a prolonged red plateau of  $\sim 350$  days. The field of ZTF 21aancgbm is not part of the regular 2-day cadence ZTF survey, so the ZTF data sample only a small portion of the light curve. We combine the ZTF data with ATLAS data, which shows that the light curve lasts for more than 400 days, and is the longest-duration LRN in our sample.

We obtained  $JHK_s$  NIR imaging with P200/WIRC on several epochs on the plateau, which shows that the transient was significantly brighter in the NIR bands (by  $> 1$  mag) than in the optical (see Fig. 8.1). The transient shows a late-time bump once it falls off the plateau, likely the result of collision with circumstellar matter (CSM) as

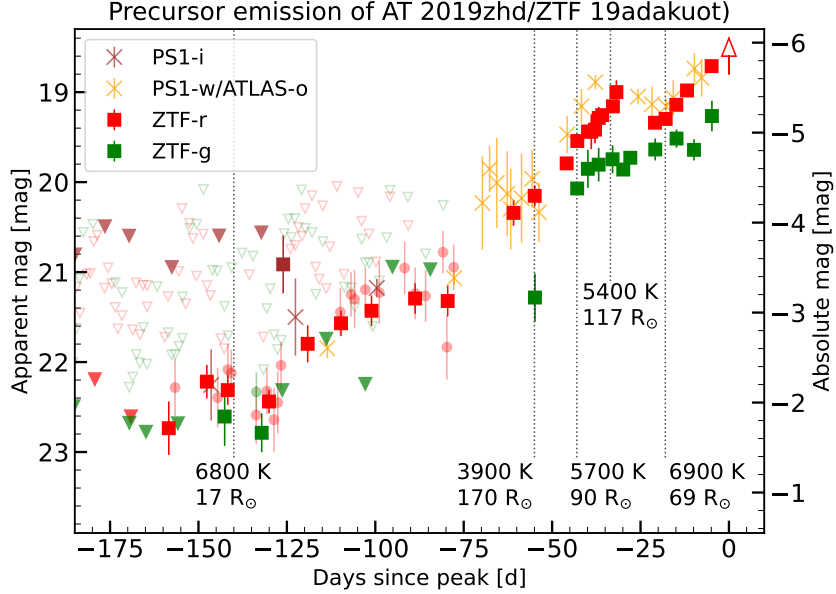


**Figure 8.4: Pre-explosion  $g$ ,  $r$ , and  $i$  detections for ZTF 19adakuot.** For phases  $< -75$  days, we bin the ZTF flux measurements taken on the same day to increase the sensitivity. These points are plotted as faint background circles. We further bin these measurements in bins of 10 days to increase their significance. The binned measurements are showed as solid squares. For phases  $> -75$  days, the squares represent ZTF forced photometry from single visits. The triangles denote  $5\sigma$  upper limits. The crosses show measurements reported previously by Pastorello et al. (2021a). At the epochs marked by the dotted vertical lines, we indicate the effective temperatures and photospheric radii to demonstrate the dramatic variations exhibited by the precursor (see text). The initial pre-explosion behavior is consistent with photosphere L2 mass loss forming an optically thick photosphere detectable by ZTF at  $\sim -150$  days, which expands and cools up to  $\sim -70$  days. Further collisions in the L2 stream or accretion onto the companion star can cause sudden increases in temperature over the next 70 days, until the transient brightens rapidly and transitions to the main explosion (marked by the red arrow).

noted by Cai et al. (2022). Our spectroscopic coverage comprises two optical spectra at +60 and +360 days since peak, and two NIR spectra at +69 and +402 days since peak. The +60 day spectrum shows a reddened continuum with weak, unresolved H $\alpha$  emission ( $v_{\text{FWHM}} \approx 350 \text{ km s}^{-1}$ ) and the Ca II NIR triplet with P Cygni line profiles ( $v_{\text{max}} \approx 400 \text{ km s}^{-1}$ ). We also detect weak [Ca II] lines with P Cygni line profiles. The +69 d NIR spectrum shows several metallic absorption lines, as well as the CO absorption bandhead. The very late-time optical spectrum at +360 days shows a highly reddened continuum with several strong molecular absorption features of TiO and VO, confirming the classification as an LRN. This spectrum also shows

strong, narrow H $\alpha$  emission (with increased  $v_{\text{FWHM}} \approx 500 \text{ km s}^{-1}$ ) and Ca II NIR lines with P Cygni profiles ( $v_{\text{max}} \approx 600 \text{ km s}^{-1}$ ).

The light-curve shape and long duration of ZTF 21aancgbm make it an interesting member of the LRN family. The 200 day plateau resembles that seen in SNe IIP, and it is tempting to posit that it is powered by hydrogen recombination. Matsumoto et al. (2022) provide scaling relations between the plateau luminosity ( $L_{\text{pl}}$ ), duration ( $t_{\text{pl}}$ ), and ejected mass ( $M_{\text{ej}}$ ) for a recombination-powered LRN plateau, given by

$$M_{\text{ej}} \approx 1.6 f_{\text{ad},0.3}^{-1} \left( \frac{t_{\text{pl}}}{100 \text{ d}} \right) \left( \frac{L_{\text{pl}}}{10^{39} \text{ erg/s}} \right) M_{\odot}, \quad (8.1)$$

where  $f_{\text{ad},0.3} \approx 1$  is a dimensionless factor quantifying inefficiencies in radiating the recombination energy. The plateau is defined as the duration between the point where the transient begins rebrightening after the first blue peak to the time when it falls off the plateau to the same brightness. We calculate an average plateau luminosity  $L_{\text{pl}} \approx 2.3 \times 10^{40} \text{ erg s}^{-1}$  and a plateau duration  $t_{\text{pl}} \approx 274 \text{ days}$ . This suggests a recombining ejecta mass of  $\sim 100 M_{\odot}$  for this LRN, implying an extremely massive progenitor. This seems unlikely, given that the correlation between peak luminosity and progenitor mass for LRNe (Blagorodnova et al. 2021) predicts the primary progenitor mass in the range  $\sim 10\text{--}50 M_{\odot}$ . Additionally, archival *Hubble Space Telescope (HST)* imaging Cai et al. (2019) suggests a progenitor mass of  $\sim 17\text{--}24 M_{\odot}$ . It is therefore very likely that the plateau luminosity is too high to be explained by H recombination alone. A plausible source of additional energy is shock interaction between the merger ejecta and pre-existing material around the binary that was ejected during the CE phase. Following Matsumoto et al. (2022), assuming that only the timescale but not the luminosity of the transient is set by H recombination, the required recombining ejected mass is

$$t_{\text{pl}} \approx 140 \rho_{i,-11}^{-1/3} \left( \frac{M_{\text{ej}}}{M_{\odot}} \right)^{1/3} \left( \frac{v_{\text{E}}}{300 \text{ km/s}} \right)^{-1} \text{ days}, \quad (8.2)$$

where  $v_{\text{E}}$  is the mean ejecta velocity and  $\rho_{i,-11} = \rho_i/10^{-11} \text{ g cm}^{-3} \approx 1$  and  $\rho_i$  is the characteristic density at which the recombination completes. We adopt  $v_{\text{E}} \approx 430 \text{ km s}^{-1}$  from Cai et al. (2022), which gives  $M_{\text{ej}} \approx 22 M_{\odot}$ . This value is larger than that derived by Cai et al. (2022) owing to the larger plateau duration that we have assumed. Assuming that this ejected mass runs into pre-existing matter ( $M_{\text{pre}} \ll M_{\text{ej}}$ ) with velocity  $v_{\text{pre}} \ll v_{\text{E}}$ , the generated shock luminosity can be written as (Matsumoto et al. 2022)

$$L_{\text{pl}}^{\text{sh}} \approx 7 \times 10^{39} \rho_{i,-11}^{-1/3} \left( \frac{M_{\text{pre}}}{0.1 M_{\text{ej}}} \right) \left( \frac{v_{\text{E}}}{300 \text{ km/s}} \right)^3 \left( \frac{M_{\text{ej}}}{M_{\odot}} \right)^{2/3} \text{ erg/s.} \quad (8.3)$$

The observed plateau luminosity can be explained by shock interactions from Eq. 8.2 and 8.3 if  $M_{\text{pre}} \approx 0.3 M_{\odot}$ . We note that the assumption  $M_{\text{pre}} \ll M_{\text{ej}}$  may not be valid, as the binary can lose a few solar masses prior to the LRN event (Blagorodnova et al. 2021). Nevertheless, these mass estimates demonstrate that strong CSM interaction can plausibly explain the high luminosities of this transient. Given the very late-time bump in the light curve of this LRN, it is not unreasonable to expect significant CSM around the binary, providing a plausible explanation for its plateau. The CSM interaction could also be in the form of collimated outflows interacting with previously ejected spherical shells, as suggested for some other LRNe by Soker et al. (2021) and Soker (2020).

**5. ZTF 21aagppzg (AT 2021blu, Smith et al. 2021b; Pastorello et al. 2022)** is located on the outskirts of the galaxy UGC 5829. It was first classified as an LBV outburst (Uno et al. 2021); however, our late-time NIR spectra show strong molecular absorption features, indicating that this is an LRN. We adopt the extinction to be dominated by the Milky Way, as our early-time optical spectra do not show any strong Na ID absorption lines.

The light curve is characteristic of LRNe and shows two pronounced peaks — an initial blue peak for  $\sim 50$  days, followed by a second red peak lasting  $\sim 200$  days. Unlike ZTF 21aancgbm, the second peak does not show a plateau but has a smooth rise and decline. The P200/WIRC NIR photometry indicates that ZTF 21aagppzg was also significantly brighter in the NIR than in the optical. Particularly at late times when the transient has faded below ZTF detection limits in  $r$  ( $> 21$  mag), it continues to be detected at  $\sim 17$  mag in the  $K$  band (see Fig. 8.1). We stack the ZTF forced photometry prior to the outburst in 5 day bins and recover some archival detections. The first detection in  $r$  is  $\sim 1040$  days prior to peak brightness with  $m_r = 22.3 \pm 0.2$  mag. The transient was detected again at four epochs in  $r$  and  $g$  between 400 and 300 days before peak, at roughly constant magnitudes of  $m_r = 22.4 \pm 0.3$  and  $m_g = 22.5 \pm 0.3$ . Finally, it is detected again 95 days before peak at  $m_r = 21.8 \pm 0.3$  mag, brightens to  $m_r = 20.9 \pm 0.2$  mag 65 days before peak, and fades back to  $m_r = 21.9 \pm 0.3$  mag at 27 days before peak. It is also detected in the  $i$  band during this time period, with  $m_i = 21.0 \pm 0.3$  mag.

Our spectroscopic coverage comprises four optical spectra at  $-5$ ,  $+6$ ,  $+34$ , and  $+54$  days since peak brightness and three NIR spectra at  $+63$ ,  $+301$ , and  $+395$  days since peak. The two early-time optical spectra are characterized by a hot blue continuum with strong Balmer emission lines. The  $\text{H}\alpha$  emission line has

$v_{\text{FWHM}} \approx 500\text{--}600 \text{ km s}^{-1}$ . The  $\text{H}\beta$  line profile appears to be a superposition of a broad component with a narrow component; however, our spectral resolution is not sufficient to distinguish between the two. These spectra do not show the Ca II NIR triplet lines. The third optical spectrum has lower resolution and a lower signal-to-noise ratio (S/N). It shows a reddened continuum, with  $\text{H}\alpha$  being the only prominent feature. The final optical spectrum was obtained two months post-peak and reveals a reddened continuum. The strength and velocity of the Balmer emission decreased, the  $\text{H}\alpha$  line developed a double-peaked profile, and  $\text{H}\beta$  is not detected. This spectrum also shows weak Ca II NIR triplet absorption lines, along with a forest of metallic absorption lines. The NIR spectrum at +63 days exhibits hydrogen emission lines with some metallic absorption lines. Our two final late-time NIR spectra show strong molecular absorption features of  $\text{TiO}$ ,  $\text{VO}$ , and  $\text{H}_2\text{O}$ .

Similar to ZTF 21aancgbm, we can use scaling relations to determine the ejecta masses. We estimate the median luminosity on the red plateau  $L_{\text{pl}} \approx 1.6 \times 10^{40} \text{ erg s}^{-1}$  and a plateau duration  $t_{\text{pl}} \approx 180 \text{ days}$ . Using  $v_{\text{E}} \approx 500 \text{ km s}^{-1}$  and Eq. 8.2 gives the recombining ejecta mass  $M_{\text{ej}} \approx 10 \text{ M}_{\odot}$ , although the estimate is very sensitive to the assumed ejecta velocity. Similar to ZTF 21aancgbm, recombination alone is not sufficient to explain the luminosity of the plateau, and Eq. 8.3 implies interaction with pre-existing mass  $M_{\text{pre}} \approx 0.2 \text{ M}_{\odot}$ . Pastorello et al. (2022) discuss archival *HST* and ground-based imaging of this transient, and the properties of the putative progenitor. We note that in addition to the data presented in their paper, this transient has archival *Spitzer Space Telescope*/IRAC imaging from 2007 December 27. We detect a marginal source at the location of the transient with  $m_{3.6} = 20.48 \pm 0.16 \text{ mag}$  and  $m_{4.5} = 19.79 \pm 0.21 \text{ mag}$  (Vega system). We leave a more detailed analysis of this LRN and its progenitor properties to a future study.

**6. ZTF 21acpkzcc (AT 2021aess)** is the most luminous LRN in our sample, with peak  $M_{\text{r}} = -15.12 \pm 0.15 \text{ mag}$ . We do not identify strong Na I D in our early-time spectra, although this is possibly due to low S/N. We assume that the extinction is dominated by the Milky Way, but caution that extinction from the host galaxy could increase the peak-luminosity estimates for this transient. Similar to the other LRNe described above, the light curve shows two distinct peaks — a blue initial peak lasting  $\sim 40$  days followed by a reddened plateau. However, our photometric coverage stops at  $\sim 50$  days into the plateau as the transient experienced solar conjunction. Similar to the previous two LRNe, ZTF 21acpkzcc is brighter in the NIR (by  $> 1$  mag) than in the optical bands. Stacking the archival ZTF light curve in 3 day bins shows some

archival detections  $\sim$ 70 days before peak at  $m_g = 21 \pm 0.3$  and  $m_r = 21.1 \pm 0.3$  mag. Our spectroscopic coverage comprises three optical spectra at +4, +46, and +68 days since peak brightness and one NIR spectrum at +54 days since peak. The early-time spectra show narrow H $\alpha$  with  $\nu_{\text{FWHM}} \approx 500 \text{ km s}^{-1}$ , which grows weaker and narrower with time (FWHM  $< 350 \text{ km s}^{-1}$  at 46 days). The +68 d spectrum exhibits a weak P Cygni profile for H $\alpha$ . The early-time spectra also show a forest of Fe II lines and the Ca II NIR triplet lines with P Cygni profiles. The initial blue light-curve peak with a red plateau together with weakening H $\alpha$  with time and NIR excess suggest that ZTF21 acpkzcc is an LRN. The high luminosity of ZTF21acpkzcc is similar to the LRN AT 2017jfs (Pastorello et al. 2019b), suggesting a massive binary origin.

We note that two additional LRNe were reported in the last three years — AT 2018bwo (Blagorodnova et al. 2021) and AT 2020kog (Pastorello et al. 2021b). AT 2020kog was missed by ZTF because it landed in the chip gaps of the ZTF detector. AT 2018bwo was discovered on 2018 May 22, when ZTF was in the reference-building phase. The first ZTF visit to the field of AT 2018bwo was two months later on 2018 July 14. No alerts were generated as this field did not have a ZTF reference image. We ran post-facto image subtractions and measured forced PSF photometry, recovering two detections of AT 2018bwo in the  $r$  band at  $19.76 \pm 0.08$  and  $20.15 \pm 0.12$  mag on 2018 July 21 and 2018 July 24, respectively.

### LRN-silver

This category includes two sources that do not show all hallmarks of a LRN, but resemble LRNe in several aspects. Their light curves are plotted in Fig. 8.1 and their optical and NIR spectra are shown in Fig. 8.2 and 8.3, respectively.

**1. ZTF 18abwxrhi (AT 2018gzz)** has peak  $M_r = -14.82 \pm 0.17$  mag and shows two pronounced light-curve features: a blue first peak followed by a longer lasting red peak/plateau. Our photometric data are sparse for the red peak/plateau as the transient did not brighten significantly above the ZTF sensitivity limits. However, the light-curve evolution inferred from the available data is strikingly similar to that of the LRNe in the gold sample. Additionally, a spectrum taken during the first blue peak shows narrow, marginally resolved Balmer emission lines with  $\nu_{\text{FWHM}} \approx 300 \text{ km s}^{-1}$  (ruling out a supernova origin), narrow, unresolved Ca II NIR triplet lines with P Cygni profiles, and narrow Ca II H&K absorption lines. We do not detect Na I D in this spectrum, and hence assume negligible host-galaxy extinction.

There is no spectroscopic coverage at late times. Given these similarities with LRNe, ZTF 18abwxrhi is most likely an LRN, and we include it in the LRN-silver category.

**2. ZTF 21aaekeqd (AT 2021afy)** is located on the outskirts of the galaxy UGC 10043. While Pastorello et al. (2022) classify this transient as an LRN, their late-time spectra do not show obvious molecular absorption features (e.g., like those seen in ZTF 21aancgbm). We also do not identify similar molecular features in any of our spectra. As noted by Pastorello et al. (2022), the light curve differs from that of other LRNe with similar luminosities. For these reasons, we include ZTF 21aaekeqd in our LRN-silver sample. It is possible that obvious molecular features appear at later times, where spectroscopic coverage does not exist.

The transient has a 100 day light curve with two low-contrast peaks and is detected only in the  $r$  and  $i$  bands by ZTF. In our earliest spectrum, we detect Na I D absorption with equivalent width  $1.8 \pm 0.6 \text{ \AA}$ , consistent with Pastorello et al. (2022). This corresponds to  $E(B - V)_{\text{host}} \approx 0.28 \pm 0.10 \text{ mag}$ , assuming that the interstellar medium is alone responsible for the Na I D absorption. However, we caution that this is unlikely, given the remote location of the transient in the host. It is possible that the sodium absorption originates in circumstellar dust around the progenitor of the explosion, in which case the extinction estimate will be incorrect (Poznanski et al. 2012). Accounting for the Galactic component, we adopt a total  $E(B - V) = 0.33 \pm 0.10 \text{ mag}$ . With this, the transient reaches  $M_{r, \text{peak}} = -13.95 \pm 0.16 \text{ mag}$ , and is one of the more luminous members of our sample. We obtained an epoch of  $J$ -band imaging at +60 days since peak brightness with  $J - r \approx 1 \text{ mag}$ , similar to other LRNe.

Our spectroscopic coverage comprises three optical spectra at phases of +33 d, +89 d, and +114 d, and one NIR spectrum at +92 d since first peak. The +33 d spectrum shows a reddened continuum with narrow H $\alpha$  ( $v_{\text{FWHM}} \approx 650 \text{ km s}^{-1}$ ) and the Ca II NIR triplet in absorption. Of the three Ca II triplet lines, we detect only the 8542  $\text{\AA}$  and 8662  $\text{\AA}$  absorption lines. This is likely because the transition probability for the 8498  $\text{\AA}$  line is a factor of  $\sim 10$  smaller than for the other two. Notably, the absorption lines are unresolved, with  $v_{\text{FWHM}} \leq 200 \text{ km s}^{-1}$  (the instrumental resolution in this wavelength range is  $v_{\text{inst}} \approx 250 \text{ km s}^{-1}$ , measured from night-sky emission lines). This velocity is much lower than the H $\alpha$  photospheric velocity at this phase ( $\sim 650 \text{ km s}^{-1}$ ). These absorption lines likely originate in a dense, slow-moving shell of CSM outside the photosphere that was likely ejected prior to

the explosion, possibly during the CE phase. The +89 d spectrum shows a more reddened continuum with slower, marginally resolved H $\alpha$  ( $v_{\text{FWHM}} \approx 400 \text{ km s}^{-1}$ ) and narrow H $\beta$  ( $v_{\text{FWHM}} \approx 300 \text{ km s}^{-1}$ ). The Ca II NIR triplet lines are now seen as a superposition of an emission component with  $v \approx 500 \text{ km s}^{-1}$ , and a central narrow absorption component (see Fig. 8.5). A possible explanation for this is that the ejecta have crashed into the CSM at this epoch, and the resulting shock has swept up only part of the CSM. A photosphere forms at the shock interface from where the emission lines originate (Ca II predominantly excited by collisions). The narrow, weak absorption component originates from the unshocked CSM shell lying outside the photosphere. The +80 d NIR spectrum shows similar narrow hydrogen emission lines. The spectrum also exhibits a weak, broad feature in the  $H$  band, which is similar to the H<sub>2</sub>O absorption seen in ZTF 21aagppzg.

The final optical spectrum at +113 d shows a very weak continuum, but extraordinarily strong H $\alpha$  ( $v_{\text{FWHM}} \approx 300 \text{ km s}^{-1}$ ) and strong, unresolved H $\beta$  ( $v_{\text{FWHM}} < 400 \text{ km s}^{-1}$ ). The Ca II NIR triplet is seen purely in emission. This suggests that the shock has swept up all the CSM. The Balmer decrement in this spectrum is  $\beta \approx 7$ , supporting the notion that the emission originates in an interaction-dominated region. The absorption to emission transition of the Ca II line profiles suggests that there is a dense, slow-moving shell of CSM around the progenitor. None of the other LRNe in our sample undergo such a transition. The late-time spectrum with very strong emission lines is unlike the late-time optical spectra of other LRNe in our sample (e.g., ZTF 21aancgbm at 360 d) that show strong molecular absorption bands.

### LRN-bronze

This category includes three sources (ZTF 18aajqkmr, ZTF 20abjgdec, and ZTF 21aabfwwl) that show multiple peaks in their light curves but do not have spectroscopic coverage (see Fig. 8.1). These transients have peak absolute magnitudes of  $-15.36$ ,  $-14.37$ , and  $-15.72$  mag, respectively. ZTF 21aabfwwl was initially classified as a Type II SN (Hinkle 2021), but the spectrum available on TNS is noisy and no H lines are clearly visible. We list these three transients as candidate LRNe.

### ILRT-gold

This category includes six sources that we spectroscopically classify as ILRTs. Their light curves are shown in Fig. 8.6. We calculate the distances and extinction due to

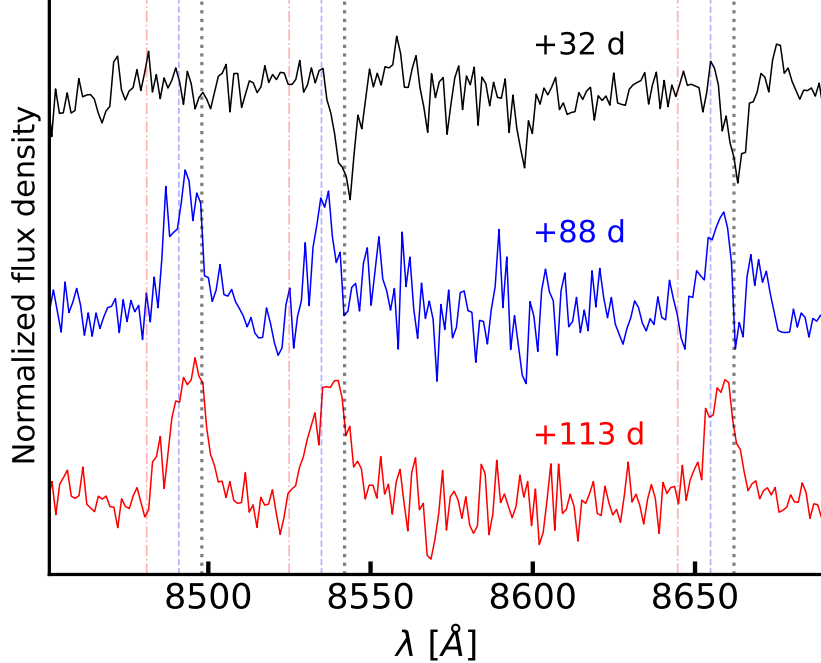


**Figure 8.5: Evolution of Ca II line profiles of ZTF 21aaekeqd.** In the earliest spectrum (+32 d, black), the lines are seen purely in absorption, and likely originate from a shell of slow-moving CSM around the binary. In the second spectrum, the profile has transitioned to emission with a narrow absorption component. This is likely because the ejecta have crashed into the CSM, and swept up only part of the CSM. The shocks in the ejecta produce the emission, while the absorption comes from the unshocked, dense CSM shell outside the photosphere. In the final optical spectrum, the line profiles are pure emission, suggesting that all of the CSM has been swept up by the ejecta.

the Milky Way as was done for the LRNe (see Sec. 8.2). It is challenging to estimate the host-galaxy extinctions because ILRTs have extremely dusty progenitors, and often exhibit variable Na I D originating in outflows (Cai et al. 2021; Smith et al. 2009; also, see discussion of ZTF 19acoaiub below). Instead, we use the peak optical  $g - r$  colors of ILRTs to estimate the host-galaxy extinction, similar to Humphreys et al. (2011), Smith et al. (2009), and Jencson et al. (2019a). The spectra of ILRTs at peak brightness show F-type absorption features, suggesting  $T \approx 7500$  K. Cai et al. (2021) find that the ILRTs in their sample have peak  $B - V$  colors in the range 0.2–0.4 mag, consistent with this interpretation. We use the peak colors of the ILRTs in our sample to estimate the value of  $E(B - V)_{\text{host}}$  required to bring the colors into this range. We estimate a non-negligible extinction for two ILRTs in our sample —  $E(B - V) \approx 0.7$  mag for ZTF 19aadyppr (consistent with Jencson et al.

Table 8.3: Photometric properties of LRN and ILRTs<sup>a</sup>

Name	DM <sup>b</sup> (mag)	$E(B - V)$ <sup>c</sup> (mag)	$m_{r, \text{peak}}$ (mag)	$M_{r, \text{peak}}$ (mag)	MJD <sub>peak</sub> (d)	$L_{\text{peak}}$ (erg s <sup>-1</sup> )
ZTF18acbwfza	31.60	0.250	$18.47 \pm 0.02$	$-13.82 \pm 0.15$	$58430.9 \pm 0.2$	$9.3_{-0.3}^{+0.3} \times 10^{40}$
ZTF19adakuot	24.45	0.055	$15.00 \pm 0.01$	$-9.60 \pm 0.15$	$58891.6 \pm 0.1$	$2.0_{-0.1}^{+0.1} \times 10^{39}$
ZTF20aawdwch	28.97	0.093	$17.79 \pm 0.02$	$-11.43 \pm 0.15$	$58963.0 \pm 1.2$	$> 1.2 \times 10^{40}$
ZTF21aagppzg	29.90	0.020	$16.45 \pm 0.01$	$-13.50 \pm 0.15$	$59258.9 \pm 0.1$	$7.9_{-0.1}^{+0.1} \times 10^{40}$
ZTF21aancgbm	29.43	0.261	$16.28 \pm 0.03$	$-13.86 \pm 0.15$	$59252.9 \pm 0.5$	$> 8.9 \times 10^{40}$
ZTF21acpkzcc	32.09	0.032	$17.05 \pm 0.03$	$-15.12 \pm 0.15$	$59545.5 \pm 0.2$	$3.3_{-0.2}^{+0.2} \times 10^{41}$
ZTF18abwxrhi	33.70	0.047	$19.33 \pm 0.06$	$-14.50 \pm 0.16$	$58386.2 \pm 0.9$	$1.9_{-0.3}^{+1.5} \times 10^{41}$
ZTF21aaekeqd	32.87	0.330	$19.82 \pm 0.06$	$-13.95 \pm 0.16$	$59229.2 \pm 1.6$	$6.0_{-4.6}^{+6.4} \times 10^{41}$
ZTF18aaajgqmr	35.00	0.018	$19.69 \pm 0.09$	$-15.36 \pm 0.17$	$58969.7 \pm 1.0$	$3.3_{-0.4}^{+0.7} \times 10^{41}$
ZTF20abjgdec	33.78	0.141	$19.80 \pm 0.06$	$-14.37 \pm 0.16$	$59045.6 \pm 2.1$	$2.4_{-1.2}^{+13.3} \times 10^{41}$
ZTF21aabfwwl	33.99	0.043	$18.39 \pm 0.05$	$-15.72 \pm 0.16$	$59239.5 \pm 1.8$	$5.2_{-0.7}^{+1.1} \times 10^{42}$
ZTF18acdyopn	33.92	0.064	$19.76 \pm 0.11$	$-14.33 \pm 0.19$	$58426.8 \pm 2.4$	$2.2_{-1.0}^{+21.7} \times 10^{41}$
ZTF19aadyppr	29.45	0.705	$16.65 \pm 0.01$	$-14.73 \pm 0.15$	$58534.7 \pm 0.5$	$2.3_{-0.1}^{+0.1} \times 10^{41}$
ZTF19acoaiub	31.83	0.038	$17.31 \pm 0.02$	$-14.62 \pm 0.15$	$58799.1 \pm 0.1$	$2.0_{-0.2}^{+0.2} \times 10^{41}$
ZTF19acdrkbh	34.33	0.051	$19.85 \pm 0.12$	$-14.62 \pm 0.20$	$58764.3 \pm 1.9$	$1.8_{-0.4}^{+0.9} \times 10^{41}$
ZTF19aagqkrq	30.76	0.200	$17.58 \pm 0.03$	$-13.72 \pm 0.15$	$58538.3 \pm 1.1$	$8.0_{-0.4}^{+0.5} \times 10^{40}$
ZTF21aclzzex	33.89	0.019	$18.26 \pm 0.06$	$-15.68 \pm 0.16$	$59528.6 \pm 1.7$	$5.2_{-1.2}^{+3.7} \times 10^{41}$
ZTF21abtdua	33.22	0.022	$< 18.31$	$< -14.96 \pm 0.15$	$< 59522.5$	$> 1.3 \times 10^{41}$
ZTF21abfxjld	33.43	0.106	$< 19.51$	$< -14.21 \pm 0.20$	$< 59359.8$	$> 8.0 \times 10^{40}$
ZTF19aavwbxs	33.26	0.038	$18.92 \pm 0.08$	$-14.44 \pm 0.17$	$58644.7 \pm 8.1$	$2.2_{-0.3}^{+0.6} \times 10^{41}$
ZTF18acrygkg	33.35	0.036	$< 19.31$	$< -14.14 \pm 0.16$	$< 58447.5$	

a: The two classes LRN and ILRT are separated by a horizontal line.

b: The distance moduli have uncertainties of 0.15 mag and are taken from NED.

c: Galactic extinction values are taken from Schlafly et al. (2011); host-galaxy extinction is calculated as described in the text.

2019a) and  $E(B - V) \approx 0.2$  mag for ZTF 19aagqkrq. For the other transients, we assume the extinction to be dominated by the Galactic component. We calculate pseudobolometric luminosities by fitting blackbodies to the available data. Table 8.3 lists the derived photometric properties of the ILRTs. Our optical and NIR spectra of these transients are shown in Figs. 8.7 and 8.8, respectively. Similar to the LRNe, we derive line velocities by fitting Lorentzian profiles and list the derived values in Table 8.4. We briefly discuss the properties of the transients here.

Two of these transients (ZTF 19aadyppr and ZTF 21aclzzex) have spectroscopic coverage extending to late times. Of these, ZTF 19aadyppr is in the galaxy M51 and has been studied in detail by Jencson et al. (2019a), who identified its red, dusty progenitor. The object shows a single-peaked red light curve, and its spectra exhibit narrow H $\alpha$  and [Ca II] emission, characteristic of ILRTs.

ZTF 21aclzzex is the brightest ILRT in our sample, with peak  $M_r = -15.68 \pm$

0.16 mag. Our light-curve coverage is sparse and noisy, but the available data show indications that the transient is red, and possibly has multiple peaks. However, our spectroscopic coverage extends to 163 d since peak, and resembles the evolution of ILRTs. An early-time spectrum at 9 d since peak brightness shows a blue continuum with narrow H $\alpha$ , H $\beta$ , Ca II, and [Ca II] emission. The spectrum also has Ca II H&K absorption. The next optical spectrum obtained at 84 d since peak shows a reddened continuum with narrow H $\alpha$ , Ca II, and [Ca II] emission, as well as Ca II H&K absorption. [O I] is detected as a weak emission line. The 118 d optical spectrum displays similar features, except [O I] has become stronger. Similar [O I] emission was observed in the ILRT AT 2013la (Cai et al. 2021). The 134 d NIR spectrum shows strong, narrow hydrogen emission lines, as well as He I and O I emission. Although the light curve is not informative enough to classify the transient, the spectroscopic evolution is strikingly similar to that of several ILRTs, especially with [Ca II] emission seen consistently in all spectra. For this reason, we classify it as an ILRT.

The other four transients have only early-time spectroscopic coverage. Analogous to the other ILRTs, they all exhibit narrow H $\alpha$  and [Ca II] emission in their spectra. We note that while the LRN AT 2018hso also showed [Ca II] emission in its early spectra, it also had two pronounced peaks in its light curve. None of these four transients show multiple peaks and are not AT 2018hso-like LRNe. We thus classify them as ILRTs based on narrow H $\alpha$  and [Ca II] emission and the lack of multipeaked light curves.

Of these four, ZTF 19acoaiub (AT 2019udc) and ZTF 19aagqkrq (AT 2019ahd) have the best-sampled light curves. ZTF 19acoaiub is located in NGC 718 and has peak  $M_r = -14.68 \pm 0.04$  mag and a relatively fast-declining, single-peaked light curve. The ZTF light curve also samples the pre-peak rise. Seven days before peak, the transient was extremely red with  $g - r \approx 0.8$  mag. As it brightens, the transient also evolves to bluer colors of  $g - r \approx 0.4$  mag five days before peak and  $g - r \approx 0.2$  mag at peak brightness. The transient then declines at a rate of  $\sim 0.03$  mag day $^{-1}$  for the next 60 days as it evolves back to redder colors. Our only optical spectrum was obtained 7 days before the peak and shows strong H $\alpha$  emission with  $v_{\text{FWHM}} \approx 1300$  km s $^{-1}$ . This spectrum also displays narrow Ca II and [Ca II] emission, similar to several other ILRTs. This pre-peak spectrum shows very strong Na I D absorption with  $\text{EW} \approx 4.8 \pm 0.7$  Å consistent with its pre-peak red colors. A likely explanation for this behavior is that the progenitor of ZTF 19acoaiub was dust-enshrouded. The

circumstellar dust was destroyed by the explosion, causing the transient to evolve to bluer colors as it brightened. This transient demonstrates the issue with using early-time Na I D features to estimate the host-galaxy extinction.

ZTF 19aagqkrq (AT 2019ahd) has peak  $M_r = -13.72 \pm 0.15$  mag and a blue color up to a few days before peak, but rapidly transitions to red colors. Our spectroscopic coverage comprises two optical spectra obtained on successive nights at peak brightness and 1 day post-peak. Both spectra show  $\text{H}\alpha$  emission with  $v_{\text{FWHM}} \approx 700 \text{ km s}^{-1}$  and strong Ca II and [Ca II] emission lines.

The remaining two — ZTF 18acdyopn and ZTF 19acdrkbh — have relatively sparse light-curve sampling. ZTF 18acdyopn has a peak absolute magnitude  $M_r = -14.33 \pm 0.19$  mag and declines by 1.5 mag in the  $r$  band in 80 days. Although our light curve does not sample the peak, the available data show that the transient had red colors a few days post-peak. An optical spectrum taken five days since peak shows narrow hydrogen Balmer emission lines ( $v_{\text{FWHM}} \approx 300 \text{ km s}^{-1}$ ), [Ca II], Ca II H&K, as well as Ca II NIR triplet emission lines. Similarly, ZTF 19acdrkbh has peak  $M_r = -14.62 \pm 0.15$  mag, was detected at the threshold of ZTF sensitivity, and has  $g - r \approx 0.6$  mag at peak. An optical spectrum at +19 days since peak shows narrow  $\text{H}\alpha$  ( $v_{\text{FWHM}} \approx 600 \text{ km s}^{-1}$ ) emission and possible Na I D absorption, similar to other ILRTs.

### ILRT-silver

This category includes two sources (ZTF 21abduah and ZTF 21abfxjld) that show luminosities and spectral evolution broadly similar to ILRTs, but do not have [Ca II] emission. Although [Ca II] emission in ILRTs is a sign of interaction with the surrounding CSM, its strength is sensitive to the CSM density (Humphreys et al. 2011). For example, the proposed ILRT AT 2019krl did not exhibit Ca II emission in several of its spectra (Andrews et al. 2021).

For both transients, our light-curve coverage does not sample the peak, and it is unclear whether they have multiple peaks. For ZTF 21abduah, our light curve samples the brightening and fading of the transient (see Fig. 8.6). We estimate a fiducial peak time by fitting a polynomial to these points. For ZTF 21abfxjld, the ZTF light curve samples the fading of the object. However, the ATLAS  $o$ -band light curve shows two measurements separated by 5 days that do not demonstrate significant evolution, suggesting that the transient peaked around then. We determine the peak time by fitting a polynomial to the ATLAS  $o$ -band light curve. We have late-

Table 8.4: Spectroscopic properties of LRNe and ILRTs

Name	MJD (d)	Phase (d)	$v_{\text{H}\alpha, \text{FWHM}}^a$ (km s $^{-1}$ )	$v_{\text{H}\beta, \text{FWHM}}^a$ (km s $^{-1}$ )	$\beta$
LRNe					
ZTF18acbfza	58424	-7.1	$510 \pm 60$		
ZTF18acbfza	58424	-7.1	$450 \pm 30$	$750 \pm 60$	$2.1 \pm 0.1$
ZTF18acbfza	58432	+0.9	$350 \pm 40$	$760 \pm 120$	$2.2 \pm 0.2$
ZTF18abwxrhi	58379	-9.3	$280 \pm 40$	$250 \pm 120$	$3.8 \pm 0.7$
ZTF21aaekeqd	59262	+33.4	$650 \pm 20$		
ZTF21aaekeqd	59318	+89.3	$340 \pm 30$	$260 \pm 70$	$2.1 \pm 0.2$
ZTF21aaekeqd	59343	+113.8	$300 \pm 20$	$< 370$	$7.6 \pm 0.6$
ZTF21aagppzg	59253	-5.9	$490 \pm 60$	$760 \pm 100$	$2.5 \pm 0.2$
ZTF21aagppzg	59265	+6.1	$420 \pm 40$	$700 \pm 80$	$2.7 \pm 0.2$
ZTF21aagppzg	59313	+54.1	$500 \pm 60$		
ZTF21aancgbm	59313	+60.1	$< 350$		
ZTF21aancgbm	59613	+360.1	$460 \pm 40$		
ZTF21acpkzcc	59549	+4.6	$470 \pm 50$	$540 \pm 70$	$3.7 \pm 0.3$
ZTF21acpkzcc	59591	+46.6	$< 340$		
ZTF21acpkzcc	59613	+68.6	$< 300$		
ILRTs					
ZTF18acdyopn	58432	+5.1	$300 \pm 40$	$630 \pm 120$	$3.3 \pm 0.4$
ZTF19aadyppr	58509	-25.7	$330 \pm 50$	$< 250$	$2.5 \pm 0.3$
ZTF19aadyppr	58526	-8.7	$640 \pm 80$	$680 \pm 180$	$2.4 \pm 0.4$
ZTF19aadyppr	58537	+2.2	$470 \pm 170$	$2400 \pm 850$	$0.9 \pm 0.3$
ZTF19aadyppr	58549	+14.3	$530 \pm 120$		
ZTF19aadyppr	58558	+23.2	$710 \pm 180$		
ZTF19aadyppr	58586	+51.3	$400 \pm 70$		
ZTF19aadyppr	58616	+81.3	$330 \pm 40$		
ZTF19acoaiub	58792	-7.1	$1250 \pm 300$	$2000 \pm 850$	$3.4 \pm 1.1$
ZTF19acdrkbh	58783	+18.7	$590 \pm 80$		
ZTF19aagqkrq	58525	-13.4	$< 850$	$1000 \pm 200$	$2.3 \pm 0.3$
ZTF19aagqkrq	58526	-12.4	$670 \pm 50$	$2000 \pm 500$	$1.6 \pm 0.2$
ZTF21aclzzex	59530	+1.9	$670 \pm 60$	$1200 \pm 180$	$3.5 \pm 0.5$
ZTF21aclzzex	59605	+76.9	$500 \pm 60$	$380 \pm 110$	$5.5 \pm 1.9$
ZTF21aclzzex	59639	+110.3	$550 \pm 40$	$300 \pm 70$	$7.9 \pm 0.9$
ZTF21abduah	59524	+1.5	$1170 \pm 100$		
ZTF21abduah	59549	+26.5	$1290 \pm 100$		
ZTF21abduah	59613	+90.5	$870 \pm 30$	$690 \pm 70$	$8.4 \pm 0.6$
ZTF21abduah	59641	+118.5	$770 \pm 30$	$780 \pm 60$	$10.6 \pm 0.6$
ZTF21abfxjld	59401	+41.7	$< 290$	$< 250$	$3.6 \pm 0.5$
ZTF21abfxjld	59440	+80.2	$< 270$	$< 260$	$4.6 \pm 0.4$

The velocities have been corrected for instrumental resolutions listed in Table 8.2. Upper limits are reported for unresolved lines.

time spectroscopic coverage of both these transients. In a spectrum taken 24 days since the (fiducial) peak, ZTF 21abtduah shows  $\text{H}\alpha$  with  $v_{\text{FWHM}} \approx 1200 \text{ km s}^{-1}$ . A second spectrum obtained at 48 days since peak shows a double-peaked  $\text{H}\alpha$  profile, suggesting interaction with slow-moving CSM, or absorption in an external shell. This spectrum also shows the narrow Ca II NIR triplet in emission. The final spectrum taken at 140 days since peak displays strong  $\text{H}\alpha$ ,  $\text{H}\beta$ , Ca II NIR, and O I emission lines, similar to ZTF 21aclzzex and AT 2013la (however, [Ca II] lines are not seen). The  $\text{H}\alpha$  profile in this spectrum is also double-peaked. ZTF 21abfxjld has spectra at +44 d and 83 d since peak, both of which show  $\text{H}\alpha$  emission with  $v_{\text{FWHM}} \leq 300 \text{ km s}^{-1}$ , and narrow [Ca II] emission. We also have two NIR spectra taken at +26 d and +125 d since peak. The +26 d NIR spectrum has narrow H emission lines. However, the 125 d spectrum shows strong but narrow H and He absorption in the  $J$  band. Such features are not seen in any other ILRTs.

The low expansion velocities of these transients argue against a core-collapse SN origin for them. The lack of any molecular features at late times rules out LRNe. None of them show any significant outbursts in archival data. The nature of these transients is not completely clear. Their spectral features point toward CSM interaction. The lack of Ca II emission suggests that the CSM is denser than in typical ILRTs. These transients could represent a peculiar variety of ILRTs. For these reasons, we classify these as ILRT-silver sources.

### ILRT-bronze

This category includes two sources — ZTF 19aavwxbs and ZTF 18acrygkg. ZTF 19aavwxbs shows a single peak lasting 20 days in the ZTF and ATLAS light curve before it went into solar conjunction. A low-resolution ( $R \approx 100$ ) spectrum of ZTF 19aavwxbs taken with the Spectral Energy Distribution Machine (SEDM; Blagorodnova et al. 2018; Rigault et al. 2019) spectrograph on the 60-inch telescope at Palomar Observatory shows  $\text{H}\alpha$  emission with  $v_{\text{FWHM}} \leq 3000 \text{ km s}^{-1}$ . No other features are discernible in the spectrum. ZTF 18acrygkg has a light curve lasting for 40 days in the ZTF data. There is no spectroscopic data for ZTF 18acrygkg. It is possible that both of these transients are low-luminosity Type II SNe, so we only list them as ILRT candidates.

## Ambiguous Sources

Finally, we have seven sources with no spectroscopic coverage and the photometric data are insufficient to determine a tentative classification. Most of these sources are likely SNe where the ZTF data sample the late-time phases. The  $5\sigma$  alert light curves of these transients have durations shorter than 25 days.

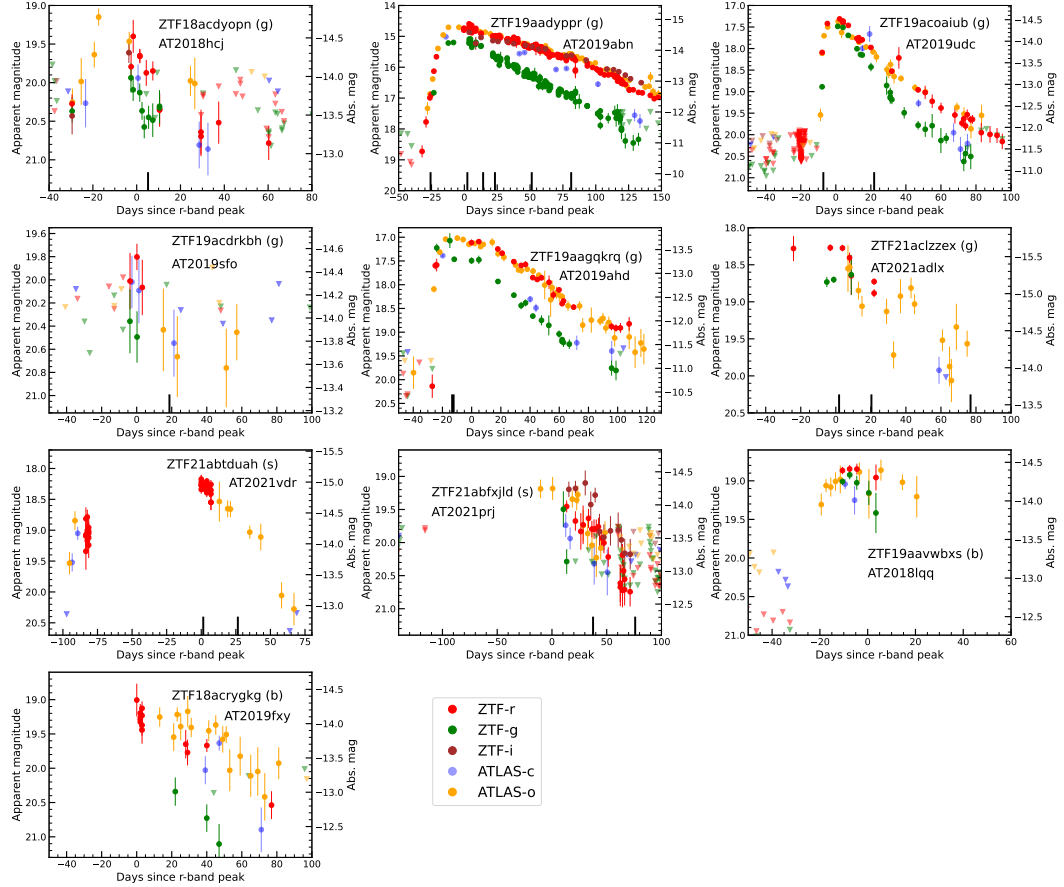


**Figure 8.6: Forced-photometry light curves of the 10 ILRTs in our sample.** The transients in the gold, silver, and bronze samples are marked in parentheses with “g,” “s,” and “b,” respectively. The ZTF-*g*, ZTF-*r*, ZTF-*i*, ATLAS-*c*, and ATLAS-*o* datapoints are plotted in green, red, brown, blue, and orange circles, respectively. Downward-pointing triangles indicate  $5\sigma$  upper limits. The days are in the observer frame. The light curves have been corrected for extinction using the values listed in Table 8.3. Solid black vertical lines indicate epochs at which spectra were obtained.

## 8.3 Volumetric rate

To estimate the volumetric rates, we simulate the ZTF survey from 2018 June 01 to 2022 February 20 with the Python package `simsurvey` (Feindt et al. 2019) using the ZTF pointing history and actual ZTF difference images to estimate the limiting

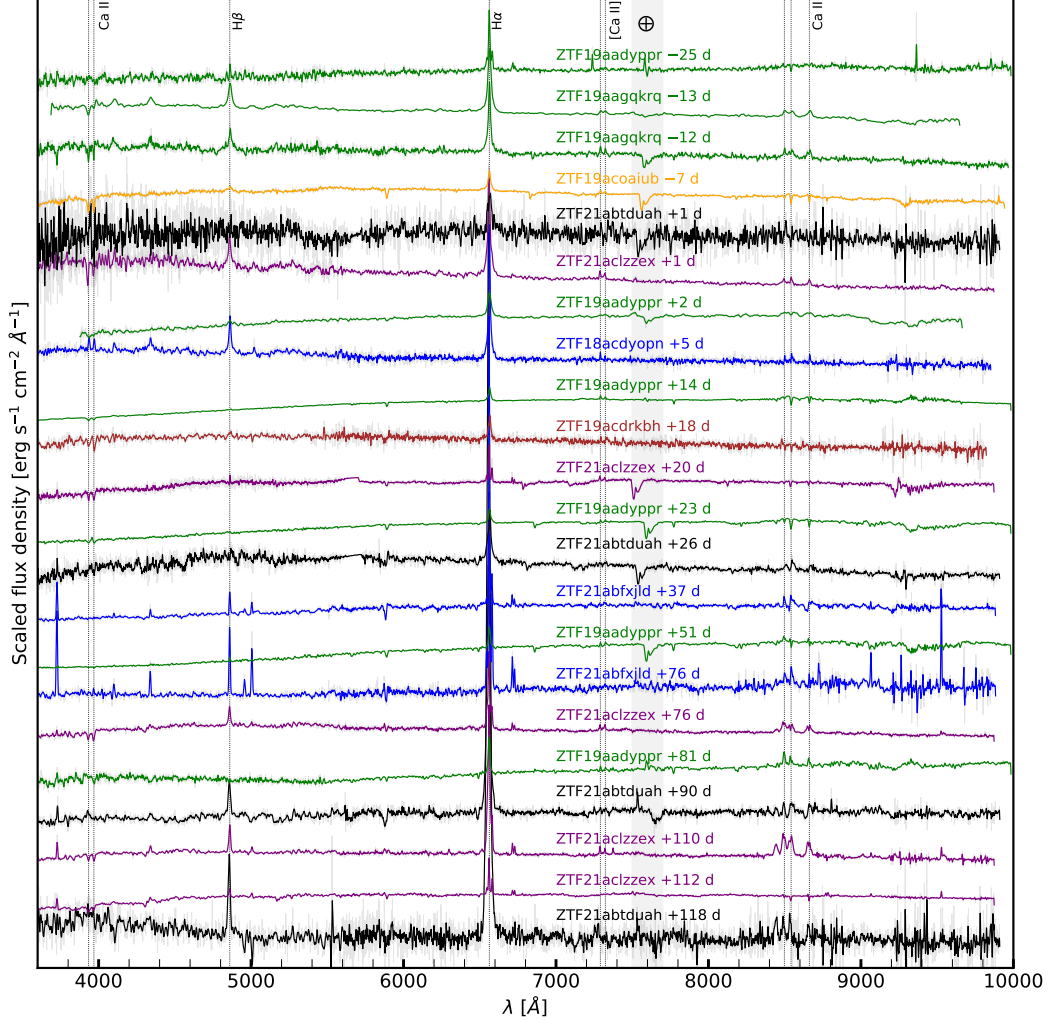


Figure 8.7: Optical spectra of ILRTs presented in this paper.

magnitudes of each pointing. Using template light curves, we then inject LRNe and ILRTs for a range of possible rates and identify the number of transients that would be detected by the selection criteria of our experiment. Comparing simulations to the observed LRN/ILRT sample gives a first estimate of the rate. This estimate is then corrected for selection effects such as the spectroscopic completeness of the CLU experiment and the CLU galaxy catalog.

### Luminosity Function

In this paper, we have presented the first controlled sample of LRNe and ILRTs from a systematic survey. We use this sample to calculate the luminosity function of LRNe and ILRTs.

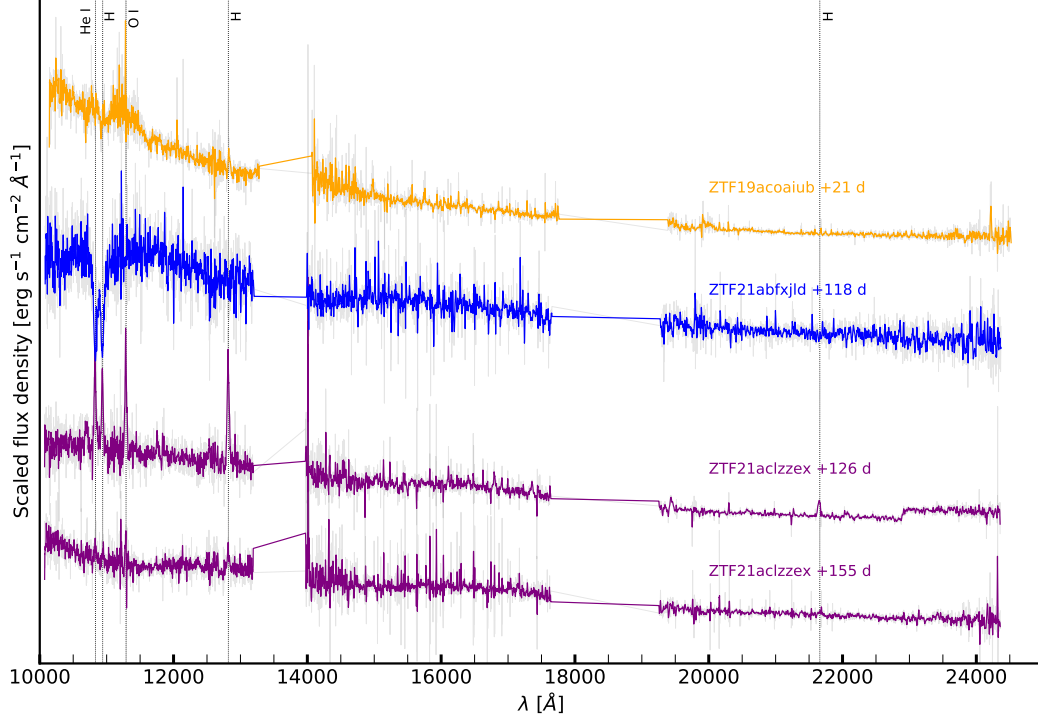


Figure 8.8: NIR spectra of ILRTs presented in this paper.

We restrict ourselves to all gold and silver LRNe that have peak absolute magnitudes brighter than  $-11$ . Fig. 8.9 shows a histogram of the peak absolute magnitudes of the events in the ZTF sample. As the events are detectable out to different volumes (all smaller than the CLU volume limit of  $200$  Mpc), the histogram needs to be volume corrected to determine an accurate luminosity function. The volume-corrected distribution of peak absolute magnitudes of LRNe in our sample is plotted in Fig. 8.9 with a different color. Each event has been weighted by  $1/V_{\max}$ , where  $V_{\max}$  is the maximum volume out to which that event can be detected ( $V_{\max} \propto 10^{\frac{3}{5}(20-M_{r,peak})}$ ). The volume-corrected distribution shows a steep decline of the event rate with increasing peak luminosity. Fig. 8.9 also shows the distribution of the ZTF events combined with events from the literature (taken from Blagorodnova et al. 2021). The distribution of the ZTF events is broadly consistent with that of the ZTF+literature events (although there are significant biases associated with the literature sample). The peak-luminosity distribution of ZTF events is well-fit by a straight line (in log space) with slope  $0.6 \pm 0.1$ . This corresponds to  $dN/dL \propto L^{-2.5 \pm 0.3}$ , significantly steeper than the luminosity function derived for low-luminosity ( $M_V > -10$  mag) LRNe (Kochanek et al. 2014). The implications of these differences are discussed in Sec. 8.4.

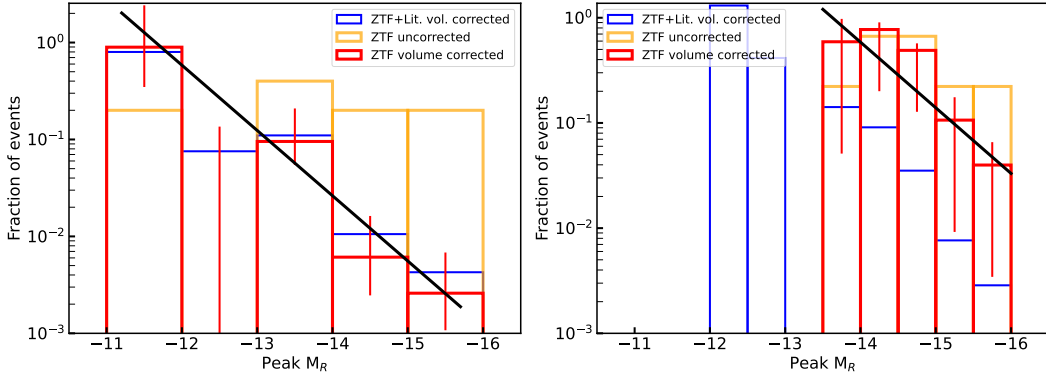


Figure 8.9: **Distribution of the peak absolute magnitudes of LRNe (left) and ILRTs (right) in our sample.** The volume-corrected ZTF sample with Poisson error bars is shown in red, and the volume-corrected ZTF+literature sample is shown in blue. The black line illustrates a linear fit to these data (in log space). We derive a luminosity scaling  $dN/dL \propto L^{-2.5 \pm 0.3}$  for LRNe and  $dN/dL \propto L^{-2.5 \pm 0.5}$  for ILRTs.

Similarly, we calculate the ILRT luminosity function using the eight gold and silver events from our sample. Fig. 8.9 (right panel) shows the volume-corrected distribution of the peak absolute magnitudes of ZTF ILRTs. We fit a straight line with slope  $0.6 \pm 0.2$  to the distribution (in log space), for  $M_r < -13.5$  mag. This corresponds to a luminosity function of  $dN/dL \propto L^{-2.5 \pm 0.5}$ . This scaling only samples the brighter end of the ILRT luminosity function. Fig. 8.9 also shows the distribution of previously known events from literature together with the ZTF sample, which extends to lower luminosities than the ZTF sample ( $M_r \approx -12$  mag). We note that for both LRNe and ILRTs, including the bronze or excluding the silver sample does not significantly change the derived luminosity function.

### Sub-sample for rate estimates

As mentioned in Sec. 8.2, only 19 of the 34 transients in Table 8.1 have spectra. The low spectroscopic completeness of this sample compared to the full CLU experiment is because it includes several transients with sparse photometric coverage (Sec. 8.2). These transients either entered solar conjunction soon after discovery or were discovered after they emerged from solar conjunction and faded away before any spectra were obtained. To exclude such transients from the sample, we introduce an additional selection criterion — a minimum threshold of 25 days on the duration of the ZTF light curve (i.e., the  $5\sigma$  detections in  $g$  or  $r$  should span at least 25 days). Of the 21 sources that satisfy this criterion, 16 have spectra giving a spectroscopic

completeness of  $\sim 80\%$  for the sample — consistent with that of the full CLU experiment.

We then build a subsample from these 21 candidates to use for LRN/ILRT rate calculations. All sources listed as potential LBVs are naturally excluded, and all “ambiguous” sources are excluded by the light-curve-duration criterion. Of the remaining sources, we only include those transients that have spectroscopic coverage (i.e., the gold and silver categories) to obtain an estimate of the rate, as this estimate is subsequently corrected for spectroscopic completeness. The subsample used for rate calculations is marked with an asterisk in Table 8.1.

The LRN subsample used for rate estimates comprises seven out of the eight gold and silver LRNe from Table 8.1. ZTF 19adakuot is excluded because of its low luminosity (Sec. 8.3). As noted in Sec. 8.2, the LRNe AT 2018bwo and AT 2020kog were not detected in the ZTF alert stream. Two detections of AT 2018bwo were recovered post-facto, but this object is excluded by the light-curve-duration criterion. AT 2020kog is excluded because it was in the chip gaps of the ZTF camera, an effect that is taken into account by our survey simulations. The ILRT subsample comprises five out of the eight gold and silver ILRTs. The remaining three do not satisfy the light-curve-duration criterion.

### Volumetric Rates

The luminosity functions and template light curves were used to simulate LRNe and ILRTs, and the `simsurvey` simulations of the ZTF survey were used to count how many of them would be detected by our experiment. We apply the selection criteria described in Sec. 8.2 and the light-curve-duration criterion from Sec. 8.3 to the simulated transients. We conduct 100 iterations of simulations for each rate to estimate the median and  $1\sigma$  uncertainties on the number of transients recovered for each rate.

The top-left panel of Fig. 8.10 shows the number of LRNe that would be detected by our selection criteria as a function of their volumetric rate. The top-right panel of Fig. 8.10 gives a histogram of the fraction of simulations where the number of detected simulated transients equals the observed number of seven LRN-gold and LRN-silver events. We fit the distribution with a skewed Gaussian function to estimate the median and 68 percentile confidence limits. Accounting for an additional Poisson uncertainty associated with the seven observed events, we derive a volumetric rate of  $r_{\text{LRN},u} = 5.7_{-2.7}^{+4.4} \times 10^{-5} \text{ Mpc}^{-3} \text{ yr}^{-1}$ .

This estimate does not account for four factors which may result in underestimation compared to the true LRN rate: (1) the CLU experiment is limited to 100" or 30 kpc from nuclei of galaxies and will miss farther transients, (2) the CLU experiment is not 100% spectroscopically complete, (3) the CLU experiment relies on the CLU galaxy catalog and is affected by its completeness, and (4) some LRNe will be missed owing to inefficiencies of the ZTF image-subtraction pipeline. First, we note that all literature events have been discovered within 100" or 30 kpc of their respective hosts. We searched through transients classified as part of the ZTF BTS — an all-sky, magnitude-limited survey with ZTF — and did not find any additional LRNe. For this reason, we believe that the CLU offset criterion does not have a significant effect on the rate estimate. Second, the CLU experiment is  $\sim$ 80% spectroscopically complete for  $mr < 20$  mag transients. This suggests that the completeness-corrected rate is  $7.1_{-3.4}^{+5.9} \times 10^{-5} \text{ Mpc}^{-3} \text{ yr}^{-1}$ . However, the CLU completeness is a function of apparent magnitude, and varies from 100% for  $mr < 18$  mag to 95% for  $mr < 19$  mag. To account for this, we calculate the completeness as a function of apparent magnitude in bins of 1 mag. For each simulation of each of our rates, we bin the simulated transients by peak apparent magnitude, and count only the fraction of events that would be classified based on the CLU criteria. This exercise gives a value consistent with the simplified approach described above because a majority of the events have faint apparent magnitudes, and the (large) uncertainties on this estimate are dominated by small-number statistics.

Third, to correct for the incompleteness of the galaxy catalog, we used the redshift completeness factor (RCF) derived from the BTS. As all events in our sample come from star-forming galaxies, we calculate the RCF for star-forming galaxies in the BTS sample as a function of redshift ( $z$ ) and WISE 3.36  $\mu\text{m}$  absolute magnitude ( $M_{W1}$ ) as described by Fremling et al. (2020). We then use the redshifts and  $M_{W1}$  magnitudes of the host galaxies of LRNe in our sample and weight each event by  $1/RCF(z, M_{W1})$  to estimate the effect of galaxy-catalog incompleteness. We find that this leads to an underestimation of the rate by  $\sim$ 10%.

Finally, the ZTF image-subtraction pipeline has two possible sources of inefficiency that are relevant for this calculation. In each science image, the pipeline actively masks pixels that are affected by quality cuts (e.g., saturation owing to high brightness, cosmic rays, bad pixels). This introduces a time-dependent source of incompleteness. This dynamic masking does not have a significant effect as LRNe and ILRTs have long durations and are picked up by the pipeline eventually. A

more serious issue pertains to the reduced efficiency of the image-subtraction algorithm on bright galaxy backgrounds, as are common for the LRNe and ILRTs in our sample. The ZTF pipeline efficiency as a function of background brightness has not been studied to date, and this analysis is outside the scope of this paper. We therefore caution that our rates are possibly lower limits. Applying the corrections described above (except pipeline efficiency), we derive a corrected rate of  $r_{\text{LRNe}} = 7.8^{+6.5}_{-3.7} \times 10^{-4} \text{ Mpc}^{-3} \text{ yr}^{-1}$  for LRNe.

Similarly, using the ILRT luminosity function and `simsurvey` simulations, we derive an uncorrected rate  $r_{\text{ILRT,u}} = 1.9^{+1.3}_{-1.0} \times 10^{-6} \text{ Mpc}^{-3} \text{ yr}^{-1}$  (see bottom panel of Fig. 8.10). Correcting for the incompleteness effects described above gives  $r_{\text{ILRT}} = 2.6^{+1.8}_{-1.4} \times 10^{-6} \text{ Mpc}^{-3} \text{ yr}^{-1}$ .

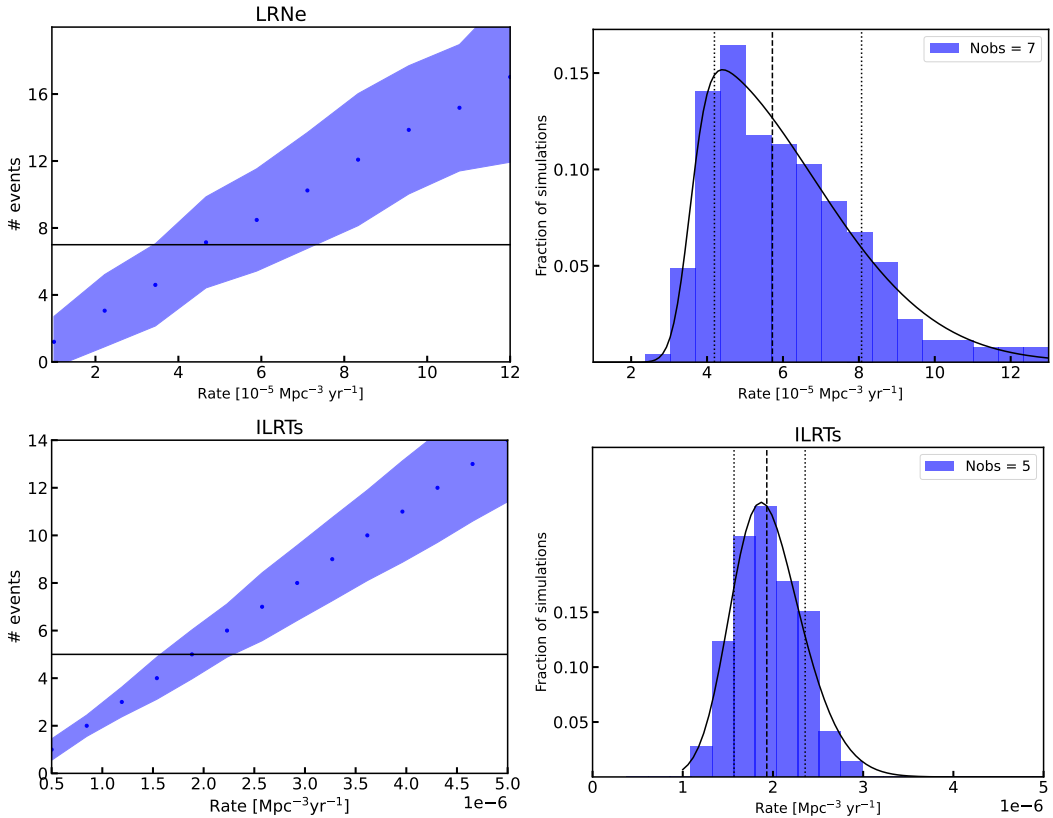


Figure 8.10: **The volumetric rates of LRNe and ILRTs.** *Left:* The number of simulated LRNe (top) and ILRTs (bottom) that pass our filtering criteria as a function of their volumetric rate. *Right:* The fraction of simulations where the number of simulated transients that pass the filtering criteria equals the observed number of LRNe (top) or ILRTs (bottom). The distributions are fit by a skewed Gaussian function, indicated as black solid curves. The vertical dashed and dotted lines show the median and 68 percentile confidence limits of the distribution, respectively.

## 8.4 Discussion

### LRNe

Kochanek et al. (2014) used three Galactic mergers to estimate the rate of low-luminosity stellar mergers with  $M_V \geq -10$  mag. They find that the luminosity function of these mergers is roughly  $dN/dL \propto L^{-1.4 \pm 0.3}$  and the rates of events brighter than  $M_{V,\text{peak}} = -3$  ( $-10$ ) is  $\sim 0.5$  ( $0.03$ )  $\text{yr}^{-1}$ . Our ZTF sample shows that their scaling does not extend to higher luminosities. For transients brighter than  $M_{r,\text{peak}} = -11$  mag, the luminosity function drops at a much steeper rate ( $dN/dL \propto L^{-2.5}$ ), suggesting a broken power-law luminosity function for LRNe. Fig. 8.11 shows the LRN rate as a function of peak absolute magnitude derived from our ZTF sample and the Kochanek et al. (2014) scaling. To convert the Galactic rate measurements from Kochanek et al. (2014) to volumetric rates, we follow Howitt et al. (2020) and assume that the LRN rate scales with star formation. We use a star-formation rate of  $2 \text{ M}_\odot \text{ yr}^{-1}$  for the Milky Way (Licquia et al. 2015) and an average cosmic star-formation rate of  $0.015 \text{ M}_\odot \text{ yr}^{-1}$  (Madau et al. 2014). The ZTF and Kochanek et al. (2014) rate estimates diverge at high luminosities. The volumetric rate of LRNe brighter than  $M_r = -11$  mag ( $-13$  mag) derived from the ZTF sample is lower by a factor of  $\sim 5$  ( $100$ ) than that extrapolated from the Kochanek et al. (2014) scaling.

A steeper luminosity function at the brighter end has also been predicted by binary population synthesis (BPS) models (Howitt et al. 2020). They follow the binary evolution of a population of binary systems with masses drawn from a Kroupa IMF and a binary fraction of unity, and find that 45% of the simulated binaries undergo some form of unstable mass transfer. 38% of these binaries result in stellar mergers while the remaining 62% result in CE ejections. Qualitatively similar results were also obtained by the population synthesis study of Politano et al. (2010), although they focused on the remnants of CEE rather than the associated transients. Howitt et al. (2020) used analytical expressions to approximate light curves associated with their simulated mergers and CE ejections, and determined the Galactic rate of LRNe as a function of their peak luminosity. Fig. 8.11 also shows the volumetric LRN rate from these BPS simulations as a function of peak magnitude. We derive the volumetric rate using the Galactic and average cosmic star-formation rates as described above. As noted by Howitt et al. (2020), the BPS rate agrees with the Kochanek et al. (2014) value for low luminosities, but diverges for  $M_{\text{bol}} \leq -10$  mag. The steep decline in the LRN rate seen in the BPS simulations is consistent with the rates derived from our ZTF sample.

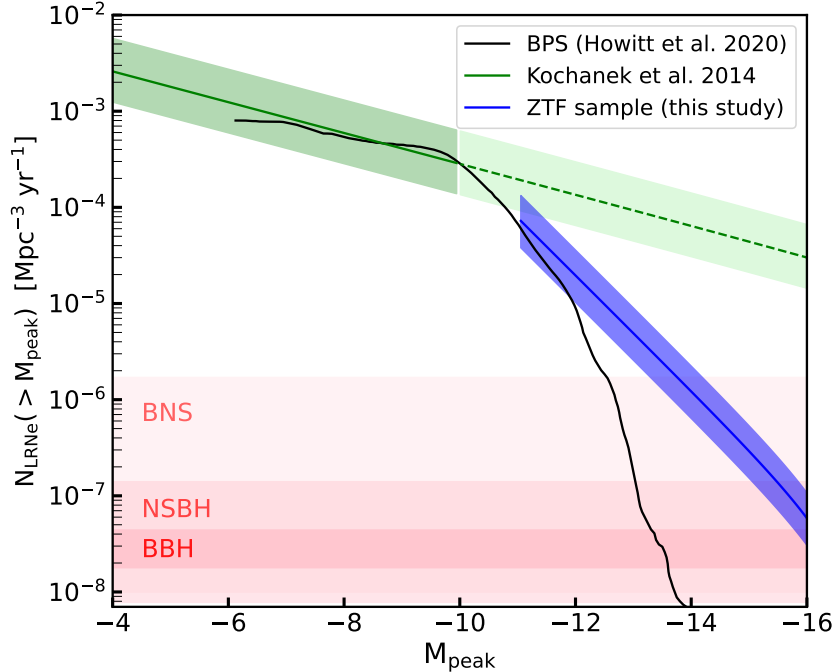


Figure 8.11: **The rate of LRNe brighter than a given absolute magnitude** as determined from our ZTF sample (blue), the Galactic sample of Kochanek et al. (2014) sample (green), and the binary population synthesis models of Howitt et al. (2020) (black line). The Kochanek et al. (2014) sample was restricted to  $-10 \leq M_V \leq -4$  mag, while the ZTF sample is restricted to  $-16 \leq M_r \leq -11$  mag. The green dashed line indicates the Galactic rate extrapolation to brighter luminosities. It is evident that the Galactic scaling overpredicts the observed ZTF rate by several orders of magnitude. The steeper drop of the LRN rate at higher luminosities is also seen in the BPS models. The BPS models underpredict the brightest ( $M_r \leq -13$  mag) rate of LRNe, which could be attributed to specific assumptions about CE physics in the models. The pink shaded regions indicate the constraints on the rates of BNS, NSBH, and BBH mergers as measured by LIGO (The LIGO Scientific Collaboration et al. 2021a). The rates of the brightest LRNe are consistent with a significant fraction of them being progenitors of these compact merging systems.

However, we note that the BPS simulations underpredict the rates for LRNe with  $M_r < -13$  mag. This could be a result of several assumptions about the LRN light curves, binary populations, or CE physics used in the BPS simulations. Most importantly, Howitt et al. (2020) assumed that the LRN light curve is powered solely by hydrogen recombination and used analytical scaling relations from Ivanova et al. (2013a) to estimate an LRN light curve. But, as noted in their analysis, this model is unable to reach the luminosities of the highest-luminosity LRNe. Similar light-curve modeling by Matsumoto et al. (2022) also shows that hydrogen recombination

alone cannot explain the light curves of the highest-luminosity LRNe. Additionally, hydrogen recombination is believed to power the plateau in LRNe, and not the initial blue peak (which is used for our and Kochanek et al. 2014 rate calculations). Using the recombination-powered light-curve model thus underpredicts the LRN rate at the high-luminosity end. More accurate models of LRN light curves are required to reconcile the predicted rate with the observed rate. Several other parameters about binary populations and CE physics can also contribute to the observed discrepancy. For example, a uniform binary fraction was assumed in the simulations, but the binary fraction increases with stellar mass (Moe et al. 2017). This would mean the number of massive binaries is higher, which would produce additional LRNe at the bright end.

Here, we note that the Kochanek et al. (2014) analysis is based on only three events, all discovered by amateur astronomers over a span of three decades. It is impossible to accurately quantify the completeness associated with the discoveries in this sample. It is thus possible that the LRN luminosity function at low luminosities differs from that derived by Kochanek et al. (2014). For example, as discussed in their paper, if they assume that the searches that discovered the Galactic LRNe had a shallower limiting magnitude ( $m_{\text{lim}, I} = 9$  mag instead of 13), their luminosity function scales as  $L^{-1.7 \pm 0.5}$ . This is closer to the value derived in this paper for the more-luminous extragalactic LRNe. A systematic census of Galactic stellar mergers is required to confirm the slope of the luminosity function at low luminosities.

The broken power-law shape, if confirmed, has interesting implications for our sample of LRNe. Observations as well as theoretical models of LRNe predict that the peak luminosities and durations of LRNe directly correlate with their progenitor masses (Kochanek et al. 2014; Blagorodnova et al. 2021; Ivanova et al. 2013b; Matsumoto et al. 2022; Cai et al. 2022). Using the relation  $L \propto M^{-2.2 \pm 0.3}$  from Cai et al. (2022), our luminosity scaling implies a mass function of  $dN/dM \propto M^{-4.3 \pm 1.1}$ , different from standard IMF models. Kochanek et al. (2014) found that the lower-luminosity Galactic LRNe have progenitors consistent with the stellar IMF. An interesting possibility to explain this difference is to postulate that the low-luminosity Galactic events are mergers while the more-luminous extragalactic events are CE ejections. For a binary system with a given primary mass, the associated LRN is brighter and longer lived if it undergoes complete CE ejection rather than a merger where only a small fraction of the envelope is ejected. From their simulations, Howitt et al. (2020) find that the bright LRNe ( $M_{\text{bol}} \leq -10$  mag) result almost exclusively

from envelope ejections, while mergers result in lower-luminosity transients. The broken power law would then suggest that the luminous CE ejections are much rarer than the less-luminous stellar mergers. The range of peak luminosities and durations of the ZTF sample events presented here is consistent with the CE ejections of Howitt et al. (2020). Thus, in this picture, most if not all of the events in the ZTF sample analyzed here could be CE ejections. In this case, our derived rate would represent the rate of CE ejections in massive binaries — an important step in the formation of double compact objects (DCOs; Vigna-Gómez et al. 2020).

It is interesting to compare our rate to the rate of DCO mergers detected by LIGO. The LIGO Scientific Collaboration et al. (2021b) determined the volumetric rate of binary neutron star (BNS), neutron-star-black-hole (NSBH), and binary black hole (BBH) mergers to be  $10\text{--}1700 \text{ Gpc}^{-3} \text{ yr}^{-1}$ ,  $7.8\text{--}140 \text{ Gpc}^{-3} \text{ yr}^{-1}$ , and  $17\text{--}44 \text{ Gpc}^{-3} \text{ yr}^{-1}$ , respectively. The shaded pink regions in Fig. 8.11 indicate these DCO merger rates. The plot shows that the brightest LRNe are consistent with a significant fraction of them being progenitors of DCO mergers. However, we reiterate that there is no direct evidence to suggest that the more-luminous LRNe come from CE ejections as opposed to mergers. Klencki et al. (2021) show that for successful CE in DCO progenitors, the primary needs to be a convective-envelope red supergiant (RSG), contrary to the few LRNe with progenitor identifications where the progenitor is a yellow supergiant with a radiative envelope. While none of the very luminous ( $M_r \leq -15$  mag) LRNe have progenitor identifications, it remains to be seen whether their photometric and spectroscopic properties conform to those expected from a RSG-CE ejection.

Finally, we note another possible source of bias that could affect the LRN rate determined here. Metzger et al. (2017) predict a population of LRNe originating in mergers involving giant primaries that should be completely dust enshrouded, and emit most of their radiation at IR wavelengths. MacLeod et al. (2022) also show that dust formation in pre-merger outflows could obscure the binary system, causing the resulting LRNe to be observable only at IR wavelengths. Some of the IR-only transients (dubbed SPRITES) that were discovered by the *Spitzer Space Telescope* and had no optical counterparts are potential examples of such dust-enshrouded LRNe (Kasliwal et al. 2017b). Searches for LRNe at IR wavelengths are required to probe this dust-enshrouded population of LRNe. Upcoming NIR time-domain surveys such as the Wide-field Infrared Transient Explorer (WINTER; Lourie et al. 2020a) at Palomar Observatory and Dynamic REd All-sky Monitoring

Survey (DREAMS; Soon et al. 2020) at Siding Springs Observatory that are slated to commence operations in the first half of 2023 will help achieve this. Targeted surveys of nearby galaxies with these NIR telescopes will help discover and study IR-only LRNe, and shed light on the complete LRN landscape. Additionally, as all LRNe are brighter and longer lived at NIR wavelengths than in the optical, the NIR surveys will also increase the population of optically-selected LRNe similar to those presented in this paper. Of particular importance will be additional discoveries of lower-luminosity LRNe ( $-9.5 > M_{r,\text{peak}} > -11$  mag) — a luminosity range that has not been probed by our sample as they have much shorter optical light curves and can lack the early blue optical peak seen in their brighter counterparts (Blagorodnova et al. 2021). The upcoming NIR surveys will thus provide an unbiased and more precise measurement of the LRN luminosity function and volumetric rate.

## ILRTs

We derive an ILRT rate of  $R_{<-13.5} \approx 2.6 \times 10^{-6} \text{ Mpc}^{-3} \text{ yr}^{-1}$  for ILRTs that are more luminous than  $M_r = -13.5$  mag. This rate is smaller than the LRN rate by two orders of magnitude, but we note that the luminosity threshold of our ILRT sample is brighter than that of our LRN sample. We cannot constrain the luminosity function of ILRTs with luminosities lower than  $M_r = -13.5$  mag, as none of our events lie in this luminosity range. In the literature, there are four ILRTs with  $-12 \geq M_r \geq -13.5$  mag, all discovered long before the start of ZTF (Cai et al. 2021). Assuming our luminosity function extends to  $M_r \approx -12$  mag, the total rate of ILRTs is  $R_{<-12} \approx 2 \times 10^{-5} \text{ Mpc}^{-3} \text{ yr}^{-1}$ . Additional discoveries of ILRTs in this low-luminosity range are required to map out the lower end of the ILRT luminosity function.

Cai et al. (2021) derived a lower limit on the ILRT rate of  $9 \times 10^{-6} \text{ Mpc}^{-3} \text{ yr}^{-1}$ . They used a sample of 12 ILRTs discovered in the last 12 yr within 30 Mpc to estimate the ILRT rate, but their analysis did not include a luminosity function or completeness of the surveys. Additionally, their sample included two events with lower luminosities than our threshold, and their lower limit is consistent with the rough estimate  $R_{<-12}$  above. Comparing to the core-collapse SN rate of  $\sim 1.01 \times 10^{-4} \text{ Mpc}^{-3} \text{ yr}^{-1}$  (Perley et al. 2020), we find that the rate of ILRTs ( $R_{<-13.5}$ ) is  $\sim 3^{+1.5}_{-1.5}\%$  of the CCSN rate. It remains to be seen how much the lower-luminosity events contribute to this rate.

Our rate is also lower than that of Thompson et al. (2009), who estimated the ILRT rate is  $\sim 20\%$  of the CCSN rate based on the two ILRTs SN 2008S and NGC 300OT.

We note that NGC 300OT is below the luminosity threshold of our sample, and the rough estimate  $R_{<-12}$  is consistent with their result.

Given the possible association of ILRT with ECSNe, it is worth comparing our rate to theoretical predictions. Poelarends et al. (2008a) determine the range of stellar masses expected to undergo ECSN for different mass-loss and convective dredge-up prescriptions, and determine their rate to be  $\sim 4\%-24\%$  of the CCSN rate. The rate also depends sensitively on the metallicity; for example, Poelarends (2007) find that for  $Z = 0.02$ , the ECSN rate is  $\sim 3\%$  of the CCSN rate, but for  $Z = 10^{-4}$ , the rate is  $\sim 25\%$ . On the contrary, Doherty et al. (2015) use a different metallicity dependence for the mass-loss rate and find that the ECSN rate is  $\sim 2\%-5\%$  of the CCSN rate for all metallicities in the range  $Z = [10^{-5}, 0.02]$ . Our measured ILRT rate ( $R_{<-13.5}$ ) is on the lower side, but still consistent with the wide range of theoretical calculations, and it is in line with the interpretation that several ILRTs could be ECSNe.

However, we cannot rule out that some of the ILRTs presented here are LBV outbursts. Dusty LBV outbursts can also result in red, low-luminosity transients with spectra showing narrow H with Ca II and [Ca II] features, similar to ILRTs (Andrews et al. 2021). While the transients in our sample do not show any archival activity for the last  $\sim 10$  yr, it is possible that they experienced previous outbursts. Nevertheless, the connection of IRLTs to ECSNe is supported by strong evidence related to their dust-enshrouded progenitors with masses of  $8\text{--}15 M_{\odot}$  (Thompson et al. 2009; Botticella et al. 2009; Jencson et al. 2019a) and the fact that their remnants faded below their progenitor luminosities (Adams et al. 2016a). Progenitors are not detectable for most of the ILRTs in our sample. As this will also be the case for a large number of ILRTs that will be detected by future large-scale deep surveys such as the Vera Rubin Observatory (VRO; Ivezić et al. 2019a), it is important to identify additional ways of distinguishing ILRTs from LBV outbursts to confirm their nature as ECSNe. Possible ways to achieve this are extensive nebular-phase observations of ILRTs. On the one hand, late-time photometric observations would allow us to detect the presence and estimate the amount of Ni generated in the explosion (see Cai et al. 2021). On the other hand, nebular spectroscopic observations would allow us to determine the composition of the ILRT ejecta where the presence of stronger Ni than Fe lines, weak O, Mg, C, and Fe lines, and a low  $[O\ I]/[Ca\ II]$  ratio would be evidence for the ECSN scenario (similar to AT 2018zd; Hiramatsu et al. 2021).



Figure 8.12: **Host galaxies of the ILRTs in our sample.** The positions of the ILRTs are indicated with a yellow cross, on top of color-coded PS1 images obtained from <http://ps1images.stsci.edu/cgi-bin/ps1cutouts>. Similar to LRNe, all ILRTs in our sample are located in star-forming galaxies.

### Host Galaxies of LRNe and ILRTs

Fig. 8.12 shows thumbnails of the host galaxies of the ZTF ILRTs presented in this paper. The ZTF ILRTs belong to star-forming galaxies, similar to all ILRTs discovered to date (see Cai et al. 2021). As neither ZTF nor the CLU galaxy catalog are biased toward star-forming galaxies (Cook et al. 2019), the sample confirms that ILRTs occur in predominantly young environments — consistent with their ECSN or LBV interpretations.

Fig. 8.13 shows thumbnails of the host galaxies of the ZTF LRNe presented in this paper. All ZTF LRNe also belong to late-type star-forming galaxies (see Table 8.1 for host-galaxy morphologies), similar to all LRNe discovered in the last decade (see Pastorello et al. 2019a; Blagorodnova et al. 2021). This confirms that the luminous ( $M_r \leq -11$  mag) LRNe occur more commonly in star-forming environments. This is consistent with the expectation that LRNe in this luminosity range have massive ( $\geq 10 M_\odot$ ) progenitors (Blagorodnova et al. 2021). Early-type galaxies are expected

to have LRNe with lower-mass progenitors and hence lower luminosities, making time-domain surveys less sensitive to detecting them.

Only three LRNe have been discovered in old environments — OGLE 2002-BLG-360 in the Galactic bulge (Tylenda et al. 2013), M31RV in the bulge of M31 (Rich et al. 1989), and M85 OT in the S0-type galaxy M85 (Kulkarni et al. 2007). Of these, M85 OT does not follow the LRN peak luminosity vs. progenitor mass correlation (Kochanek et al. 2014; Blagorodnova et al. 2021). The progenitor mass of M85 OT has been constrained to  $< 7 M_{\odot}$  (Ofek et al. 2008). This is expected to produce an LRN with  $M_{r,\text{peak}} \geq -10$  mag — much fainter than its actual peak  $M_r \approx -12$  mag. As it is not a canonical LRN, M85 OT has been suggested to be an ILRT. However, ILRTs have star-forming hosts, unlike M85 OT. Its progenitor mass is also incompatible with the ECSN or LBV scenario for ILRTs, suggesting that it is not a canonical ILRT either. An intriguing possibility is that M85 OT is the merger of a white dwarf (WD) with a companion evolved star. Such “CV mergers” are believed to produce transients with observational characteristics similar to those of LRNe (Metzger et al. 2021). A WD progenitor would be consistent with the old environment of M85 OT. As this is not a canonical merger of two stars, we would not expect the transient to follow the correlations observed in other LRNe. The Galactic slow nova CK Vul has been proposed to be a merger involving a WD progenitor (Eyles et al. 2018; Metzger et al. 2021). M85 OT could be an extragalactic member of this class of outbursts. Discoveries of additional LRNe in early-type galaxies will shed further light on the origin of this population.

## 8.5 Summary and the future

Despite the discovery of a dozen LRNe and ILRTs in the last decade, their rate remained uncertain. In this paper, we compiled a systematic sample of LRNe and ILRTs using the Census of the Local Universe experiment on the Zwicky Transient Facility to address this issue. We present a sample of eight LRNe and eight ILRTs identified by the CLU experiment. We discuss the properties of these transients, and present new data for the precursor emission in AT 2019zhd and line-profile evolution in ZTF 21aaekeqd (AT 2021afy). We conduct simulations of the ZTF survey using actual ZTF observation history and correct for the completeness of CLU to derive a rate of  $7.8_{-3.7}^{+6.5} \times 10^{-5} \text{ Mpc}^{-3} \text{ yr}^{-1}$  for LRNe with absolute magnitudes  $M_r$  in the range  $[-11, -16]$ , and  $2.6_{-1.4}^{+1.8} \times 10^{-6} \text{ Mpc}^{-3} \text{ yr}^{-1}$  for ILRTs with  $M_r < -13.5$  mag.

The rates of LRNe in this luminosity range are much lower than those extrapolated



Figure 8.13: **Host galaxies of the LRNe in our sample.** The positions of the LRNe are indicated with a yellow cross. ZTF 19adakuot is located in M31. All LRNe in our sample (including LRN-bronze events) are located in star-forming galaxies.

from Galactic measurements of low-luminosity Galactic LRNe by Kochanek et al. (2014). Specifically, we find that the luminosity function of LRNe scales as  $\propto L^{-2.5}$  in the range  $-11 < M_r < -16$  mag, as opposed to  $L^{-1.4}$  derived by Kochanek et al. (2014) for  $-4 < M_V < -10$  mag. This steeper decline at higher luminosities is broadly consistent with binary population synthesis models of Howitt et al. (2020); however, the BPS models underpredict the rates for  $M_r < -13$  mag by as much as two orders of magnitude. This discrepancy is likely due to assumptions about the light-curve models used in the BPS simulation. The rates of the brightest LRNe in our sample are consistent with a significant fraction of them being progenitors of double compact object systems. We note that all LRNe in our sample and those discovered in the last decade belong to star-forming host galaxies. There have been no analogs of M85 OT, which was discovered in an S0-type galaxy.

The ILRT rate corresponds to  $2.6^{+1.8}_{-1.4}\%$  of the local core-collapse SN rate. However, our sample only probes the high-luminosity end of the ILRT luminosity function. Assuming our scaling extrapolates to lower luminosities, our measurement is con-

sistent with previously measured constraints on the ILRT rate by Thompson et al. (2009) and Cai et al. (2021). The ILRT rate is also consistent with the wide range of theoretical predictions of rates of electron-capture SNe by Poelarends et al. (2008b) and Doherty et al. (2015). Additional nebular-phase observations of ILRTs and observations of their progenitors are required to confidently establish them as electron-capture SNe.

The future holds exciting prospects for studies of LRNe and ILRTs. Upcoming NIR time-domain surveys such as WINTER and DREAMS will enable substantial progress in the next few years. These surveys will provide the first unbiased sample of the dusty, red transients and will be instrumental in uncovering hidden populations that could be missed by optical surveys. These results will set the stage for the Vera Rubin Observatory. Based on our rate estimates, we calculate that VRO will discover between 300 to 1500 LRNe and 200–700 ILRTs (with  $M_{r,\text{peak}} < -13.5$  mag) per year (assuming a sensitivity of  $mr \approx 24.2$  mag). While most of these will be too faint for spectroscopic classifications, these transients can be identified based on their low luminosities, long-duration light curves, and red photometric colors. An experiment similar to CLU that keeps track of VRO transients in cataloged galaxies will be instrumental in the study of LRNe and ILRTs.

## 8.6 Acknowledgements

We thank the anonymous referee for providing useful comments. Based on observations obtained with the Samuel Oschin 48-inch Telescope and the 60-inch Telescope at Palomar Observatory as part of the Zwicky Transient Facility (ZTF) project. ZTF is supported by the National Science Foundation (NSF) under grants AST-1440341 and AST-2034437, and a collaboration including current partners Caltech, IPAC, the Weizmann Institute of Science, the Oskar Klein Center at Stockholm University, the University of Maryland, Deutsches Elektronen-Synchrotron and Humboldt University, the TANGO Consortium of Taiwan, the University of Wisconsin at Milwaukee, Trinity College Dublin, Lawrence Livermore National Laboratories, IN2P3, University of Warwick, Ruhr University Bochum, Northwestern University, and former partners the University of Washington, Los Alamos National Laboratories, and Lawrence Berkeley National Laboratories. Operations are conducted by COO, IPAC, and UW. The ZTF forced-photometry service was funded under the Heising-Simons Foundation grant 12540303 (PI M. Graham). The SED Machine is based upon work supported by the NSF under grant 1106171. This work is also based in part on observations made with the Nordic Optical Telescope, owned in col-

laboration by the University of Turku and Aarhus University, and operated jointly by Aarhus University, the University of Turku, and the University of Oslo (respectively, representing Denmark, Finland, and Norway), the University of Iceland, and Stockholm University, at the Observatorio del Roque de los Muchachos, La Palma, Spain, of the Instituto de Astrofísica de Canarias. The Liverpool Telescope is operated on the island of La Palma by Liverpool John Moores University in the Spanish Observatorio del Roque de los Muchachos of the Instituto de Astrofísica de Canarias with financial support from the UK Science and Technology Facilities Council. This work is part of the research program VENI, with project number 016.192.277, which is partially financed by the Netherlands Organisation for Scientific Research (NWO). A major upgrade of the Kast spectrograph on the Shane 3 m telescope at Lick Observatory, led by Brad Holden, was made possible through generous gifts from the Heising-Simons Foundation, William and Marina Kast, and the University of California Observatories. Research at Lick Observatory is partially supported by a generous gift from Google. Some of the data presented herein were obtained at the W. M. Keck Observatory, which is operated as a scientific partnership among the California Institute of Technology, the University of California, and NASA; the observatory was made possible by the generous financial support of the W. M. Keck Foundation. A.V.F.’s group acknowledges generous support from the Christopher R. Redlich Fund, Sunil Nagaraj, Landon Noll, Sandy Otellini, and many additional donors.

## 8.7 Data availability

Light curves and spectra of the LRNe, ILRTs, and possible LBVs presented in this paper, as well as template LRN and ILRT light curves, are available online at Zenodo (Karambelkar et al. 2023a). The spectra will also be posted to WISEREP. The ZTF pointing-history logs will be made available upon request to the corresponding author.

## 8.8 Appendix: Properties of Sources Classified as Possible LBV Outbursts

The light curves of the six sources we classify as potential LBV outbursts are shown in Fig. 8.14 and their spectra are displayed in Fig. 8.15. We discuss the individual objects below.

- **ZTF 19acpmbvd (AT 2019wbg)** is located in the galaxy NGC 4045, and shows a bumpy, red light curve with at least three peaks. The transient was

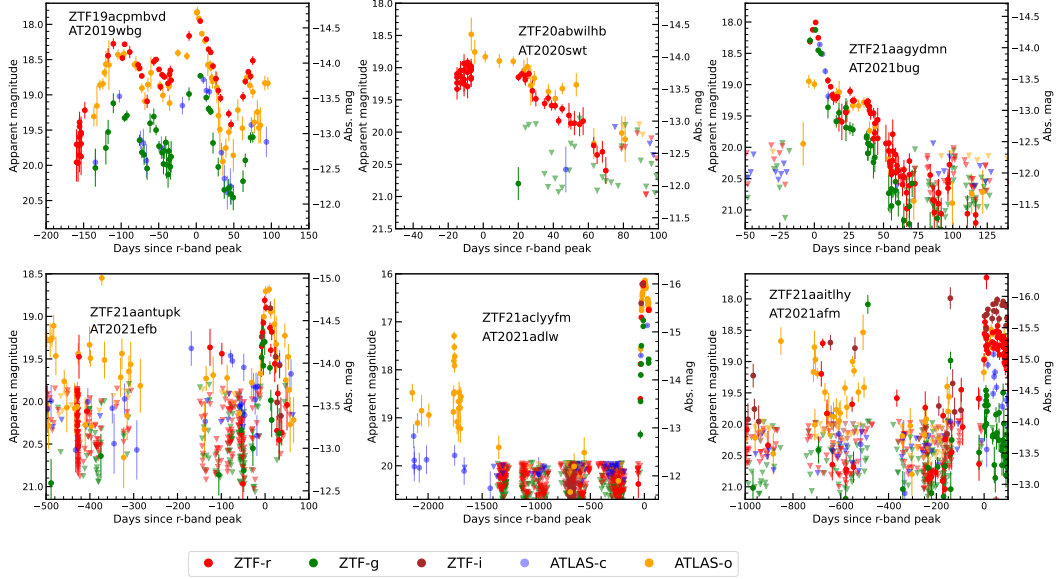


Figure 8.14: Light curves of transients that are possible LBV outbursts.

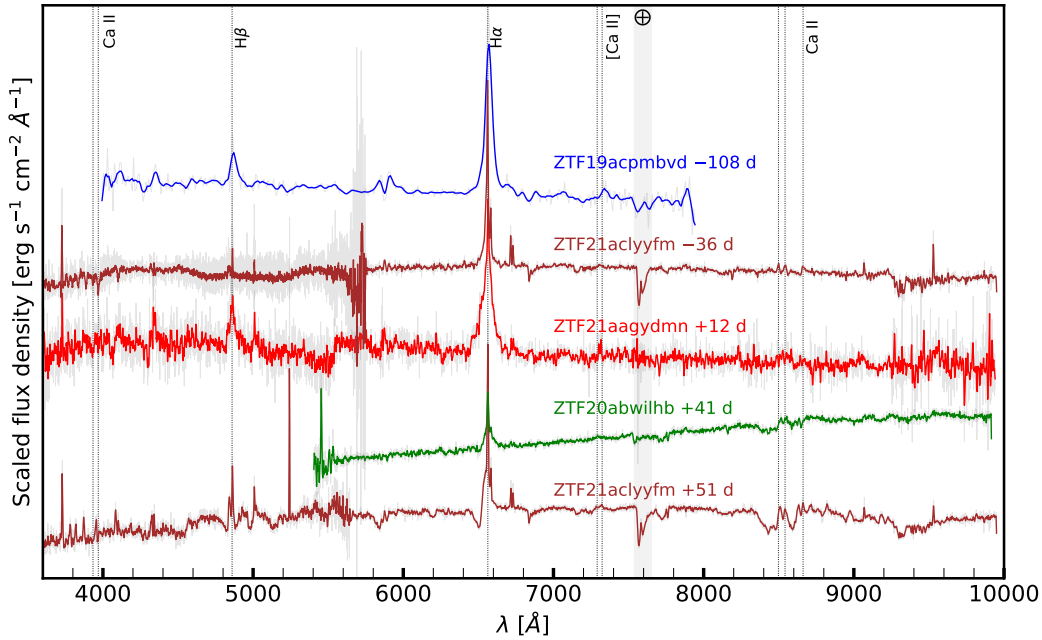


Figure 8.15: Optical spectra of transients that are possible LBV outbursts.

detected in 2016 in iPTF data with  $m_g \approx 22$  mag. It was redetected in ZTF in 2022 at  $m_r \approx 19.5$  mag. A spectrum taken during this outburst shows H $\alpha$  emission with  $\nu_{\text{FWHM}} \approx 1700 \text{ km s}^{-1}$ .

- **ZTF 20abwilhb (AT 2020swt)** is located in the galaxy UGC 03820. The light

curve does not show multiple peaks, but exhibits signs of a  $\sim$ 40 day plateau, after which the transient declines. The optical spectrum has  $\text{H}\alpha$  emission with  $v_{\text{FWHM}} \approx 3300 \text{ km s}^{-1}$ , suggesting that this transient could be an LBV outburst or a low-luminosity Type II SN.

- **ZTF 21aagydmn (AT 2021bug)** is located in the galaxy NGC 4533 and exhibits an unusual light curve that peaks at  $M_r \approx -14.4$  mag, thereafter declining quickly. Once off the first decline, the light curve plateaus for  $\sim$ 10 days, and then continues to decline. The spectrum shows  $\text{H}\alpha$  emission with  $v_{\text{FWHM}} \approx 2600 \text{ km s}^{-1}$ ; however, the light curve does not have a long-duration plateau as seen in low-luminosity Type II SNe. The true nature of this source is unclear, but an outburst in a massive star is a possibility.
- **ZTF 21aantupk (AT 2021efb)** is located at the nucleus of the galaxy CGC 003-005. The light curve shows erratic activity in the ATLAS and the ZTF data for several hundred days prior to the main explosion in 2021. We suggest that this source is either an LBV outburst or AGN activity.
- **ZTF 21aclyyfm (AT 2021adlw)** is located in the galaxy NGC 3813, and reached  $M_r \approx -16$  mag in the 2021 outburst. Archival ATLAS data show that it underwent a similar outburst ( $M_o \approx -15$  mag) about 1800 days prior to this outburst. An optical spectrum taken at an early phase during the 2021 outburst shows narrow  $\text{H}\alpha$  emission with  $v_{\text{FWHM}} \approx 1000 \text{ km s}^{-1}$ ; however, late-time spectra reveal ejecta with much larger velocities. This source is likely an LBV outburst or a “weak” Type IIn SN.
- **ZTF 21aaithy (AT 2021afm)** is located close to the center of the galaxy NGC 5657. It had several detections in ATLAS and ZTF data in the  $\sim$ 1000 days leading up to the 2021 explosion. We also detect the transient in the  $g$  band in PTF data taken during July 2011 and April 2016 at  $m_g \approx 20$  mag. Owing to the extensive archival activity, we categorize this source as a possible LBV outburst.

**HOT SPRINGS AND DUST RESERVOIRS: JWST REVEALS  
THE DUSTY, MOLECULAR AFTERMATH OF  
EXTRAGALACTIC MASSIVE STAR MERGERS**

To be submitted to ApJ.

V. R. Karambelkar<sup>1</sup>, M. M. Kasliwal<sup>1</sup>, N. Blagorodnova<sup>2</sup>, J. Jencson<sup>3</sup>, R. Lau<sup>4</sup>,  
K. De<sup>5</sup>, H. Tranin<sup>2</sup>, M. Wavaseur<sup>2</sup>

<sup>1</sup>Cahill Center for Astrophysics, California Institute of Technology, Pasadena, CA 91125,  
USA

<sup>2</sup>Institut de Ciències del Cosmos (ICCUB), Universitat de Barcelona (UB), c. Martí i  
Franquès, 1, 08028 Barcelona, Spain

<sup>3</sup>IPAC, California Institute of Technology, Pasadena, CA 91125, USA

<sup>4</sup>NSF NOIRLab, 950 N. Cherry Ave., Tucson, AZ 85719, USA

<sup>5</sup>Columbia University, 538 West 120th Street 704, MC 5255, New York, NY 10027

**Abstract**

We present *James Webb Space Telescope (JWST)* observations of four Luminous Red Novae (LRNe) : dusty, extragalactic transients from massive stellar mergers. These four LRNe — AT 2021blu, AT 2021biy, AT 2018bwo, and M31-LRN-2015 — span a broad range in progenitor primary masses ( $\approx 3$ – $20 M_{\odot}$ ) and phases since merger ( $\approx 1100$ – $3700$  days) at the time of the *JWST* observations. Our *JWST* observations comprise multiband 5–25  $\mu\text{m}$  photometry with the Mid-Infrared Instrument (MIRI) for all four sources, and additionally 5–12  $\mu\text{m}$  spectra with Low-Resolution Spectrograph (LRS) for AT 2021blu and AT 2021biy. The LRS spectra are dominated by absorption features of water vapor, CO, and SiO. We measure water vapor column densities of  $\approx 10^{22} \text{ cm}^{-2}$  that are larger than normal red supergiant stars, but consistent with those seen in Galactic stellar mergers. Our detection of water vapor streaming away from stellar merger remnants supports the association of water fountain sources with common-envelope events. We model the full infrared SEDs of these LRNe using the radiative transfer code DUSTY and derive dust masses of

$\approx 4.2 \times 10^{-5}$ ,  $3 \times 10^{-4}$ ,  $7.5 \times 10^{-5}$ , and  $7.7 \times 10^{-4} M_{\odot}$  for the four LRNe, respectively. These dust masses are  $\approx 10\%$ ,  $60\%$ ,  $6\%$  and  $12\%$  of the median expected dust masses in CCSNe at similar phases. Accounting for their occurrence rates, the total dust contribution of LRNe is  $\sim 25\%$  of CCSNe. The total dust masses formed are lower than those expected from total ejected masses by at least an order of magnitude, suggesting that dust formation occurs on much longer timescales around these sources. Our results advocate for *JWST* observations of a broader sample of LRNe covering even older phases to measure their terminal dust yields, quantify their contribution to the cosmic dust budget, study the evolution of molecules, and probe pre-merger mass loss during the CE phase.

## 9.1 Introduction

Luminous Red Novae (LRNe) are transient eruptions associated with stellar mergers as a consequence of common-envelope evolution (CEE) in binary stars (Pastorello et al. 2019a; Ivanova et al. 2013b; Blagorodnova et al. 2021; Kulkarni et al. 2007; Kasliwal et al. 2011). These transients provide a valuable opportunity to study CEE — a crucial but poorly understood phase in binary evolution that plays a key role in the formation of double compact objects, which are important sources of gravitational waves (Ivanova et al. 2013a; Vigna-Gómez et al. 2020; Dominik et al. 2012; Postnov et al. 2014; Marchant et al. 2021). Additionally, LRNe are prolific dust producers, and offer insights into the contribution of CEE events to the cosmic dust budget (Bermúdez-Bustamante et al. 2024; Lü et al. 2013).

LRNe span a wide range of peak luminosities ( $-15 \leq M_r \leq -3$  mag), which are correlated with the mass of the primary star (Blagorodnova et al. 2021; Pastorello et al. 2019a). The lower-luminosity members of this class, often referred to as red novae (RNe), are primarily Galactic events with primary star masses between  $\approx 1 - 8 M_{\odot}$  (Tylenda et al. 2011a; Munari et al. 2002; Tylenda et al. 2005; Tylenda et al. 2013). In contrast, more luminous LRNe ( $M_{r,peak} \leq -10$  mag) are extragalactic transients involving primary stars more massive than  $10 M_{\odot}$  (Blagorodnova et al. 2021). Despite their broad luminosity range, these transients exhibit similar late-time behaviors, marked by a shift of the emitted light to infrared (IR) wavelengths due to dust-formation, and spectra resembling M-type supergiant stars with strong absorption features due to oxygen-rich molecules (Blagorodnova et al. 2020; Karambelkar et al. 2023b; Tylenda 2005). Furthermore, LRNe have high occurrence rates, with Galactic low mass red novae having an estimated rate of  $\sim 0.5 \text{ yr}^{-1}$  (Kochanek et al. 2014) and extragalactic massive LRNe occurring at a volumetric rate that is

$\approx 77\%$  of the local core-collapse supernova (CCSN) rate (Karambelkar et al. 2023b).

Given their high occurrence rates and dusty nature, LRNe may be significant contributors to the cosmic dust budget (Lü et al. 2013; Bermúdez-Bustamante et al. 2024). Late-time IR and sub-mm observations of the Galactic RNe show that their remnants are enshrouded in substantial amounts of dust and molecules (Nicholls et al. 2013; Lynch et al. 2007a; Banerjee et al. 2004; Banerjee et al. 2007; Woodward et al. 2021; Steinmetz et al. 2025). The more luminous extragalactic LRNe have larger ejected masses (Matsumoto et al. 2022) and are thus expected to produce even more dust than their Galactic counterparts. Given their volumetric rate is comparable to CCSNe — considered to be major cosmic dust sources (Nozawa et al. 2003; Sarangi et al. 2015) — these LRNe could represent an equally important dust production channel. Moreover, while CCSN-generated dust can be partially destroyed by reverse shocks propagating through their ejecta, the lower velocities of LRNe suggest a reduced destruction fraction (e.g., Nozawa et al. 2007; Slavin et al. 2015; Slavin et al. 2020). Thus, extragalactic LRNe could be major contributors to the cosmic dust budget and could explain unusually dusty galaxies in the early universe (Dwek et al. 2007). However, no LRNe have been observed at late times at mid-IR wavelengths, leaving their dust production largely unquantified.

In addition to dust, late-time observations of LRNe can shed light on the formation and evolution of molecules as they condense to form ice and dust. IR and sub-mm observations of Galactic RNe years after their eruptions reveal complex, bipolar ejecta structures rich in gaseous molecules such as water vapor, CO, SiO, AlO (Kamiński et al. 2011; Kamiński et al. 2021; Kamiński et al. 2018; Steinmetz et al. 2024) as well as conglomerates such as water ice (Banerjee et al. 2004). However the molecular aftermath of the more massive LRNe has not been studied. Late-time observations also provide crucial insights about the CEE phase, as the dust masses can be used to infer whether CEE resulted in a stellar merger or an envelope ejection (MacLeod et al. 2017; Blagorodnova et al. 2017). Additionally, late-time rebrightenings in LRNe (Cai et al. 2022) are believed to be powered by interactions of the ejecta with circumstellar material (CSM), and provide a way to trace pre-merger mass loss during CEE. Despite their importance, late-time observations of the extragalactic LRNe have been limited in the past due to a lack of sensitive IR telescopes.

In this paper, we present the first late-time mid-IR observations of four LRNe obtained with the *James Webb Space Telescope (JWST)*. We model the observations

to measure the dust masses produced in these events and estimate their contribution to the cosmic dust budget relative to CCSNe. We also study the molecular content of the remnants and use the *JWST* observations to probe the late-time evolution of massive stellar merger remnants. We describe the properties of the four LRNe in Section 9.2, our *JWST* observations in Section 9.3, our modeling in Section 9.4, and discuss the implications of our findings in Section 9.5. We conclude with a summary of our results in Section 9.6.

## 9.2 The Luminous Red Novae

Four LRNe are presented in this paper — AT 2021blu (Pastorello et al. 2022; Karambelkar et al. 2023b), AT 2021biy (Cai et al. 2022; Karambelkar et al. 2023b), AT 2018bwo (Blagorodnova et al. 2021), and M31-LRN-2015 (Williams et al. 2015; MacLeod et al. 2017).

AT 2021blu and AT 2021biy were both discovered in early 2021 in the galaxies UGC 5829 (9.5 Mpc<sup>1</sup>) and NGC 4631 (7.7 Mpc), respectively. Their peak absolute magnitudes were  $M_{r,\text{peak}} = -13.50 \pm 0.15$  and  $-13.86 \pm 0.15$ , respectively, putting them at the luminous end of the LRN-luminosity function. Their lightcurves showed an initial blue peak of  $\approx 50$  days duration followed by a long plateau lasting a few hundred days. While this plateau in AT 2021blu lasted  $\approx 180$  days, the plateau-duration in AT 2021biy exceeded 250 days, substantially longer than seen in other LRNe with similar luminosities. The maximum light spectra show strong and narrow ( $v \leq 1000 \text{ km s}^{-1}$ ) emission lines of hydrogen. At late times, both transients evolve show strong infrared excesses (Karambelkar et al. 2023b) indicating dust-formation, and their spectra show the characteristic broad absorption bands of oxygen-rich molecules such as water vapour, TiO, VO. Archival pre-eruption imaging shows that the primary stars in the progenitor primary stars of both these transients were luminous yellow supergiant stars with masses between  $\approx 13\text{--}18 M_{\odot}$  for AT 2021blu (Pastorello et al. 2022) and  $\approx 17\text{--}24 M_{\odot}$  for AT 2021biy (Cai et al. 2022).

AT 2018bwo and M31-LRN-2015 were discovered in May 2018 and January 2015 in the galaxies NGC 45 (6.7 Mpc) and M 31 (0.77 Mpc), respectively. The transients reached peak absolute magnitudes of  $M_{r,\text{peak}} = -10.97 \pm 0.11$  and  $-9.5 \pm 0.1$ , respectively — placing them at the low luminosity end of extragalactic LRNe. In addition to their lower luminosities compared to AT,2021blu and AT,2021biy, they also had shorter durations, with initial blue peaks lasting  $\sim 10$  days and

---

<sup>1</sup>All distances taken from ned.ipac.caltech.edu, corrected for infall into the Virgo, GA, and Shapley clusters and assuming  $H_0 = 73 \text{ km s}^{-1} \text{ Mpc}^{-1}$ .

subsequent plateaus lasting  $\approx$ 41 days each. Despite this, they show characteristic LRN signatures with low expansion velocities ( $\sim$ 100 km s $^{-1}$ ) and late-time spectra that resemble M-type stars with molecular absorption features. Archival imaging revealed the progenitor primary masses of 12–16 M $_{\odot}$  for AT 2018bwo, and 3–5 M $_{\odot}$  for M31-LRN-2015.

The differences in luminosities and durations observed in these LRNe have been attributed to different ejecta masses (Matsumoto et al. 2022) which likely correlate with the progenitor masses (Blagorodnova et al. 2021). The range of luminosities, durations, progenitor masses, and phases since eruption spanned by these four LRNe allow for studying dust-formation across a wide range of the stellar merger phase space.

### 9.3 Observations and data reduction

All *JWST* observations of the four LRNe were conducted as part of the GO Program 4244 (PI Karambelkar).

#### AT 2021blu

##### JWST observations

AT 2021blu was observed with the Mid-Infrared Instrument (MIRI, Wright et al. 2023) aboard the *JWST* on 2024 April 3. The observations comprised of a R $\sim$  100 spectrum covering 5–12  $\mu$ m obtained with the Low-Resolution Spectrometer (LRS) and broadband imaging observations in the F1280W, F1500W, F1800W, F2100W and F2550W filters. Calibrated data were downloaded from the MAST portal. The LRS data were reduced using version 1.13.3 of the *JWST* science calibration pipeline and calibrated using version 11.17.14 of the CRDS with the 1223 CRDS context. The LRS spectra were extracted using the optimal extraction algorithm (Horne 1986) and LRS observations of the flux standard BD+60 1753 as a reference profile. The optimal extraction was implemented by adapting routines in the *JWST* data analysis tool notebook for MIRI LRS observations<sup>2</sup>

For the final spectral extraction of AT 2021blu, we used an extraction aperture with a full width of 11 pixels and background regions between 6 and 11 pixels from the center of the profile trace on either side. The background at the central trace position was determined using the average of the fluxes in the background regions. AT 2021blu is offset from its host galaxy and is relatively isolated, so we do not

---

<sup>2</sup>[https://spacetelescope.github.io/jdat\\_notebooks/](https://spacetelescope.github.io/jdat_notebooks/)

detect any structure in the background emission in the 2D-spectrum.

For the broadband imaging, we performed aperture photometry at the locations of AT 2021blu (RA=160.643049, Dec = +34.437396) on the MIRI images using an aperture that encloses 70% of the total flux and aperture corrections from `jwst_miri_apcorr_0010.fits`<sup>3</sup>.

### NEOWISE mid-IR observations

The field of AT 2021blu was observed multiple times by NEOWISE (Mainzer et al. 2014b) in the W1 and W2 bands as part of its survey on 2024 April 27 (24 days after the *JWST* observations). We stacked the NEOWISE frames from using the online NEOWISE image coadding service<sup>4</sup>. We constructed W1 and W2 reference images by coadding observations of the field from 2018. We subtracted the new images from the reference images using the ZOGY algorithm and performed PSF photometry at the location of AT 2021blu in the difference image. The measured flux values are listed in Table 9.1.

### NIR observations

We observed AT 2021blu in the NIR *J*, *H* and *Ks* bands with the Wide-field Infrared Camera (WIRC, Wilson et al. 2003b) on the 200-inch Hale telescope on 2024-06-05. The WIRC data were reduced using the python package `wircpipe` and PSF photometry was performed at the location of AT 2021blu to extract the fluxes. The NIR flux measurements are listed in Table 9.1.

We also obtained a NIR 1–2.5  $\mu\text{m}$  spectrum of AT 2021blu with the Near-infrared Echelle Spectrograph (NIRES, Wilson et al. 2004) on the Keck II 10 m telescope on 2024-06-16. The spectra were reduced, extracted and telluric corrected using the software `spextool` Vacca et al. (2003) and Cushing et al. (2004).

### AT 2021biy

*JWST* observations of AT 2021biy were conducted on 2024 June 8 and comprised of a 5–12  $\mu\text{m}$  MIRI LRS spectrum and MIRI imaging in the F1280W, F1500W, F1800W, F2100W, and F2550W filters. The spectra and images were reduced using the same methods described in Section 9.3.

---

<sup>3</sup>Downloaded from <https://jwst-crds.stsci.edu/>

<sup>4</sup><https://irsa.ipac.caltech.edu/applications/ICORE/>

Table 9.1: Infrared fluxes of the four LRNe

Filter	Date	Flux μJy
AT 2021blu		
J	2024-06-05	7.0 ± 1.8
H	2024-06-05	15.4 ± 3.1
Ks	2024-06-05	42.0 ± 4.2
W1	2024-04-27	150 ± 15
W2	2024-04-27	93 ± 23
F560W	2024-04-03	116.4 ± 1.2
F1280W	2024-04-03	100.7 ± 2.2
F1500W	2024-04-03	89.3 ± 2.7
F1800W	2024-04-03	73.1 ± 5.0
F2100W	2024-04-03	59.7 ± 6.8
F2550W	2024-04-03	51.0 ± 17.1
AT 2021biy		
F560W	2024-06-08	252.9 ± 7.0
F1280W	2024-06-08	359.0 ± 9.7
F1500W	2024-06-08	309.2 ± 8.4
F1800W	2024-06-08	293.9 ± 10.9
F2100W	2024-06-08	274.4 ± 13.0
F2550W	2024-06-08	247.0 ± 24.6
AT 2018bwo		
F560W	2024-07-04	86.0 ± 1.0
F770W	2024-07-04	114.1 ± 1.2
F1000W	2024-07-04	159.8 ± 1.3
F1130W	2024-07-04	172.9 ± 3.5
F1280W	2024-07-04	170.3 ± 2.1
F1500W	2024-07-04	167.9 ± 2.4
F1800W	2024-07-04	154.9 ± 3.6
F2100W	2024-07-04	134.6 ± 4.3
F2550W	2024-07-04	95.6 ± 16.5
M31-LRN-2015		
F560W	2025-01-16	46.2 ± 0.9
F770W	2025-01-16	227.0 ± 0.9
F1000W	2025-01-16	51.3 ± 1.2
F1130W	2025-01-16	162.4 ± 3.2
F1280W	2025-01-16	551.1 ± 2.7
F1500W	2025-01-16	740.8 ± 3.8
F1800W	2025-01-16	755.8 ± 4.6
F2100W	2025-01-16	1069.2 ± 5.3
F2550W	2025-01-16	1490.4 ± 17.9

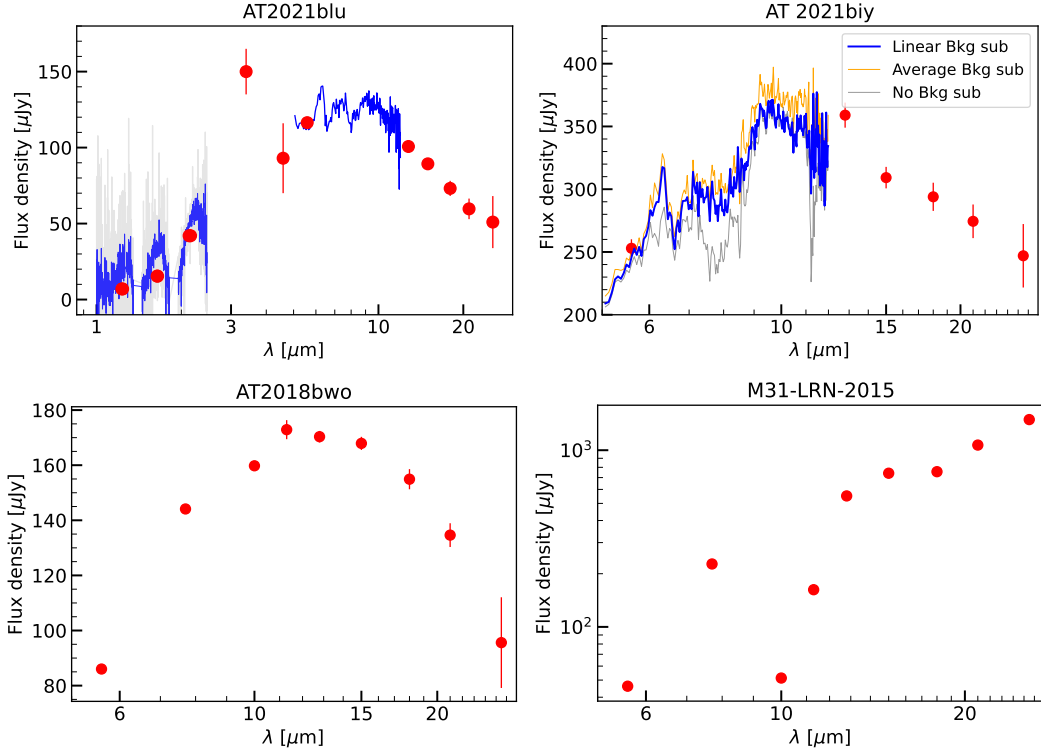


Figure 9.1: **The infrared spectral energy distributions of the four LRNe.** For AT 2021biy (top right), three reductions of the LRS spectrum are plotted with different methods of background subtraction (see text). In the rest of the paper, the reduction with linear background subtraction (blue) is adopted.

In contrast to AT 2021blu, AT 2021biy is located on top of a star-forming region within its host galaxy. Consequently, the 2D-spectrum shows a complex background profile, esp. in the  $8-10\text{ }\mu\text{m}$  range. For AT 2021biy, we used background regions between 5 and 13 pixels from the center of the profile trace on either side. We determined the background at the central trace location by fitting a linear function to the flux profiles in the left and right background regions. Fig. 9.1 shows a comparison of the extracted spectra of AT 2021biy with this linear-background subtraction, an average-background subtraction (similar to AT 2021blu) and without any background subtraction. Without background subtraction, the flux from AT 2021biy is significantly underestimated between  $8-10\text{ }\mu\text{m}$ . The linear and average-background subtracted spectra are broadly consistent with each other and only show slight differences in the profiles of the features. We use the linear-background subtracted spectrum for our analysis in this paper, but note that it is possible that some flux measurements in this wavelength range could be affected by the uncertain background levels.

For the imaging observations, we performed aperture photometry at the location of AT 2021biy (RA = 190.516707, Dec = +32.535532) using the process described in Section 9.3.

### AT 2018bwo and M31-LRN-2015

The MIRI observations of AT 2018bwo and M31-LRN-2015 were conducted on 2024 July 04, and 2025 January 16, respectively, and comprised of broadband imaging with the F560W, F770W, F1000W, F1130W, F1280W, F1500W, F1800W, F2100W, and F2550W filters for both sources. The data were processed and fluxes were measured using the same method described in Section 9.3 by performing aperture photometry at the locations of AT 2018bwo (RA=3.507175, Dec=−23.1932145) and M31-LRN-2015 (RA=10.533503, Dec=40.9169811).

The measured broadband fluxes and uncertainties are listed in Table 9.1. The LRS spectra are available online.

## 9.4 Analysis

### SEDs and Comparison with Galactic mergers

Figure 9.1 shows the infrared spectral energy distributions (SEDs) of the four LRNe. AT 2021blu and AT 2021biy have spectroscopic and photometric observations. The 5–12  $\mu\text{m}$  spectra of both these sources are dominated by strong features at 6  $\mu\text{m}$ , 7.5  $\mu\text{m}$  and a broad feature spanning 8–10  $\mu\text{m}$ . In the following sections, we show that these features can be explained by a combination of dust and O-rich molecules around the merger remnant. Molecular absorption from TiO and water vapor is also seen in the NIR spectrum of AT 2021blu. The AT 2021blu SED peaks around 5  $\mu\text{m}$ , while AT 2021biy peaks around 10  $\mu\text{m}$ , suggesting a colder dust temperature. AT 2018bwo and M31-LRN-2015 have only photometric observations, so we cannot identify any circumstellar molecules in them. The SED of AT 2018bwo peaks around 11  $\mu\text{m}$  and declines at longer wavelengths, similar to AT 2021biy. In contrast, the SED of M31-LRN-2015 rises sharply from 15 to 25  $\mu\text{m}$ , indicating much colder dust. The SED also shows a deep absorption feature at 10  $\mu\text{m}$ , generally attributed to silicate dust.

Fig. 9.2 compares the *JWST* mid-IR SEDs of the four LRNe to the Galactic stellar mergers V1309Sco (taken from Nicholls et al. 2013), V4332Sgr (Banerjee et al. 2007) and V838Mon (Woodward et al. 2021). In addition to these published data, we also downloaded reduced archival Spitzer Infrared Spectrograph (IRS; Houck et al. 2004) spectra for V838Mon and V4332Sgr from the Combined Atlas of Sources

with Spitzer IRS Spectra (CASSIS<sup>5</sup>; Lebouteiller et al. 2011; Lebouteiller et al. 2015). AT 2021blu and AT 2021biy were observed with *JWST* at 1144 and 1216 days since their optical *r*-band peaks. The shape of the mid-IR SEDs of AT 2021blu and AT 2021biy bear closest resemblance to that of V838Mon at a phase of 900 days since peak. The 6.3  $\mu\text{m}$  feature of AT 2021blu and AT 2021biy is also seen in the 6200 day spectrum of V838 Mon and has been attributed to water vapor Woodward et al. (2021), similar to T Tauri Stars (Sargent et al. 2014). Notably absent from their spectra are the strong, broad silicate absorption from 8–10  $\mu\text{m}$  that dominate the mid-IR spectra of V1309Sco at a phase of 700 days since peak, and V838 Mon and V4332 Sgr at phases >2000 days. AT 2018bwo and M31-LRN-2015 were observed at later phases of 2235 days and 3647 days since their respective peaks. AT 2018bwo shows a sharp rise from 5 to 8  $\mu\text{m}$  that is steeper than the other three LRNe, indicative of an emission feature. In the next section, we find that this behavior can be explained by silicate emission. M31-LRN-2015 shows a strong silicate absorption feature spanning 7 to 13  $\mu\text{m}$  similar to the very late time SEDs of V4332 Sgr and V838 Mon. Similar to these events, the SED of M31-LRN-2015 rises sharply towards wavelengths longer than 25  $\mu\text{m}$ .

### SED modeling

We now model the infrared SEDs of the four LRNe to constrain their dusty and molecular content. A detailed 3-D radiative transfer analysis is outside the scope of this paper. Here, we construct spherically symmetric models comprising a central star surrounded by shells of dust, using the radiative transfer code DUSTY. For the two sources with spectroscopic observations, we include an additional spherical shell with molecules to constrain column densities of different molecules.

### AT 2021blu and AT 2021biy

As the infrared spectra of AT 2021blu and AT 2021biy are dominated by strong molecular features, we attempt to model the SED as a combination of a central star surrounded by a dust shell and a second outer molecular shell. This geometry is motivated by ALMA observations of the Galactic stellar mergers (Kamiński et al. 2018; Kamiński et al. 2021), which show that the remnants are enshrouded in dust and molecules, with the molecules generally extending to larger radii than the dust. Under this assumption, we first model radiation from the star emerging through a dust shell using the radiative transfer code DUSTY (Ivezic et al. 1997; Ivezic et al.

---

<sup>5</sup><https://cassis.sirtf.com>; AORKeys : 10523136, 25433344, 10523392, 14867968, 25432064

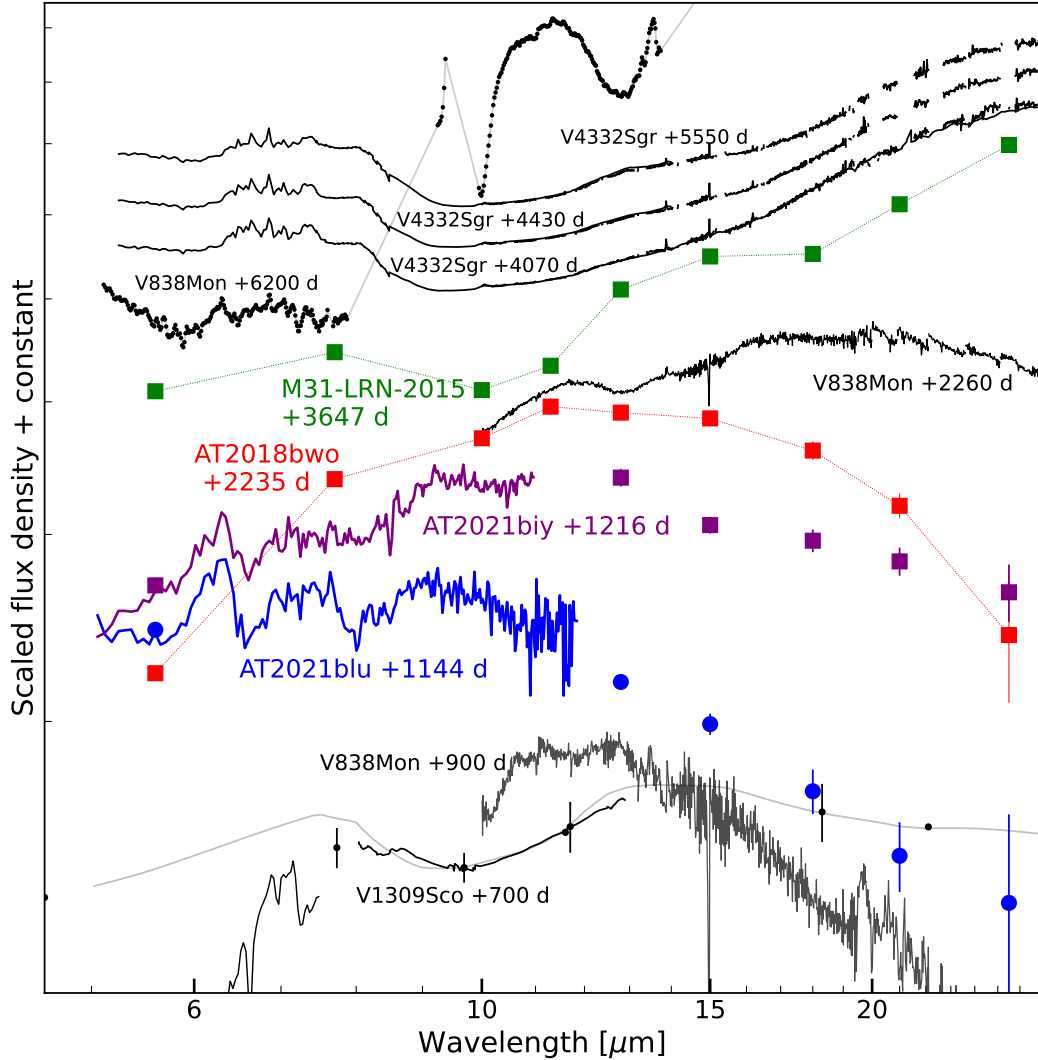


Figure 9.2: Comparison of the spectral energy distributions of the four LRNe (colored) to Galactic stellar mergers (black).

1999). Then we model the emergent radiation when the DUSTY output passes through the outer molecular shell to derive the column densities of molecules encountered in the outer regions of the CSM. A full description and calculation of our model is given in Appendix A.

For the DUSTY models, we assumed a standard Mathis et al. (1977) distribution for the dust grain sizes that assumes minimum and maximum grain sizes of  $0.005 \mu\text{m}$  and  $0.25 \mu\text{m}$ , respectively, and a grain-size power-law index of  $-3.5$ . We assumed a  $r^{-2}$  radial density profile for the dust shell and a shell-thickness ratio of 2. For the dust composition, we assumed a mixture of silicate and compact alumina dust

using the Sil-DL and Al2O3-comp opacities available in DUSTY. We assumed a silicate-to-alumina ratio of 0.5 (similar to V 838Mon; Woodward et al. 2021).

For the molecular modeling, we adopt a simple approach commonly used in stellar atmospheric modeling (see, e.g., Yamamura et al. 1999b; Yamamura et al. 1999a; Cami 2002; Sargent et al. 2014) in which the atmosphere is modeled using the plane-parallel approximation under local-thermodynamic equilibrium (LTE). In this approach, the molecular layer is characterized by four parameters — the excitation temperature, radius, column density and turbulent velocity. For our modeling, we assume a single circular molecular slab of temperature  $T_{\text{mol}}$  and radius  $R_{\text{mol}}$  comprising CO, H<sub>2</sub>O and SiO molecules with column densities  $N_{\text{CO}}$ ,  $N_{\text{H}_2\text{O}}$  and  $N_{\text{SiO}}$ , respectively, placed in front of the star and its dust shell. For AT 2021biy, we do not include CO as we do not have any NIR data to constrain this molecule. The absorption cross-sections for H<sub>2</sub>O and CO were calculated using data from the HITEMP online database<sup>6</sup> (Rothman et al. 2010), and from the Exomol database for SiO<sup>7</sup> (Yurchenko et al. 2021). The turbulent velocity of this layer is fixed to  $v_{\text{turb}} = 10 \text{ km s}^{-1}$ .

Our choice of these three molecules is motivated by their common occurrence in O-rich environments such as M-type stars and their high opacities in the wavelengths covered by our observations (see Sloan et al. (2015) for mid-IR spectra of M giants with these molecular features). All three molecules have been identified in the near to mid-infrared spectra of V838 Mon (Lynch et al. 2004; Woodward et al. 2021). Furthermore, the NIR spectra of AT 2021blu shows strong absorption features due to water vapor. Although we do not have NIR observations of AT 2021biy contemporaneous with the *JWST* observations, an older NIR spectrum presented in (Karambelkar et al. 2023b) shows similar water-vapor and CO absorption. It is therefore natural to include these molecules in the analysis of the mid-IR spectra. Water vapor has several strong transitions in the 5–8  $\mu\text{m}$  range that are expected to significantly absorb the continuum radiation in this region. The strong apparent emission feature peaking at 6.3  $\mu\text{m}$  in both our LRNe is actually caused by a minimum of water vapor opacity in the narrow wavelength range from 6–7  $\mu\text{m}$ . In addition to AT 2021blu and AT 2021biy, this feature has been detected in V838 Mon, several RSG stars (Tsuiji 2003) and outbursting FU-Ori stars (Sargent et al. 2014). SiO gas is also an important ingredient of molecules around RSGs and is responsible for the dip seen at 8  $\mu\text{m}$  in our spectra.

---

<sup>6</sup><https://hitran.org/hitemp>

<sup>7</sup><https://www.exomol.com/data/molecules/SiO/28Si-16O/SiOUVenIR/>

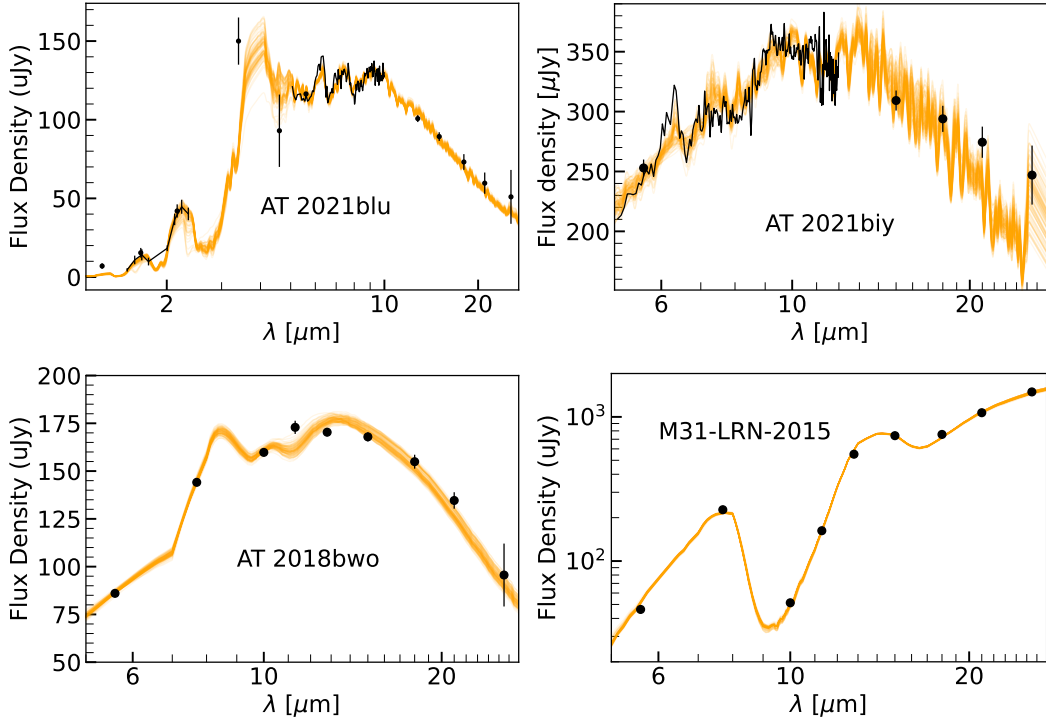


Figure 9.3: **Range of best-fit models (orange) from MCMC fits to the SEDs (black dots).**

In total, our model comprises eight free parameters (three DUSTY and five molecular) for AT 2021blu, and seven free parameters for AT 2021biy. We use Markov Chain Monte Carlo (MCMC) sampling implemented in the python package emcee (Foreman-Mackey et al. 2013a) to derive posterior distributions on these parameters, using wide and uniform priors. The resulting medians, 16<sup>th</sup> and 84<sup>th</sup> percentile values for the derived parameters are listed in Table 9.2. Fig. 9.3 shows the best-fit models for the two sources. The individual contributions of dust and molecules are shown in Figure 9.6 and the posterior distributions on all parameters are shown in Figures 9.7 and 9.8 in Appendix A.

For AT 2021blu, we find that the SED can be reproduced with a central star having a temperature  $\approx 2200$  K, surrounded by a shell of warm dust with  $T_{\text{dust}} \approx 1100$  K,  $\tau_V \approx 22$ , and an inner shell radius of  $\approx 100$  A.U. The molecular shell has a colder temperature of  $\approx 670$  K, and extends to a radius of  $\approx 170$  A.U.

In contrast, for AT 2021biy, we find the central star temperature is not very well constrained, possibly due to lack of near-infrared data. The dust shell is much colder and larger, with  $T_{\text{dust}} \approx 700$  K,  $\tau_V \approx 20$  and an inner radius of  $\approx 250 \pm 30$  A.U.

Table 9.2: Inferred dust and molecular parameters for the four LRNe

Source	AT 2021blu	AT 2021biy	AT 2018bwo	M31-LRN-2015
Phase [d]	+1144	+1216	+2235	+3647
Distance (Mpc)	9.5	7.7	6.74	0.77
$T_{\text{star}}$ [K]	$2200^{+200}_{-200}$	$2400^{+600}_{-600}$	$2600^{+400}_{-300}$	$6000^{+500}_{-300}$
$T_{\text{dust}}$ [K]	$1100^{+50}_{-50}$	$700^{+70}_{-70}$	$670^{+30}_{-30}$	$385^{+10}_{-10}$
$\tau_V, \text{tot}$	$22.4^{+1.2}_{-1.3}$	$20.3^{+2.8}_{-2.3}$	$15.0^{+0.8}_{-0.7}$	$100^{+5}_{-5}$
$a_{\text{sil}}$	0.5 (fixed)	0.5 (fixed)	$0.57^{+0.05}_{-0.05}$	$0.40^{+0.01}_{-0.01}$
$T_{\text{mol}}$ [K]	$670^{+30}_{-30}$	$660^{+110}_{-30}$	–	–
$\log(N_{\text{H}_2\text{O}}/\text{cm}^{-2})$	$22.0^{+0.1}_{-0.1}$	$22.5^{+0.2}_{-1.2}$	–	–
$\log(N_{\text{CO}}/\text{cm}^{-2})$	$21.1^{+0.7}_{-1.7}$	–	–	–
$\log(N_{\text{SiO}}/\text{cm}^{-2})$	$19.9^{+0.3}_{-0.3}$	$19.8^{+0.5}_{-0.5}$	–	–
$R_{\text{mol}}/10^{15}\text{cm}$	$2.1^{+0.2}_{-0.6}$	$2.7^{+0.7}_{-0.7}$	–	–
$R_{\text{dust,in}}/10^{15}\text{cm}$	$1.3^{+0.2}_{-0.2}$	$3.6^{+0.5}_{-0.5}$	$2.1^{+0.2}_{-0.2}$	$2.7^{+0.1}_{-0.1}$
$M_{\text{dust}}/10^{-5}\text{M}_{\odot}$	$4.2^{+0.7}_{-0.7}$	$30^{+5}_{-5}$	$7.5^{+1.0}_{-1.0}$	$77^{+5}_{-5}$
$L_{\text{tot}}/10^5\text{L}_{\odot}$	$3.3^{+0.2}_{-0.2}$	$4.2^{+0.2}_{-0.2}$	$1.48^{+0.06}_{-0.06}$	$4.62^{+0.07}_{-0.05} \times 10^{-2}$

The temperature of the molecular shell is  $\approx 660$  K, very similar to the dust shell temperature (unlike in AT 2021blu). The derived column densities of the molecules are similar to AT 2021blu.

### AT 2018bwo and M31-LRN-2015

As we do not have any spectroscopic data for AT 2018bwo and M31-LRN-2015, we do not attempt to constrain their molecular content. Instead, we model their SEDs assuming only a central star surrounded by a dust shell using DUSTY. These sources were observed  $\approx 7$  and 10 years since their eruptions, respectively. At these late phases, silicate dust features are expected to dominate the molecular features in the 8–10  $\mu\text{m}$  region (see, e.g., V838 Mon, Woodward et al. 2021), so adding molecules to our models is not expected to substantially change the inferred dust properties. M31-LRN-2015 in particular shows a very deep silicate absorption feature in its SED, and so we are confident that our modeling will recover the true dust properties despite excluding molecules. We discuss the possible effects of molecular contributions to AT 2018bwo in the next subsection.

We model the multiband fluxes of these two sources using DUSTY with four free parameters ( $T_{\text{star}}$ ,  $T_{\text{dust}}$ ,  $\tau_V$ , and  $a_{\text{sil}}$ ), where  $a_{\text{sil}}$  is the relative abundance fraction of silicate dust. We assume similar dust grain sizes and density profiles as described in Section 9.4. For AT 2018bwo, we assume a dust composition comprising alumina

and silicate dust as before, but the ratio of silicate ( $a_{sil}$ ) is a free parameter. For M31-LRN-2015, we do not find satisfactory fits using silicate and alumina dust. Instead, we find good matches with silicates and glassy olivines — similar to the composition inferred for the Galactic merger OGLE-2002-BLG-360 (Steinmetz et al. 2025). Based on this, we assume that the dust composition for M31-LRN-2015 a mixture of silicates and glassy olivines, with their relative ratio as a free parameter. We use `emcee` to fit the models to the data and derive posterior distributions on the parameters. The derived parameters are listed in Table 9.2. The best-fit models are plotted in Figure 9.3. The posteriors are shown in Figures 9.9 and 9.10 in the Appendix.

For AT 2018bwo, we find a central star temperature of  $\approx 2600$  K with a dust shell having  $T_{dust} \approx 650$  K,  $\tau_V \approx 17$  and  $a_{sil} \approx 0.6$ , and an inner radius of  $\approx 150$  A.U. In contrast, for M31-LRN-2015, we find a much cooler dust shell with  $T_{dust} \approx 320$  K and a much larger  $\tau_V \approx 100$ . The best-fit silicate fraction  $a_{sil} \approx 0.4$ , and the outer radius of the dust shell is  $\approx 200$  A.U.

## Caveats

First, we note that AT 2021blu and AT 2021biy do not show any pronounced silicate features due to molecules, so their dust masses could be overestimated by our modeling. To test this, we attempted to fit their SEDs using models comprised of a blackbody stellar photosphere surrounded by molecules, without any dust. We find that while these models fit the 5–8  $\mu$ m region reasonably well, they underestimate the continuum flux at longer wavelengths. The characteristic continuum shape produced by the DUSTY models is required to reproduce these longer wavelength observations. Furthermore, for the best fitting no-dust models, the underlying blackbody photosphere has a temperature of  $\approx 900$  K. No stars have such low photospheric temperatures, suggesting that the underlying photosphere is indeed formed by a warm dust shell. Through our MCMC modeling, we are able to constrain the properties of this dust shell reasonably well, suggesting that the reported dust masses are unlikely to be substantially overestimated, but future observations when more dust has formed and the silicate feature dominates the SED will verify the masses presented here for these two sources.

Next, the dust-masses of AT 2018bwo and M31-LRN-2015 could be affected by molecules which we do not model, as only photometric data is available for these two sources. The effect of molecules is likely very small for M31-LRN-2015, as the

dust properties are very well constrained by the strong silicate absorption feature that dominates its SED. For AT 2018bwo, the effect of molecules could be higher. To test this, we converted the *JWST* observations of AT 2021blu to multiband photometric measurements by convolving the LRS spectrum with the transmission curves of the *JWST* filters, and fit it with DUSTY models without any molecules. We find a dust mass of  $\approx 5 \times 10^{-5} M_{\odot}$ , slightly larger than the value of  $4.2 \times 10^{-5} M_{\odot}$  derived from dust+molecules modeling. Thus, we conclude that while the dust masses for AT 2018bwo could be overestimated, it is unlikely to be substantially lower than the value reported here.

Finally, for our modeling, we have assumed a simple spherically symmetric geometry for dust, surrounded by molecules. In reality, the geometry is likely more complicated, with dust and molecules mixed with each other. Sub-mm observations reveal the complex bipolar morphology of this ejected material around the remnant (Kamiński et al. 2018; Kamiński et al. 2021). Although our simple models provide reasonably good fits to the SEDs, future studies that conduct 3D radiative transfer simulations can provide more information about the geometry of the ejecta.

## 9.5 Discussion

### Dust masses and contribution to the cosmic dust budget

We use the dust shell parameters derived from DUSTY modeling to determine the mass of the dust formed around the LRNe using the following relation derived by Lau et al. 2025 (in prep.) :

$$\frac{M_d}{M_{\odot}} \approx 2.4 \times 10^{-11} \left( \frac{R_{\text{in}}}{50 R_{\odot}} \right)^2 \left( \frac{\tau_V}{0.7} \right) \left( \frac{Y}{5} \right) \left( \frac{\kappa_V^d}{10^4 \text{ cm}^2 \text{ g}^{-1}} \right)^{-1}. \quad (9.1)$$

The dust masses measured for the four LRNe are  $\approx 4.2 \times 10^{-5}$ ,  $3 \times 10^{-4}$ ,  $7.5 \times 10^{-5}$ , and  $7.7 \times 10^{-4} M_{\odot}$  for AT 2021blu, AT 2021biy, AT 2018bwo, and M31-LRN-2015, respectively. The exact values and uncertainties are reported in Table 9.2. Of these four sources, dust masses have previously been reported only for M31-LRN-2015 at phases of 43 to 1276 days since maximum (Blagorodnova et al. 2020). The dust masses measured in their study increased from  $\approx 10^{-7} M_{\odot}$  at 46 days to  $\sim 10^{-3} M_{\odot}$  at 1276 days during this period. This does not agree with our late-time measurement of  $7.7 \times 10^{-4} M_{\odot}$  at +3647 days. However, the SEDs modeled in that study contained data only at wavelengths shorter than 5  $\mu\text{m}$ , with the final epoch (1276 days) SED comprising only one detection at 4.5  $\mu\text{m}$  and three non-

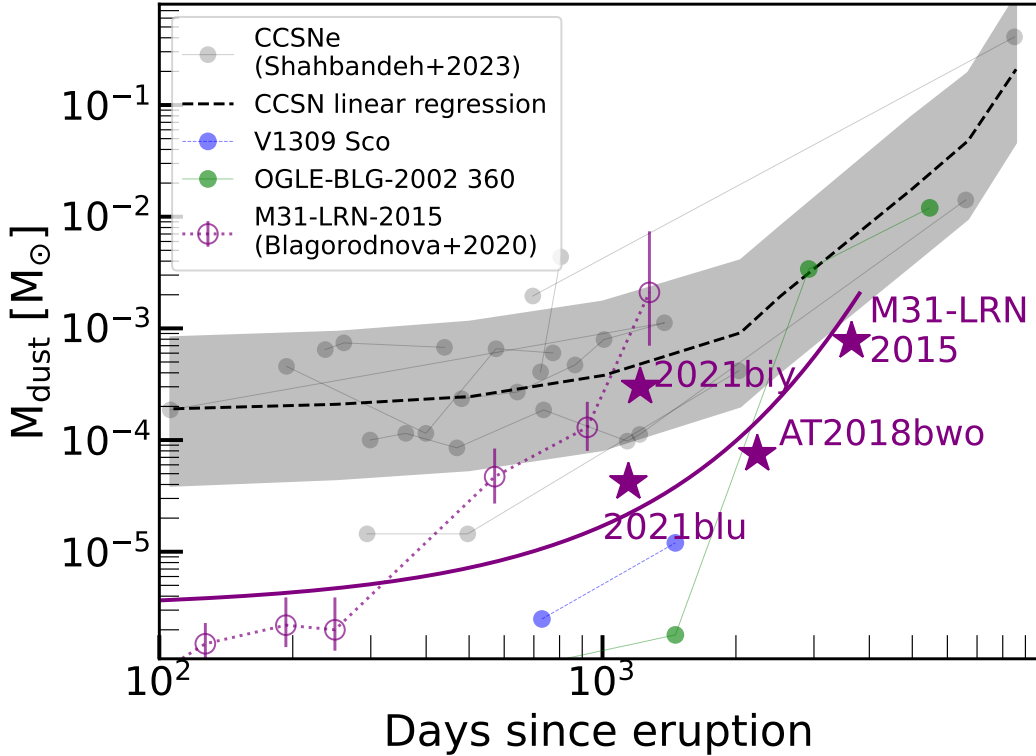


Figure 9.4: Dust masses inferred for the four LRNe in this paper (purple stars), compared with CCSNe (black dots), previous NIR-based measurements for M31-LRN-2015 (hollow purple circles), and Galactic LRNe V1309 Sco (blue) and OGLE-2002-BLG-360 (green) with regression fits to LRNe (purple solid line) and CCSNe (black dashed line). The dust masses of the LRNe AT 2021blu, AT 2021biy, AT 2018bwo, and M31-LRN-2015 are  $\approx 10\%$ ,  $60\%$ ,  $6\%$  and  $12\%$  of the median expected dust masses in CCSNe at similar phases. After accounting for occurrence rates relative to CCSNe, we estimate that the total dust produced by these LRNe is  $\sim 25\%$  of CCSNe.

detections at shorter wavelengths. Consequently, some of their measurements are likely inaccurate, and at least the final-epoch measurement is inconsistent with our longer wavelength observations.

Figure 9.4 shows our dust mass measurements of the four LRNe as a function of the time since their eruption (purple stars). We also include the previous measurements of M31-LRN-2015 for comparison as hollow circles. In general, the dust masses appear to increase with phase since the eruption. To visualize this, we fit a gaussian process regression model to the LRN measurements and plot the range of expected dust masses as a purple shaded region in Figure 9.4. For this fit, we included all four of our measurements and all but the last two epochs of the previous M31-LRN-2015

measurements. Also plotted in Figure 9.4 are the dust-masses for core collapse supernovae (CCSNe, taken from Shahbandeh et al. 2023) and a regression fit to the CCSN dust masses (also from Shahbandeh et al. 2023). Comparing our *JWST* measurements to CCSNe, we find that the dust masses for AT 2021blu, AT 2021biy, AT 2018bwo, and M31-LRN-2015 are  $\approx 10\%$ ,  $60\%$ ,  $6\%$  and  $12\%$  of the median expected dust masses in CCSNe at similar phases. The previous Blagorodnova et al. (2020) M31-LRN-2015 measurements, if to be believed, suggest lower dust masses ( $\approx 2\%$ ) compared to CCSNe at phases  $< 500$  days. Clearly AT 2021biy is an outlier, and has a larger dust mass than AT 2021blu at a similar phase. This is likely due to a combination of a larger ejected mass from the more massive progenitor of AT 2021biy, and dust-formation in the outer layers of the ejecta due to shock-interactions with CSM.

To estimate the contribution of LRNe to the cosmic-dust budget relative to CCSNe, we convolve the dust masses with the LRN-volumetric rates. We use the rates and luminosity function derived in Karambelkar et al. (2023b) (which is valid for  $M_{r,\text{peak}} < -11$  mag) for AT 2018bwo, AT 2021blu, and AT 2021biy. For M31-LRN-2015 ( $M_{r,\text{peak}} = -9.5$  mag), we use the Galactic merger rate and luminosity function from Kochanek et al. (2014), which predicts a rate of  $\sim 0.03 \text{ yr}^{-1}$  for mergers with  $M_V \approx -10$  mag. We assume a local volumetric CCSN rate of  $\approx 10^{-4} \text{ Mpc}^{-3} \text{ yr}^{-1}$  (Perley et al. 2020) and a Galactic CCSN rate of  $\approx 0.016 \text{ yr}^{-1}$  (Rozwadowska et al. 2021) to convert LRN rates to those relative to CCSNe. We find that the rate-corrected total dust mass in these four LRNe is  $\sim 25\%$  of the median dust mass in CCSNe, dominated by M31-LRN-2015 which is the least luminous and hence the most common of the four LRNe. We note that if we extrapolate the Karambelkar et al. (2023b) luminosity function to the luminosity of M31-LRN-2015, we obtain a larger dust mass of  $\approx 40\%$  of CCSNe. Our estimate suggests that the dust contribution of LRNe to the cosmic dust-budget is  $\approx 25\%$  of CCSNe. However, this is likely a lower limit, due to the following reasons.

First, for all four LRNe, dust formation probably continues beyond the epochs probed by the *JWST* observations. All four LRNe have different progenitor masses and luminosities, and likely have different dust-formation timescales. For example, we find the largest dust mass for M31-LRN-2015 — the source with the lowest luminosity and the lowest progenitor mass in our sample. AT 2018bwo, AT 2021blu and AT 2021biy have progenitors  $\sim 4\text{--}7$  times more massive than M31-LRN-2015 and their luminosities suggest about an order of magnitude more ejected mass than

M31-LRN-2015. Thus, they are expected to produce more dust in the long term than M31-LRN-2015, which would bring their terminal dust yields closer to CCSNe. However, the presence of a more massive remnant could keep the ejecta warm for longer periods, prolonging the dust formation timescales compared to M31-LRN-2015. Long-term, multi-epoch IR monitoring of LRNe together with theoretical studies of dust-formation in LRNe is required to address this issue and determine the terminal dust yields of LRNe.

Second, while CCSNe produce large amounts of dust, a substantial fraction of this dust can be destroyed by the reverse shock passing through the supernova ejecta. Several theoretical studies have attempted to estimate the efficiency of dust destruction in SNe and found results ranging from little to complete destruction, depending on the grain size and dust composition. In general, smaller grains are easily destroyed, while larger grains can survive longer (Nozawa et al. 2007). For silicate dust, several studies have found dust survival fractions of  $\sim 10\text{--}20\%$  (Slavin et al. 2020; Micelotta et al. 2016; Silvia et al. 2010; Bianchi et al. 2007). Lower survival fractions of a few percent are predicted by Bocchio et al. (2016), Kirchschlager et al. (2019), and Priestley et al. (2022), and higher survival fractions are supported by Nozawa et al. (2007) (0.2 - 1.0) and Nath et al. (2008) ( $>80\%$ ). Biscaro et al. (2016) find that dust survival also depends on the SN type with most of the dust destroyed in Type IIb SNe, 14-45% dust surviving in Type II-P SNe, 6–11% survival in CasA, and 42–98% survival in dense ejecta of SN 1987A. While the dust-destruction in LRNe has not been quantified, their substantially lower velocities ( $\sim 100 \text{ km s}^{-1}$ ) compared to CCSNe ( $\sim 1000 \text{ km s}^{-1}$ ) suggest lesser dust destruction. The rate of dust destruction is expected to increase steeply with shock velocity (see, e.g., McKee 1989; Jones et al. 1994). Slavin et al. (2020) find that the surviving fraction of dust depends on the relative velocity of the dust grains and the shocked gas, with a dust survival rate of more than 90% for a relative velocity of  $100 \text{ km s}^{-1}$ , and less than 40% for a relative velocity of  $1000 \text{ km s}^{-1}$ . Thus, a large fraction of the dust produced in LRNe could eventually make its way into the ISM, unlike CCSNe. A dust survival rate of 10–20% for CCSNe would then imply comparable contributions from LRNe and CCSNe to the cosmic dust budget. Future studies quantifying the destruction of dust by low-velocity shocks in LRNe will help address this.

Finally, our four LRNe do not capture the full variety of stellar mergers. The progenitors of all four LRNe had YSG primaries, but stellar mergers with red giant

or supergiant primaries are expected to produce more dust (MacLeod et al. 2022). In Figure 9.4, we also show the inferred dust masses for the Galactic stellar merger OGLE-BLG-2002-360 — the only known example of a giant star merger (taken from Tylenda et al. 2013; Steinmetz et al. 2025). About fifteen years since its eruption, this source has formed  $\approx 10^{-2} M_{\odot}$  of dust, similar to CCSNe at this phase. Historically, optical surveys have missed these dusty mergers but this population is being unveiled by the advent of infrared time-domain surveys. Future IR observations of the wider variety of stellar mergers will be crucial to quantify the full dust contributions of stellar mergers to the cosmic dust budget.

In conclusion, our observations suggest that the dust masses produced in LRNe are  $\sim 25\%$  of those in CCSNe. However, the higher dust destruction fraction in CCSNe compared to LRNe together with possibly longer timescales of dust formation in massive stellar mergers could make the dust contributions of LRNe comparable to CCSNe. Our results strongly advocate for multi-epoch IR monitoring of a wider variety of LRNe to trace their dust formation timescales and terminal dust yields.

### Water vapor and molecules

The *JWST* spectra of AT 2021blu and AT 2021biy are dominated by features of water vapor and other O-rich molecules. This is not surprising, as large molecular-rich clouds have been detected around the Galactic stellar mergers (Lynch et al. 2004; Lynch et al. 2007a; Kamiński et al. 2015; Kamiński et al. 2018; Kamiński et al. 2021), and NIR spectra of several LRNe show absorption features due to these molecules (Karambelkar et al. 2023b; Blagorodnova et al. 2020; Pastorello et al. 2022; Cai et al. 2022). We used our *JWST* observations to estimate the column densities of these molecules for the two extragalactic LRNe. The derived molecular column densities from Table 9.2 for water vapor, CO, and SiO of  $\approx 10^{22}$ ,  $10^{21}$ , and  $10^{20} \text{ cm}^{-2}$  are similar to the values measured for V838 Mon (Lynch et al. 2004).

The water vapor column densities in LRNe are generally higher than those measured in red giant and supergiant stars, which have column densities of  $\sim 10^{18} \text{ cm}^{-2}$  (Tsuji 2003). Some supergiants, such as Betelgeuse and  $\mu$ Cep, have been identified with possible molecular spheres outside of their photospheres (a.k.a. *molspheres* Tsuji 2006) with water vapor column densities of  $\approx 10^{20} \text{ cm}^{-2}$  (Tsuji 2000; Ohnaka 2004; Tsuji 2006) — still lower than the values found for LRNe. The molecular shell radii measured for our LRNe suggest expansion velocities of  $\sim 250$  and  $300 \text{ km s}^{-1}$  for AT 2021blu and AT 2021biy — consistent with the molecules being formed in the

outer layers of expanding ejecta. The enhanced column densities in the LRNe thus suggest large amounts of water vapor streaming away from the merger remnant. Using the radii, we estimate the mass of the water vapor to be  $\sim 1 - 3 \times 10^{-3} M_{\odot}$  for AT 2021blu and  $10^{-3} - 10^{-2} M_{\odot}$  for AT 2021biy.

Our observation of large amounts of water vapor streaming away from stellar merger remnants supports the recent association of Galactic water-fountain sources with common-envelope events (Khouri et al. 2021). These water fountains are characterized by  $> 100 \text{ km s}^{-1}$  water maser emission arising from jets excavating dusty circumstellar envelopes, and have unusually high mass loss rates that can be explained by a recent common-envelope event. They also have a characteristic geometry with bipolar lobes around the remnant surrounded by slow expanding gas in a toroidal configuration perpendicular to the lobes (Sahai et al. 2017). Future 3-D modeling of our observations of AT 2021blu and AT 2021biy is required to test whether such a geometry is present around their remnants.

Finally, the detection of molecules in the mid-IR spectra of these massive stellar mergers provides an opportunity to study the long-term evolution of molecules in oxygen-rich environments. It will be particularly interesting to study the transition of water-vapor to water-ice, which has been detected in the late-time IR spectrum of the Galactic stellar merger V4332 Sgr (Banerjee et al. 2004) through its broad absorption feature at  $3 \mu\text{m}$ . Continued spectroscopic observations of the  $8 - 10 \mu\text{m}$  range that covers the silicate-dust feature will enable studying the dust-condensation sequence of oxygen-rich environments, as more dust condenses onto the molecular seeds (e.g., Verhoelst et al. 2009).

### Late-time evolution of LRNe

We now use our *JWST* observations to study the late-time evolution of LRN remnants. Figure 9.5 shows the evolution of the luminosities, dust-shell radii, stellar and dust temperatures for the four LRNe. In addition to our *JWST* measurements, the previous values of these parameters for these sources are taken from Blagorodnova et al. (2020) and MacLeod et al. (2022) for M31-LRN-2015, Cai et al. (2021) and Karambelkar et al. (2023b) for AT 2021biy, Pastorello et al. (2022) for AT 2021blu, and (Blagorodnova et al. 2018) for AT 2018bwo.

The *JWST* luminosities show that all four LRNe have faded since their previous observations (Fig. 9.5 top panel). However, all four are brighter than extrapolations from their previous trends, suggesting that the luminosity decline has slowed down.

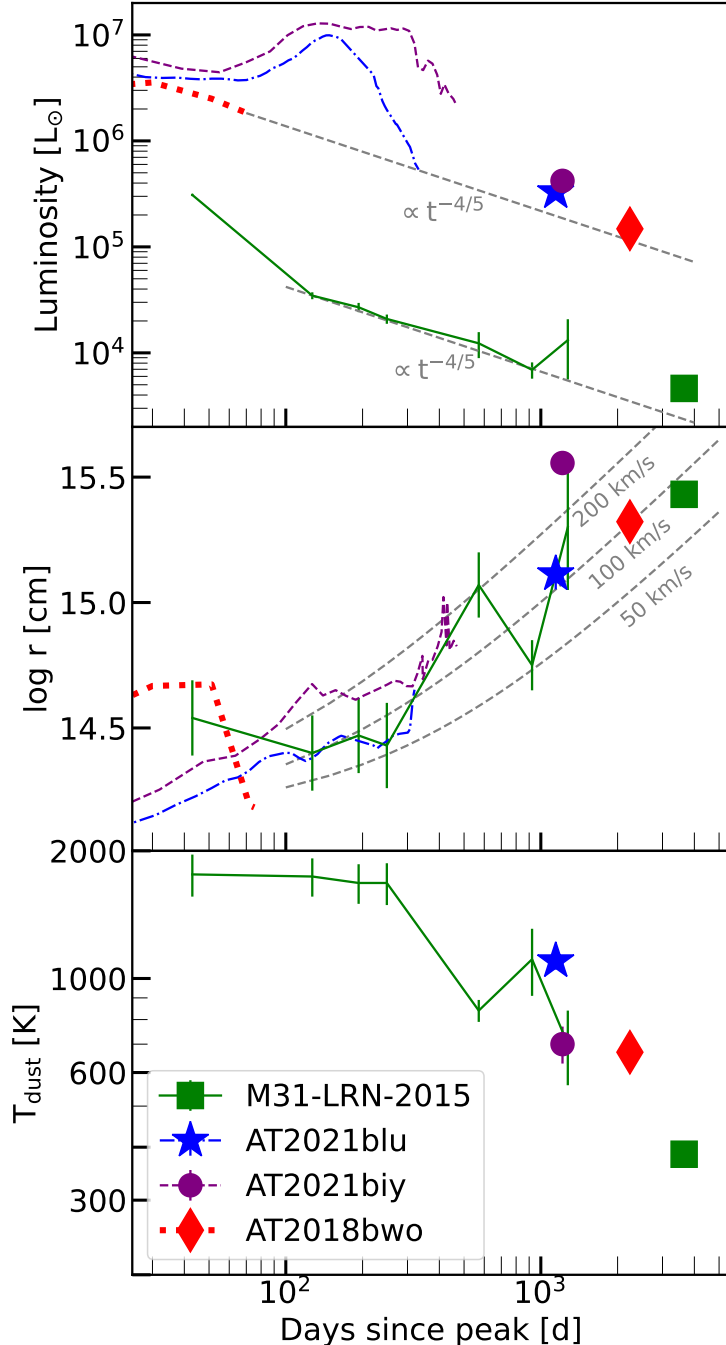


**Figure 9.5: Late-time evolution of LRN properties.** JWST measurements are indicated with stars, while solid lines show previous measurements wherever available. *Top:* The JWST luminosities of all four LRNe are higher than that extrapolated from their previous trends. The luminosities are inconsistent with gravitational contraction of an inflated remnant ( $\propto t^{-4/5}$ ), and suggest shock-interactions with CSM. *Middle:* The dust shell inner radii are consistent with expansion velocities of  $100\text{--}250\text{ km s}^{-1}$ , with the highest velocity for AT 2021biy that has the most massive progenitor of the four LRNe. AT 2021biy also has a colder dust shell temperature than AT 2021blu at a similar phase (*Bottom panel*).

This has been observed previously in V838 Mon, V4332 Sgr, and M31-LRN-2015, whose luminosities at late times declined as  $L \propto t^{-4/5}$ , consistent with the expectation for a gravitationally contracting inflated envelope around the remnant (Tylenda 2005; Tylenda et al. 2005; Blagorodnova et al. 2020). For M31-LRN-2015, this trend was observed for 2.5 years after the peak, following which its luminosity appeared to increase, possibly due to shocks (Blagorodnova et al. 2020). The *JWST* luminosity of M31-LRN-2015 is higher than the expectation from the  $t^{-4/5}$  trend by a factor  $\approx 3$ , indicative of a luminosity increase due to shocks. Similarly, the other three LRNe also do not decline as  $t^{-4/5}$ , suggesting that their late-time luminosity evolution is governed by shocks. We note that all LRNe are more luminous than their progenitors at the time of the *JWST* observations.

The second and bottom panel of Figure 9.5 shows the evolution of the inner radii and temperatures of the dust shells, respectively. The radii of AT 2021blu, AT 2018bwo, and M31-LRN-2015 are consistent with expansion speeds of  $\approx 100 \text{ km s}^{-1}$ , while AT 2021biy has a larger expansion velocity of  $250 \text{ km s}^{-1}$ . The dust temperatures generally decline with time. We note that while AT 2021blu and AT 2021biy were observed at similar phases of  $\approx 1200$  days, AT 2021biy has a dust-shell that is three times larger,  $\approx 400$  K cooler (Figure 9.5, bottom panel), and eight times more massive than AT 2021blu. AT 2021biy also had the longest lightcurve plateau of all LRNe, showed late-time rebrightenings likely powered by shocks, is the most luminous of the four LRNe in our sample, and has the most massive progenitor of the four (Cai et al. 2022). These properties suggest a larger ejected mass in AT 2021biy than the other LRNe, and also point to stronger CSM interaction that can produce large amounts of dust in the outer layers of the ejecta due to shocks.

Finally, converting the dust masses to total ejecta masses using a gas-to-dust ratio of 100 suggests low total ejected masses of  $4 \times 10^{-3} M_{\odot}$ ,  $3 \times 10^{-2} M_{\odot}$ ,  $8 \times 10^{-3} M_{\odot}$  and  $8 \times 10^{-2} M_{\odot}$  for AT 2021blu, AT 2021biy, AT 2018bwo, and M31-LRN-2015, respectively. These are much lower than the ejected masses estimated from the lightcurves, of a few tenths of a solar mass for M31-LRN-2015 (MacLeod et al. 2017; Williams et al. 2015; Matsumoto et al. 2022) and several solar masses for the other three LRNe (Pastorello et al. 2022; Karambelkar et al. 2023b). This suggests that the dust-formation occurs over a much longer timescale than that probed by our observations. Simulations of binaries undergoing CEE show that dust formation continues in the inner regions of the ejecta for several years after the dynamical inspiral (Iaconi et al. 2020). González-Bolívar et al. (2024) and Bermúdez-Bustamante

et al. (2024) simulated carbon dust formation in CE interactions of low mass AGB stars with a  $0.6M_{\odot}$  companion. They find that dust formation starts about 2-3 years into their simulations during the early inspiral phase, but really takes off ten years later when it reaches  $\approx 10^{-3} M_{\odot}$  and increases steadily to a plateau of  $\approx 10^{-2} M_{\odot}$  after 30-40 years. Iaconi et al. (2020) find that for a  $0.88 M_{\odot}$  red-giant primary, the dust formation occurs between 300 – 5000 days after the dynamical inspiral ends, reaching terminal values of  $\sim 10^{-3} M_{\odot}$  at 5000 days. While these simulated systems differ from the LRN-progenitors studied in this paper, it seems reasonable that the dust masses in LRNe will continue to increase for several decades since eruption, beyond the maximum phase of ten years that is probed by our observations. Future observations of even older LRNe will be crucial to trace the dust formation curve in LRNe, determine their terminal dust yields, and use dust masses to estimate the total ejected masses in these sources.

## 9.6 Summary and way forward

In this paper, we presented *JWST* observations of four LRNe originating from extragalactic massive stellar mergers. The four LRNe spanned a wide progenitor primary mass range ( $3-20 M_{\odot}$ ) and a wide range of phases since merger (1100 – 3600 days). We modeled the infrared SEDs of these LRNe to measure their dust and molecular content. We find –

- The dust masses in the four LRNe AT 2021blu, AT 2021biy, AT 2018bwo, and M31-LRN-2015 are  $\approx 4.2 \times 10^{-5}$ ,  $3 \times 10^{-4}$ ,  $7.5 \times 10^{-5}$ , and  $7.7 \times 10^{-4} M_{\odot}$ . This corresponds to  $\approx 10\%$ ,  $60\%$ ,  $6\%$  and  $12\%$  of the median expected dust masses in CCSNe at similar phases.
- After accounting for occurrence rates, the total dust mass produced in LRNe is estimated to be  $\sim 25\%$  of that produced in CCSNe. This is likely a lower limit, as dust-formation is expected to continue beyond the epochs covered by our observations. Furthermore, a lower dust-destruction fraction in LRNe than CCSNe may make the dust contributions of LRNe comparable to CCSNe.
- We also find large column densities of water vapor, CO, and SiO around the merger remnant, making LRNe important laboratories to study the evolution of these molecules as they potentially transition to form ices with future observations. The detection of water vapor also supports the association of water fountain sources with CEE remnants.

- The late-time luminosities of LRNe are higher than extrapolated from their previous trends, indicating that they might be undergoing shock-powered rebrightenings due to interaction with CSM.
- The measured dust masses for all four LRNe are lower than those expected from lightcurve-based ejecta masses by at least one order of magnitude. This suggests that dust forms on a much longer timescale than that probed by our observations.

This work highlights the potential of LRNe in understanding cosmic dust sources, studying dust-formation and evolution of molecules, and probing mass-loss during CEE phase. Future observations with *JWST* of a broader sample of LRNe will be crucial to determine the terminal dust yields of LRNe, and study the evolution of the dust and molecular properties. These studies will set the stage for future IR missions such as the *Nancy Grace Roman Space Telescope* and PRobe far-Infrared Mission for Astrophysics (PRIMA).

## 9.7 Appendix: Modeling the dust and molecular emission

As discussed in Section 9.4, we model the emission from a central star and dust using DUSTY, and then add a plane-parallel layer of molecules around it. We assume the outer radius of the star+dust shell configuration is  $R_*$ , and the molecular slab is characterized by its temperature ( $T_{\text{mol}}$ ), radius ( $R_{\text{mol}}$ ) and optical depth ( $\tau_\nu$ ) with  $R_{\text{mol}} > R_*$ . Under these conditions, the radiative transfer equation is

$$I_\nu = I_{\nu_0} e^{-\tau_\nu} + B_\nu(T)(1 - e^{-\tau_\nu}) \quad (9.2)$$

and the emergent flux density (given that  $I_{\nu_0} = 0$  for  $R_{\text{mol}} > r > R_*$ ) is given by

$$f_\nu = \frac{\pi R_*^2}{D^2} I_{\nu_0} e^{-\tau_\nu} + \frac{\pi R_{\text{mol}}^2}{D^2} (1 - e^{-\tau_\nu}) = f_\nu^d e^{-\tau_\nu} + \frac{\pi R_{\text{mol}}^2}{D^2} B_\nu(T)(1 - e^{-\tau_\nu}) \quad (9.3)$$

where  $f_\nu^d = \frac{\pi R_*^2}{D^2} I_{\nu_0}$  is the emergent flux density from the star+dust unaffected by the presence of molecules.

Unfortunately, DUSTY outputs neither  $f_\nu^d$  nor  $I_{\nu_0}$ , but instead outputs the shape of the spectrum i.e. normalized  $\nu f_\nu$ . From this, we can only determine a normalized flux density  $f_\nu^{d,n}$  such that  $\int f_\nu^{d,n} d\nu = 1$  and the required model flux density  $f_\nu^d = C f_\nu^{d,n}$ .

$$f_\nu = C f_\nu^{d,n} e^{-\tau_\nu} + \frac{\pi R_{\text{mol}}^2}{D^2} B_\nu(T) (1 - e^{-\tau_\nu}) = \frac{\pi R_{\text{mol}}^2}{D^2} \times [C_1 f_\nu^{d,n} e^{-\tau_\nu} + B_\nu(T) (1 - e^{-\tau_\nu})] \quad (9.4)$$

In our fitting process, the free parameters are  $R_{\text{mol}}$ ,  $C_1$  and  $\tau_\nu$  (which incorporates the column densities as free parameters). Once  $C_1$  and  $R_{\text{mol}}$  are determined, the radius of the dust shell can be estimated using the  $r_1$  parameter provided as part of DUSTY output. We first calculate the integrated bolometric luminosity of the DUSTY model alone

$$L_d = \int 4\pi D^2 f_\nu^d d\nu = \int 4\pi D^2 \frac{\pi R_{\text{mol}}^2}{D^2} C_1 f_\nu^{d,n} d\nu = 4\pi^2 R_{\text{mol}}^2 C_1 \int f_\nu^{d,n} d\nu = 4\pi^2 R_{\text{mol}}^2 C_1 \quad (9.5)$$

and then use this to calculate the radius

$$R_* = r_1 \left( \frac{L_d}{10^4 L_\odot} \right)^{\frac{1}{2}} Y = r_1 \left( \frac{4\pi^2 R_{\text{mol}}^2 C_1}{10^4 L_\odot} \right)^{\frac{1}{2}} Y \quad (9.6)$$

where  $Y$  is the shell-thickness.

An example of the different model components is shown in Figure 9.6.

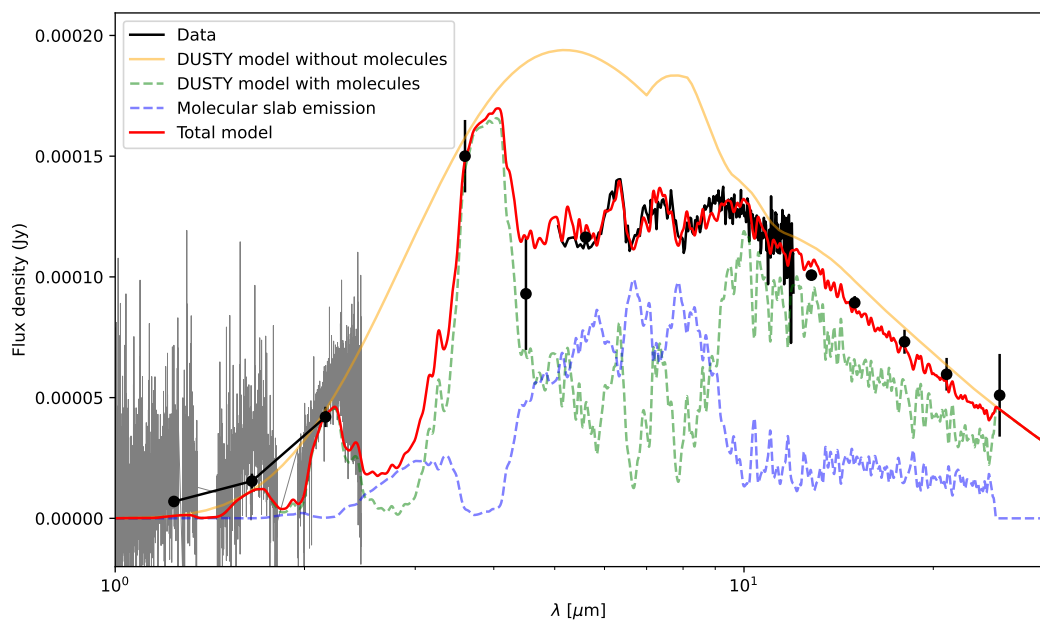


**Figure 9.6: A breakdown of the different model components for AT 2021blu:**  
 DUSTY model (blackbody star + dust shell, orange), DUSTY model attenuated with molecules (dashed green line), emission from molecular shell (dashed blue line), total model (red line = green + blue) that fit to the data (black)

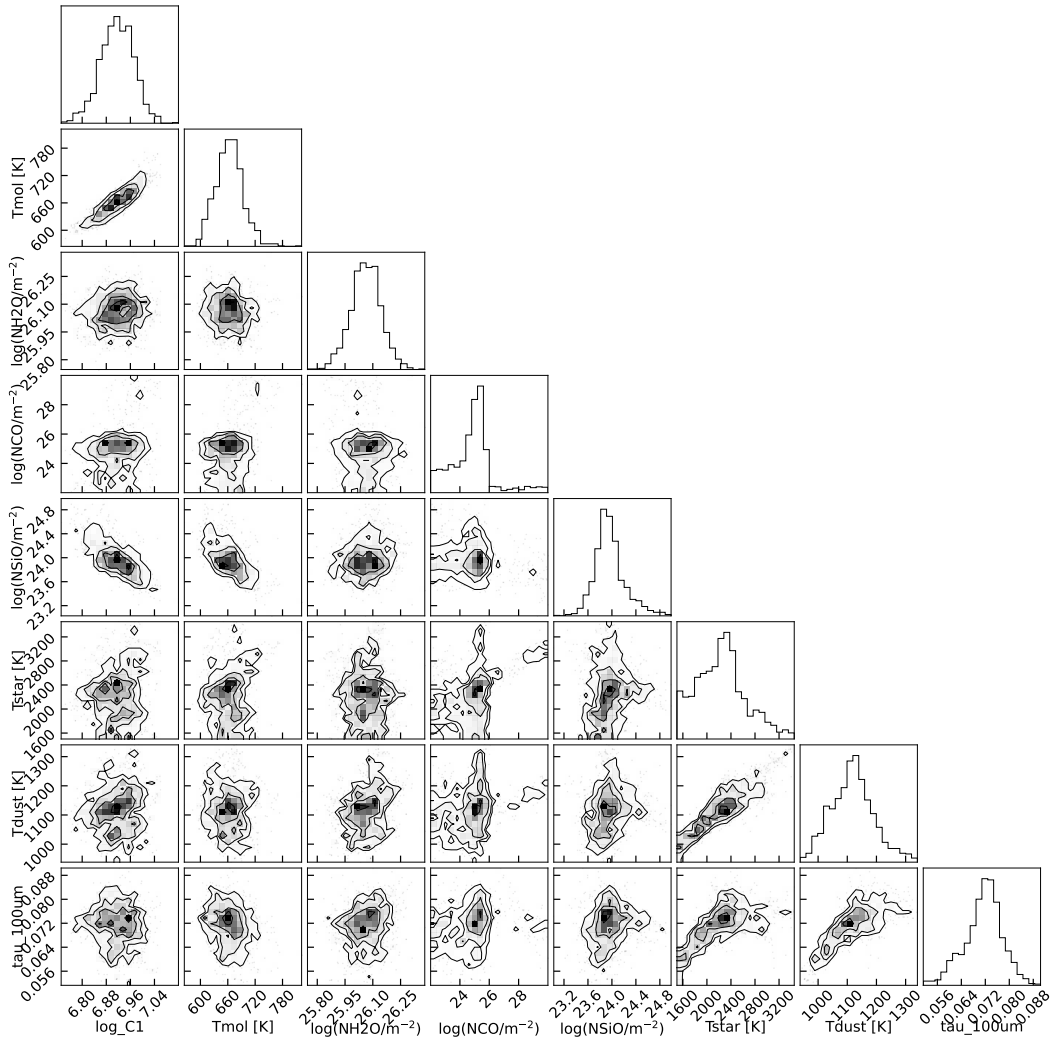


**Figure 9.7: Posterior probability distributions of parameters for AT 2021blu.**  
 Note that  $\tau_{100}$  represents the dust optical depth at 100  $\mu\text{m}$ .

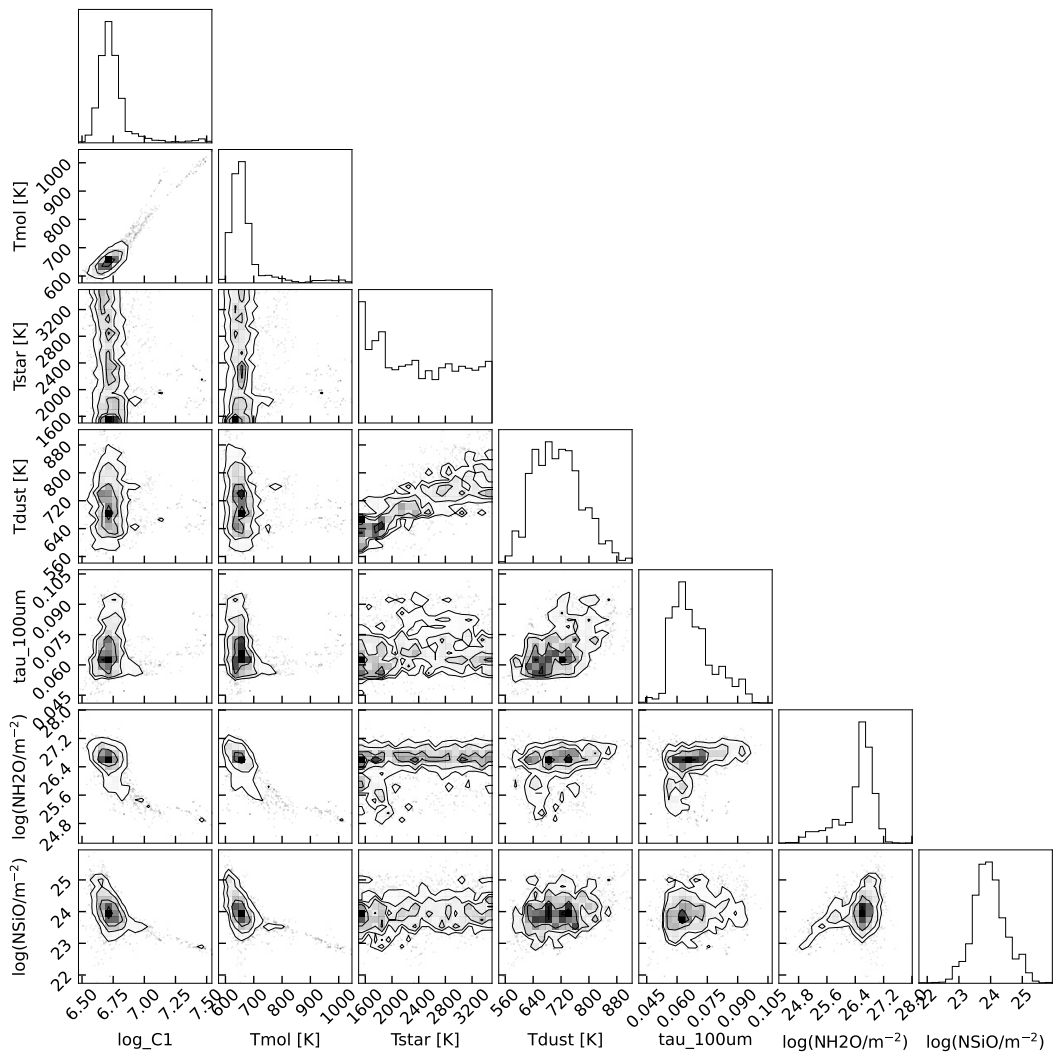


**Figure 9.8: Posterior probability distributions of parameters for AT 2021biy.**  
 Note that  $\tau_{100}$  represents the dust optical depth at 100  $\mu\text{m}$ .

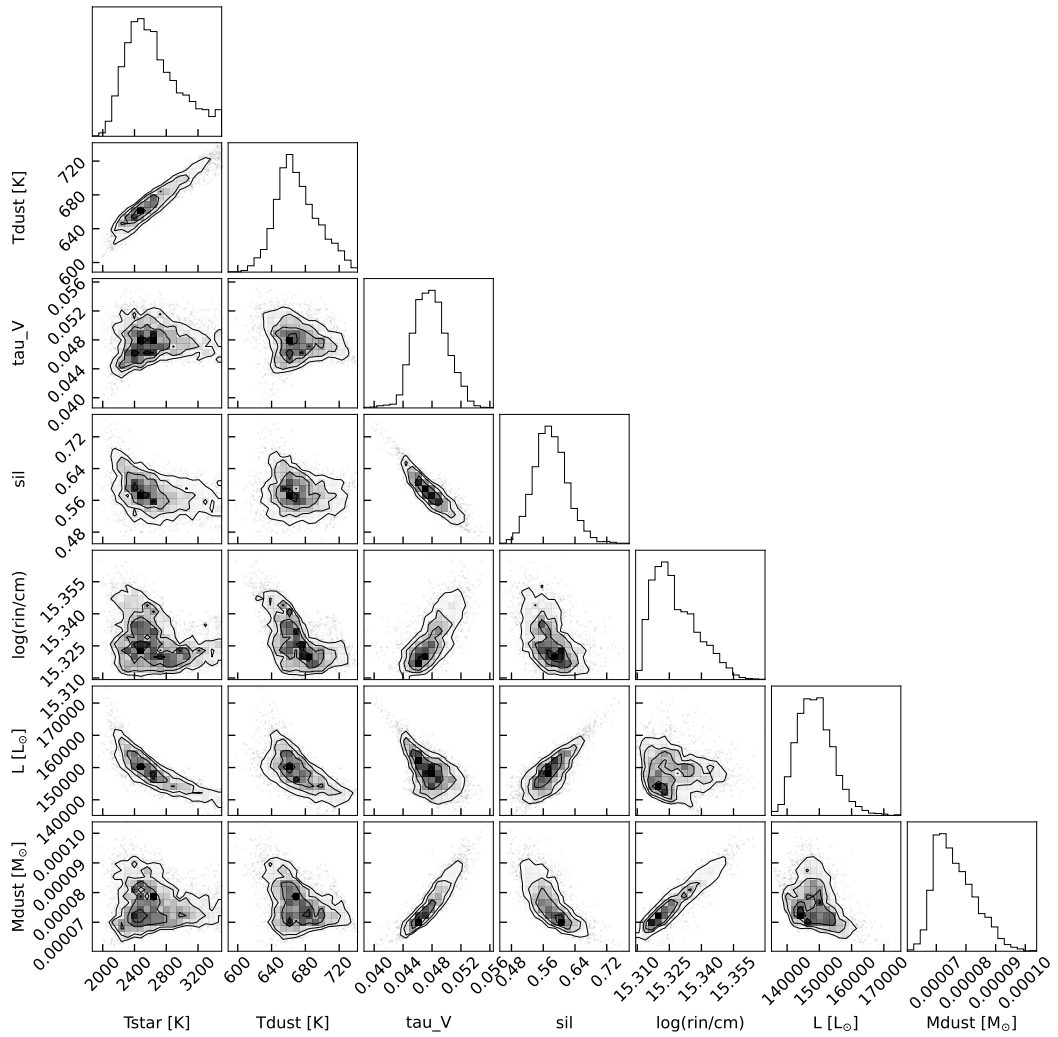


**Figure 9.9: Posterior probability distributions of parameters for AT 2018bwo.**  
 The model has four free parameters: Tstar, Tdust, tau\_V, and sil, and  $r_{in}$ , L,  $M_{dust}$  are derived parameters.

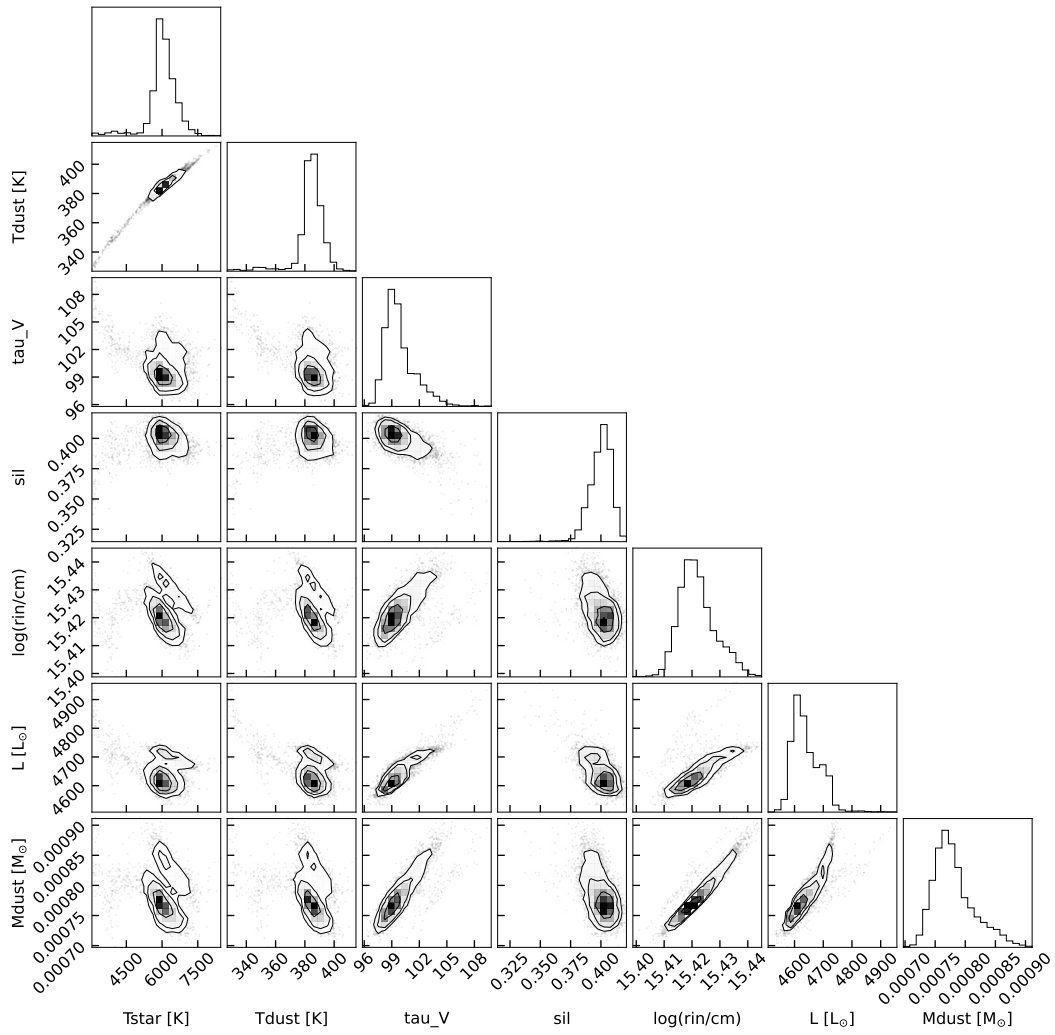


Figure 9.10: **Posterior probability distributions of parameters for M31-LRN-2015.** The model has four free parameters:  $T_{\text{star}}$ ,  $T_{\text{dust}}$ ,  $\tau_{\text{V}}$ , and  $\text{sil}$ , and  $r_{in}$ ,  $L$ ,  $M_{\text{dust}}$  are derived parameters.

THE SLOW BRIGHTENING OF WNTR23BZDIQ /  
 WTP19AALZLK : POSSIBLE ONSET OF  
 COMMON-ENVELOPE EVOLUTION IN AN ASYMPTOTIC  
 GIANT BRANCH STAR?

Under review in ApJ.

V. R. Karambelkar<sup>1</sup>, M. M. Kasliwal<sup>1</sup>, K. De<sup>2</sup>, D. Frostig<sup>3</sup>, R. Stein<sup>4,5,6</sup>, G. Mo<sup>7</sup>,  
 N. Lourie<sup>7</sup>, R. Simcoe<sup>7</sup>, N. Blagorodnova<sup>8</sup>

<sup>1</sup>Cahill Center for Astrophysics, California Institute of Technology, Pasadena, CA 91125,  
 USA

<sup>2</sup>Columbia University, 538 West 120th Street 704, MC 5255, New York, NY 10027

<sup>3</sup>Center for Astrophysics | Harvard & Smithsonian, 60 Garden Street, Cambridge, MA  
 02138, USA

<sup>4</sup>Joint Space-Science Institute, University of Maryland, College Park, MD 20742, USA

<sup>5</sup>Department of Astronomy, University of Maryland, College Park, MD 20742, USA

<sup>6</sup>Astrophysics Science Division, NASA Goddard Space Flight Center, Mail Code 661,  
 Greenbelt, MD 20771, USA

<sup>7</sup>MIT-Kavli Institute for Astrophysics and Space Research, 77 Massachusetts Ave.,  
 Cambridge, MA 02139, USA

<sup>8</sup>Institut de Ciències del Cosmos (ICCUB), Universitat de Barcelona (UB), c. Martí i  
 Franquès, 1, 08028 Barcelona, Spain

**Abstract**

We present WNTR23bzdiq/WTP19aalzlk, a slow eruption of an early-asymptotic giant branch (AGB) star in M 31 identified by the Wide-field Infrared Transient Explorer (WINTER) near-infrared and the NEOWISE mid-infrared surveyors. This source brightened gradually over seven years: a 0.5 mag optical rise (2018–2021), a 1-mag optical outburst lasting  $\sim$ 1000 days (2021–2023), and another 1 mag optical rebrightening in 2024. This was accompanied by a steady mid-IR brightening of 1 mag over ten years in NEOWISE data. Archival optical data show only erratic,

small amplitude ( $< 0.3$  mag) brightness variations from 2003 to 2015, revealing a progenitor star with  $T_{\text{eff}} \approx 3500$  K and  $L \approx 1.6 \times 10^4 L_{\odot}$  — consistent with a  $7 \pm 2 M_{\odot}$  star in its early-AGB phase. During the eruption, the luminosity rose to  $\approx 5 \times 10^4 L_{\odot}$  with slow photospheric expansion ( $\approx 5 \text{ km s}^{-1}$ ) and constant temperatures ( $\approx 3600$  K) inferred from the spectral energy distribution. Optical and NIR spectra of the eruption resemble late M-type stars, with a mixed-temperature behavior — transitioning from M1 in the optical to M7/M8 in the NIR. These properties of WNTR23bzdiq resemble those of stellar merger transients, particularly the giant star merger OGLE-2002-BLG-360, but on longer timescales. As such, WNTR23bzdiq potentially marks the onset of common-envelope evolution (CEE) in a binary with an AGB primary, and is possibly a member of the emerging population of infrared transients from CEE in giant stars. Continued multiwavelength monitoring, particularly mid-IR observations with *JWST* to quantify dust production, will shed further light on WNTR23bzdiq.

## 10.1 Introduction

Common envelope evolution (CEE) is an important evolutionary phase in the lives of binary stars (Paczynski 1976; Webbink 1984). This phase is triggered when mass transfer in the binary system becomes dynamically unstable, causing the primary star to engulf the secondary star in a shared common envelope. Dynamical friction then triggers an inspiral of the binary system, which can result either in a stellar merger, or an envelope ejection that leaves behind a stable binary in a closer orbit (Ivanova et al. 2013a). Thus, CEE can produce the rapid orbital shrinkage required to explain the formation of double compact objects in very close orbits that can merge by radiating gravitational waves within the Hubble time (Dominik et al. 2012; Ivanova et al. 2013a; Postnov et al. 2014; Vigna-Gómez et al. 2020; Marchant et al. 2021). Despite its vital role in the formation pathways of gravitational wave sources, CEE remains poorly understood due to a lack of direct observations of this short-lived phase (Ivanova et al. 2013a).

The final stage of CEE — merger or envelope ejection — powers luminous stellar eruptions. A class of transients called Luminous Red Novae (LRNe) has been associated with binary systems undergoing CEE (Pastorello et al. 2019a; Blagorodnova et al. 2021; Tylenda et al. 2011a; Kasliwal et al. 2011; Munari et al. 2002; Kulkarni et al. 2007). These events offer an important probe into understanding the physical processes involved in CEE. Most LRNe have been identified by optical time-domain surveys based on a sharp increase in the system’s luminosity lasting tens to a few

hundred days (Karambelkar et al. 2023b; Pastorello et al. 2021a; Pastorello et al. 2021b; Pastorello et al. 2022; Cai et al. 2022). These eruptions typically exhibit multi-peaked lightcurves, a rapid transition from blue to red colors due to dust formation, and a spectroscopic transition to M-type spectra with strong molecular absorption features (Munari et al. 2002; Tylenda et al. 2011a; Kochanek et al. 2014; Pastorello et al. 2019a; Karambelkar et al. 2023b). While LRNe span a wide range of progenitor masses, the evolutionary stages are largely limited to stars on the main-sequence or stars crossing the Hertzsprung gap (Blagorodnova et al. 2017; MacLeod et al. 2017; Blagorodnova et al. 2021; MacLeod et al. 2022). Of the more than two dozen LRNe discovered to date, only one has a giant star progenitor (Tylenda et al. 2013).

The paucity of CEE transients from giant stars has been attributed to their markedly different appearance compared to typical LRNe (MacLeod et al. 2022). Owing to their extended envelopes and longer dynamical timescales, giant star merger transients are expected to evolve much more slowly than LRNe. Furthermore, these stars are predicted to lose a lot more mass upon the initiation of CEE and are expected to be more enshrouded in dust than their lesser evolved counterparts (MacLeod et al. 2022). Consequently, giant star mergers are predicted to manifest as slow-evolving, long-lived, primarily infrared transients — significantly different from optical LRNe (MacLeod et al. 2022; Pejcha et al. 2016; Metzger et al. 2017).

The Galactic transient OGLE-2002-BLG-360 is the only CE transient with a confirmed red giant progenitor (Tylenda et al. 2013). This eruption, originating from a K-type giant star, lasted for over two thousand days, exhibited multiple lightcurve peaks along with a spectral evolution to an M-type star at late times. While its overall morphology resembled LRNe, its duration was nearly an order of magnitude longer than typical optical LRNe. Infrared and sub-mm observations show that it is the dustiest among Galactic stellar mergers (Steinmetz et al. 2025), establishing it as the prototypical event for a slow, dusty transient from CEE in a binary system with a giant primary. Beyond OGLE-BLG, the historical long-duration eruption of CK Vul (Kato 2003; Tylenda et al. 2013) and the population of IR transients discovered by the *Spitzer Space Telescope* without any optical counterparts (termed SPRITES, Kasliwal et al. 2017b; Jencson et al. 2019b) have been attributed to mergers or envelope ejections involving evolved, giant stars. Nonetheless, the phase space of giant star mergers and envelope ejections remains largely unexplored, primarily due to a lack of infrared time-domain surveys.

In this paper, we present WNTR23bzdiq/WTP19aalzlk — a slow, ongoing infrared eruption of a giant star in M 31, whose properties align with the expectations for CEE involving a giant star. This source was independently identified by two infrared searches: the new Wide-field Infrared Transient Explorer (WINTER, Lourie et al. 2020a; Frostig et al. 2024a) in the near-IR (NIR), and a dedicated pipeline for detecting mid-IR transients using the NEOWISE survey (De et al. 2023; De et al. 2024; Meisner et al. 2019; Mainzer et al. 2014b). Archival photometry indicates that the giant progenitor of WNTR23bzdiq was an early asymptotic giant branch (AGB) star, making it the most evolved star associated with a possible CE transient.

This paper is organized as follows — Section 10.2 describes the observations of this source, Section 10.3 analyzes the photometric and spectroscopic properties, Section 10.4 discusses possible origin scenarios for this eruption, and Section 10.5 concludes with a summary of our results and path forward.

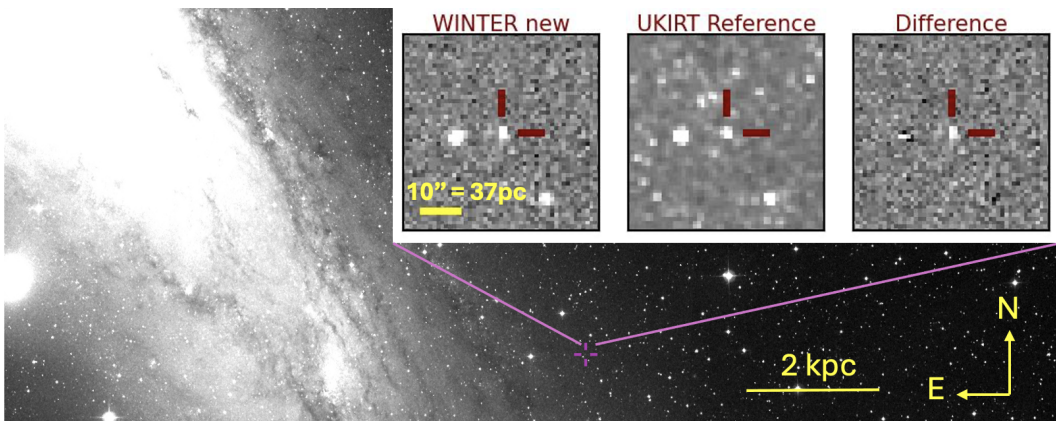


Figure 10.1: **The location of WNTR23bzdiq.** WNTR23bzdiq (pink cross) is located in the outskirts of M31, at an angular separation of  $\approx 0.9$  deg from its center corresponding to a distance of  $\approx 12$  kpc. *Inset:* A comparison of a new  $J$ -band WINTER image from 2023, an archival  $J$ -band UKIRT Hemisphere survey reference image from 2014, and the difference image of these two. The position of WNTR23bzdiq is marked by cross-hairs. The background image is taken from the Digitized Sky Survey II.

## 10.2 Observations

### Identification

The WINTER surveyor is a 1.2 sq deg. field-of-view InGaAs camera mounted on a 1 m robotic telescope at Palomar observatory operating at the NIR  $Y$ ,  $J$ , and  $Hs$  bands (Lourie et al. 2020a; Frostig et al. 2024a). WINTER is conducting a Nearby Galaxies Survey that routinely images galaxies within 25 Mpc in the  $J$ -band

to search for infrared transients. The source WNTR23bzdiq was identified as a candidate transient in the outskirts of M 31 in the WINTER data stream on UT 2023-12-17 at  $\alpha=00:38:48.6$ ,  $\delta =+40:46:08.2$  by its automated transient detection pipeline. The full details of the WINTER transient detection pipeline will be outlined in a forthcoming paper (Karambelkar & Stein et al., in prep). Briefly, the pipeline generates astrometrically and photometrically calibrated stacks of dithered observations and performs image subtraction relative to archival images from the UKIRT Hemisphere Survey (UHS, Dye et al. 2018). Transient candidates identified from the difference images are broadcast to Skyportal/Fritz (Coughlin et al. 2023d) for human scanning and vetting of interesting sources. WNTR23bzdiq was flagged during scanning, and was coincident with a point source in the archival UHS image, suggesting that it was a star that had brightened since the UHS epoch. Figure 10.1 shows cutouts of the new WINTER science image, UHS reference image, and difference image of the detection.

This source was independently identified as WTP19aalzlk — a large-amplitude, long-duration mid-IR transient — by the NEOWISE transient detection pipeline (De et al. 2024), which searches for transients in unWISE stacks (Meisner et al. 2019) of NEOWISE images. The source has been steadily brightening by  $\approx 1$  mag in both W1 and W2 filters for the last ten years.

## Photometry

Since its discovery, WNTR23bzdiq was observed in the *J*-band at several epochs as part of the regular WINTER survey. We performed aperture photometry at the position of the source in the stacked WINTER images to construct a *J* band lightcurve.

To supplement the WINTER *J*-band observations, we compiled publicly available optical data from the Zwicky Transient Facility (ZTF, Bellm et al. 2019a). This field was observed as part of the ZTF routine survey in the *g, r*, and *i* bands. Science-frame photometry up to UT 2024-06-29 was retrieved from the source catalogs in ZTF Data Release 22. Photometry for the later epochs was obtained through the ZTF forced photometry service (Masci et al. 2019). The difference fluxes from the forced photometry service were converted to the science fluxes adding flux of the nearest source in the reference image to the forced photometry. The ZTF fluxes were binned into 5-day bins to increase their signal-to-noise ratios.

Mid-infrared observations from the NEOWISE mission (Mainzer et al. 2014b) from

2014 to 2024 were obtained from the NEOWISE Single exposure source table in the final data release hosted on IRSA<sup>1</sup>. The NEOWISE fluxes from each pointing were binned together.

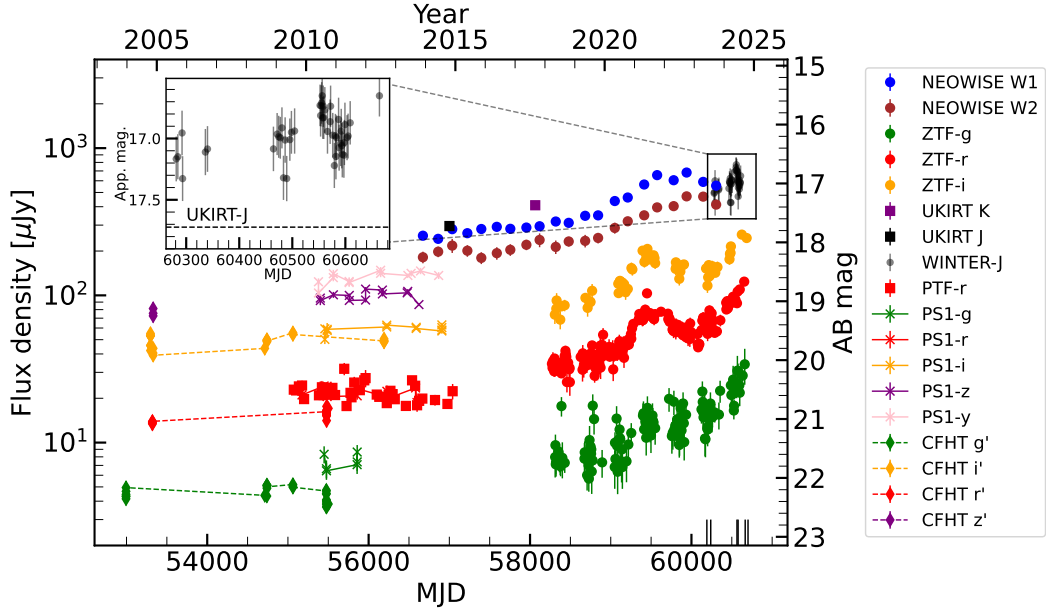


Figure 10.2: **Multiband lightcurve of WNTR23bzdiq.** The *J*-band discovery lightcurve from WINTER is displayed in the inset plot, which shows a slow brightening from 2023 to 2024 relative to the 2014 UKIRT measurement. The full plot shows the optical to mid-IR photometry spanning 2003 to 2025. In the optical data available until 2015, the source only shows small amplitude ( $< 0.3$  mag) erratic brightness variations. In 2018, it starts brightening smoothly, undergoes a 1000-day outburst from 2021 to 2023, and has continued rebrightening since. The NEOWISE mid-IR data shows a smooth brightening from 2016 to 2023, following which it decines slightly. Importantly, the mid-IR fluxes continued to increase even when the optical luminosity faded in 2023. The black vertical lines mark the epochs of the spectroscopic observations.

Archival optical observations were compiled from the Palomar Transient Factory (PTF, (Law et al. 2009)), the intermediate Palomar Transient Factory (iPTF Cao et al. 2016), the PanSTARRS survey (PS1, Chambers et al. 2016c; Magnier et al. 2013; Flewelling et al. 2020), and the Canada France Hawaii Telescope (CFHT). PTF/iPTF *g* and *r*-band lightcurves from 973 observations taken from 2010 to 2015 were downloaded from the point-source catalogs (Ofek et al. 2012; Laher et al. 2014) hosted at IRSA<sup>2</sup>. The PTF/iPTF observations were binned into 30-day

<sup>1</sup><https://irsa.ipac.caltech.edu/Missions/wise.html>

<sup>2</sup><https://irsa.ipac.caltech.edu/Missions/ptf.html>

bins to increase fidelity. PS1 *grizy* fluxes for ten epochs spanning 2010 to 2015 were downloaded from the PS1 source catalogs hosted on MAST<sup>3</sup>. Even older observations from 2003 to 2012 were obtained from the CFHT MegaPrime data archive.<sup>4</sup> Reduced and calibrated  $g'$ ,  $r',i'$  and  $z'$ -band MegaPrime images were downloaded from the archive and photometry was performed at the location of WNTR23bzdiq to construct the lightcurves. Archival infrared observations were compiled from the 2MASS point source catalog (Cutri et al. 2003; one epoch each in  $JHKs$  bands), the United Kingdom Infrared Telescope (UKIRT) M31 catalog (Neugent et al. 2020; one epoch each in  $J$  and  $Ks$  bands), the ALLWISE data release (Cutri et al. 2021; detections in W1 and W2 bands), and the Spitzer IRAC point source catalogs of M31 (Khan 2017; one epoch, detections in channels 1, 2, and 3). Finally, archival *Gaia* observations from 2016 confirm the membership of this source in M31 (see Neugent et al. 2020).

These optical and infrared lightcurves of WNTR23bzdiq are shown in Figure 10.2. Overall, we find good agreement between different photometry sources where they overlap, with small differences ( $\sim 0.1$  mag) likely due to differences in filter profiles. Fig. 10.2 suggests that this source did not show any significant brightness variations over a fifteen year period (2003 to 2018), following which it underwent an outburst lasting  $\approx 1000$  days, and has brightened again subsequently.

## Spectroscopy

We obtained three optical spectra of this source, one with the Binospec spectrograph (Fabricant et al. 2019) on the MMT telescope (PI: MacLeod) on 2023-10-22 one with the Double Beam Spectrograph (DBSP, Oke et al. 1982,  $R \approx 1000$ ) on the 200-inch Hale telescope at Palomar Observatory on 2024-09-25, and one with the Low Resolution Imaging Spectrometer (LRIS, Oke et al. 1995,  $R \approx 750$ ) on the Keck I telescope at Mauna Kea Observatory on 2025-01-26. Additionally, we obtained three near-infrared spectra, two with the Near-Infrared Echelle Spectrograph (NIRES, Wilson et al. 2004,  $R \approx 2500$ ) on the Keck II telescope on 2023-09-04 (NASA Program ID: 2023B-N258, PI: De) and 2024-09-11, and one with the Triple-spec spectrograph (Herter et al. 2008,  $R \approx 2700$ ) on the 200-inch Hale telescope on 2024-12-22. The DBSP spectrum was reduced using the python package `dbsp_drp` (Mandigo-Stoba et al. 2022). The LRIS spectrum was reduced using the `idl` package `1pipe` (Perley et al. 2020). The NIRES and TripleSpec spectra were reduced

---

<sup>3</sup><https://catalogs.mast.stsci.edu/panstarrs/>

<sup>4</sup><https://www.cadc-ccda.hia-ihc.nrc-cnrc.gc.ca/en/cfht/>

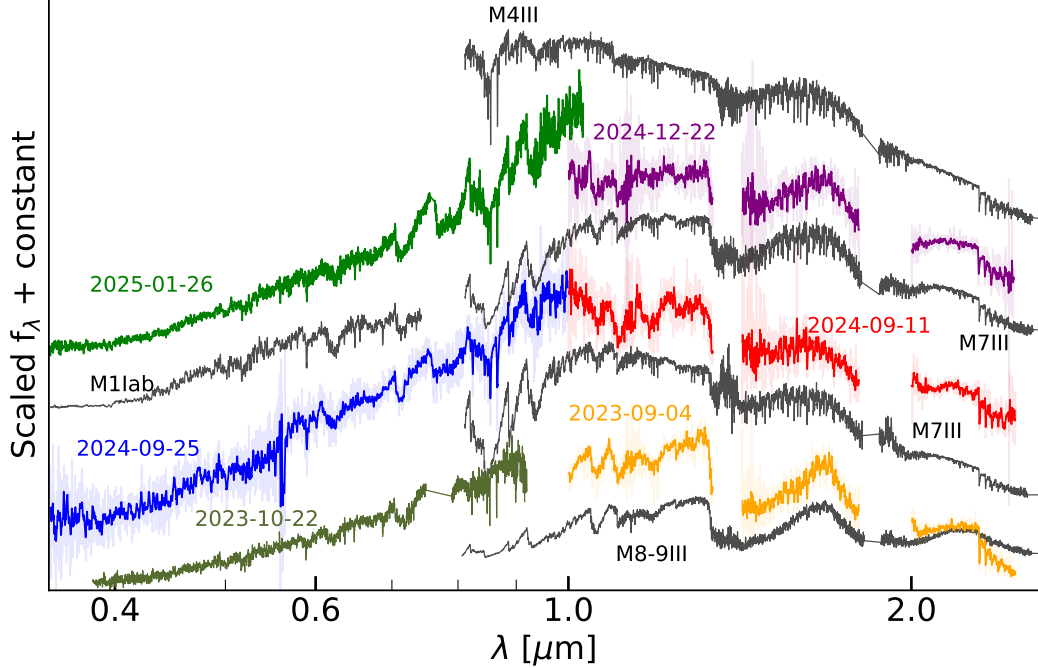


Figure 10.3: **Optical-NIR spectra of WNTR23bzdiq** (colored) compared to stellar spectral templates (black). The spectra of WNTR23bzdiq resemble those of late M-type giant stars. We find that the NIR spectral type varies from an M8-9 in our earliest spectrum that was taken at the end of the 2021 outburst (orange) to M7 in the next two spectra (red, purple) taken during the 2024 rebrightening. Additionally, the spectra at the two later epochs have mixed-spectral types, where the optical spectra match an M1 spectral type template while the NIR spectra match later M7 type templates. This behavior resembles the Galactic stellar merger V838 Mon. *Inset:* Continuum normalized optical spectra zoomed-in around the H $\alpha$  line, showing no strong H $\alpha$  emission.

using the idl package `spextool` (Cushing et al. 2004) and corrected for telluric absorption using the package `xtellcor` (Vacca et al. 2003). These optical and NIR spectra are shown in in Figure 10.3. The black vertical lines in Figure 10.2 mark the epochs of the spectroscopic observations. The spectra show strong absorption bands of oxygen-rich molecules and resemble late M-type stars. The locations of the molecular absorption bands are consistent with the redshift of M31, confirming the M31 membership of this source.

### Distance and reddening

For the analysis in this paper, we assume a distance to M 31 of 0.77 Mpc (Ferrarese et al. 2000). We correct for a Galactic line-of-sight extinction of  $E_{B-V} = 0.09$  mag

(Schlafly et al. 2012). We do not adopt any additional reddening from M 31, as the source is located on the outskirts of the galaxy where the interstellar dust obscuration is expected to be low, and we do not find any evidence for additional reddening in our modeling.

### 10.3 Analysis

#### Progenitor modeling

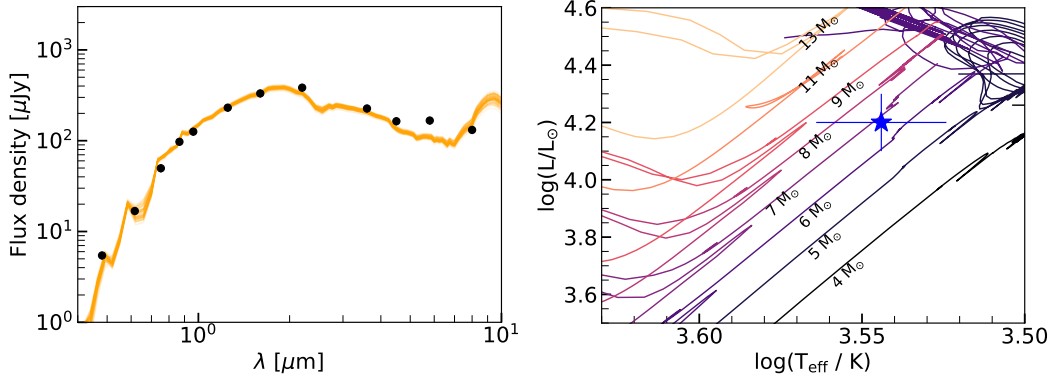


Figure 10.4: **Modeling the progenitor of WNTR23bzdiq.** *Left:* Spectral energy distribution of the progenitor star (black dots) together with the range of best-fit PHOENIX+DUSTY models (orange). Our modeling suggests the progenitor has  $T_{\text{eff}} \approx 3500$  K and a total luminosity  $\log L = 4.2 L_{\odot}$ . *Right:* Comparing these progenitor properties (blue star) to MIST stellar evolutionary tracks (colored lines) in the HR diagram suggests the progenitor is a  $7 \pm 2 M_{\odot}$  star in its early AGB phase.

We use the archival photometry to model the nature of the progenitor star of WNTR23bzdiq. We construct the progenitor's spectral energy distribution (SED) using the PS1 *grizy* band, the UKIRT *J* and *Ks* band, 2MASS *H*-band, ALLWISE 3.4 and 4.6 $\mu\text{m}$ , and Spitzer IRAC 5.8 and 8.0 $\mu\text{m}$  fluxes. We first fit the SED using a combination of PHOENIX model photospheres (Husser et al. 2013) and the radiative transfer code DUSTY (Ivezic et al. 1997; Ivezic et al. 1999). We downloaded solar metallicity PHOENIX stellar models available online<sup>5</sup> and used them as inputs to DUSTY. DUSTY models the emergent radiation from the star through a dust shell, assuming spherical symmetry. We used the  $\log g=0.0$  PHOENIX models for our analysis. For the DUSTY models, we assumed silicate dust grains (motivated by the oxygen-rich molecular features in our spectra) with a standard MRN distribution for dust grain sizes, a wind-like  $r^{-2}$  radial density profile for the dust shell, and a

<sup>5</sup><https://www.stsci.edu/hst/instrumentation/reference-data-for-calibration-and-tools/astronomical-catalogs/phoenix-models-available-in-synphot>

shell-thickness ratio of 2.0. First, we computed a grid of DUSTY models for stars with  $T_{\text{eff}}$  ranging from 2100 to 4500 K with increments of 100 K (limited by availability of the PHOENIX models), dust temperatures  $T_d$  ranging from 500 to 2000 K with increments of 100 K, and for fifteen values of the dust optical depth in the  $V$ -band (0.55  $\mu\text{m}$ )  $\tau_V$  uniformly sampled in log space from  $\tau_V = 0.01$  to 10. Then, we interpolated between this grid using a convolutional neural network (CNN) model. The CNN model was implemented using pytorch (Ansel et al. 2024), comprises two hidden dense layers (with 64 and 128 units, respectively) with ReLU activation, and an output layer with 203 units that predicts the SED from 0.1 – 20  $\mu\text{m}$  for three input parameters ( $T_{\text{eff}}$ ,  $T_{\text{star}}$ ,  $\tau_V$ ) described above. The model was trained using the Adam optimizer (Kingma et al. 2014) with an initial learning rate of 0.001 for 100 epochs using the grid of 6000 models with a 80-20% train-test split. We find that the CNN model is able to predict the DUSTY SEDs very well, with differences between the predicted and true SEDs smaller than 1% in the wavelength range from 0.1 to 20  $\mu\text{m}$ , well below the errorbars on the observations. We used this model to derive posterior distributions of  $T_{\text{eff}}$ ,  $T_{\text{dust}}$ , and  $\tau_V$  using Markov Chain Monte Carlo (MCMC) sampling implemented in the python package `emcee` (Foreman-Mackey et al. 2013a).

Our DUSTY modeling suggests that the progenitor is a star with  $T_{\text{eff}} = 3500_{-150}^{+150}$  K, surrounded by a dust shell with temperature  $T_d = 1450_{-100}^{+130}$  K and optical depth  $\tau_V = 2.7_{-0.4}^{+0.4}$ . Figure 10.4 (left panel) shows the range of best-fit models to the progenitor SED. We note that for such optical depths, the optical and NIR data can place strong constraints on  $T_{\text{eff}}$ , but mid-IR data at longer wavelengths (especially covering the 10  $\mu\text{m}$  silicate feature) are required for strong constraints on the dust parameters. As our SED coverage ends at 8  $\mu\text{m}$ , it is possible that our dust estimates are subject to inaccuracies or error-underestimations in the mid-IR Spitzer bands. For this reason, while we are confident about the effective temperature estimates, we caution that our dust estimates may not be accurate. The total integrated luminosity of the progenitor obtained from the DUSTY fitting is  $\log(L/L_{\odot}) = 4.20 \pm 0.02$ .

To test for any systematics associated with our DUSTY modeling, we also fit the progenitor SED using the Grid of Red supergiant and Asymptotic Giant Branch ModelS (GRAMS; Sargent et al. 2010; Sargent et al. 2011; Srinivasan et al. 2011) and the approach described in Jencson et al. (2022). This suite of radiative transfer models consists of a base grid of 1225 spectra of stars with constant mass-loss rates and spherically symmetric shells of silicate dust around them. The spectra are

computed using PHOENIX model photospheres (Kučinskas et al. 2005; Kučinskas et al. 2006) combined with the dust radiative transfer code 2-Dust (Ueta et al. 2003). The published grid uses  $1 M_{\odot}$  stars with effective temperatures  $T_{\text{eff}}$  between 2100 and 4700 K, at a fixed subsolar metallicity  $\log(Z/Z_{\odot}) = -0.5$  and a fixed surface gravity  $\log g = -0.5$ . The circumstellar dust is characterized by the dust temperature at the inner radius of the dust shell  $T_{\text{in}}$  and the optical depth at  $1 \mu\text{m}$   $\tau_1$ , which can be converted to a dust mass-loss rate  $\dot{M}_d$  assuming a wind speed. An additional parameter is the inner radius of the dust shell,  $R_{\text{in}}$ . Similar to Jencson et al. (2022), we find that our derived parameters are largely insensitive to this parameter, and we fix it to  $R_{\text{in}} = 11.0 R_{\ast}$ . The best-fit model has  $T_{\text{eff}} = 3500$  K  $\tau_1 = 0.46$  (corresponding to  $\tau_V = 1.9$  for silicate dust),  $T_{\text{in}} = 1000$  K — consistent with the values from the DUSTY modeling. The total luminosity of the progenitor from the GRAMS modeling is  $\log(L/L_{\odot}) = 4.20^{+0.06}_{-0.03}$ .

In summary, our modeling suggests that the progenitor is a cold star with conservative estimates of  $T_{\text{eff}} = 3500^{+200}_{-200}$  and luminosity  $\log(L/L_{\odot}) = 4.2 \pm 0.1$ , moderately enshrouded in hot dust with temperature  $T_{\text{dust}} \approx 1000\text{--}1500$  K and  $\tau_V \approx 2\text{--}3$ . The photospheric radius is calculated to be  $350 \pm 50 R_{\odot}$  while the inner radius of the dust shell is  $\approx 1800 \pm 400 R_{\odot}$ . We compare the luminosity and effective temperature to stellar evolutionary tracks from MESA Isochrones and Stellar Tracks (MIST; Dotter 2016; Choi et al. 2016)<sup>6</sup> in the right panel of Figure 10.4. Comparing the position of the star in the HR diagram to the stellar tracks suggests that the progenitor is a star with a zero-age main-sequence (ZAMS) mass of  $7 \pm 2 M_{\odot}$  in its early-AGB phase.

### Lightcurve evolution

The multiband lightcurve of WNTR23bzdiq is shown in Figure 10.2. No substantial variations ( $> 0.3$  mag) are seen in the available optical data from 2003 to 2018. Starting in 2018, the ZTF data reveal a gradual brightening — an increase of a few tenths of a magnitude over three years. This was followed by a 1 mag eruption beginning in 2021, which lasted for roughly 1000 days. The star faded towards the end of 2023, then rebrightened in 2024 and continues to brighten at the time of writing. The NEOWISE data show a smooth and steady increase in the mid-IR brightness from 2016 to 2023, followed by a decline in the next year. The mid-IR fading lags behind the optical, with the mid-IR fading beginning about a thousand days after the optical fading. No mid-IR data are available during the 2024 rebrightening.

---

<sup>6</sup>downloaded from <https://waps.cfa.harvard.edu/MIST/>

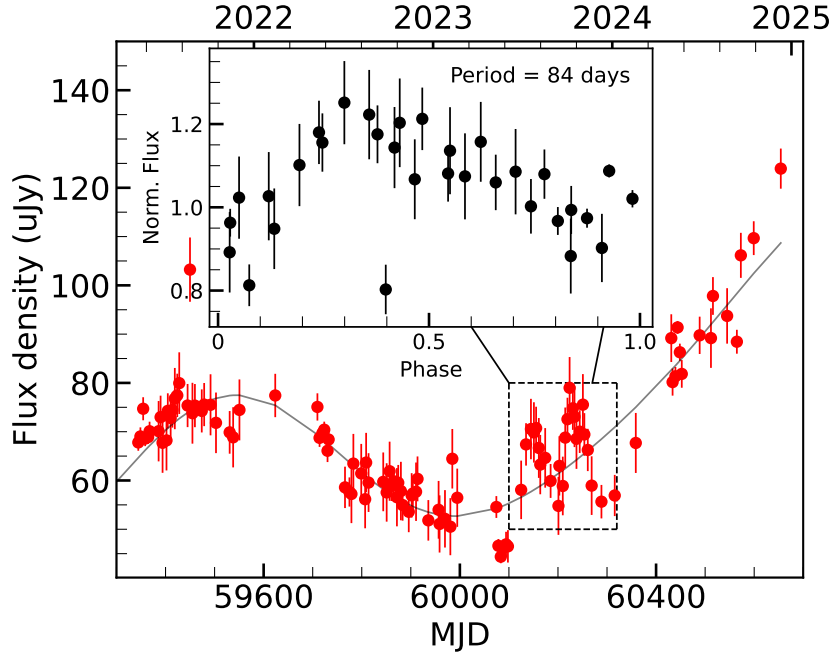


Figure 10.5: The *r*-band lightcurve of WNTR23bzdiq (red points) showing an indication of periodicity at the end of the first eruption in 2023, with two successive bumps of  $\approx 0.2$  mag amplitude (dashed square). The inset shows a phase-folded lightcurve of these two bumps, where the flux has been normalized by a smooth gaussian process fit (black line) and phase folded at the derived period of 84 days.

We do not find any clear periodic signatures in the lightcurve. At the end of the first eruption in 2023, the *r*-band lightcurve shows two sharp, consecutive bumps, each  $\approx 0.2$  mag in amplitude (Figure 10.5). A Lomb Scargle analysis of this segment yields a period of  $\approx 84$  days. However, these two sharp bumps are unlikely to be caused by orbital motion of the binary, but could be due to accretion episodes on the secondary. Outside this, we do not detect any clear periodic signatures in the ZTF or the archival PTF data, although the larger uncertainties in the PTF and early ZTF data limit sensitivity to low-amplitude variations.

We derived the evolution of the bolometric luminosity, effective temperature, stellar radius, and dust properties using the multi-band light curves, applying DUSTY modeling combined with MCMC sampling as described in Section 10.3. To build spectral energy distributions (SEDs) at several epochs between 2018 and 2025, we used Gaussian Process (GP) regression to interpolate the light curves and fill temporal gaps. The GP model, implemented with the python package `scikit-learn` (Pedregosa et al. 2011), employed a Radial Basis Function kernel with an added

White kernel to account for observational noise. For epochs between 2018 and 2023, the SEDs include five bands (*griW1W2*). We find that the *W1* and *W2* measurements are essential for accurately constraining the bolometric luminosity; omitting them results in underestimates by factors of up to two. In contrast, for 2024 and 2025, only optical (*gri*) and NIR (*J*) data are available. As a result, we cannot accurately estimate stellar parameters during this period. We report values by assuming the  $r - W1$  and  $r - W2$  colors remain similar to those in late 2023 — an assumption supported by the minimal color variations observed in the previous lightcurve.

In 2018, the bolometric luminosity was  $\approx 20000 L_{\odot}$ , already brighter than the progenitor’s 2015 luminosity of  $\approx 16000 L_{\odot}$ . This slow brightening continued through 2020, after which the luminosity increased more rapidly, reaching  $\approx 40000 L_{\odot}$  by the end of 2022. Notably, this luminosity increase began  $\approx 200$  days prior to the *r*-band outburst and was driven primarily by the brightening in the *W1* and *W2* bands. The luminosity plateaued for the next five hundred days before declining slightly to  $\approx 35000 L_{\odot}$  in late 2023. Based on the 2024 data, we infer a further increase to  $\approx 50000 L_{\odot}$  by the end of that year; however, we caution that these estimates are uncertain due to the lack of mid-IR data during this time.

The effective temperature in 2018 is estimated to be  $\approx 3650$  K, marginally ( $1\sigma$ ) warmer than the progenitor. Over the subsequent years, the temperature remains nearly constant, with small fluctuations of  $\approx 50$  K that are consistent with the NIR spectroscopic evolution (Section 10.3). For instance, the temperature in 2024 is predicted to be slightly higher than in 2023, consistent with the warmer spectral types inferred from the 2024 NIR spectra.

The dust optical depth remains roughly constant between 2018 and mid-2022 at  $\tau_V \approx 3.2$ , slightly higher than that of the progenitor ( $2.7 \pm 0.4$ ). In early 2023,  $\tau_V$  increases to  $\approx 3.6$  before declining thereafter. This evolution mirrors the optical light curve: the optical depth peaks when the mid-IR flux is at its maximum and the optical emission is fading. During this time (2018 to 2025), the dust shell temperature remains steady at  $\approx 1200$  K, while the inner radius of the shell expands from  $\approx 3000 R_{\odot}$  to  $\approx 5000 R_{\odot}$ . We estimate the dust mass from the DUSTY model parameters using the prescription from Lau et al. (2025), finding an increase from  $\sim 1 \times 10^{-7} M_{\odot}$  to  $\sim 4 \times 10^{-7} M_{\odot}$  over this period. While the inferred dust evolution aligns well with the multi-wavelength photometric changes, we reiterate that these estimates are based on data at wavelengths  $\lesssim 5 \mu\text{m}$ , where the impact of dust is not most prominent. Observations at longer wavelengths are essential to robustly

constrain the dust properties and their evolution in this system.

### Spectroscopic evolution

Figure 10.3 shows the optical and near-IR spectra of WNTR23bzdiq, along with the closest matching stellar spectral templates from the Jacoby-Hunter-Christian Atlas (Jacoby et al. 1984) and the IRTF spectral library (Rayner et al. 2009). The spectra generally resemble late M-type giant stars; however, the spectral sub-types evolve between epochs. No strong emission lines are detected in any of the spectra.

Our earliest NIR spectrum, taken towards the end of the first outburst, shows strong absorption bands of TiO, H<sub>2</sub>O, and CO. The *H*-band bump shaped by water-vapor absorption on either sides resembles that of very late M8-M9 type stars. An optical spectrum from a month later also exhibits molecular absorption bands of TiO and atomic absorption such as the Ca H&K, Na ID doublet, Mg, and the Ca NIR triplet. This optical spectrum is more consistent with an M1-type star — in contrast to the much colder NIR spectrum — implying a “mixed-temperature.”

The next set of spectra — an optical and an NIR pair taken two weeks apart in September 2024, roughly a year into the second brightening — show similar behavior. The NIR spectrum continues to show strong molecular absorption bands, though with a noticeable change in the appearance of the *H*-band shape, now resembling an M7-type star. The optical spectrum remains consistent with an M1-type. Even within the optical spectrum, the redder wavelengths around 0.9 – 1  $\mu$ m resemble an M4-type star. This is confirmed by comparing the spectral types derived from the equivalent widths (EW) of the CO 2.29  $\mu$ m absorption bandhead and the depth of the TiO 0.8859  $\mu$ m band. The EW of the CO bandhead is  $\approx$ 25  $\text{\AA}$ , corresponding to an M7 spectral type (Davies et al. 2007) in the 2–2.5  $\mu$ m range, while the depth of the TiO band is  $\approx$ 0.25, corresponding to an M3 spectral type (Dorda et al. 2016) in the 0.8–0.9  $\mu$ m range. These comparisons suggest a transition from M1 to M7 spectral type from optical to NIR wavelengths. This mixed-temperature behavior persists in the later spectra from December 2024 and January 2025.

Such mixed-temperature spectra have previously been observed in outbursting young stellar objects (YSO), where optical emission originates from the star and NIR emission from the accretion disk (Rigliaco et al. 2012). However, the high luminosity of WNTR23bzdiq rules out a YSO origin. Similar spectral behavior has been seen in the stellar merger eruption V838Mon (Lynch et al. 2004; Lynch et al. 2007b;

Loebman et al. 2015) and recently in the planet-star merger ZTF-SLRN-2020 (De et al. 2023). Both sources underwent a transition from initial hot spectra to cool, M-type, mixed-temperature spectra at late times. In these events, the mixed-temperature spectrum is interpreted as arising from a multi-layered photosphere formed by the material ejected during the merger. For V 838Mon, Lynch et al. (2004) and Lynch et al. (2007b) model the visible to mid-IR spectra using a configuration of a stellar blackbody viewed through dense outer shells. This configuration creates a complex, non-grey photosphere where longer wavelengths probe the outer regions of the envelope while shorter wavelengths probe the inner regions, producing the observed mixed-temperature spectrum.

The mixed-temperature spectra of WNTR23bzdiq point towards a similar configuration of a dense envelope of ejecta around the star. Unlike V838 Mon, where a clear transition from a hot progenitor to a cool M-type spectrum was observed, WNTR23bzdiq began as an M-type star. Nonetheless, the near-IR spectrum at the end of the first outburst indicates a transition to a slightly cooler spectral type than the progenitor. This is followed by a shift toward somewhat warmer M7-type spectra during the rebrightening phase. These spectral changes, though subtler than in V838 Mon, reinforce the parallel with merger-driven eruptions. We further explore these similarities and the broader context of merger transients in Section 10.4.

## 10.4 Discussion

### The nature of WNTR23bzdiq

We now discuss possible origins for the slow eruption of WNTR23bzdiq. AGB stars are known to exhibit brightness variations due to pulsations, being in symbiotic binaries, eclipses by companions, or due to thermal pulses. The variability in WNTR23bzdiq is also reminiscent of the class of “slow variables” showing small luminosity changes over a span of several years (see Petz et al. 2025 for a recent summary). Known classes of slow variables include some YSOs, Teixeira et al. 2018, magnetically active main sequence (MS) and K-giant stars (Baliunas et al. 1990; Phillips et al. 1978), and precursors to stellar mergers (Tylenda et al. 2011b; Blagorodnova et al. 2020; Addison et al. 2022; Tranin et al. 2024). However, this phase space of stellar variability has not been characterized extensively, and several examples exist that have not been fully explained. We examine each of these scenarios below.

First, WNTR23bzdiq is unlike the typical pulsation-driven variability seen in AGB

stars (Whitelock et al. 2003). These stars exhibit periodic or semi-regular brightness variations on timescales ranging from a few hundred days to a few thousand days (Whitelock et al. 2003; Riebel et al. 2015; Karambelkar et al. 2020), unlike the eruptive nature of the WNTR23bzdiq variations.

Second, cool giants in symbiotic binaries can exhibit erratic brightness variations driven by accretion events or dust formation episodes, often appearing as long-duration outbursts or dimmings (De et al. 2022). However, symbiotic stars typically exhibit strong emission lines of hydrogen and helium from ionized gas, which are absent in all spectra of WNTR23bzdiq. This makes a symbiotic binary origin unlikely.

Third, eclipses by stellar companions or debris disks produce long-duration dimming events in cool giants (Rowan et al. 2021; Tzanidakis et al. 2023; Torres et al. 2022). One possibility is that WNTR23bzdiq is brightening because it recently emerged from such a dimming phase. However, this would require the star to have been at its minimum state since at least 2009 (as no dimming events are seen in the PTF and NEOWISE lightcurves). Such a duration would exceed the previous record for dimming giants by over three years (Tzanidakis et al. 2023). The CFHT data further suggest either that the dimming lasted for at least 14 years or that the star underwent a brightening and fading episode between 2005 and 2008. The latter seems unlikely given the long brightening timescale observed post-2020 data, while the former would be unprecedented.

Fourth, while several known classes of slow variables such as YSOs, active MS or K-type giants are ruled out by the AGB progenitor of WNTR23bzdiq, some giant and AGB stars exhibit slow variations whose mechanisms are not fully understood. Recently, Petz et al. (2025) cataloged slow variables from the ASAS-SN survey, noting that while most of the AGB stars exhibit large amplitude, semi-regular periodic variations, some giant stars exhibit steady brightening or dimming trends over several years. WNTR23bzdiq is more similar to this latter group and may represent a more evolved member. However, it does not closely resemble any of the individual examples of slow giants presented in their paper.<sup>7</sup>.

---

<sup>7</sup>The closest resemblance is to the red giant NSV 1610 (a.k.a. 2MASSJ04282152-0148343, their Fig. 11) which was at roughly constant brightness for six years (2014–2020) following which it underwent an 1 mag outburst for three years. However, the full lightcurve of this source from ASAS-SN Skypatrolv2 shows that before 2014, the star had a higher brightness, underwent a decline of 1.5 mag in 2012 and stayed at this low luminosity for the next 8 years. The 2020 outburst was a rebrightening to its initial brightness, unlike WNTR23bzdiq.

Fifth, we examined ZTF light curves for 1,700 red giants and supergiants in the outskirts of M31 compiled by Neugent et al. (2020), and found no source with variability resembling WNTR23bzdiq. All variables in this sample show changes on timescales of a few hundred days, typical of standard RSG or AGB variability. We also searched the database of mid-IR transients in M31 from the NEOWISE survey (De et al. 2024) and found no comparable events. Taken together, these comparisons suggest that WNTR23bzdiq appears to be unlike known classes of slow variable stars.

Sixth, thermal pulses and hot-bottom burning can produce surface luminosity variations of up to  $\sim 0.5$  dex in AGB stars (Marigo et al. 2007; Marigo et al. 2008; Marigo et al. 2013). With  $\approx 10^3$  AGB stars in M31 brighter than  $m_H < 16.5$  mag (similar to WNTR23bzdiq, Gavetti et al. 2025) and an interpulse duration of  $\approx 10^4$  years (Marigo et al. 2007), such events are expected roughly once per decade. It is therefore plausible that the observed brightening of WNTR23bzdiq is linked to a thermal pulse. However, thermal pulse-driven luminosity changes are predicted to occur over a timescale of  $\sim 10^4$  years, much slower than WNTR23bzdiq, whose luminosity increased by 0.5 dex over a few years. Additionally, the MIST models suggest that the progenitor was on the early-AGB, before the onset of thermal pulses, making this explanation less likely. If this event is indeed a thermal pulse, WNTR23bzdiq would offer a rare opportunity to study this process. To our knowledge, the only other candidate is the donor star in the symbiotic binary IGR J17329-2731, which has brightened by 4 magnitudes over the last four decades, possibly due to a thermal pulse (Bozzo et al. 2018).

Finally, a compelling explanation links WNTR23bzdiq to eruptions associated with stellar mergers triggered by CEE. Binary systems undergoing CEE often exhibit slow, years-long brightenings from mass loss during the dynamical inspiral (Tylenda et al. 2011a; Blagorodnova et al. 2020; Addison et al. 2022; Tranin et al. 2024). When the primary is a giant or AGB star, the full merger is accompanied by a gradual increase in luminosity over several years (Pejcha et al. 2016; MacLeod et al. 2022), similar to that seen in WNTR23bzdiq. The spectroscopic similarities with the Galactic stellar merger V838 Mon, discussed in Section 10.3, further support a merger association. In the following Section, we explore the resemblance between WNTR23bzdiq and the Galactic giant star merger OGLE-2002-BLG-360, and examine whether WNTR23bzdiq may mark the onset of CEE in an AGB star.

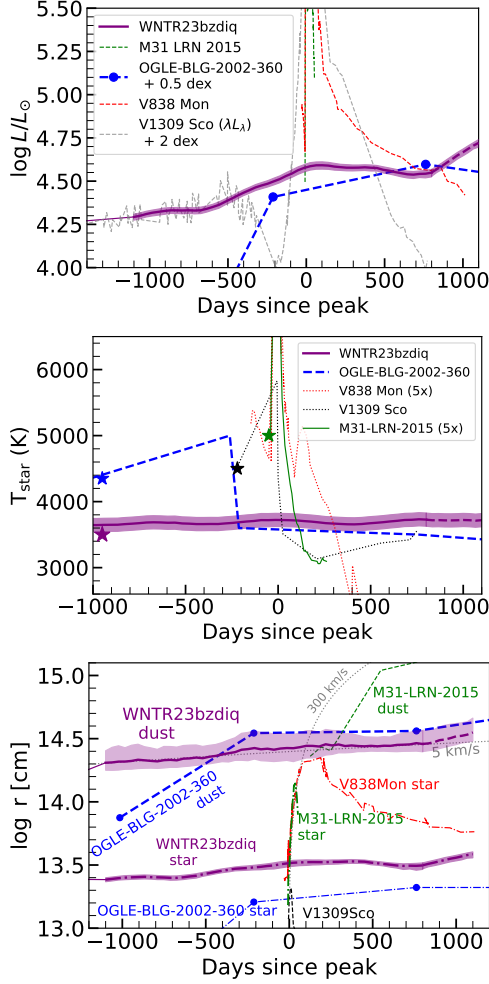


**Figure 10.6: Comparison of properties of WNTR23bzdiq (purple) to the giant star merger OGLE-BLG (blue) and classical LRNe V838 Mon (red), V1309 Sco (black), and M31-LRN-2015 (green).** *Top* The classical LRNe are relatively short lived-eruptions with a sharp rise to maximum, while OGLE-BLG shows a slower rise and longer duration than the classical LRNe. WNTR23bzdiq has an even slower rise and longer duration, consistent with its progenitor being more evolved and extended than that of OGLE-BLG. *Middle:* During their eruptions, all stellar mergers become hotter than their progenitors (indicated by stars) at initial times and then cool rapidly to resemble cold M-type stars. The progenitor of WNTR23bzdiq is a M-type star to begin with, and so it is not expected to show these sharp transitions. The long term temperature is similar to that reached by OGLE-BLG. *Bottom:* The LRNe show rapid photospheric and dust-shell expansions with velocities of  $\approx 300 \text{ km s}^{-1}$  (black dotted line). In contrast, WNTR23bzdiq and OGLE-BLG show a much slower radius evolution with dust-radius expansion velocities of  $\approx 5 \text{ km s}^{-1}$ .

### WNTR23bzdiq: a slower analog of OGLE-2002-BLG-360?

The Galactic transient OGLE-2002-BLG-360 (OGLE-BLG, Tylenda et al. 2013) is considered to be the prototypical (and the only unambiguous) example of a giant star merger. Its eruption began in 2002 with a four magnitude rise over five hundred days, followed by three lightcurve peaks and a transition to an M-type supergiant, consistent with the hallmarks of stellar mergers such as V838 Mon and V1309 Sco. However, OGLE-BLG’s eruption spanned  $\approx$ 2000 days — over an order of magnitude longer than the other mergers — likely due to its extended giant primary, unlike the MS progenitors of V838 Mon and V1309 Sco (MacLeod et al. 2022). The orbital period at the surface of the progenitor of OGLE-BLG ( $M \approx 1 - 3 M_{\odot}$ ,  $R \approx 30 R_{\odot}$ ,  $T_{\text{eff}} \approx 4350$  K) is  $\approx$ 19 days — substantially longer than the other mergers (e.g., 1.4 days for V1309 Sco, Tylenda et al. 2011a). The slow bumpy eruption of WNTR23bzdiq is reminiscent of OGLE-BLG, though with even longer timescales. This is expected in the merger scenario, as the AGB progenitor of WNTR23bzdiq is more extended than that of OGLE-BLG (orbital period at surface  $\approx$ 270 days), and would produce an even slower merger than OGLE-BLG. Motivated by this, we examine WNTR23bzdiq as a possible analog of OGLE-BLG-2002-360.

Figure 10.6 compares the luminosities, temperatures and radii of WNTR23bzdiq with OGLE-BLG (Tylenda et al. 2013) and the more classical stellar mergers (or LRNe) V838Mon (Munari et al. 2002; Tylenda 2005), V1309Sco (Tylenda et al. 2011a), and M31-LRN-2015 (MacLeod et al. 2017; Blagorodnova et al. 2020). The luminosity evolution (top panel) of WNTR23bzdiq qualitatively resembles that of OGLE-BLG, but has a lower amplitude (a factor of 2 increase versus 40) and is stretched out over a longer duration. Both WNTR23bzdiq and OGLE-BLG evolve over much longer timescales than the main eruptions of the three LRNe. However, WNTR23bzdiq resembles the slow *I*-band rise observed in V1309 Sco for several years before its main eruption, which has been attributed to pre-merger mass loss from the binary (Pejcha 2014).

The middle panel shows the evolution of the stellar effective temperatures. All comparison LRNe had progenitors warmer than 4000 K (marked by stars), with temperatures that typically rose at the onset of the eruption before rapidly dropping to  $\leq$  3500 K as they evolved into M-type stars. In contrast, WNTR23bzdiq was an M-type star to start with, and continued to stay at  $\approx$ 3500–3600 K without any significant changes throughout its eruption. OGLE-BLG (blue dashed line) started out warmer (at 4300 K) but reached a similar temperature of  $\approx$ 3500 K at late times.

The bottom panel compares the evolution of the photospheric and dust shell radii. Both the stellar and dust shell radii of WNTR23bzdiq closely track those of OGLE-BLG during its eruption, with similarly slow expansion velocities of  $\approx 5 \text{ km s}^{-1}$ . In contrast, classical LRNe exhibit much faster expansion, around  $\approx 300 \text{ km s}^{-1}$ . The slow expansion velocities for OGLE-BLG and WNTR23bzdiq can be explained by a slow wind from the stellar surface over the course of its eruption, maintaining the dust shell at roughly the same radius (Steinmetz et al. 2025), unlike LRNe that are marked by a rapid mass-ejection episode at the time of merger which expands with high velocities. This is in line with the expectation that CE stripping in extended giants occurs as a steady wind over several years, rather than a sudden mass ejection seen in less extended stars (MacLeod et al. 2022).

Thus, WNTR23bzdiq shares several similarities with OGLE-BLG, appearing as a scaled-down, stretched-out analog, consistent with its more extended, cooler M-type AGB progenitor compared to OGLE-BLG. To assess the plausibility of a CE origin for WNTR23bzdiq, we compare the energetics of the eruption and with the orbital energy losses.

The total radiated energy of WNTR23bzdiq is  $\approx 10^{46} \text{ erg}$ . The magnitude of the orbital energy of a  $\sim 1 M_{\odot}$  companion at the surface of the progenitor star is  $\sim 10^{47} \text{ erg}$ , suggesting that  $\sim 10\%$  of the orbital energy has been radiated if the companion has not inspiraled deeper within the envelope. If the stellar orbit has shrunk by a factor of ten, only  $\sim 1\%$  of the lost orbital energy needs to be radiated. In this case, the lost orbital energy would approach the envelope's binding energy ( $\sim 10^{48} \text{ erg}$ ), making envelope ejection possible. In the extreme case of a full merger, the radiated energy corresponds to  $\sim 0.1\%$  of the orbital energy lost.

We estimate the expected luminosity from a CE inspiral using the formalism described in (MacLeod et al. 2018). If a  $\sim 1 M_{\odot}$  companion spirals through the progenitor's outer envelope, the rate of orbital energy loss ( $L_{\text{decay}}$ ) is  $\sim 10^{39} \text{ erg s}^{-1}$ . The peak radiated luminosity in WNTR23bzdiq is  $\sim 10^{38} \text{ erg s}^{-1}$  — about 10% of  $L_{\text{decay}}$ . Since  $L_{\text{decay}} \propto R^{-5/2}$ , the orbital energy is lost more rapidly if the companion is embedded deeper within the envelope. This may be the case if the 84 day cycles observed at the end of the first eruption reflects the orbital period, implying an orbital separation of  $\approx 160 R_{\odot}$ , about half its initial size. In all cases, these estimates suggest that only a fraction of the orbital energy is required to power the observed luminosity and radiated energy of WNTR23bzdiq. Future observations of this ongoing eruption will determine whether the energetics remain consistent with the CE

explanation.

In summary, WNTR23bzdiq appears to be a slower analog of OGLE-BLG, consistent with a cooler, more extended AGB progenitor. The multi-peaked, slow eruption is ongoing and provides a valuable opportunity for continued multiwavelength follow-up.

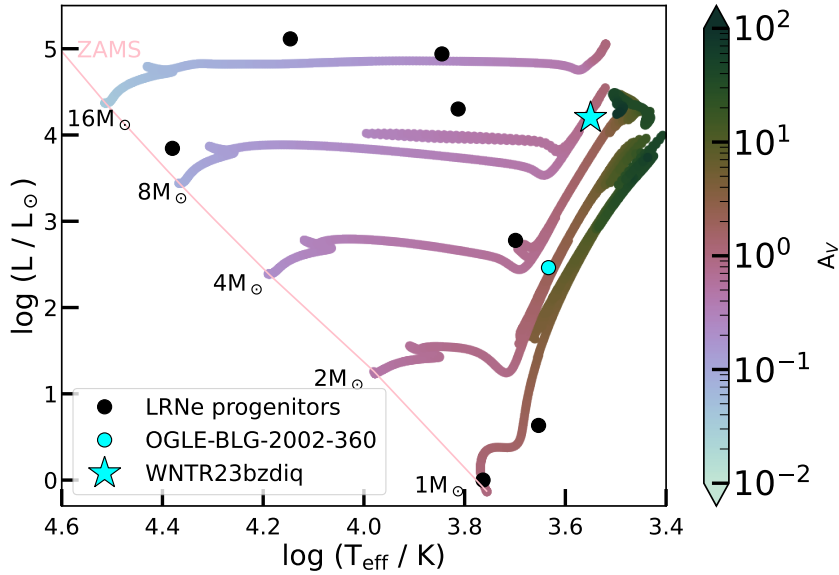


**Figure 10.7: HR-diagram with the progenitors of classical LRNe (black dots), OGLE-BLG (cyan dot) and WNTR23bzdiq (cyan star) with MIST stellar evolutionary tracks.** The stellar tracks are color-coded with the expected dust obscurations ( $A_V$ ) from the wind-model of MacLeod et al. (2022). The progenitor of WNTR23bzdiq is colder than that of any other merger transient, and is the only progenitor on the AGB — potentially providing a unique opportunity to study the outcomes of common-envelope evolution in an AGB star.

### WNTR23bzdiq in the context of common-envelope transients

Figure 10.7 shows the HR diagram locations of the progenitor primary stars of WNTR23bzdiq and other LRNe. The AGB progenitor of WNTR23bzdiq (cyan star) is cooler and more evolved than the MS or Hertzsprung-Gap progenitors of all LRNe. As noted before, giant star primaries are rare in this sample, with OGLE-BLG being the only other example (cyan dot). This scarcity has been attributed to large dust obscuration due to pre-merger mass loss in such systems (MacLeod et al. 2022). Overlaid stellar evolutionary tracks in Figure 10.7 (colored by dust obscuration from the wind model of MacLeod et al. 2022) show that for a  $1 M_\odot$  companion, the WNTR23bzdiq progenitor would have  $A_V \approx 0.5\text{--}0.7$ , slightly lower than the

value of  $A_V \approx 2\text{--}3$  from our DUSTY modeling. This discrepancy could reflect a more massive companion ( $\sim 3 M_\odot$ ), or the limitations of the DUSTY modeling discussed in Section 10.3. In any case, WNTR23bzdiq sits at an intermediate level of dust obscuration between MS/HG LRN progenitors ( $A_V \leq 0.1$ ) and low-mass giants and AGB stars ( $A_V > 10$  mag). While optical time-domain surveys will continue to discover more LRNe, upcoming IR time-domain searches will be crucial to probe the dustier transients.

In the CE scenario, the extended progenitor of WNTR23bzdiq makes it a candidate for a successful envelope ejection rather than a stellar merger. LRN progenitors typically have radiative envelopes with high binding energies and are more likely to merge with their companions after CEE, while a successful CE ejection requires a cool, extended envelope with lower binding energies (Klencki et al. 2021; MacLeod et al. 2022). Our estimates for WNTR23bzdiq show that the orbital energy lost exceeds the binding energy of the envelope if the inspiral shrinks the orbit by a factor of ten. Future observations to measure the mass of the ejected material will help clarify the outcome of this event.

The properties of WNTR23bzdiq are also consistent with theoretical simulations of CEE. The multiple bumps in its lightcurve could arise from mild shocks that form when envelope layers ejected at later times collide with the previously ejected layers (Ricker et al. 2012; Iaconi et al. 2018; Iaconi et al. 2019), or due to instabilities during the slow self-regulated phase that produce large amplitude pulsations in the envelope (Clayton et al. 2017). The current dust mass ( $\sim 10^{-7} M_\odot$ ) is broadly consistent with early-phase predictions from CEE simulations (González-Bolívar et al. 2024; Bermúdez-Bustamante et al. 2024; Iaconi et al. 2020; Lü et al. 2013), which predict substantial dust formation ( $10^{-3} - 10^{-2} M_\odot$ ) only  $\sim 10$  years after the onset of CEE. Future *JWST* observations to trace the evolution of the dust content will be key to confirming the CE origin for WNTR23bzdiq.

## 10.5 Summary and way forward

In this paper, we presented WNTR23bzdiq / WTP19aalzlk — a slow eruption of an early-AGB star in the M 31 galaxy identified by the WINTER near-infrared and the NEOWISE mid-infrared surveyors, that exhibits the following properties —

- The source showed a slow, bumpy increase in its optical flux beginning in 2018. From 2018 to 2021, it steadily brightened by 0.5 mag in the  $r$ -band. In 2021, it underwent a sharp outburst with an amplitude of 1 mag lasting for a total of a

thousand days. In 2024, the source rebrightened by 1 mag and has continued to rise since. At the time of writing, the source has brightened by 2 magnitudes since its quiescent state in the last ten years.

- The optical outburst was accompanied by a slow mid-IR brightening (1 mag over ten years) seen in the NEOWISE data. The mid-IR flux increases smoothly in this duration and continued to rise even when the optical flux faded in 2022.
- No substantial photometric variations were seen in the optical bands from 2003 to 2015. Modeling the quiescent data suggests that the progenitor was an early-AGB star with a  $L \approx 16000 L_\odot$  and  $T_{\text{eff}} \approx 3500$  K.
- The bolometric luminosity rose to  $\approx 40000 L_\odot$  during the 2021 eruption, plateaued for the next two years, and has risen to  $\approx 50000 L_\odot$  since then. The temperature stayed mostly constant at  $\approx 3600$  K throughout the eruption. The stellar and dust shell radii suggest slow photospheric expansion velocities of  $\approx 5 \text{ km s}^{-1}$ , indicating a prolonged mass-loss event. The dust mass produced thus far is  $\sim 4 \times 10^{-7} M_\odot$ .
- Optical and NIR spectra taken during the outburst show strong molecular absorption features of TiO and resemble late M-type stars. The spectra exhibit mixed-temperature behavior where the spectral type transitions from M1 in the optical to M7/8 in the NIR, similar to that seen in the Galactic stellar merger V838 Mon.

WNTR23bzdiq is unlike known classes of slow giant variables such as pulsating AGB stars, symbiotic binaries, and giant star eclipses. While its variability could be triggered by a thermal pulse in an isolated AGB star, the observed timescales are significantly faster than those predicted by theoretical models. The spectroscopic and photometric properties also resemble those of stellar merger transients — particularly the giant star merger OGLE-2002-BLG-360 — but on much longer timescales, consistent with those expected from its colder and more extended AGB progenitor. As such, the slow eruption of WNTR23bzdiq possibly marks the onset of CEE in a binary with an AGB primary, providing a rare opportunity to study CEE in such systems. Continued monitoring — particularly mid-IR observations with *JWST* to trace the evolution of dust masses and multiband observations to measure the energetics of the eruption — will help confirm the association with CEE.

WNTR23bzdiq is possibly a member of the emerging class of slow, infrared-bright transients from CEE in cold giant primaries, whose extended envelopes have low

binding energies, making them more likely to eject their envelopes as a consequence of CEE. New and upcoming infrared transient searches such as WINTER, PRime Focus Infrared Microlensing Experiment (PRIME, Kondo et al. 2023), Dynamic Red All-sky Monitoring Survey (DREAMS Tranin et al. 2024), and Cryoscope (Kasliwal et al. 2025a) will be instrumental in mapping the largely uncharted landscape of such transients. These surveys will set the stage for more sensitive infrared searches with the *Nancy Grace Roman Space Telescope*.

## 10.6 Acknowledgements

VK acknowledges Yashvi Sharma for assistance with the machine learning interpolator, and Jacob Jencson for helping with the GRAMS modeling. WINTER’s construction is made possible by the National Science Foundation under MRI grant number AST-1828470 with early operations supported by AST-1828470. Significant support for WINTER also comes from the California Institute of Technology, the Caltech Optical Observatories, the Bruno Rossi Fund of the MIT Kavli Institute for Astrophysics and Space Research, the David and Lucille Packard Foundation, and the MIT Department of Physics and School of Science. This work was supported by a NASA Keck PI Data Award, administered by the NASA Exoplanet Science Institute. We acknowledge the support of the National Aeronautics and Space Administration through ADAP grant number 80NSSC24K0663. This research has made use of the Keck Observatory Archive (KOA), which is operated by the W. M. Keck Observatory and the NASA Exoplanet Science Institute (NExSci), under contract with the National Aeronautics and Space Administration. N. B. acknowledges to be funded by the European Union (ERC, CET-3PO, 101042610). Views and opinions expressed are however those of the author(s) only and do not necessarily reflect those of the European Union or the European Research Council Executive Agency. Neither the European Union nor the granting authority can be held responsible for them. Some of the data presented herein were obtained at Keck Observatory, which is a private 501(c)3 non-profit organization operated as a scientific partnership among the California Institute of Technology, the University of California, and the National Aeronautics and Space Administration. The Observatory was made possible by the generous financial support of the W. M. Keck Foundation. The authors wish to recognize and acknowledge the very significant cultural role and reverence that the summit of Maunakea has always had within the Native Hawaiian community. We are most fortunate to have the opportunity to conduct observations from this mountain.

## SUMMARY AND PATH FORWARD

In this final chapter, I summarize the progress made in this thesis on the open questions outlined in Chapter 1 (see Figure 11.1), and highlight the exciting potential of upcoming surveys that are poised to significantly advance our understanding of the merger landscape. In particular, I discuss scientific opportunities from the following forthcoming surveys:

- The Vera Rubin Observatory’s Legacy Survey of Space and Time (LSST, Ivezić et al. 2019b) will be the deepest time-domain survey conducted to date, covering  $\approx 18000$  sq. deg in six filters to a depth of  $\approx 24.2$  mag for the next ten years. The trifecta of unprecedented depth, color information, and temporal baseline offers a unique opportunity to discover and characterize low-luminosity transients and variable stars. Through a combination of cross-matching with galaxy catalogs and efficient filtering strategies, LSST will enable the study of stellar and white-dwarf mergers on an unprecedented scale.
- The Spectro-Photometer for the History of the Universe, Epoch of Reionization, and Ices Explorer (SPHEREx, Crill et al. 2020) mission was launched on March 11, 2025 and will conduct a spectroscopic survey of the entire sky from  $0.75 - 5.0$   $\mu\text{m}$  at a spectral resolution of  $40 - 130$  every six months over its two-year-long baseline (Crill et al. 2020). SPHEREx’s infrared sensitivity matches those of the mid-IR ALLWISE survey (Cutri et al. 2021) and its NE-OWISE reactivation mission (Mainzer et al. 2014a). The multiplicative power of combining SPHEREx spectra with data from these IR surveys provides an exciting opportunity to study the dustiest stellar mergers in our Milky Way.
- The *Nancy Grace Roman Space Telescope* (Roman, Akeson et al. 2019), scheduled to launch in 2027, will provide unprecedented wide-field NIR sensitivity ( $\approx 27$  mag over  $0.281$  sq. deg.) heralding a new era in infrared time-domain astronomy. Near-realtime transient searches with the RAPID

pipeline<sup>1</sup> using Roman data provide an exciting opportunity for studying the dustiest stellar mergers and searches for neutron star mergers.

- Cryoscope (Kasliwal et al. 2025a) is a planned wide-field (49.6 sq. deg.) K-dark band time-domain surveyor at Dome C in Antarctica, reaching a depth of  $\approx 24$  mag, enabling large-scale IR searches for neutron star mergers and the dustiest massive star mergers.

### 11.1 Uncovering the demographics of He-CO WD mergers

Part I of this thesis focused on the outcomes of WD mergers. In Chapters 2 and 3, I presented systematic infrared searches for dusty, variable RCB stars which revealed that their Galactic number is between 250–400, corresponding to a Galactic He-CO WD merger rate of  $0.8\text{--}5 \times 10^{-3} \text{ yr}^{-1}$ . This rate provides an observational benchmark to validate binary population synthesis models that estimate the number of WD binary systems detectable by LISA (Lamberts et al. 2019). However, this estimate does not include the uncertain contribution of the dustless-HdC (dHdC) stars, which are seemingly identical to RCB stars in almost all major aspects, except for variability and dust composition (Clayton 2012). With the growing number of known RCB and dHdC stars (Tisserand et al. 2022), it is now possible to conduct comparative studies aimed at identifying differences between the two populations (Crawford et al. 2022). In Chapter 4, I presented oxygen isotope ratios for the largest sample of RCB and dHdC stars to date using medium-resolution spectra. These measurements revealed that dHdC stars tend to exhibit lower oxygen isotope ratios than RCB stars, suggesting that the two populations may originate from WD binaries with different total masses or mass ratios — with RCB stars likely arising from more massive systems.

A natural next step involves high-resolution spectroscopic observations of this expanded sample to enable more detailed elemental abundance studies. As a first step towards this, Mehla et al. (2024)<sup>2</sup> presented the highest resolution NIR spectra for the largest sample of RCB and dHdC stars to date from the iSHell spectrograph on IRFT (Program: 2022B065, PI: Karambelkar), and showed a correlation between oxygen isotope ratios and stellar effective temperatures. Similar trends are observed in simulations of WD merger outcomes, driven by the total mass and mass ratios of the merging white dwarfs (Crawford et al. 2024). The possible mass difference

---

<sup>1</sup><https://rapid.ipac.caltech.edu/>

<sup>2</sup>Study led by an undergraduate student mentored by VK

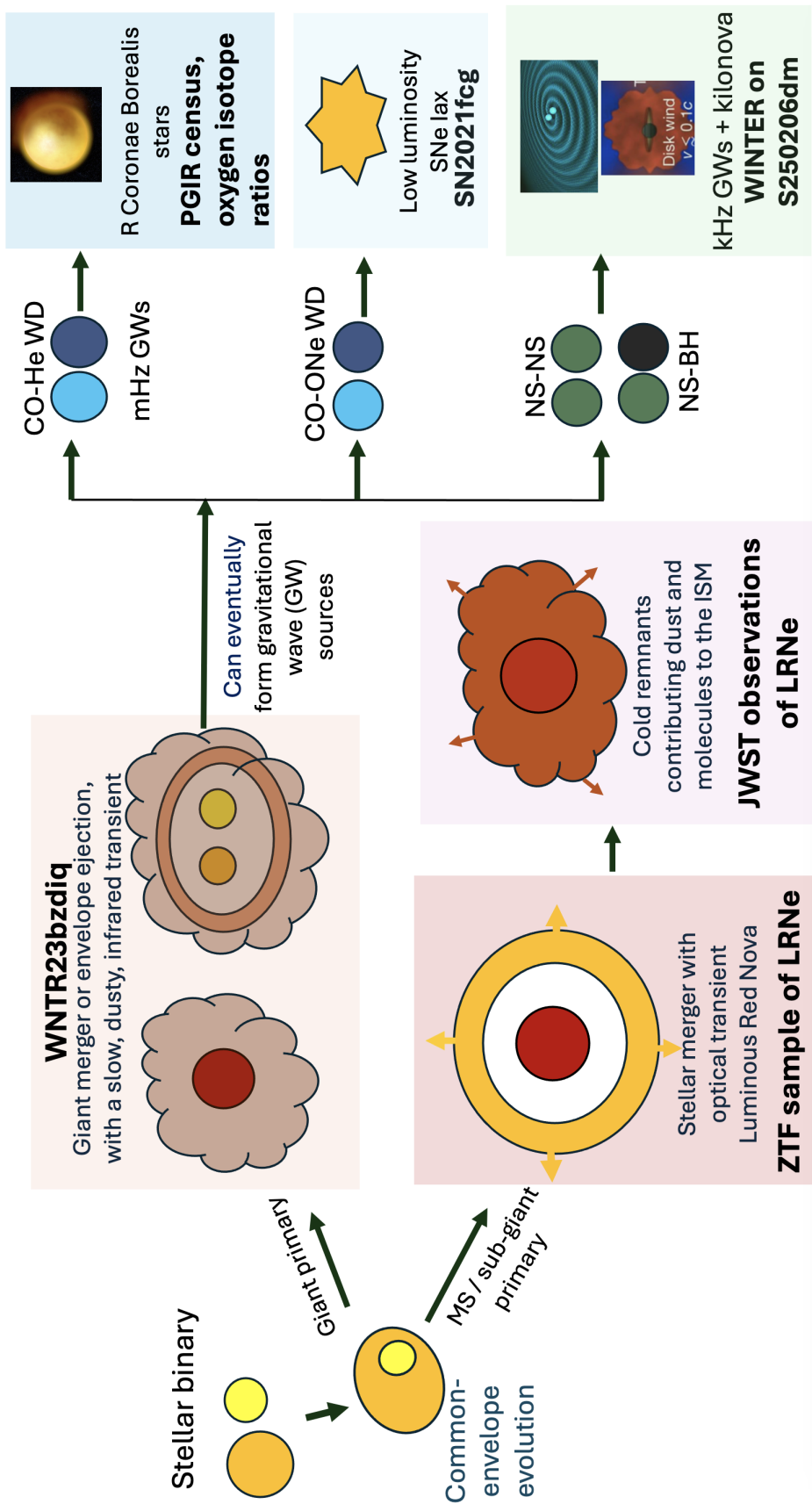


Figure 11.1: A schematic of the landscape of merging stars, merging white dwarfs, and merging neutron stars explored in this thesis.

between RCBs and dIaCs can also be probed through asteroseismology (Wong et al. 2024) using high-cadenced observations from *TESS* and long-term variability data from AAVSO. Finally, sub-mm observations of dIaC stars to search for cold dust around them will determine whether they ever underwent a dusty phase in their evolutionary history. These observational studies will provide insights into the distinct progenitor properties of dIaC and RCB stars, helping to resolve their dust puzzle and yielding a more complete picture of the He-CO WD binaries in the Milky Way. Looking ahead, upcoming surveys like Rubin and Roman will extend these studies beyond the Milky Way, enabling identifications of RCB stars in galaxies to a distance of  $\sim 10$  Mpc, opening a new window into low-mass WD binaries in diverse environments.

### 11.2 Populating the landscape of low-luminosity SNe Iax

In Chapter 5, I presented SN 2021fcg — the least luminous SN Iax identified to date — whose properties are consistent with a failed detonation from an ONe-CO WD merger. As a next step for this supernova, deep late-time optical observations with the *Hubble Space Telescope* (Program ID: 17083, PI: Karambelkar) and infrared observations with *JWST* to search for a remnant will provide additional constraints on the explosion mechanism (Shen et al. 2017). More broadly, only three other SNe occupy this low-luminosity end of the SN Iax population (Srivastav et al. 2020; Stritzinger et al. 2015; Foley et al. 2009). Rubin will play a crucial role in expanding this sample, with a detection horizon of  $\approx 200$  Mpc, five times larger than the  $\approx 40$  Mpc reach of current surveys. A targeted experiment similar to the ZTF Census of the Local Universe (De et al. 2020c; Das et al. 2023) that keeps track of Rubin transients in cataloged nearby galaxies will be instrumental in identifying these low-luminosity SNe.

### 11.3 The infrared quest for the next kilonova

Part II of this thesis focused on infrared searches for electromagnetic counterparts to neutron star mergers. In Chapter 6, I outlined the data reduction pipeline for the new WINTER infrared surveyor at Palomar Observatory, designed for near-IR electromagnetic followup of GW alerts during the International Gravitational Wave Network’s fourth (O4) observing run. In Chapter 7, I described WINTER’s follow-up of the GW alert S250206dm. While no compelling kilonova counterpart was identified by WINTER and other surveys (Ahumada et al. in prep.), the search demonstrated the benefit of NIR observations and highlighted the need for more

sensitive wide-field infrared searches. WINTER will continue to respond to GW alerts from BNS and NSBH mergers for the remainder of O4, which is scheduled to run through October 7, 2025. In addition to WINTER, deeper infrared searches conducted by the PRIME surveyor (1.8 m, 1.56 sq. deg., Guiffreda et al. 2024; Kondo et al. 2023; Durbak et al. 2024; Kutyrev et al. 2023 will aid the IR quest for the next kilonova during O4.

Beyond O4, IGWN’s fifth observing run (O5) is scheduled to begin in late 2027. O5 is expected to increase the median detection horizons for BNS and NSBH mergers to  $\approx 700$  and  $\approx 1300$  Mpc, respectively (Kiendrebeogo et al. 2023). IR searches for kilonovae during O5 will be led by Roman and Cryoscope. Roman’s unparalleled infrared sensitivity (depth of 27.6 mag in an hour in the F129 filter<sup>3</sup>) over a field of 0.28 sq. deg. enables it to discover kilonovae from well-localized GW alerts to a distance of  $\approx 3$  Gpc. Meanwhile, Cryoscope’s much wider 49.6 sq. deg. FOV enables it to tile larger localization regions. Cryoscope can discover all kilonovae within 300 Mpc, regardless of the localization size, and kilonovae within 1 Gpc for events better localized than 100 sq deg (Kasliwal et al. 2025a). With this powerful suite of infrared surveys and the improving sensitivity of GW detectors in the coming years, the infrared quest for kilonovae is set to strike gold.

#### 11.4 The (IR) bright future of common-envelope transients

Part II of this thesis focused on exploring the multiple facets of transients originating in massive stellar mergers and common-envelope ejections.

##### Building a robust sample of LRNe to study CEE

In Chapter 8, I presented the first systematic sample study of Luminous Red Novae — extragalactic transients from massive stellar mergers — and measured their volumetric rate and luminosity function. The cumulative rate of extragalactic LRNe with  $M_{\text{peak}} < -11$  mag is  $\approx 70^{+70}_{-40}\%$  of the local core-collapse supernova rate, and declines with luminosity as  $dN/dL \sim L^{-2.5}$ . While this is broadly consistent with predictions from binary population synthesis simulations, the models tend to underpredict the rate of the most luminous events ( $M_{r,\text{peak}} \leq -13$  mag). The current uncertainties in the LRN rate are dominated by the small sample size of nine events, limiting our ability to constrain common envelope evolution (CEE) models robustly via comparison to population synthesis models. Looking forward, Rubin will dramatically overcome this limitation, discovering over 500 LRNe annually (Howitt

---

<sup>3</sup>[https://roman.gsfc.nasa.gov/science/WFI\\_technical.html](https://roman.gsfc.nasa.gov/science/WFI_technical.html)

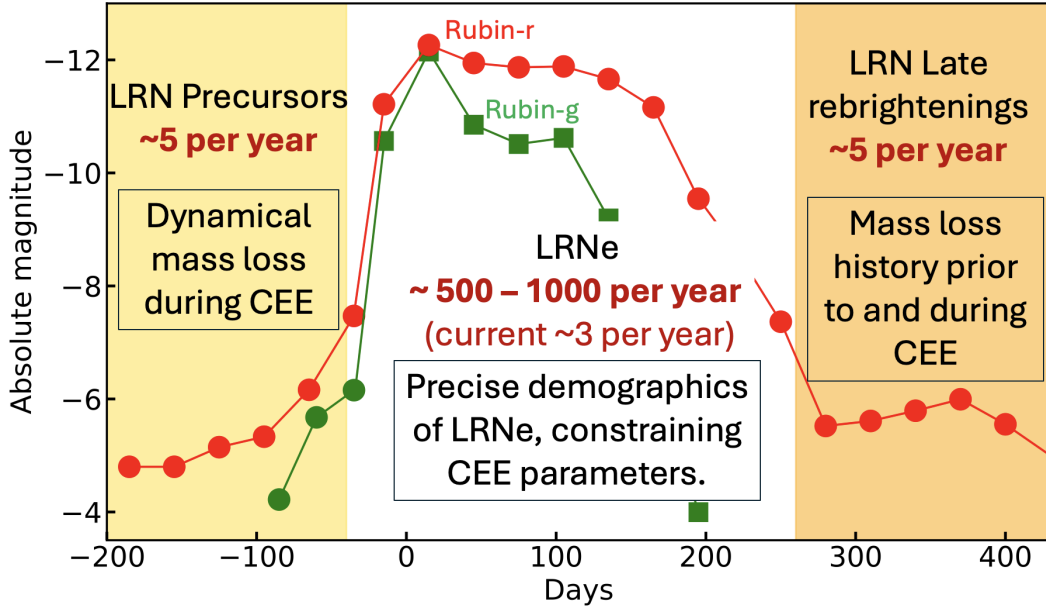


Figure 11.2: **The landscape of LRNe in the Rubin era.** Rubin will revolutionize the study of stellar mergers with a hundred-fold increase in sensitivity to LRNe, and unprecedented precursor and late-time observations of nearby LRNe

et al. 2020). Remarkably, many of these events can be identified photometrically, without requiring spectroscopic confirmation, due to their distinctive signatures. By cross-matching Rubin’s alert stream with galaxy catalogs (e.g., NED-LVS; Cook et al. 2023) and selecting transients with intermediate luminosities ( $M_{\text{abs},r}$  between  $-10$  and  $-16$  mag) and color evolution from blue to red (see Fig. 11.2), a robust photometric selection of LRNe becomes feasible. This will enable the construction of a large, statistically significant sample of massive stellar mergers, yielding volumetric rate and luminosity function measurements to better than 10% precision. In addition to increasing the sample size, Rubin’s depth and cadence will provide valuable observations both prior to and long after the merger, capturing signatures of pre-merger mass loss that can be ejected months to decades before the merger (Pejcha et al. 2017; Cai et al. 2021; Tranin et al. 2024). These observations will open up a new phase space for LRN studies (Blagorodnova et al. 2020), offering deeper insight into the dynamical processes driving common envelope evolution.

### Uncovering the landscape of the missing dusty mergers and envelope ejections

In Chapter 10, I presented a slow infrared transient in M 31 identified by WINTER and NEOWISE, that may mark the onset of common envelope evolution (CEE) in a binary system with an AGB primary. This event is a member of an emerging

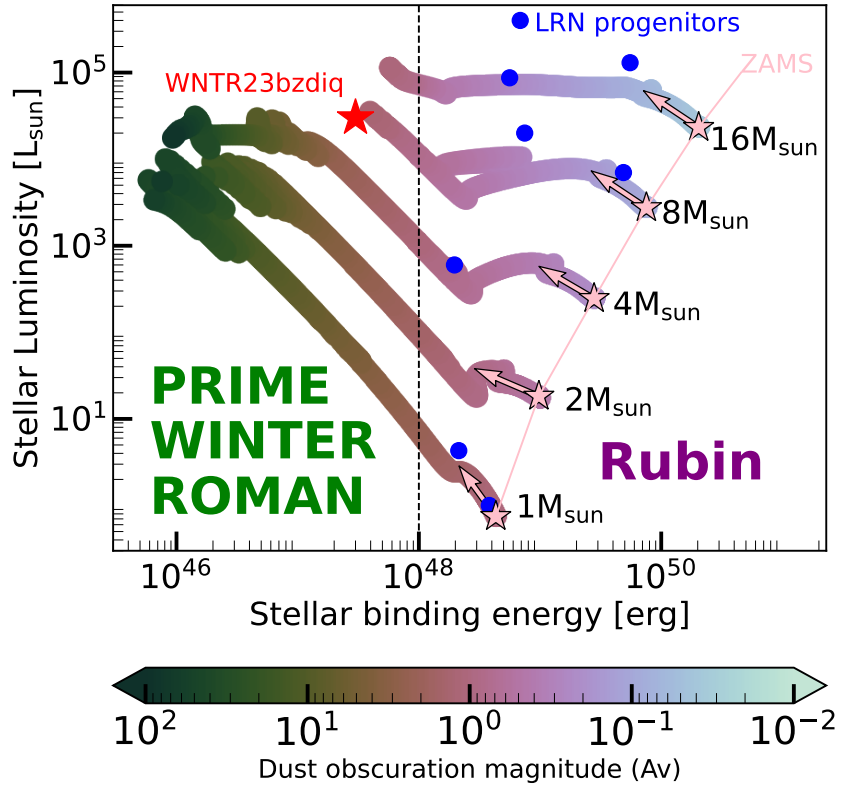
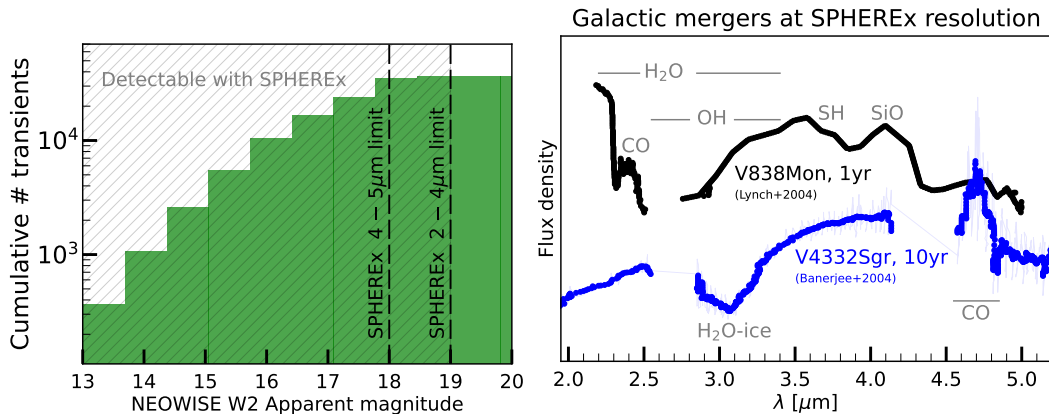


Figure 11.3: **The landscape of stellar merger discovery for Rubin and upcoming infrared surveys.** Colored lines show stellar evolutionary tracks for the primary star in a binary system, color-coded by the amount of dust formed when it engulfs its companion (from MacLeod et al. 2022). All known LRN progenitors (blue dots), discovered by optical telescopes, are moderately evolved stars with high binding energies and relatively low dust. The Rubin Observatory will discover hundreds of such mergers annually. Meanwhile, new infrared surveys such as PRIME, WINTER, Roman, and Cryoscope will explore the largely uncharted territory of giant stars with lower binding energies that are more likely to eject their envelopes and are missed by optical surveys due to large dust obscuration.

class of dusty infrared transients linked to CEE in evolved giant star primaries (De et al. in prep) — distinct from LRNe, which involve mergers with main-sequence or Hertzsprung Gap primaries (MacLeod et al. 2022). These dusty transients have been missed by previous optical surveys and are only now being uncovered with the advent of new IR time-domain searches. These mergers can provide crucial insights about the formation of compact object binaries, as the extended envelopes of giant stars make them more prone to eject their envelopes rather than undergo a merger (Klencki et al. 2020), unlike LRNe. Going forward, NIR searches with WINTER, PRIME, Roman, and Cryoscope will help uncover this largely uncharted landscape

of giant star mergers and envelope ejections (Figure 11.4).

Closer to home, the NEOWISE and SPHEREx missions are set to uncover the population of missing, dusty stellar mergers in the Milky Way. The Galactic merger rate is estimated to be as high as one per year (Kochanek et al. 2014), yet only three have been identified in the last thirty years, indicating they may be missed due to dust or their rate may be overestimated. A new pipeline to identify mid-IR transients using NEOWISE data has uncovered a plethora of dusty Galactic transients from the last decade that were missed by optical surveys (De et al. 2023). SPHEREx, with a comparable mid-IR sensitivity to NEOWISE, is set to provide infrared spectra that will classify the vast majority of these sources and will identify dusty, low-mass stellar mergers in the Milky Way based on broad molecular and ice features in their 2–5  $\mu\text{m}$  spectra (Figure 11.4). This will provide a census of the missing mergers in the Milky Way, providing a rate of low-mass mergers and a sample of nearby events for detailed follow-up studies.



**Figure 11.4: Searching for missing mergers in the Milky Way with NEOWISE and SPHEREx.** *Left:* The NEOWISE survey has identified thousands of slow-evolving infrared transients over the last fifteen years (De et al. 2023) that will be detected by SPHEREx. SPHEREx 2–5  $\mu\text{m}$  spectra for these transients will search for missed low-mass mergers in the Milky Way, identifying them by their mid-IR spectra that exhibit absorption bands of volatile molecules and ice (*right*, Lynch et al. 2004; Banerjee et al. 2004).

### Quantifying the dust and molecular contents of stellar mergers

In Chapter 9, motivated by the comparable rates of LRNe and CCSNe, I presented a *JWST* study to measure the dust masses of four LRNe (Program ID: 4244, PI: Karambelkar). We found that the dust contribution of LRNe is  $\approx 25\%$  of CCSNe, suggesting that LRNe could be important cosmic dust sources. Our *JWST* observa-

tions also revealed substantial amounts of oxygen-rich molecules, including water vapor, CO, and SiO, surrounding these merger remnants, highlighting their potential as key laboratories for studying the evolution of molecules as they condense into dust and ice conglomerates (Banerjee et al. 2004). Future *JWST* observations targeting a broader sample of LRNe will be essential to quantifying the dust yields. Some of these observations will be carried out as part of our approved *JWST* Cycle 4 program focused on dust production in gap transients (Program ID: 7040). Continued mid-infrared spectroscopic monitoring with *JWST* will enable detailed tracking of molecular evolution around the remnants, providing new insights into their fascinating post-merger chemistry and dust formation (Kamiński et al. 2021). In addition to *JWST*, mid-IR spectra from SPHEREx will trace hot-dust emission and molecular and ice absorption around stellar mergers (Figure 11.4).

Thus, the exciting suite of upcoming surveys is poised to transform our understanding of the different facets of common-envelope transients. The future of mergers is undoubtedly (IR) bright.

## BIBLIOGRAPHY

Aartsen, M. G. et al. (Mar. 2017). “The IceCube Neutrino Observatory: instrumentation and online systems”. In: *Journal of Instrumentation* 12.3, P03012. doi: 10.1088/1748-0221/12/03/P03012.

Aasi, J. et al. (2015). “Advanced LIGO”. In: *Class. Quant. Grav.* 32, p. 074001. doi: 10.1088/0264-9381/32/7/074001.

Abbasi, R. et al. (Feb. 2023). “IceCube Search for Neutrinos Coincident with Gravitational Wave Events from LIGO/Virgo Run O3”. In: *ApJ* 944.1, 80, p. 80. doi: 10.3847/1538-4357/aca5fc.

Abbott, B. P. et al. (Feb. 2016). “Observation of Gravitational Waves from a Binary Black Hole Merger”. In: *PRL* 116.6, 061102, p. 061102. doi: 10.1103/PhysRevLett.116.061102.

Abbott, B. P. et al. (Nov. 2017a). “A gravitational-wave standard siren measurement of the Hubble constant”. In: *Nature* 551.7678, pp. 85–88. doi: 10.1038/nature24471.

Abbott, B. P. et al. (Oct. 2017b). “Gravitational Waves and Gamma-Rays from a Binary Neutron Star Merger: GW170817 and GRB 170817A”. In: *ApJ* 848.2, L13, p. L13. doi: 10.3847/2041-8213/aa920c.

Abbott, B. P. et al. (Oct. 2017c). “GW170817: Observation of Gravitational Waves from a Binary Neutron Star Inspiral”. In: *PRL* 119.16, 161101, p. 161101. doi: 10.1103/PhysRevLett.119.161101.

Abbott, B. P. et al. (Oct. 2017d). “GW170817: Observation of Gravitational Waves from a Binary Neutron Star Inspiral”. In: *Physical Review Letters* 119.16. doi: 10.1103/physrevlett.119.161101.

- (Oct. 2017e). “GW170817: Observation of Gravitational Waves from a Binary Neutron Star Inspiral”. In: *Physical Review Letters* 119.16. doi: 10.1103/physrevlett.119.161101.
- (Oct. 2017f). “Multi-messenger Observations of a Binary Neutron Star Merger”. In: *ApJ* 848.2, p. L12. doi: 10.3847/2041-8213/aa91c9.

Abbott, R. et al. (June 2021a). “GWTC-2: Compact Binary Coalescences Observed by LIGO and Virgo during the First Half of the Third Observing Run”. In: *Physical Review X* 11.2. doi: 10.1103/physrevx.11.021053.

- (June 2021b). “Observation of Gravitational Waves from Two Neutron Star–Black Hole Coalescences”. In: *ApJ* 915.1, p. L5. doi: 10.3847/2041-8213/ac082e.

Abbott, R. et al. (Oct. 2023). “GWTC-3: Compact Binary Coalescences Observed by LIGO and Virgo during the Second Part of the Third Observing Run”. In: *Physical Review X* 13.4, 041039, p. 041039. doi: 10.1103/PhysRevX.13.041039.

Acernese, F. et al. (Dec. 2014). “Advanced Virgo: a second-generation interferometric gravitational wave detector”. In: *Classical and Quantum Gravity* 32.2, p. 024001. doi: 10.1088/0264-9381/32/2/024001.

Adams, S. M. et al. (Aug. 2016a). “Almost gone: SN 2008S and NGC 300 2008OT-1 are fainter than their progenitors”. In: *MNRAS* 460, pp. 1645–1657. doi: 10.1093/mnras/stw1059.

Adams, T. et al. (2016b). “Low-latency analysis pipeline for compact binary coalescences in the advanced gravitational wave detector era”. In: *Class. Quant. Grav.* 33.17, p. 175012. doi: 10.1088/0264-9381/33/17/175012.

Addison, H. et al. (Dec. 2022). “Searching for the next Galactic Luminous red nova”. In: *MNRAS* 517.2, pp. 1884–1900. doi: 10.1093/mnras/stac2685.

Ahumada, T. et al. (Dec. 2024). “EP 241217a: Possible J-band detection with WINTER”. In: *GRB Coordinates Network* 38626, p. 1.

Akeson, R. et al. (Feb. 2019). “The Wide Field Infrared Survey Telescope: 100 Hubbles for the 2020s”. In: *arXiv e-prints*, arXiv:1902.05569, arXiv:1902.05569. doi: 10.48550/arXiv.1902.05569.

Akutsu, T. et al. (Aug. 2020). “Overview of KAGRA: Detector design and construction history”. In: *Progress of Theoretical and Experimental Physics* 2021.5, 05A101. doi: 10.1093/ptep/ptaa125.

Alcock, C. et al. (June 2001). “The MACHO Project LMC Variable Star Inventory. X. The R Coronae Borealis Stars”. In: *ApJ* 554.1, pp. 298–315. doi: 10.1086/321369.

Alksnis, A. et al. (Jan. 2001). “General Catalog of Galactic Carbon Stars by C. B. Stephenson. Third Edition”. In: *Baltic Astronomy* 10, pp. 1–318. doi: 10.1515/astro-2001-1-202.

Allen, B. (2005). “ $\chi^2$  time-frequency discriminator for gravitational wave detection”. In: *Phys. Rev. D* 71, p. 062001. doi: 10.1103/PhysRevD.71.062001.

Allen, B. et al. (2012). “FINDCHIRP: An Algorithm for detection of gravitational waves from inspiraling compact binaries”. In: *Phys. Rev. D* 85, p. 122006. doi: 10.1103/PhysRevD.85.122006.

Alvarez, R. et al. (Feb. 1998). “Near-infrared narrow-band photometry of M-giant and Mira stars: models meet observations”. In: *A&A* 330, pp. 1109–1119.

Amaro-Seoane, P. et al. (Feb. 2017). “Laser Interferometer Space Antenna”. In: *arXiv e-prints*, arXiv:1702.00786, arXiv:1702.00786.

Andrews, J. E. et al. (Aug. 2021). “The Blue Supergiant Progenitor of the Supernova Imposter AT 2019krl”. In: *ApJ* 917.2, 63, p. 63. doi: 10.3847/1538-4357/ac09e1.

Ansel, J. et al. (Apr. 2024). “PyTorch 2: Faster Machine Learning Through Dynamic Python Bytecode Transformation and Graph Compilation”. In: *29th ACM International Conference on Architectural Support for Programming Languages and Operating Systems, Volume 2 (ASPLOS '24)*. ACM. doi: 10.1145/3620665.3640366.

Antier, S. et al. (June 2020). “GRANDMA observations of advanced LIGO’s and advanced Virgo’s third observational campaign”. In: *Monthly Notices of the Royal Astronomical Society* 497.4, pp. 5518–5539. doi: 10.1093/mnras/staa1846.

Arnett, W. D. (Feb. 1982). “Type I supernovae. I - Analytic solutions for the early part of the light curve”. In: *ApJ* 253, pp. 785–797. doi: 10.1086/159681.

Aso, Y. et al. (2013). “Interferometer design of the KAGRA gravitational wave detector”. In: *Phys. Rev. D* 88.4, p. 043007. doi: 10.1103/PhysRevD.88.043007.

Asplund, M. et al. (Jan. 2000). “The R Coronae Borealis stars - atmospheres and abundances”. In: *A&A* 353, pp. 287–310.

Astropy Collaboration et al. (Oct. 2013). “Astropy: A community Python package for astronomy”. In: *A&A* 558, A33, A33. doi: 10.1051/0004-6361/201322068.

Astropy Collaboration et al. (Sept. 2018). “The Astropy Project: Building an Open-science Project and Status of the v2.0 Core Package”. In: *AJ* 156.3, 123, p. 123. doi: 10.3847/1538-3881/aabc4f.

Astropy Collaboration et al. (Aug. 2022). “The Astropy Project: Sustaining and Growing a Community-oriented Open-source Project and the Latest Major Release (v5.0) of the Core Package”. In: *ApJ* 935.2, 167, p. 167. doi: 10.3847/1538-4357/ac7c74.

Aubin, F. et al. (2021). “The MBTA pipeline for detecting compact binary coalescences in the third LIGO–Virgo observing run”. In: *Class. Quant. Grav.* 38.9, p. 095004. doi: 10.1088/1361-6382/abe913.

Bailer-Jones, C. A. L. et al. (Aug. 2018). “Estimating Distance from Parallaxes. IV. Distances to 1.33 Billion Stars in Gaia Data Release 2”. In: *AJ* 156.2, 58, p. 58. doi: 10.3847/1538-3881/aacb21.

Baliunas, S. et al. (Dec. 1990). “Evidence for long-term brightness changes of solar-type stars”. In: *Nature* 348.6301, pp. 520–523. doi: 10.1038/348520a0.

Banerjee, D. P. K. et al. (Sept. 2007). “Spitzer Observations of V4332 Sagittarii: Detection of Alumina Dust”. In: *ApJ* 666.1, pp. L25–L28. doi: 10.1086/521528.

Banerjee, D. P. K. et al. (2004). “L & M band infrared studies of V4332 Sagittarii - Detection of the water-ice absorption band at 3.05 microns and the CO fundamental band in emission”. In: *Astrophys. J. Lett.* 615, pp. L53–L56. doi: 10.1086/425963.

Barnes, J. et al. (2013). “Effect of a High Opacity on the Light Curves of Radioactively Powered Transients from Compact Object Mergers”. In: *Astrophys. J.* 775, p. 18. doi: 10.1088/0004-637X/775/1/18.

Barnes, J. et al. (2016). “Radioactivity and thermalization in the ejecta of compact object mergers and their impact on kilonova light curves”. In: *Astrophys. J.* 829.2, p. 110. doi: 10.3847/0004-637X/829/2/110.

Bayer, M. (2012). “SQLAlchemy”. In: *The Architecture of Open Source Applications Volume II: Structure, Scale, and a Few More Fearless Hacks*. Ed. by A. Brown et al. aosabook.org.

Becerra, R. L. et al. (Feb. 2025). “LIGO/Virgo/KAGRA S250206dm: DDOTI Upper Limit for the Neutrino IceCube Candidate”. In: *GRB Coordinates Network* 39198, p. 1.

Becker, A. (Apr. 2015). *HOTPANTS: High Order Transform of PSF AND Template Subtraction*. Astrophysics Source Code Library, record ascl:1504.004.

Bell, R. A. et al. (Jan. 1976). “A grid of model atmospheres for metal-deficient giant stars. II.” In: *A&AS* 23, pp. 37–95.

Bellm, E. C. et al. (Dec. 2018). “The Zwicky Transient Facility: System Overview, Performance, and First Results”. In: *Publications of the Astronomical Society of the Pacific* 131.995, p. 018002. doi: 10.1088/1538-3873/aaecbe.

Bellm, E. C. et al. (Jan. 2019a). “The Zwicky Transient Facility: System Overview, Performance, and First Results”. In: *PASP* 131.995, p. 018002. doi: 10.1088/1538-3873/aaecbe.

– (Jan. 2019b). “The Zwicky Transient Facility: System Overview, Performance, and First Results”. In: *PASP* 131.995, p. 018002. doi: 10.1088/1538-3873/aaecbe.

Bermúdez-Bustamante, L. C. et al. (Sept. 2024). “Dust formation in common envelope binary interactions - II: 3D simulations with self-consistent dust formation”. In: *MNRAS* 533.1, pp. 464–481. doi: 10.1093/mnras/stae1841.

Bertin, E. (July 2006). “Automatic Astrometric and Photometric Calibration with SCAMP”. In: *Astronomical Data Analysis Software and Systems XV*. Ed. by C. Gabriel et al. Vol. 351. Astronomical Society of the Pacific Conference Series, p. 112.

– (July 2011). “Automated Morphometry with SExtractor and PSFEx”. In: *Astronomical Data Analysis Software and Systems XX*. Ed. by I. N. Evans et al. Vol. 442. Astronomical Society of the Pacific Conference Series, p. 435.

Bertin, E. et al. (June 1996). “SExtractor: Software for source extraction.” In: *A&AS* 117, pp. 393–404. doi: 10.1051/aas:1996164.

Bertin, E. et al. (Jan. 2002). “The TERAPIX Pipeline”. In: *Astronomical Data Analysis Software and Systems XI*. Ed. by D. A. Bohlender et al. Vol. 281. Astronomical Society of the Pacific Conference Series, p. 228.

Bhowmick, A. et al. (Feb. 2018). “Are DY Persei Stars Cooler Cousins of R Coronae Borealis Stars?” In: *ApJ* 854.2, 140, p. 140. doi: 10.3847/1538-4357/aaaae4.

Bianchi, S. et al. (June 2007). “Dust formation and survival in supernova ejecta”. In: *Monthly Notices of the Royal Astronomical Society* 378.3, pp. 973–982. doi: 10.1111/j.1365-2966.2007.11829.x.

Bildsten, L. et al. (June 2007). “Faint Thermonuclear Supernovae from AM Canum Venaticorum Binaries”. In: *ApJ* 662.2, pp. L95–L98. doi: 10.1086/519489.

Biscaro, C. et al. (May 2016). “Molecules and dust in Cassiopeia A. II. Dust sputtering and diagnosis of supernova dust survival in remnants”. In: *A&A* 589, A132, A132. doi: 10.1051/0004-6361/201527769.

Blagorodnova, N. et al. (Jan. 2017). “Common Envelope Ejection for a Luminous Red Nova in M101”. In: *ApJ* 834, 107, p. 107. doi: 10.3847/1538-4357/834/2/107.

Blagorodnova, N. et al. (Aug. 2020). “Progenitor, precursor, and evolution of the dusty remnant of the stellar merger M31-LRN-2015”. In: *MNRAS* 496.4, pp. 5503–5517. doi: 10.1093/mnras/staa1872.

Blagorodnova, N. et al. (Mar. 2018). “The SED Machine: A Robotic Spectrograph for Fast Transient Classification”. In: *PASP* 130.985, p. 035003. doi: 10.1088/1538-3873/aaa53f.

Blagorodnova, N. et al. (Sept. 2021). “The luminous red nova AT 2018bwo in NGC 45 and its binary yellow supergiant progenitor”. In: *A&A* 653, A134, A134. doi: 10.1051/0004-6361/202140525.

Blanco, V. M. (Jan. 1958). “Carbon Stars at Intermediate Galactic Latitudes.” In: *ApJ* 127, p. 191. doi: 10.1086/146450.

Bocchio, M. et al. (Mar. 2016). “Dust grains from the heart of supernovae”. In: *A&A* 587, A157, A157. doi: 10.1051/0004-6361/201527432.

Bopp, B. W. et al. (Aug. 1981). “The FK COM stars.” In: *ApJ* 247, pp. L131–L134. doi: 10.1086/183606.

Botticella, M. T. et al. (Sept. 2009). “SN 2008S: an electron-capture SN from a super-AGB progenitor?” In: *MNRAS* 398, pp. 1041–1068. doi: 10.1111/j.1365-2966.2009.15082.x.

Bozzo, E. et al. (May 2018). “IGR J17329-2731: The birth of a symbiotic X-ray binary”. In: *A&A* 613, A22, A22. doi: 10.1051/0004-6361/201832588.

Bramall, D. G. et al. (July 2010). “The SALT HRS spectrograph: final design, instrument capabilities, and operational modes”. In: *Ground-based and Airborne Instrumentation for Astronomy III*. Ed. by I. S. McLean et al. Vol. 7735. Society of Photo-Optical Instrumentation Engineers (SPIE) Conference Series, 77354F, 77354F. doi: 10.1117/12.856382.

Broekgaarden, F. S. et al. (Dec. 2021). “Impact of Massive Binary Star and Cosmic Evolution on Gravitational Wave Observations II: Double Compact Object Rates and Properties”. In: *arXiv e-prints*, arXiv:2112.05763, arXiv:2112.05763.

Brown, W. R. et al. (Jan. 2020). “The ELM Survey. VIII. Ninety-eight Double White Dwarf Binaries”. In: *ApJ* 889.1, p. 49. doi: 10.3847/1538-4357/ab63cd.

Bulla, M. (2019). “POSSIS: predicting spectra, light curves and polarization for multi-dimensional models of supernovae and kilonovae”. In: *Mon. Not. Roy. Astron. Soc.* 489.4, pp. 5037–5045. doi: 10.1093/mnras/stz2495.

– (Apr. 2023). “The critical role of nuclear heating rates, thermalization efficiencies, and opacities for kilonova modelling and parameter inference”. In: *MNRAS* 520.2, pp. 2558–2570. doi: 10.1093/mnras/stad232.

Burdge, K. B. et al. (Sept. 2020). “A systematic search of Zwicky Transient Facility data for ultracompact binary LISA-detectable gravitational-wave sources”. In: *arXiv e-prints*, arXiv:2009.02567, arXiv:2009.02567.

Cai, Y. .- et al. (Dec. 2019). “The transitional gap transient AT 2018hso: new insights into the luminous red nova phenomenon”. In: *A&A* 632, L6, p. L6. doi: 10.1051/0004-6361/201936749.

Cai, Y. .- et al. (Oct. 2021). “Intermediate-luminosity red transients: Spectrophotometric properties and connection to electron-capture supernova explosions”. In: *A&A* 654, A157, A157. doi: 10.1051/0004-6361/202141078.

Cai, Y. .- et al. (July 2022). “Observations of the luminous red nova AT 2021biy in the nearby galaxy NGC 4631”. In: *arXiv e-prints*, arXiv:2207.00734, arXiv:2207.00734.

Cami, J. (June 2002). “Molecular gas and dust around evolved stars”. PhD thesis. University of Amsterdam, Netherlands.

Cannon, K. et al. (June 2021). “GstLAL: A software framework for gravitational wave discovery”. In: *SoftwareX* 14, 100680, p. 100680. doi: 10.1016/j.softx.2021.100680.

Cao, Y. et al. (Nov. 2016). “Intermediate Palomar Transient Factory: Realtime Image Subtraction Pipeline”. In: *PASP* 128.11, p. 114502. doi: 10.1088/1538-3873/128/969/114502.

Chambers, K. C. et al. (Dec. 2016a). “The Pan-STARRS1 Surveys”. In: *arXiv e-prints*, arXiv:1612.05560, arXiv:1612.05560. doi: 10.48550/arXiv.1612.05560.

– (Dec. 2016b). “The Pan-STARRS1 Surveys”. In.

Chambers, K. C. et al. (Dec. 2016c). “The Pan-STARRS1 Surveys”. In: *arXiv:1612.05560*.

Chen, M. C. et al. (May 2014). “The dependence of the evolution of Type Ia SN progenitors on the C-burning rate uncertainty and parameters of convective boundary mixing”. In: *MNRAS* 440.2, pp. 1274–1280. doi: 10.1093/mnras/stu108.

Choi, J. et al. (June 2016). “Mesa Isochrones and Stellar Tracks (MIST). I. Solar-scaled Models”. In: *ApJ* 823.2, 102, p. 102. doi: 10.3847/0004-637X/823/2/102.

Clayton, G. C. (June 2012). “What Are the R Coronae Borealis Stars?” In: *Journal of the American Association of Variable Star Observers (JAAVSO)* 40, p. 539.

Clayton, G. C. (Mar. 1996). “The R Coronae Borealis Stars”. In: *PASP* 108, p. 225. doi: 10.1086/133715.

Clayton, G. C. et al. (Oct. 1992). “Observations of R Coronae Borealis Stars in Decline: Empirical Arguments for Dust Formation near the Stellar Surface”. In: *ApJ* 397, p. 652. doi: 10.1086/171821.

Clayton, G. C. et al. (Sept. 2003). “Winds in R Coronae Borealis Stars”. In: *ApJ* 595.1, pp. 412–417. doi: 10.1086/377336.

Clayton, G. C. et al. (Apr. 2005). “An Extremely Large Excess of  $^{18}\text{O}$  in the Hydrogen-deficient Carbon Star HD 137613”. In: *ApJ* 623.2, pp. L141–L144. doi: 10.1086/430110.

Clayton, G. C. et al. (June 2007). “Very Large Excesses of  $^{18}\text{O}$  in Hydrogen-deficient Carbon and R Coronae Borealis Stars: Evidence for White Dwarf Mergers”. In: *ApJ* 662.2, pp. 1220–1230. doi: 10.1086/518307.

Clayton, G. C. et al. (Dec. 2011). “The Circumstellar Environment of R Coronae Borealis: White Dwarf Merger or Final-helium-shell Flash?” In: *ApJ* 743.1, 44, p. 44. doi: 10.1088/0004-637X/743/1/44.

Clayton, G. C. et al. (Aug. 2013). “Variable Winds and Dust Formation in R Coronae Borealis Stars”. In: *AJ* 146.2, 23, p. 23. doi: 10.1088/0004-6256/146/2/23.

Clayton, M. et al. (Sept. 2017). “Episodic mass ejections from common-envelope objects”. In: *MNRAS* 470.2, pp. 1788–1808. doi: 10.1093/mnras/stx1290.

Collaboration, T. L. S. et al. (2021). “GWTC-2.1: Deep Extended Catalog of Compact Binary Coalescences Observed by LIGO and Virgo During the First Half of the Third Observing Run”. In.

Cook, D. O. et al. (Sept. 2023). “Completeness of the NASA/IPAC Extragalactic Database (NED) Local Volume Sample”. In: *ApJS* 268.1, 14, p. 14. doi: 10.3847/1538-4365/acdd06.

Cook, D. O. et al. (July 2019). “Census of the Local Universe (CLU) Narrowband Survey. I. Galaxy Catalogs from Preliminary Fields”. In: *ApJ* 880.1, 7, p. 7. doi: 10.3847/1538-4357/ab2131.

Coughlin, M. W. et al. (Aug. 2018). “Constraints on the neutron star equation of state from AT2017gfo using radiative transfer simulations”. In: *Monthly Notices of the Royal Astronomical Society* 480.3, pp. 3871–3878. doi: 10.1093/mnras/sty2174.

Coughlin, M. W. et al. (July 2020a). “Implications of the search for optical counterparts during the second part of the Advanced LIGO’s and Advanced Virgo’s third observing run: lessons learned for future follow-up observations”. In: *Monthly Notices of the Royal Astronomical Society* 497.1, pp. 1181–1196. doi: 10.1093/mnras/staa1925.

Coughlin, M. W. et al. (Nov. 2019a). “GROWTH on S190425z: Searching Thousands of Square Degrees to Identify an Optical or Infrared Counterpart to a Binary Neutron Star Merger with the Zwicky Transient Facility and Palomar Gattini-IR”. In: *ApJ* 885.1, L19, p. L19. doi: 10.3847/2041-8213/ab4ad8.

Coughlin, M. W. et al. (2019b). “Multimessenger Bayesian parameter inference of a binary neutron star merger”. In: *Mon. Not. Roy. Astron. Soc.* 489.1, pp. L91–L96. doi: 10.1093/mnrasl/slz133.

Coughlin, M. W. et al. (2020b). “Standardizing kilonovae and their use as standard candles to measure the Hubble constant”. In: *Phys. Rev. Res.* 2.2, p. 022006. doi: 10.1103/PhysRevResearch.2.022006.

Coughlin, M. W. et al. (July 2023a). “A Data Science Platform to Enable Time-domain Astronomy”. In: *The Astrophysical Journal Supplement Series* 267.2, p. 31. doi: 10.3847/1538-4365/acdee1.

Coughlin, M. W. et al. (Aug. 2023b). “A Data Science Platform to Enable Time-domain Astronomy”. In: *ApJS* 267.2, 31, p. 31. doi: 10.3847/1538-4365/acdee1.

– (Aug. 2023c). “A Data Science Platform to Enable Time-domain Astronomy”. In: *ApJS* 267.2, 31, p. 31. doi: 10.3847/1538-4365/acdee1.

Coughlin, M. W. et al. (July 2023d). “A Data Science Platform to Enable Time-domain Astronomy”. In: *The Astrophysical Journal Supplement Series* 267.2, p. 31. doi: 10.3847/1538-4365/acdee1.

Coulter, D. A. et al. (Dec. 2017). “Swope Supernova Survey 2017a (SSS17a), the optical counterpart to a gravitational wave source”. In: *Science* 358.6370, pp. 1556–1558. doi: 10.1126/science.aap9811.

Crawford, C. L. et al. (Aug. 2020). “Modelling R Coronae Borealis stars: effects of He-burning shell temperature and metallicity”. In: *MNRAS* 498.2, pp. 2912–2924. doi: 10.1093/mnras/staa2526.

Crawford, C. L. et al. (Nov. 2022). “Peculiar hydrogen-deficient carbon stars: strontium-rich stars and the s-process”. In: *A&A* 667, A85, A85. doi: 10.1051/0004-6361/202142882.

Crawford, C. L. et al. (May 2023). “A spectral classification system for hydrogen-deficient carbon stars”. In: *MNRAS* 521.2, pp. 1674–1699. doi: 10.1093/mnras/stad324.

Crawford, C. L. et al. (Oct. 2024). “Modelling hydrogen-deficient carbon stars in MESA - the effects of total mass and mass ratio”. In: *MNRAS* 534.2, pp. 1018–1027. doi: 10.1093/mnras/stae2149.

Crill, B. P. et al. (Dec. 2020). “SPHEREx: NASA’s near-infrared spectrophotometric all-sky survey”. In: *Space Telescopes and Instrumentation 2020: Optical, Infrared, and Millimeter Wave*. Ed. by M. Lystrup et al. Vol. 11443. Society of Photo-Optical Instrumentation Engineers (SPIE) Conference Series, 114430I, p. 114430I. doi: 10.1117/12.2567224.

Cushing, M. C. et al. (Apr. 2004). “Spextool: A Spectral Extraction Package for SpeX, a 0.8-5.5 Micron Cross-Dispersed Spectrograph”. In: *PASP* 116.818, pp. 362–376. doi: 10.1086/382907.

Cutri, R. M. et al. (June 2003). *VizieR Online Data Catalog: 2MASS All-Sky Catalog of Point Sources (Cutri+ 2003)*.

Cutri, R. M. et al. (Feb. 2021). *VizieR Online Data Catalog: AllWISE Data Release (Cutri+ 2013)*.

Czekaj, M. A. et al. (Apr. 2014). “The Besançon Galaxy model renewed. I. Constraints on the local star formation history from Tycho data”. In: *A&A* 564, A102, A102. doi: 10.1051/0004-6361/201322139.

Dal Canton, T. et al. (Aug. 2020). “Realtime search for compact binary mergers in Advanced LIGO and Virgo’s third observing run using PyCBC Live”. In.

Dan, M. et al. (Aug. 2011). “Prelude to A Double Degenerate Merger: The Onset of Mass Transfer and Its Impact on Gravitational Waves and Surface Detonations”. In: *ApJ* 737.2, 89, p. 89. doi: 10.1088/0004-637X/737/2/89.

Dan, M. et al. (Feb. 2014). “The structure and fate of white dwarf merger remnants”. In: *MNRAS* 438.1, pp. 14–34. doi: 10.1093/mnras/stt1766.

Das, K. K. et al. (Dec. 2023). “Probing the Low-mass End of Core-collapse Supernovae Using a Sample of Strongly-stripped Calcium-rich Type I Ib Supernovae from the Zwicky Transient Facility”. In: *ApJ* 959.1, 12, p. 12. doi: 10.3847/1538-4357/acfeeb.

Davies, B. et al. (Dec. 2007). “A Massive Cluster of Red Supergiants at the Base of the Scutum-Crux Arm”. In: *ApJ* 671.1, pp. 781–801. doi: 10.1086/522224.

Davies, G. S. et al. (2020). “Extending the PyCBC search for gravitational waves from compact binary mergers to a global network”. In: *Phys. Rev. D* 102.2, p. 022004. doi: 10.1103/PhysRevD.102.022004.

Davis, K. et al. (Nov. 2021). “UCSC Transient Classification Report for 2021-11-19”. In: *Transient Name Server Classification Report 2021-3967*, pp. 1–3967.

De, K. et al. (Feb. 2020a). “Palomar Gattini-IR: Survey Overview, Data Processing System, On-sky Performance and First Results”. In: *PASP* 132.1008, p. 025001. doi: 10.1088/1538-3873/ab6069.

– (Feb. 2020b). “Palomar Gattini-IR: Survey Overview, Data Processing System, On-sky Performance and First Results”. In: *PASP* 132.1008, 025001, p. 025001. doi: 10.1088/1538-3873/ab6069.

De, K. et al. (Dec. 2020c). “The Zwicky Transient Facility Census of the Local Universe. I. Systematic Search for Calcium-rich Gap Transients Reveals Three Related Spectroscopic Subclasses”. In: *ApJ* 905.1, 58, p. 58. doi: 10.3847/1538-4357/abb45c.

De, K. et al. (Aug. 2022). “SRGA J181414.6-225604: A New Galactic Symbiotic X-Ray Binary Outburst Triggered by an Intense Mass-loss Episode of a Heavily Obscured Mira Variable”. In: *ApJ* 935.1, 36, p. 36. doi: 10.3847/1538-4357/ac7c6e.

De, K. et al. (May 2023). “An infrared transient from a star engulfing a planet”. In: *Nature* 617.7959, pp. 55–60. doi: 10.1038/s41586-023-05842-x.

De, K. et al. (Oct. 2024). “The disappearance of a massive star marking the birth of a black hole in M31”. In: *arXiv e-prints*, arXiv:2410.14778, arXiv:2410.14778. doi: 10.48550/arXiv.2410.14778.

De Marco, O. et al. (June 2002). “What Are the Hot R Coronae Borealis Stars?” In: *AJ* 123.6, pp. 3387–3408. doi: 10.1086/340569.

de Mink, S. E. et al. (Feb. 2014). “The Incidence of Stellar Mergers and Mass Gainers among Massive Stars”. In: *ApJ* 782.1, 7, p. 7. doi: 10.1088/0004-637X/782/1/7.

Dekany, R. et al. (Mar. 2020). “The Zwicky Transient Facility: Observing System”. In: *PASP* 132.1009, 038001, p. 038001. doi: 10.1088/1538-3873/ab4ca2.

Denissenkov, P. A. et al. (Mar. 2015). “Hybrid C-O-Ne white dwarfs as progenitors of Type Ia supernovae: dependence on Urca process and mixing assumptions”. In: *MNRAS* 447.3, pp. 2696–2705. doi: 10.1093/mnras/stu2589.

Dietrich, T. et al. (2020). “Multimessenger constraints on the neutron-star equation of state and the Hubble constant”. In: *Science* 370.6523, pp. 1450–1453. doi: 10.1126/science.abb4317.

Dobie, D. et al. (Dec. 2019). “An ASKAP Search for a Radio Counterpart to the First High-significance Neutron Star–Black Hole Merger LIGO/Virgo S190814bv”. In: *ApJ* 887.1, p. L13. doi: 10.3847/2041-8213/ab59db.

Doherty, C. L. et al. (Jan. 2015). “Super- and massive AGB stars - IV. Final fates - initial-to-final mass relation”. In: *MNRAS* 446.3, pp. 2599–2612. doi: 10.1093/mnras/stu2180.

Dominik, M. et al. (Nov. 2012). “Double Compact Objects. I. The Significance of the Common Envelope on Merger Rates”. In: *ApJ* 759, 52, p. 52. doi: 10.1088/0004-637X/759/1/52.

Dorda, R. et al. (Nov. 2016). “Characterisation of red supergiants in the Gaia spectral range”. In: *A&A* 595, A105, A105. doi: 10.1051/0004-6361/201628422.

Dotter, A. (Jan. 2016). “MESA Isochrones and Stellar Tracks (MIST) 0: Methods for the Construction of Stellar Isochrones”. In: *ApJS* 222.1, 8, p. 8. doi: 10.3847/0067-0049/222/1/8.

Driebe, T. et al. (Nov. 1998). “The evolution of helium white dwarfs. I. The companion of the millisecond pulsar PSR J1012+5307”. In: *A&A* 339, pp. 123–133.

Duev, D. A. et al. (2019a). “Real-bogus classification for the Zwicky Transient Facility using deep learning”. In: *Monthly Notices of the Royal Astronomical Society* 489.3, pp. 3582–3590.

Duev, D. A. et al. (Nov. 2019b). “Real-bogus classification for the Zwicky Transient Facility using deep learning”. In: *MNRAS* 489.3, pp. 3582–3590. doi: 10.1093/mnras/stz2357.

Durbak, J. et al. (Aug. 2024). “The PRIME camera: results and performance after continuous observations”. In: *X-Ray, Optical, and Infrared Detectors for Astronomy XI*. Ed. by A. D. Holland et al. Vol. 13103. Society of Photo-Optical Instrumentation Engineers (SPIE) Conference Series, 1310327, p. 1310327. doi: 10.1117/12.3020680.

Dwek, E. et al. (June 2007). “The Evolution of Dust in the Early Universe with Applications to the Galaxy SDSS J1148+5251”. In: *ApJ* 662.2, pp. 927–939. doi: 10.1086/518430.

Dye, S. et al. (Feb. 2018). “The UKIRT Hemisphere Survey: definition and J-band data release”. In: *MNRAS* 473.4, pp. 5113–5125. doi: 10.1093/mnras/stx2622.

Dyer, M. J. et al. (July 2018). “A telescope control and scheduling system for the Gravitational-wave Optical Transient Observer (GOTO)”. In: *Observatory Operations: Strategies, Processes, and Systems VII*. Vol. 10704. Society of Photo-Optical Instrumentation Engineers (SPIE) Conference Series, 107040C, p. 107040C. doi: 10.1117/12.2311865.

Eikenberry, S. S. et al. (Sept. 2004). “FLAMINGOS-2: the facility near-infrared wide-field imager and multi-object spectrograph for Gemini”. In: *Ground-based Instrumentation for Astronomy*. Ed. by A. F. M. Moorwood et al. Vol. 5492. Society of Photo-Optical Instrumentation Engineers (SPIE) Conference Series, pp. 1196–1207. doi: 10.1117/12.549796.

Elias, J. H. et al. (June 2006). “Performance of the Gemini near-infrared spectrograph”. In: *Society of Photo-Optical Instrumentation Engineers (SPIE) Conference Series*. Ed. by I. S. McLean et al. Vol. 6269. Society of Photo-Optical

Instrumentation Engineers (SPIE) Conference Series, 626914, p. 626914. doi: 10.1117/12.671765.

Elitzur, M. et al. (Oct. 2001). “Dusty winds - I. Self-similar solutions”. In: *MNRAS* 327, pp. 403–421. doi: 10.1046/j.1365-8711.2001.04706.x.

Evans, P. A. et al. (Dec. 2017). “Swift and NuSTAR observations of GW170817: Detection of a blue kilonova”. In: *Science* 358.6370, pp. 1565–1570. doi: 10.1126/science.aap9580.

Ewing, B. et al. (2024). “Performance of the low-latency GstLAL inspiral search towards LIGO, Virgo, and KAGRA’s fourth observing run”. In: *Phys. Rev. D* 109.4, p. 042008. doi: 10.1103/PhysRevD.109.042008.

Eyer, L. et al. (June 2023). “Gaia Data Release 3. Summary of the variability processing and analysis”. In: *A&A* 674, A13, A13. doi: 10.1051/0004-6361/202244242.

Eyres, S. P. S. et al. (Dec. 2018). “ALMA reveals the aftermath of a white dwarf–brown dwarf merger in CK Vulpeculae”. In: *MNRAS* 481.4, pp. 4931–4939. doi: 10.1093/mnras/sty2554.

Fabricant, D. et al. (July 2019). “Binospec: A Wide-field Imaging Spectrograph for the MMT”. In: *PASP* 131.1001, p. 075004. doi: 10.1088/1538-3873/ab1d78.

Feast, M. W. (Jan. 1996). “Introductory review: Some general problems concerning RCB stars”. In: *Hydrogen Deficient Stars*. Ed. by C. S. Jeffery et al. Vol. 96. Astronomical Society of the Pacific Conference Series, p. 3.

– (Feb. 1997). “The R Coronae Borealis stars - II. Further inferences from the infrared data”. In: *MNRAS* 285.2, pp. 339–357. doi: 10.1093/mnras/285.2.339.

Feast, M. W. et al. (Feb. 1997). “The R Coronae Borealis stars - I. Infrared photometry and long-term variations”. In: *MNRAS* 285.2, pp. 317–338. doi: 10.1093/mnras/285.2.317.

Feindt, U. et al. (Oct. 2019). “simsurvey: estimating transient discovery rates for the Zwicky transient facility”. In: *Journal of Cosmology and Astroparticle Physics* 2019.10, pp. 005–005. doi: 10.1088/1475-7516/2019/10/005.

Ferrarese, L. et al. (Feb. 2000). “The Hubble Space Telescope Key Project on the Extragalactic Distance Scale. XXVI. The Calibration of Population II Secondary Distance Indicators and the Value of the Hubble Constant”. In: *ApJ* 529.2, pp. 745–767. doi: 10.1086/308309.

Ferrario, L. et al. (Nov. 2009). “The origin of magnetism on the upper main sequence”. In: *MNRAS* 400.1, pp. L71–L74. doi: 10.1111/j.1745-3933.2009.00765.x.

Filippenko, A. V. et al. (Oct. 1992). “The Subluminous, Spectroscopically Peculiar Type 1a Supernova 1991bg in the Elliptical Galaxy NGC 4374”. In: *AJ* 104, p. 1543. doi: 10.1086/116339.

Fink, M. et al. (Dec. 2007). “Double-detonation supernovae of sub-Chandrasekhar mass white dwarfs”. In: *A&A* 476.3, pp. 1133–1143. doi: 10.1051/0004-6361:20078438.

Fink, M. et al. (Feb. 2014). “Three-dimensional pure deflagration models with nucleosynthesis and synthetic observables for Type Ia supernovae”. In: *MNRAS* 438.2, pp. 1762–1783. doi: 10.1093/mnras/stt2315.

Flesch, E. W. (Dec. 2023). “The Million Quasars (Milliquas) Catalogue, v8”. In: *The Open Journal of Astrophysics* 6, 49, p. 49. doi: 10.21105/astro.2308.01505.

Flewelling, H. A. et al. (Nov. 2020). “The Pan-STARRS1 Database and Data Products”. In: *ApJS* 251.1, 7, p. 7. doi: 10.3847/1538-4365/abb82d.

Foley, R. J. et al. (Aug. 2009). “SN 2008ha: An Extremely Low Luminosity and Exceptionally Low Energy Supernova”. In: *AJ* 138.2, pp. 376–391. doi: 10.1088/0004-6256/138/2/376.

Foley, R. J. et al. (Apr. 2013). “Type Iax Supernovae: A New Class of Stellar Explosion”. In: *ApJ* 767.1, 57, p. 57. doi: 10.1088/0004-637X/767/1/57.

Foley, R. J. et al. (Sept. 2014). “Possible Detection of the Stellar Donor or Remnant for the Type Iax Supernova 2008ha”. In: *ApJ* 792.1, 29, p. 29. doi: 10.1088/0004-637X/792/1/29.

Fong, W. et al. (Dec. 2015). “A Decade of Short-duration Gamma-Ray Burst Broad-band Afterglows: Energetics, Circumburst Densities, and Jet Opening Angles”. In: *ApJ* 815.2, 102, p. 102. doi: 10.1088/0004-637X/815/2/102.

Foreman-Mackey, D. et al. (Mar. 2013a). “emcee: The MCMC Hammer”. In: *PASP* 125.925, p. 306. doi: 10.1086/670067.

– (Mar. 2013b). “emcee: The MCMC Hammer”. In: *PASP* 125.925, p. 306. doi: 10.1086/670067.

Fremling, C. et al. (May 2020). “The Zwicky Transient Facility Bright Transient Survey. I. Spectroscopic Classification and the Redshift Completeness of Local Galaxy Catalogs”. In: *ApJ* 895.1, 32, p. 32. doi: 10.3847/1538-4357/ab8943.

Frostig, D. et al. (Dec. 2020). “Design requirements for the Wide-field Infrared Transient Explorer (WINTER)”. In: *Society of Photo-Optical Instrumentation Engineers (SPIE) Conference Series*. Vol. 11447. Society of Photo-Optical Instrumentation Engineers (SPIE) Conference Series, 1144767, p. 1144767. doi: 10.1117/12.2562842.

Frostig, D. et al. (Feb. 2022a). “An Infrared Search for Kilonovae with the WINTER Telescope. I. Binary Neutron Star Mergers”. In: *ApJ* 926.2, 152, p. 152. doi: 10.3847/1538-4357/ac4508.

Frostig, D. et al. (Aug. 2022b). “Readout and cooling of the WINTER InGaAs camera”. In: *X-Ray, Optical, and Infrared Detectors for Astronomy X*. Ed. by A. D. Holland et al. Vol. 12191. Society of Photo-Optical Instrumentation Engineers (SPIE) Conference Series, 121912N, 121912N. doi: 10.1117/12.2630602.

Frostig, D. et al. (July 2024a). “WINTER commissioning and early performance: a new time-domain near-IR facility”. In: *Ground-based and Airborne Instrumentation for Astronomy X*. Ed. by J. J. Bryant et al. Vol. 13096. Society of Photo-Optical Instrumentation Engineers (SPIE) Conference Series, 130963J, 130963J. doi: 10.1117/12.3019165.

– (July 2024b). “WINTER commissioning and early performance: a new time-domain near-IR facility”. In: *Ground-based and Airborne Instrumentation for Astronomy X*. Ed. by J. J. Bryant et al. Vol. 13096. Society of Photo-Optical Instrumentation Engineers (SPIE) Conference Series, 130963J, 130963J. doi: 10.1117/12.3019165.

Fryer, C. L. et al. (July 2008). “On the Road to Understanding Type Ia Progenitors: Precision Simulations of Double Degenerate Mergers”. In: *Hydrogen-Deficient Stars*. Ed. by A. Werner et al. Vol. 391. Astronomical Society of the Pacific Conference Series, p. 335.

Fryer, C. et al. (May 1999). “What Can the Accretion-induced Collapse of White Dwarfs Really Explain?” In: *ApJ* 516.2, pp. 892–899. doi: 10.1086/307119.

Fuenmayor, F. J. (Dec. 1981). “A deep near infrared objective prism survey for carbon stars toward the galactic center and anticenter.” In: *Rev. Mexicana Astron. Astrofis.* 6, pp. 83–93.

Gaia Collaboration et al. (May 2021). “Gaia Early Data Release 3. Summary of the contents and survey properties”. In: *A&A* 649, A1, A1. doi: 10.1051/0004-6361/202039657.

Gaia Collaboration et al. (June 2023). “Gaia Data Release 3. Summary of the content and survey properties”. In: *A&A* 674, A1, A1. doi: 10.1051/0004-6361/202243940.

García-Hernández, D. A. et al. (May 2009). “CNO Abundances of Hydrogen-Deficient Carbon and R Coronae Borealis Stars: A View of the Nucleosynthesis in a White Dwarf Merger”. In: *ApJ* 696.2, pp. 1733–1754. doi: 10.1088/0004-637X/696/2/1733.

García-Hernández, D. A. et al. (May 2010). “Oxygen Isotopic Ratios in Cool R Coronae Borealis Stars”. In: *ApJ* 714.1, pp. 144–154. doi: 10.1088/0004-637X/714/1/144.

García-Hernández, D. A. et al. (May 2023). “The Carbon Star DY Persei May Be a Cool R Coronae Borealis Variable”. In: *ApJ* 948.1, 15, p. 15. doi: 10.3847/1538-4357/acc574.

Gautschy, A. (Dec. 2023). “À Propos Nonlinear Pulsations of R CrB Variables”. In: *arXiv e-prints*, arXiv:2312.14693, arXiv:2312.14693. doi: 10.48550/arXiv.2312.14693.

Gautschy-Loidl, R. et al. (July 2004). “Dynamic model atmospheres of AGB stars. IV. A comparison of synthetic carbon star spectra with observations”. In: *A&A* 422, pp. 289–306. doi: 10.1051/0004-6361:20035860.

Gavetti, C. et al. (Apr. 2025). “A study of Andromeda to improve our knowledge on the evolution and dust production by AGB stars”. In: *arXiv e-prints*, arXiv:2504.12940, arXiv:2504.12940.

Geballe, T. R. et al. (June 2009). “Do Hydrogen-Deficient Carbon Stars have Winds?” In: *ApJ* 698.1, pp. 735–739. doi: 10.1088/0004-637X/698/1/735.

Geiss, J. et al. (Oct. 2002). “Chemical Evolution in Our Galaxy during the Last 5 Gyr”. In: *ApJ* 578.2, pp. 862–867. doi: 10.1086/342869.

Gezer, I. et al. (Oct. 2015). “The WISE view of RV Tauri stars”. In: *MNRAS* 453.1, pp. 133–146. doi: 10.1093/mnras/stv1627.

Goldstein, A. et al. (Oct. 2017). “An Ordinary Short Gamma-Ray Burst with Extraordinary Implications: Fermi-GBM Detection of GRB 170817A”. In: *ApJ* 848.2, p. L14. doi: 10.3847/2041-8213/aa8f41.

Goldstein, D. A. et al. (Aug. 2019). “GROWTH on S190426c: Real-time Search for a Counterpart to the Probable Neutron Star-Black Hole Merger using an Automated Difference Imaging Pipeline for DECam”. In: *ApJ* 881.1, L7, p. L7. doi: 10.3847/2041-8213/ab3046.

Gompertz, B. P. et al. (July 2020). “Searching for electromagnetic counterparts to gravitational-wave merger events with the prototype Gravitational-Wave Optical Transient Observer (GOTO-4)”. In: *Monthly Notices of the Royal Astronomical Society* 497.1, pp. 726–738. doi: 10.1093/mnras/staa1845.

Gonneau, A. et al. (May 2016). “Carbon stars in the X-Shooter Spectral Library”. In: *A&A* 589, A36, A36. doi: 10.1051/0004-6361/201526292.

González-Bolívar, M. et al. (Jan. 2024). “Dust formation in common envelope binary interaction - I: 3D simulations using the Bowen approximation”. In: *MNRAS* 527.3, pp. 9145–9158. doi: 10.1093/mnras/stad3748.

Goorvitch, D. (Dec. 1994). “Infrared CO Line List for the X 1 Sigma + State”. In: *ApJS* 95, p. 535. doi: 10.1086/192110.

Goswami, A. et al. (Nov. 2010). “HE 1015-2050: Discovery of a Hydrogen-deficient Carbon Star at High Galactic Latitude”. In: *ApJ* 723.2, pp. L238–L242. doi: 10.1088/2041-8205/723/2/L238.

Graham, M. J. et al. (July 2019). “The Zwicky Transient Facility: Science Objectives”. In: *PASP* 131.1001, p. 078001. doi: 10.1088/1538-3873/ab006c.

Grankin, K. N. et al. (Jan. 2007). “Results of the ROTOR-program. I. The long-term photometric variability of classical T Tauri stars”. In: *A&A* 461.1, pp. 183–195. doi: 10.1051/0004-6361:20065489.

Gray, R. O. et al. (2009). *Stellar Spectral Classification*.

Green, G. M. et al. (Dec. 2019). “A 3D Dust Map Based on Gaia, Pan-STARRS 1, and 2MASS”. In: *ApJ* 887.1, 93, p. 93. doi: 10.3847/1538-4357/ab5362.

Groot, P. J. et al. (Nov. 2024). “The BlackGEM Telescope Array. I. Overview”. In: *PASP* 136.11, 115003, p. 115003. doi: 10.1088/1538-3873/ad8b6a.

Grossman, D. et al. (2014). “The long-term evolution of neutron star merger remnants – II. Radioactively powered transients”. In: *Mon. Not. Roy. Astron. Soc.* 439.1, pp. 757–770. doi: 10.1093/mnras/stt2503.

Guiffreda, O. et al. (Apr. 2024). “LIGO/Virgo/KAGRA S240422ed: PRIME near-infrared observations”. In: *GRB Coordinates Network* 36306, p. 1.

Gustafsson, B. et al. (Sept. 1975). “Reprint of 1975A&A....42..407G. A grid of model atmospheres for metal-deficient giant stars. I.” In: *A&A* 500, pp. 67–92.

Gustafsson, B. et al. (Aug. 2008). “A grid of MARCS model atmospheres for late-type stars. I. Methods and general properties”. In: *A&A* 486, pp. 951–970. doi: 10.1051/0004-6361:200809724.

Haggard, D. et al. (2017). “A Deep Chandra X-ray Study of Neutron Star Coalescence GW170817”. In: *Astrophys. J. Lett.* 848.2, p. L25. doi: 10.3847/2041-8213/aa8ede.

Hallinan, G. et al. (Dec. 2017). “A radio counterpart to a neutron star merger”. In: *Science* 358.6370, pp. 1579–1583. doi: 10.1126/science.aap9855.

Han, Z. et al. (Oct. 2002). “The origin of subdwarf B stars - I. The formation channels”. In: *MNRAS* 336.2, pp. 449–466. doi: 10.1046/j.1365-8711.2002.05752.x.

Han, Z. et al. (May 2003). “The origin of subdwarf B stars - II”. In: *MNRAS* 341.2, pp. 669–691. doi: 10.1046/j.1365-8711.2003.06451.x.

Han, Z. (June 1998a). “The formation of double degenerates and related objects”. In: *MNRAS* 296.4, pp. 1019–1040. doi: 10.1046/j.1365-8711.1998.01475.x.

– (June 1998b). “The formation of double degenerates and related objects”. In: *MNRAS* 296.4, pp. 1019–1040. doi: 10.1046/j.1365-8711.1998.01475.x.

Han, Z. et al. (Feb. 1995). “The formation of bipolar planetary nebulae and close white dwarf binaries”. In: *MNRAS* 272.4, pp. 800–820. doi: 10.1093/mnras/272.4.800.

Hanna, C. et al. (2020). “Fast evaluation of multidector consistency for real-time gravitational wave searches”. In: *Phys. Rev. D* 101.2, p. 022003. doi: 10.1103/PhysRevD.101.022003.

Hansen, C. J. et al. (2004). “Stellar Energy Sources”. In: *Stellar Interiors: Physical Principles, Structure, and Evolution*. New York, NY: Springer New York, pp. 271–327. doi: 10.1007/978-1-4419-9110-2\_6.

Harris, C. R. et al. (Sept. 2020). “Array programming with NumPy”. In: *Nature* 585.7825, pp. 357–362. doi: 10.1038/s41586-020-2649-2.

Hedrosa, R. P. et al. (May 2013). “Nitrogen Isotopes in Asymptotic Giant Branch Carbon Stars and Presolar SiC Grains: A Challenge for Stellar Nucleosynthesis”. In: *ApJ* 768.1, L11, p. L11. doi: 10.1088/2041-8205/768/1/L11.

Heger, A. et al. (July 2003). “How Massive Single Stars End Their Life”. In: *ApJ* 591, pp. 288–300. doi: 10.1086/375341.

Hema, B. P. et al. (Oct. 2017). “Abundance Analyses of the New R Coronae Borealis Stars: ASAS-RCB-8 and ASAS-RCB-10”. In: *PASP* 129.980, p. 104202. doi: 10.1088/1538-3873/aa7f25.

Herter, T. L. et al. (July 2008). “The performance of TripleSpec at Palomar”. In: *Proc. SPIE*. Vol. 7014. Society of Photo-Optical Instrumentation Engineers (SPIE) Conference Series, 70140X, p. 70140X. doi: 10.1117/12.789660.

Hills, J. G. et al. (Feb. 1976). “Stellar Collisions in Globular Clusters”. In: *Astrophysical Letters* 17, p. 87.

Hinkle, J. (Jan. 2021). “SCAT Transient Classification Report for 2021-01-06”. In: *Transient Name Server Classification Report* 2021-64, pp. 1–64.

Hinrichsen, E. et al. (Dec. 2020). “Opto-mechanical design of the Wide-Field Infrared Transient Explorer (WINTER) fly’s eye camera”. In: *Ground-based and Airborne Instrumentation for Astronomy VIII*. Ed. by C. J. Evans et al. Vol. 11447. Society of Photo-Optical Instrumentation Engineers (SPIE) Conference Series, 114479F, 114479F. doi: 10.1117/12.2562912.

Hirai, R. et al. (Oct. 2022). “A Two-stage Formalism for Common-envelope Phases of Massive Stars”. In: *ApJ* 937.2, L42, p. L42. doi: 10.3847/2041-8213/ac9519.

Hiramatsu, D. et al. (June 2021). “The electron-capture origin of supernova 2018zd”. In: *Nature Astronomy* 5, pp. 903–910. doi: 10.1038/s41550-021-01384-2.

Høg, E. et al. (Mar. 2000). “The Tycho-2 catalogue of the 2.5 million brightest stars”. In: *A&A* 355, pp. L27–L30.

Hook, I. M. et al. (May 2004). “The Gemini-North Multi-Object Spectrograph: Performance in Imaging, Long-Slit, and Multi-Object Spectroscopic Modes”. In: *PASP* 116.819, pp. 425–440. doi: 10.1086/383624.

Horne, K. (June 1986). “An optimal extraction algorithm for CCD spectroscopy.” In: *PASP* 98, pp. 609–617. doi: 10.1086/131801.

Hotokezaka, K. et al. (Jan. 2018). “Neutron star mergers as sites of r-process nucleosynthesis and short gamma-ray bursts”. In: *International Journal of Modern Physics D* 27.13, 1842005, p. 1842005. doi: 10.1142/S0218271818420051.

Houck, J. R. et al. (Oct. 2004). “The infrared spectrograph on the Spitzer Space Telescope”. In: *Optical, Infrared, and Millimeter Space Telescopes*. Ed. by J. C. Mather. Vol. 5487. Society of Photo-Optical Instrumentation Engineers (SPIE) Conference Series, pp. 62–76. doi: 10.1117/12.550517.

Howitt, G. et al. (Mar. 2020). “Luminous Red Novae: population models and future prospects”. In: *MNRAS* 492.3, pp. 3229–3240. doi: 10.1093/mnras/stz3542.

Hu, L. et al. (Sept. 2022). “Image Subtraction in Fourier Space”. In: *ApJ* 936.2, 157, p. 157. doi: 10.3847/1538-4357/ac7394.

Humphreys, R. M. et al. (Sept. 1999). “Eta Carinae’s Second Eruption and the Light Curves of the eta Carinae Variables”. In: *PASP* 111, pp. 1124–1131. doi: 10.1086/316420.

Humphreys, R. M. et al. (Dec. 2011). “The Photometric and Spectral Evolution of the 2008 Luminous Optical Transient in NGC 300”. In: *ApJ* 743, 118, p. 118. doi: 10.1088/0004-637X/743/2/118.

Husser, T. .- et al. (May 2013). “A new extensive library of PHOENIX stellar atmospheres and synthetic spectra”. In: *A&A* 553, A6, A6. doi: 10.1051/0004-6361/201219058.

Iaconi, R. et al. (June 2018). “The effect of binding energy and resolution in simulations of the common envelope binary interaction”. In: *MNRAS* 477.2, pp. 2349–2365. doi: 10.1093/mnras/sty794.

Iaconi, R. et al. (Nov. 2019). “Properties of the post-inspiral common envelope ejecta - I. Dynamical and thermal evolution”. In: *MNRAS* 489.3, pp. 3334–3350. doi: 10.1093/mnras/stz2312.

Iaconi, R. et al. (Sept. 2020). “Properties of the post in-spiral common envelope ejecta II: dust formation”. In: *MNRAS* 497.3, pp. 3166–3179. doi: 10.1093/mnras/staa2169.

Iben, I. et al. (Jan. 1996). “On the origin of R CrB and other hydrogen-deficient stars”. In: *Hydrogen Deficient Stars*. Ed. by C. S. Jeffery et al. Vol. 96. Astronomical Society of the Pacific Conference Series, p. 409.

Iben Jr., I. et al. (Dec. 1993). “Common Envelopes in Binary Star Evolution”. In: *PASP* 105, p. 1373. doi: 10.1086/133321.

Iben Jr., I. et al. (Jan. 1997). “Helium and Carbon-Oxygen White Dwarfs in Close Binaries”. In: *ApJ* 475.1, pp. 291–299. doi: 10.1086/303525.

Iben I., J. et al. (Feb. 1984). “Supernovae of type I as end products of the evolution of binaries with components of moderate initial mass.” In: *ApJS* 54, pp. 335–372. doi: 10.1086/190932.

IceCube Collaboration (Feb. 2025). “LIGO/Virgo/KAGRA S250206dm: Two counterpart neutrino candidates from IceCube neutrino searches”. In: *General Coordinates Network* 39176, p. 1.

Ivanova, N. et al. (Feb. 2013a). “Common envelope evolution: where we stand and how we can move forward”. In: *A&A Rev.* 21, 59, p. 59. doi: 10.1007/s00159-013-0059-2.

Ivanova, N. et al. (Jan. 2013b). “Identification of the Long-Sought Common-Envelope Events”. In: *Science* 339, p. 433. doi: 10.1126/science.1225540.

Ivezic, Z. et al. (June 1997). “Self-similarity and scaling behaviour of infrared emission from radiatively heated dust - I. Theory”. In: *MNRAS* 287, pp. 799–811.

Ivezic, Z. et al. (Oct. 1999). “User Manual for DUSTY”. In: *astro-ph/9910475*.

Ivezić, Ž. et al. (Mar. 2019a). “LSST: From Science Drivers to Reference Design and Anticipated Data Products”. In: *ApJ* 873, 111, p. 111. doi: 10.3847/1538-4357/ab042c.

Ivezić, Ž. et al. (Mar. 2019b). “LSST: From Science Drivers to Reference Design and Anticipated Data Products”. In: *ApJ* 873.2, 111, p. 111. doi: 10.3847/1538-4357/ab042c.

Jacoby, G. H. et al. (Oct. 1984). “A library of stellar spectra”. In: *ApJS* 56, pp. 257–281. doi: 10.1086/190983.

Jayasinghe, T. et al. (July 2018). “The ASAS-SN catalogue of variable stars I: The Serendipitous Survey”. In: *MNRAS* 477.3, pp. 3145–3163. doi: 10.1093/mnras/sty838.

Jeffery, C. S. et al. (July 2011). “Double white dwarf mergers and elemental surface abundances in extreme helium and R Coronae Borealis stars”. In: *MNRAS* 414.4, pp. 3599–3616. doi: 10.1111/j.1365-2966.2011.18667.x.

Jencson, J. E. et al. (Aug. 2019a). “Discovery of an Intermediate-luminosity Red Transient in M51 and Its Likely Dust-obsured, Infrared-variable Progenitor”. In: *ApJ* 880.2, L20, p. L20. doi: 10.3847/2041-8213/ab2c05.

Jencson, J. E. et al. (Nov. 2019b). “The SPIRITS Sample of Luminous Infrared Transients: Uncovering Hidden Supernovae and Dusty Stellar Outbursts in Nearby Galaxies”. In: *ApJ* 886.1, 40, p. 40. doi: 10.3847/1538-4357/ab4a01.

Jencson, J. E. et al. (May 2022). “An Exceptional Dimming Event for a Massive, Cool Supergiant in M51”. In: *ApJ* 930.1, 81, p. 81. doi: 10.3847/1538-4357/ac626c.

Jha, S. W. (2017). “Type Iax Supernovae”. In: *Handbook of Supernovae*. Ed. by A. W. Alsabti et al., p. 375. doi: 10.1007/978-3-319-21846-5\\_42.

Johnson, J. A. et al. (Sept. 2020). “The origin of the elements: a century of progress”. In: *Philosophical Transactions of the Royal Society of London Series A* 378.2180, 20190301, p. 20190301. doi: 10.1098/rsta.2019.0301.

Jones, A. P. et al. (Oct. 1994). “Grain Destruction in Shocks in the Interstellar Medium”. In: *ApJ* 433, p. 797. doi: 10.1086/174689.

Jordan George C., I. et al. (Dec. 2012). “Failed-detonation Supernovae: Subluminous Low-velocity Ia Supernovae and their Kicked Remnant White Dwarfs with Iron-rich Cores”. In: *ApJ* 761.2, L23, p. L23. doi: 10.1088/2041-8205/761/2/L23.

Justham, S. et al. (Mar. 2006). “Magnetic braking of Ap/Bp stars: application to compact black-hole X-ray binaries”. In: *MNRAS* 366.4, pp. 1415–1423. doi: 10.1111/j.1365-2966.2005.09907.x.

Kamiński, T. et al. (Mar. 2011). “Strong linear polarization of V4332 Sagittarii: a dusty disc geometry”. In: *A&A* 527, A75, A75. doi: 10.1051/0004-6361/201015950.

Kamiński, T. et al. (Aug. 2015). “Post-outburst spectra of a stellar-merger remnant of V1309 Scorpii: from a twin of V838 Monocerotis to a clone of V4332 Sagittarii”. In: *A&A* 580, A34, A34. doi: 10.1051/0004-6361/201526212.

Kamiński, T. et al. (Oct. 2018). “Submillimeter-wave emission of three Galactic red novae: cool molecular outflows produced by stellar mergers”. In: *A&A* 617, A129, A129. doi: 10.1051/0004-6361/201833165.

Kamiński, T. et al. (Nov. 2021). “V838 Monocerotis as seen by ALMA: A remnant of a binary merger in a triple system”. In: *A&A* 655, A32, A32. doi: 10.1051/0004-6361/202141526.

Karakas, A. I. et al. (Aug. 2015). “R Coronae Borealis Stars Are Viable Factories of Pre-solar Grains”. In: *ApJ* 809.2, 184, p. 184. doi: 10.1088/0004-637X/809/2/184.

Karambelkar, V. et al. (Nov. 2022). “R Coronae Borealis and dustless hydrogen-deficient carbon stars likely have different oxygen isotope ratios”. In: *A&A* 667, A84, A84. doi: 10.1051/0004-6361/202142918.

Karambelkar, V. et al. (Feb. 2024). “Transient EPW20240219aa: J-band upper limits from WINTER”. In: *GRB Coordinates Network* 35807, p. 1.

Karambelkar, V. R. et al. (Dec. 2020). “Census of R Coronae Borealis stars I: Infrared light curves from Palomar Gattini IR”. In: *arXiv e-prints*, arXiv:2012.11629, arXiv:2012.11629.

Karambelkar, V. R. et al. (Nov. 2021). “Faintest of Them All: ZTF 21aaoryiz/SN 2021fcg-Discovery of an Extremely Low Luminosity Type Iax Supernova”. In: *ApJ* 921.1, L6, p. L6. doi: 10.3847/2041-8213/ac2e90.

Karambelkar, V. R. et al. (Feb. 2023a). *Lightcurves, spectra and model-lightcurves of Luminous Red Novae and Intermediate Luminosity Red Transients by the Zwicky Transient Facility*. Zenodo. doi: 10.5281/zenodo.7651607.

Karambelkar, V. R. et al. (May 2023b). “Volumetric Rates of Luminous Red Novae and Intermediate-luminosity Red Transients with the Zwicky Transient Facility”. In: *ApJ* 948.2, 137, p. 137. doi: 10.3847/1538-4357/acc2b9.

Kasen, D. et al. (2013). “Opacities and Spectra of the *r*-process Ejecta from Neutron Star Mergers”. In: *Astrophys. J.* 774, p. 25. doi: 10.1088/0004-637X/774/1/25.

Kasen, D. et al. (2017). “Origin of the heavy elements in binary neutron-star mergers from a gravitational wave event”. In: *Nature* 551, p. 80. doi: 10.1038/nature24453.

Kashyap, R. et al. (Dec. 2018). “Double-degenerate Carbon-Oxygen and Oxygen-Neon White Dwarf Mergers: A New Mechanism for Faint and Rapid Type Ia Supernovae”. In: *ApJ* 869.2, 140, p. 140. doi: 10.3847/1538-4357/aaedb7.

Kasliwal, M. M. et al. (Dec. 2017a). “Illuminating gravitational waves: A concordant picture of photons from a neutron star merger”. In: *Science* 358.6370, pp. 1559–1565. doi: 10.1126/science.aap9455.

Kasliwal, M. M. et al. (Feb. 2019a). “The GROWTH Marshal: A Dynamic Science Portal for Time-domain Astronomy”. In: *Publications of the Astronomical Society of the Pacific* 131.997, p. 038003. doi: 10.1088/1538-3873/aafbc2.

Kasliwal, M. M. et al. (Jan. 2019b). “Spitzer mid-infrared detections of neutron star merger GW170817 suggests synthesis of the heaviest elements”. In: *Monthly Notices of the Royal Astronomical Society: Letters* 510.1, pp. L7–L12. doi: 10.1093/mnrasl/slz007.

Kasliwal, M. M. (Jan. 2011). “Bridging the gap : elusive explosions in the local universe”. PhD thesis. California Institute of Technology.

Kasliwal, M. M. et al. (Nov. 2010). “Rapidly Decaying Supernova 2010X: A Candidate “.Ia” Explosion”. In: *ApJ* 723.1, pp. L98–L102. doi: 10.1088/2041-8205/723/1/L98.

Kasliwal, M. M. et al. (Apr. 2011). “PTF 10fqs: A Luminous Red Nova in the Spiral Galaxy Messier 99”. In: *ApJ* 730.2, 134, p. 134. doi: 10.1088/0004-637X/730/2/134.

Kasliwal, M. M. et al. (Apr. 2017b). “SPIRITS: Uncovering Unusual Infrared Transients with Spitzer”. In: *ApJ* 839.2, 88, p. 88. doi: 10.3847/1538-4357/aa6978.

Kasliwal, M. M. et al. (Dec. 2020). “Kilonova Luminosity Function Constraints Based on Zwicky Transient Facility Searches for 13 Neutron Star Merger Triggers during O3”. In: *ApJ* 905.2, p. 145. doi: 10.3847/1538-4357/abc335.

Kasliwal, M. M. et al. (Feb. 2025a). “Cryoscope: A Cryogenic Infrared Survey Telescope”. In: *arXiv e-prints*, arXiv:2502.06950, arXiv:2502.06950. doi: 10.48550/arXiv.2502.06950.

Kasliwal, M. M. et al. (Feb. 2025b). “Cryoscope: A Cryogenic Infrared Survey Telescope”. In: *arXiv e-prints*, arXiv:2502.06950, arXiv:2502.06950. doi: 10.48550/arXiv.2502.06950.

Kato, T. (Feb. 2003). “CK Vul as a candidate eruptive stellar merging event”. In: *A&A* 399, pp. 695–697. doi: 10.1051/0004-6361:20021808.

Khan, R. (Jan. 2017). “Spitzer Photometry of  $\sim$ 1 Million Stars in M31 and 15 Other Galaxies”. In: *ApJS* 228.1, 5, p. 5. doi: 10.3847/1538-4365/228/1/5.

Khouri, T. et al. (Dec. 2021). “Observational identification of a sample of likely recent common-envelope events”. In: *Nature Astronomy* 6, pp. 275–286. doi: 10.1038/s41550-021-01528-4.

Kiendrebeogo, R. W. et al. (Nov. 2023). “Updated Observing Scenarios and Multimessenger Implications for the International Gravitational-wave Networks O4 and O5”. In: *ApJ* 958.2, p. 158. doi: 10.3847/1538-4357/acfc1.

Kijbunchoo, N. et al. (Oct. 2011). “NSV 11154 Is a New R Coronae Borealis Star”. In: *PASP* 123.908, p. 1149. doi: 10.1086/662435.

Kilkenny, D. et al. (May 1989). “NSV 6708 : hydrogen in an R Coronae Borealis star.” In: *MNRAS* 238, 1P–6. doi: 10.1093/mnras/238.1.1P.

Kim, Y. .- et al. (Feb. 2022). “New Modules for the SEDMachine to Remove Contaminations from Cosmic Rays and Non-target Light: BYECR and CONTSEP”. In: *PASP* 134.1032, 024505, p. 024505. doi: 10.1088/1538-3873/ac50a0.

Kingma, D. P. et al. (Dec. 2014). “Adam: A Method for Stochastic Optimization”. In: *arXiv e-prints*, arXiv:1412.6980, arXiv:1412.6980. doi: 10.48550/arXiv.1412.6980.

Kirchschlager, F. et al. (Nov. 2019). “Dust survival rates in clumps passing through the Cas A reverse shock - I. Results for a range of clump densities”. In: *MNRAS* 489.4, pp. 4465–4496. doi: 10.1093/mnras/stz2399.

Klencki, J. et al. (June 2020). “It has to be cool: on supergiant progenitors of binary black hole mergers from common-envelope evolution”. In: *arXiv e-prints*, arXiv:2006.11286, arXiv:2006.11286.

Klencki, J. et al. (Jan. 2021). “It has to be cool: Supergiant progenitors of binary black hole mergers from common-envelope evolution”. In: *A&A* 645, A54, A54. doi: 10.1051/0004-6361/202038707.

Kochanek, C. S. et al. (Sept. 2014). “Stellar mergers are common”. In: *MNRAS* 443, pp. 1319–1328. doi: 10.1093/mnras/stu1226.

Kondo, I. et al. (June 2023). “Prediction of Planet Yields by the PRime-focus Infrared Microlensing Experiment Microlensing Survey”. In: *AJ* 165.6, 254, p. 254. doi: 10.3847/1538-3881/acccf9.

Kool, E. C. et al. (Feb. 2018). “First results from GeMS/GSAOI for project SUN-BIRD: Supernovae UNmasked By Infra-Red Detection”. In: *MNRAS* 473.4, pp. 5641–5657. doi: 10.1093/mnras/stx2463.

Koposov, S. et al. (July 2006). “Q3C, Quad Tree Cube – The new Sky-indexing Concept for Huge Astronomical Catalogues and its Realization for Main Astronomical Queries (Cone Search and Xmatch) in Open Source Database PostgreSQL”. In: *Astronomical Data Analysis Software and Systems XV*. Ed. by C. Gabriel et al. Vol. 351. Astronomical Society of the Pacific Conference Series, p. 735.

Kourkchi, E. et al. (July 2017). “Galaxy Groups Within  $3500 \text{ km s}^{-1}$ ”. In: *ApJ* 843.1, 16, p. 16. doi: 10.3847/1538-4357/aa76db.

Kromer, M. et al. (Mar. 2013). “3D deflagration simulations leaving bound remnants: a model for 2002cx-like Type Ia supernovae”. In: *MNRAS* 429.3, pp. 2287–2297. doi: 10.1093/mnras/sts498.

Kromer, M. et al. (July 2015). “Deflagrations in hybrid CONe white dwarfs: a route to explain the faint Type Iax supernova 2008ha”. In: *MNRAS* 450.3, pp. 3045–3053. doi: 10.1093/mnras/stv886.

Kučinskas, A. et al. (Oct. 2005). “Broad-band photometric colors and effective temperature calibrations for late-type giants. I.  $Z = 0.02$ ”. In: *A&A* 442.1, pp. 281–308. doi: 10.1051/0004-6361:20053028.

Kučinskas, A. et al. (June 2006). “Broad-band photometric colors and effective temperature calibrations for late-type giants. II.  $Z < 0.02$ ”. In: *A&A* 452.3, pp. 1021–1038. doi: 10.1051/0004-6361:20054431.

Kulkarni, S. R. (Oct. 2005). “Modeling Supernova-like Explosions Associated with Gamma-ray Bursts with Short Durations”. In: *arXiv e-prints*, astro-ph/0510256, astro-ph/0510256. doi: 10.48550/arXiv.astro-ph/0510256.

Kulkarni, S. R. et al. (May 2007). “An unusually brilliant transient in the galaxy M85”. In: *Nature* 447, pp. 458–460. doi: 10.1038/nature05822.

Kutyrev, A. et al. (Oct. 2023). “The PRIME project large format near infrared camera for the microlensing events survey”. In: *Society of Photo-Optical Instrumentation Engineers (SPIE) Conference Series*. Vol. 12680. Society of Photo-Optical Instrumentation Engineers (SPIE) Conference Series, 126802O, 126802O. doi: 10.1117/12.2692417.

Laher, R. R. et al. (July 2014). “IPAC Image Processing and Data Archiving for the Palomar Transient Factory”. In: *PASP* 126, pp. 674–710. doi: 10.1086/677351.

Lambert, D. L. et al. (Mar. 1994). “The R Coronae Borealis stars - a few mere facts.” In: *Journal of Astrophysics and Astronomy* 15, pp. 47–67. doi: 10.1007/BF03010404.

Lamberts, A. et al. (Dec. 2019). “Predicting the LISA white dwarf binary population in the Milky Way with cosmological simulations”. In: *MNRAS* 490.4, pp. 5888–5903. doi: 10.1093/mnras/stz2834.

Lang, D. et al. (2010). “Astrometry.net: Blind astrometric calibration of arbitrary astronomical images”. In: *AJ* 137. arXiv:0910.2233, pp. 1782–2800.

Lau, M. Y. M. et al. (June 2022). “Common envelopes in massive stars: towards the role of radiation pressure and recombination energy in ejecting red supergiant envelopes”. In: *MNRAS* 512.4, pp. 5462–5480. doi: 10.1093/mnras/stac049.

Lau, R. M. et al. (Apr. 2025). “Revealing a Main-sequence Star that Consumed a Planet with JWST”. In: *ApJ* 983.2, 87, p. 87. doi: 10.3847/1538-4357/adb429.

Lauer, A. et al. (Sept. 2019). “Evolving R Coronae Borealis stars with MESA”. In: *MNRAS* 488.1, pp. 438–450. doi: 10.1093/mnras/stz1732.

Law, N. M. et al. (Dec. 2009). “The Palomar Transient Factory: System Overview, Performance, and First Results”. In: *PASP* 121, pp. 1395–1408. doi: 10.1086/648598.

Lawson, W. A. et al. (Oct. 1989). “The R Coronae Borealis star NSV 6708.” In: *MNRAS* 240, pp. 689–700. doi: 10.1093/mnras/240.3.689.

Lawson, W. A. et al. (Nov. 1990). “The photometric characteristics of cool hydrogen-deficient carbon stars.” In: *MNRAS* 247, p. 91.

Lawson, W. A. et al. (Jan. 1996). “The observational characterization of hydrogen-deficient carbon stars as pulsating stars”. In: *Hydrogen Deficient Stars*. Ed. by C. S. Jeffery et al. Vol. 96. Astronomical Society of the Pacific Conference Series, p. 349.

Lawson, W. A. et al. (Feb. 1997). “The radial velocity variations of cool hydrogen-deficient carbon stars”. In: *MNRAS* 285.2, pp. 266–276. doi: 10.1093/mnras/285.2.266.

Lebouteiller, V. et al. (Sept. 2011). “CASSIS: The Cornell Atlas of Spitzer/Infrared Spectrograph Sources”. In: *ApJS* 196.1, 8, p. 8. doi: 10.1088/0067-0049/196/1/8.

Lebouteiller, V. et al. (June 2015). “CASSIS: The Cornell Atlas of Spitzer/Infrared Spectrograph Sources. II. High-resolution Observations”. In: *ApJS* 218.2, 21, p. 21. doi: 10.1088/0067-0049/218/2/21.

Lee, C. .-. (Mar. 2015). “Mining R Coronae Borealis stars from Catalina surveys”. In: *A&A* 575, A2, A2. doi: 10.1051/0004-6361/201424638.

Lee, C.-H. et al. (Jan. 2020). “ZTF18abhjrcf: The First R Coronae Borealis Star from the Zwicky Transient Facility Public Survey”. In: *The Astronomical Journal* 159.2, p. 61. doi: 10.3847/1538-3881/ab5b10.

Lee, O. J. et al. (Jan. 1947). “Carbon Stars in Zones 40[degrees] to 90[degrees]. Dearborn Survey of Faint Red Stars”. In: *Annals of the Dearborn Observatory* 5, pp. 287–292.

Levan, A. J. et al. (July 2020). “Electromagnetic counterparts of gravitational wave sources at the Very Large Telescope”. In: *Nature Reviews Physics* 2.9, pp. 455–457. doi: 10.1038/s42254-020-0216-2.

Li, W. et al. (Apr. 2003). “SN 2002cx: The Most Peculiar Known Type Ia Supernova”. In: *PASP* 115.806, pp. 453–473. doi: 10.1086/374200.

Li, L.-X. et al. (1998). “Transient events from neutron star mergers”. In: *Astrophys. J. Lett.* 507, p. L59. doi: 10.1086/311680.

Li, Z. et al. (Feb. 2019). “Formation of Extremely Low-mass White Dwarfs in Double Degenerates”. In: *ApJ* 871.2, 148, p. 148. doi: 10.3847/1538-4357/aaf9a1.

Licquia, T. C. et al. (June 2015). “Improved Estimates of the Milky Way’s Stellar Mass and Star Formation Rate from Hierarchical Bayesian Meta-Analysis”. In: *ApJ* 806.1, 96, p. 96. doi: 10.1088/0004-637X/806/1/96.

Lidov, M. L. (Oct. 1962). “The evolution of orbits of artificial satellites of planets under the action of gravitational perturbations of external bodies”. In: *Planetary and Space Science* 9.10, pp. 719–759. doi: 10.1016/0032-0633(62)90129-0.

LIGO–Virgo–KAGRA Collaboration (Feb. 2025a). “LIGO/Virgo/KAGRA S250206dm: Identification of a GW compact binary merger candidate”. In: *General Coordinates Network* 39175, p. 1.

– (Feb. 2025b). “LIGO/Virgo/KAGRA S250206dm: Updated Sky localization and EM Bright Classification”. In: *General Coordinates Network* 39231, p. 1.

Lipunov, V. M. et al. (June 1988). “The Joint Evolution of Normal and Compact Magnetized Stars in Close Binaries - Analytical Description and Statistical Simulation”. In: *Ap&SS* 145.1, pp. 1–45. doi: 10.1007/BF00645692.

Lira, P. et al. (Jan. 1998). “Optical Light Curves of the Type IA Supernovae SN 1990N and SN 1991T”. In: *AJ* 115.1, pp. 234–246. doi: 10.1086/300175.

Livio, M. et al. (June 1988). “The Common Envelope Phase in the Evolution of Binary Stars”. In: *ApJ* 329, p. 764. doi: 10.1086/166419.

Loebman, S. R. et al. (Jan. 2015). “The Continued Optical to Mid-Infrared Evolution of V838 Monocerotis”. In: *AJ* 149, 17, p. 17. doi: 10.1088/0004-6256/149/1/17.

Lomb, N. R. (Feb. 1976). “Least-squares frequency analysis of unequally spaced data”. In: *Ap&SS* 39, pp. 447–462. doi: 10.1007/BF00648343.

Lourie, N. P. et al. (Dec. 2020a). “The wide-field infrared transient explorer (WIN-TER)”. In: *Society of Photo-Optical Instrumentation Engineers (SPIE) Conference Series*. Vol. 11447. Society of Photo-Optical Instrumentation Engineers (SPIE) Conference Series, 114479K, 114479K. doi: 10.1117/12.2561210.

Lourie, N. P. et al. (2020b). “The wide-field infrared transient explorer (WINTER)”. In: *Ground-based and Airborne Instrumentation for Astronomy VIII*. Ed. by C. J. Evans et al. Vol. 11447. International Society for Optics and Photonics. SPIE, pp. 2064–2077. doi: 10.1117/12.2561210.

Lü, G. et al. (Apr. 2013). “DUST FORMATION IN THE EJECTA OF COMMON ENVELOPE SYSTEMS”. In: *ApJ* 768.2, p. 193. doi: 10.1088/0004-637X/768/2/193.

Lynch, D. K. et al. (May 2004). “0.8-13 Micron Spectroscopy of V838 Monocerotis and a Model for Its Emission”. In: *ApJ* 607, pp. 460–473. doi: 10.1086/382667.

Lynch, D. K. et al. (Apr. 2007a). “Recent Infrared Spectroscopy of V838 Monocerotis and the Current Model”. In: *The Nature of V838 Mon and its Light Echo*. Ed. by R. L. M. Corradi et al. Vol. 363. Astronomical Society of the Pacific Conference Series, p. 39.

– (Apr. 2007b). “Recent Infrared Spectroscopy of V838 Monocerotis and the Current Model”. In: *The Nature of V838 Mon and its Light Echo*. Ed. by R. L. M. Corradi et al. Vol. 363. Astronomical Society of the Pacific Conference Series, p. 39.

MacLeod, M. et al. (Feb. 2017). “Lessons from the Onset of a Common Envelope Episode: the Remarkable M31 2015 Luminous Red Nova Outburst”. In: *ApJ* 835, 282, p. 282. doi: 10.3847/1538-4357/835/2/282.

MacLeod, M. et al. (Jan. 2018). “Planetary Engulfment in the Hertzsprung-Russell Diagram”. In: *ApJ* 853.1, L1, p. L1. doi: 10.3847/2041-8213/aaa5fa.

MacLeod, M. et al. (Oct. 2022). “Dusty, Self-obsured Transients from Stellar Coalescence”. In: *ApJ* 937.2, 96, p. 96. doi: 10.3847/1538-4357/ac8c31.

Madau, P. et al. (Aug. 2014). “Cosmic Star-Formation History”. In: *ARA&A* 52, pp. 415–486. doi: 10.1146/annurev-astro-081811-125615.

Maehara, H. et al. (Jan. 1987). “A search for cool carbon stars. I. Cassiopeia region.” In: *Annals of the Tokyo Astronomical Observatory* 21, pp. 293–310.

Magee, M. R. et al. (May 2016). “The type Iax supernova, SN 2015H. A white dwarf deflagration candidate”. In: *A&A* 589, A89, A89. doi: 10.1051/0004-6361/201528036.

Magnier, E. A. et al. (Apr. 2013). “The Pan-STARRS 1 Photometric Reference Ladder, Release 12.01”. In: *ApJS* 205, 20, p. 20. doi: 10.1088/0067-0049/205/2/20.

Mainzer, A. et al. (Sept. 2014a). “Initial Performance of the NEOWISE Reactivation Mission”. In: *ApJ* 792.1, 30, p. 30. doi: 10.1088/0004-637X/792/1/30.

– (Sept. 2014b). “Initial Performance of the NEOWISE Reactivation Mission”. In: *ApJ* 792.1, 30, p. 30. doi: 10.1088/0004-637X/792/1/30.

Maíz Apellániz, J. et al. (Sept. 2023). “Stellar variability in Gaia DR3. I. Three-band photometric dispersions for 145 million sources”. In: *A&A* 677, A137, A137. doi: 10.1051/0004-6361/202346759.

Malonis, A. C. et al. (2020). “Detector architecture of the wide-field infrared transient explorer (WINTER) InGaAs camera”. In: *X-Ray, Optical, and Infrared Detectors for Astronomy IX*. Ed. by A. D. Holland et al. Vol. 11454. International Society for Optics and Photonics. SPIE, pp. 514–519. doi: 10.1117/12.2561228.

Mandigo-Stoba, M. S. et al. (Feb. 2022). “DBSP\_DRP: A Python package for automated spectroscopic data reduction of DBSP data”. In: *The Journal of Open Source Software* 7.70, 3612, p. 3612. doi: 10.21105/joss.03612.

Marchant, P. et al. (June 2021). “The role of mass transfer and common envelope evolution in the formation of merging binary black holes”. In: *A&A* 650, A107, A107. doi: 10.1051/0004-6361/202039992.

Margalit, B. et al. (2017). “Constraining the Maximum Mass of Neutron Stars From Multi-Messenger Observations of GW170817”. In: *Astrophys. J. Lett.* 850.2, p. L19. doi: 10.3847/2041-8213/aa991c.

Margutti, R. et al. (Oct. 2017). “The Electromagnetic Counterpart of the Binary Neutron Star Merger LIGO/Virgo GW170817. V. Rising X-Ray Emission from an Off-axis Jet”. In: *ApJ* 848.2, p. L20. doi: 10.3847/2041-8213/aa9057.

Marigo, P. et al. (July 2007). “Evolution of asymptotic giant branch stars. I. Updated synthetic TP-AGB models and their basic calibration”. In: *A&A* 469.1, pp. 239–263. doi: 10.1051/0004-6361:20066772.

Marigo, P. et al. (May 2008). “Evolution of asymptotic giant branch stars. II. Optical to far-infrared isochrones with improved TP-AGB models”. In: *A&A* 482, pp. 883–905. doi: 10.1051/0004-6361:20078467.

Marigo, P. et al. (Sept. 2013). “Evolution of thermally pulsing asymptotic giant branch stars - I. The COLIBRI code”. In: *MNRAS* 434.1, pp. 488–526. doi: 10.1093/mnras/stt1034.

Marrese, P. M. et al. (Jan. 2019). “Gaia Data Release 2. Cross-match with external catalogues: algorithms and results”. In: *A&A* 621, A144, A144. doi: 10.1051/0004-6361/201834142.

Marsh, T. R. et al. (May 2004). “Mass transfer between double white dwarfs”. In: *MNRAS* 350.1, pp. 113–128. doi: 10.1111/j.1365-2966.2004.07564.x.

Martini, P. et al. (Aug. 1999). “Nova Sagittarii 1994 1 (V4332 Sagittarii): The Discovery and Evolution of an Unusual Luminous Red Variable Star”. In: *AJ* 118, pp. 1034–1042. doi: 10.1086/300951.

Masci, F. J. et al. (Jan. 2019). “The Zwicky Transient Facility: Data Processing, Products, and Archive”. In: *PASP* 131.995, p. 018003. doi: 10.1088/1538-3873/aae8ac.

Masi, G. (Feb. 2025). “IGO/Virgo/KAGRA S250206dm: Virtual Telescope Project upper limit for the Neutrino IceCube Candidate”. In: *GRB Coordinates Network* 39204, p. 1.

Mason, E. et al. (June 2010). “The peculiar nova V1309 Scorpii/nova Scorpii 2008. A candidate twin of V838 Monocerotis”. In: *A&A* 516, A108, A108. doi: 10.1051/0004-6361/200913610.

Mathis, J. S. et al. (Oct. 1977). “The size distribution of interstellar grains.” In: *ApJ* 217, pp. 425–433. doi: 10.1086/155591.

Matsumoto, T. et al. (Feb. 2022). “Light Curve Model for Luminous Red Novae and Inferences about the Ejecta of Stellar Mergers”. In: *arXiv e-prints*, arXiv:2202.10478, arXiv:2202.10478.

Mauerhan, J. C. et al. (Jan. 2018). “The dusty aftermath of SN Hunt 248: merger-burst remnant?” In: *MNRAS* 473.3, pp. 3765–3775. doi: 10.1093/mnras/stx2500.

McCrea, W. H. (Jan. 1964). “Extended main-sequence of some stellar clusters”. In: *MNRAS* 128, p. 147. doi: 10.1093/mnras/128.2.147.

McCully, C. et al. (Aug. 2014). “A luminous, blue progenitor system for the type Iax supernova 2012Z”. In: *Nature* 512.7512, pp. 54–56. doi: 10.1038/nature13615.

McCully, C. et al. (June 2021). “The Progenitor System of SN 2012Z Did Not Disappear: Comparing Hubble Space Telescope Observations a Decade Apart”. In: *arXiv e-prints*, arXiv:2106.04602, arXiv:2106.04602.

McKee, C. (Jan. 1989). “Dust Destruction in the Interstellar Medium”. In: *Interstellar Dust*. Ed. by L. J. Allamandola et al. Vol. 135. IAU Symposium, p. 431.

Mehla, A. et al. (Dec. 2024). “Oxygen Isotope Ratios in Hydrogen-Deficient Carbon Stars: A Correlation with Effective Temperature and Implications for White Dwarf Merger Outcomes”. In: *arXiv e-prints*, arXiv:2412.03664, arXiv:2412.03664. doi: 10.48550/arXiv.2412.03664.

Meisner, A. M. et al. (Dec. 2019). “unWISE Coadds: The Five-year Data Set”. In: *PASP* 131.1006, p. 124504. doi: 10.1088/1538-3873/ab3df4.

Messick, C. et al. (2017). “Analysis Framework for the Prompt Discovery of Compact Binary Mergers in Gravitational-wave Data”. In: *Phys. Rev. D* 95.4, p. 042001. doi: 10.1103/PhysRevD.95.042001.

Metzger, B. D. et al. (2010). “Electromagnetic Counterparts of Compact Object Mergers Powered by the Radioactive Decay of R-process Nuclei”. In: *Mon. Not. Roy. Astron. Soc.* 406, p. 2650. doi: 10.1111/j.1365-2966.2010.16864.x.

Metzger, B. D. et al. (Nov. 2017). “Shock-powered light curves of luminous red novae as signatures of pre-dynamical mass-loss in stellar mergers”. In: *MNRAS* 471, pp. 3200–3211. doi: 10.1093/mnras/stx1768.

Metzger, B. D. (2020). “Kilonovae”. In: *Living Rev. Rel.* 23.1, p. 1. doi: 10.1007/s41114-019-0024-0.

Metzger, B. D. et al. (Dec. 2021). “Transients from the Cataclysmic Deaths of Cataclysmic Variables”. In: *ApJ* 923.1, 100, p. 100. doi: 10.3847/1538-4357/ac2a39.

Micelotta, E. R. et al. (May 2016). “Dust destruction by the reverse shock in the Cassiopeia A supernova remnant”. In: *A&A* 590, A65, A65. doi: 10.1051/0004-6361/201527350.

Minniti, D. et al. (July 2010). “VISTA Variables in the Via Lactea (VVV): The public ESO near-IR variability survey of the Milky Way”. In: *New Astronomy* 15.5, pp. 433–443. doi: 10.1016/j.newast.2009.12.002.

Misner, C. W. et al. (1973). *Gravitation*.

Mo, G. et al. (May 2024). “GRB 240529A: J-band detections with WINTER”. In: *GRB Coordinates Network* 36569, p. 1.

Moe, M. et al. (June 2017). “Mind Your Ps and Qs: The Interrelation between Period (P) and Mass-ratio (Q) Distributions of Binary Stars”. In: *ApJS* 230.2, 15, p. 15. doi: 10.3847/1538-4365/aa6fb6.

Montiel, E. J. et al. (Oct. 2018). “The Double Dust Envelopes of R Coronae Borealis Stars”. In: *AJ* 156.4, 148, p. 148. doi: 10.3847/1538-3881/aad772.

Mooley, K. P. et al. (Feb. 2018). “A mildly relativistic wide-angle outflow in the neutron-star merger event GW170817”. In: *Nature* 554.7691, pp. 207–210. doi: 10.1038/nature25452.

Moore, A. M. et al. (Aug. 2016). “Unveiling the dynamic infrared sky with Gattini-IR”. In: *Ground-based and Airborne Telescopes VI*. Ed. by H. J. Hall et al. Vol. 9906. Society of Photo-Optical Instrumentation Engineers (SPIE) Conference Series, 99062C, p. 99062C. doi: 10.1117/12.2233694.

Moore, A. M. et al. (Jan. 2019). “Unveiling the dynamic infrared sky”. In: *Nature Astronomy* 3, pp. 109–109. doi: 10.1038/s41550-018-0675-x.

Morgan, D. H. et al. (Sept. 2003). “Suspected cool R Coronae Borealis stars in the Magellanic Clouds”. In: *MNRAS* 344.1, pp. 325–335. doi: 10.1046/j.1365-8711.2003.06822.x.

Moriya, T. et al. (Oct. 2010). “Faint Core-Collapse Supernovae withFallback”. In: *Deciphering the Ancient Universe with Gamma-ray Bursts*. Ed. by N. Kawai et al. Vol. 1279. American Institute of Physics Conference Series, pp. 224–226. doi: 10.1063/1.3509269.

Morris, T. et al. (Feb. 2007). “The Triple-Ring Nebula Around SN 1987A: Fingerprint of a Binary Merger”. In: *Science* 315.5815, p. 1103. doi: 10.1126/science.1136351.

Mould, J. et al. (Apr. 1990). “A Nova-like Red Variable in M31”. In: *ApJ* 353, p. L35. doi: 10.1086/185702.

Mould, J. R. et al. (Feb. 2000). “The Hubble Space Telescope Key Project on the Extragalactic Distance Scale. XXVIII. Combining the Constraints on the Hubble Constant”. In: *ApJ* 529.2, pp. 786–794. doi: 10.1086/308304.

Munari, U. et al. (July 2002). “The mysterious eruption of V838 Mon”. In: *A&A* 389, pp. L51–L56. doi: 10.1051/0004-6361:20020715.

Munson, B. et al. (Apr. 2021). “R Coronae Borealis Star Evolution: Simulating 3D Merger Events to 1D Stellar Evolution Including Large-scale Nucleosynthesis”. In: *ApJ* 911.2, 103, p. 103. doi: 10.3847/1538-4357/abeb6c.

“United Kingdom Infrared Telescope” (2000). In: *Encyclopedia of Astronomy and Astrophysics*. Ed. by P. Murdin, 4351, p. 4351. doi: 10.1888/0333750888/4351.

Narayan, R. et al. (Aug. 1992). “Gamma-Ray Bursts as the Death Throes of Massive Binary Stars”. In: *ApJ* 395, p. L83. doi: 10.1086/186493.

Nassau, J. J. et al. (Jan. 1957). “Carbon Stars in Two Northern Milky way Zones.” In: *ApJ* 125, p. 195. doi: 10.1086/146293.

Nath, B. B. et al. (Aug. 2008). “Dust Sputtering by Reverse Shocks in Supernova Remnants”. In: *ApJ* 682.2, pp. 1055–1064. doi: 10.1086/589224.

Neugent, K. F. et al. (Jan. 2020). “The Luminosity Function of Red Supergiants in M31”. In: *ApJ* 889.1, 44, p. 44. doi: 10.3847/1538-4357/ab5ba0.

Neumann, J. von (1941). “Distribution of the Ratio of the Mean Square Successive Difference to the Variance”. In: *The Annals of Mathematical Statistics* 12.4, pp. 367–395. doi: 10.1214/aoms/1177731677.

Nicholls, C. P. et al. (Apr. 2013). “The dusty aftermath of the V1309 Sco binary merger.” In: *MNRAS* 431, pp. L33–L37. doi: 10.1093/mnrasl/slt003.

Nitz, A. H. et al. (2017). “Detecting binary compact-object mergers with gravitational waves: Understanding and Improving the sensitivity of the PyCBC search”. In: *Astrophys. J.* 849.2, p. 118. doi: 10.3847/1538-4357/aa8f50.

Nordin, J. et al. (Nov. 2019). “Transient processing and analysis using AMPEL: alert management, photometry, and evaluation of light curves”. In: *A&A* 631, A147, A147. doi: 10.1051/0004-6361/201935634.

Nozawa, T. et al. (Dec. 2003). “Dust in the Early Universe: Dust Formation in the Ejecta of Population III Supernovae”. In: *ApJ* 598.2, pp. 785–803. doi: 10.1086/379011.

Nozawa, T. et al. (Sept. 2007). “Evolution of Dust in Primordial Supernova Remnants: Can Dust Grains Formed in the Ejecta Survive and Be Injected into the Early Interstellar Medium?” In: *ApJ* 666.2, pp. 955–966. doi: 10.1086/520621.

Ofek, E. O. et al. (Feb. 2008). “The Environment of M85 Optical Transient 2006-1: Constraints on the Progenitor Age and Mass”. In: *ApJ* 674, 447–450, pp. 447–450. doi: 10.1086/524350.

Ofek, E. O. et al. (Jan. 2012). “The Palomar Transient Factory Photometric Calibration”. In: *PASP* 124, pp. 62–73. doi: 10.1086/664065.

Ofek, E. O. et al. (June 2023). “The Large Array Survey Telescope-System Overview and Performances”. In: *PASP* 135.1048, 065001, p. 065001. doi: 10.1088/1538-3873/acd8f0.

Ohnaka, K. (July 2004). “Warm water vapor envelope in the supergiants  $\alpha$  Ori and  $\alpha$  Her and its effects on the apparent size from the near-infrared to the mid-infrared”. In: *A&A* 421, pp. 1149–1158. doi: 10.1051/0004-6361:20035668.

Oke, J. B. et al. (June 1982). “An Efficient Low Resolution and Moderate Resolution Spectrograph for the Hale Telescope”. In: *PASP* 94, p. 586. doi: 10.1086/131027.

Oke, J. B. et al. (Apr. 1995). “The Keck Low-Resolution Imaging Spectrometer”. In: *PASP* 107, p. 375. doi: 10.1086/133562.

Oskinova, L. M. et al. (Dec. 2020). “X-rays observations of a super-Chandrasekhar object reveal an ONe and a CO white dwarf merger product embedded in a putative SN Iax remnant”. In: *A&A* 644, L8, p. L8. doi: 10.1051/0004-6361/202039232.

Otero, S. et al. (June 2014). “New R Coronae Borealis and DY Persei Star Candidates and Other Related Objects Found in Photometric Surveys”. In: *Journal of the American Association of Variable Star Observers (AAVSO)* 42.1, p. 13.

Paczynski, B. (Jan. 1976). “Common Envelope Binaries”. In: *Structure and Evolution of Close Binary Systems*. Ed. by P. Eggleton et al. Vol. 73. IAU Symposium, p. 75.

Pandas Development Team (Sept. 2024). *pandas-dev/pandas: Pandas*. Version v2.2.3. doi: 10.5281/zenodo.13819579.

Pandey, G. et al. (Dec. 2007). “Fluorine in R Coronae Borealis and Extreme Helium Stars”. In: *arXiv e-prints*, arXiv:0712.3971, arXiv:0712.3971.

Pastorello, A. et al. (Oct. 2019a). “Luminous red novae: Stellar mergers or giant eruptions?” In: *A&A* 630, A75, A75. doi: 10.1051/0004-6361/201935999.

Pastorello, A. et al. (May 2019b). “The evolution of luminous red nova AT 2017jfs in NGC 4470”. In: *A&A* 625, L8, p. L8. doi: 10.1051/0004-6361/201935511.

Pastorello, A. et al. (Feb. 2021a). “Forbidden hugs in pandemic times. I. Luminous red nova AT 2019zhd, a new merger in M 31”. In: *A&A* 646, A119, A119. doi: 10.1051/0004-6361/202039952.

Pastorello, A. et al. (Mar. 2021b). “Forbidden hugs in pandemic times. II. The luminous red nova variety: AT 2020hat and AT 2020kog”. In: *A&A* 647, A93, A93. doi: 10.1051/0004-6361/202039953.

Pastorello, A. et al. (Aug. 2022). “Panchromatic evolution of three luminous red novae: Forbidden hugs in pandemic times – IV”. In: *arXiv e-prints*, arXiv:2208.02782, arXiv:2208.02782.

Pastorello, A. et al. (Aug. 2019c). “Supernova impostors and other gap transients”. In: *Nature Astronomy* 3, pp. 676–679. doi: 10.1038/s41550-019-0809-9.

Patterson, M. T. et al. (Jan. 2019). “The Zwicky Transient Facility Alert Distribution System”. In: *PASP* 131.995, p. 018001. doi: 10.1088/1538-3873/aae904.

Pedersen, P. P. et al. (July 2024). “Infrared photometry with InGaAs detectors: first light with SPECULOOS”. In: *Ground-based and Airborne Instrumentation for Astronomy X*. Ed. by J. J. Bryant et al. Vol. 13096. Society of Photo-Optical Instrumentation Engineers (SPIE) Conference Series, 130963X, p. 130963X. doi: 10.1117/12.3018320.

Pedregosa, F. et al. (2011). “Scikit-learn: Machine Learning in Python”. In: *Journal of Machine Learning Research* 12, pp. 2825–2830.

Pejcha, O. (June 2014). “Burying a Binary: Dynamical Mass Loss and a Continuous Optically thick Outflow Explain the Candidate Stellar Merger V1309 Scorpii”. In: *ApJ* 788, 22, p. 22. doi: 10.1088/0004-637X/788/1/22.

Pejcha, O. et al. (Feb. 2016). “Cool and luminous transients from mass-losing binary stars”. In: *MNRAS* 455, pp. 4351–4372. doi: 10.1093/mnras/stv2592.

Pejcha, O. et al. (Nov. 2017). “Pre-explosion Spiral Mass Loss of a Binary Star Merger”. In: *ApJ* 850.1, 59, p. 59. doi: 10.3847/1538-4357/aa95b9.

Percy, J. R. (June 2023). “Studies of R CrB Star Pulsation Using ASAS-SN Photometry”. In: *JAAVSO* 51.1, p. 64.

Perley, D. A. (Aug. 2019). “Fully Automated Reduction of Longslit Spectroscopy with the Low Resolution Imaging Spectrometer at the Keck Observatory”. In: *PASP* 131.1002, p. 084503. doi: 10.1088/1538-3873/ab215d.

Perley, D. A. et al. (Nov. 2020). “The Zwicky Transient Facility Bright Transient Survey. II. A Public Statistical Sample for Exploring Supernova Demographics”. In: *ApJ* 904.1, 35, p. 35. doi: 10.3847/1538-4357/abbd98.

Perlmutter, S. et al. (June 1999). “Measurements of  $\Omega$  and  $\Lambda$  from 42 High-Redshift Supernovae”. In: *ApJ* 517.2, pp. 565–586. doi: 10.1086/307221.

Petz, S. et al. (Jan. 2025). “Life in the Slow Lane: A Search for Long Term Variability in ASAS-SN”. In: *arXiv e-prints*, arXiv:2501.14058, arXiv:2501.14058. doi: 10.48550/arXiv.2501.14058.

Phillips, M. J. et al. (Aug. 1978). “Long-term variability of dMe stars.” In: *ApJ* 224, pp. 182–184. doi: 10.1086/156363.

Plez, B. (Dec. 2008). “MARCS model atmospheres”. In: *Physica Scripta Volume T* 133, 014003, p. 014003. doi: 10.1088/0031-8949/2008/T133/014003.

Podsiadlowski, P. et al. (May 2003). “On the formation and evolution of black hole binaries”. In: *MNRAS* 341.2, pp. 385–404. doi: 10.1046/j.1365-8711.2003.06464.x.

Poelarends, A. J. T. (Jan. 2007). “Stellar evolution on the borderline of white dwarf and neutron star formation”. PhD thesis. University of Utrecht, Netherlands.

Poelarends, A. J. T. et al. (Mar. 2008a). “The Supernova Channel of Super-AGB Stars”. In: *ApJ* 675.1, pp. 614–625. doi: 10.1086/520872.

– (Mar. 2008b). “The Supernova Channel of Super-AGB Stars”. In: *ApJ* 675, pp. 614–625. doi: 10.1086/520872.

Politano, M. et al. (Sept. 2010). “Population Synthesis of Common Envelope Mergers. I. Giant Stars with Stellar or Substellar Companions”. In: *ApJ* 720.2, pp. 1752–1766. doi: 10.1088/0004-637X/720/2/1752.

Postnov, K. A. et al. (Dec. 2014). “The Evolution of Compact Binary Star Systems”. In: *Living Reviews in Relativity* 17.1, 3, p. 3. doi: 10.12942/lrr-2014-3.

Pozanenko, A. S. et al. (Jan. 2018). “GRB 170817A Associated with GW170817: Multi-frequency Observations and Modeling of Prompt Gamma-Ray Emission”. In: *ApJ* 852.2, L30, p. L30. doi: 10.3847/2041-8213/aaa2f6.

Poznanski, D. et al. (Jan. 2010). “An Unusually Fast-Evolving Supernova”. In: *Science* 327.5961, p. 58. doi: 10.1126/science.1181709.

Poznanski, D. et al. (Oct. 2012). “An empirical relation between sodium absorption and dust extinction”. In: *MNRAS* 426.2, pp. 1465–1474. doi: 10.1111/j.1365-2966.2012.21796.x.

Priestley, F. D. et al. (Jan. 2022). “Dust destruction and survival in the Cassiopeia A reverse shock”. In: *MNRAS* 509.3, pp. 3163–3171. doi: 10.1093/mnras/stab3195.

Prieto, J. L. et al. (July 2008). “Discovery of the Dust-Enshrouded Progenitor of SN 2008S with Spitzer”. In: *ApJ* 681, pp. L9–L12. doi: 10.1086/589922.

Pumo, M. L. et al. (Nov. 2009). “EC-SNe from Super-Asymptotic Giant Branch Progenitors: Theoretical Models Versus Observations”. In: *ApJ* 705.2, pp. L138–L142. doi: 10.1088/0004-637X/705/2/L138.

Putney, A. (Oct. 1997). “Surveying DC White Dwarfs for Magnetic Fields”. In: *ApJS* 112.2, pp. 527–556. doi: 10.1086/313037.

Raghavan, D. et al. (Sept. 2010). “A Survey of Stellar Families: Multiplicity of Solar-type Stars”. In: *ApJS* 190.1, pp. 1–42. doi: 10.1088/0067-0049/190/1/1.

Ramírez, S. (2024). *FastAPI*.

Ramsay Howat, S. K. et al. (Sept. 2004). “The commissioning of and first results from the UIST imager spectrometer”. In: *Ground-based Instrumentation for Astronomy*. Ed. by A. F. M. Moorwood et al. Vol. 5492. Society of Photo-Optical Instrumentation Engineers (SPIE) Conference Series, pp. 1160–1171. doi: 10.1117/12.551673.

Rao, N. K. et al. (Jan. 1996). “Surface composition of the RCB stars - refinement of a few mere facts”. In: *Hydrogen Deficient Stars*. Ed. by C. S. Jeffery et al. Vol. 96. Astronomical Society of the Pacific Conference Series, p. 43.

Rao, N. K. et al. (Feb. 2008). “High-resolution spectroscopy of the R Coronae Borealis star V Coronae Australis”. In: *MNRAS* 384.2, pp. 477–488. doi: 10.1111/j.1365-2966.2007.12643.x.

– (Mar. 2015). “Mid-infrared variations of R Coronae Borealis stars”. In: *MNRAS* 447.4, pp. 3664–3677. doi: 10.1093/mnras/stu2748.

Rau, A. et al. (Dec. 2009). “Exploring the Optical Transient Sky with the Palomar Transient Factory”. In: *PASP* 121, p. 1334. doi: 10.1086/605911.

Rayner, J. T. et al. (Mar. 2003). “SpeX: A Medium-Resolution 0.8-5.5 Micron Spectrograph and Imager for the NASA Infrared Telescope Facility”. In: *PASP* 115.805, pp. 362–382. doi: 10.1086/367745.

Rayner, J. T. et al. (Dec. 2009). “The Infrared Telescope Facility (IRTF) Spectral Library: Cool Stars”. In: *ApJS* 185.2, pp. 289–432. doi: 10.1088/0067-0049/185/2/289.

Reguitti, A. et al. (Feb. 2021). “Low-luminosity Type II supernovae - III. SN 2018hwm, a faint event with an unusually long plateau”. In: *MNRAS* 501.1, pp. 1059–1071. doi: 10.1093/mnras/staa3730.

Rich, R. M. et al. (June 1989). “Luminous M giants in the bulge of M31”. In: *ApJ* 341, pp. L51–L54. doi: 10.1086/185455.

Ricker, G. R. et al. (Jan. 2015). “Transiting Exoplanet Survey Satellite (TESS)”. In: *Journal of Astronomical Telescopes, Instruments, and Systems* 1, 014003, p. 014003. doi: 10.1117/1.JATIS.1.1.014003.

Ricker, P. M. et al. (Feb. 2012). “An AMR Study of the Common-envelope Phase of Binary Evolution”. In: *ApJ* 746.1, 74, p. 74. doi: 10.1088/0004-637X/746/1/74.

Riddle, R. L. et al. (2012). “The Robo-AO software: fully autonomous operation of a laser guide star adaptive optics and science system”. In: *Adaptive Optics Systems III*. Ed. by B. L. Ellerbroek et al. Vol. 8447. International Society for Optics and Photonics. SPIE, pp. 993–1001. doi: 10.1117/12.925475.

Riebel, D. et al. (July 2015). “SAGE-Var: An Infrared Survey of Variability in the Magellanic Clouds”. In: *ApJ* 807.1, 1, p. 1. doi: 10.1088/0004-637X/807/1/1.

Riess, A. G. et al. (Sept. 1998). “Observational Evidence from Supernovae for an Accelerating Universe and a Cosmological Constant”. In: *AJ* 116.3, pp. 1009–1038. doi: 10.1086/300499.

Rigault, M. et al. (July 2019). “Fully automated integral field spectrograph pipeline for the SEDMachine: pysedm”. In: *A&A* 627, A115, A115. doi: 10.1051/0004-6361/201935344.

Rigliaco, E. et al. (Dec. 2012). “X-shooter spectroscopy of young stellar objects. I. Mass accretion rates of low-mass T Tauri stars in  $\sigma$  Orionis”. In: *A&A* 548, A56, A56. doi: 10.1051/0004-6361/201219832.

Roberts, L. F. et al. (2011). “Electromagnetic Transients Powered by Nuclear Decay in the Tidal Tails of Coalescing Compact Binaries”. In: *Astrophys. J. Lett.* 736, p. L21. doi: 10.1088/2041-8205/736/1/L21.

Rosswog, S. (2005). “Mergers of neutron star black hole binaries with small mass ratios: Nucleosynthesis, gamma-ray bursts and electromagnetic transients”. In: *Astrophys. J.* 634, p. 1202. doi: 10.1086/497062.

Rosswog, S. et al. (Feb. 2024). “Heavy Elements and Electromagnetic Transients from Neutron Star Mergers”. In: *Annalen der Physik* 536.2, 2200306, p. 2200306. doi: 10.1002/andp.202200306.

Rothman, L. S. et al. (Oct. 2010). “HITEMP, the high-temperature molecular spectroscopic database”. In: *JQSRT* 111, pp. 2139–2150. doi: 10.1016/j.jqsrt.2010.05.001.

Rowan, D. M. et al. (June 2021). “ASASSN-21co: A Detached Eclipsing Binary with an 11.9 yr Period”. In: *Research Notes of the American Astronomical Society* 5.6, 147, p. 147. doi: 10.3847/2515-5172/ac0c83.

Rozwadowska, K. et al. (Feb. 2021). “On the rate of core collapse supernovae in the milky way”. In: *New Astronomy* 83, 101498, p. 101498. doi: 10.1016/j.newast.2020.101498.

Ruiter, A. J. et al. (July 2009). “Rates and Delay Times of Type Ia Supernovae”. In: *ApJ* 699.2, pp. 2026–2036. doi: 10.1088/0004-637X/699/2/2026.

Sachdev, S. et al. (Jan. 2019). “The GstLAL Search Analysis Methods for Compact Binary Mergers in Advanced LIGO’s Second and Advanced Virgo’s First Observing Runs”. In: *arXiv e-prints*.

Sahai, R. et al. (Jan. 2017). “ALMA Observations of the Water Fountain Pre-planetary Nebula IRAS 16342-3814: High-velocity Bipolar Jets and an Expanding Torus”. In: *ApJ* 835.1, L13, p. L13. doi: 10.3847/2041-8213/835/1/L13.

Saio, H. (July 2008). “Radial and Nonradial Pulsations in RCB and EHe-B Stars”. In: *Hydrogen-Deficient Stars*. Ed. by A. Werner et al. Vol. 391. Astronomical Society of the Pacific Conference Series, p. 69.

Saio, H. et al. (Apr. 2000). “The evolution of a rapidly accreting helium white dwarf to become a low-luminosity helium star”. In: *MNRAS* 313.4, pp. 671–677. doi: 10.1046/j.1365-8711.2000.03221.x.

– (June 2002). “Merged binary white dwarf evolution: rapidly accreting carbon-oxygen white dwarfs and the progeny of extreme helium stars”. In: *MNRAS* 333.1, pp. 121–132. doi: 10.1046/j.1365-8711.2002.05384.x.

Saito, R. K. et al. (Sept. 2024). “The VISTA Variables in the Vía Láctea extended (VVVX) ESO public survey: Completion of the observations and legacy”. In: *A&A* 689, A148, A148. doi: 10.1051/0004-6361/202450584.

Sana, H. et al. (July 2012). “Binary Interaction Dominates the Evolution of Massive Stars”. In: *Science* 337, pp. 444–. doi: 10.1126/science.1223344.

Sarangi, A. et al. (Mar. 2015). “Condensation of dust in the ejecta of Type II-P supernovae”. In: *A&A* 575, A95, A95. doi: 10.1051/0004-6361/201424969.

Sargent, B. A. et al. (Sept. 2014). “Emission from Water Vapor and Absorption from Other Gases at 5–7.5  $\mu\text{m}$  in Spitzer-IRS Spectra of Protoplanetary Disks”. In: *ApJ* 792.2, 83, p. 83. doi: 10.1088/0004-637X/792/2/83.

Sargent, B. A. et al. (June 2010). “The Mass-loss Return from Evolved Stars to the Large Magellanic Cloud. II. Dust Properties for Oxygen-rich Asymptotic Giant Branch Stars”. In: *ApJ* 716.1, pp. 878–890. doi: 10.1088/0004-637X/716/1/878.

Sargent, B. A. et al. (Feb. 2011). “The Mass-loss Return from Evolved Stars to the Large Magellanic Cloud. IV. Construction and Validation of a Grid of Models for Oxygen-rich AGB Stars, Red Supergiants, and Extreme AGB Stars”. In: *ApJ* 728.2, 93, p. 93. doi: 10.1088/0004-637X/728/2/93.

Scargle, J. D. (Dec. 1982). “Studies in astronomical time series analysis. II - Statistical aspects of spectral analysis of unevenly spaced data”. In: *ApJ* 263, pp. 835–853. doi: 10.1086/160554.

Scherbak, P. et al. (Jan. 2023). “White dwarf binaries suggest a common envelope efficiency  $\alpha \approx 1/3$ ”. In: *MNRAS* 518.3, pp. 3966–3984. doi: 10.1093/mnras/stac3313.

Schlafly, E. F. et al. (Aug. 2011). “Measuring Reddening with Sloan Digital Sky Survey Stellar Spectra and Recalibrating SFD”. In: *ApJ* 737, 103, p. 103. doi: 10.1088/0004-637X/737/2/103.

Schlafly, E. F. et al. (Sept. 2012). “Photometric Calibration of the First 1.5 Years of the Pan-STARRS1 Survey”. In: *ApJ* 756, 158, p. 158. doi: 10.1088/0004-637X/756/2/158.

Schneider, F. R. N. et al. (May 2015). “Evolution of Mass Functions of Coeval Stars through Wind Mass Loss and Binary Interactions”. In: *ApJ* 805.1, 20, p. 20. doi: 10.1088/0004-637X/805/1/20.

Schneider, F. R. N. et al. (Apr. 2016). “Rejuvenation of stellar mergers and the origin of magnetic fields in massive stars”. In: *MNRAS* 457.3, pp. 2355–2365. doi: 10.1093/mnras/stw148.

Schneider, F. R. N. et al. (June 2024). “Pre-supernova evolution and final fate of stellar mergers and accretors of binary mass transfer”. In: *A&A* 686, A45, A45. doi: 10.1051/0004-6361/202347854.

Schneider, F. R. N. et al. (Oct. 2019). “Stellar mergers as the origin of magnetic massive stars”. In: *Nature* 574.7777, pp. 211–214. doi: 10.1038/s41586-019-1621-5.

Schwab, J. (Nov. 2019). “Evolutionary Models for R Coronae Borealis Stars”. In: *ApJ* 885.1, 27, p. 27. doi: 10.3847/1538-4357/ab425d.

Shahbandeh, M. et al. (Aug. 2023). “JWST observations of dust reservoirs in type IIP supernovae 2004et and 2017eaw”. In: *MNRAS* 523.4, pp. 6048–6060. doi: 10.1093/mnras/stad1681.

Shappee, B. J. et al. (June 2014). “The Man behind the Curtain: X-Rays Drive the UV through NIR Variability in the 2013 Active Galactic Nucleus Outburst in NGC 2617”. In: *ApJ* 788.1, 48, p. 48. doi: 10.1088/0004-637X/788/1/48.

Shen, K. J. (May 2015). “Every Interacting Double White Dwarf Binary May Merge”. In: *ApJ* 805.1, L6, p. L6. doi: 10.1088/2041-8205/805/1/L6.

Shen, K. J. et al. (June 2010). “Thermonuclear Ia Supernovae from Helium Shell Detonations: Explosion Models and Observables”. In: *ApJ* 715.2, pp. 767–774. doi: 10.1088/0004-637X/715/2/767.

Shen, K. J. et al. (Jan. 2017). “Wait for It: Post-supernova Winds Driven by Delayed Radioactive Decays”. In: *ApJ* 834.2, 180, p. 180. doi: 10.3847/1538-4357/834/2/180.

Shen, K. J. et al. (Feb. 2018). “Sub-Chandrasekhar-mass White Dwarf Detonations Revisited”. In: *ApJ* 854.1, 52, p. 52. doi: 10.3847/1538-4357/aaa8de.

Shields, J. V. et al. (Mar. 2019). “An all-sky search for R Coronae Borealis stars in ASAS-SN”. In: *MNRAS* 483.4, pp. 4470–4478. doi: 10.1093/mnras/sty3445.

Silvia, D. W. et al. (June 2010). “Numerical Simulations of Supernova Dust Destruction. I. Cloud-crushing and Post-processed Grain Sputtering”. In: *ApJ* 715.2, pp. 1575–1590. doi: 10.1088/0004-637X/715/2/1575.

Sim, S. A. et al. (May 2010). “Detonations in Sub-Chandrasekhar-mass C+O White Dwarfs”. In: *ApJ* 714.1, pp. L52–L57. doi: 10.1088/2041-8205/714/1/L52.

Simcoe, R. A. et al. (Feb. 2019a). “Background-limited Imaging in the Near Infrared with Warm InGaAs Sensors: Applications for Time-domain Astronomy”. In: *AJ* 157.2, 46, p. 46. doi: 10.3847/1538-3881/aae094.

Simcoe, R. A. et al. (2019b). “Background-limited Imaging in the Near Infrared with Warm InGaAs Sensors: Applications for Time-domain Astronomy”. In: *Astron. J.* 157.2, p. 46. doi: 10.3847/1538-3881/aae094.

Skrutskie, M. F. et al. (Feb. 2006). “The Two Micron All Sky Survey (2MASS)”. In: *AJ* 131.2, pp. 1163–1183. doi: 10.1086/498708.

Slavin, J. D. et al. (Apr. 2015). “Destruction of Interstellar Dust in Evolving Supernova Remnant Shock Waves”. In: *ApJ* 803, 7, p. 7. doi: 10.1088/0004-637X/803/1/7.

Slavin, J. D. et al. (Oct. 2020). “The Dynamics, Destruction, and Survival of Supernova-formed Dust Grains”. In: *ApJ* 902.2, 135, p. 135. doi: 10.3847/1538-4357/abb5a4.

Sloan, G. C. et al. (Sept. 2015). “Infrared Spectral Properties of M Giants”. In: *ApJ* 811.1, 45, p. 45. doi: 10.1088/0004-637X/811/1/45.

Smith, K. W. et al. (Aug. 2020a). “Design and Operation of the ATLAS Transient Science Server”. In: *PASP* 132.1014, 085002, p. 085002. doi: 10.1088/1538-3873/ab936e.

– (Aug. 2020b). “Design and Operation of the ATLAS Transient Science Server”. In: *PASP* 132.1014, 085002, p. 085002. doi: 10.1088/1538-3873/ab936e.

Smith, K. W. et al. (Jan. 2021a). “ATLAS21dfy (AT2021biy): discovery of a transient in NGC 4631 (4 Mpc)”. In: *Transient Name Server AstroNote* 33, pp. 1–33.

Smith, K. W. et al. (Feb. 2021b). “ATLAS21dic (AT2021blu): discovery of a transient in UGC 05829 (8 Mpc)”. In: *Transient Name Server AstroNote* 43, pp. 1–43.

Smith, N. et al. (May 2009). “SN 2008S: A Cool Super-Eddington Wind in a Supernova Impostor”. In: *ApJ* 697, pp. L49–L53. doi: 10.1088/0004-637X/697/1/L49.

Smith, N. et al. (July 2011). “Luminous blue variable eruptions and related transients: diversity of progenitors and outburst properties”. In: *MNRAS* 415, pp. 773–810. doi: 10.1111/j.1365-2966.2011.18763.x.

Smith, N. et al. (Feb. 2016). “The Persistent Eruption of UGC 2773-OT: finally, a decade-long extragalactic Eta Carinae analogue”. In: *MNRAS* 455.4, pp. 3546–3560. doi: 10.1093/mnras/stv2507.

Smith, N. et al. (Aug. 2018). “Light echoes from the plateau in Eta Carinae’s Great Eruption reveal a two-stage shock-powered event”. In: *MNRAS* 480.2, pp. 1466–1498. doi: 10.1093/mnras/sty1500.

Soberman, G. E. et al. (Nov. 1997). “Stability criteria for mass transfer in binary stellar evolution.” In: *A&A* 327, pp. 620–635. doi: 10.48550/arXiv.astro-ph/9703016.

Soker, N. (Apr. 2020). “Efficiently Jet-powered Radiation in Intermediate-luminosity Optical Transients”. In: *ApJ* 893.1, 20, p. 20. doi: 10.3847/1538-4357/ab7dbb.

Soker, N. et al. (May 2021). “Explaining recently studied intermediate luminosity optical transients (ILOTs) with jet powering”. In: *Research in Astronomy and Astrophysics* 21.4, 090, p. 090. doi: 10.1088/1674-4527/21/4/90.

Somiya, K. (2012). “Detector configuration of KAGRA: The Japanese cryogenic gravitational-wave detector”. In: *Class. Quant. Grav.* 29. Ed. by M. Hannam et al., p. 124007. doi: 10.1088/0264-9381/29/12/124007.

Soon, J. et al. (Jan. 2020). “Wide-field dynamic astronomy in the near-infrared with Palomar Gattini-IR and DREAMS”. In: *Advances in Optical Astronomical Instrumentation*, p. 5. doi: 10.1117/12.2539594.

Soon, J. et al. (Aug. 2022). “DREAMS: status update and assembly/alignment challenges”. In: *Ground-based and Airborne Telescopes IX*. Ed. by H. K. Marshall et al. Vol. 12182. Society of Photo-Optical Instrumentation Engineers (SPIE) Conference Series, 121822K, 121822K. doi: 10.1117/12.2629072.

Soszyński, I. et al. (Dec. 2009). “The Optical Gravitational Lensing Experiment. The OGLE-III Catalog of Variable Stars. V. R Coronae Borealis Stars in the Large Magellanic Cloud”. In: *AcA* 59.4, pp. 335–347. doi: 10.48550/arXiv.0912.2097.

Soyano, T. et al. (Jan. 1991). “A search for cool carbon stars. V. Perseus - Camelopardalis ( $l \equiv 150^\circ$ ) region.” In: *Publications of the National Astronomical Observatory of Japan* 2, pp. 203–223.

Srinivasan, S. et al. (Aug. 2011). “The mass-loss return from evolved stars to the Large Magellanic Cloud. V. The GRAMS carbon-star model grid”. In: *A&A* 532, A54, A54. doi: 10.1051/0004-6361/201117033.

Srivastav, S. et al. (Apr. 2020). “The Lowest of the Low: Discovery of SN 2019gsc and the Nature of Faint Iax Supernovae”. In: *ApJ* 892.2, L24, p. L24. doi: 10.3847/2041-8213/ab76d5.

Staff, J. E. et al. (Sept. 2012). “Do R Coronae Borealis Stars Form from Double White Dwarf Mergers?” In: *ApJ* 757.1, 76, p. 76. doi: 10.1088/0004-637X/757/1/76.

Staff, J. E. et al. (July 2018). “The Role of Dredge-up in Double White Dwarf Mergers”. In: *ApJ* 862.1, 74, p. 74. doi: 10.3847/1538-4357/aaca3d.

Steeghs, D. et al. (Apr. 2022). “The Gravitational-wave Optical Transient Observer (GOTO): prototype performance and prospects for transient science”. In: *MNRAS* 511.2, pp. 2405–2422. doi: 10.1093/mnras/stac013.

Stein, R. et al. (Jan. 2024). “IceCube-240105A: Detection of NIR flare of PKS 0446+11 with WINTER”. In: *GRB Coordinates Network* 35584, p. 1.

Steinmetz, T. et al. (Feb. 2024). “A bipolar structure and shocks surrounding the stellar-merger remnant V1309 Scorpii”. In: *A&A* 682, A127, A127. doi: 10.1051/0004-6361/202347818.

Steinmetz, T. et al. (Feb. 2025). “OGLE-2002-BLG-360: a dusty anomaly among red nova remnants”. In: *arXiv e-prints*, arXiv:2502.18365, arXiv:2502.18365. doi: 10.48550/arXiv.2502.18365.

Stephenson, C. B. (Jan. 1973). “A general catalogue of cool carbon stars”. In: *Publications of the Warner & Swasey Observatory*.

Stern, D. et al. (July 2012). “Mid-infrared Selection of Active Galactic Nuclei with the Wide-Field Infrared Survey Explorer. I. Characterizing WISE-selected Active Galactic Nuclei in COSMOS”. In: *ApJ* 753.1, 30, p. 30. doi: 10.1088/0004-637X/753/1/30.

Stritzinger, M. D. et al. (Jan. 2014). “Optical and near-IR observations of the faint and fast 2008ha-like supernova 2010ae”. In: *A&A* 561, A146, A146. doi: 10.1051/0004-6361/201322889.

Stritzinger, M. D. et al. (Jan. 2015). “Comprehensive observations of the bright and energetic Type Iax SN 2012Z: Interpretation as a Chandrasekhar mass white dwarf explosion”. In: *A&A* 573, A2, A2. doi: 10.1051/0004-6361/201424168.

Sun, M. et al. (May 2018). “Formation of Extremely Low-mass White Dwarf Binaries”. In: *ApJ* 858.1, 14, p. 14. doi: 10.3847/1538-4357/aab9a4.

Swift, J. J. et al. (Apr. 2015). “Miniature Exoplanet Radial Velocity Array I: design, commissioning, and early photometric results”. In: *Journal of Astronomical Telescopes, Instruments, and Systems* 1.2, p. 027002. doi: 10.1117/1.jatis.1.2.027002.

Tachibana, Y. et al. (Dec. 2018a). “A Morphological Classification Model to Identify Unresolved PanSTARRS1 Sources: Application in the ZTF Real-time Pipeline”. In: *PASP* 130.994, p. 128001. doi: 10.1088/1538-3873/aae3d9.

– (Dec. 2018b). “A Morphological Classification Model to Identify Unresolved PanSTARRS1 Sources: Application in the ZTF Real-time Pipeline”. In: *PASP* 130.994, p. 128001. doi: 10.1088/1538-3873/aae3d9.

Tanaka, M. et al. (2013). “Radiative Transfer Simulations of Neutron Star Merger Ejecta”. In: *Astrophys. J.* 775, p. 113. doi: 10.1088/0004-637X/775/2/113.

Tanaka, M. et al. (Aug. 2020). “Systematic opacity calculations for kilonovae”. In: *MNRAS* 496.2, pp. 1369–1392. doi: 10.1093/mnras/staa1576.

Tang, S. et al. (Apr. 2013). “R Coronae Borealis Stars in M31 from the Palomar Transient Factory”. In: *ApJ* 767.2, L23, p. L23. doi: 10.1088/2041-8205/767/2/L23.

Tanvir, N. R. et al. (Oct. 2017). “The Emergence of a Lanthanide-rich Kilonova Following the Merger of Two Neutron Stars”. In: *ApJ* 848.2, L27, p. L27. doi: 10.3847/2041-8213/aa90b6.

Taubenberger, S. et al. (Apr. 2011). “High luminosity, slow ejecta and persistent carbon lines: SN 2009dc challenges thermonuclear explosion scenarios”. In: *MNRAS* 412.4, pp. 2735–2762. doi: 10.1111/j.1365-2966.2010.18107.x.

Taubenberger, S. (2017). “The Extremes of Thermonuclear Supernovae”. In: *Handbook of Supernovae*. Ed. by A. W. Alsabti et al., p. 317. doi: 10.1007/978-3-319-21846-5\_37.

Teixeira, G. D. C. et al. (Nov. 2018). “Photometric variability of massive young stellar objects”. In: *A&A* 619, A41, A41. doi: 10.1051/0004-6361/201833667.

The LIGO Scientific Collaboration et al. (Nov. 2021a). “GWTC-3: Compact Binary Coalescences Observed by LIGO and Virgo During the Second Part of the Third Observing Run”. In: *arXiv e-prints*, arXiv:2111.03606, arXiv:2111.03606.

The LIGO Scientific Collaboration et al. (Nov. 2021b). “The population of merging compact binaries inferred using gravitational waves through GWTC-3”. In: *arXiv e-prints*, arXiv:2111.03634, arXiv:2111.03634.

Theureau, G. et al. (Apr. 2007). “Kinematics of the Local Universe. XIII. 21-cm line measurements of 452 galaxies with the Nançay radiotelescope, JHK Tully-Fisher relation, and preliminary maps of the peculiar velocity field”. In: *A&A* 465, pp. 71–85. doi: 10.1051/0004-6361:20066187.

Thompson, T. A. et al. (Nov. 2009). “A New Class of Luminous Transients and a First Census of their Massive Stellar Progenitors”. In: *ApJ* 705, pp. 1364–1384. doi: 10.1088/0004-637X/705/2/1364.

Tisserand, P. (Mar. 2012). “Tracking down R Coronae Borealis stars from their mid-infrared WISE colours”. In: *A&A* 539, A51, A51. doi: 10.1051/0004-6361/201117874.

Tisserand, P. et al. (Sept. 2004). “EROS 2 photometry of probable R Coronae Borealis stars in the Small Magellanic Cloud”. In: *A&A* 424, pp. 245–252. doi: 10.1051/0004-6361:20040386.

Tisserand, P. et al. (Apr. 2008). “R Coronae Borealis stars in the Galactic bulge discovered by EROS-2”. In: *A&A* 481.3, pp. 673–690. doi: 10.1051/0004-6361:20078814.

Tisserand, P. et al. (July 2009). “New Magellanic Cloud R Coronae Borealis and DY Persei type stars from the EROS-2 database: the connection between RCBs, DYPers, and ordinary carbon stars”. In: *A&A* 501.3, pp. 985–998. doi: 10.1051/0004-6361/200911808.

Tisserand, P. et al. (May 2011). “New R Coronae Borealis stars discovered in OGLE-III Galactic bulge fields from their mid- and near-infrared properties”. In: *A&A* 529, A118, A118. doi: 10.1051/0004-6361/201014220.

Tisserand, P. et al. (Mar. 2013). “The ongoing pursuit of R Coronae Borealis stars: the ASAS-3 survey strikes again”. In: *A&A* 551, A77, A77. doi: 10.1051/0004-6361/201220713.

Tisserand, P. et al. (Mar. 2020). “A plethora of new R Coronae Borealis stars discovered from a dedicated spectroscopic follow-up survey”. In: *A&A* 635, A14, A14. doi: 10.1051/0004-6361/201834410.

Tisserand, P. et al. (Dec. 2021). “The dawn of a new era for dustless HdC stars with GAIA eDR3”. In: *arXiv e-prints*, arXiv:2112.07693, arXiv:2112.07693.

Tisserand, P. et al. (Nov. 2022). “The dawn of a new era for dustless HdC stars with Gaia eDR3”. In: *A&A* 667, A83, A83. doi: 10.1051/0004-6361/202142916.

Tisserand, P. et al. (Apr. 2024a). “HdC and EHe stars through the prism of Gaia DR3. 3D distribution and Gaia’s chromatic PSF effects”. In: *A&A* 684, A131, A131. doi: 10.1051/0004-6361/202348005.

- (Apr. 2024b). “HdC and EHe stars through the prism of Gaia DR3. Evolution of RV amplitude and dust formation rate with effective temperature”. In: *A&A* 684, A130, A130. doi: 10.1051/0004-6361/202348004.

Tomasella, L. et al. (Aug. 2020). “Observations of the low-luminosity Type Iax supernova 2019gsc: a fainter clone of SN 2008ha?” In: *MNRAS* 496.2, pp. 1132–1143. doi: 10.1093/mnras/staa1611.

Tonry, J. L. et al. (June 2018). “ATLAS: A High-cadence All-sky Survey System”. In: *PASP* 130.988, p. 064505. doi: 10.1088/1538-3873/aabadf.

Toonen, S. et al. (Oct. 2012). “Supernova Type Ia progenitors from merging double white dwarfs. Using a new population synthesis model”. In: *A&A* 546, A70, A70. doi: 10.1051/0004-6361/201218966.

Torres, G. et al. (Oct. 2022). “ $\eta$  Geminorum: an eclipsing semiregular variable star orbited by a companion surrounded by an extended disc”. In: *MNRAS* 516.2, pp. 2514–2521. doi: 10.1093/mnras/stac2322.

Tranin, H. et al. (Sept. 2024). “Hertzsprung gap stars in nearby galaxies and the Quest for Luminous Red Novae Progenitors”. In: *arXiv e-prints*, arXiv:2409.11347, arXiv:2409.11347. doi: 10.48550/arXiv.2409.11347.

Travouillon, T. D. et al. (2020). “DREAMS telescope: opto-mechanical design”. In: *Ground-based and Airborne Telescopes VIII*. Ed. by H. K. Marshall et al. Vol. 11445. International Society for Optics and Photonics. SPIE. doi: 10.1117/12.2562980.

Troja, E. et al. (Oct. 2017). “The X-ray counterpart to the gravitational-wave event GW170817”. In: *Nature* 551.7678, pp. 71–74. doi: 10.1038/nature24290.

Tsuiji, T. (Aug. 2000). “Water on the Early M Supergiant Stars  $\alpha$  Orionis and  $\mu$  Cephei”. In: *ApJ* 538.2, pp. 801–807. doi: 10.1086/309185.

Tsuiji, T. (2003). “Water observed in red giant and supergiant stars - Manifestation of a novel picture of the stellar atmosphere or else evidence against the classical model stellar photosphere”. In: *ESA Spec. Publ.* 511, p. 93.

- (July 2006). “Infrared Spectra and Visibilities as Probes of the Outer Atmospheres of Red Supergiant Stars”. In: *ApJ* 645.2, pp. 1448–1463. doi: 10.1086/504585.

Tsukada, L. et al. (2023). “Improved ranking statistics of the GstLAL inspiral search for compact binary coalescences”. In: *Phys. Rev. D* 108.4, p. 043004. doi: 10.1103/PhysRevD.108.043004.

Tsuna, D. et al. (July 2020). “Intermediate Luminosity Red Transients by Black Holes Born from Erupting Massive Stars”. In: *ApJ* 897.2, L44, p. L44. doi: 10.3847/2041-8213/aba0ac.

Turatto, M. et al. (Jan. 2003). “Variety in Supernovae”. In: *From Twilight to High-light: The Physics of Supernovae*. Ed. by W. Hillebrandt et al., p. 200. doi: 10.1007/10828549\_26.

Tutukov, A. V. et al. (June 1994). “Merging of Binary White Dwarfs Neutron Stars and Black-Holes Under the Influence of Gravitational Wave Radiation”. In: *MNRAS* 268, p. 871. doi: 10.1093/mnras/268.4.871.

Tylenda, R. (June 2005). “Evolution of V838 Monocerotis during and after the 2002 eruption”. In: *A&A* 436, pp. 1009–1020. doi: 10.1051/0004-6361:20052800.

Tylenda, R. et al. (Aug. 2005). “V4332 Sagittarii revisited”. In: *A&A* 439, pp. 651–661. doi: 10.1051/0004-6361:20041581.

Tylenda, R. et al. (Apr. 2011a). “V1309 Scorpii: merger of a contact binary”. In: *A&A* 528, A114, A114. doi: 10.1051/0004-6361/201016221.

– (Apr. 2011b). “V1309 Scorpii: merger of a contact binary”. In: *A&A* 528, A114, A114. doi: 10.1051/0004-6361/201016221.

Tylenda, R. et al. (July 2013). “OGLE-2002-BLG-360: from a gravitational microlensing candidate to an overlooked red transient”. In: *A&A* 555, A16, A16. doi: 10.1051/0004-6361/201321647.

Tzanidakis, A. et al. (Sept. 2023). “Gaia17bpp: A Giant Star with the Deepest and Longest Known Dimming Event”. In: *ApJ* 955.1, 69, p. 69. doi: 10.3847/1538-4357/aceda7.

Ueta, T. et al. (Apr. 2003). “2-DUST: A Dust Radiative Transfer Code for an Axisymmetric System”. In: *ApJ* 586.2, pp. 1338–1355. doi: 10.1086/367818.

Uno, K. et al. (Feb. 2021). “Transient Classification Report for 2021-02-08”. In: *Transient Name Server Classification Report* 2021-393, pp. 1–393.

Usman, S. A. et al. (Oct. 2016). “The PyCBC search for gravitational waves from compact binary coalescence”. In: *Classical and Quantum Gravity* 33.21, p. 215004. doi: 10.1088/0264-9381/33/21/215004.

Vacca, W. D. et al. (Mar. 2003). “A Method of Correcting Near-Infrared Spectra for Telluric Absorption”. In: *PASP* 115.805, pp. 389–409. doi: 10.1086/346193.

Valenti, S. et al. (Feb. 2008). “The broad-lined Type Ic supernova 2003jd”. In: *MNRAS* 383.4, pp. 1485–1500. doi: 10.1111/j.1365-2966.2007.12647.x.

Valenti, S. et al. (June 2009). “A low-energy core-collapse supernova without a hydrogen envelope”. In: *Nature* 459.7247, pp. 674–677. doi: 10.1038/nature08023.

van den Heuvel, E. P. J. (Jan. 1976). “Late Stages of Close Binary Systems”. In: *Structure and Evolution of Close Binary Systems*. Ed. by P. Eggleton et al. Vol. 73. IAU Symposium, p. 35.

VanderPlas, J. T. et al. (Oct. 2015). “Periodograms for Multiband Astronomical Time Series”. In: *ApJ* 812.1, 18, p. 18. doi: 10.1088/0004-637X/812/1/18.

Verhoelst, T. et al. (Apr. 2009). “The dust condensation sequence in red supergiant stars”. In: *A&A* 498.1, pp. 127–138. doi: 10.1051/0004-6361/20079063.

Vigna-Gómez, A. et al. (May 2019). “Massive Stellar Mergers as Precursors of Hydrogen-rich Pulsational Pair Instability Supernovae”. In: *ApJ* 876.2, L29, p. L29. doi: 10.3847/2041-8213/ab1bdf.

Vigna-Gómez, A. et al. (2020). “Common envelope episodes that lead to double neutron star formation”. In: *Publications of the Astronomical Society of Australia* 37, e038. doi: 10.1017/pasa.2020.31.

Virtanen, P. et al. (2020). “SciPy 1.0: Fundamental Algorithms for Scientific Computing in Python”. In: *Nature Methods* 17, pp. 261–272. doi: 10.1038/s41592-019-0686-2.

Walt, S. J. van der et al. (May 2019a). “SkyPortal: An Astronomical Data Platform”. In: *Journal of Open Source Software* 4.37. doi: 10.21105/joss.01247.

– (2019b). “SkyPortal: An Astronomical Data Platform”. In: *Journal of Open Source Software* 4.37, p. 1247. doi: 10.21105/joss.01247.

Warner, B. (Jan. 1967). “The hydrogen-deficient carbon stars”. In: *MNRAS* 137, p. 119. doi: 10.1093/mnras/137.2.119.

Webbink, R. F. (July 1975). “The evolution of low-mass close binary systems”. PhD thesis. University of Cambridge, UK.

– (Jan. 1979). “The Formation of White Dwarfs in Close Binary Systems”. In: *IAU Colloq. 53: White Dwarfs and Variable Degenerate Stars*. Ed. by H. M. van Horn et al., p. 426.

– (Feb. 1984). “Double white dwarfs as progenitors of R Coronae Borealis stars and Type I supernovae”. In: *ApJ* 277, pp. 355–360. doi: 10.1086/161701.

White, C. J. et al. (Jan. 2015). “Slow-speed Supernovae from the Palomar Transient Factory: Two Channels”. In: *ApJ* 799.1, 52, p. 52. doi: 10.1088/0004-637X/799/1/52.

Whitelock, P. A. et al. (June 2003). “Obscured asymptotic giant branch variables in the Large Magellanic Cloud and the period-luminosity relation”. In: *MNRAS* 342.1, pp. 86–104. doi: 10.1046/j.1365-8711.2003.06514.x.

Williams, S. C. et al. (June 2015). “A Luminous Red Nova in M31 and its Progenitor System”. In: *ApJ* 805, L18, p. L18. doi: 10.1088/2041-8205/805/2/L18.

Wilson, J. C. et al. (Mar. 2003a). “A Wide-Field Infrared Camera for the Palomar 200-inch Telescope”. In: *Instrument Design and Performance for Optical/Infrared Ground-based Telescopes*. Ed. by M. Iye et al. Vol. 4841. Society of Photo-Optical Instrumentation Engineers (SPIE) Conference Series, pp. 451–458. doi: 10.1117/12.460336.

– (Mar. 2003b). “A Wide-Field Infrared Camera for the Palomar 200-inch Telescope”. In: *Instrument Design and Performance for Optical/Infrared Ground-based Telescopes*. Ed. by M. Iye et al. Vol. 4841. Society of Photo-Optical Instrumentation Engineers (SPIE) Conference Series, pp. 451–458. doi: 10.1117/12.460336.

Wilson, J. C. et al. (Sept. 2004). “Mass producing an efficient NIR spectrograph”. In: *Ground-based Instrumentation for Astronomy*. Ed. by A. F. M. Moorwood et al. Vol. 5492. Society of Photo-Optical Instrumentation Engineers (SPIE) Conference Series, pp. 1295–1305. doi: 10.1117/12.550925.

Wong, T. L. S. et al. (Feb. 2024). “The Asteroseismological Richness of RCB and dLdC Stars”. In: *ApJ* 962.1, 20, p. 20. doi: 10.3847/1538-4357/ad0cfa.

Woodward, C. E. et al. (Nov. 2021). “The Infrared Evolution of Dust in V838 Monocerotis”. In: *AJ* 162.5, 183, p. 183. doi: 10.3847/1538-3881/ac1f1e.

Woosley, S. E. et al. (Nov. 2002). “The evolution and explosion of massive stars”. In: *Reviews of Modern Physics* 74, pp. 1015–1071. doi: 10.1103/RevModPhys.74.1015.

Wright, E. L. et al. (Dec. 2010). “The Wide-field Infrared Survey Explorer (WISE): Mission Description and Initial On-orbit Performance”. In: *AJ* 140.6, pp. 1868–1881. doi: 10.1088/0004-6256/140/6/1868.

Wright, G. S. et al. (May 2023). “The Mid-infrared Instrument for JWST and Its In-flight Performance”. In: *Publications of the Astronomical Society of the Pacific* 135.1046, p. 048003. doi: 10.1088/1538-3873/acbe66.

Wyatt, S. D. et al. (May 2020). “The Gravitational Wave Treasure Map: A Tool to Coordinate, Visualize, and Assess the Electromagnetic Follow-up of Gravitational-wave Events”. In: *ApJ* 894.2, 127, p. 127. doi: 10.3847/1538-4357/ab855e.

Yama, H. et al. (Jan. 2023). “Optical Alignment Method for the PRIME Telescope”. In: *Journal of Astronomical Instrumentation* 12.3, 2350004, p. 2350004. doi: 10.1142/S2251171723500046.

Yamamura, I. et al. (Jan. 1999a). “Detection of warm SO<sub>2</sub> gas in oxygen-rich AGB stars”. In: *A&A* 341, pp. L9–L12.

Yamamura, I. et al. (Aug. 1999b). “Infrared emission of hot water in the atmosphere of Mira”. In: *A&A* 348, pp. L55–L58.

Yang, S. et al. (Nov. 2021). “A low-energy explosion yields the underluminous Type IIP SN 2020cxd”. In: *A&A* 655, A90, A90. doi: 10.1051/0004-6361/202141244.

Yao, Y. et al. (Dec. 2019). “ZTF Early Observations of Type Ia Supernovae. I. Properties of the 2018 Sample”. In: *ApJ* 886.2, 152, p. 152. doi: 10.3847/1538-4357/ab4cf5.

York, D. G. et al. (Sept. 2000). “The Sloan Digital Sky Survey: Technical Summary”. In: *AJ* 120.3, pp. 1579–1587. doi: 10.1086/301513.

Yungelson, L. R. et al. (Jan. 1994). “Are the Observed Frequencies of Double Degenerates and SN IA Contradictory?” In: *ApJ* 420, p. 336. doi: 10.1086/173563.

Yurchenko, S. N. et al. (Nov. 2021). “ExoMol line lists – XLIV. Infrared and ultra-violet line list for silicon monoxide (28Si16O)”. In: *Monthly Notices of the Royal Astronomical Society* 510.1, pp. 903–919. doi: 10.1093/mnras/stab3267.

Yurchenko, S. N. et al. (Nov. 2018). “ExoMol line lists XXXI: spectroscopy of lowest eight electronic states of C<sub>2</sub>”. In: *MNRAS* 480.3, pp. 3397–3411. doi: 10.1093/mnras/sty2050.

Zackay, B. et al. (Oct. 2016a). “Proper Image Subtraction—Optimal Transient Detection, Photometry, and Hypothesis Testing”. In: *ApJ* 830.1, 27, p. 27. doi: 10.3847/0004-637X/830/1/27.

– (Oct. 2016b). “Proper Image Subtraction—Optimal Transient Detection, Photometry, and Hypothesis Testing”. In: *ApJ* 830.1, 27, p. 27. doi: 10.3847/0004-637X/830/1/27.

Začs, L. et al. (Sept. 2007). “A comprehensive analysis of the cool RCB star DY Persei”. In: *A&A* 472.1, pp. 247–256. doi: 10.1051/0004-6361:20066923.

Zaniewski, A. et al. (Nov. 2005). “Discovery of Five New R Coronae Borealis Stars in the MACHO Galactic Bulge Database”. In: *AJ* 130.5, pp. 2293–2302. doi: 10.1086/466516.

Zhang, X. et al. (Jan. 2012). “Evolutionary models for double helium white dwarf mergers and the formation of helium-rich hot subdwarfs”. In: *MNRAS* 419.1, pp. 452–464. doi: 10.1111/j.1365-2966.2011.19711.x.

Zhang, X. et al. (Nov. 2014). “Post-merger evolution of carbon-oxygen + helium white dwarf binaries and the origin of R Coronae Borealis and extreme helium stars”. In: *MNRAS* 445.1, pp. 660–673. doi: 10.1093/mnras/stu1741.

Zhu, J.-P. et al. (Aug. 2021a). “Kilonova Emission from Black Hole–Neutron Star Mergers. II. Luminosity Function and Implications for Target-of-opportunity Observations of Gravitational-wave Triggers and Blind Searches”. In: *ApJ* 917.1, p. 24. doi: 10.3847/1538-4357/abfe5e.

Zhu, J.-P. et al. (Nov. 2021b). “No Detectable Kilonova Counterpart is Expected for O3 Neutron Star–Black Hole Candidates”. In: *ApJ* 921.2, p. 156. doi: 10.3847/1538-4357/ac19a7.